Technische Universität Kaiserslautern

Fachbereich Chemie

Magnetic and Structural Characterization of Isolated Gaseous Ions by XMCD and IRMPD Spectroscopy

Am Fachbereich Chemie der Technischen Universität Kaiserslautern zur Erlangung

des akademischen Grades “Doktor der Naturwissenschaften” genehmigte

Dissertation

(D386)

vorgelegt von

Dipl.-Chem. Joachim Hewer

Betreuer: Prof. Dr. G. Niedner-Schatteburg

Tag der wissenschaftlichen Aussprache: 08. August 2017

Technische Universität Kaiserslautern 2017

Die vorliegende Arbeit wurde im Zeitraum von Oktober 2013 bis Juni 2017 im Fachbereich Chemie der Technischen Universität Kaiserslautern unter Betreuung von Prof. Dr. G. Niedner-Schatteburg angefertigt.

Datum des Antrags der Eröffnung des Promotionsverfahrens: 03.05.2017

Promotionskommision:

Vorsitzender	Prof. Dr.-Ing. S. Ernst
1. Berichterstatter	Prof. Dr. G. Niedner-Schatteburg
2. Berichterstatter	Prof. Dr. M. Gerhards

Für meine Familie

„Ich bin immernoch verwirrt, aber auf einem höheren Niveau.“

\- Enrico Fermi –

Content

1 Introduction ... 1

1.1 References ... 4

2 Experimental Setup and Methods ... 9

2.1 Electrospray Ionization (ESI) ... 9

2.1.1 The Apollo II ESI Source ... 11

2.1.2 The Custom-Built ESI source ... 12

2.2 Ion Trap Mass Spectrometers ... 13

2.2.1 The Bruker amaZon SL mass spectrometer ... 13

2.2.2 The NanoCluster Trap setup ... 18

2.3 Photon Generation ... 21

2.3.1 LaserVision Optical Parametric Oscillator / Amplifier IR Laser System ... 21

2.3.2 Soft X-ray Synchrotron Radiation at the UE52-PGM Beamline at BESSY II ... 25

2.4 Methods ... 27

2.4.1 InfraRed Multiple Photon Dissociation (IRMPD) spectroscopy ... 27

2.4.2 Density Functional Theory (DFT) ... 30

2.4.3 X-ray Absorption and X-ray Magnetic Circular Dichroism (XMCD) Spectroscopy ... 31

2.5 References ... 47

3 Intrinsic Magnetism of Hetero-Bimetallic 3*d*-4*f* Complexes by XMCD Spectroscopy ... 53

3.1 Preamble ... 53

3.2 Abstract ... 54

3.3 Introduction ... 54

3.4 Experimental methods and setup ... 56

3.5 Results and Discussion ... 63

3.5.1 XMCD Spectroscopy of isolated $[Mn_2Ln](H)_2^+$ ... 64

3.5.2 Estimate of the Ion Temperature ... 73

3.5.3 Magnetometry of Bulk Samples ... 76

3.6 Conclusions ... 80

3.7 Acknowledgements ... 81

3.8 References ... 81

3.9 Supplementary Material ... 87

4 Gas Phase XMCD Spectroscopy of an Octahedral Iron(II) Spin-Crossover Complex ... 107

4.1 Preamble ... 107

4.2 Abstract ... 108

4.3 Introduction 108
4.4 Computational and Experimental methods 109
  4.4.1 Theoretical methods 109
  4.4.2 Experimental methods and setup 110
4.5 Results and Discussion 113
  4.5.1 DFT calculations 113
  4.5.2 XMCD spectroscopy at the Fe $L_{3,2}$ absorption edges 117
4.6 Conclusions 130
4.7 Acknowledgements 131
4.8 Appendix 133
4.9 References 140
4.10 Supplementary Material 145

5 Structural Characterization of (Methylated) Thymine/Uracil-Tetracyanoplatinate(II)-Aggregates by Two Color Enhanced Infrared Multiple Photon Dissociation (IRMPD) Spectroscopy 169
5.1 Preamble 169
5.2 Abstract 170
5.3 Introduction 170
5.4 Experimental and computational methods 172
5.5 Results and Discussion 174
  5.5.1 Thymine – Tetracyanoplatinate(II): $[T \cdot Pt(CN)_4]^{2-}$ 175
  5.5.2 Methylthymine – Tetracyanoplatinate(II): $[1\text{-mT} \cdot Pt(CN)_4]^{2-}$ 178
  5.5.3 Uracil – Tetracyanoplatinate(II): $[U \cdot Pt(CN)_4]^{2-}$ 182
  5.5.4 1-Methyluracil – Tetracyanoplatinate(II): $[1\text{-mU} \cdot Pt(CN)_4]^{2-}$ 184
5.6 Conclusions 187
5.7 References 189
5.8 Supplementary Material 193

6 Gas Phase Structure of Fluorescein, 2,7-Dichlorofluorescein and 5-Nitrofluorescein Ions by Infrared Multiple Photon Dissociation Spectroscopy and Density Functional Theory 217
6.1 Preamble 217
6.2 Abstract 218
6.3 Introduction 218
6.4 Experimental and Computational methods 220
6.5 Results and Discussion 222
  6.5.1 Dianions 223
  6.5.2 Cations 228
  6.5.3 Monoanions 241

6.6 Conclusions 251
6.7 References 252
6.8 Supplementary Material 257

7 Summary and Outlook 275

8 Zusammenfassung und Ausblick 281

9 Appendix: Joint Publications 287
9.1 Infrared spectroscopy of N_2 adsorption on size selected cobalt cluster cations in isolation........ 289
9.1.1 Preamble 289
9.1.2 Reprint 290
9.2 Vibrational Blue Shift of Coordinated N_2 in $[Fe_3O(OAc)_6(N_2)_n]^+$: “Non Classical” Dinitrogen Complexes 297
9.2.1 Preamble 297
9.2.2 Reprint 298
9.3 Doubly Regioselective C-H Hydroarylation of Unsymmetrical Alkynes Using Carboxylates as Deciduous Directing Groups 303
9.3.1 Preamble 303
9.3.2 Reprint 304

Lebenslauf 309

List of Publications 311

Danksagung 315

1 Introduction

Mass spectrometry in combination with optical spectroscopy has proven to be a powerful tool to study the intrinsic properties of isolated ionic molecular systems, such as their structure[1-9], reactivity[10-15], catalytic activity[16-22], absorption[23-31] and magnetism[32-48]. Several techniques have been developed for the ionization of samples or the transfer of ionic species into the gas phase for subsequent examination, e.g. laser vaporization sources (LVAP) [32, 33, 49-53], matrix assisted laser desorption/ionization (MALDI)[54-56], and most notably the electrospray ionization[57-60] (ESI) technique. ESI is a popular soft ionization technique, allowing e.g. for the transfer of intact metal complexes, reaction intermediates and thermally labile biomolecules into the gas phase.

Transition metal complexes exhibit diverse optical, catalytic or magnetic properties making them indispensable in synthesis or various industrial and medical applications. They are used in homogenous catalysis[61], in chemical industry and research, or as pharmaceuticals[62, 63] in the treatment of e.g. cancer. The applicability of metal complexes depends heavily on their stability, reactivity, binding motifs etc., which are dictated by the molecular geometry. Hence, the elucidation of the molecular structure is essential to gain fundamental insight into the intrinsic properties of metal complexes.

Infrared absorption spectroscopy is commonly applied in order to obtain structural information on molecular systems in the gas phase. However, due to the typically low particle density in the gas phase, measuring absorption spectra by directly detecting the attenuation of incident light is not possible. Instead, an action scheme, the so called infrared (multiple) photon dissociation (IR(M)PD) spectroscopy is used.[1-3, 5, 16, 64] Infrared photons are absorbed resonantly and excite particular vibrations within the molecule. The received energy is spread across the whole molecule via internal vibrational redistribution (IVR), allowing for re-excitation of the same vibrational coordinate. This process is repeated until a dissociation threshold of the molecule is overcome and the ion fragments. The low density of vibrational states in small systems can impede IVR, and together with vibrational anharmonicities, results in a bottleneck for multiple photon absorption and hence for dissociation.[65, 66] Large molecules and clusters have generally large heat capacities and may require more laser power for weaker bands to appear in IRMPD spectra.[67] The resonant two-color IRMPD technique enhances fragmentation efficiencies and thus, may reveal otherwise “dark bands”.[66, 68]

To gain structural information from experimental IRMPD spectra, comparison to calculated IR absorption spectra is required. For this purpose, density functional theory (DFT) has proven to produce reliable linear harmonic absorption spectra at low cost.[69, 70]

The magnetic properties of a sample strongly correlate with surrounding of molecular units. In solid state physics, for example, the magnetism is based on the spin (intrinsic angular momentum and an additional angular momentum induced by the spatial motion of electrons), long range magnetic order and their respective coupling.[71] For transition metals (bulk ferromagnets Fe, Co, Ni), the bulk magnetism is dominated by the spin magnetic moment, as the orbital magnetic moment is often quenched by orbital hybridization and reduced symmetry.[72] Reducing the size of the investigated system, i.e. going from bulk to transition metal clusters down to the single atom, the orbital moment is gradually restored.[34] Single Molecule Magnets (SMM) provide another highly interesting form of magnetism, as their magnetic properties, including high magnetic moments and anisotropy barriers, do not originate from long range magnetic ordering, but are intrinsic properties of the individual molecule.[73] X-ray magnetic circular dichroism (XMCD) spectroscopy in combination with sum rule analysis allows for an element selective detection and assignment of spin and orbital contributions to the magnetic moment.[74, 75] The technique was initially applied to surface samples, thin films and deposited clusters,[76-79] and in the recent past successfully extended to gas phase experiments, allowing for the investigation of magnetic moments devoid of environmental influences.[32-35, 41, 47, 48, 80, 81] Recently, a first proof-of-principle study on the model SMM Mn_{12}-acetate in the gas phase confirmed the XMCD signature of bulk measurements.[82] Building on the success of our previous gas phase XMCD experiments, we present expanded investigations on further mono- and multimetallic metal complexes.

This thesis comprises four independent research projects (chapters 3 to 6) using XMCD spectroscopy, IRMPD spectroscopy and DFT calculations for magnetic and structural characterization of isolated gaseous ions. All chapters are prepared as manuscript for publication, containing a preamble that declares the individual contributions of the co-authors to the projects.

The experimental setups and methods are introduced and explained in detail in chapter 2. This includes the different ESI sources, ion trap mass spectrometers, photon sources via table-top laser and synchrotron, as well as the spectroscopic (IRMPD, XAS, XMCD) and theoretical (DFT) methods employed. Chapter 3 deals with XMCD spectroscopic investigations on a set of isostructural trinuclear heterobimetallic complexes containing two manganese(II) and a lanthanide(III) metal centers. We address the element selective contributions of the spin and orbital magnetic moments quantitatively and compare the results to magnetic data obtained by bulk magnetometry. Chapter 4 presents the characterization of an iron(II) Spin-Crossover complex by temperature dependent XMCD spectroscopy in the gas phase and DFT modeling. Chapter 5 reports on the structural elucidation of self-assembled aggregates of (methylated) nucleobases and tetracyanoplatinate(II) by two-color IRMPD spectroscopy in conjunction with DFT calculations. Chapter 6 elucidates the gas phase structures of some selected fluorescein derivatives in different charged states by IRMPD spectroscopy together with DFT computations. A summary of the results is given in chapters 7 and 8.

1.1 References

[1] L. MacAleese, P. Maître, "*Infrared spectroscopy of organometallic ions in the gas phase: From model to real world complexes*", *Mass Spectrom. Rev.*, **2007**, *26*, 583-605.

[2] J. S. Brodbelt, J. J. Wilson, "*Infrared multiphoton dissociation in quadrupole ion traps*", *Mass Spectrom. Rev.*, **2009**, *28*, 390-424.

[3] N. C. Polfer, J. Oomens, "*Vibrational spectroscopy of bare and solvated ionic complexes of biological relevance*", *Mass Spectrom. Rev.*, **2009**, *28*, 468-494.

[4] T. D. Fridgen, "*Infrared consequence spectroscopy of gaseous protonated and metal ion cationized complexes*", *Mass Spectrom. Rev.*, **2009**, *28*, 586-607.

[5] N. C. Polfer, "*Infrared multiple photon dissociation spectroscopy of trapped ions*", *Chem. Soc. Rev.*, **2011**, *40*, 2211-2221.

[6] R. Wu, T. B. McMahon, "*An investigation of protonation sites and conformations of protonated amino acids by IRMPD spectroscopy*", *ChemPhysChem*, **2008**, *9*, 2826-2835.

[7] J. S. Prell, M. Demireva, J. Oomens, E. R. Williams, "*Role of Sequence in Salt-Bridge Formation for Alkali Metal Cationized GlyArg and ArgGly Investigated with IRMPD Spectroscopy and Theory*", *J. Am. Chem. Soc.*, **2009**, *131*, 1232-1242.

[8] S. H. Yoon, J. Chamot-Rooke, B. R. Perkins, A. E. Hilderbrand, J. C. Poutsma, V. H. Wysocki, "*IRMPD Spectroscopy Shows That AGG Forms an Oxazolone* b_2^+ *Ion*", *J. Am. Chem. Soc.*, **2008**, *130*, 17644-17645.

[9] N. C. Polfer , J. Oomens, R. C. Dunbar, "*Alkali Metal Complexes of the Dipeptides PheAla and AlaPhe: IRMPD Spectroscopy*", *ChemPhysChem*, **2008**, *9*, 579-589.

[10] V. B. Di Marco, G. G. Bombi, "*Electrospray mass spectrometry (ESI-MS) in the study of metal–ligand solution equilibria*", *Mass Spectrom. Rev.*, **2006**, *25*, 347-379.

[11] E. Kuhn, J. Wu, J. Karl, H. Liao, W. Zolg, B. Guild, "*Quantification of C-reactive protein in the serum of patients with rheumatoid arthritis using multiple reaction monitoring mass spectrometry and 13C-labeled peptide standards*", *Proteomics*, **2004**, *4*, 1175-1186.

[12] J. Murray, S. W. Taylor, B. Zhang, S. S. Ghosh, R. A. Capaldi, "*Oxidative Damage to Mitochondrial Complex I Due to Peroxynitrite: IDENTIFICATION OF REACTIVE TYROSINES BY MASS SPECTROMETRY*", *J. Biol. Chem.*, **2003**, *278*, 37223-37230.

[13] P. Longevialle, "*Ion–neutral complexes in the unimolecular reactivity of organic cations in the gas phase*", *Mass Spectrom. Rev.*, **1992**, *11*, 157-192.

[14] A. Ding, P. Zia-Amirhosseini, A. F. McDonagh, A. L. Burlingame, L. Z. Benet, "*Reactivity of tolmetin glucuronide with human serum albumin. Identification of binding sites and mechanisms of reaction by tandem mass spectrometry*", *Drug Metab. Dispos.*, **1995**, *23*, 369.

[15] M. Zhu, L. Ma, H. Zhang, W. G. Humphreys, "*Detection and Structural Characterization of Glutathione-Trapped Reactive Metabolites Using Liquid Chromatography−High-Resolution Mass Spectrometry and Mass Defect Filtering*", *Anal. Chem.*, **2007**, *79*, 8333-8341.

[16] J. Roithová, "*Characterization of reaction intermediates by ion spectroscopy*", *Chem. Soc. Rev.*, **2012**, *41*, 547-559.

[17] A. Škríba, J. Schulz, J. Roithová, "*Monitoring of Reaction Intermediates in the Gas Phase: Ruthenium-Catalyzed C–C Coupling*", *Organometallics*, **2014**, *33*, 6868-6878.

[18] D. A. Plattner, "*Electrospray mass spectrometry beyond analytical chemistry: studies of organometallic catalysis in the gas phase*", *Int. J. Mass Spectrom.*, **2001**, *207*, 125-144.

[19] J. Wassenaar, E. Jansen, Z.-J. van, F. M. Bickelhaupt, M. A. Siegler, A. L. Spek, N. H. ReekJoost, "*Catalyst selection based on intermediate stability measured by mass spectrometry*", *Nat Chem*, **2010**, *2*, 417-421.

[20] R. A. J. O'Hair, G. N. Khairallah, "*Gas Phase Ion Chemistry of Transition Metal Clusters: Production, Reactivity, and Catalysis*", *J. Cluster Sci.*, **2004**, *15*, 331-363.

[21] H. Schwarz, "*Chemistry with Methane: Concepts Rather than Recipes*", *Angew. Chem. Int. Ed.*, **2011**, *50*, 10096-10115.

[22] B. L. Tjelta, P. B. Armentrout, "*Ligand Effects in C−H and C−C Bond Activation by Gas-Phase Transition Metal−Ligand Complexes*", *J. Am. Chem. Soc.*, **1996**, *118*, 9652-9660.

[23] D. W. Lupo, M. Quack, "*IR-laser photochemistry*", *Chem. Rev.*, **1987**, *87*, 181-216.

[24] S. L. Chin, "*Multiphoton Ionization of Molecules*", *Phys. Rev. A*, **1971**, *4*, 992-996.

[25] A. Sen, T. F. M. Luxford, N. Yoshikawa, C. E. H. Dessent, "*Solvent evaporation versus proton transfer in nucleobase-Pt(CN)$_{4,6}^{2-}$ dianion clusters: a collisional excitation and electronic laser photodissociation spectroscopy study*", *Phys. Chem. Chem. Phys.*, **2014**, *16*, 15490-15500.

[26] P. D. McQueen, S. Sagoo, H. Yao, R. A. Jockusch, "*On the Intrinsic Photophysics of Fluorescein*", *Angewandte Chemie International Edition*, **2010**, *49*, 9193-9196.

[27] A. Sen, C. E. H. Dessent, "*Communication: Photoactivation of nucleobase bound platinumII metal complexes: Probing the influence of the nucleobase*", *J. Chem. Phys.*, **2014**, *141*, 241101.

[28] A. Sen, C. E. H. Dessent, "*Mapping the UV Photophysics of Platinum Metal Complexes Bound to Nucleobases: Laser Spectroscopy of Isolated Uracil·Pt(CN)$_4^{2-}$ and Uracil·Pt(CN)$_6^{2-}$ Complexes*", *J. Phys. Chem. Lett.*, **2014**, *5*, 3281-3285.

[29] A. Sen, G.-L. Hou, X.-B. Wang, C. E. H. Dessent, "*Electron Detachment as a Probe of Intrinsic Nucleobase Dynamics in Dianion-Nucleobase Clusters: Photoelectron Spectroscopy of the Platinum II Cyanide Dianion Bound to Uracil, Thymine, Cytosine, and Adenine*", *J. Phys. Chem. B*, **2015**, *119*, 11626-11631.

[30] A. Sen, E. M. Matthews, G.-L. Hou, X.-B. Wang, C. E. H. Dessent, "*Photoelectron spectroscopy of hexachloroplatinate-nucleobase complexes: Nucleobase excited state decay observed via delayed electron emission*", *J. Chem. Phys.*, **2015**, *143*, 184307.

[31] H. Yao, R. A. Jockusch, "*Fluorescence and Electronic Action Spectroscopy of Mass-Selected Gas-Phase Fluorescein, 2′,7′-Dichlorofluorescein, and 2′,7′-Difluorofluorescein Ions*", *J. Chem. Phys. A*, **2013**, *117*, 1351-1359.

[32] S. Peredkov, M. Neeb, W. Eberhardt, J. Meyer, M. Tombers, H. Kampschulte, G. Niedner-Schatteburg, "*Spin and Orbital Magnetic Moments of Free Nanoparticles*", *Phys. Rev. Lett.*, **2011**, *107*, 233401.

[33] S. Peredkov, A. Savci, S. Peters, M. Neeb, W. Eberhardt, H. Kampschulte, J. Meyer, M. Tombers, B. Hofferberth, F. Menges, G. Niedner-Schatteburg, "*X-ray absorption spectroscopy of mass-selected transition metal clusters using a cyclotron ion trap: An experimental setup for measuring XMCD spectra of free clusters*", *J. Electron Spectrosc. Relat. Phenom.*, **2011**, *184*, 113-118.

[34] J. Meyer, M. Tombers, C. van Wüllen, G. Niedner-Schatteburg, S. Peredkov, W. Eberhardt, M. Neeb, S. Palutke, M. Martins, W. Wurth, "*The spin and orbital contributions to the total magnetic moments of free Fe, Co, and Ni clusters*", *J. Chem. Phys.*, **2015**, *143*, 104302.

[35] D. Dieleman, M. Tombers, L. Peters, J. Meyer, S. Peredkov, J. Jalink, M. Neeb, W. Eberhardt, T. Rasing, G. Niedner-Schatteburg, "*Orbit and spin resolved magnetic*

properties of size selected $[\mathrm{Co}_N\mathrm{Rh}]^+$ *and* $[\mathrm{Co}_N\mathrm{Au}]^+$ *nanoalloy clusters*", *Phys. Chem. Chem. Phys.*, **2015**, *17*, 28372-28378.

[36] J. T. Lau, J. Rittmann, V. Zamudio-Bayer, M. Vogel, K. Hirsch, P. Klar, F. Lofink, T. Möller, B. v. Issendorff, "*Size Dependence of* $L_{2,3}$ *Branching Ratio and 2p Core-Hole Screening in X-Ray Absorption of Metal Clusters*", *Phys. Rev. Lett.*, **2008**, *101*, 153401.

[37] J. T. Lau, K. Hirsch, A. Langenberg, J. Probst, R. Richter, J. Rittmann, M. Vogel, V. Zamudio-Bayer, T. Möller, B. von Issendorff, "*Localized high spin states in transition-metal dimers: X-ray absorption spectroscopy study*", *Phys. Rev. B*, **2009**, *79*, 241102.

[38] K. Hirsch, J. T. Lau, K. Ph, A. Langenberg, J. Probst, J. Rittmann, M. Vogel, V. Zamudio-Bayer, T. Möller, B. v. Issendorff, "*X-ray spectroscopy on size-selected clusters in an ion trap: from the molecular limit to bulk properties*", *J. Phys. B*, **2009**, *42*, 154029.

[39] J. T. Lau, M. Vogel, A. Langenberg, K. Hirsch, J. Rittmann, V. Zamudio-Bayer, T. Möller, B. v. Issendorff, "*Communication: Highest occupied molecular orbital–lowest unoccupied molecular orbital gaps of doped silicon clusters from core level spectroscopy*", *J. Chem. Phys.*, **2011**, *134*, 041102.

[40] K. Hirsch, V. Zamudio-Bayer, F. Ameseder, A. Langenberg, J. Rittmann, M. Vogel, T. Möller, B. v. Issendorff, J. T. Lau, "*2p X-ray Absorption of Free Transistion-Metal Cations Across the 3D Transition Elements: Calcium Through Copper*", *Phys. Rev. A*, **2012**, *85*, 062501.

[41] M. Niemeyer, K. Hirsch, V. Zamudio-Bayer, A. Langenberg, M. Vogel, M. Kossick, C. Ebrecht, K. Egashira, A. Terasaki, T. Möller, B. v. Issendorff, J. T. Lau, "*Spin Coupling and Orbital Angular Momentum Quenching in Free Iron Clusters*", *Phys. Rev. Lett.*, **2012**, *108*, 057201.

[42] V. Zamudio-Bayer, L. Leppert, K. Hirsch, A. Langenberg, J. Rittmann, M. Kossick, M. Vogel, R. Richter, A. Terasaki, T. Möller, "*Coordination-driven magnetic-to-nonmagnetic transition in manganese-doped silicon clusters*", *Phys. Rev. B*, **2013**, *88*, 115425.

[43] A. Langenberg, K. Hirsch, A. Ławicki, V. Zamudio-Bayer, M. Niemeyer, P. Chmiela, B. Langbehn, A. Terasaki, B. v. Issendorff, J. T. Lau, "*Spin and orbital magnetic moments of size-selected iron, cobalt, and nickel clusters*", *Phys. Rev. B*, **2014**, *90*, 184420.

[44] K. Hirsch, V. Zamudio-Bayer, A. Langenberg, M. Niemeyer, B. Langbehn, T. Möller, A. Terasaki, B. v. Issendorff, J. T. Lau, "*Magnetic Moments of Chromium-Doped Gold Clusters: The Anderson Impurity Model in Finite Systems*", *Phys. Rev. Lett.*, **2015**, *114*, 087202.

[45] V. Zamudio-Bayer, K. Hirsch, A. Langenberg, M. Niemeyer, M. Vogel, A. Ławicki, A. Terasaki, J. T. Lau, B. von Issendorff, "*Maximum Spin Polarization in Chromium Dimer Cations as Demonstrated by X-ray Magnetic Circular Dichroism Spectroscopy*", *Angew. Chem. Int. Ed.*, **2015**, *54*, 4498-4501.

[46] V. Zamudio-Bayer, K. Hirsch, A. Langenberg, A. Ławicki, A. Terasaki, B. v. Issendorff, J. Lau, "*Electronic ground states of* Fe_2^+ *and* Co_2^+ *as determined by x-ray absorption and x-ray magnetic circular dichroism spectroscopy*", *J. Chem. Phys.*, **2015**, *143*, 244318.

[47] S. T. Akin, V. Zamudio-Bayer, K. Duanmu, G. Leistner, K. Hirsch, C. Bülow, A. Ławicki, A. Terasaki, B. v. Issendorff, D. G. Truhlar, J. T. Lau, M. A. Duncan, "*Size-Dependent Ligand Quenching of Ferromagnetism in* $\mathrm{Co}_3(\mathrm{benzene})_N^+$ *Clusters Studied with X-ray Magnetic Circular Dichroism Spectroscopy*", *J. Phys. Chem. Lett.*, **2016**, *7*, 4568-4575.

[48] V. Zamudio-Bayer, R. Lindblad, C. Bülow, G. Leistner, A. Terasaki, B. v. Issendorff, J. T. Lau, "*Electronic ground state of* Ni_2^+", *J. Chem. Phys.*, **2016**, *145*, 194302.

[49] C. Berg, T. Schindler, G. Niedner-Schatteburg, V. E. Bondybey, "*Reactions of simple hydrocarbons with Nb_N^+: Chemisorption and physisorption on ionized niobium clusters*", *J. Chem. Phys.*, **1995**, *102*, 4870-4884.

[50] M. Tombers, L. Barzen, G. Niedner-Schatteburg, "*Inverse H/D Isotope Effects in Benzene Activation by Cationic and Anionic Cobalt Clusters*", *J. Phys. Chem. A*, **2013**, *117*, 1197-1203.

[51] L. Barzen, M. Tombers, C. Merkert, J. Hewer, G. Niedner-Schatteburg, "*Benzene activation and H/D isotope effects in reactions of mixed cobalt platinum clusters: The influence of charge and of composition*", *Int. J. Mass Spectrom.*, **2012**, *330–332*, 271-276.

[52] J. Mohrbach, S. Dillinger, G. Niedner-Schatteburg, "*Cryo Kinetics and Spectroscopy of Cationic Nickel Clusters: Rough and Smooth Surfaces*", *J. Phys. Chem. C*, **2017**, *121*, 10907-10918.

[53] S. Dillinger, J. Mohrbach, J. Hewer, M. Gaffga, G. Niedner-Schatteburg, "*Infrared spectroscopy of N_2 adsorption on size selected cobalt cluster cations in isolation*", *Phys. Chem. Chem. Phys.*, **2015**, *17*, 10358-10362.

[54] M. Karas, R. Krüger, "*Ion Formation in MALDI: The Cluster Ionization Mechanism*", *Chem. Rev.*, **2003**, *103*, 427-440.

[55] S. Berkenkamp, F. Kirpekar, F. Hillenkamp, "*Infrared MALDI Mass Spectrometry of Large Nucleic Acids*", *Science*, **1998**, *281*, 260.

[56] K. Dreisewerd, S. Berkenkamp, A. Leisner, A. Rohlfing, C. Menzel, "*Fundamentals of matrix-assisted laser desorption/ionization mass spectrometry with pulsed infrared lasers*", *Int. J. Mass Spectrom.*, **2003**, *226*, 189-209.

[57] M. Yamashita, J. B. Fenn, "*Negative ion production with the electrospray ion source*", *J. Phys. Chem.*, **1984**, *88*, 4671-4675.

[58] M. Yamashita, J. B. Fenn, "*Electrospray ion source. Another variation on the free-jet theme*", *J. Phys. Chem.*, **1984**, *88*, 4451-4459.

[59] J. B. Fenn, M. Mann, C. K. Meng, S. F. Wong, C. M. Whitehouse, "*Electrospray ionization–principles and practice*", *Mass Spectrom. Rev.*, **1990**, *9*, 37-70.

[60] J. B. Fenn, "*Electrospray Wings for Molecular Elephants (Nobel Lecture)*", *Angew. Chem. Int. Ed.*, **2003**, *42*, 3871-3894.

[61] A. Behr, P. Neubert, "*Applied homogeneous catalysis*", John Wiley & Sons, **2012**.

[62] M. Galanski, V. B. Arion, M. A. Jakupec, B. K. Keppler, "*Recent Developments in the Field of Tumor-Inhibiting Metal Complexes*", *Curr. Pharm. Des.*, **2003**, *9*, 2078-2089.

[63] C. X. Zhang, S. J. Lippard, "*New metal complexes as potential therapeutics*", *Curr. Opin. Chem. Biol.*, **2003**, *7*, 481-489.

[64] N. C. Polfer, J. Oomens, R. C. Dunbar, "*IRMPD spectroscopy of metal-ion/tryptophan complexes*", *Phys. Chem. Chem. Phys.*, **2006**, *8*, 2744-2751.

[65] T. Pankewitz, A. Lagutschenkov, G. Niedner-Schatteburg, S. S. Xantheas, Y.-T. Lee, "*Infrared spectrum of $NH_4^+(H_2O)$: Evidence for mode specific fragmentation*", *J. Chem. Phys.*, **2007**, *126*, 074307.

[66] Y. Nosenko, F. Menges, C. Riehn, G. Niedner-Schatteburg, "*Investigation by two-color IR dissociation spectroscopy of Hoogsteen-type binding in a metalated nucleobase pair mimic*", *Phys. Chem. Chem. Phys.*, **2013**, *15*, 8171-8178.

[67] A. Simon, C. Joblin, N. Polfer, J. Oomens, "*Infrared Spectroscopy of $[XFeC_{24}H_{12}]^+$ ($X=C_5H_5$, $C_5(CH_3)_5$) Complexes in the Gas Phase: Experimental and Computational Studies of Astrophysical Interest*", *J. Phys. Chem. A*, **2008**, *112*, 8551-8560.

[68] Y. Nosenko, C. Riehn, G. Niedner-Schatteburg, "*SELF-PAIRING OF 1-METHYLTHYMINE MEDIATED BY TWO AND THREE AG(I) IONS: A GAS PHASE STUDY USING INFRARED DISSOCIATION SPECTROSCOPY AND DENSITY FUNCTIONAL THEORY*", *Phys. Chem. Chem. Phys.*, **2016**, *18*, 8491-8501.

[69] F. Neese, "*PREDICTION OF MOLECULAR PROPERTIES AND MOLECULAR SPECTROSCOPY WITH DENSITY FUNCTIONAL THEORY: FROM FUNDAMENTAL THEORY TO EXCHANGE-COUPLING*", *Coord. Chem. Rev.*, **2009**, *253*, 526-563.

[70] I. Ciofini, C. A. Daul, "*DFT CALCULATIONS OF MOLECULAR MAGNETIC PROPERTIES OF COORDINATION COMPOUNDS*", *Coord. Chem. Rev.*, **2003**, *238–239*, 187-209.

[71] C.-G. Stefanita, "*MAGNETISM: BASICS AND APPLICATIONS*", Springer Science & Business Media, **2012**.

[72] M. Tombers, "*SPIN AND ORBITAL MAGNETIC MOMENTS OF ISOLATED SINGLE MOLECULE MAGNETS AND TRANSITION METAL CLUSTERS*", **2015**.

[73] G. Christou, D. Gatteschi, D. N. Hendrickson, R. Sessoli, "*SINGLE-MOLECULE MAGNETS*", *MRS Bull.*, **2000**, *25*, 66-71.

[74] B. T. Thole, P. Carra, F. Sette, G. van der Laan, "*X-RAY CIRCULAR DICHROISM AS A PROBE OF ORBITAL MAGNETIZATION*", *Phys. Rev. Lett.*, **1992**, *68*, 1943-1946.

[75] P. Carra, B. T. Thole, M. Altarelli, X. Wang, "*X-RAY CIRCULAR DICHROISM AND LOCAL MAGNETIC FIELDS*", *Phys. Rev. Lett.*, **1993**, *70*, 694-697.

[76] M. Tischer, O. Hjortstam, D. Arvanitis, J. Hunter Dunn, F. May, K. Baberschke, J. Trygg, J. M. Wills, B. Johansson, O. Eriksson, "*ENHANCEMENT OF ORBITAL MAGNETISM AT SURFACES: CO ON CU(100)*", *Phys. Rev. Lett.*, **1995**, *75*, 1602-1605.

[77] C. T. Chen, Y. U. Idzerda, H. J. Lin, N. V. Smith, G. Meigs, E. Chaban, G. H. Ho, E. Pellegrin, F. Sette, "*EXPERIMENTAL CONFIRMATION OF THE X-RAY MAGNETIC CIRCULAR DICHROISM SUM RULES FOR IRON AND COBALT*", *Phys. Rev. Lett.*, **1995**, *75*, 152-155.

[78] A. Baniodeh, Y. Lan, G. Novitchi, V. Mereacre, A. Sukhanov, M. Ferbinteanu, V. Voronkova, C. E. Anson, A. K. Powell, "*MAGNETIC ANISOTROPY AND EXCHANGE COUPLING IN A FAMILY OF ISOSTRUCTURAL* $Fe^{III}_2Ln^{III}_2$ *COMPLEXES*", *Dalton Trans.*, **2013**, *42*, 8926-8938.

[79] J. T. Lau, A. Föhlisch, M. Martins, R. Nietubyc, M. Reif, W. Wurth, "*SPIN AND ORBITAL MAGNETIC MOMENTS OF DEPOSITED SMALL IRON CLUSTERS STUDIED BY X-RAY MAGNETIC CIRCULAR DICHROISM SPECTROSCOPY*", *New Journal of Physics*, **2002**, *4*, 98.

[80] J. T. Lau, K. Hirsch, P. Klar, A. Langenberg, F. Lofink, R. Richter, J. Rittmann, M. Vogel, V. Zamudio-Bayer, T. Möller, B. v. Issendorff, "*X-RAY SPECTROSCOPY REVEALS HIGH SYMMETRY AND ELECTRONIC SHELL STRUCTURE OF TRANSITION-METAL-DOPED SILICON CLUSTERS*", *Phys. Rev. A*, **2009**, *79*, 053201.

[81] K. Hirsch, J. Lau, P. Klar, A. Langenberg, J. Probst, J. Rittmann, M. Vogel, V. Zamudio-Bayer, T. Möller, B. Von Issendorff, "*X-RAY SPECTROSCOPY ON SIZE-SELECTED CLUSTERS IN AN ION TRAP: FROM THE MOLECULAR LIMIT TO BULK PROPERTIES*", *J. Phys. B: At., Mol. Opt. Phys.*, **2009**, *42*, 154029.

[82] M. Tombers, J. Meyer, J. Meyer, A. Lawicki, V. Zamudio-Bayer, K. Hirsch, J. T. Lau, B. von Issendorf, A. Terasaki, T. Schlathölter, R. Hoekstra, S. Schmidt, A. K. Powell, E. Kessler, M. H. Prosenc, C. van Wüllen, G. Niedner-Schatteburg, "*A SINGLE MOLECULE MAGNET STUDIED AS SINGLE MOLECULE*", *submitted to Nature Chemistry*, **2016**.

2 Experimental Setup and Methods

2.1 Electrospray Ionization (ESI)

The Electrospray ionization (ESI) allows for a gentle transfer of ions from the solution into the gas phase. The fundamentals for this method have been described by ZELENY in 1917 and realized by DOLE 1968.[1, 2] First experiments were conducted with heavy molecular ions like polystyrenes or lysozyme, but the mass – charge ratio was not resolved by the used mass spectrometers. YAMASHITA and FENN combined the ESI-source with a quadrupole mass spectrometer and FENN was rewarded with the Nobel Prize for the application.[3-6] The ESI technique was initially used in analyses of biomolecules and proteins, but has become a valuable tool in mass spectrometry in all scientific fields.[7-11]

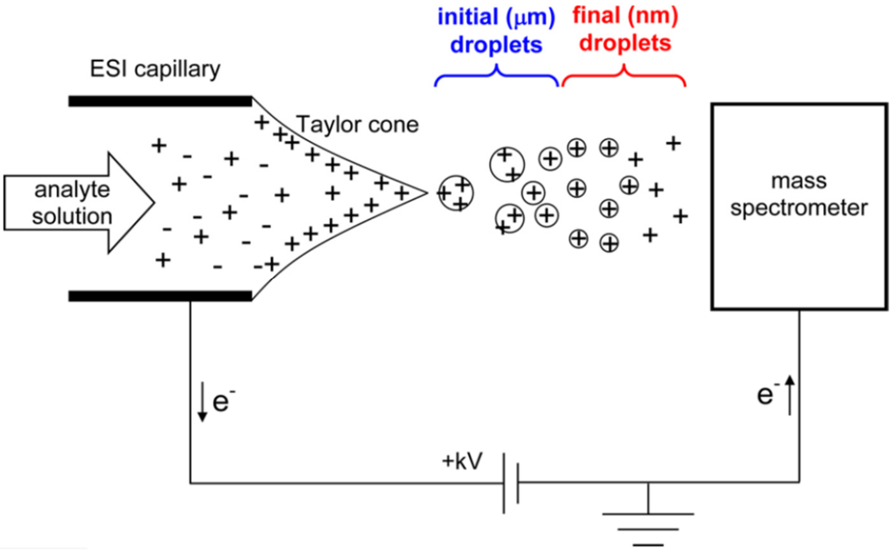

Figure 1:[12] Schematic depiction of an ESI source, operated in positive ion mode.

In the ESI process, a solution of a sample is pinched through an electroconductive capillary by a syringe pump. The capillary itself is held on a potential of some kV with respect to the counterelectrode. The strong electric field causes a charge separation in the electrolyte and the ions of the corresponding polarity approach the liquid surface.[13] The emerging liquid jet is deformed to the so called TAYLOR-cone.[1, 14] By the interplay of viscosity and surface tension the liquid jet becomes instable and breaks into small droplets. The size of the droplets depends on parameters like the difference in potential, flow rate and type of solvent etc.[13, 15] According to the polarity of the applied potential, the droplets provide a surplus charge. The coulomb repulsion causes a divergence of the droplets. By evaporation of solvent molecules, the diameter of the droplets decreases steadily and the surface charge density increases up to the so called Rayleigh limit. The Coulomb repulsion exceeds the surface tension and the droplets disintegrate into much smaller droplets.[12, 13] This process is repeated several times until the droplets are nanometer-sized (cf. Fig. 1). The release of the ions into the gas phase is discussed in three different models.[12]

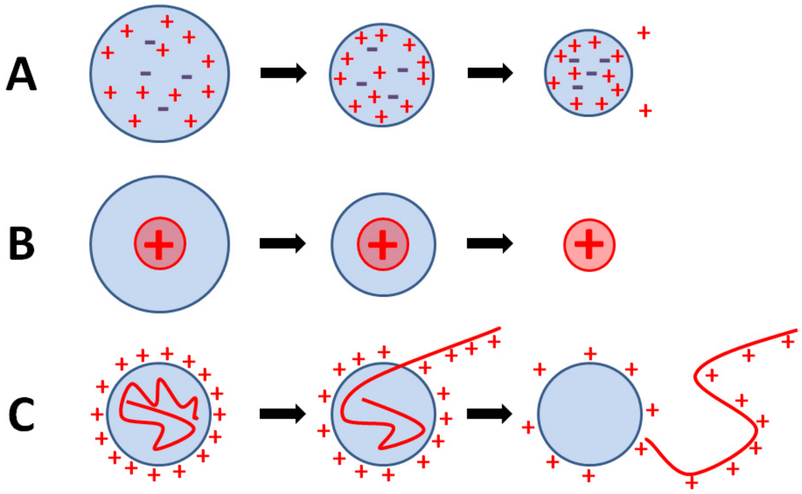

Figure 2: Schematic depiction of the discussed ESI models.

In the **ion evaporation model**, small ions are directly emitted from the surface of the nanodroplets due to the exalted charge density (cf. Fig. 2**A**).[12, 16, 17]

In the **charge residue model**, small nanodroplets provide single ions and the solvent evaporates successively, leaving the bare ions in the gas phase (cf. Fig. 2**B**).[2, 18, 19]

The **chain ejection model** describes the transfer of unfolded proteins from the solution into the gas phase. Nonpolar domains that are directed to the inside of the protein in the folded state interact with the solvent and approach the droplet surface. The protein is ejected step by step from the droplet into the gas phase (cf. Fig. 2**C**).[12, 20, 21]

It should be mentioned, that the term ionization may be misleading. The process does not describe an ionization process in the proper meaning of the word, but rather a transfer of ions from a solution into the gas phase.

2.1.1 The Apollo II ESI Source

The Bruker Apollo II ESI source serves to transfer the ions from the solvated state into the gas phase. The source consists of the spray needle, the spray chamber and the transfer capillary (cf. Fig. 3).

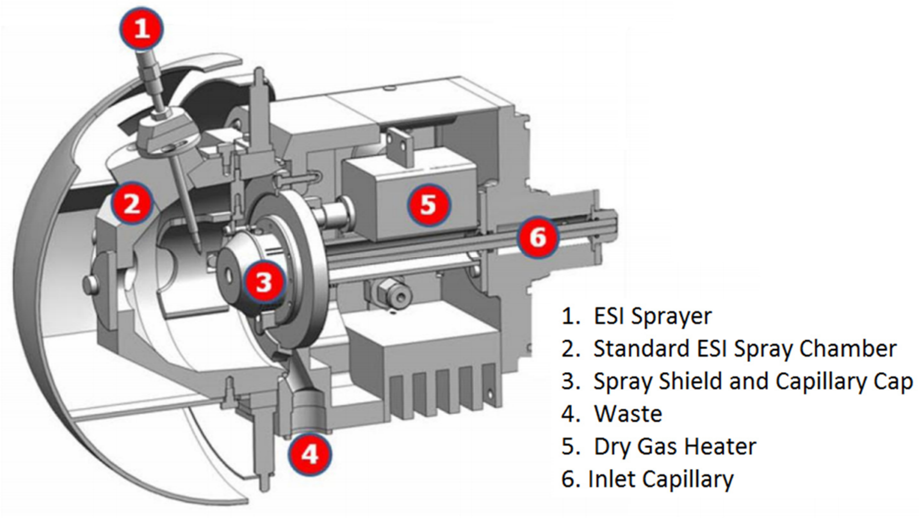

Figure 3:[22] 3D-model of the Bruker Apollo Electrospray Ionization (ESI) source.

The sample solution is injected into the spray needle using a syringe pump. The nebulizer gas (nitrogen) is used to nebulize the solution to an aerosol and provide a constant ion current. The dry gas (nitrogen) is used to reduce the solvents' droplet size. Neutral particles and solvent molecules are drained by the waste pump. A kV potential is applied to the spray shield in order to attract the charged droplets and ions from the spray needle. The polarity of the potential is adapted to the polarity of the species of interest – anions or cations. Another potential of 500 V is used to focus the ions to the aperture of the transfer capillary or inlet capillary. The capillary serves to transfer the ions from the chamber at ambient pressure to the first vacuum stage of the mass spectrometer and represents a barrier between two pressure areas. The internal diameter and the length of the inlet capillary define the gas flow and hence the pressure of the first vacuum stage. The tails of the capillary are metal coated in order to enable a voltage gradient for the ion transfer.

2.1.2 The Custom-Built ESI source

The ion source for the X-ray magnetic circular dichroism (XMCD) experiments is different to the commercially available Apollo II ESI source described in chapter 2.1.1. The custom-built ESI was provided by the group of Thomas SCHLATHÖLTER (Zernike Institute for Advanced Materials, University of Groningen, The Netherlands).[23] The main components are the spray needle (stainless steel), the transfer capillary (stainless steel) and the radio frequency (RF) ion funnel. The spray needle is located on a x,y,z translation stage in order to allow for an optimization of the needle position resulting in a maximum ion signal intensity. A high voltage of 3 to 5 kV is applied to the spray needle to form the TAYLOR-cone and enable optimum spray conditions. The generated ions are transferred into the vacuum by the transfer capillary, which is heated by a constant voltage of 10 to 30 V. After the capillary, the ions are captured by a RF operated ion funnel consisting of 26 ion lenses with tapering diameter. The RF voltage has a frequency of approx. 250 kHz and a peak to peak amplitude of 250 mV. The RF field is superimposed on a constant potential gradient, decreasing from 120 V on the first ion lens to 30 V on the last ion lens. After the ion funnel the ions are directly forwarded to the first hexapole ion guide of the NanoCluster Trap (cf. chapter 2.2.2). The samples are injected by a syringe pump at a flow rate of about 0.2 ml/h. In contrast to the Apollo II ESI source, no nebulizer or dry gas is used in the custom-built ESI source.[22]

2.2 Ion Trap Mass Spectrometers

2.2.1 The Bruker amaZon SL mass spectrometer

A modified Bruker amaZon SL mass spectrometer was used for the InfraRed multiple photon Dissociation (IRMPD) experiments. The main parts of the spectrometer are shown in Fig. 4.

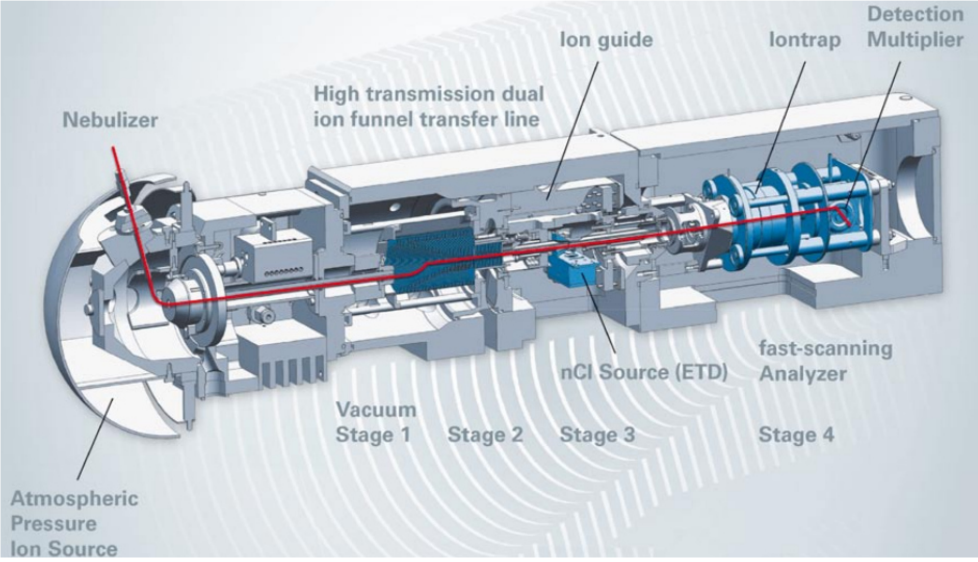

Figure 4:[22] The Bruker amaZon SL mass spectrometer.

The vacuum system

The ion transfer into the gas phase occurs in the spray chamber at ambient pressure, the mass detection occurs at a high vacuum in the range of 10^{-6} mbar. The amaZon SL is differentially pumped in four stages to bridge almost nine orders of magnitude pressure differences.

The ions and the spray gas enter the mass spectrometer via the inlet capillary. The tiny inner diameter allows for a backing pump to maintain an equilibrium pressure of a few milibars (cf. Fig. 5). The next vacuum stage is separated by a skimmer, evacuated by a split-flow turbomolecular pump. Both following vacuum stages, which are separated by skimmers, are connected to the split-flow turbomolecular pump by different valves. This arrangement allows for a pressure of approx. 10^{-6} mbar in the fourth stage.

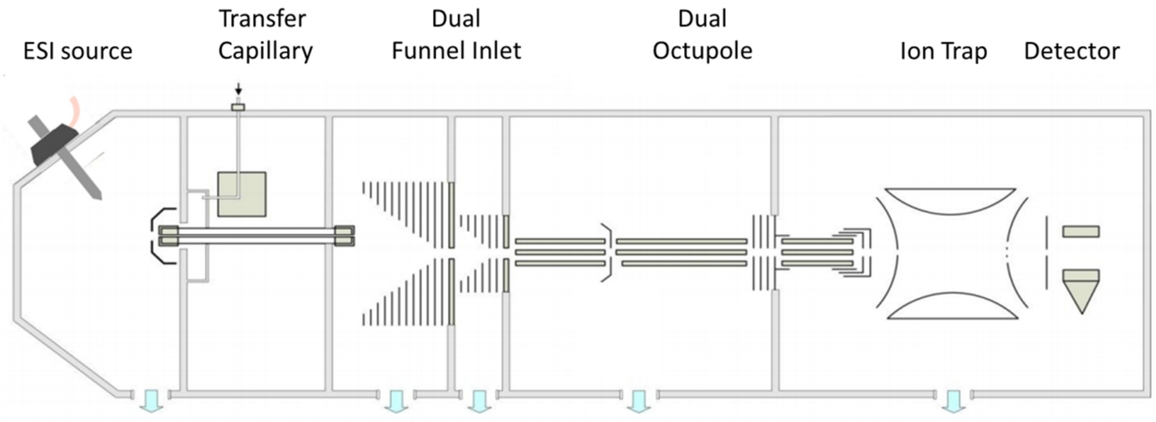

Figure 5:[22] Schematic depiction of the differentially pumped mass spectrometer.

Double ion funnel and multipole ion optic

The biggest challenge for mass spectrometers with atmospheric pressure ionization (API) is the transfer of the ions from ambient pressure to the first vacuum stage.

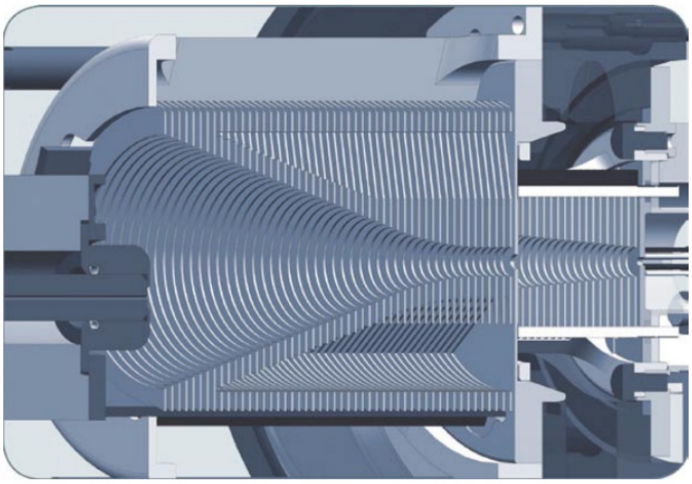

Figure 6:[22] The double ion funnel.

The double ion funnel is shown in Fig. 6. In contrast to common ion optics, the ion funnel focuses the ions from a large initial volume to a small outlet nozzle. The ions are focused regardless to their mass to charge ratio and a large tolerance with respect to their direction of propagation. A radio frequency (RF) voltage applied to the stacked apertures of the ion funnel generates an effective potential trapping the ions in the funnel. The ion funnel is arranged off-axis to the inlet capillary to avoid contamination of the subsequent ion optics. Two adjustable direct voltages at the first and last aperture serve to guide the ions through the aperture at the funnel end. The funnel aperture itself defines the barrier to the next vacuum stage. An ensuing RF voltage operated multipole guides the ions via several focusing lenses into the ion trap.

The ion trap: PAUL-trap

The ion trap conduces to the trapping and mass detection of the ions. It consists of an ion conditioning unit, the actual ion trap and a detection unit (cf. Fig. 7).

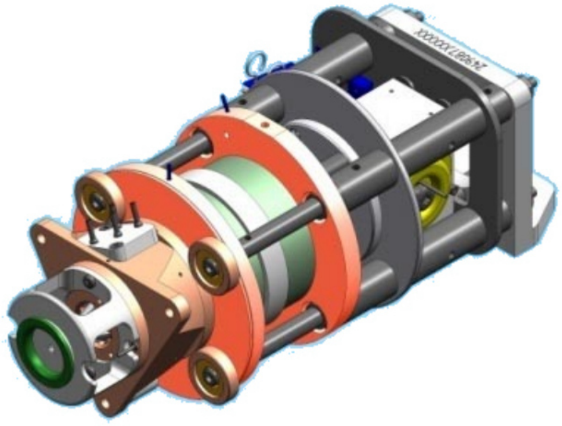

Figure 7:[22] Construction drawing of the PAUL-trap used in the Bruker amaZon SL mass spectrometer.

The ion trap itself is composed of the entrance and exit cap and a ring electrode (cf. Fig. 8). The entrance and exit cap provide a pinhole to enable injection and ejection of the ions. The hyperbolic geometry of the electrodes generates a quadrupolar trapping potential, superimposed to higher order components. Helium is used to thermalize the ions and facilitate an efficient ion trapping. The Helium partial pressure is a sensitive parameter, affecting signal intensities and peak width. The Helium pressure is stabilized by a high precision proportional integral derivative (PID).

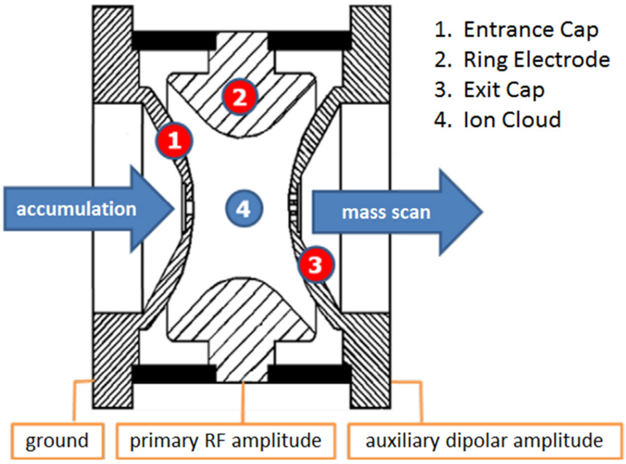

Figure 8: [22] Schematic depiction of a PAUL-trap.

The ions are detected by a DALY-detector, consisting of an aluminium-coated steel electrode that generates secondary electrons at preceding ion impact. The secondary electrons are accelerated to a scintillator creating photons detected by a photomultiplier.[24] The DALY-detector allows for the detection of anions and cations with a simultaneous minimization of mass distortion of electron multipliers.

The ion trap has various tasks. The ions are accumulated, stored, isolated, excited, (collision induced dissociation, CID) and ejected for mass detection. The flexibility of PAUL-type traps offers several advantages in comparison to linear quadrupole instruments with respect to sensitivity and mass-selectivity.

In the first part of the analysis cycle, the ions are accumulated in the ion trap. The continuous ion current has to be suspended for the subsequent mass analysis. A high voltage gate lens is used to deflect the ion current from the trap beyond the accumulation period. During the accumulation period a RF voltage of 781 kHz is applied to the ring electrode, the endcaps are grounded. The oscillating potential difference between the ring electrode and the endcaps generates a quadrupolar electric field. Ions of certain mass to charge ratios can be stored in the trap, depending on the RF voltage. The quadrupolar field can be compared to a three dimensional pseudopotential well, where the depth depends on the ion mass and the RF voltage. An auxiliary voltage applied to the endcaps in order to isolate, fragment and detect precursor ions and their fragment ions. Entering the trap, the ions lose kinetic energy by collisions with the Helium background gas and can be trapped in the ion trap. The trapping efficiency depends on the m/z – ratio, the ion mass, the depth of the pseudopotential well and the phase of the RF voltage at the time of the injection. The accumulation time is typically in the range of 0.01 – 200 ms.

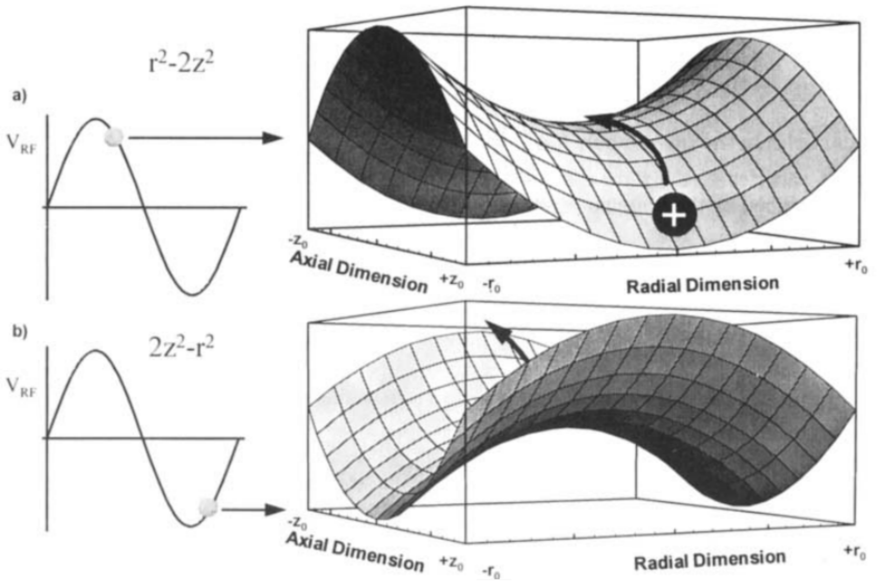

Figure 9:[25] The time depending potential well of the RF is shown for **(a)** a phase angle of 90° where the ions are trapped in the radial-dimension but not in the axial-dimension, and **(b)** a phase angle of 270° where the ions are trapped in only the axial direction. An ion injected in the axial direction must have kinetic energy to overcome the potential barrier presented in **(a),** and contrarily should not have too much kinetic energy to be trapped if injected during situation **(b)**.

In order to enable IR photon irradiation of the trapped ions, the PAUL-trap was modified in collaboration with the manufacturer of the mass spectrometer Bruker Daltonic GmbH. Two holes of 2 mm in diameter (inner surface) and 6 mm (outer surface) were drilled into the ring electrode (cf. Fig. 10). The aperture at the inner surface was reduced to minimize Helium loss from the trap and the apertures are additionally used as iris for laser alignment.[26] The laser beam enters the vacuum chamber by a barium fluoride window (BaF_2, W1, W2, cf. Fig. 10) attached to the vacuum chamber cover by Viton® gaskets. The beam of the tuneable IR laser (IR_{scan}) is led vertically through the center of the ion trap to allow for a maximum overlap between laser beam and ion cloud. The laser beam is deflected by two silver mirrors (M1, M2) and diverted off the vacuum chamber passing the second barium fluoride window (W2). In the two color experiments, the IR laser beams (IR_{scan}, IR_{fix}) are arranged counterpropagating.

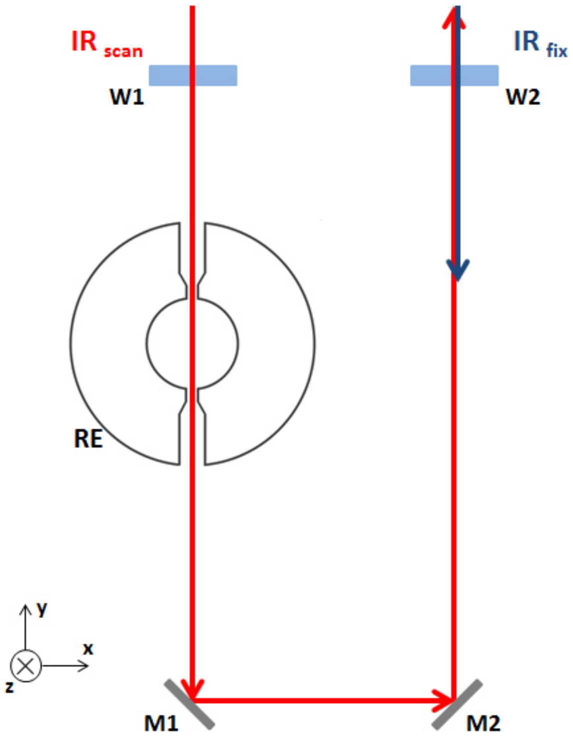

Figure 10:[26] Schematic depiction of the IR beam path through the ring electrode (RE) of the PAUL-trap. W1, W2: barium fluoride windows; M1, M2 deflection mirrors.

2.2.2 The NanoCluster Trap setup

The NanoCluster Trap is a custom-built ion trap mass spectrometer for gas-phase X-ray magnetic circular dichroism (XMCD) experiments. The setup was built by the groups of Thomas MÖLLER, Bernd von ISSENDORF and Tobias LAU and is operated and supervised by Tobias LAU at the UE52 beamline at BESSY II in Berlin. The required superconducting magnet was supplied by Akira TERASAKI.

The NanoCluster Trap is a custom-built ion trap mass spectrometer to record total ion yield (TIY) gas phase X-ray absorption spectra (XAS) with linear polarized light, as well as XAS spectra with circularly polarized light for XMCD studies.[27-39] The ion source can be chosen among the Electrospray Ionization (ESI) source or a magnetron sputter source. The generated ions are transferred via a hexapole ion guide into a quadrupole mass filter (Extrel, 40 – 4000 amu), where the ion of interest can be mass selected (cf. Fig. 11). The selected ions are transferred

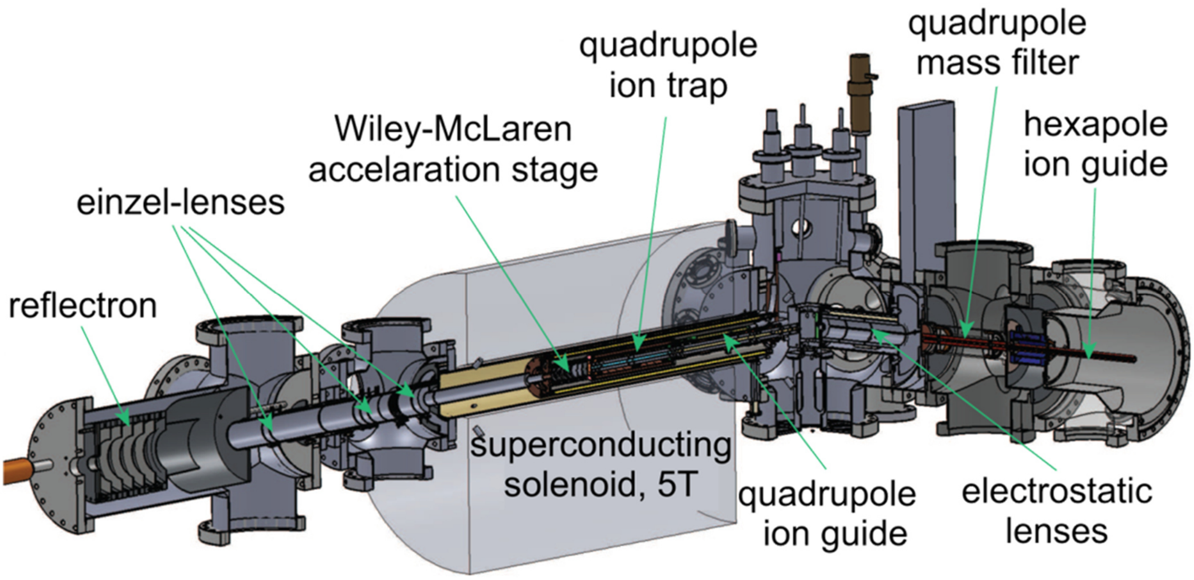

Figure 11:[40] Schematic drawing of the NanoCluster Trap setup, built by the groups of Thomas Möller, Bernd von Issendorf and Tobias Lau, operated by the group of Tobias Lau at the UE52 beamline at BESSY II. The 5 T magnet superconducting magnet was provided by Akira Terasaki. The ion source is not shown in the figure.

via various electrostatic lenses into a quadrupole ion beam bender that bends the ion beam by 90 degrees onto the axis of the superconducting magnet and the X-ray propagation axis. The ion loss due to the deflection by the stray field of the magnet is partially compensated by the electrostatic lenses prior to the ion beam bender. After the bender, a quadrupole ion guide transfers the ions into the linear quadrupole ion trap (cf. Fig. 12). The trap is located in the high field region (5T) of the superconducting solenoid. Depending on the mass of the ions of interest, the ion trap is operated at frequencies between 2 and 4 MHz. The cooling of the ion trap is performed by evaporative liquid Helium cooling to temperatures of 3.5 – 4 K and the ions are cooled by collisional cooling at a constant Helium backing pressure of 10^{-7} to 10^{-6} mbar. The effective ion temperature is higher at approx. 10 – 20 K, due to the RF heating from the operation of the ion trap.[35] The ions are ejected from the trap at a frequency of about 100 Hz to the reflectron time of flight (TOF) mass spectrometer to record mass spectra. The X-ray beam enters the NanoCluster Trap setup at the quadrupole ion beam bender, passes the ion guide and irradiates the ions in the linear quadrupole ion trap. A GaAsP-diode is located at the reflectron stage of the TOF mass spectrometer to record the photon flux of the beamline for normalization of the XA spectra. Depending on the absorption edge and the number of chromophores, the trapped ions are irradiated for 5 to 15 s at an exit slit width of 200 to 500 µm at a certain photon energy. The resulting spectral resolution is in between the range of 0.5 to 2.5 eV.

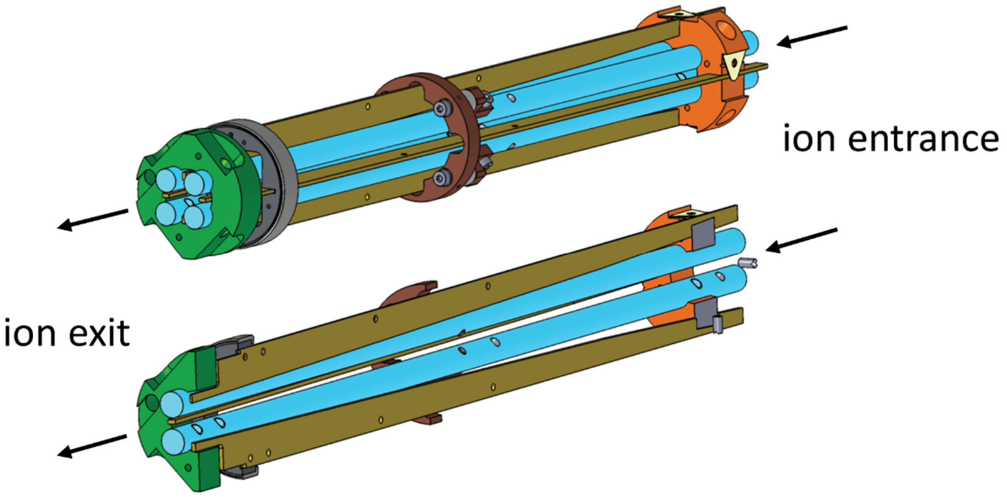

Figure 12:[40] Top: Schematic drawing of the cryogenically cooled quadrupole ion trap. It comprises four parallel rods (d = 6 mm, L = 25 cm) along with four shack fins (side electrodes). The fins generate a static potential gradient that pushes the ions continuously to the trap exit aperture, allowing for a more efficient emptying and trapping. The rods and side electrodes are made of non-magnetic molybdenum, since the trap is located in the high field region of the superconducting solenoid.

2.3 Photon Generation

2.3.1 LaserVision Optical Parametric Oscillator / Amplifier IR Laser System

The IR photons are generated via two *LaserVision* optical parametric oscillator / amplifier (OPO / A) systems, pumped by a *Continuum Powerlite DLS 8000* Nd:YAG laser (cf. Fig. 13).[41-44] The Nd:YAG laser has a repetition rate of 10 Hz and the pulse length of the fundamental beam (1064 nm) is approx. 7 ns. The pulse energy is in the range of 550 – 600 mJ/pulse. A beam splitter divides the fundamental beam into one third directed towards the OPO stage and two thirds directed towards the OPA stage. The OPO part of the fundamental is frequency doubled to 532 nm in a potassium titanyl phosphate crystal (KTP, second harmonic generation, SHG).[45] The non-converted fundamental beam is dumped, and the green 532 nm beam is used to pump the OPO stage. The optical parametric oscillator consists of two potassium titanyl phosphate (KTP) crystals and a resonator. The pumping frequency ν_{532nm} is split into the signal and idler waves $\nu_{1,s}$ and $\nu_{1,I}$ and it is $\nu_{532nm} = \nu_{1,s} + \nu_{1,i}$. The energetic distribution of the signal and idler waves is tuned by the angle between the crystal and the incident pumping laser beam. The OPO generates idler radiation in the range of 7400 – 4700 cm^{-1}, and signal radiation in the range of 14000 – 11300 cm^{-1}.

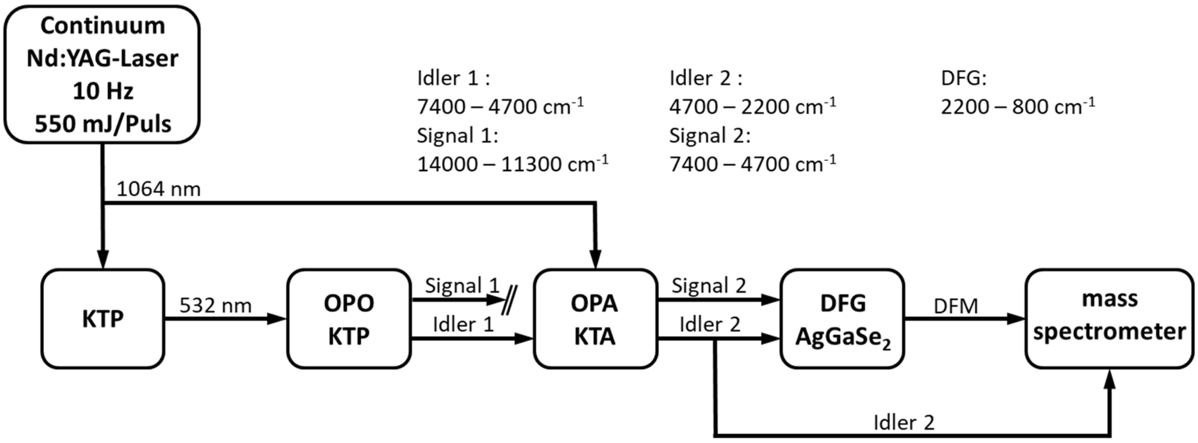

Figure 13: Principle scheme of the LaserVision KTP/KTA OPO/OPA laser system, revealing the non-linear optical processes for the generation of IR photons.

In this regard the two OPO/A systems differ. One system is a narrowband system (nb) and one system is a broadband system (bb). An optical grating is used in the nb system to reduce the bandwidth of the signal and idler radiation (single mode operation, cf. Fig. 14). The nb system has a spectral resolution of less than 0.3 cm^{-1}, the bb system 0.9 cm^{-1} though.

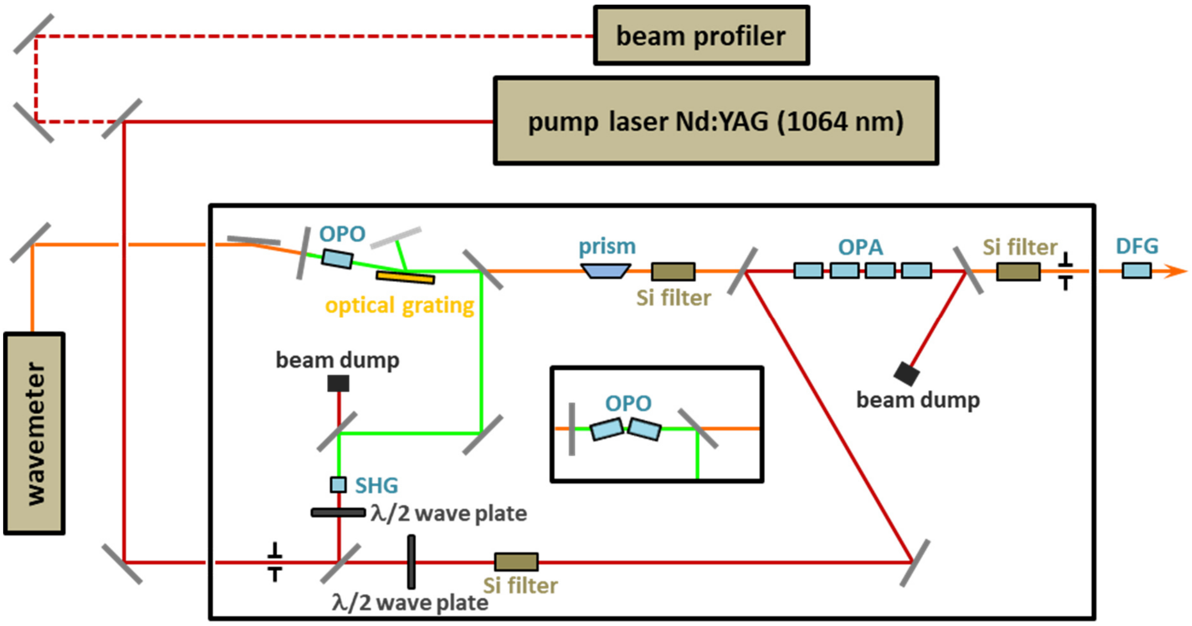

Figure 14: Schematic representation of the beam path of the narrowband (nb) LaserVision OPO/OPA laser system. Inset: alternative OPO setup in the broadband (bb) system.

The signal radiation $\nu_{1,s}$ of the OPO stage is separated by a silicon filter in the Brewster angle and the idler radiation $\nu_{1,i}$ directed to the OPA stage, where the fundamental ν_{1064nm} is decomposed into a signal and idler wave. The amplification process does not require a resonator and the signal wave is represented by the OPO idler wave $\nu_{1,i}$.[46] The OPA stage consists of four potassium titanyl arsenate (KTA) crystals illuminated by the remaining two-thirds of the ν_{1064nm} beam collinear with the OPO idler wave $\nu_{1,i}$. The process generates the signal 2 ($\nu_{2,s}$) and idler 2 ($\nu_{2,i}$) waves, whereby the idler 1 wave corresponds to the signal 2 ($\nu_{1,i} = \nu_{2,s}$). The Signal 2 is in the range of 7400 – 4700 cm^{-1} and the idler 2 is in the range of 2700 – 2200 cm^{-1}. Due to the energy conservation it is:

$$\nu_{1064nm} = \nu_{2,s} + \nu_{2,i} = \nu_{1,i} + \nu_{2,i} = \nu_{532nm} - \nu_{1,s} + \nu_{2,i} \tag{1}$$

The idler 2 wave is suitable for IRMPD measurements in the stretching vibration region (OH, NH, CH). The signal 2 wave is suitable for measurements in the near IR region e.g. for the detection of low lying electronic transitions. The spectral range below 2500 cm^{-1} is accessible by difference frequency generation (DFG) using the signal 2 and idler 2 waves. The DFG is proceeded in a silver gallium diselenide ($AgGaSe_2$) crystal that generates IR radiation in the range of approx. 800 – 2200 cm^{-1} ($\nu_{DFM} = \nu_{2,s} - \nu_{2,i}$).[47] The residual signal and idler radiation is deflected by a zinc-selenide (ZnSe) window. The overall IR radiation intensity varies from approx. 0.1 – 20 mJ/pulse, due to inherent absorption of the crystals and windows, water and carbon dioxide absorption. The lower limit for The IRMPD experiments is at approx. 1000 cm^{-1}, owing to the inherent absorption of the BaF_2 windows. An exemplary laser energy curve is shown in Fig. 15.

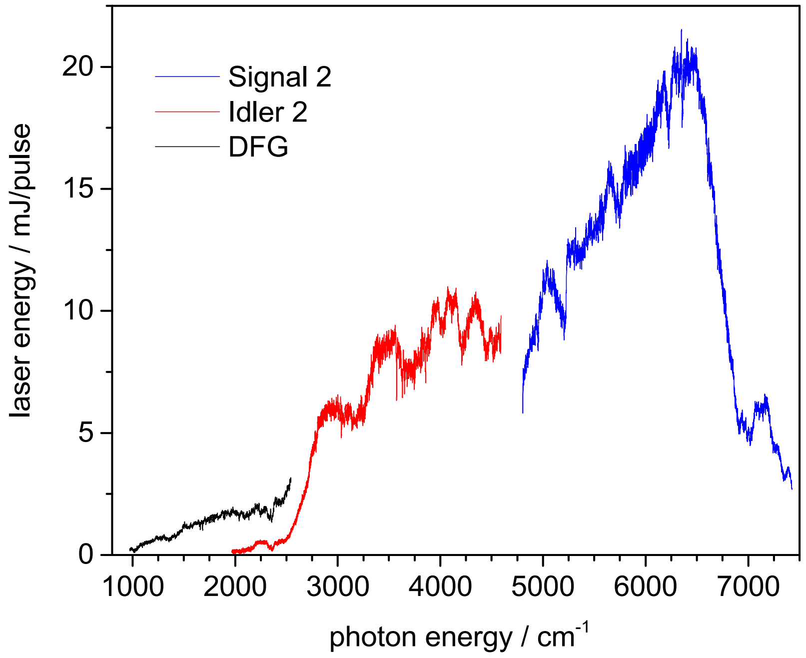

Figure 15: Energy curve of the LaserVision broadband (bb) OPO/A system.

The IR radiation of the bb system is focused by a calcium fluoride (CaF_2) lens with a focal length of 0.5 m, to a spot located 8 cm in front of the first deflection mirror in the mass spectrometer to prevent damages at the optics. The DFG radiation is focused by a parabolic mirror with a focal length of 0.152 m. The IR radiation of the nb system is focused by a CaF_2 lens with a focal length of 0.75 m into the Paul-trap. A delay generator (*DG645, Stanford Research Systems*) is used for the synchronization of the laser systems and the mass spectrometer. The ion packages can be irradiated by one to ten laser pulses each. The time delay of the laser pulses of the bb and nb system can be adjusted by the delay generator, the default value for the two color experiments is $t_{IR,fix} - t_{IR,tuned} = 100$ ns.

The beam path of the LaserVision OPO/A systems is shown in Fig. 14. The various nonlinear processes for the frequency conversions require different beam polarizations. The polarization and thus the IR output energy can be adjusted by the half-wave plates (λ/2-plate) shifting the polarization of the ν_{1064nm} radiation. The emerging horizontal (h) and vertical (v) beam polarizations at different optical elements are summarized in Tab. 1. The IR frequency was calibrated using a wave meter (bb system: *Bristol Instruments: 821B-NIR*, nb system: *Toptica Photonics: HighFinesse IRII-WS7*).

Table 1: Beam polarization before and after different optical elements of the LaserVision OPO/A IR laser system (cf. Fig. 14).[26]

optical element	In	Out
OPO λ/2-plate	ν_{1064nm} (h)	ν_{1064nm} (v)
SHG KTP	ν_{1064nm} (v)	ν_{532nm} (v)
OPO KTP	ν_{532nm} (v)	$\nu_{1,s}$ (h) + $\nu_{1,i}$ (v)
dove prism and wave	$\nu_{1,s}$ (h) + $\nu_{1,i}$ (v)	$\nu_{1,s}$ (v) + $\nu_{1,i}$ (h)
silicon filter 1	$\nu_{1,s}$ (v) + $\nu_{1,i}$ (h)	$\nu_{1,i}$ (h) = $\nu_{2,s}$ (h)
OPA λ/2-plate	ν_{1064nm} (h)	ν_{1064nm} (v)
OPA KTA	ν_{1064nm} (v) & $\nu_{1,i}$ (h)	ν_{1064nm} (v) + $\nu_{2,s}$ (h) + $\nu_{2,i}$
silicon filter 2	$\nu_{2,s}$ (h) + $\nu_{2,i}$ (v)	$\nu_{2,s}$ (h) or $\nu_{2,i}$ (v)
$AgGaSe_2$ crystal	$\nu_{2,s}$ (h) + $\nu_{2,i}$ (v)	ν_{DFM}

2.3.2 Soft X-ray Synchrotron Radiation at the UE52-PGM Beamline at BESSY II

The presented X-ray absorption spectra were recorded with the NanoCluster Trap setup at the Helmholtz-Zentrum Berlin für Materialien und Energie. The required photons are generated at the soft X-ray undulator beamline UE52. In the following, a short overview on synchrotron radiation and undulators is given. A detailed description is given elsewhere.[48]

If electrons are accelerated to relativistic velocities on a circular orbit, they emit electromagnetic radiation called synchrotron radiation. At the BESSY II synchrotron facility, the electrons are accelerated to approx. 1.7 GeV and then transferred into the storage ring. In the storage ring there are straight beam path sections alternating with dipole, quadrupole, and sixtupole magnets for the deflection, focusing and correction of the electron beam. The dipole magnets bend the electron beam to form a circular beam path. The spatial deflection generates bremsstrahlung, which can be focused, monochromatized and used in X-ray experiments. The energy loss of the electrons is compensated by reacceleration in RF cavities located in the storage ring.

Another possibility of generating highly brilliant synchrotron radiation is the use of so called undulators, which are located in the straight beam paths of the storage ring. The undulators are built of concatenated permanent magnets with alternating polarity (cf. Fig. 16). The magnet arrangement causes an oscillatory motion of the electrons, generating X-rays. One electron emits multiple light waves passing through the magnet array, which can interfere constructively and generate highly brilliant X-radiation. The photon energy is adjusted by manipulating the gap between the permanent magnets.

The beamline UE52 used for the presented XMCD experiments is equipped with an APPLE 2 (advanced planar polarized light emitter) undulator.[50-53] It is built up of 4 rows of permanent magnets of alternating polarization. All rows of magnets can be shifted individually against each other. The undulator can generate linear (horizontal and vertical) and circular (left and right handed) polarized radiation, depending on the magnet gap and shift (cf. Fig. 16). The UE52 beamline is a soft X-ray beamline, providing an energy range of 85 to 1600 eV (cf. Tab. 2). The spectral resolution is adjusted by variation of the exit slit width of the used plane-grating mirror (PGM) monochromator. The storage ring is operated in the “top up” mode, resulting in a periodic electron injection (every few minutes) to keep a constant ring current of 260 mA.

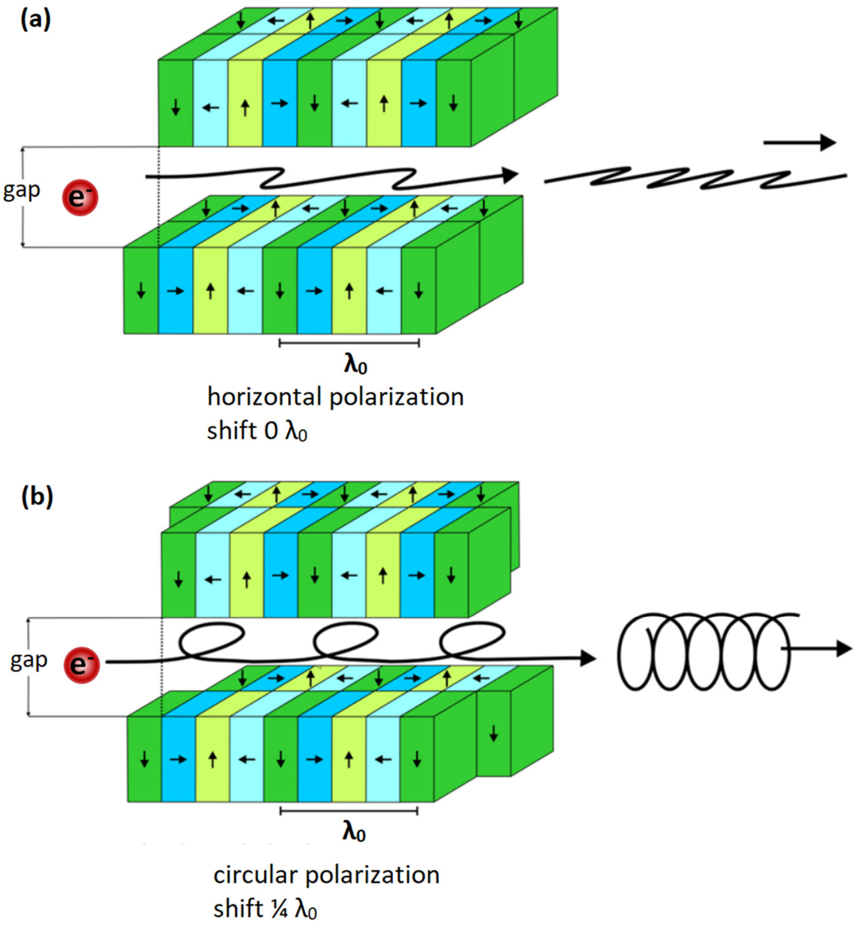

Figure 16:[49] Arrangement of the concatenated permanent magnets of an APPLE 2 (advanced planar polarized light emitter) undulator.[50-52] **(a)** Magnet arrangement for horizontal photon polarization and **(b)** arrangement for circular photon polarization.

Table 2.2: Technical specifications of the UE52-PGM beamline at BESSY II.[54]

energy range	85 – 1600 eV (soft X-ray regime)
resolving power at 400 eV	> 10000
polarization	variable
degree of polarization	90 %
photon flux (500 – 1000 eV)	> 1012 photons / s
divergence	0.8 mrad x 0.2 mrad

2.4 Methods

2.4.1 InfraRed Multiple Photon Dissociation (IRMPD) spectroscopy

The infrared spectroscopy is a powerful tool for the structural elucidation of diverse substances. It provides information on the position of a charge (at ions, e.g. protonated functional group), the presence of certain functional groups (-OH, $-NH_2$, -C=O), symmetry and presence of hydrogen bonds.[55] The structure of a molecule is strongly related to its vibrational fingerprint. In the condensed phase, the decrease of the intensity of the infrared light by absorption is measured. Due to the low particle density in ion traps of often less than 10^8 cm^{-3}, a decrease in the photon intensity of the incident IR beam cannot be detected.[55]

The infrared multiple photon dissociation (IRMPD) spectroscopy represents an action spectroscopy. The species of interest is isolated in the ion trap and the ion cloud is irradiated by a tuneable IR laser. When the IR laser frequency is in resonance with a vibrational mode of the isolated ion, the ion absorbs photons and the energy is redistributed among the whole molecule. Thus, the internal energy of the ions increases until the dissociation barrier is reached and weak bonds break.[55] The fragment ions are detected by the mass spectrometer. The IRMPD spectrum is obtained by plotting the fragmentation efficiency vs. the IR laser frequency. In the IRMPD process, the absorption of several photons is necessary for a fragmentation and by this, the fragmentation efficiency is not linearly correlated to the absorption cross section and the laser power. Hence, IRMPD absorption bands may differ significantly in intensity or disappear completely compared to calculated harmonic absorption spectra.[56-58] The absorption of multiple photons is an incoherent process and thus, the absorbed energy is quickly dissipated by the internal vibrational redistribution (IVR) process to all vibrational degrees of freedom. This leads to an effective heating of the molecular ion.[55, 59] Multiple cycles, involving the photon energy redistribution and the subsequent increase of the internal energy are sketched in Fig. 17.

The photon energy in the IR spectroscopy regime is approx. 800 – 4000 cm^{-1}, which corresponds to 10 – 50 kJ/mol. Thus, single photons can only break very weak molecular bonds. Binding energies of organic molecules are one order of magnitude higher in energy. (e.g. C – C 348 kJ/mol, C = O 743 kJ/mol, O – H 463 kJ/mol, N – H 388 kJ/mol).[60] Hence, in order to break covalent bonds, multiple IR photons are necessary.[58]

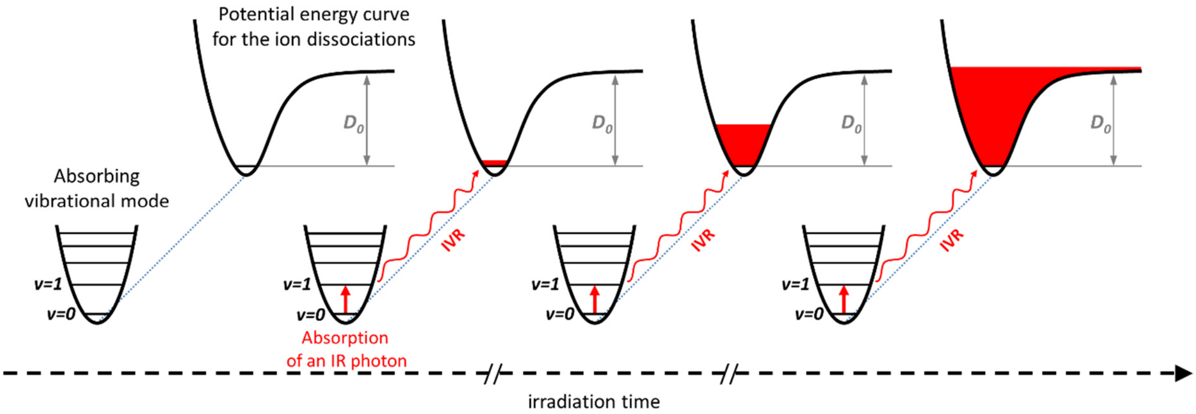

Figure 17: Schematic representation of the infrared multiple photon dissociation spectroscopy, involving the cycles of photon absorption and internal vibrational redistribution (IVR).[58]

In order to fragment very stable ions, tagging represents an alternative technique.[61] Instead of isolating the species of interest, a weakly bound and chemically unreactive atom or molecule is attached to the species (e.g. Argon, Helium atoms or Hydrogen molecules). A resonant absorption of IR photons induces a cleavage of the bond between the ion and the tag. The cryogenic temperatures required for the tagging technique are only accessible in supersonic expansion jets or cryogenically cooled ion traps. The perturbation of the tag is assumed to be negligible in the evaluation of tagged IR(M)PD spectra.[58]

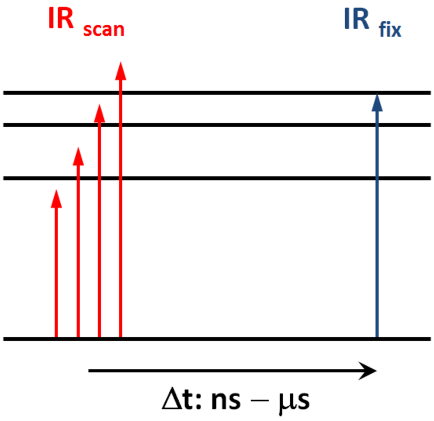

Figure 2.18: Timing scheme of the scanning IR laser (IR_{scan}) and the frequency fixed IR laser (IR_{fix}).

Besides the already pictured IRMPD experiments using a single IR OPO/A, the so-called two-color IRMPD technique was used as well. The first laser is set to a fixed frequency, resonant to a vibrational absorption mode and the second laser is tuned to record the spectrum. The temporal succession is flexible in the range of microseconds (µs) to nanoseconds (ns) (cf. Fig. 2.18). Our experience has shown, that the irradiation of the tuned laser prior to the frequency fixed laser is preferable. A reversed scheme leads to heating of the ions, resulting in a band broadening. The second laser enables the absorption of additional photons in order to augment the fragmentation efficiency or IRMPD yield or overcome IVR bottlenecks and reveal otherwise "dark" bands.[62]

The two-color IRMPD process is shown in Fig. 19 (based on the depiction of ROITHOVÀ[58]). The absorption of a second (blue) IR photons is feasible when the energy of the first IR photon is redistributed via IVR across the molecule. The restriction is does not apply for the red photon which is absorbed immediately. The energy input is expedited and the dissociation threshold is reached more quickly.

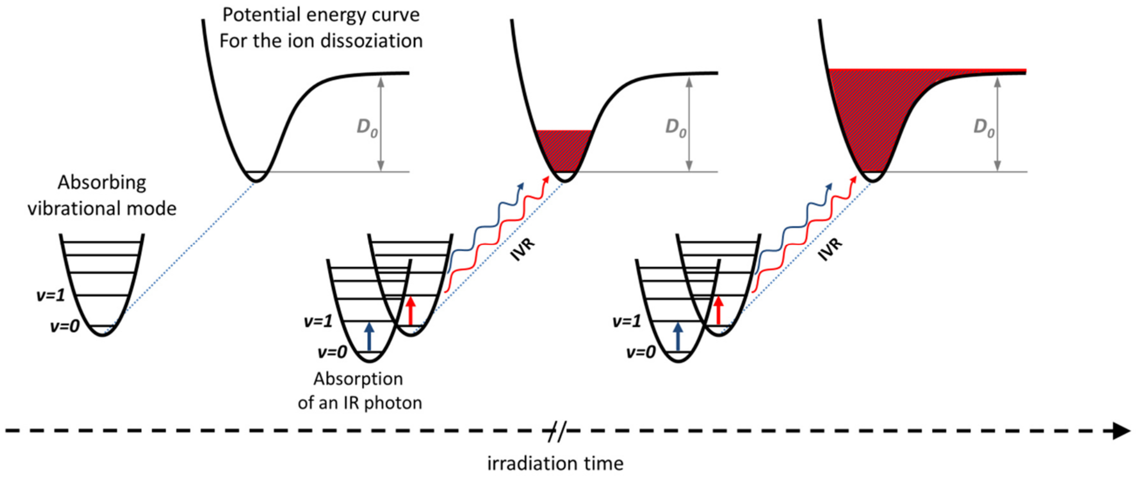

Figure 19: Schematic representation of the IRMPD process using the two-color IRMPD technique.

2.4.2 Density Functional Theory (DFT)

The interpretation of various experimental results is facilitated by comparison with quantum chemical calculations. Density functional Theory (DFT) represents a computationally cheap approach for the calculation of diverse molecular properties like bond lengths, bond energies, IR frequencies and electronic properties.[63-67] The basic idea of DFT is the possibility to qualify the energy of an electronic systems by its electron density $\rho(\vec{r})$, described by THOMAS and FERMI.[68, 69] The electron shell is treated as electron gas, whereas the kinetic and electrostatic energy is expressed by the electron density $\rho(\vec{r})$.[70] This model is not able to qualify chemical bonds, since the energy of a molecule is always higher than the sum of the single atom energies.[71] The theorem of KOHN and HOHENBERG showed in 1964, that the electronic ground state energy and all other properties of the ground state are determined by the ground state electron density and the variational principle is able to assess the ground state energy.[72]

The minimization of the energy, using the variational principle was derived by KOHN and SHAM.[73] The energy is described as a function of the electron density $\rho(\vec{r})$:

$$E(\rho) = T_S(\rho) + \int dr\, \rho(\vec{r})(V_{ext}(\vec{r}) + \frac{1}{2}\varphi(\vec{r})) + E_{XC}(\rho) \tag{2}$$

$T_S(\rho)$ is the kinetic energy, $\varphi(\vec{r})$ represents the Coulomb potential and the exchange-correlation energy is given by $E_{XC}(\rho)$, describing the electron-electron interaction. The KOHN-SHAM wavefunction is a single slater determinant, which is constructed using a set of orbitals that are the lowest energy solution to

$$\left(-\frac{\hbar^2}{2m}\nabla^2 + V_{eff}(\vec{r})\right)\Phi_i(r) = \varepsilon_i\Phi_i(r) \tag{3}$$

with the orbital energy ε_i of the corresponding Kohn-Sham orbital i. The electron density of the entire system is described as:

$$\rho(\vec{r}) = \sum_i^N |\Phi_i(r)|^2 \tag{4}$$

The estimation of the exchange-correlation energy $E_{XC}(\rho)$ plays a crucial role within DFT as it inherits all unknown factors and the amount strongly depends on the used functionals. The kinetic energy and the integral in equation (2) instead are calculated cheaply, since they cover only one and two electron integrals.

The local density approach (LDA) describes the exchange-correlation energy per particle in a homogeneous electron gas, where spin up and spin down electron density is considered differentiated.[65] Generalized gradient approximations (GGA) are used to calculate the exchange-correlation energies according to Hartree-Fock methods. The combination of LDA and GGA in so-called hybrid functionals has proven to achieve reasonable results in the computation of atomic and molecular properties.[74, 75]

The determination of structural properties is conducted by performing geometry optimizations with all possible start geometries, resulting in different local minimum structures. Comparison of the energy of the local minima allow for the determination of the global minimum structure. The comparison of calculated harmonic frequencies of the most favourable minimum structures with experimental IRMPD or IR absorption spectra allows for a reliable structural assignment.[76]

All quantum chemical calculations in the presented work were performed using the Gaussian 09 program package.[77] The choice of specific functionals and basis sets is discussed in the respective chapters. The calculations were gratefully performed on the computing clusters of the TU Kaiserslautern under the supervision of Prof. Dr. Christoph VAN WÜLLEN.

2.4.3 X-ray Absorption and X-ray Magnetic Circular Dichroism (XMCD) Spectroscopy

The absorption of photons of the X-ray regime, usually leads to an excitation of core electrons within an atom. The absorption is either resonant or non-resonant. In the latter case, the core electron is excited into a free-electron like continuum state. The photon energy (hv) exceeds the binding energy (E_b) of the electron and the excess energy is converted into kinetic energy (E_{kin}) of the electron. This process is described by the photoelectric effect (cf. eq. (5), with ϕ being the work function).

$$E_{kin} \leq hv - E_b - \phi \tag{5}$$

In the case of a resonant absorption, the core electron is excited into an empty valence state (or valence hole) of the atom. In both cases the system is left with an empty core state (or core hole). The hole can be filled by an electron dropping down from an energetically higher level. The released energy corresponds to the difference between the dropping electron and the core hole and can be emitted either as radiation (fluorescence) or by ejection of another valence electron (AUGER electron).

In the following, the resonant absorption as excitation from an initial core state to a valence hole will be described in a one electron portrait and in terms of a process of first order. Hence, a time dependent perturbation of the system by the electromagnetic field of the X-rays leads to a prompt excitation from the initial state $|i\rangle$ to an empty valence or final state $|f\rangle$ without interference from intermediate states $|n\rangle$.

The transition probability T_{if} from $|i\rangle$ to $|f\rangle$ is described by FERMI's golden rule, taking only the first order term into account as derived by DIRAC:[78]

$$T_{if} = \frac{2\pi}{\hbar} \left| \langle f | \hat{H}_{int} | i \rangle \right|^2 \delta\left(\varepsilon_i - \varepsilon_f\right) \rho\left(\varepsilon_f\right) \tag{6}$$

$\hat{H}_{int}$	interaction Hamiltonian
$\varepsilon_{i,f}$	energy of the initial and final state
$\rho(\varepsilon_f)$	density of final states per unit energy

The interaction Hamiltonian for resonant X-ray absorption can be described as the product of the momentum operator $\boldsymbol{p}$ and the vector potential $\boldsymbol{A}$ with the elementary charge $\boldsymbol{e}$ and the electron mass m_e:[79-82]

$$\hat{H}_{int} = \frac{e}{m_e} \boldsymbol{p} \cdot \boldsymbol{A} \tag{7}$$

The initial and final states and the matrix elements provide an electronic and a photon part. After evaluation of the photon part and quantization of the electromagnetic field, the corresponding matrix elements M can be described as a transition between two electronic states $|a\rangle$ and $|b\rangle$:[83]

$$M = \langle b | \boldsymbol{p} \cdot \boldsymbol{\varepsilon} \, e^{i\boldsymbol{k}\cdot\boldsymbol{r}} | a \rangle \tag{8}$$

with $\boldsymbol{\varepsilon}$ being the unit photon polarization operator. If the dipole approximation is applied, the dependence from the photon wave vector $\boldsymbol{k}$ is eliminated through a series expansion of the exponential function and truncation after the first term. The electron momentum operator $\boldsymbol{p}$ can be expressed by the length operator $\boldsymbol{r}$:[79]

$$M = \langle b | \boldsymbol{p} \cdot \boldsymbol{\varepsilon} \, (1 + i\boldsymbol{k} \cdot \boldsymbol{r} + \cdots) | a \rangle \cong \langle b | \boldsymbol{p} \cdot \boldsymbol{\varepsilon} | a \rangle = i m_e \omega \langle b | \boldsymbol{r} \cdot \boldsymbol{\varepsilon} | a \rangle \tag{9}$$

With m_e being the electron rest mass and $\omega = \omega_b - \omega_a$ the photon frequency associated with the transistion from $|a\rangle$ to $|b\rangle$. The dipole approximation assumes that the size of the absorbing atomic shell is small relative to the X-ray wavelength:[79]

$$|\boldsymbol{r}| \ll \frac{1}{|\boldsymbol{k}|} = \frac{\lambda}{2\pi} \tag{10}$$

This means the electric field which drives the electronic transition is constant across the atomic volume. The derived absorption cross section σ^{abs} is expressd by:

$$\sigma^{abs} = 4\pi^2 \frac{e^2}{4\pi\varepsilon_0 \hbar c} \hbar\omega |\langle b | \boldsymbol{\varepsilon} \cdot \boldsymbol{r} | a \rangle|^2 \delta\big(\hbar\omega - (E_b - E_a)\big) \rho(E_b) \tag{11}$$

The X-ray absorption resonance intensity I_{res} is given by the integration over the absorption cross section after normalization of the electronic states $|a\rangle$ and $|b\rangle$:

$$I_{res} = 4\pi^2 \frac{e^2}{4\pi\varepsilon_0 \hbar c} \hbar\omega |\langle b | \boldsymbol{\varepsilon} \cdot \boldsymbol{r} | a \rangle|^2 = A |\langle b | \boldsymbol{\varepsilon} \cdot \boldsymbol{r} | a \rangle|^2 \tag{12}$$

$A = 4\pi^2 \alpha_f \hbar\omega$	proportionality factor
$\alpha_f = \frac{e^2}{4\pi\varepsilon_0 \hbar c}$	fine structure constant

When polarized photons are considered, the polarization dependent dipole operator P_α^q must be included into the product $\boldsymbol{\varepsilon} \cdot \boldsymbol{r}$. The angular momentum of the light is expressed by $\hbar q$. In the case of linear polarized light $q = 0$, for circularly polarized light $q = \pm 1$ and α indicates the X-ray incident direction in Cartesian coordinates.

$$P_\alpha^q = \boldsymbol{\varepsilon}_\alpha^q \cdot \boldsymbol{r} = \boldsymbol{\varepsilon} \cdot \boldsymbol{r} \tag{13}$$

For the X-ray absorption resonance intensity I_{res} follows

$$I_{res} = A|\langle b|\boldsymbol{\varepsilon} \cdot \boldsymbol{r}|a\rangle|^2 = A\left|\langle b\middle|\boldsymbol{\varepsilon}_\alpha^q \boldsymbol{r}\middle|a\rangle\right|^2 = A\left|\langle b\middle|P_\alpha^q\middle|a\rangle\right|^2 \tag{14}$$

The polarization dependent dipole operator P_α^q may be expressed by spherical harmonics $Y_{l,m_l}(\vartheta,\varphi)$or RACAH's spherical tensor operators $C_m^{(l)}$.[84, 85] In an one electron picture, the initial $|a\rangle$ and final $|b\rangle$ electronic states can be expressed by the following simple wave function:

$$R_{n,l}(r) Y_{l,m_l} \chi_{s,m_s} = \left|R_{n,l}(r); l, m_l, s, m_s\right\rangle \tag{15}$$

$R_{n,l}(r)$	radial component of the wave function
Y_{l,m_l}	angular part of the wave function
χ_{s,m_s}	spin part of the wave function
l, m_l, s, m_s	quantum numbers

The transition matrix elements factor into a spin, radial and angular part (eq. 16). Since the spin part is not influenced by the dipole operator, the spin is maintained upon excitation. The polarization dependence is preserved in the angular part, whereas the angle integrated transition strength is expressed in the radial factor of the wave function.

$$\left\langle b\middle|P_\alpha^q\middle|a\right\rangle = \left\langle R_{n',l}(r); l, m_l, s, m_s'\middle|P_\alpha^q\middle|R_{n,c}(r); c, m_c, s, m_s\right\rangle \tag{16a}$$

$$\left\langle b\middle|P_\alpha^q\middle|a\right\rangle = \delta(m_s', m_s)\left\langle R_{n',l}(r)\middle|r\middle|R_{n,c}(r)\right\rangle \sum\nolimits_{m_c,m_l,p} \left(e_{\alpha,p}^q \left\langle l, m_l\middle|C_p^{(1)}\middle|c, m_c\right\rangle\right) \tag{16b}$$

$$\left\langle b\middle|P_\alpha^q\middle|a\right\rangle = \quad \boldsymbol{spin} \qquad \boldsymbol{radial} \qquad \boldsymbol{angular}$$

The inspection of the non-zero matrix elements of equation (16b) allows for the derivation of the dipole selection rules for X-ray excitations:

- $\Delta l = l' - l = \pm 1$
- $\Delta m_l = m_l' - m_l = q = 0, \pm 1$
- $\Delta s = s' - s = 0$
- $\Delta m_s = m_s' - m_s = 0$

Intensity sum rule for the charge

Following the definition of the X-ray propagation (α) and the polarization dependent dipole operator P_α^q, one can define the resonant X-ray absorption intensity, independent of the orientation (white line intensity)

$$\langle I \rangle = \frac{1}{3}\left(I_x^q + I_y^q + I_z^q\right) = \frac{1}{3}\left(I_\alpha^{-1} + I_\alpha^{0} + I_\alpha^{+1}\right) \tag{17}$$

This can be deduced from the average over three orthogonal measurements on nonmagnetic samples with higher than monoclinic symmetry as sum over q or α. If the sample possesses a spherical symmetry a single measurement is enough.

The white line intensity for magnetic samples can be determined using linear polarized light and an angular average. When circularly polarized light is used, the sample must be magnetically saturated with an orientation parallel and antiparallel to the X-ray propagation direction (α) and one has to sum over both intensities. The orientation independent X-ray absorption intensity is directly proportional to the number of d states above the FERMI level, that is, the number of holes in the d band (cf. Fig. 20).[79]

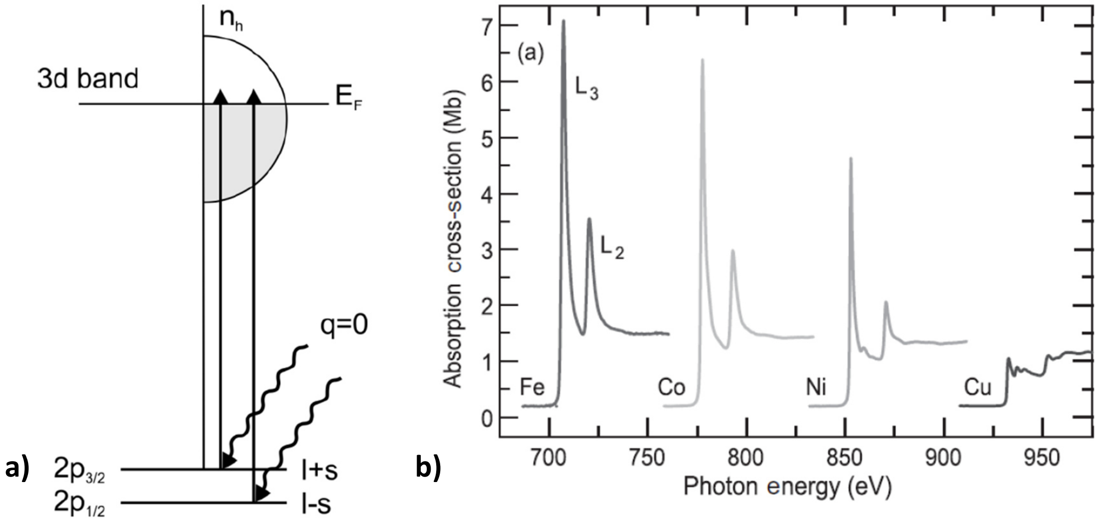

Figure 20:[79, 86, 87] Illustration of the intensity sum rule by **a)** a scheme of the absorption of linear polarized X-ray photons and **b)** normalized $L_{2,3}$ edge X-ray absorption spectra of the 3d metals iron, cobalt, nickel and copper.
The absorption intensity drops with increasing number of 3d electrons, that is, less holes in the valence band.

The white line intensity for a transition from a core (n, c)state to a valence state (n', L) with $c = L - 1$ is proportional to the number of unoccupied states in the valence shell N_h:

$$\langle I \rangle = C \cdot N_h \tag{18}$$

$$C = AR^2 \frac{L}{3(2L+1)}, \tag{19}$$

$$A = \frac{4\pi^2 \hbar\omega}{137}, \tag{20}$$

where R is the radial matrix element for the transition $n, c \rightarrow n', L$.

XMCD and sum rule analysis

If the intensity sum rule for the charge is considered using circularly polarized light, the X-ray absorption can be derived as spin dependent. This implicates the possibility to identify characteristics in the “spin-up” and “spin-down” holes in the valence orbitals by evaluating the differences in the X-ray absorption intensities and allows for the determination of magnetic moments.

The spin dependence in the X-ray absorption intensities can be explained by a two-step model (cf. Fig. 21):[87]

A) The circularly polarized X-ray photon is absorbed by an electron in the spin-orbit split initial ground state $|i\rangle$. For the $2p \rightarrow 3d$ transition ($L_{2,3}$ absorption edges) in e.g. transition metals, this corresponds to the $2p_{3/2}$ and the $2p_{1/2}$levels. The spin-orbit coupling of the ground state causes the angular momentum of the X-ray photon to be partially transferred to the spin of the excited electron, leading to its spin polarization. This spin polarization is opposite for the $2p_{3/2}$ and $2p_{1/2}$ levels, since the spin-orbit coupling is opposite as well (l + s and l - s). The quantization axis of the excited electron and the photon angular momentum are identical, parallel or antiparallel to the propagation direction of the X-rays.

B) The spin polarized electrons are excited into an exchange split valence shell with an odd number of electrons, thus uneven population of “spin-up” and “spin-down” electron holes. The electron holes serve as a detector for the spin polarized excited electrons. The maximum difference in the X-ray absorption (XMCD effect) can be observed if the spin moments of the valence electrons are aligned to the photon angular momentum which coincides with the X-ray propagation direction.

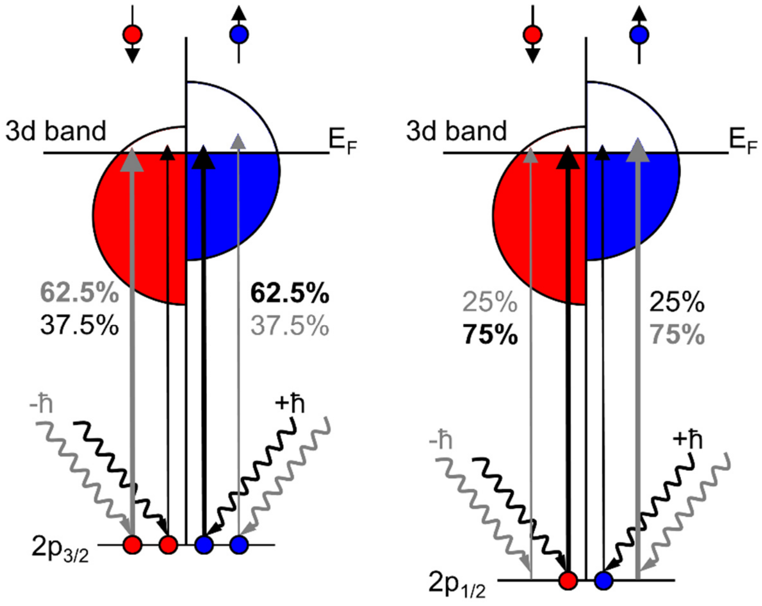

(a) **(b)**

Figure 21:[86, 87] Relative transition probabilities for “spin-up” (↑) and “spin-down” (↓) electrons from the spin orbit split 2p levels, i.e. $2p_{3/2}$ **(a)** and $2p_{1/2}$ **(b)** level upon excitation with circularly polarized photons with q = ± 1 (q = -1 = -ħ = transition marked in grey and q = +1 = +ħ = transitions marked in black). Transition probabilities for the excitation of spin up or spin down electrons switch when the photon helicity is reversed. Positive (q = +1) circularly polarized light predominantly excites spin up electrons at the L_3 edge ($2p_{3/2} \rightarrow 3d$) and at the L_2 edge ($2p_{1/2} \rightarrow 3d$), it mostly excites spin down electrons. The situation is reversed for negative (q = -1) circularly polarized photons.

The statistical weight of the different transition probabilities for a transition from an initial state $|a\rangle$. with the configuration $|c, m_c, m_s\rangle$ to a final state $|b\rangle$ with the configuration $|l, m_l, m_{s'}\rangle$ can be derived from the transition matrix elements, taking the dipole selection rules into consideration. According to Stöhr and Wu, the transition matrix elements can be expressed by:[88-90]

$$\langle n', l, m_l | P_{(1)}^{+1} | n, c, m_c \rangle = \sqrt{\frac{(c+m_c+2)(c+m_c+1)}{2(2c+3)(2c+1)}} R \tag{21}$$

$$\langle n', l, m_l | P_{(1)}^{-1} | n, c, m_c \rangle = \sqrt{\frac{(c-m_c+2)(c-m_c+1)}{2(2c+3)(2c+1)}} R \tag{22}$$

$$l = c + 1 \tag{23}$$

$n\ (n')$	main quantum number of the core (final) state
$c\ (l)$	orbital angular momentum quantum number of the core (final) state
$m_c\ (m_l)$	orbital magnetic quantum number of the core (final) state

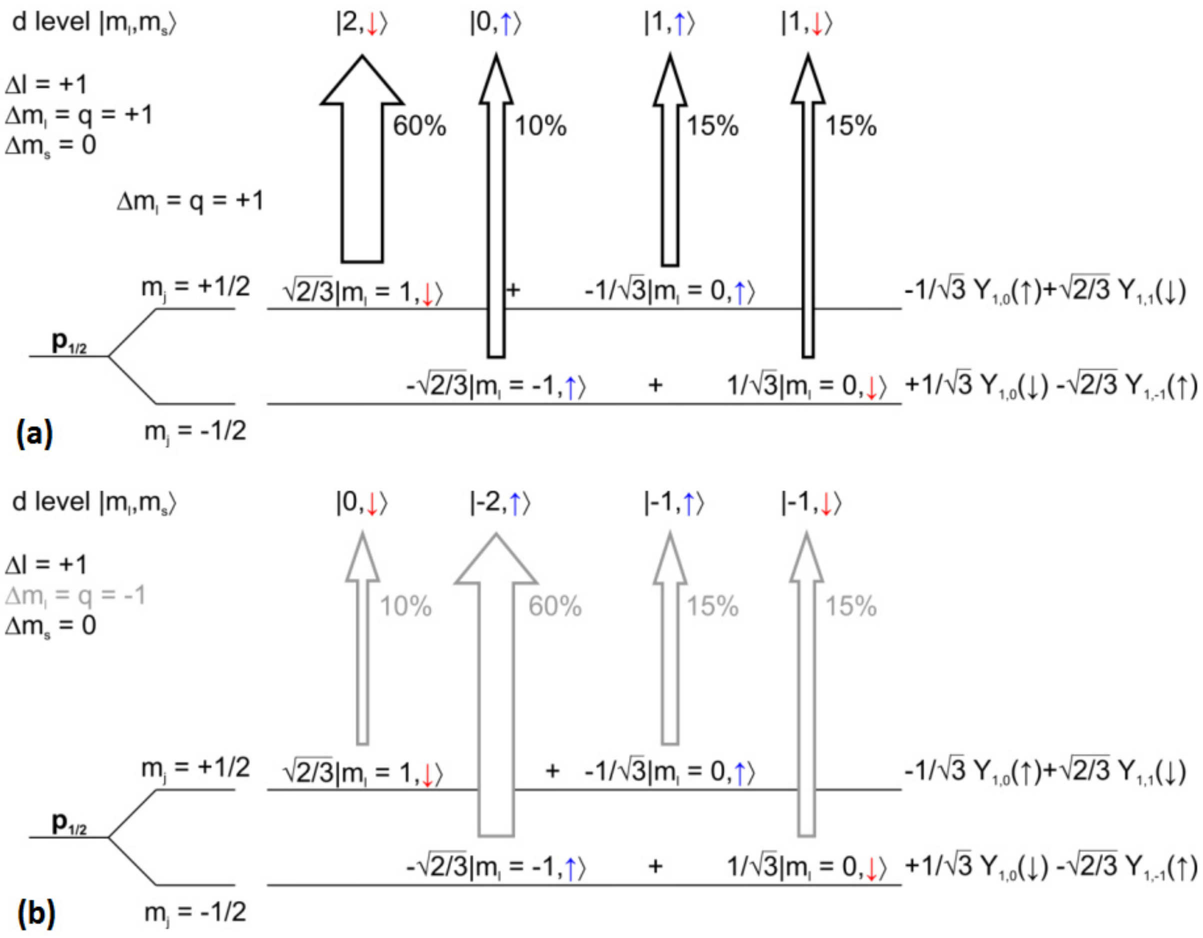

Figure 22:[86, 87] Transition probabilities from the different $m_j = \pm ½$ states (degenerated) of the $p_{1/2}$ spin orbit split level into final d states in a LS coupling scheme (modified from Ref [91]). The statistical weights of the individual transitions are given for the absorption of either a photon with angular momentum **(a)** q = +ħ or (**b**) q = -ħ. Thus, $\Delta m_l = +1$ for Fig. 22 **(a)** and $\Delta m_l = -1$ for Fig. 22 **(b).** ↑denotes spin up and ↓ spin down states. The representation of the electronic state in terms of spherical harmonics is given on the right.

The photon angular momentum is not completely transferred to the electron spin, instead some of it is transferred to the electron angular momentum. The angular momentum is as well sensed by the valence shell if the valence shell has an angular momentum $l \neq 0$. When a negative circularly polarized photon $(q = -1 = -\hbar)$ is absorbed, only transitions with $\Delta m_l = -1$ are allowed. The other way round, when a positive circularly polarized photon $(q = +1 = +\hbar)$ is absorbed only transitions with $\Delta m_l = +1$ are allowed. The dipole selection rules are illustrated in Fig. 23:

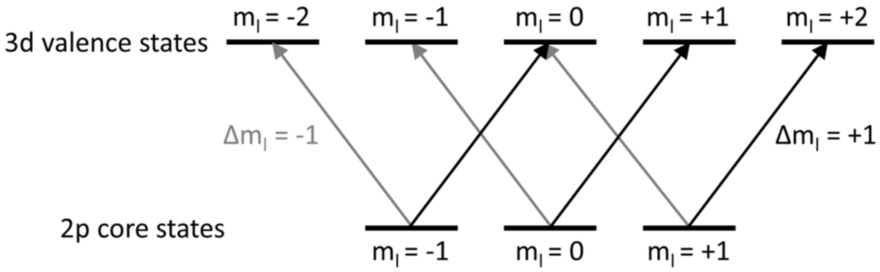

Figure 23: Sensitivity of the XMCD effect of orbital magnetism.[86, 87, 92]

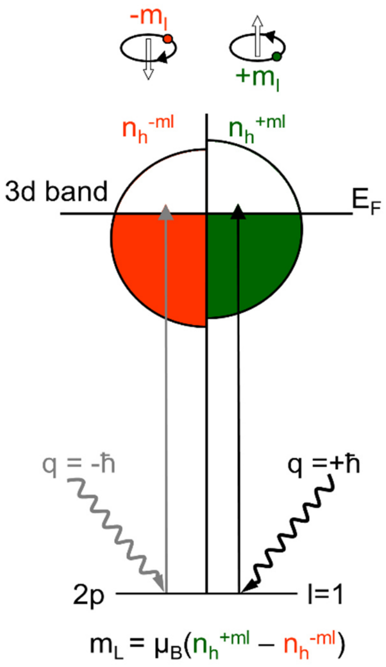

Figure 24:[86, 87] Probing of orbital angular momentum by XMCD spectroscopy. If the valence shell has an orbital angular momentum l ≠ 0, a net orbital angular momentum can arise if the m_L states are not equally occupied.

Due to the conservation of momentum, the angular momentum of the absorbed circular polarized X-ray photon is transferred to the excited electron in terms of different spin and orbital momentum degrees of freedom. This can be detected by a magnetic valence shell and results in different absorption intensities for positive and negative circularly polarized X-rays.

In the early 1990's, THOLE and CARRA derived the contributions of spin and orbital angular momenta to the XMCD effect.[93, 94] The so called "sum rules" give access to quantitative information about the expectation value of the spin $\langle S_z \rangle$ and orbital angular momentum $\langle L_z \rangle$. In the general formulation for a dipole transition $|c, l^n\rangle \rightarrow |c^{-1}, l^{n-1}\rangle$ from a ground (core) state with an orbital angular momentum c into an excited (valence) state with an orbital angular momentum l and n being the population and a quantization axis in z-direction, they read as:[92-95]

$$\frac{\int_{j_+ + j_-} (\mu^+ - \mu^-) d\omega}{\int_{j_+ + j_-} (\mu^+ + \mu^- + \mu^0) d\omega} = \frac{1}{2} \frac{c(c+1) - l(l+1) - 2}{l(l+1)(4l+2-n)} \langle L_z \rangle \tag{24}$$

for the expectation value of the orbital angular momentum and

$$\begin{aligned} \frac{\int_{j_+} (\mu^+ - \mu^-) d\omega - \left(\frac{c+1}{c}\right) \int_{j_-} (\mu^+ - \mu^-) d\omega}{\int_{j_+ + j_-} (\mu^+ + \mu^- + \mu^0) d\omega} &= \frac{l(l+1) - 2 - c(c+1)}{3c(4l+2-n)} \langle S_z \rangle \\ &+ \frac{l(l+1)[l(l+1) + 2c(c+1) + 4] - 3(c-1)^2(c+2)^2}{6lc(l+1)(4l+2-n)} \langle T_z \rangle \end{aligned} \tag{25}$$

for the expectation value of the spin with:

j_+, j_-	Transitions from spin orbit split levels
μ^+	XA spectrum recorded with positive circularly polarized
μ^-	XA spectrum recorded with negative circularly polarized
μ^0	XA spectrum recorded with linearly polarized light (q = 0)

In a more clearly, simplified expression, these formulas can be rewritten as:

$$\frac{\int_{j_+ + j_-} (\mu^+ - \mu^-) d\omega}{\int_{j_+ + j_-} (\mu^+ - \mu^- + \mu^0) d\omega} = a \frac{\langle L_z \rangle}{n_h} \tag{26}$$

and

$$\frac{-\left(\int_{j_+}(\mu^+ - \mu^-)d\omega - b\int_{j_-}(\mu^+ - \mu^-)d\omega\right)}{\int_{j_+ + j_-}(\mu^+ - \mu^- + \mu^0)d\omega} = \frac{c\langle S_z\rangle + d\langle T_z\rangle}{n_h} \tag{27}$$

with

n_h number of holes in the final state / shell (= $4l_f + 2 - n$)
a, b, c, d sum rule related prefactors

The quantization axis (z) coincides with the X-ray propagation direction and the magnetic field. The expectation value for the magnetic dipole term $\langle T_z\rangle$ describes an aspheric spin contribution in a non-cubic system. If there is an anisotropy in the distribution of the spins, that is, a spin asymmetry along the quantization axis, the magnetic dipole term may alter der spin magnetic moment by up to 20 % in anisotropic media.[96-98]

The integration limits j_+ and j_- for a $2p \rightarrow 3d$ transition ($c = 1, l = 2$; typical for first row transition metals) correspond to the L_3 and L_2 absorption edges. The magnetism of the f-electrons in rare earth compounds is usually studied at the transition $3d \rightarrow 4f$ ($M_{5,4}$ absorption edge). In general, if the orbital angular momentum of the initial state is l_i and of the final state is l_f, the sum rule related prefactors are summarized in Tab. 3.

Table 3: Sum rule related prefactors for different dipole transitions.[91]

l_i	l_f	a	b	c	d
s: 0	p: 1	1	-	-	-
p: 1	d: 2	1/2	2	2/3	7/3
d: 2	f: 3	1/3	3/2	2/3	2

Since usual X-ray absorption spectra are only recorded for negative (μ^-) and positive (μ^+) circularly polarized light, the XA spectrum of the linearly polarized light (μ^0) is unknown in most cases. However, for systems with cubic symmetry the denominator of the sum rules can be approximated by:[97, 99]

$$\mu^+ + \mu^- + \mu^0 \approx \mu^+ + \mu^- + \frac{(\mu^+ + \mu^-)}{2} = \frac{3}{2}(\mu^+ + \mu^-) \tag{28}$$

For non-cubic systems, the deviation is still quite low and the integral of eq. 28 remains a reasonable approximation.

The expectation values for the spin $\langle S_z \rangle$ and orbital angular momentum $\langle L_z \rangle$ are directly related to the spin m_s, orbital m_l and total magnetic moment m_J by the following relation:

$$m_S = -g_S \mu_B \langle S_z \rangle \tag{29}$$

$$m_L = -g_L \mu_B \langle L_z \rangle \tag{30}$$

$$m_J = m_S + m_L = -\mu_B(g_S\langle S_z \rangle - g_L\langle L_z \rangle) = -\mu_B(\langle L_z \rangle + 2\langle S_z \rangle) = -\mu_B g_J \langle J_z \rangle \tag{31}$$

g_S	g-factor of the electron spin $g_S = 2.0$
g_L	g-factor of the orbital momentum $g_L = 1.0$
g_J	g-factor of the total magnetic moment.
$\langle J_z \rangle$	expectation value of the total magnetic moment.

For a $2p \rightarrow 3d$ transition, (29) and (30) can be rewritten using equations (26) and (27):

$$m_S = -g_S \mu_B \frac{-\left(\int_{L_3}(\mu^+ - \mu^-)d\omega - 2\int_{L_2}(\mu^+ - \mu^-)d\omega\right)}{\frac{2}{3}\int_{L_3+L_2}(\mu^+ + \mu^- + \mu^0)d\omega} n_h - g_S \mu_B \frac{7}{2}\langle T_z \rangle \tag{32}$$

$$m_L = -g_L \mu_B \frac{\int_{L_3+L_2}(\mu^+ - \mu^-)d\omega}{\frac{1}{2}\int_{L_3+L_2}(\mu^+ + \mu^- + \mu^0)d\omega} n_h \tag{33}$$

When abbreviating the integrations as follows:

$$A = \int_{L_3}(\mu^+ - \mu^-)d\omega \tag{34}$$

$$B = \int_{L_2}(\mu^+ - \mu^-)d\omega \tag{35}$$

$$C = \frac{2}{3}\int_{L_3+L_2}(\mu^+ + \mu^- + \mu^0)d\omega \tag{36}$$

one may write:

$$m_S = g_S \mu_B \frac{(A-2B)}{C} n_h - g_S \mu_B \frac{7}{2} \langle T_z \rangle \tag{37}$$

$$m_L = -g_L \mu_B \frac{4}{3} \frac{A+B}{C} n_h \tag{38}$$

From the equations (32) and to(38) the ratio of orbital to spin magnetic moment can be derived for a $2p \rightarrow 3d$ transition:

$$\frac{m_L}{m_S} \approx \frac{\mu_B \langle L_z \rangle}{2\mu_B \langle S_z \rangle} = \frac{2}{3} \frac{\int_{L_3+L_2} (\mu^+ - \mu^-) d\omega}{\int_{L_3} (\mu^+ - \mu^-) d\omega - 2 \int_{L_2} (\mu^+ - \mu^-) d\omega} = \frac{2}{3} \frac{A+B}{A-2B} \tag{39}$$

The ratio $\langle L_z \rangle$ to $2\langle S_z \rangle + \langle T_z \rangle$ provides a contribution from the magnetic dipole operator. However, this contribution is neglected in the following since it can be expected to be small in the investigated systems and under the experimental conditions (< 5%, cf. chapters 3 and 4).[92, 100] The ratio m_L/m_s can be determined without knowing the number of electron holes n_h in the valence shell and the normalisation with the sum spectrum $\mu^+ + \mu^- + \mu^0$ and the incomplete polarization of the synchrotron radiation. Thus, some sources of errors from the applications of some rules vanish, making the determination of m_L/m_s more precise than the individual determination of m_L or m_s.[92]

Remarks on the application and correction of sum rules

The derivation of the sum rules is based on several approximations. The presented two-step model and the application of the sum rules have some requirements to fulfil.

- The dipole selection rules allow for transitions from a 2p ground state into both, the 4s and 3d states. The application of sum rules is only valid, if transition from 2p to 4s are negligible. For the $L_{3,2}$ absorption edges of 3d transition metals, the contribution is less than 5 % and can be removed by subtraction of a two-step function (cf. chapters 3 and 4).[92-94, 99, 101]

- The energy dependence of the radial matrix elements and spin orbit coupling constant is not taken into account. This happens if the electrons of the final states are bound weaker and more delocalized in comparison to final state excitations close to the absorption threshold.[97]
- The contribution of relativistic effects on the radial matrix elements should be negligible. This means that the radial matrix elements for the $l_i + ½$ and $l_i - ½$ excitations should be the same.
- The dipole approximation neglects higher terms in the series expansion. Higher terms e.g. the quadrupolar transition should have less spectral weight than the error bar.
- For the application of the spin sum rule, the L_3 and L_2 edges must be separable in energy, hence the spin orbit splitting must be sufficiently large. This includes spectral overlap and quantum mechanical mixing, that is a mixture of $l_i + ½$ and $l_i - ½$ excitations of the same energy induced by an additional interaction like the 2p – 3d Coulomb interaction.[102]

The deviation of the spin sum rule due to core-valence Coulomb interaction has not been quantified in the original derivation of the sum rule by CARRA.[100] This effect largely depends on the atomic species and its electron configuration. JO et al. have numerically investigated the deviation from the XMCD spin sum rule for selected 3d transition metal ions and trivalent 4f rare earth ions by atomic calculations taking into account the multipole electron-electron interaction. The deviations reach from about 7 % for Ni^{3+} to more than 30 % for Mn^{3+} for the 3d transition metal ions and from less than 1 % for Er^{3+} to 230 % for Sm^{3+} for the rare earth ions.[100, 103] The presented magnetic moments calculated by the spin sum rule in this work have been corrected as explained in the respective chapters.

Temperature and magnetic field dependence of magnetizations

The alignment (or magnetization) of samples providing a magnetic dipole and a respective magnetic moment with respect to the quantization axis (z) depends on the temperature and the external magnetic field strength. The quantization axis coincides with the axis of the external magnetic field. The degree of the alignment corresponds to the projection ($m_{S/L/J}^{(z)}$) of the intrinsic magnetic moment ($m_{S/L/J}$) onto the quantization axis. At 100 % alignment, the projection is equal to the intrinsic magnetic moment. Strong external magnetic fields improve the alignment whereas high temperatures decrease the alignment by thermal randomization (cf. Fig. 25).[87] The Brillouin functions (equations 40-42) describe the spin, orbital and total magnetizations depending on the temperature T and the magnetic field strength B.

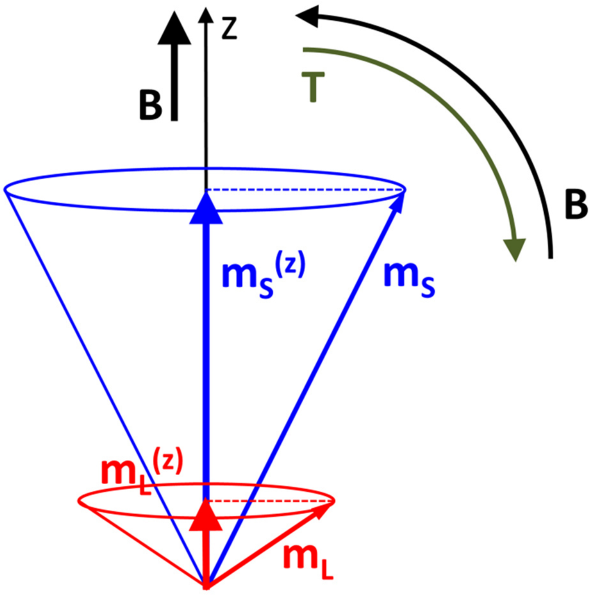

Figure 25:[87] Schematic depiction of the intrinsic spin (m_S) and orbital (m_L) magnetic moments and their projection (magnetizations) onto the quantization axis ($m_S^{(z)}$ and $m_L^{(z)}$). The influences of temperature and magnetic field strength on the alignment are indicated by the green and black arrow.

$$m_S^{(z)} = g_S \mu_B S \left(\frac{2S+1}{2S} \coth\left(\frac{2S+1}{2S} \frac{\mu_B g_S S B}{k_B T} \right) - \frac{1}{2S} \coth\left(\frac{1}{2S} \frac{\mu_B g_S S B}{k_B T} \right) \right) \tag{40}$$

$$m_L^{(z)} = g_L \mu_B L \left(\frac{2L+1}{2L} \coth\left(\frac{2L+1}{2L} \frac{\mu_B g_L L B}{k_B T} \right) - \frac{1}{2L} \coth\left(\frac{1}{2L} \frac{\mu_B g_L L B}{k_B T} \right) \right) \tag{41}$$

$$m_J^{(z)} = g_J \mu_B J \left(\frac{2J+1}{2J} \coth\left(\frac{2J+1}{2J} \frac{\mu_B g_J J B}{k_B T} \right) - \frac{1}{2J} \coth\left(\frac{1}{2J} \frac{\mu_B g_J J B}{k_B T} \right) \right) \tag{42}$$

$m_{S/L/J}^{(z)}$	projection of the spin/orbital/total intrinsic magnetic moment onto the quantization axis
S, L, J	total spin, orbital and total angular momentum, J = L + S
g_S	Landé-factor of the electron spin, $g_S = 2.0$
g_L	Landé-factor of the orbital magnetic moment, $g_L = 1.0$
g_J	Landé-factor of the total magnetic moment
B	magnetic field strength
T	temperature

The Brillouin functions allow for a scaling of experimental magnetizations at a given magnetic field and temperature to the projection at 0 K and infinite magnetic field equal to the intrinsic magnetic moments. Alternatively, the experimental magnetization can be utilized in order to determine the temperature of a system with a certain magnetic moment at a known magnetic field. The spin orbit coupling in the systems presented in this work, hence the coupling between spin (S) and orbital (L) angular momentum to the total angular momentum (J), exceeds the individual coupling of S or L to the external magnetic field.[33, 35, 104] Thus, considerations of this matter are confined to the total angular momentum.

Data Treatment

Due to the relatively small amount of metal ions in the investigated samples, the fragment ion intensity amounts only several percent of the parent ion signal intensity. An assignment of the fragment ion peaks was hardly possible, since the calibration of the time of flight mass spectrometer was sacrificed to the optimization of the fragment ion signal intensity. The polarization dependent XA spectra were recorded in an alternating scheme. For every polarization at a specific absorption edge, five to ten raw spectra were averaged. A detailed description of the Data Treatment can be read in the PhD thesis of Matthias Tombers.[87]

2.5 References

[1] J. Zeleny, "*Instability of Electrified Liquid Surfaces*", *Phys. Rev.*, **1917**, *10*, 1-6.

[2] M. Dole, L. L. Mack, R. L. Hines, R. C. Mobley, L. D. Ferguson, M. B. Alice, "*Molecular Beams of Macroions*", *J. Chem. Phys.*, **1968**, *49*, 2240-2249.

[3] J. B. Fenn, "*Electrospray Wings for Molecular Elephants (Nobel Lecture)*", *Angew. Chem. Int. Ed.*, **2003**, *42*, 3871-3894.

[4] J. B. Fenn, M. Mann, C. K. Meng, S. F. Wong, C. M. Whitehouse, "*Electrospray ionization–principles and practice*", *Mass Spectrom. Rev.*, **1990**, *9*, 37-70.

[5] M. Yamashita, J. B. Fenn, "*Negative ion production with the electrospray ion source*", *J. Phys. Chem.*, **1984**, *88*, 4671-4675.

[6] M. Yamashita, J. B. Fenn, "*Electrospray ion source. Another variation on the free-jet theme*", *J. Phys. Chem.*, **1984**, *88*, 4451-4459.

[7] D. A. Plattner, "*Electrospray mass spectrometry beyond analytical chemistry: studies of organometallic catalysis in the gas phase*", *Int. J. Mass Spectrom.*, **2001**, *207*, 125-144.

[8] A. Škríba, J. Schulz, J. Roithová, "*Monitoring of Reaction Intermediates in the Gas Phase: Ruthenium-Catalyzed C–C Coupling*", *Organometallics*, **2014**, *33*, 6868-6878.

[9] I. I. Stewart, "*Electrospray mass spectrometry: a tool for elemental speciation*", *Spectrochim. Acta, Part A*, **1999**, *54*, 1649-1695.

[10] K. L. Vikse, Z. Ahmadi, J. Scott McIndoe, "*The application of electrospray ionization mass spectrometry to homogeneous catalysis*", *Coord. Chem. Rev.*, **2014**, *279*, 96-114.

[11] G. T. T. Gibson, S. M. Mugo, R. D. Oleschuk, "*Nanoelectrospray emitters: Trends and perspective*", *Mass Spectrom. Rev.*, **2009**, *28*, 918-936.

[12] L. Konermann, E. Ahadi, A. D. Rodriguez, S. Vahidi, "*Unraveling the Mechanism of Electrospray Ionization*", *Anal. Chem.*, **2013**, *85*, 2-9.

[13] S. J. Gaskell, "*Erratum: Electrospray: Principles and Practice by Simon Gaskell, J. Mass Spectrom.32, 677 (1997)*", *J. Mass Spectrom.*, **1997**, *32*, 1378-1378.

[14] G. Taylor, "*Disintegration of Water Drops in an Electric Field*", *Proc. R. Soc. London, A*, **1964**, *280*, 383-397.

[15] M. S. Wilm, M. Mann, "*Electrospray and Taylor-Cone theory, Dole's beam of macromolecules at last?*", *Int. J. Mass Spectrom. Ion Processes*, **1994**, *136*, 167-180.

[16] J. V. Iribarne, B. A. Thomson, "*On the evaporation of small ions from charged droplets*", *J. Chem. Phys.*, **1976**, *64*, 2287-2294.

[17] B. A. Thomson, J. V. Iribarne, "*Field induced ion evaporation from liquid surfaces at atmospheric pressure*", *J. Chem. Phys.*, **1979**, *71*, 4451-4463.

[18] G. Schmelzeisen-Redeker, L. Bütfering, F. W. Röllgen, "*Desolvation of ions and molecules in thermospray mass spectrometry*", *Int. J. Mass Spectrom. Ion Processes*, **1989**, *90*, 139-150.

[19] A. T. Iavarone, E. R. Williams, "*Mechanism of Charging and Supercharging Molecules in Electrospray Ionization*", *J. Am. Chem. Soc.*, **2003**, *125*, 2319-2327.

[20] E. Ahadi, L. Konermann, "*Modeling the Behavior of Coarse-Grained Polymer Chains in Charged Water Droplets: Implications for the Mechanism of Electrospray Ionization*", *J. Phys. Chem. B*, **2012**, *116*, 104-112.

[21] L. Konermann, A. D. Rodriguez, J. Liu, "*On the Formation of Highly Charged Gaseous Ions from Unfolded Proteins by Electrospray Ionization*", *Anal. Chem.*, **2012**, *84*, 6798-6804.

[22] "*Bruker Daltonics: amaZon SL Series User Manual*".

[23] E. Dmitrii, S. Bari, H. Ronnie, L. Arkadiusz, H. Konstantin, Z.-B. Vicente, L. Tobias, I. Bernd von, S. Thomas, "*An intense electrospray ionization source for soft X-ray photoionization of gas phase protein ions*", *J. Phys. Conf. Ser.*, **2015**, *635*, 112083.

[24] N. R. Daly, "*Scintillation Type Mass Spectrometer Ion Detector*", *Rev. Sci. Instrum.*, **1960**, *31*, 264-267.

[25] C. Weil, M. Nappi, C. D. Cleven, H. Wollnik, R. G. Cooks, "*Multiparticle Simulation of Ion Injection into the Quadrupole Ion Trap Under the Influence of Helium Buffer Gas Using Short Injection Times and DC Pulse Potentials*", *Rapid Commun. Mass Spectrom.*, **1996**, *10*, 742-750.

[26] F. Menges, "*Structure and Reactivity of Isolated Mononuclear and Oligonuclear Metal Complexes*", **2013**.

[27] J. T. Lau, J. Rittmann, V. Zamudio-Bayer, M. Vogel, K. Hirsch, P. Klar, F. Lofink, T. Möller, B. v. Issendorff, "*Size Dependence of $L_{2,3}$ Branching Ratio and 2p Core-Hole Screening in X-Ray Absorption of Metal Clusters*", *Phys. Rev. Lett.*, **2008**, *101*, 153401.

[28] J. T. Lau, K. Hirsch, A. Langenberg, J. Probst, R. Richter, J. Rittmann, M. Vogel, V. Zamudio-Bayer, T. Möller, B. von Issendorff, "*Localized high spin states in transition-metal dimers: X-ray absorption spectroscopy study*", *Phys. Rev. B*, **2009**, *79*, 241102.

[29] J. T. Lau, K. Hirsch, P. Klar, A. Langenberg, F. Lofink, R. Richter, J. Rittmann, M. Vogel, V. Zamudio-Bayer, T. Möller, B. v. Issendorff, "*X-ray spectroscopy reveals high symmetry and electronic shell structure of transition-metal-doped silicon clusters*", *Phys. Rev. A*, **2009**, *79*, 053201.

[30] K. Hirsch, J. T. Lau, K. Ph, A. Langenberg, J. Probst, J. Rittmann, M. Vogel, V. Zamudio-Bayer, T. Möller, B. v. Issendorff, "*X-ray spectroscopy on size-selected clusters in an ion trap: from the molecular limit to bulk properties*", *J. Phys. B*, **2009**, *42*, 154029.

[31] J. T. Lau, M. Vogel, A. Langenberg, K. Hirsch, J. Rittmann, V. Zamudio-Bayer, T. Möller, B. v. Issendorff, "*Communication: Highest occupied molecular orbital–lowest unoccupied molecular orbital gaps of doped silicon clusters from core level spectroscopy*", *J. Chem. Phys.*, **2011**, *134*, 041102.

[32] K. Hirsch, V. Zamudio-Bayer, F. Ameseder, A. Langenberg, J. Rittmann, M. Vogel, T. Möller, B. v. Issendorff, J. T. Lau, "*2p X-ray Absorption of Free Transistion-Metal Cations Across the 3d Transition Elements: Calcium Through Copper*", *Phys. Rev. A*, **2012**, *85*, 062501.

[33] M. Niemeyer, K. Hirsch, V. Zamudio-Bayer, A. Langenberg, M. Vogel, M. Kossick, C. Ebrecht, K. Egashira, A. Terasaki, T. Möller, B. v. Issendorff, J. T. Lau, "*Spin Coupling and Orbital Angular Momentum Quenching in Free Iron Clusters*", *Phys. Rev. Lett.*, **2012**, *108*, 057201.

[34] V. Zamudio-Bayer, L. Leppert, K. Hirsch, A. Langenberg, J. Rittmann, M. Kossick, M. Vogel, R. Richter, A. Terasaki, T. Möller, B. v. Issendorff, S. Kümmel, J. T. Lau, "*Coordination-driven magnetic-to-nonmagnetic transition in manganese-doped silicon clusters*", *Phys. Rev. B*, **2013**, *88*, 115425.

[35] A. Langenberg, K. Hirsch, A. Ławicki, V. Zamudio-Bayer, M. Niemeyer, P. Chmiela, B. Langbehn, A. Terasaki, B. v. Issendorff, J. T. Lau, "*Spin and orbital magnetic moments of size-selected iron, cobalt, and nickel clusters*", *Phys. Rev. B*, **2014**, *90*, 184420.

[36] V. Zamudio-Bayer, K. Hirsch, A. Langenberg, M. Niemeyer, M. Vogel, A. Ławicki, A. Terasaki, J. T. Lau, B. von Issendorff, "*Maximum Spin Polarization in Chromium Dimer Cations as Demonstrated by X-ray Magnetic Circular Dichroism Spectroscopy*", *Angew. Chem. Int. Ed.*, **2015**, *54*, 4498-4501.

[37] K. Hirsch, V. Zamudio-Bayer, A. Langenberg, M. Niemeyer, B. Langbehn, T. Möller, A. Terasaki, B. v. Issendorff, J. T. Lau, "*Magnetic Moments of Chromium-Doped Gold Clusters: The Anderson Impurity Model in Finite Systems*", *Phys. Rev. Lett.*, **2015**, *114*, 087202.

[38] V. Zamudio-Bayer, R. Lindblad, C. Bülow, G. Leistner, A. Terasaki, B. v. Issendorff, J. T. Lau, "*Electronic ground state of* Ni_2^+", *J. Chem. Phys.*, **2016**, *145*, 194302.

[39] S. T. Akin, V. Zamudio-Bayer, K. Duanmu, G. Leistner, K. Hirsch, C. Bülow, A. Ławicki, A. Terasaki, B. v. Issendorff, D. G. Truhlar, J. T. Lau, M. A. Duncan, "*Size-Dependent Ligand Quenching of Ferromagnetism in* $Co_3(benzene)_N^+$ *Clusters Studied with X-ray Magnetic Circular Dichroism Spectroscopy*", *J. Phys. Chem. Lett.*, **2016**, *7*, 4568-4575.

[40] A. Langenberg, "*Magnetische Momente freier, massenselektierter Eisen-, Cobalt- und Nickelcluster*", PhD thesis thesis, **2013**.

[41] R. L. Byer, R. L. Herbst, in *Nonlinear Infrared Generation* (Ed.: Y. R. Shen), Springer Berlin Heidelberg, **1977**, pp. 81-137.

[42] J. A. Giordmaine, R. C. Miller, "*Tunable Coherent Parametric Oscillation in LiNbO3 at Optical Frequencies*", *Phys. Rev. Lett.*, **1965**, *14*, 973-976.

[43] W. R. Bosenberg, D. R. Guyer, "*Single-frequency optical parametric oscillator*", *Appl. Phys. Lett.*, **1992**, *61*, 387-389.

[44] W. R. Bosenberg, D. R. Guyer, "*Broadly tunable, single-frequency optical parametric frequency-conversion system*", *J. Opt. Soc. Am. B*, **1993**, *10*, 1716-1722.

[45] P. A. Franken, A. E. Hill, C. W. Peters, G. Weinreich, "*Generation of Optical Harmonics*", *Phys. Rev. Lett.*, **1961**, *7*, 118-119.

[46] M. Moser, "*Aufbau und Charakterisierung eines optischen parametrischen Verstärkers im nahen infraroten Spektralbereich*", Hochschule für angewandte Wissenschaften-FH München **2008**.

[47] M. Gerhards, "*High energy and narrow bandwidth mid IR nanosecond laser system*", *Opt. Commun.*, **2004**, *241*, 493-497.

[48] G. Margaritondo, "*A Primer in Synchrotron Radiation: Everything You Wanted to Know about SEX (Synchrotron Emission of X-rays) but Were Afraid to Ask*", *J. Synchrotron Radiat.*, **1995**, *2*, 148-154.

[49] W. Heiko, "*Recent advances in x-ray absorption spectroscopy*", *Reports on Progress in Physics*, **2004**, *67*, 2105.

[50] S. Sasaki, K. Kakuno, T. Takada, T. Shimada, K.-i. Yanagida, Y. Miyahara, "*Design of a new type of planar undulator for generating variably polarized radiation*", *Nucl. Instrum. Methods Phys. Res., Sect. A*, **1993**, *331*, 763-767.

[51] S. Sasaki, "*Analyses for a planar variably-polarizing undulator*", *Nucl. Instrum. Methods Phys. Res., Sect. A*, **1994**, *347*, 83-86.

[52] J. Bahrdt, W. Frentrup, A. Gaupp, M. Scheer, W. Gudat, G. Ingold, S. Sasaki, "*A quasi-periodic hybrid undulator at BESSY II*", *Nucl. Instrum. Methods Phys. Res., Sect. A*, **2001**, *467–468, Part 1*, 130-133.

[53] J. Bahrdt, W. Frentrup, A. Gaupp, M. Scheer, W. Gudat, G. Ingold, S. Sasaki, "*Elliptically polarizing insertion devices at BESSY II*", *Nucl. Instrum. Methods Phys. Res., Sect. A*, **2001**, *467–468, Part 1*, 21-29.

[54] https://www.helmholtz-berlin.de/pubbin/igama_output?modus=einzel&sprache=en&gid=1927.

[55] N. C. Polfer, "*Infrared multiple photon dissociation spectroscopy of trapped ions*", *Chem. Soc. Rev.*, **2011**, *40*, 2211-2221.

[56] D. Schröder, H. Schwarz, P. Milko, J. Roithová, "*Dissociation Routes of Protonated Toluene Probed by Infrared Spectroscopy in the Gas Phase*", *J. Phys. Chem. A*, **2006**, *110*, 8346-8353.

[57] A. Simon, C. Joblin, N. Polfer, J. Oomens, "*Infrared Spectroscopy of $[XFeC_{24}H_{12}]^+$ ($X = C_5H_5$, $C_5(CH_3)_5$) Complexes in the Gas Phase: Experimental and Computational Studies of Astrophysical Interest*", *J. Phys. Chem. A*, **2008**, *112*, 8551-8560.

[58] J. Roithová, "*Characterization of reaction intermediates by ion spectroscopy*", *Chem. Soc. Rev.*, **2012**, *41*, 547-559.

[59] E. R. Grant, P. A. Schulz, A. S. Sudbo, Y. R. Shen, Y. T. Lee, "*Is Multiphoton Dissociation of Molecules a Statistical Thermal Process?*", *Phys. Rev. Lett.*, **1978**, *40*, 115-118.

[60] P. W. Atkins, J. De Paula, "*Physikalische Chemie*", John Wiley & Sons, **2001**.

[61] N. R. Walker, R. S. Walters, M. K. Tsai, K. D. Jordan, M. A. Duncan, "*Infrared Photodissociation Spectroscopy of $Mg^+(H_2O)Ar_N$ Complexes: Isomers in Progressive Microsolvation*", *J. Phys. Chem. A*, **2005**, *109*, 7057-7067.

[62] Y. Nosenko, F. Menges, C. Riehn, G. Niedner-Schatteburg, "*Investigation by two-color IR dissociation spectroscopy of Hoogsteen-type binding in a metalated nucleobase pair mimic*", *Phys. Chem. Chem. Phys.*, **2013**, *15*, 8171-8178.

[63] K. Capelle, "*A bird's-eye view of density-functional theory*", *Braz. J. Phys.*, **2006**, *36*, 1318-1343.

[64] N. S. Ostlund, A. Szabo, "*Modern quantum chemistry: introduction to advanced electronic structure theory*", Dover Publications Inc New edition edn, **1996**.

[65] W. Kohn, A. D. Becke, R. G. Parr, "*Density Functional Theory of Electronic Structure*", *J. Phys. Chem.*, **1996**, *100*, 12974-12980.

[66] R. G. Parr, W. Yang, "*Density-functional theory of the electronic structure of molecules*", *Annu. Rev. Phys. Chem.*, **1995**, *46*, 701-728.

[67] W. Koch, M. C. Holthausen, "*A chemist's guide to density functional theory*", John Wiley & Sons, **2015**.

[68] L. H. Thomas, in *Mathematical Proceedings of the Cambridge Philosophical Society, Vol. 23*, Cambridge Univ Press, **1927**, pp. 542-548.

[69] E. Fermi, "*Eine statistische Methode zur Bestimmung einiger Eigenschaften des Atoms und ihre Anwendung auf die Theorie des periodischen Systems der Elemente*", *Z. Phys.*, **1928**, *48*, 73-79.

[70] T. Ziegler, "*Approximate density functional theory as a practical tool in molecular energetics and dynamics*", *Chem. Rev.*, **1991**, *91*, 651-667.

[71] E. Teller, "*On the Stability of Molecules in the Thomas-Fermi Theory*", *Rev. Mod. Phys.*, **1962**, *34*, 627-631.

[72] P. Hohenberg, W. Kohn, "*Inhomogeneous Electron Gas*", *Phys. Rev.*, **1964**, *136*, B864-B871.

[73] W. Kohn, L. J. Sham, "*Self-Consistent Equations Including Exchange and Correlation Effects*", *Phys. Rev.*, **1965**, *140*, A1133-A1138.

[74] A. D. Becke, "*Density-functional thermochemistry. III. The role of exact exchange*", *J. Chem. Phys.*, **1993**, *98*, 5648-5652.

[75] A. D. Becke, "*A new mixing of Hartree–Fock and local density-functional theories*", *J. Chem. Phys.*, **1993**, *98*, 1372-1377.

[76] J. P. Perdew, J. A. Chevary, S. H. Vosko, K. A. Jackson, M. R. Pederson, D. J. Singh, C. Fiolhais, "*Atoms, molecules, solids, and surfaces: Applications of the generalized gradient approximation for exchange and correlation*", *Phys. Rev. B*, **1992**, *46*, 6671-6687.

[77] M. J. Frisch, G. W. Trucks, H. B. Schlegel, G. E. Scuseria, M. A. Robb, J. R. Cheeseman, G. Scalmani, V. Barone, G. A. Petersson, H. Nakatsuji, X. Li, M. Caricato, A. Marenich, J. Bloino, B. G. Janesko, R. Gomperts, B. Menucci, H. P. Hratchian, J. V. Ortiz, A. F. Izmaylov, J. L. Sonnenberg, D. Williams-Young, F. Ding, F. Lipparini, F. Egidi, J. Goings, B. Peng, A. Petrone, T. Henderson, D. Ranasinghe, V. G. Zakrzewski, J. Gao, N. Rega, G. Zheng, W. Liang, M. Hada, M. Ehara, K. Toyota, R. Fukuda, J. Hasegawa, M. Ishida, T. Nakajima, Y. Honda, O. Kitao, H. Nakai, T. Vreven, K. Throssel, J. A. Montgomery, J. E. Peralta, F. Ogliaro, M. Bearpark, J. J. Heyd, E. Brothers, K. N. Kudin, V. N. Staroverov, T. Keith, R. Kobayashi, J. Normand, K. Raghavachari, A. Rendell, J. C. Burant, S. S. Iyengar, J. Tomasi, M. Cossi, J. M. Millam, M. Klene, C. Adamo, R. Cammi, J. W. Ochterski, R. L. Martin, K. Morokuma, O. Farkas, Fores, "*GAUSSIAN09, REVISION D.01, GAUSSIAN, INC., WALLINGFORD, CT*", *University of Minnesota, Minneapolis*, **2009**.

[78] P. A. M. Dirac, "*THE QUANTUM THEORY OF THE EMISSION AND ABSORPTION OF RADIATION*", *Proc. R. Soc. London, A*, **1927**, *114*, 243-265.

[79] J. Stöhr, H. C. Siegmann, "*MAGNETISM*", *Solid-State Sciences. Springer, Berlin, Heidelberg*, **2006**, *5*.

[80] L. I. Schiff, "*QUANTUM MECHANICS 3RD*", *New York: McGraw-Hill*, **1968**, 61-62.

[81] F. Mandl, G. Shaw, "*QUANTUM FIELD THEORY*", John Wiley & Sons, **2010**.

[82] J. Als-Nielsen, D. McMorrow, "*ELEMENTS OF MODERN X-RAY PHYSICS*", John Wiley & Sons, **2011**.

[83] H. A. Kramers, W. Heisenberg, "*ÜBER DIE STREUUNG VON STRAHLUNG DURCH ATOME*", *Z. Phys.*, **1925**, *31*, 681-708.

[84] B. W. Shore, D. H. Menzel, "*PRINCIPLES OF ATOMIC SPECTRA*", John Wiley & Sons Ltd., New York, **1968**.

[85] R. D. Cowan, "*THE THEORY OF ATOMIC STRUCTURE AND SPECTRA*", Univ of California Press, **1981**.

[86] J. Meyer, "*SPIN AND ORBITAL CONTRIBUTIONS TO THE MAGNETIC MOMENT OF ISOLATED TRANSITION METAL CLUSTERS AND COMPLEXES*", **2014**.

[87] M. Tombers, "*SPIN AND ORBITAL MAGNETIC MOMENTS OF ISOLATED SINGLE MOLECULE MAGNETS AND TRANSITION METAL CLUSTERS*", **2015**.

[88] T. Funk, A. Deb, S. J. George, H. Wang, S. P. Cramer, "*X-RAY MAGNETIC CIRCULAR DICHROISM—A HIGH ENERGY PROBE OF MAGNETIC PROPERTIES*", *Coord. Chem. Rev.*, **2005**, *249*, 3-30.

[89] J. Stöhr, Y. Wu, in *New Directions in Research with Third-Generation Soft X-Ray Synchrotron Radiation Sources* (Eds.: A. S. Schlachter, F. J. Wuilleumier), Springer Netherlands, Dordrecht, **1994**, pp. 221-250.

[90] H. A. Bethe, E. E. Salpeter, "*QUANTUM MECHANICS OF ONE-AND TWO-ELECTRON ATOMS*", Springer Science & Business Media, **2012**.

[91] G. Schütz, E. Goering, H. Stoll, in *Handbook of Magnetism and Advanced Magnetic Materials*, John Wiley & Sons, Ltd, **2007**.

[92] J. T. Lau, "*MAGNETISCHE EIGENSCHAFTEN KLEINER MASSENSEPARIERTER ÜBERGANGSMETALL-CLUSTER*", **2002**.

[93] B. T. Thole, P. Carra, F. Sette, G. van der Laan, "*X-RAY CIRCULAR DICHROISM AS A PROBE OF ORBITAL MAGNETIZATION*", *Phys. Rev. Lett.*, **1992**, *68*, 1943-1946.

[94] P. Carra, B. T. Thole, M. Altarelli, X. Wang, "*X-RAY CIRCULAR DICHROISM AND LOCAL MAGNETIC FIELDS*", *Phys. Rev. Lett.*, **1993**, *70*, 694-697.

[95] H. Ebert, G. Schütz, in *Lecture Notes in Physics, Berlin Springer Verlag, Vol. 466*, **1996**.

[96] O. Šipr, J. Minár, H. Ebert, "*ON THE IMPORTANCE OF THE MAGNETIC DIPOLE TERM T Z IN ANALYZING X-RAY MAGNETIC CIRCULAR DICHROISM SPECTRA OF CLUSTERS*", *EPL*, **2009**, *87*, 67007.

[97] R. Wu, A. J. Freeman, "*LIMITATION OF THE MAGNETIC-CIRCULAR-DICHROISM SPIN SUM RULE FOR TRANSITION METALS AND IMPORTANCE OF THE MAGNETIC DIPOLE TERM*", *Phys. Rev. Lett.*, **1994**, *73*, 1994-1997.

[98] J. Stöhr, H. König, "*DETERMINATION OF SPIN- AND ORBITAL-MOMENT ANISOTROPIES IN TRANSITION METALS BY ANGLE-DEPENDENT X-RAY MAGNETIC CIRCULAR DICHROISM*", *Phys. Rev. Lett.*, **1995**, *75*, 3748-3751.

[99] C. T. Chen, Y. U. Idzerda, H. J. Lin, N. V. Smith, G. Meigs, E. Chaban, G. H. Ho, E. Pellegrin, F. Sette, "*EXPERIMENTAL CONFIRMATION OF THE X-RAY MAGNETIC CIRCULAR DICHROISM SUM RULES FOR IRON AND COBALT*", *Phys. Rev. Lett.*, **1995**, *75*, 152-155.

[100] Y. Teramura, A. Tanaka, T. Jo, "*EFFECT OF COULOMB INTERACTION ON THE X-RAY MAGNETIC CIRCULAR DICHROISM SPIN SUM RULE IN 3 D TRANSITION ELEMENTS*", *Journal of the Physical Society of Japan*, **1996**, *65*, 1053-1055.

[101] M. Altarelli, "*SUM RULES FOR X-RAY MAGNETIC CIRCULAR DICHROISM*", *Nuovo Cimento D*, **1998**, *20*, 1067-1073.

[102] G. van der Laan, "*SUM RULE PRACTICE*", *J. Synchrotron Radiat.*, **1999**, *6*, 694-695.

[103] Y. Teramura, A. Tanaka, B. T. Thole, T. Jo, "*EFFECT OF COULOMB INTERACTION ON THE X-RAY MAGNETIC CIRCULAR DICHROISM SPIN SUM RULE IN RARE EARTHS*", *J. Phys. Soc. Jpn.*, **1996**, *65*, 3056-3059.

[104] K. Fauth, B. Münzing, "*UNTERDRÜCKTER IMPULS*", *Phys. J.*, **2012**, *11*, 22.

3 Intrinsic Magnetism of Hetero-Bimetallic 3*d*-4*f* Complexes by XMCD Spectroscopy

Joachim M. Hewer[a], Matthias Tombers[a], Johannes Lang[a], Sebastian Schmitt[f], Yanhua Lan[f], Annie K. Powell[f,g], Vicente Zamudio-Bayer[b], J. Tobias Lau[b], Bernd von Issendorff[c], Akira Terasaki[d], Thomas Schlathölter[e], Ronnie Hoekstra[e], Asamanjoy Bhunia[f], Munendra Yadav[f], Ravi Yadav[f], Peter W. Roesky[f], and Gereon Niedner-Schatteburg[a]

(a) Fachbereich Chemie und Forschungszentrum OPTIMAS, Kaiserslautern, Germany
(b) Institut für Methoden und Instrumentierung der Forschung mit Synchrotronstrahlung, Helmholtz-Zentrum Berlin für Materialien und Energie, Berlin, Germany
(c) Physikalisches Institut, Universität Freiburg, Germany
(d) Department of Chemistry, Kyushu University, Fukuoka, Japan
(e) Zernike Institute for Advanced Materials, University of Groningen, Groningen, The Netherlands
(f) Institut für Anorganische Chemie, Karlsruher Institut für Technologie, Karlsruhe, Germany
(g) Institute of Nanotechnology, Karlsruhe Institute of Technology, Germany

3.1 Preamble

The following chapter is prepared as a manuscript for publication. I conducted the XMCD experiments, data evaluation and the simulations. I received experimental support by Matthias Tombers and Johannes Lang and Vicente Zamudio-Bayer. Asamanjoy Bhunia, Munendra Yadav and Ravi Yadav synthesized the samples in the group of Peter W. Roesky. Sebastian Schmitt and Yanhua Lan conducted the SQUID measurements in the group of Annie Powell. Tobias Lau, Bernd von Issendorf and Akira Terasaki operate the NanoCluster Trap experimental setup at the BESSY II synchrotron. Thomas Schlathölter and Ronnie Hoekstra provided the Electrospray Ionization (ESI). I wrote the manuscript and revised it with the help of Matthias Tombers, Peter W. Roesky, Annie K. Powell and Gereon Niedner-Schatteburg.

3.2 Abstract

We report polarization dependent gas phase X-ray absorption (XA) spectra of hetero-bimetallic 3*d*-4*f* complex ions in terms of X-ray magnetic circular dichroism (XMCD) spectroscopy. The magnetic coupling of the metal centers of trimetallic [Mn_2Ln] –type complexes (Ln = Nd, Eu, Gd, Dy, Lu) is very weak. The element selectivity of the XMCD technique in combination with the sum rule analysis allows for decomposition of the total magnetic moments into its individual parts, that is, spin and orbital angular momentum of the respective metal ion. The consequences of this are checked through variation of the incorporated lanthanide ion. The findings are compared to bulk SQUID magnetometry and are in very good agreement. The experimental magnetic moments are analyzed by temperature dependent Brillouin functions to enable a temperature estimation of the investigated complex ions in the gas phase. The temperature findings are in accordance to similar experiments on metal clusters.

3.3 Introduction

Molecular magnetism especially in the so called single molecule magnets (SMMs) has become a growing field of research since the discovery of the archetypal manganese acetate coordination cluster [$Mn_{12}O_{12}(OAc)_{16}(H_2O)_4$] in the early 1980s, and the subsequent discovery of its magnetic bistability or SMM behavior. Potential applications for SMMs include quantum computing and information storage.[1-9] A large number of mono- and polynuclear metal complexes with manifold molecular architectures have been reported. [6, 10-16] Much effort is currently spent on the design of heterometallic SMMs that combine 3*d* transition metal ions and 4*f* lanthanide ions.[17-22] The objective is the combination of high spin ground states by the 3*d* ions and large single-ion anisotropy by the 4*f* ions at the same time.[23]

Characterization of the aforementioned complexes is usually performed inter alia by means of SQUID magnetometry in ac and dc mode, EPR, NMR, µSR, PND, INS.[10] Besides this, the synchrotron based techniques e.g. X-ray absorption spectroscopy (XAS) with circularly polarized light have been used thoroughly in molecular magnetism due to their unique capability to obtain element specific magnetic information, as well as the separation of spin and orbital angular momenta.[24-30] The experiments are in general carried out on solid crystals, diluted powder samples, or surface deposited molecules. The determined magnetic moments and e.g. the anisotropy energies are ascribed to the intrinsic properties of the isolated molecules. However, the environment of the molecules can have an influence. This can be observed for surface deposited molecules, where charge transfer from the surface to the molecule may lead to a partial reduction of the metal ions and therefore to perturbed magnetic properties.[31, 32]

In previous work, gas phase X-ray magnetic circular dichroism (XMCD) spectroscopy on trapped and cooled metal cluster ions has been demonstrated as a valuable tool to characterize the magnetic properties of pure metal clusters, alloyed clusters and metal cluster adsorbates since any perturbation due to crystal lattice, substrate-surface interaction, solvation effects etc. can be avoided.[33-45] The comparison of spin and orbital magnetic moments of small clusters or nanoparticles with their bulk values shows, that the per-atom magnetic moments for clusters can be significantly higher.[33, 39]

In this work, we use XMCD spectroscopy to characterize the magnetic properties of a set of five structurally identical 3*d*-4*f* bimetallic complexes of the [Mn_2Ln]-type where we can vary the lanthanide ion to give Ln = Nd, Eu, Gd, Dy, Lu (Fig. 1). We study these in detail for the first time in the gas phase and can compare the results to those from standard bulk magnetometry. In addition, we look for a benchmark for future gas phase characterization of magnetic properties of interesting magnetic compounds like single-molecule magnets.

The [Mn_2Ln]-core of the compounds is stabilized using the Schiff base 2,2'-{[(2-aminoethyl)imino]bis[2,1-ethanediyl-nitriloethylidyne]}bis-2-hydroxy-benzoic acid (H_4L) as proligand. This proligand has three potential coordination pockets, which enable the coordination of one or three metal ions allowing for the possible formation of mono- and tri-nuclear complexes. Within this concept, we recently published the trinuclear mixed 3*d*-4*f* complex $(NHEt_3)_2[Dy\{Mn(L)\}_2](ClO_4)\cdot 2(H_2O)$ (abbreviated as [Mn_2Dy]; Fig. 1).[46, 47] Herein, we also report the synthesis and characterization of the analogues Nd, Eu, Gd, and Lu compounds (Fig. 1).

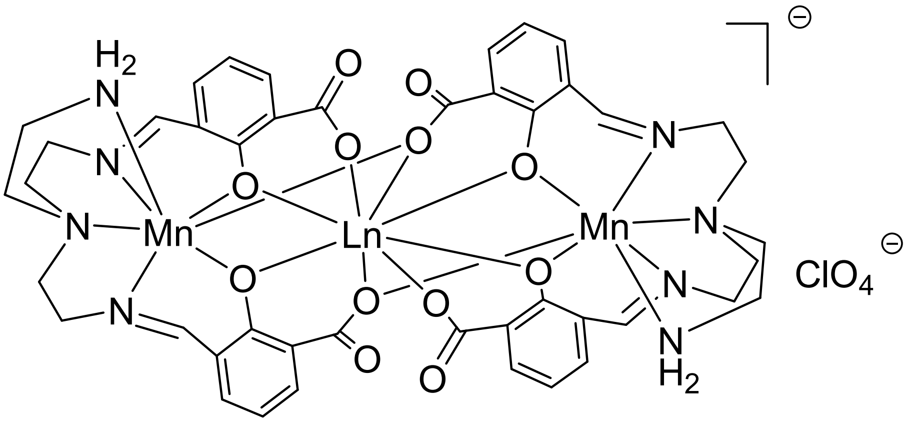

2 $HNEt_3^{\oplus}$

Ln = Nd, Eu, Gd, Dy, Lu

Figure 1: [Mn_2Ln]-type complexes.[46]

3.4 Experimental methods and setup

Recording XMCD spectra of isolated complexes

The presented polarization dependent X-ray Absorption (XA) spectra were recorded at the NanoCluster Trap which is connected to the UE52-PGM soft X-ray beamline at the BESSY II synchrotron facility of the Helmholtz-Zentrum Berlin. The NanoCluster Trap is a custom built mass spectrometer to record Total Ion Yield (TIY) gas phase XA spectra.[38, 39, 43] For our experiments we used a custom built Electro Spray Ionization (ESI) source to transfer our multi metal complexes into the gas phase.[41]

The samples for our gas phase measurements were prepared as a solution in acetonitrile (CH_3CN) at a concentration of approx. 10^{-3} mol/L. The investigated cationic species [$C_{44}H_{46}N_8O_{12}LnMn_2$]$^+$ (abbreviated as[Mn_2Ln]($H)_2^+$) are formed out of the trimetallic anion by protonation of two carboxylic groups coordinated to the central lanthanide ion during the ESI process.

The cation of interest ([Mn_2Ln]($H)_2^+$)) is mass selected in a linear quadrupole mass filter (Extrel, 40 – 4000 amu). The ions are guided into and stored in a linear quadrupole ion trap which is located within the high field region (5 T) of a superconducting solenoid. The trap is operated at frequencies between 2 and 4 MHz depending on the mass of the investigated ions. The linear quadrupole ion trap is cooled down to temperatures < 4 K by evaporative liquid He cooling. The ions are cooled down by collisional cooling in the vacuum chamber at a constant He backing pressure in the range of 10^{-6} to 10^{-7} mbar. The ions are thermalized at a somewhat higher temperature of approx. 10 – 15 K caused by radio frequency (RF) heating caused by the ion trap operation.[39] The trap is filled by a constant ion current from the source. The ions are ejected from the trap into the time of flight (TOF) mass spectrometer at a frequency of approx. 100 Hz. The XA is recorded by TIY spectroscopy whereas the ions are irradiated by the X-rays for 10 – 15 s at a fixed photon energy.[34, 35, 48, 49] A GaAsP diode records the X-ray intensity coming from the undulator beamline which is used for normalization of the XA spectra to the photon flux. The spectra at the Mn $L_{2,3}$ absorption edge were recorded with an exit slit size of 200 µm and a corresponding spectral resolution of ~200 meV. The spectra at the lanthanide $M_{4,5}$ absorption edges were recorded with an exit slit size of 500 µm and a corresponding spectral resolution of ~2.5 eV. The fragment intensity amounts to only a small fraction of the parent ion intensity. The XA spectra were alternately taken for left (negative) and right handed (positive) circularly polarized light.

Sum rule analysis of XMCD effects

The so called sum rules link the spectral intensities of the XA spectra of different photon helicity to the projection of the spin and orbital magnetizations of a sample.[50-53] The recorded XMCD spectra were analyzed in terms of sum rule analysis:

$$m_S^{(z)} = g_S \mu_B \frac{A - bB}{c\frac{3}{2}C} n_h - g_S \mu_B \frac{d}{c} \langle T_Z \rangle$$

$$m_L^{(z)} = -g_L \mu_B \frac{A + B}{a\frac{3}{2}C} n_h$$

where n_h is the number of electron holes in the final state, g_S and g_L the g-factors for the electron spin and orbital angular momentum ($g_S = 2.0$, $g_L = 1.0$), μ_B the Bohr magneton and *a*,*b*,*c* and *d* are sum rule related prefactors. In this work, we assume Mn^{2+} and Ln^{3+} to be in an $3d^5$ and $4f^n$ high spin state ($n = 3, 6, 7, 9$ for Ln = Nd, Eu, Gd, Dy, respectively). The Lu $M_{4,5}$ absorption edge was not measured for the $[Mn_2Lu](H)_2^+$ compound, due to the minor photon flux in this energy region. We chose the number of unoccupied valence orbitals to be $n_h = 5$ for Mn^{2+} and $n_h = 11, 8, 7$, or 5 for Nd^{3+}, Eu^{3+}, Gd^{3+} and Dy^{3+}, respectively. The prefactors *a*,*b*,*c* and *d* are 1/2, 2, 2/3, and 7/3 for the Mn $L_{3,2}$ absorption edges and 1/3, 3/2, 2/3, and 2 for the Ln $M_{5,4}$ absorption edges.[54]

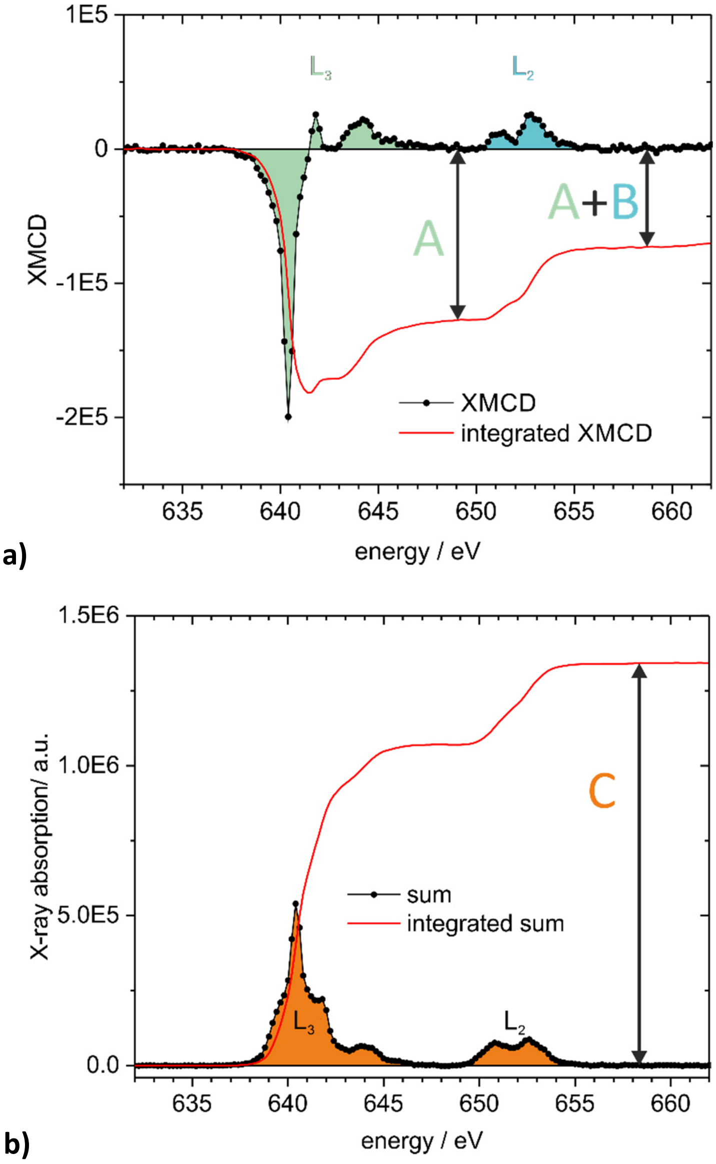

Figure 2: a) XMCD spectrum and the integrated XMCD intensity for the Mn $L_{3,2}$ absorption edges of the $[Mn_2Eu](H)_2^+$ ion. The Integral over the L_3 edge is labeled **A**, the integral over the L_2 edge is labeled **B**. **b)** Sum of the XA spectra for right and left handed circular polarity and its integral of the $[Mn_2Eu](H)_2^+$ ion. The integral over the L_3 and L_2 absorption edge is labeled **C**. Note, that the XAS at the respective lanthanide M_5 and M_4 absorption edges are considered for the lanthanides' local magnetizations.

The integrals **A**, **B** and **C** are extracted from the XMCD spectrum (difference spectrum of XAS with different helicities) and the sum spectrum (sum of the XAS with different helicities) at the manganese $L_{3,2}$ and the lanthanide $M_{5,4}$ absorption edges, respectively (cf. Fig. 2). A two-step function is subtracted from the XA sum spectra to eliminate the non-resonant absorption. We follow the procedure described by Chen at al. (cf. Fig. S6).[50] Sum rule analysis allows us to extract the projection ($m_S^{(z)}$ and $m_L^{(z)}$) of the intrinsic spin and orbital magnetic moments (m_S and m_L) onto the quantization axis. In the following, $m_S^{(z)}$ and $m_L^{(z)}$ are called spin and orbital magnetization. The quantization axis coincides with the magnetic field and the X-ray propagation direction.

Correction factors:

The sum rules only apply to transitions between well-defined shells. For the manganese ions we consider the transition from the 2p core state to a 3*d* valence state, for the lanthanide ions we consider the transition from the 3*d* core state to a 4*f* valence state. The valence states are not always separated, even if they appear so. This leads to inaccuracies in the magnetic moments calculated by the sum rules, particularly for the spin sum rule.[55] The imprecision of the sum rules has been reviewed in many publications.[55-63] Teramura *et al*. have introduced correction factors for the spin sum rule based on calculations on an atomic model, taking into account the Coulomb interaction in the $L_{2,3}/M_{4,5}$ absorption and the expectation value for the magnetic dipole operator $<T_z>$, which is not accessible in our XMCD experiment.[59-64] The presented magnetizations in this work are corrected by the suggested procedure of Teramura (cf. Tabs. S1, S2), for the uncorrected data see supplement (Figs. S8, S9, Tab. S3, S4).

Bulk phase Magnetometry

The bulk phase magnetometry measurements were conducted using a Quantum Design SQUID magnetometer MPMS. The magnetometer works in a temperature range between 1.8 and 400 K for dc applied fields ranging from -70 to +70 kOe. Measurements were performed on the polycrystalline samples dispersed in Apeizon grease. The magnetic data were corrected for the sample holder and the diamagnetic contributions estimated from Pascal constants.[46]

General Procedure for the Synthesis of Complexes $(NHEt_3)_2[Dy\{Mn(L)\}_2](ClO_4)\cdot 2(H_2O)$ [47]

General considerations: Elemental analyses were carried out with an Elementar vario EL III analyzer. IR spectra were obtained on a Bruker IFS 113v FTIR spectrometer. 3-Formyl salicylic acid, tris-(2-aminoethyl)amine, all lanthanide nitrates, $Mn(ClO_4)_2\cdot 6H_2O$, and all solvents were used as purchased from commercial sources without further purification.

Synthesis: 3-Formylsalicylic acid (67 mg, 0.4 mmol) and tris(2-aminoethyl)amine (0.03 mL, 0.2 mmol) were dissolved in ethanol / water (15 mL / 5 mL) mixture. Then triethylamine (0.14 mL, 1 mmol) was added dropwise with stirring. To the resulting solution $Mn(ClO_4)_2(H_2O)_6$ (75 mg, 0.2 mmol) and $Ln(NO_3)_3\cdot(H_2O)_m$ (m = 5 (Nd, Eu, Gd) and m = 6 (Lu)) (0.1 mmol) were added and the subsequent mixture was stirred for another 12 h. The solution was then filtered and kept for crystallization. Within one week, needle shaped yellow crystals were collected, washed with diethyl ether and dried in vacuum.

$(NHEt_3)_2[Nd\{Mn(L)\}_2](ClO_4)\cdot 2(H_2O)$

Yield: 46 mg, 31%. (based on Nd). IR (KBr pellet): $\bar{\upsilon}$ = 3446 (br), 3415 (br), 2858 (w), 1638 (s), 1593 (s), 1552 (s), 1439 (s), 1413 (s), 1372 (w), 1297 (s), 1225 (m), 1193 (m), 1160 (m), 1094 (s), 1026 (m), 997 (m), 986 (m), 961 (m), 877 (m), 832 (m), 800 (m), 765 (s), 667 (m), 624 (m), 482 (w) cm^{-1}. Anal. Calcd for $C_{56}H_{80}ClNdMn_2N_{10}O_{18}$: C, 45.73; H, 5.48; N, 9.52. Found: C, 45.06; H, 5.44; N, 9.44.

$(NHEt_3)_2[Eu\{Mn(L)\}_2](ClO_4)\cdot 2(H_2O)$

Yield: 57 mg, 39%. (based on Eu). IR (KBr pellet): $\bar{\upsilon}$ = 3447 (br), 2907 (w), 2858 (w), 1634 (s), 1594 (s), 1554 (s), 1440 (s), 1414 (s), 1373 (w), 1332 (m), 1297 (s), 1231 (m), 1193 (m), 1159 (m), 1094 (s), 1026 (m), 997 (m), 986 (m), 962 (m), 877 (m), 832 (m), 801 (m), 764 (s), 667 (m), 624 (m), 600 (w), 483 (w), 457 (w) cm^{-1}. Anal. Calcd for $C_{56}H_{80}ClEuMn_2N_{10}O_{18}$: C, 45.49; H, 5.45; N, 9.47. Found: C, 45.41; H, 5.34; N, 9.44.

$(NHEt_3)_2[Gd\{Mn(L)\}_2](ClO_4)\cdot 2(H_2O)$

Yield: 45 mg, 30%. (based on Gd). IR (KBr pellet): ῡ = 3415 (br), 3293 (w), 3246 (w), 2923 (m), 2864 (w), 2360 (m) 1635(s), 1558 (s), 1440 (s), 1406 (m), 1295 (s), 1233 (w), 1094 (s), 1028 (m), 986 (w), 961 (w), 876 (m), 833 (w), 803 (w), 765 (w), 666 (w), 624 (w), 480 (w) cm^{-1}. Anal. Calcd for $C_{56}H_{80}ClGdMn_2N_{10}O_{18}$: C, 45.33; H, 5.43; N, 9.44. Found: C, 44.87; H, 5.43; N, 9.39.

$(NHEt_3)_2[Lu\{Mn(L)\}_2](ClO_4)\cdot 2(H_2O)$

Yield: 59 mg, 39%. (based on Lu). IR (KBr pellet): ῡ = 3438 (br), 2902 (w), 2857 (w), 1630 (s), 1594 (m), 1552 (m), 1462 (s), 1440 (m), 1414 (m), 1335 (w), 1301 (m), 1231 (m), 1194 (w), 1162 (w), 1096 (s), 1026 (w), 986 (w), 966 (m), 960 (m), 878 (m), 833 (w), 805 (w), 761 (m), 669 (m), 624 (m), 603 (w), 551 (w), 482 (w), 455 (w), 409 (w) cm^{-1}. Anal. Calcd for $C_{56}H_{80}ClLuMn_2N_{10}O_{18}$: C, 44.79; H, 5.37; N, 9.33. Found: C, 45.40; H, 5.44; N, 9.17.

X-ray crystallographic studies of $(NHEt_3)_2[Dy\{Mn(L)\}_2](ClO_4)\cdot 2(H_2O)$: The details of the X-ray crystallography measurements in the compound with Ln = Dy were reported previously.[46] The other compounds were measured analogously. Thus a suitable crystal of $(NHEt_3)_2$-$[Dy\{Mn(L)\}_2](ClO_4)\cdot 2(H_2O)$ was covered in mineral oil (Aldrich) and mounted onto a glass fiber and transferred directly into the cold stream of a Stoe IPDS 2 diffractometer.

All structures were solved by using the program SHELXS/T.[65] The remaining non-hydrogen atoms were located from successive difference Fourier map calculations. The refinements were carried out by using full-matrix least-squares techniques on F^2 by using the program SHELXL.[65] The hydrogen atom contributions of all of the compounds were calculated, but not refined. In each case, the locations of the largest peaks in the final difference Fourier map calculations, as well as the magnitude of the residual electron densities, were of no chemical significance.

Crystal data for Mn_2Nd: $C_{44}H_{44}Mn_2N_8NdO_{12}\bullet ClO_4\bullet 2(H_2O)\bullet 2(C_6H_{16}N)$, M = 1470.87, a = 10.7964(3) Å, b = 15.8740(5) Å, c = 19.6279(6) Å, α = 77.872(2)°, β = 84.929(2)°, γ = 73.340(2)°, V = 3149.31(17) $Å^3$, T = 100 K, space group P-1, Z = 2, $\mu(MoK\alpha)$ = 1.327 mm^{-1}, 34019 reflections measured, 15284 independent reflections (R_{int} = 0.0578). The final R_1 values were 0.0427 (I >

$2\sigma(I)$). The final $wR(F^2)$ values were 0.0856 ($I > 2\sigma(I)$). The final R_1 values were 0.0729 (all data). The final $wR(F^2)$ values were 0.0949 (all data). The goodness of fit on F^2 was 0.941.

Crystal data for Mn_2Eu: $C_{44}H_{44}EuMn_2N_8O_{12}\bullet ClO_4\bullet 2(H_2O)\bullet 2(C_6H_{16}N)$, M = 1478.59, a = 10.8074(5) Å, b = 15.8727(8) Å, c = 19.6925(9) Å, α = 77.729(4)°, β = 85.158(4)°, γ = 73.222(4)°, V = 3159.4(3) Å^3, T = 150 K, space group P-1, Z = 2, μ(MoKα) = 1.493 mm^{-1}, 34767 reflections measured, 34767 independent reflections. The final R_1 values were 0.1416 ($I > 2\sigma(I)$). The final $wR(F^2)$ values were 0.3287 ($I > 2\sigma(I)$). The final R_1 values were 0.1922 (all data). The final $wR(F^2)$ values were 0.3636 (all data). The goodness of fit on F^2 was 1.285.

Crystal data for Mn_2Tm: $C_{44}H_{44}Mn_2N_8O_{12}Gd\bullet ClO_4\bullet 2(H_2O)\bullet 2(C_6H_{16}N)$, M = 1483.88, a = 10.7923(7) Å, b = 15.8330(9) Å, c = 19.7272(11) Å, α = 77.652(4)°, β = 85.215(5)°, γ = 73.203(5)°, V = 3151.6(3) Å^3, T = 200 K, space group P-1, Z = 2, μ(MoKα) = 1.554 mm^{-1}, 46115 reflections measured, 46115 independent reflections. The final R_1 values were 0.1002 ($I > 2\sigma(I)$). The final $wR(F^2)$ values were 0.2380 ($I > 2\sigma(I)$). The final R_1 values were 0.1811 (all data). The final $wR(F^2)$ values were 0.2758 (all data). The goodness of fit on F^2 was 0.969.

Crystal data for Mn_2Lu: $C_{44}H_{44}LuMn_2N_8O_{12}\bullet ClO_4\bullet 2(H_2O)\bullet 2(C_6H_{16}N)$, M = 1501.60, a = 10.8378(3) Å, b = 15.7953(5) Å, c = 20.2009(6) Å, α = 76.445(2)°, β = 86.642(2)°, γ = 72.035(2)°, V = 3197.54(17) Å^3, T = 200 K, space group P-1, Z = 2, μ(MoKα) = 2.04 mm^{-1}, 95545 reflections measured, 95545 independent reflections. The final R_1 values were 0.0901 ($I > 2\sigma(I)$). The final $wR(F^2)$ values were 0.2363 ($I > 2\sigma(I)$). The final R_1 values were 0.1112 (all data). The final $wR(F^2)$ values were 0.2606 (all data). The goodness of fit on F^2 was 1.034.

3.5 Results and Discussion

Following the earlier published procedures for $(NHEt_3)_2[Dy\{Mn(L)\}_2](ClO_4)\cdot 2(H_2O)$, we generated 2,2'-{[(2-aminoethyl)imino]bis[2,1-ethanediyl-nitriloethylidyne]}bis-2-hydroxy-benzoic acid H_4L *in situ* as proligand. Further reaction in an EtOH / H_2O (3:1) mixture with triethylamine, $Mn(ClO_4)_2\cdot 6H_2O$ and $Ln(NO_3)_3\cdot 5H_2O$ (10:2:1) resulted in the trinuclear mixed 3*d*-4*f* complexes $(NHEt_3)_2[Ln\{Mn(L)\}_2](ClO_4)\cdot 2(H_2O)$ (Ln = Nd, Eu, Gd, Lu; (abbreviated as $[Mn_2Ln]$) (Scheme 2). All new compounds were characterized by standard analytical / spectroscopic techniques and the solid-state structures were established by single crystal X-ray diffraction (Figure 3). All compounds are isostructural to the earlier described dysprosium species $(NHEt_3)_2[Ln\{Mn(L)\}_2](ClO_4)\cdot 2(H_2O)$ and will thus only be described here briefly. The asymmetric unit of each contains two $(NHEt_3)^+$ cations, one $(ClO_4)^-$, one $[Ln\{Mn(L)\}_2]^-$ coordination anion and two water molecules. The central Ln(III) atom is 8-fold coordinated, being in the center of a distorted square antiprism coordination polyhedron. The two manganese ions are 7-fold coordinated by four nitrogen atoms of the tris-(2-aminoethyl)amine subunit and three oxygen atoms of which two are phenoxy groups and the remaining one is part of a carboxyl group (Figures S1-S4). By considering the lanthanide contraction, bonding parameters of all compounds are in comparison to $[Mn_2Dy]$ in a similar range and thus will not be discussed here.

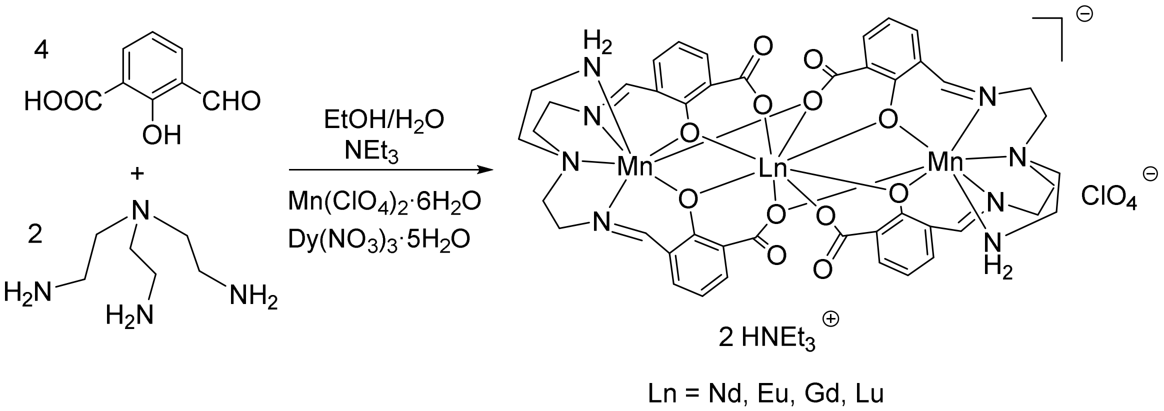

Scheme 2: Synthesis of $(NHEt_3)_2[Ln\{Mn(L)\}_2](ClO_4)\cdot 2(H_2O)$ (Ln = Nd, Eu, Gd, Lu).

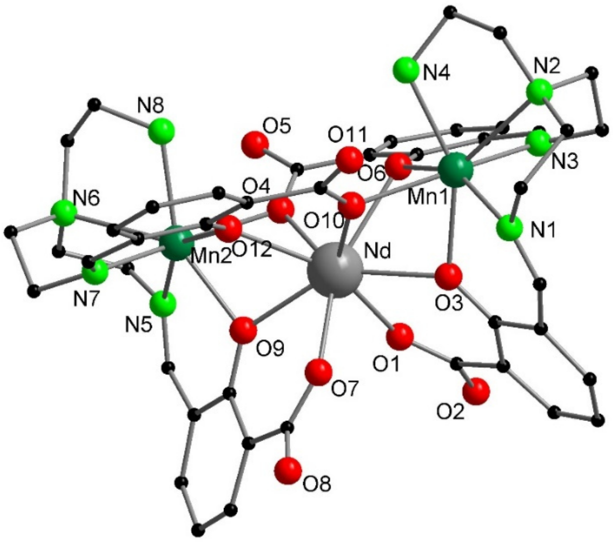

Figure 3: Solid state structure of the $[Nd\{Mn(L)\}_2]^-$ anion of $(NHEt_3)_2$-$[Ln\{Mn(L)\}_2](ClO_4)\cdot 2(H_2O)$, omitting hydrogen atoms for clarity. The corresponding Eu, Gd and Lu compounds are isostructural (see ESI, Figs. S1-S4).

3.5.1 XMCD Spectroscopy of isolated $[Mn_2Ln](H)_2^+$

3.5.1.1 The Mn Absorption Edges L_2, L_3

To address the magnetism of the incorporated manganese ions of the isolated complexes, we recorded XA spectra of $[Mn_2Ln](H)_2^+$ for positively and negatively circularly polarized X-rays at the manganese $2p_{3/2}$ / $2p_{1/2}$ (L_3/L_2) absorption edges, corresponding to a $2p \rightarrow 3d$ excitation, by TIY spectroscopy.

The polarization dependent XA spectra measured at the Mn $L_{3,2}$ absorption edge show a substantial dichroic effect (cf. Fig. 4). The Mn ions in the investigated complexes are expected to be in a +II oxidation state with a $3d^5$ electron configuration which means that we have either one unpaired electron in a low spin state or five unpaired electrons in a high spin state. At the given ligand field, the Mn^{2+} ions are expected to be in a high spin state with five unpaired electrons. This orbital occupation entails a significant spin magnetic moment of 5 μ_B per atom (m_S) and an orbital magnetic moment of 0 µB per atom (m_L) according to HUND's rules.

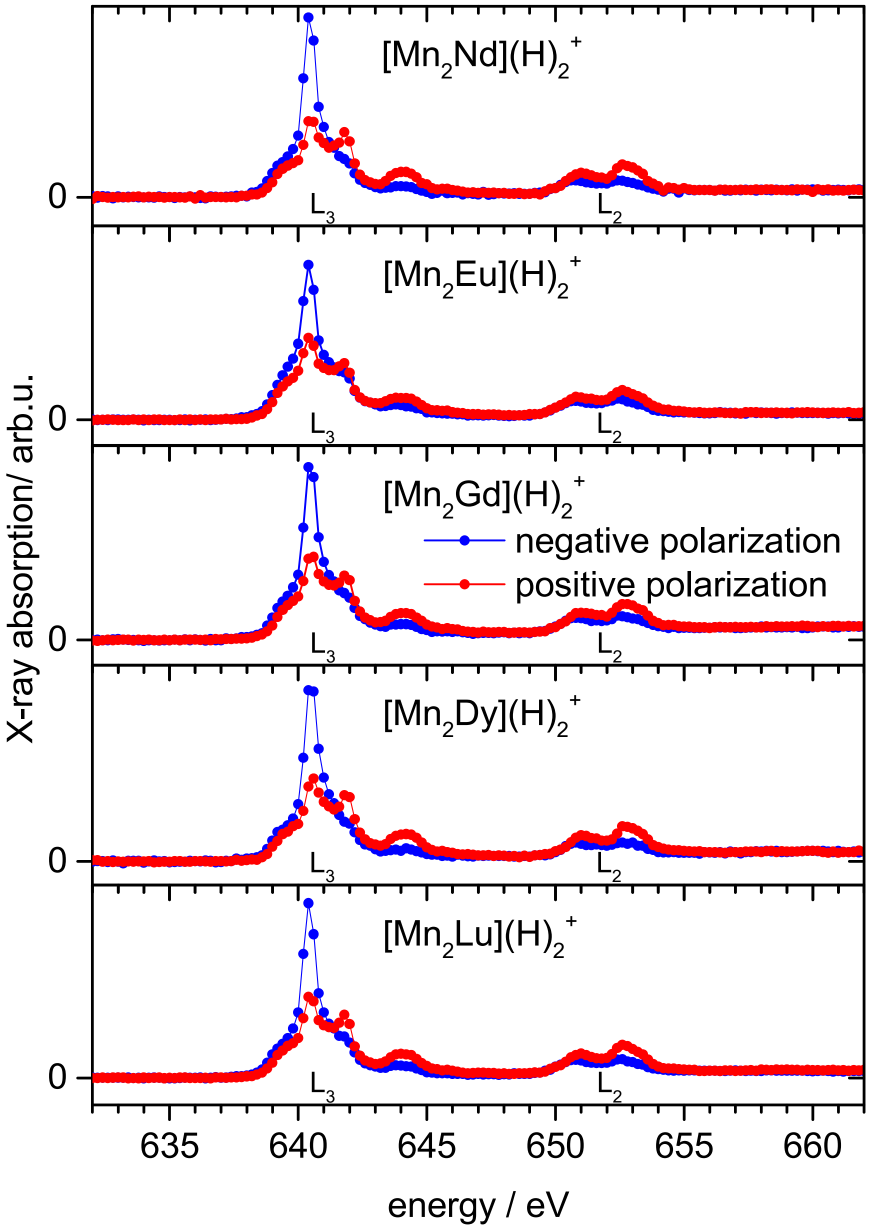

Figure 4: The manganese $L_{3,2}$ edges: Polarization dependent XA spectra for negative (blue) and positive (red) circular photon polarization for the five isostructural, bimetallic 3*d*-4*f* trinuclear complexes $[Mn_2Ln](H)_2^+$ (Ln = Nd, Eu, Gd, Dy, Lu).

The measured XAS spectra for positive and negative polarization of the five complexes differing only in the incorporated lanthanide ion look similar (cf. Fig. 4). The dichroic effect at the first subpeak of the L_3 absorption peak around 640.5 eV is approximately the same magnitude. There are minor differences in the second and third subpeak of the L_3 absorption at 641.8 and 644.0 eV. The dichroic effects in the spectra of $[Mn_2Eu](H)_2^+$ and $[Mn_2Gd](H)_2^+$ seem less pronounced compared to the other three complexes. The L_2 absorption peaks look much alike except for the $[Mn_2Eu](H)_2^+$ species, where the dichroic effect seems smaller as well. These findings can also be discerned in the XMCD spectra (cf. Fig. S7)

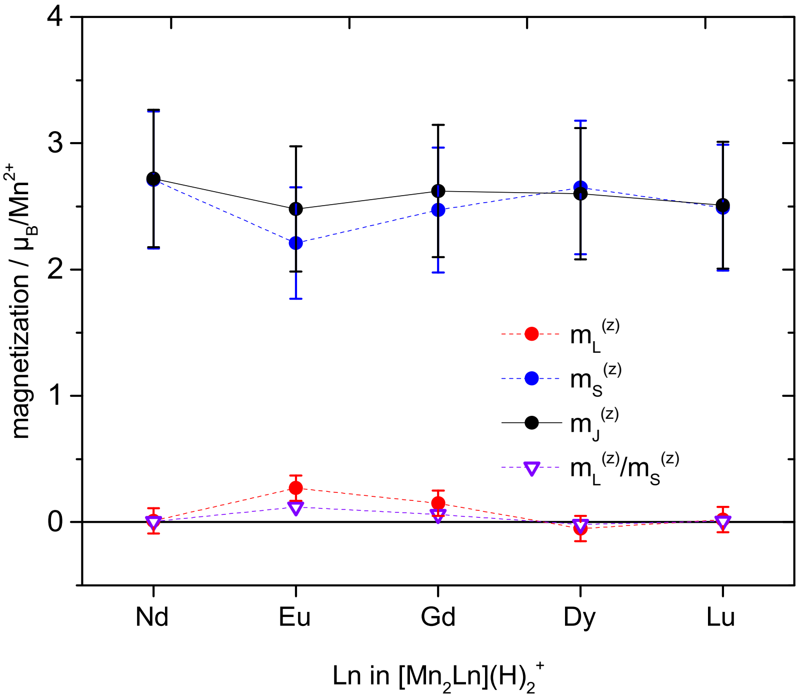

Figure 5: Magnetizations of the Mn^{2+} cations: contributions by spin ($m_S^{(z)}$, filled blue circles), contributions by orbit ($m_L^{(z)}$, filled red squares), total values ($m_J^{(z)}$, filled black triangles); together with the $m_L^{(z)}$ to $m_S^{(z)}$ ratio (open purple triangles) on the manganese ions within the investigated mixed 3*d*-4*f* trinuclear complexes of the type $[Mn_2Ln](H)_2^+$.

The magnetizations at the Mn atoms are extracted by sum rule analyses of the XAS spectra at the Mn $L_{3,2}$ absorption edges (cf. Fig. 5). The background subtraction from the manganese XA sum spectra due to excitations into higher unoccupied (nonmagnetic) d states is performed by a two-step function. The step height for the L_3 edge is 2/3, the step height at the L_2 edge 1/3 of the full edge jump, according to the degeneracy of the spin-orbit split 2p initial states (cf. Fig. S6).[39, 50, 54] The total magnetizations per atom/ion ($m_J^{(z)}$) for all complexes is in the range of 2.48 – 2.72 μ_B / Mn^{2+} and is almost exclusively contributed by the spin magnetic moment ($m_S^{(z)}$ = 2.21 – 2.71 μ_B / Mn^{2+}) (cf. Fig 5). The orbital magnetic moments of the Nd, Dy, and Lu species match the predicted value of $m_L = 0$ for a d^5 high spin configuration with 5 singly occupied d-orbitals very well. The Eu and Gd species seem to have a minor orbital contribution of up to $m_L^{(z)} = 0.27\ \mu_B / Mn^{2+}$ (for Eu) to the total magnetization of the Mn^{2+} ions (cf. integrated XMCD signal Fig. S7). The residual $m_L^{(z)}$ values may for example be explained by a distorted ligand field and/or partial low spin configurations of the d^5 configuration. Detailed structural studies of the complexes may reveal slight differences in the molecular geometry. For all complexes the magnetizations of the manganese ions correspond very well to the expected values for decoupled Mn^{2+} ions in an octahedral ligand environment, in between the error bars. Also the $m_L/m_S \approx 0$ corresponds to the Mn^{2+} ground state (S = 5/2, L = 0, J = 5/2). Due to the substantial spin magnetizations, an antiferromagnetic coupling scheme between the manganese ions can be excluded. The extracted spin and orbital magnetizations by sum rule analyses as well as the total magnetization and the orbital to spin magnetization ratio are summarized in Tab. 1.

Table 1: Experimental orbital ($m_L^{(z)}$), spin ($m_S^{(z)}$), total ($m_J^{(z)}$) magnetization and the orbital to spin ratios ($m_L^{(z)}/m_S^{(z)}$) at the manganese ions of the $[Mn_2Ln](H)_2^+$ complexes.

	$m_L^{(z)}$ / μ_B/Mn^{2+}	$m_S^{(z)}$ / μ_B/Mn^{2+}	$m_J^{(z)}$ / μ_B/Mn^{2+}	$m_L^{(z)}/m_S^{(z)}$
$[Mn_2Nd](H)_2^+$	0.01	2.71	2.72	0.00
$[Mn_2Eu](H)_2^+$	0.27	2.21	2.48	0.12
$[Mn_2Gd](H)_2^+$	0.15	2.47	2.62	0.06
$[Mn_2Dy](H)_2^+$	-0.05	2.65	2.60	-0.02
$[Mn_2Lu](H)_2^+$	0.02	2.49	2.51	0.01

3.5.1.2 The Lanthanide Absorption Edges M_4, M_5

In order to push the limits of the combination of XMCD spectroscopy and sum rule analysis to differentiate the magnetic properties of the incorporated lanthanide ions, we recorded X-ray absorption spectra at the respective lanthanide $M_{5,4}$ absorption edges corresponding to the excitation $3d^{10}4f^{n} \rightarrow 3d^{9}4f^{n+1}$. Due to decreasing photon flux at the undulator with increasing photon energy, we were not able to record the XA spectra for $[Mn_2Lu](H)_2^+$ at the Lu $M_{5,4}$ absorption edge (> 1500 eV). Since Lu^{3+} has a diamagnetic $4d^{10}4f^{14}$ ground state electron configuration, no contribution of Lu^{3+} to the magnetic properties of $[Mn_2Lu](H)_2^+$ is expected.

XMCD spectroscopy at the Nd 3d ($M_{5,4}$) absorption edge

The XA spectra of the $[Mn_2Nd](H)_2^+$ ion in the range of 955 – 1030 eV show a rather small dichroic effect on the M_5 absorption at 979 eV and a substantial dichroic effect on the M_4 absorption at 1000 eV (Fig. 6, left), indicating a magnetic moment at the Nd^{III} center. The non-resonant background was subtracted using a two-step function.[50] The step height at the M_5 edge is ¼, at the M_4 edge ¾ of the full edge jump. The statistically expected ratio of 3:2 based on the 3*d* orbital degeneracy is not observed in our experiment due to the 3*d*-4*f* interaction.[66] The XA sum integral and the XMCD integral show two plateaus after the first and after the second absorption edge (990 and 1020 eV), giving the integrals A, B and C (cf. chapter 2). Our gas phase XA/XMCD spectra at the neodymium absorption edge closely resemble bulk spectra.[66-68] Assuming a high spin state for the neodymium giving a number of unoccupied valence orbitals $n_h = 11$ for Nd(III), sum rule analysis (inclusive spin sum rule correction) yields a spin magnetization of $m_S^{(z)} = -0.60\ \mu_B/Nd^{3+}$ and an orbital magnetization of $m_L^{(z)} = 1.23\ \mu_B\ /\ Nd^{3+}$. Note, that the spin sum rule correction has a major impact on the spin magnetization (the value of the original spin sum rule yields $m_S^{(z)} = -2.41\ \mu B\ /\ Nd^{3+}$, see Fig. S11, Tab. S6). The experimental ratio $m_L^{(z)}/m_S^{(z)} \approx -2.05$ corresponds to the ground state of Nd^{3+} in accordance with HUND's rules. The (corrected) extracted magnetizations are summarized in Tab. S6. (Tab. 2).

XMCD spectroscopy at the Eu 3d ($M_{5,4}$) absorption edge

The polarization dependent XA spectra of $[Mn_2Eu](H)_2^+$ in the range of 1100 – 1190 eV show very small dichroic effects, implying also a very small magnetic moment at the Eu^{3+} center of the complex (Fig 6, right). The non-resonant background in the sum spectrum was subtracted using a two-step function.[50] The step height at the M_5 edge is 1/3, at the M_4 edge 2/3 of the full edge jump. The statistically expected ratio of 3:2 based on the 3*d* orbital degeneracy is not observed in our experiment due to the 3*d*-4*f* interaction.[66] Although the integrated XMCD signal shows some minor dichroic effect, the intensity is so low that one can assume a negligible magnetization at the Eu^{3+} center. For the free Eu^{3+} ion in the ground state it can be deduced L = 3, S = 3 and J = 0, and thus a diamagnetic $^7F_0$ ground state, according to HUND's rules.[69] The combination of XMCD spectroscopy and sum rule analysis usually allows for distinction of the orbital and spin magnetic moments. In our case both cancel out to a total magnetic moment $m_J^{(z)} \approx 0$. Due to the low XMCD signal intensity, we skipped the use of sum rule analysis.

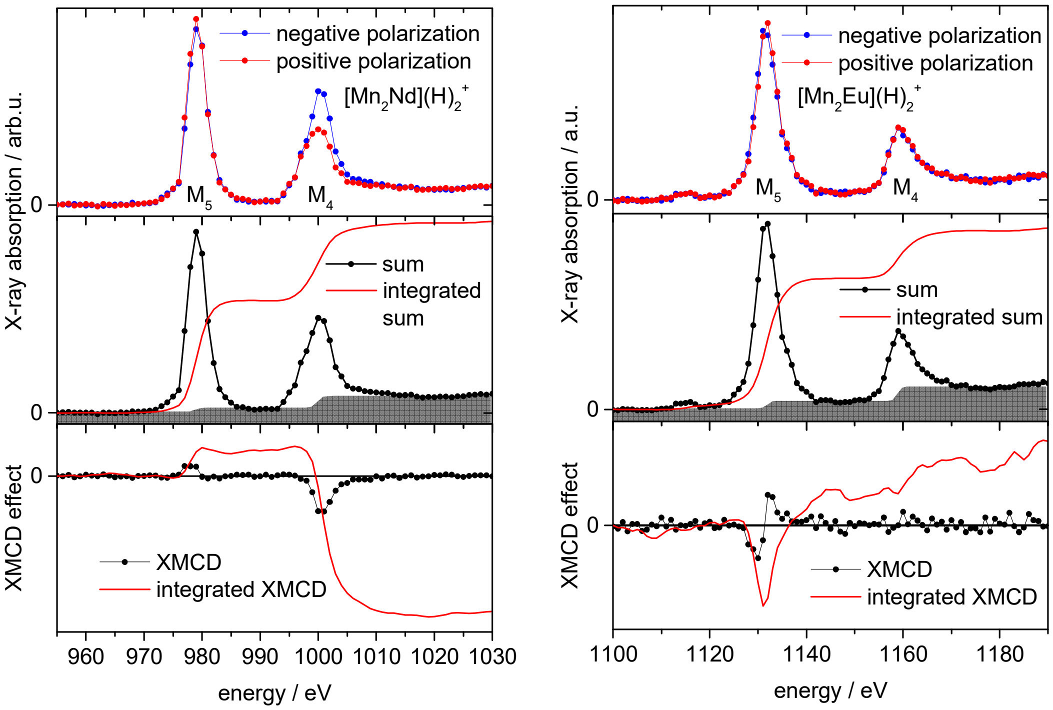

Figure 6: The lanthanide $M_{5,4}$ edges: Polarization dependent X-ray absorption spectra for negative (blue) and positive (red) circular photon polarization, the resulting XMCD spectra (black) and the integral of the XMCD signal (red) on the Nd $M_{5,4}$ (left) and the Eu $M_{5,4}$ (right) absorption edges of the [Mn$_2$Nd](H)$_2^+$ and [Mn$_2$Eu](H)$_2^+$ mixed 3*d*-4*f* trinuclear complexes. Note, that the ordinates for the sum spectra and their integrals are different.

XMCD spectroscopy at the Gd 3d ($M_{5,4}$) absorption edge

The XA spectra for negative and positive helicity of [Mn$_2$Gd](H)$_2^+$ in the range of 1165 – 1250 eV show large dichroic effects on the M_5 and M_4 absorption edges at 1184 and 1215 eV, respectively (Fig. 7, left). This indicates a large total magnetic moment at the Gd^{3+} center. The integrated sum spectrum shows two plateaus after the M_5 and after the M_4 absorption edges. We did not observe non-resonant background after normalization of the spectra. The integrated XMCD signal shows also two plateaus after both absorption edges. We assume a high spin configuration with the number of electron holes in the valence orbital $n_h = 7$. We calculated a spin magnetization of $m_S^{(z)} = 4.14\ \mu_B / Gd^{3+}$ and an orbital magnetization of $m_L^{(z)} = 0.01\ \mu_B / Gd^{3+}$, leaving a total magnetization of $m_J^{(z)} = 4.15\ \mu_B / Gd^{3+}$ and a ratio $m_L^{(z)} / m_S^{(z)} = 0$ (Tab. 2). These values are reasonable given the fact, that prediction by HUND's rules results in L = 0, S = 7/2 and J = 7/2. The experimental as well as the theoretical value for the orbital to spin magnetization ratio according to HUND's Rules agree with $m_L / m_S = 0$.

Table 2: Experimental orbital ($m_L^{(z)}$), spin ($m_S^{(z)}$), total ($m_J^{(z)}$) magnetizations and the orbital to spin ratios ($m_L^{(z)}/m_S^{(z)}$) at the Lanthanide ions of the $[Mn_2Ln](H)_2^+$ complexes.

	$m_L^{(z)}$ / μ_B / Ln^{3+}	$m_S^{(z)}$ / μ_B / Ln^{3+}	$m_J^{(z)}$ / μ_B / Ln^{3+}	$m_L^{(z)}$ / $m_S^{(z)}$
$[Mn_2Nd](H)_2^+$	1.23	-0.60	0.63	-2.05
$[Mn_2Eu](H)_2^+$			≈0	
$[Mn_2Gd](H)_2^+$	0.01	4.14	4.15	0.00
$[Mn_2Dy](H)_2^+$	2.88	3.57	6.45	0.81

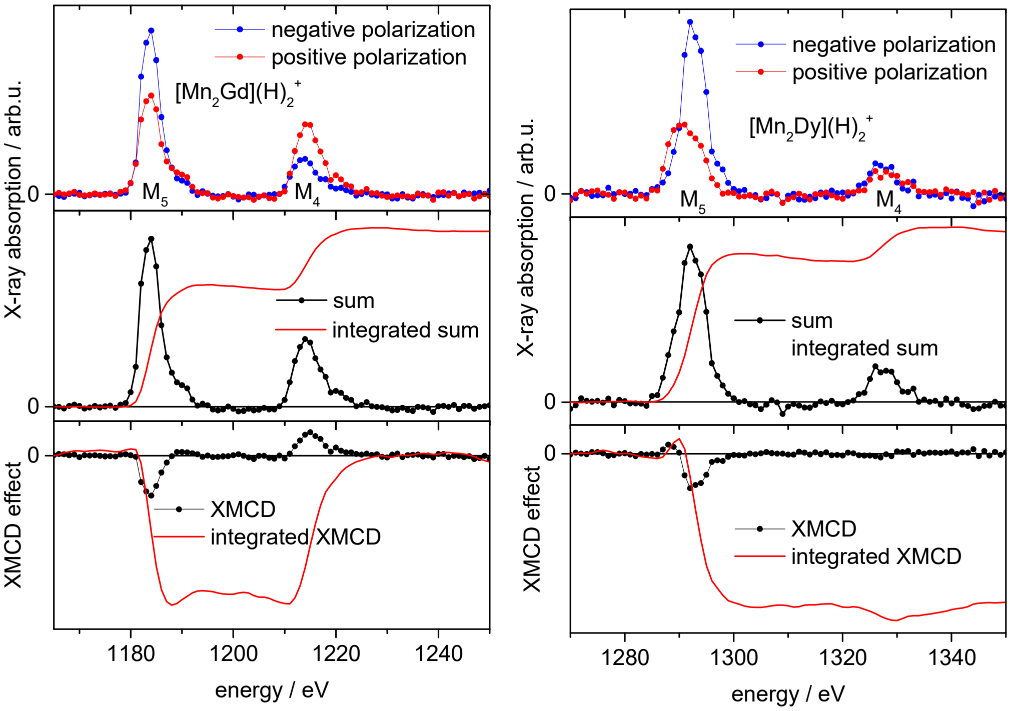

Figure 7: Polarization dependent X-ray absorption spectra for negative (blue) and positive (red) circular photon polarization, the resulting XMCD spectra (black) and the integral of the XMCD signal (red) on the Gd $M_{5,4}$ (left) and the Dy $M_{5,4}$ (right) absorption edges of the $[Mn_2Gd](H)_2^+$ and $[Mn_2Dy](H)_2^+$ mixed 3*d*-4*f* trinuclear complexes. Note, that the ordinates for the sum spectra and their integrals are different.

XMCD spectroscopy at the Dy 3d ($M_{5,4}$) absorption edge

The XA spectra of the $[Mn_2Dy](H)_2^+$ ion in the range of 1270 – 1350 eV show a very large dichroic effect on the M_5 absorption edge at 1292 eV, and almost no dichroism on the M_4 absorption edge at 1327 eV (Fig. 7, right). A contribution of spin and orbital magnetization can be expected for this species. As in the case of $[Mn_2Gd](H)_2^+$ we do not observe a non-resonant background after normalization of the absorption spectra. The integrated sum spectrum shows two pronounced plateaus after the M_5 and the M_4 absorption edges. The integral of the XMCD signal provides a plateau after the M_5 absorption edge that remains roughly constant at the M_4 absorption edge. The lanthanide ion Dy^{3+} has a $3d^{10}4f^{9}$ ground state electron configuration, we assume the number of electron holes in the valence shell to $n_h = 5$. We calculated a spin magnetization of $m_S^{(z)} = 3.57\ \mu_B / Dy^{3+}$ and an orbital magnetization of

$m_L^{(z)}$ = 2.88 μ_B / Dy^{3+}. This results in a total magnetization of $m_J^{(z)}$ = 6.45 μ_B / Dy^{3+} and an orbital to spin magnetic ratio of $m_L^{(z)}$ / $m_S^{(z)}$ = 0.81 (Tab. 3). HUND's rules predict L = 5, S = 5/2 and J = 15/2 for the ground state of Dy^{3+} and a magnetic moment ratio of m_L / m_S = 1. The calculated ratio $m_L^{(z)}$ / $m_S^{(z)}$ = 0.81 is in reasonable good accordance with this.

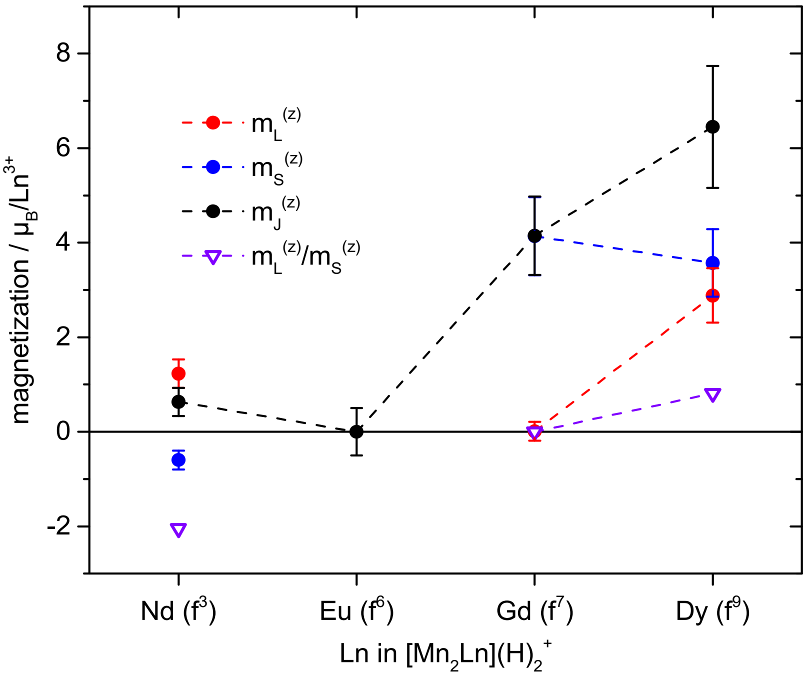

Figure 8: Spin ($m_S^{(z)}$, filled blue circles), orbital ($m_L^{(z)}$, filled red squares), total ($m_{tot}^{(z)}$, filled black triangles) magnetizations and the $m_L^{(z)}$ to $m_S^{(z)}$ ratio (open purple triangles) on the Ln atoms within the investigated bimetallic 3*d*-4*f* trinuclear complexes of the type $[Mn_2Ln](H)_2^+$.

The calculated spin ($m_S^{(z)}$), orbital ($m_L^{(z)}$), total ($m_J^{(z)}$) magnetizations and the orbital to spin magnetic ratios ($m_L^{(z)}/m_S^{(z)}$) of the investigated complexes are plotted in Fig. 8 and summarized in Tab. 3. The magnetic properties of the Ln^{3+} ions meet the expectations corresponding to the respective 4*f*^{n} electron configuration. The found magnetizations on the lanthanide ions are in line with predictions of HUND's rules for free Ln^{3+} ions. Our results support the assumption, that the magnetic f-electrons of lanthanide ions are confined and scarcely interact with surrounding ligand systems.[70-72]

Table 3: Experimental orbital to spin magnetization ratios ($m_L^{(z)}/m_S^{(z)}$) and total magnetizations ($m_J^{(z)}$) of the trivalent lanthanide ions in the $[Mn_2Ln](H)_2^+$ complexes (this work) and textbook values for free lanthanide ions Ln^{III}.[69]

	$m_L^{(z)}/m_S^{(z)}$ this work	m_L/m_S [69]	$m_{J,Ln}^{(z)}$ this work	$m_{J,Ln}$(T→ 0 K)
$[Mn_2Nd](H)_2^+$	-2.05	-2	0.63	3.27
$[Mn_2Eu](H)_2^+$		0.5		0
$[Mn_2Gd](H)_2^+$	0.00	0	4.15	7
$[Mn_2Dy](H)_2^+$	0.81	1	6.45	10

3.5.2 Estimate of the Ion Temperature

The $[Mn_2Dy]$ complex was studied in detail and the metal ions provide very weak exchange interactions ($J_{Mn-Mn} = 0.00\ cm^{-1}$, $J_{Dy-Mn} = 0.22\ cm^{-1}$).[22, 46] The magnetic moments can presumably orient independently, which allows us to estimate the $[Mn_2Ln](H)_2^+$ ion temperature by projection of the measured total magnetizations $m_J^{(z)}$ (of the manganese ions and the lanthanide ions independently) onto a Brillouin function of the temperature at a magnetic field of 5 T described by:

$$m_J^{(z)} = g_J \mu_B J \left(\frac{2J+1}{2J}\right) \coth\left(\frac{2J+1}{2J}\frac{\mu_B g_J J B}{k_B T}\right) - \frac{1}{2J}\coth\left(\frac{1}{2J}\frac{\mu_B g_J J B}{k_B T}\right)$$

with:

$m_J^{(z)}$:	projection of the total magnetic moment onto the quantization axis
J	total angular momentum, J = L + S
g_J	Landé-factor of the total magnetic moment
B	magnetic field strength
T	temperature

Table 4: Spin Orbit coupling constants for the Mn^{2+} ion ζ_{3d} and selected lanthanide ions ζ_{4f}.[73]

Ion	ζ_{3d} / cm^{-1}	ζ_{3d} / kJ/mol
Mn^{2+}	347	4.15
Ion	ζ_{4f} / cm^{-1}	ζ_{4f} / kJ/mol
Nd^{3+}	884	10.58
Eu^{3+}	1326	15.86
Gd^{3+}	1450	17.35
Dy^{3+}	1932	23.11

The total magnetic moments are approximated as a sum of the individual spin and orbital magnetic moments ($m_J \approx m_S + m_L$). This is reasonable because the strong spin-orbit coupling in the Mn^{2+} and Ln^{3+} ions (cf. Tab. 4) is more than one order of magnitude higher compared to the thermal and magnetic energy equivalents under the experimental conditions and in addition, the exchange interactions between the metal ions are weak (cf. Tabs. 4,5). In our experiments the coupling between the spin (S) and orbital (L) angular momentum to the total angular momentum (J) exceeds the individual coupling of S or L to the applied external magnetic field.[39, 40, 74, 75]

Table 5: Thermal energy (left) and magnetic energy (right) equivalents.

T / K	E / cm^{-1}	E / kJ/mol	B / T	E / cm^{-1}	E / kJ/mol
5	3.475	0.0416	0.1	0.04668	0.0006
10	6.950	0.0831	1.0	0.46686	0.0056
50	34.752	0.4157	2.0	0.93373	0.0112
100	69.503	0.8314	5.0	2.3343	0.0279
300	208.51	2.4943	7.0	3.2681	0.0391

The Brillouin function for a Mn^{2+} ion in the ground state is shown in Fig. 9. For the five investigated complexes $[Mn_2Ln](H)_2^+$ with different incorporated lanthanide ions, the same Brillouin function is plotted one below the other (see color code). The calculated $m_J^{(z)}$ values and the assumed error of 20 % are shown as a dotted horizontal line. The corresponding temperature as a projection onto the temperature axis is shown as dotted vertical line. The colored areas represent the uncertainty. The evaluated temperatures differ only slightly in the range of 12.3 to 13.9 K with an average of $\overline{T}$ = 13.3K , which is in line with the temperatures expected, even if the uncertainty is relatively high ($\Delta T \approx \pm 4$ K).

The Brillouin functions of Nd^{3+}, Gd^{3+} and Dy^{3+} in their respective ground state configuration are shown in Fig. 10. The calculated $m_J^{(z)}$ values are shown as a dotted horizontal line, the shaded area represents the assumed error of 20 % (for Gd^{3+} and Dy^{3+}) and 40 % (for Nd^{3+}), respectively. The corresponding temperature as a projection onto the temperature axis is shown as dotted vertical line, again the shaded area represents the temperature uncertainty. The evaluated temperature of the Gd^{3+} ion yields 13.8 K, the temperature of the Dy^{3+} ion yields 14.6 K. The difference of < 1 K and the average of 14.2 K is consistent with the temperatures extracted from the manganese data. The temperature uncertainty is approx. ± 4.5 K for Gd^{3+}

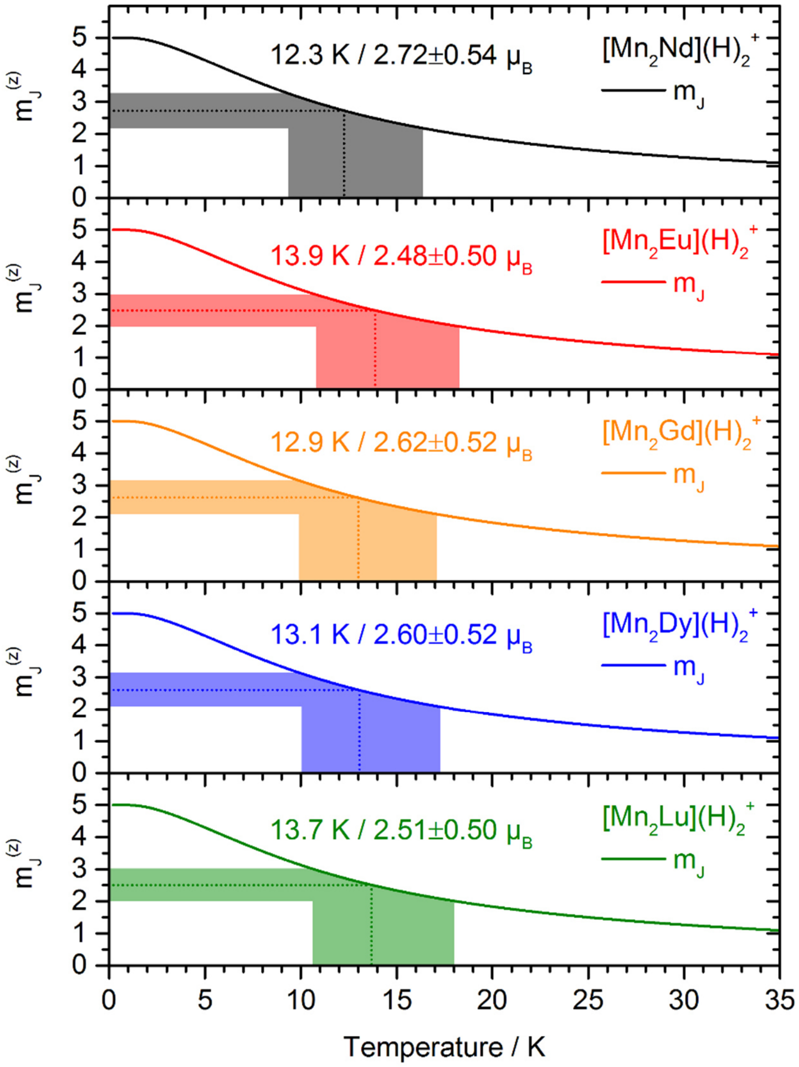

Figure 9: Simulated magnetizations $m_J^{(z)}$ of the Mn^{2+} ion in the ground state (S = 5/2, L = 0, J = 5/2), as Brillouin function of the ion temperature at a magnetic field of B = 5 T. The experimentally determined magnetizations ($m_J^{(z)}$) are projected onto the Brillouin function to identify the ion temperature.

and ± 5.5 K for Dy^{3+}. The temperature derived from the Nd^{3+} data is 23.4 ± 11 K. This value is significantly augmented compared to Gd^{3+} and Dy^{3+} but still in the expected temperature range for the experiment. The Brillouin curve for the Nd^{3+} ion is much shallower compared to Gd^{3+} or Dy^{3+}, resulting in an augmented uncertainty for the temperature. A further explanation might be a higher error in the correction of the spin sum rule.[60] The error in the original spin sum rule is > 100 %, additionally, the $<T_z>/<S>$ ratio is > 30 %. Hence the error for the experimentally determined $m_J^{(z)}$ is probably higher (estimated 40 %).

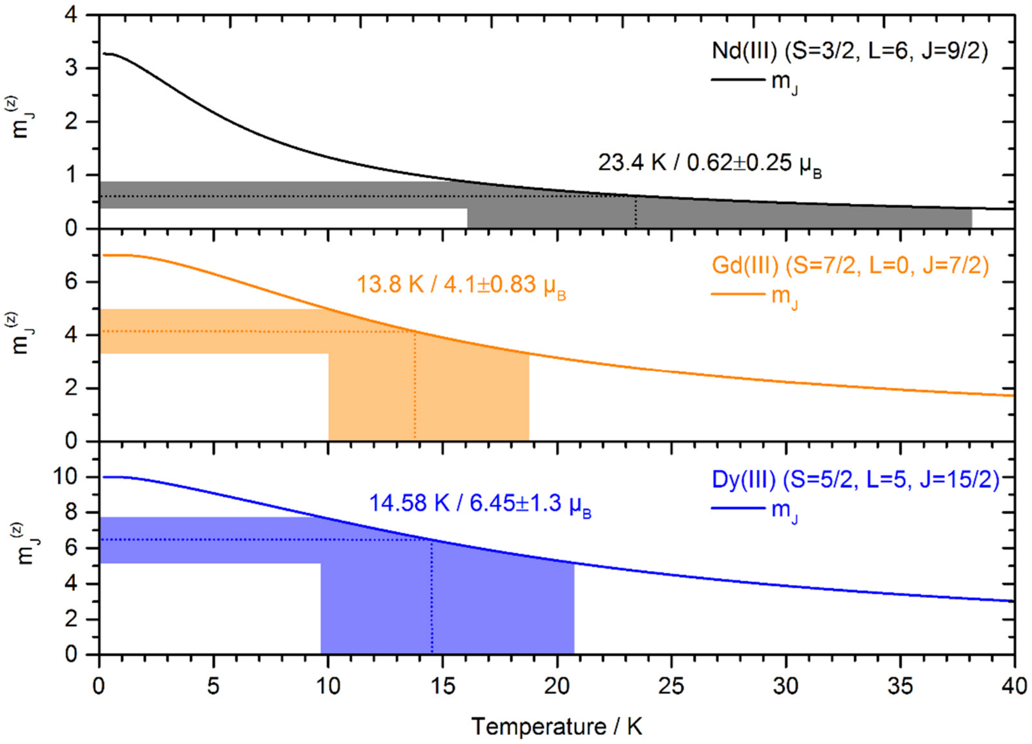

Figure 10: Simulated magnetizations $m_J^{(z)}$ of the Nd^{3+} (top, black), Gd^{3+} (middle, orange) and Dy^{3+} (bottom, blue) ions in the ground state, as Brillouin function of the ion temperature at a magnetic field of B = 5 T. The experimentally determined magnetizations ($m_J^{(z)}$) are projected onto the Brillouin function to identify the ion temperature.

All in all, the ion temperatures determined in this study are in very good agreement with those assessed in previous experiments at the NanoCluster Trap, conducted on metal cluster ions and metal cluster ion adsorbates.[37-45] Zamudio-Bayer *et al*. find ion temperatures of 7.4 to 27.3 K for Ni_2^+ under very similar experimental conditions.[45] For the $Co_3(benzene)_n^+$ cluster ion with n = 0-3, Akin *et al*. found temperatures in the range of 12 – 31 K.[37]

3.5.3 Magnetometry of Bulk Samples

The magnetic susceptibilities of the isostructural [Mn_2Ln] complexes were measured between 1.8 and 300 K under an applied field of 0.1 T. The data are summarized in Tab. 6 and shown as χT vs T plots in Fig. 11. The χT product of [Mn_2Nd] steadily decreases from 12.3 cm^3Kmol^{-1} at room temperature to a weakly defined minimum of 11.1 cm^3Kmol^{-1} at 12 K and then increases to 11.9 cm^3Kmol^{-1} (cf. Fig. 11 and Tab. 6, S3). The χT product of [Mn_2Eu] steadily decreases from 10.1 cm^{3}Kmol^{-1} at 300 K to 7.8 cm^{3}Kmol^{-1} at 1.8 K (cf. Fig. 11 and Tab. 6, S3). The χT product of [Mn$_2$Gd] remains constant at approx. 16 cm^{3}Kmol^{-1} to 40 K and then increases to reach 19.9 cm^{3}Kmol^{-1} at 1.8 K (cf. Fig. 11 and Tab. 6, S3). The χT product of [Mn$_2$Dy] steadily decreases from 23.2 cm^{3}Kmol^{-1} at 300 K to a minimum of 21.2 cm^{3}Kmol^{-1} at 11 K and then increases to 23.8 cm^{3}Kmol^{-1} at 1.8 K (cf. Fig.11 and Tab. 6, S3). The χT product of [Mn$_2$Lu] steadily decreases from 8.9 cm^{3}Kmol^{-1} at room temperature to 7.3 cm^{3}Kmol^{-1}at 1.8 K with a behavior very similar to that of the [Mn$_2$Eu] compound (cf. Fig. 11 and Tab. 6, S3).

Table 6: Experimental χT products at 1.8 K, 300 K and the sum of Curie constants for the five [Mn$_2$Ln]-type complexes.

	χT / cm^{3}Kmol^{-1} 1.8 K	**χT / cm^{3}Kmol^{-1} 300 K**	**Σ_i C_i / cm^{3}Kmol^{-1}**
[Mn$_2$Nd]	11.95	12.33	10.39
[Mn$_2$Eu]	7.83	10.09	8.75
[Mn$_2$Gd]	19.88	16.70	16.63
[Mn$_2$Dy]	23.76	23.18	22.93
[Mn$_2$Lu]	7.28	8.85	8.75

The χT products for all five complexes at room temperature under an applied DC field of 1000 Oe are consistent with the expected values for one isolated Ln(III) ion and two Mn(II) ions (cf. Tabs. 6, S3). The initial decrease in the χT product of [Mn$_2$Nd], [Mn$_2$Eu] and [Mn$_2$Dy] with temperature can be explained as a result of the thermal depopulation of the m_J levels of the Nd^{3+}, Eu^{3+} and Dy^{3+} ions, respectively.[46] The increase of the χT value for the species with paramagnetic lanthanides [Mn$_2$Nd], [Mn$_2$Gd] and [Mn$_2$Dy] below 10 K indicates weak ferromagnetic interactions between the Mn^{2+} ions and the lanthanide ions. The lanthanide ions with a diamagnetic ground state Eu^{3+} ($^7F_0$) and Lu^{3+} ($^1S_0$) should scarcely contribute to the molar susceptibilities and their χT products are expected to originate solely from the Mn^{2+} ions. The augmented χT values especially at higher temperatures for the europium species are due to thermally populated low lying excited states of the Eu^{3+} ion. This finding is widely known as Van Vleck magnetism of the Eu^{3+} ion.[76-80] (cf. Tab S4). The drop of χT of [Mn$_2$Eu] and [Mn$_2$Lu] can originate from an antiferromagnetic coupling of the manganese moments at very low temperatures.

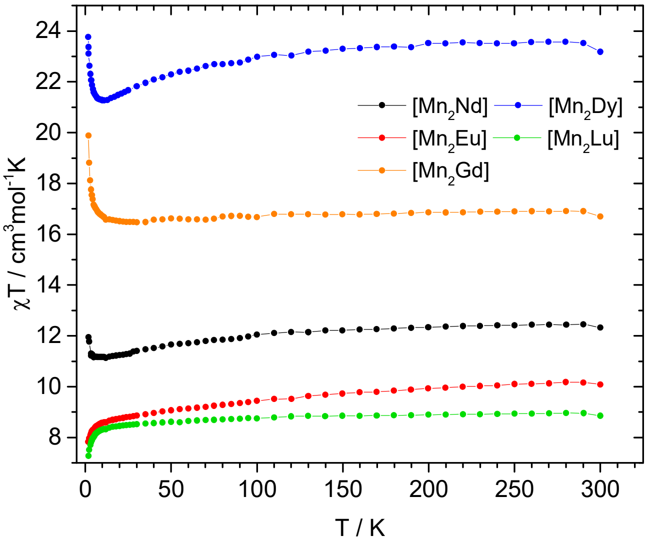

Figure 11: Measured temperature dependence of the χT product of five isostructural bimetallic complexes of the [Mn_2Ln]-type (sum formula: [$C_{44}H_{44}N_8O_{12}LnMn_2(C_6H_{16}N)_2(ClO_4)(H_2O)_2$], with Ln = Nd, Eu, Gd, Dy, Lu).

The field dependence of the magnetization was measured at 2, 3 and 5 K for all [Mn_2Ln] samples. The M vs. H plot at 2K shows a relative fast increase and an approach to saturation for all samples (cf. Fig. 12). The saturated magnetizations at maximum magnetic field (7 T) are in very good agreement with the expected values as a sum of spin-only values for very weakly exchange coupled metal ions (cf. Tab. 7). The magnetization value of 13.57 μ_B for [Mn_2Nd] is in approximate agreement with that expected of 13 μ_B which is the sum of the contribution of one Nd^{3+} (3.0 μ_B) and two Mn^{2+} (5 μ_B). For [Mn_2Eu], the magnetization of 9.99 μ_B agrees very well with the expected contribution of only two Mn^{2+} of 5.0 μ_B (with Eu^{3+} being diamagnetic). The magnetization of [Mn_2Gd] of 16.66 μ_B is also close to the expected value of 17 μ_B (7.0 μ_B for Gd^{3+} and 5.0 μ_B for each Mn^{2+}). The [Mn_2Dy] complex provides a molar magnetization of 16.02 μ_B, which is still in reasonable agreement with the expected magnetization of 15.0 μ_B (5.0 μ_B for Dy^{3+} and 5.0 μ_B for each Mn^{2+}). The magnetization of [Mn_2Lu] of 9.81 μ_B is in accordance to the solely contribution from just the two paramagnetic Mn^{2+} ions of 2 x 5.0 μ_B.

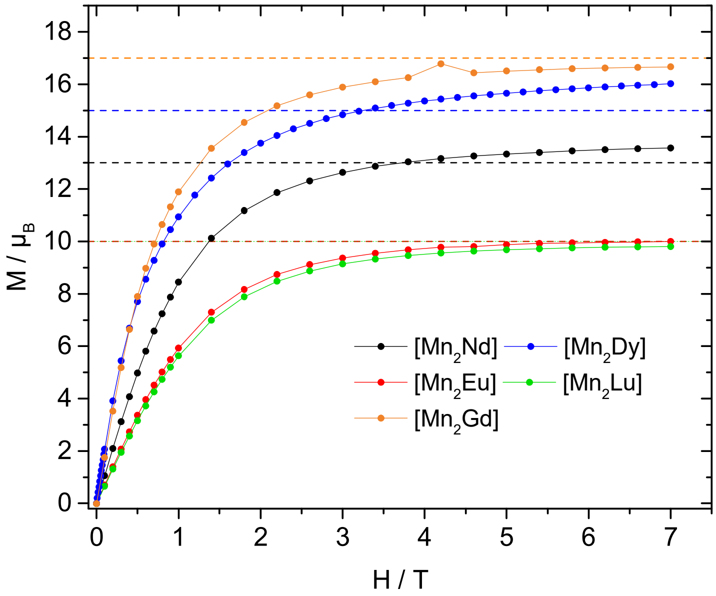

Figure 12: Molar magnetizations at 2 K of five isostructural bimetallic complexes of the [Mn_2Ln]-type (sum formula: [$C_{44}H_{44}N_8O_{12}LnMn_2(C_6H_{16}N)_2(ClO_4)(H_2O)_2$], with Ln = Nd, Eu, Gd, Dy, Lu). The horizontal dashed lines correspond to the expected values as sum of the individual spin-only contributions of one Ln(III) and two Mn(II) ions.

The saturation of the magnetization at high magnetic fields is less pronounced for [Mn_2Nd] and [Mn_2Dy]. Furthermore, the maximum measured magnetization is slightly higher compared to the calculated values (positive $\Delta M_{rel.}$, cf. Tab. 7). This indicates the presence of magnetic anisotropy and/or the population of low-lying excited states. For [Mn_2Nd] and [Mn_2Dy] the plot of M vs. H/T at different temperatures shows that the curves are not superposed on to a single master curve, supporting the assumption of either presence of magnetic anisotropy and/or population of low-lying excited states (cf. Fig. S5).[47]

Table 7: Molar magnetizations of [Mn_2Ln] measured at 2 K and 7 T ($M_{exp.}$), the expected values (spin-only, $M_{theo.}$) and the relative deviation ($\Delta M_{rel.}$) for all five complexes.

	$M_{exp.}$ / μ_B (7 T)	**$M_{theo.}$ / μ_B**	**$\Delta M_{rel.}$**
[Mn_2Nd]	13.57	13	+4.4 %
[Mn_2Eu]	9.99	10	-0.1 %
[Mn_2Gd]	16.66	17	-2.0 %
[Mn_2Dy]	16.02	15	+6.8 %
[Mn_2Lu]	9.81	10	-1.9 %

3.6 Conclusions

The combination of element selective X-ray magnetic circular dichroism spectroscopy (XMCD) and sum rule analysis allows for the assessment of the individual contributions to the total magnetic moment of a hetero-bimetallic complex. We show that we are able to extract the contribution of spin and orbital magnetizations of the manganese ions and of the lanthanide ions separately.

Due to the vanishing orbital angular momenta of the manganese ions and the substantial spin magnetizations, a high spin configuration is confirmed. The XMCD effects and the respective spin and orbital angular momenta of the lanthanide ions vary, according to the occupation of the *f*-orbitals. We have confirmed the diamagnetic ground state of Eu^{3+}. The m_L/m_S ratios reported for Nd^{3+}, Gd^{3+} and Dy^{3+} are in a very good agreement with the values expected from HUND's rules.

By comparing the experimental $m_J^{(z)}$ at the given experimental conditions with a Brillouin plot for the Mn^{2+} and the respective Ln^{3+} ground states as a function of the temperature at a constant magnetic field of 5 T, we are able to approximate the ion temperature of the hetero-bimetallic complexes. The values of around 14 K are in the expected temperature range, due to RF heating of the ions caused by the trap operation.

We have shown that the combination of XMCD spectroscopy of isolated hetero-bimetallic complexes in the gas phase with sum rule analysis is a powerful tool for the investigation of interesting magnetic compounds, free of solvation effects, crystal packing effects or interaction with surfaces.

To evaluate the magnetic data obtained from the gas phase studies, we performed bulk magnetometry of crystalline samples. The SQUID measurements show weak ferromagnetic interactions between the paramagnetic trivalent lanthanide ions (Nd^{3+}, Gd^{3+} and Dy^{3+}) and the surrounding Mn^{2+} ions at temperatures < 10 K. A magnetic coupling of the manganese ions via the diamagnetic lanthanide ions (Eu^{3+} and Lu^{3+}) is not observed. However, the susceptibility measurements reveal Van Vleck paramagnetism for [Mn_2Eu] due to thermal population of low lying excited states of the Eu^{3+} ion.

The magnetization measurements show a good agreement between the expected magnetization for weak exchange coupled ions and the measured saturation value at high fields. The less pronounced saturation of magnetization of [Mn_2Nd] and [Mn_2Dy] indicate the presence of magnetic anisotropy and/or population of low-lying excited states, supported by the M vs. H/T plots, lacking a superposition of the magnetization curves at different temperatures.

3.7 Acknowledgements

This work was supported through the DFG funded transregional collaborative research center SFB TRR 88 “3MET.de”. We gratefully acknowledge the financial support and generous allocation of X-ray beamtime from HZB and the BESSY II synchrotron radiation facility. The endstation is jointly operated by HZB and Uni Freiburg, and is partially funded by the German Federal Ministry of Education (BMBF) through grand BMBF-05K16Vf1. We thank the Toyota Technological Institute for providing the superconducting magnet used in the XMCD experiments. Dr. M. T. Gamer is acknowledged for support in solving single crystal structures.

3.8 References

[1] R. Sessoli, D. Gatteschi, A. Caneschi, M. A. Novak, "MAGNETIC BISTABILITY IN A METAL-ION CLUSTER", *Nature*, **1993**, *365*, 141-143.

[2] D. Gatteschi, A. Caneschi, L. Pardi, R. Sessoli, "LARGE CLUSTERS OF METAL IONS: THE TRANSITION FROM MOLECULAR TO BULK MAGNETS", *Science*, **1994**, *265*, 1054.

[3] L. Bogani, W. Wernsdorfer, "MOLECULAR SPINTRONICS USING SINGLE-MOLECULE MAGNETS", *Nat. Mater.*, **2008**, *7*, 179-186.

[4] S. Sanvito, A. R. Rocha, "MOLECULAR-SPINTRONICS: THE ART OF DRIVING SPIN THROUGH MOLECULES", *J. Comput. Theor. Nanosci.*, **2006**, *3*, 624-642.

[5] G. Christou, D. Gatteschi, D. N. Hendrickson, R. Sessoli, "SINGLE-MOLECULE MAGNETS", *MRS Bull.*, **2000**, *25*, 66-71.

[6] T. Lis, "PREPARATION, STRUCTURE, AND MAGNETIC PROPERTIES OF A DODECANUCLEAR MIXED-VALENCE MANGANESE CARBOXYLATE", *Acta Crystallogr., Sect. B*, **1980**, *36*, 2042-2046.

[7] M. Shiddiq, D. Komijani, Y. Duan, A. Gaita-Ariño, E. Coronado, S. Hill, "ENHANCING COHERENCE IN MOLECULAR SPIN QUBITS VIA ATOMIC CLOCK TRANSITIONS", *Nature*, **2016**, *531*, 348-351.

[8] M. N. Leuenberger, D. Loss, "QUANTUM COMPUTING IN MOLECULAR MAGNETS", *Nature*, **2001**, *410*, 789-793.

[9] K. V. Raman, A. M. Kamerbeek, A. Mukherjee, N. Atodiresei, T. K. Sen, P. Lazić, V. Caciuc, R. Michel, D. Stalke, S. K. Mandal, "*Interface-engineered templates for molecular spin memory devices*", *Nature*, **2013**, *493*, 509-513.

[10] D. Gatteschi, R. Sessoli, J. Villain, "*Molecular nanomagnets", Vol. 5*, Oxford University Press on Demand, **2006**.

[11] K. Weighardt, K. Pohl, I. Jibril, G. Huttner, "*Hydrolysis Products of the Monomeric Amine Complex $(C_6H_{15}N_3)FeCl_3$: The Structure of the Octameric Iron(III) Cation of $\{[(C_6H_{15}N_3)_6Fe_8(\mu_3\text{-}O)_2(\mu_2\text{-}OH)_{12}]Br_7(H_2O)\}Br\cdot 8H_2O$", Angew. Chem. Int. Ed. in Engl.*, **1984**, *23*, 77-78.

[12] N. Ishikawa, M. Sugita, T. Ishikawa, S. Koshihara, Y. Kaizu, "*Mononuclear lanthanide complexes with a long magnetization relaxation time at high temperatures: A new category of magnets at the single-molecular level*", *J. Phys. Chem. B*, **2004**, *108*, 11265-11271.

[13] J. D. Rinehart, M. Fang, W. J. Evans, J. R. Long, "*Strong exchange and magnetic blocking in N_2^{3-}-radical-bridged lanthanide complexes*", *Nature Chem.*, **2011**, *3*, 538-542.

[14] A. Barra, A. Caneschi, A. Cornia, F. Fabrizi de Biani, D. Gatteschi, C. Sangregorio, R. Sessoli, L. Sorace, "*Single-molecule magnet behavior of a tetranuclear iron(III) complex. The origin of slow magnetic relaxation in iron(III) clusters*", *J. Am. Chem. Soc.*, **1999**, *121*, 5302-5310.

[15] S. L. Castro, Z. Sun, C. M. Grant, J. C. Bollinger, D. N. Hendrickson, G. Christou, "*Single-molecule magnets: tetranuclear vanadium(III) complexes with a butterfly structure and an S=3 ground state*", *J. Am. Chem. Soc.*, **1998**, *120*, 2365-2375.

[16] A. M. Ako, I. J. Hewitt, V. Mereacre, R. Clérac, W. Wernsdorfer, C. E. Anson, A. K. Powell, "*A ferromagnetically coupled Mn_{19} aggregate with a record $S = 83/2$ ground spin state*", *Angew. Chem.*, **2006**, *118*, 5048-5051.

[17] V. Chandrasekhar, B. M. Pandian, R. Boomishankar, A. Steiner, J. J. Vittal, A. Houri, R. Clérac, "*Trinuclear Heterobimetallic Ni2Ln complexes $[L_2Ni_2Ln][ClO_4]$(Ln = La, Ce, Pr, Nd, Sm, Eu, Gd, Tb, Dy, Ho, and Er; LH_3 = (S)P[N(Me)N═CH−C_6H_3-2-OH-3-OMe]$_3$): From Simple Paramagnetic Complexes to Single-Molecule Magnet Behavior*", *Inorg. Chem.*, **2008**, *47*, 4918-4929.

[18] V. Chandrasekhar, B. M. Pandian, J. J. Vittal, R. Clérac, "*Synthesis, Structure, and Magnetism of Heterobimetallic Trinuclear Complexes $\{[L_2Co_2Ln][X]\}$ [Ln = Eu, X = Cl; Ln = Tb, Dy, Ho, X = NO_3; LH_3 = (S)P[N(Me)N═CH−C_6H_3-2-OH-3-OMe]$_3$]: A 3d−4f Family of Single-Molecule Magnets*", *Inorg. Chem.*, **2009**, *48*, 1148-1157.

[19] T. Yamaguchi, Y. Sunatsuki, H. Ishida, M. Kojima, H. Akashi, N. Re, N. Matsumoto, A. Pochaba, J. Mroziński, "*Synthesis, Structures, and Magnetic Properties of Face-Sharing Heterodinuclear Ni(II)–Ln(III) (Ln = Eu, Gd, Tb, Dy) Complexes*", *Inorg. Chem.*, **2008**, *47*, 5736-5745.

[20] T. Hamamatsu, K. Yabe, M. Towatari, S. Osa, N. Matsumoto, N. Re, A. Pochaba, J. Mrozinski, J.-L. Gallani, A. Barla, P. Imperia, C. Paulsen, J.-P. Kappler, "*Magnetic Interactions in Cu^{II}–Ln^{III} Cyclic Tetranuclear Complexes: Is It Possible to Explain the Occurrence of SMM Behavior in Cu^{II}–Tb^{III} and Cu^{II}–Dy^{III} Complexes?*", *Inorg. Chem.*, **2007**, *46*, 4458-4468.

[21] J. Rinck, G. Novitchi, W. Van den Heuvel, L. Ungur, Y. Lan, W. Wernsdorfer, C. E. Anson, L. F. Chibotaru, A. K. Powell, "*An Octanuclear $[Cr^{III}_4Dy^{III4}]$ 3d–4f Single-Molecule Magnet*", *Angew. Chem. Int. Ed.*, **2010**, *49*, 7583-7587.

[22] J. Dreiser, K. S. Pedersen, C. Piamonteze, S. Rusponi, Z. Salman, M. E. Ali, M. Schau-Magnussen, C. A. Thuesen, S. Piligkos, H. Weihe, H. Mutka, O. Waldmann, P. Oppeneer,

J. Bendix, F. Nolting, H. Brune, "*Direct observation of a ferri-to-ferromagnetic transition in a fluoride-bridged 3d-4f molecular cluster*", *Chem. Sci.*, **2012**, *3*, 1024-1032.

[23] R. Sessoli, A. K. Powell, "*Strategies towards single molecule magnets based on lanthanide ions*", *Coord. Chem. Rev.*, **2009**, *253*, 2328-2341.

[24] R. Sessoli, M. Mannini, F. Pineider, A. Cornia, P. Sainctavit, in *Magnetism and Synchrotron Radiation: New Trends* (Eds.: E. Beaurepaire, H. Bulou, F. Scheurer, K. Jean-Paul), Springer Berlin Heidelberg, Berlin, Heidelberg, **2010**, pp. 279-311.

[25] M.-A. Arrio, P. Sainctavit, C. C. dit Moulin, C. Brouder, F. De Groot, T. Mallah, M. Verdaguer, "*Soft X-ray magnetic circular dichroism in molecular based magnet*", *Physica B: Condensed Matter*, **1995**, *208*, 775-776.

[26] K. Baberschke, "*X-ray magnetic dichroism: the technique of choice to study magnetism element specifically*", *Phys. Scr.*, **2005**, *2005*, 49.

[27] G. Champion, N. Lalioti, V. Tangoulis, M.-A. Arrio, P. Sainctavit, F. Villain, A. Caneschi, D. Gatteschi, C. Giorgetti, F. Baudelet, "*Xmcd for monitoring exchange interactions. the role of the gd 4f and 5d orbitals in metal-nitronyl nitroxide magnetic chains*", *J. Am. Chem. Soc.*, **2003**, *125*, 8371-8376.

[28] S. Khanra, K. Kuepper, M. Prinz, M. Raekers, S. Voget, A. V. Postnikov, F. M. de Groot, S. J. George, M. Coldea, M. Neumann, "*Star-Shaped Molecule of $Mn^{II}{}_4O_6$ Core with an S_T= 10 High-Spin State. A Theoretical and Experimental Study with XPS, XMCD, and Other Magnetic Methods*", *Inorg. Chem.*, **2008**, *47*, 4605-4617.

[29] M. P. de Jong, C. Tengstedt, A. Kanciurzewska, E. Carlegrim, W. R. Salaneck, M. Fahlman, "*Chemical bonding in $V(TCNE)_x$ ($x\sim 2$) thin-film magnets grown in situ*", *Phys. Rev. B*, **2007**, *75*, 064407.

[30] M.-A. Arrio, P. Sainctavit, C. Cartier dit Moulin, C. Brouder, F. De Groot, T. Mallah, M. Verdaguer, "*Measurement of magnetic moment at the atomic scale in a high Tc molecular based magnet*", *J. Phys. Chem.*, **1996**, *100*, 4679-4684.

[31] M. Mannini, F. Pineider, P. Sainctavit, C. Danieli, E. Otero, C. Sciancalepore, A. M. Talarico, M.-A. Arrio, A. Cornia, D. Gatteschi, "*Magnetic memory of a single-molecule quantum magnet wired to a gold surface*", *Nat. Mater.*, **2009**, *8*, 194-197.

[32] M. Mannini, P. Sainctavit, R. Sessoli, C. Cartier dit Moulin, F. Pineider, M. A. Arrio, A. Cornia, D. Gatteschi, "*XAS and XMCD investigation of Mn12 monolayers on gold*", *Chem. Eur. J.*, **2008**, *14*, 7530-7535.

[33] J. Meyer, M. Tombers, C. van Wüllen, G. Niedner-Schatteburg, S. Peredkov, W. Eberhardt, M. Neeb, S. Palutke, M. Martins, W. Wurth, "*The spin and orbital contributions to the total magnetic moments of free Fe, Co, and Ni clusters*", *J. Chem. Phys.*, **2015**, *143*, 104302.

[34] S. Peredkov, M. Neeb, W. Eberhardt, J. Meyer, M. Tombers, H. Kampschulte, G. Niedner-Schatteburg, "*Spin and Orbital Magnetic Moments of Free Nanoparticles*", *Phys. Rev. Lett.*, **2011**, *107*, 233401.

[35] S. Peredkov, A. Savci, S. Peters, M. Neeb, W. Eberhardt, H. Kampschulte, J. Meyer, M. Tombers, B. Hofferberth, F. Menges, G. Niedner-Schatteburg, "*X-ray absorption spectroscopy of mass-selected transition metal clusters using a cyclotron ion trap: An experimental setup for measuring XMCD spectra of free clusters*", *J. Electron Spectrosc. Relat. Phenom.*, **2011**, *184*, 113-118.

[36] D. Dieleman, M. Tombers, L. Peters, J. Meyer, S. Peredkov, J. Jalink, M. Neeb, W. Eberhardt, T. Rasing, G. Niedner-Schatteburg, "*Orbit and spin resolved magnetic*

properties of size selected [Co_nRh]$^+$ and [Co_nAu]$^+$ nanoalloy clusters", *Phys. Chem. Chem. Phys.*, **2015**, *17*, 28372-28378.

[37] S. T. Akin, V. Zamudio-Bayer, K. Duanmu, G. Leistner, K. Hirsch, C. Bülow, A. Ławicki, A. Terasaki, B. v. Issendorff, D. G. Truhlar, J. T. Lau, M. A. Duncan, "*Size-Dependent Ligand Quenching of Ferromagnetism in Co_3(benzene)$_n^+$ Clusters Studied with X-ray Magnetic Circular Dichroism Spectroscopy*", *J. Phys. Chem. Lett.*, **2016**, *7*, 4568-4575.

[38] K. Hirsch, V. Zamudio-Bayer, A. Langenberg, M. Niemeyer, B. Langbehn, T. Möller, A. Terasaki, B. v. Issendorff, J. T. Lau, "*Magnetic Moments of Chromium-Doped Gold Clusters: The Anderson Impurity Model in Finite Systems*", *Phys. Rev. Lett.*, **2015**, *114*, 087202.

[39] A. Langenberg, K. Hirsch, A. Ławicki, V. Zamudio-Bayer, M. Niemeyer, P. Chmiela, B. Langbehn, A. Terasaki, B. v. Issendorff, J. T. Lau, "*Spin and orbital magnetic moments of size-selected iron, cobalt, and nickel clusters*", *Phys. Rev. B*, **2014**, *90*, 184420.

[40] M. Niemeyer, K. Hirsch, V. Zamudio-Bayer, A. Langenberg, M. Vogel, M. Kossick, C. Ebrecht, K. Egashira, A. Terasaki, T. Möller, B. v. Issendorff, J. T. Lau, "*Spin Coupling and Orbital Angular Momentum Quenching in Free Iron Clusters*", *Phys. Rev. Lett.*, **2012**, *108*, 057201.

[41] E. Dmitrii, S. Bari, H. Ronnie, L. Arkadiusz, H. Konstantin, Z.-B. Vicente, L. Tobias, I. Bernd von, S. Thomas, "*An intense electrospray ionization source for soft X-ray photoionization of gas phase protein ions*", *J. Phys. Conf. Ser.*, **2015**, *635*, 112083.

[42] V. Zamudio-Bayer, K. Hirsch, A. Langenberg, A. Ławicki, A. Terasaki, B. v. Issendorff, J. Lau, "*Electronic ground states of Fe_2^+ and Co_2^+ as determined by x-ray absorption and x-ray magnetic circular dichroism spectroscopy*", *J. Chem. Phys.*, **2015**, *143*, 244318.

[43] V. Zamudio-Bayer, K. Hirsch, A. Langenberg, M. Niemeyer, M. Vogel, A. Ławicki, A. Terasaki, J. T. Lau, B. von Issendorff, "*Maximum Spin Polarization in Chromium Dimer Cations as Demonstrated by X-ray Magnetic Circular Dichroism Spectroscopy*", *Angew. Chem. Int. Ed.*, **2015**, *54*, 4498-4501.

[44] V. Zamudio-Bayer, L. Leppert, K. Hirsch, A. Langenberg, J. Rittmann, M. Kossick, M. Vogel, R. Richter, A. Terasaki, T. Möller, "*Coordination-driven magnetic-to-nonmagnetic transition in manganese-doped silicon clusters*", *Phys. Rev. B*, **2013**, *88*, 115425.

[45] V. Zamudio-Bayer, R. Lindblad, C. Bülow, G. Leistner, A. Terasaki, B. v. Issendorff, J. T. Lau, "*Electronic ground state of Ni_2^+*", *J. Chem. Phys*, **2016**, *145*, 194302.

[46] A. Bhunia, M. T. Gamer, L. Ungur, L. F. Chibotaru, A. K. Powell, Y. Lan, P. W. Roesky, F. Menges, C. Riehn, G. Niedner-Schatteburg, "*From a Dy(III) single molecule magnet (SMM) to a ferromagnetic [Mn(II)Dy(III)Mn(II)] trinuclear complex*", *Inorg. Chem.*, **2012**, *51*, 9589-9597.

[47] A. Bhunia, "*Functionalized 3d/4f Coordination Oligomers and Polymers*", Cuvillier, **2011**.

[48] K. Hirsch, J. Lau, P. Klar, A. Langenberg, J. Probst, J. Rittmann, M. Vogel, V. Zamudio-Bayer, T. Möller, B. Von Issendorff, "*X-ray spectroscopy on size-selected clusters in an ion trap: from the molecular limit to bulk properties*", *J. Phys. B: At., Mol. Opt. Phys.*, **2009**, *42*, 154029.

[49] L. F. Chibotaru, L. Ungur, C. Aronica, H. Elmoll, G. Pilet, D. Luneau, "*Structure, magnetism, and theoretical study of a mixed-valence $Co^{II}_3Co^{III}_4$ heptanuclear wheel: lack of SMM behavior despite negative magnetic anisotropy*", *J. Am. Chem. Soc.*, **2008**, *130*, 12445-12455.

[50] C. T. Chen, Y. U. Idzerda, H. J. Lin, N. V. Smith, G. Meigs, E. Chaban, G. H. Ho, E. Pellegrin, F. Sette, "*Experimental Confirmation of the X-Ray Magnetic Circular Dichroism Sum Rules for Iron and Cobalt*", *Phys. Rev. Lett.*, **1995**, *75*, 152-155.

[51] B. T. Thole, P. Carra, F. Sette, G. van der Laan, "*X-ray circular dichroism as a probe of orbital magnetization*", *Phys. Rev. Lett.*, **1992**, *68*, 1943-1946.

[52] P. Carra, B. T. Thole, M. Altarelli, X. Wang, "*X-ray circular dichroism and local magnetic fields*", *Phys. Rev. Lett.*, **1993**, *70*, 694-697.

[53] P. Carra, "*X-ray circular dichroism as a probe of orbital and spin magnetizations*", *Synchrotron Radiat. News*, **1992**, *5*, 21-24.

[54] G. Schütz, E. Goering, H. Stoll, in *Handbook of Magnetism and Advanced Magnetic Materials*, John Wiley & Sons, Ltd, **2007**.

[55] C. Piamonteze, P. Miedema, F. M. F. de Groot, "*Accuracy of the spin sum rule in XMCD for the transition-metal L edges from manganese to copper*", *Phys. Rev. B*, **2009**, *80*, 184410.

[56] W. Heiko, "*Recent advances in x-ray absorption spectroscopy*", *Rep. Prog. Phys.*, **2004**, *67*, 2105.

[57] T. Funk, A. Deb, S. J. George, H. Wang, S. P. Cramer, "*X-ray magnetic circular dichroism—a high energy probe of magnetic properties*", *Coord. Chem. Rev.*, **2005**, *249*, 3-30.

[58] F. M. F. de Groot, "*X-ray absorption and dichroism of transition metals and their compounds*", *J. Electron Spectrosc. Relat. Phenom.*, **1994**, *67*, 529-622.

[59] Y. Teramura, A. Tanaka, T. Jo, "*Effect of coulomb interaction on the X-Ray magnetic circular dichroism spin sum rule in 3d transition elements*", *J. Phys. Soc. Jpn.*, **1996**, *65*, 1053-1055.

[60] Y. Teramura, A. Tanaka, B. T. Thole, T. Jo, "*Effect of Coulomb Interaction on the X-Ray Magnetic Circular Dichroism Spin Sum Rule in Rare Earths*", *J. Phys. Soc. Jpn.*, **1996**, *65*, 3056-3059.

[61] S. Qiao, A. Kimura, H. Adachi, K. Iori, K. Miyamoto, T. Xie, H. Namatame, M. Taniguchi, A. Tanaka, T. Muro, S. Imada, S. Suga, "*Direct evidence of ferromagnetism without net magnetization observed by x-ray magnetic circular dichroism*", *Phys. Rev. B*, **2004**, *70*, 134418.

[62] S. Qiao, A. Kimura, H. Adachi, K. Iori, K. Miyamoto, T. Xie, H. Namatame, M. Taniguchi, A. Tanaka, T. Muro, S. Imada, S. Suga, "*Temperature dependence of spin and orbital magnetic moments of Sm 4f electrons in (Sm, Gd)Al_2*", *J. Electron Spectrosc. Relat. Phenom.*, **2005**, *144–147*, 749-752.

[63] F. Bondino, C. Cepek, N. Tagmatarchis, M. Prato, H. Shinohara, A. Goldoni, "*Element-Specific Probe of the Magnetic and Electronic Properties of Dy incar-Fullerenes*", *J. Phys. Chem. B*, **2006**, *110*, 7289-7295.

[64] T. Jo, "*The 3d–4f exchange interaction, X-ray second-order optical processes and the magnetic circular dichroism (MCD) spin sum rule in rare earths*", *J. Electron Spectrosc. Relat. Phenom.*, **1997**, *86*, 73-82.

[65] G. Sheldrick, "*A short history of SHELX*", *Acta Crystallogr., Sect. A*, **2008**, *64*, 112-122.

[66] D. B. Xu, C. J. Sun, J. S. Chen, S. M. Heald, B. Sanyal, R. A. Rosenberg, T. J. Zhou, G. M. Chow, "*Large enhancement of magnetic moment in L 1 0 ordered FePt thin films by Nd substitutional doping*", *J. Phys. D: Appl. Phys.*, **2015**, *48*, 255001.

[67] O. Toulemonde, F. Studer, A. Barnabé, B. Raveau, J. B. Goedkoop, "*Magnetic properties of chromium doped rare earth manganites $Ln_{0.5}Ca_{0.5}Mn_{1-x}Cr_xO_3$(Ln=Pr, Nd, Sm and*

$0.05 \leqslant x \leqslant 0.10$) by soft x-ray magnetic circular dichroism", J. Appl. Phys., **1999**, *86*, 2616-2621.

[68] R. Cid, J. Díaz, L. M. Álvarez-Prado, J. M. Alameda, S. M. Valvidares, J. C. Cezar, N. B. Brookes, "*Microscopic origin of perpendicular magnetic anisotropy in amorphous Nd-Co homogeneous and compositionally modulated, thin films studied by XMCD", J. Phys. Conf. Ser.*, **2010**, *200*, 072017.

[69] A. F. Orchard, "*Magnetochemistry", Oxford chemistry primers*, **1999**, *75*.

[70] J. D. Rinehart, J. R. Long, "*Exploiting single-ion anisotropy in the design of f-element single-molecule magnets", Chem. Sci.*, **2011**, *2*, 2078-2085.

[71] G. R. Giesbrecht, J. C. Gordon, "*Lanthanide alkylidene and imido complexes", Dalton Transactions*, **2004**, 2387-2393.

[72] L. Maron, O. Eisenstein, "*Do f Electrons Play a Role in the Lanthanide−Ligand Bonds? A DFT Study of Ln(NR$_2$)$_3$; R=H, SiH$_3$", J. Phys. Chem. A*, **2000**, *104*, 7140-7143.

[73] H. Lueken, "*Magnetochemie", Teubner Studienbücher Chemie*, **1999**.

[74] J. Stöhr, "*X-ray magnetic circular dichroism spectroscopy of transition metal thin films", J. Electron Spectrosc. Relat. Phenom.*, **1995**, *75*, 253-272.

[75] K. Fauth, B. Münzing, "*Unterdrückter Impuls", Phys. J.*, **2012**, *11*, 22.

[76] A. Skaugen, E. Schierle, G. van der Laan, D. K. Shukla, H. C. Walker, E. Weschke, J. Strempfer, "*Long-range antiferromagnetic order of formally nonmagnetic Eu^{3+} Van Vleck ions observed in multiferroic Eu$_{1-x}$Y$_x$MnO$_3$", Phys. Rev. B*, **2015**, *91*, 180409.

[77] A. Frank, "*Temperature Variation of the Magnetic Susceptibility, Gyromagnetic Ratio, and Heat Capacity in Sm^{+++} and Eu^{+++}", Phys. Rev.*, **1932**, *39*, 119-129.

[78] J. H. Van Vleck, "*Magnetic Case History of the Eu^{3+} Ion", J. Appl. Phys.*, **1968**, *39*, 365-372.

[79] M. S. Tagirov, D. A. Tayurskiĭ, "*Insulating Van Vleck paramagnets at high magnetic fields (Review)", Low Temp. Phys.*, **2002**, *28*, 147-164.

[80] Y. Takikawa, S. Ebisu, S. Nagata, "*Van Vleck paramagnetism of the trivalent Eu ions", J. Phys. Chem. Solids*, **2010**, *71*, 1592-1598.

[81] W. C. Martin, R. Zalubas, L. Hagan, "*Atomic energy levels-The rare-Earth elements", NSRDS-NBS, Washington: National Bureau of Standards, US Department of Commerce*, **1978**, *1*.

3.9 Supplementary Material

Intrinsic Magnetism of Hetero-Bimetallic 3*d*-4*f* Complexes by XMCD Spectroscopy

Joachim M. Hewer[a], Matthias Tombers[a], Johannes Lang[a], Sebastian Schmitt[f], Yanhua Lan[f], Annie K. Powell[f,g], Marc H. Prosenc[a], Vicente Zamudio-Bayer[b], J. Tobias Lau[b], Bernd von Issendorff[c], Akira Terasaki[d], Thomas Schlathölter[e], Ronnie Hoekstra[e], Asamanjoy Bhunia[f], Munendra Yadav[f], Ravi Yadav[f], Peter W. Roesky[f], and Gereon Niedner-Schatteburg[a]

- *(a) Fachbereich Chemie and Forschungszentrum OPTIMAS, Kaiserslautern, Germany*
- *(b) Institut für Methoden und Instrumentierung der Forschung mit Synchrotronstrahlung, Helmholtz-Zentrum Berlin für Materialien und Energie, Berlin, Germany*
- *(c) Physikalisches Institut, Universität Freiburg, Germany*
- *(d) Department of Chemistry, Kyushu University, Fukuoka, Japan*
- *(e) Zernike Institute for Advanced Materials, University of Groningen, Groningen, The Netherlands*
- *(f) Institut für Anorganische Chemie, Karlsruher Institut für Technologie, Karlsruhe, Germany*
- *(g) Institute of Nanotechnology, Karlsruhe Institute of Technology, Germany*

Content

Figure S1: Molecular structure of [Mn_2Nd] in the solid-state.

Figure S2: Molecular structure of [Mn_2Eu] in the solid-state.

Figure S3: Molecular structure of [Mn_2Gd] in the solid-state.

Figure S4: Molecular structure of [Mn_2Lu] in the solid-state.

Table S1: The expectation values of magnetic quantities and the ratio of X_I to X_E of the S_z sum rule for Mn^{2+} calculated with 10 Dq = 1.5 eV.

Table S2: The expectation values of magnetic quantities and the ratio of X_I to X_E of the S_z sum rule for Nd^{3+}, Gd^{3+} and Dy^{3+}.

Table S3: Ground states of the ions Mn^{2+} and Ln^{3+}, and the respective calculated Curie constants.

Table S4: Lowest lying excited states of the Ln^{3+} ions.

Figure S5: DC magnetic data. Field dependence of magnetization of the $[Mn_2Ln]$-type complexes (Ln = Nd, Eu, Gd, Dy, Lu) as M vs. H/T plots.

Figure S6: Sum of positive and negative XA spectra (black) and their integrated sum (red) for five different mixed 3*d*-4*f* trinuclear complexes $[Mn_2Ln](H)_2^+$ (Ln = Nd, Eu, Gd, Dy, Lu).

Figure S7: XMCD spectra (black) and their integrated sum (red) for five different mixed 3*d*-4*f* trinuclear complexes $[Mn_2Ln](H)_2^+$ (Ln = Nd, Eu, Gd, Dy, Lu).

Figure S8: Semi-logarithmic plot of the measured temperature dependence of χT of five complexes of the $[Mn_2Ln]$-type (sum formula: $[C_{44}H_{44}N_8O_{12}LnMn_2(C_6H_{16}N)_2(ClO_4)(H_2O)_2]$, with Ln = Nd, Eu, Gd, Dy, Lu).

Figure S9: Relative orientation of the total magnetic moments $m_J^{(z)}/m_J$ as Brillouin function of the temperature for Mn^{2+}, Nd^{3+}, Gd^{3+} and Dy^{3+}.

Figure S10: Calculated Magnetizations of the Mn^{2+} cations by the original sum rules: contributions by spin ($m_S^{(z)}$, filled blue circles), contributions by orbit ($m_L^{(z)}$, filled red squares), total values ($m_J^{(z)}$, filled black triangles); together with the $m_L^{(z)}$ to $m_S^{(z)}$ ratio (open purple triangles) on the manganese ions within the investigated mixed 3*d*-4*f* trinuclear complexes of the type $[Mn_2Ln](H)_2^+$.

Table S5: Experimental orbital ($m_L^{(z)}$), spin ($m_S^{(z)}$), total ($m_{tot}^{(z)}$) magnetization and the orbital to spin ratios ($m_L^{(z)}/m_S^{(z)}$) at the manganese ions of the $[Mn_2Ln](H)_2^+$ complexes obtained by the original sum rules.

Figure S11: Calculated Spin ($m_S^{(z)}$, filled blue circles), orbital ($m_L^{(z)}$, filled red squares), total ($m_{tot}^{(z)}$, filled black triangles) magnetizations by the original sum rules and the $m_L^{(z)}$ to $m_S^{(z)}$

ratio (open purple triangles) on the Ln atoms within the investigated bimetallic 3*d*-4*f* trinuclear complexes of the type $[Mn_2Ln](H)_2^+$.

Table S6: Experimental orbital ($m_L^{(z)}$), spin ($m_S^{(z)}$), total ($m_{tot}^{(z)}$) magnetizations and the orbital to spin ratios ($m_L^{(z)}/m_S^{(z)}$) at the Ln^{3+} ions of the $[Mn_2Ln](H)_2^+$ complexes obtained by the original sum rules.

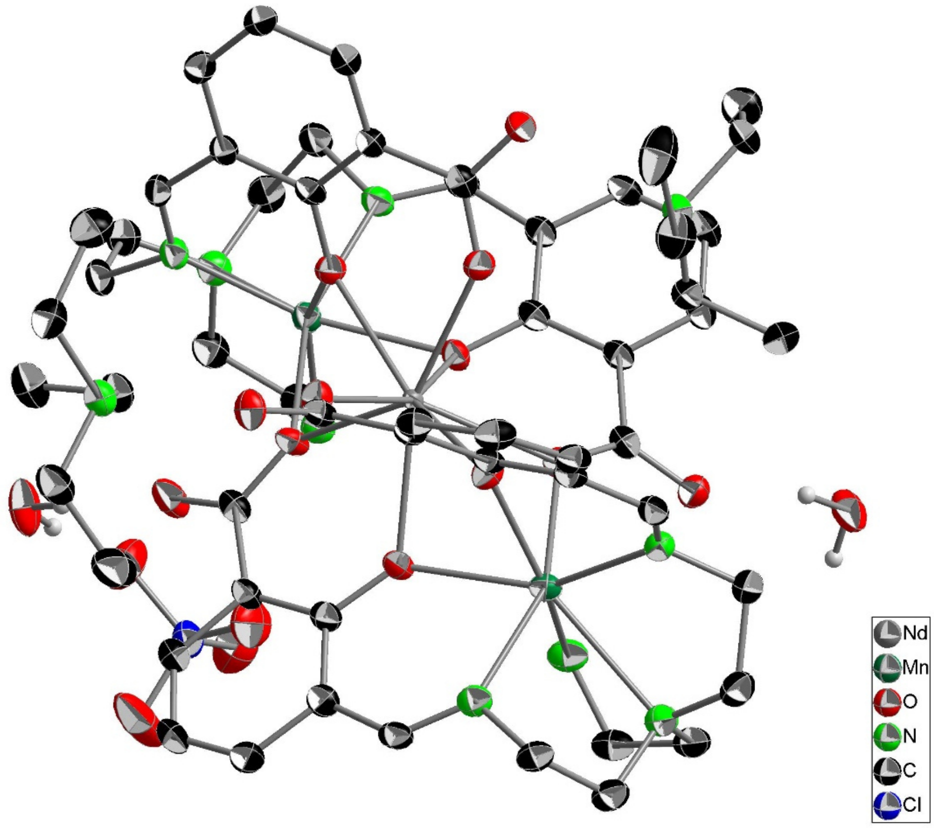

Figure S1: Molecular structure of [Mn_2Nd] in the solid-state. Hydrogen atoms are omitted for clarity. Ellipsoids displayed at 50% probability.

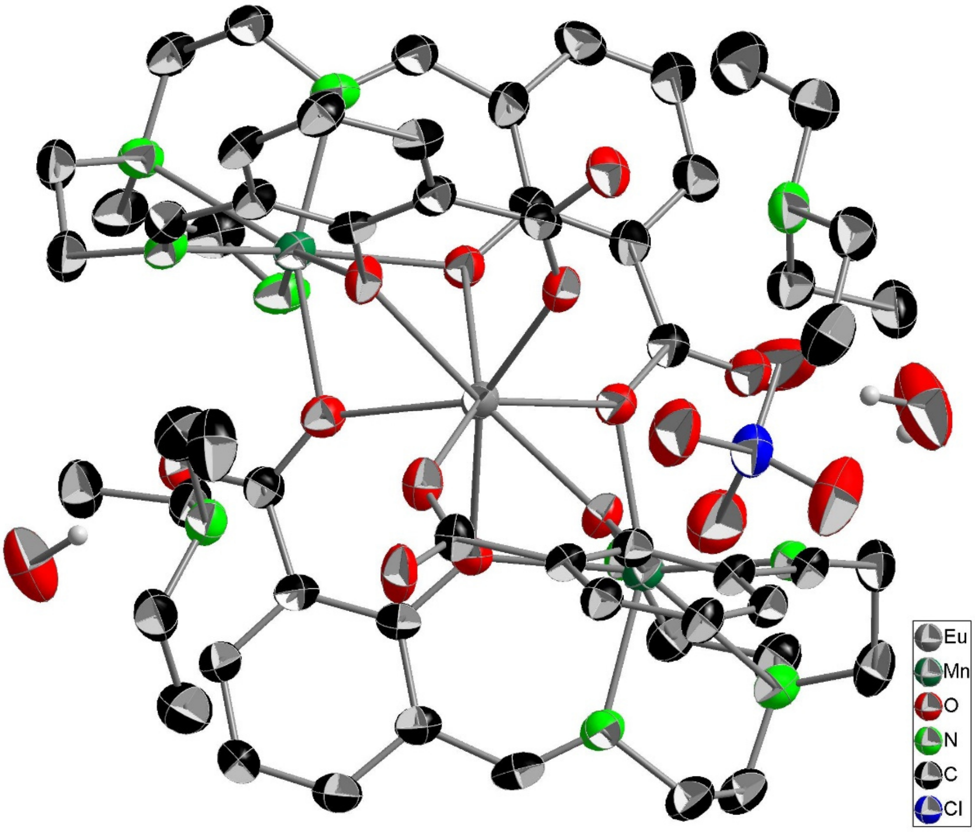

Figure S2: Molecular structure of [Mn_2Eu] in the solid-state. Hydrogen atoms are omitted for clarity. Ellipsoids displayed at 50% probability.

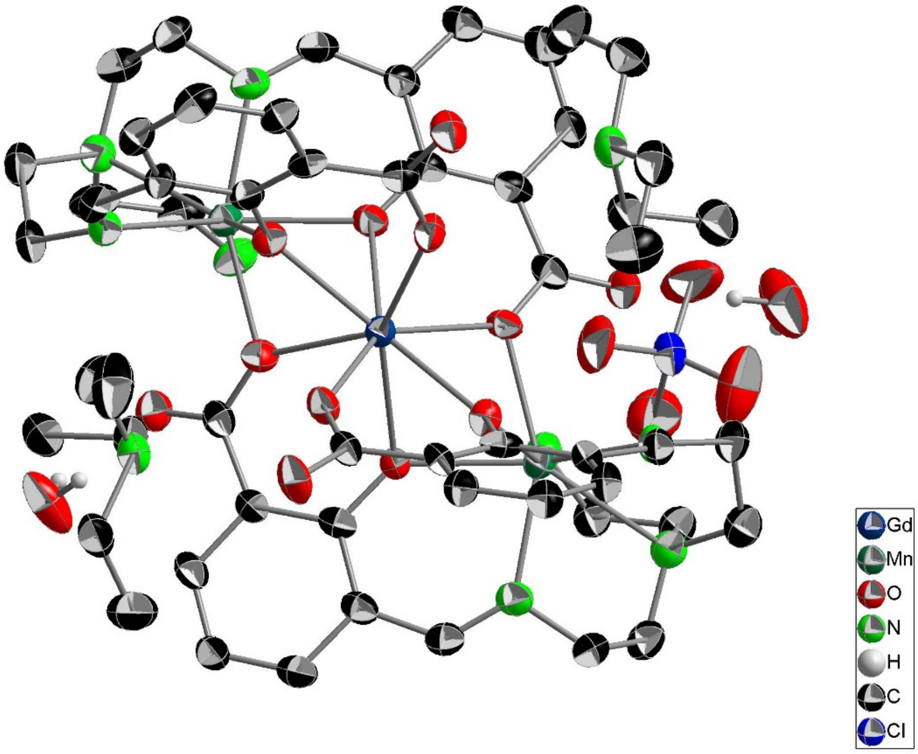

Figure S3: Molecular structure of [Mn_2Gd] in the solid-state. Hydrogen atoms are omitted for clarity. Ellipsoids displayed at 50% probability.

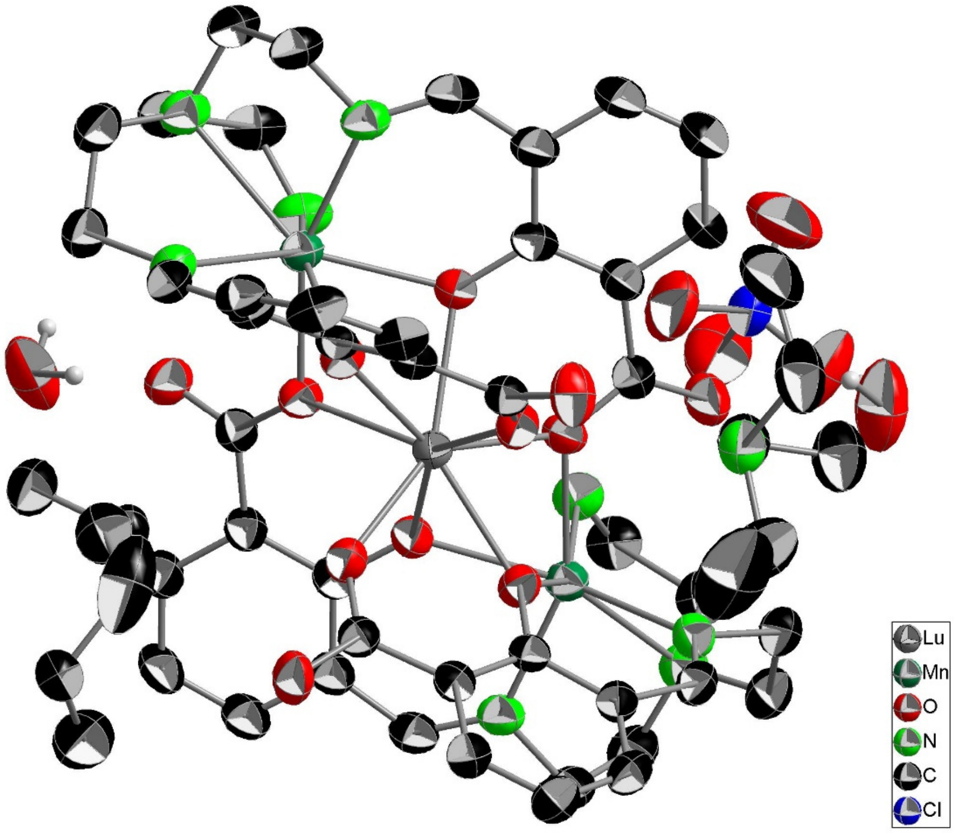

Figure S4: Molecular structure of [Mn_2Lu] in the solid-state. Hydrogen atoms are omitted for clarity. Ellipsoids displayed at 50% probability.

Correction of the spin sum rules by Takeo Jo *et al.*.[59, 60]

The S_z sum rule for the $L_{2,3}$ edge in **3*d* transition metal** systems is expressed as:

$$X_I = X_E.$$

The relative integrated magnetic circular dichroism (MCD) intensity is defined as

$$X_I = \frac{\int_{L_3}\left(\mu_+(\omega)-\mu_-(\omega)\right)d\omega - 2\int_{L_2}\left(\mu_+(\omega)-\mu_-(\omega)\right)d\omega}{\int_{L_3+L_2}\left(\mu_+(\omega)+\mu_0(\omega)+\mu_-(\omega)\right)d\omega}$$

and the expectation value is given by

$$X_E = \frac{2}{3(10-n)}\langle S_z\rangle + \frac{7}{3(10-n)}\langle T_z\rangle.$$

The absorption spectra with positive and negative light helicity are given by $\mu_{\pm}(\omega)$, with linearly polarized light by $\mu_0(\omega)$ along the *z* direction. L_3 and L_2 denote the integrated region with respect to ω, the number of 3*d* electrons is given by n.

Table S1: The expectation values of magnetic quantities and the ratio of X_I to X_E of the S_z sum rule for Mn^{2+} calculated with 10 Dq = 1.5 eV.[59]

	n	$\langle S_z\rangle$	$\langle T_z\rangle$	X_I/X_E
Mn^{2+}	5	-2.50	0.00031	0.680

The S_z sum rule for the **rare earths** is very similar:

$$X_I = X_E,$$

but the integrated MCD intensity is defined by

$$X_I = X_I(M_5) - \tfrac{3}{2} X_I(M_4)$$

and

$$X_I(M_5) = \frac{\int_{M_5} \big(\mu_-(\omega) - \mu_+(\omega)\big) d\omega}{\int_{M_5+M_4} \big(\mu_+(\omega) + \mu_0(\omega) + \mu_-(\omega)\big) d\omega},$$

$$X_I(M_4) = \frac{\int_{M_4} \big(\mu_-(\omega) - \mu_+(\omega)\big) d\omega}{\int_{M_5+M_4} \big(\mu_+(\omega) + \mu_0(\omega) + \mu_-(\omega)\big) d\omega}.$$

The expectation value is given by

$$X_E = \frac{2}{3(14-n)} \langle S_z \rangle + \frac{7}{14-n} \langle T_z \rangle.$$

The absorption spectra with positive and negative light helicity are given by $\mu_{\pm}(\omega)$, with linearly polarized light by $\mu_0(\omega)$ along the *z* direction. M_5 and M_4 denote the integrated region with respect to ω, the number of 4*f* electrons is given by n.

Table S2: The expectation values of magnetic quantities and the ratio of X_I to X_E of the S_z sum rule for Nd^{3+}, Gd^{3+} and Dy^{3+}.[60]

	n	$\langle S_z \rangle$	$\langle T_z \rangle$	X_I/X_E
Nd^{3+}	3	1.20	0.378	2.076
Gd^{3+}	7	-3.466	0.010	0.949
Dy^{3+}	9	-2.417	0.128	0.919

Table S3: Ground states of the Mn^{2+} and Ln^{3+} ions and the respective calculated Curie constants.

Ion	e^--config.	S	L	J	$^{2S+1}L_J$	g_J	C / cm^3Kmol^{-1}
Mn(II)	[Ar] $3d^5$	5/2	0	5/2	$^6S_{5/2}$	2	4.377
Nd(III)	[Xe] $4f^3$	3/2	6	9/2	$^4I_{9/2}$	8/11	1.637
Eu(III)	[Xe] $4f^6$	3	3	0	$^7F_0$		
Gd(III)	[Xe] $4f^7$	7/2	0	7/2	$^8S_{7/2}$	2	7.878
Dy(III)	[Xe] $4f^9$	5/2	5	15/2	$^6H_{15/2}$	4/3	14.172
Lu(III)	[Xe] $4f^{14}$	0	0	0	$^1S_0$		

Table S4: Lowest lying excited states of the Ln^{3+} ions.[81]

Ion	e⁻-config.	Term	Level / cm⁻¹
Nd(III)	[Xe] 4*f*³	$^4I_{9/2}$	0
		$^4I_{11/2}$	1880
		$^4I_{13/2}$	3860
		$^4I_{15/2}$	5910
		$^4F_{3/2}$	11290
		$^4F_{5/2}$	12320
		$^4F_{7/2}$	13280
		$^4F_{9/2}$	14570
Eu(III)	[Xe] 4*f*⁶	$^7F_0$	0
		$^7F_1$	370
		$^7F_2$	1040
		$^7F_3$	1890
		$^7F_4$	2860
		$^7F_5$	3910
		$^7F_6$	4940
Gd(III)	[Xe] 4*f*⁷	$^8S_{7/2}$	0
		$^6P_{7/2}$	32120
		$^6P_{5/2}$	32720
		$^6P_{3/2}$	33290
Dy(III)	[Xe] 4*f*⁹	$^6H_{15/2}$	0
		$^6H_{9/2}$	
		$^6H_{13/2}$	3460
		$^6H_{11/2}$	5780
		$^6H_{7/2}$	9060
		$^6H_{5/2}$	10100
		$^6F_{1/2}$	
		$^6F_{11/2}$	
		$^6F_{9/2}$	8950
		$^6F_{7/2}$	10870
		$^6F_{5/2}$	12270
		$^6F_{3/2}$	13060
Lu(III)	[Xe] 4*f*¹⁴	$^1S_0$	0
		$^2F_{7/2}$	90433
		$^2F_{7/2}$	94768

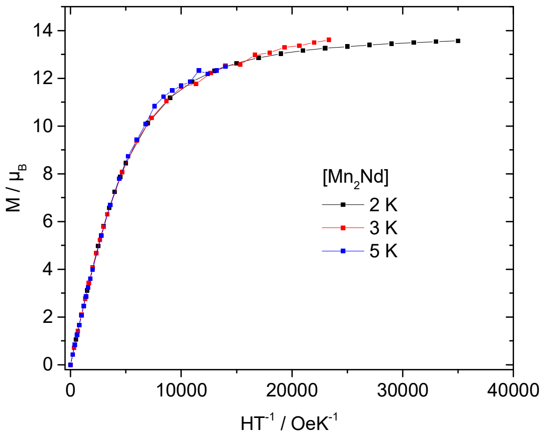
M / μ_B
0
2
4
6
8
10
12
14
0
10000
20000
30000
40000
HT^{-1} / OeK^{-1}
[Mn$_2$Nd]
2 K
3 K
5 K

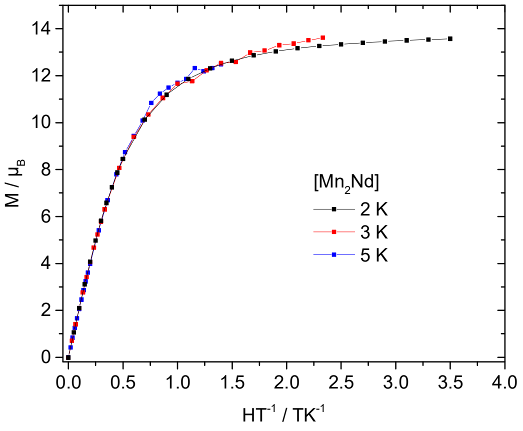
M / μ_B
0
2
4
6
8
10
12
14
0.0
0.5
1.0
1.5
2.0
2.5
3.0
3.5
4.0
HT^{-1} / TK^{-1}
[Mn$_2$Nd]
2 K
3 K
5 K

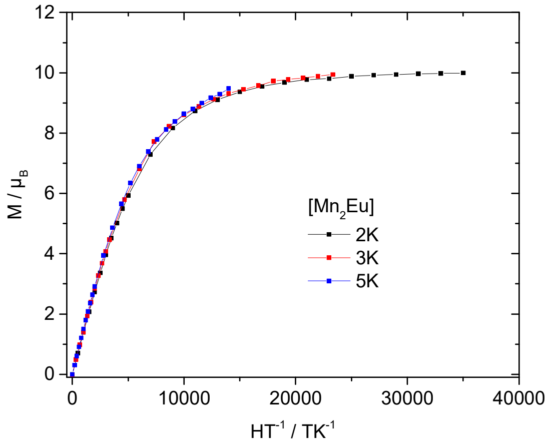
M / μ_B
0
2
4
6
8
10
12
0
10000
20000
30000
40000
HT^{-1} / TK^{-1}
[Mn$_2$Eu]
2K
3K
5K

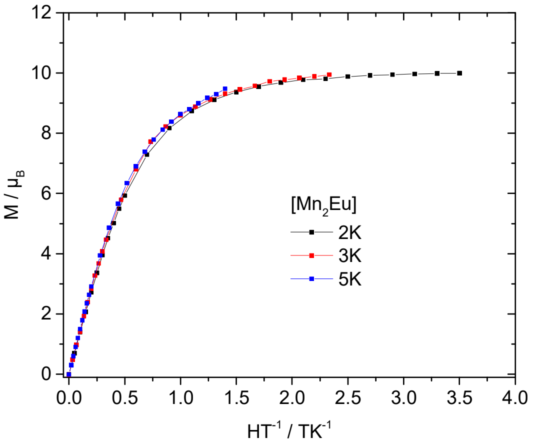
M / μ_B
0
2
4
6
8
10
12
0.0
0.5
1.0
1.5
2.0
2.5
3.0
3.5
4.0
HT^{-1} / TK^{-1}
[Mn$_2$Eu]
2K
3K
5K

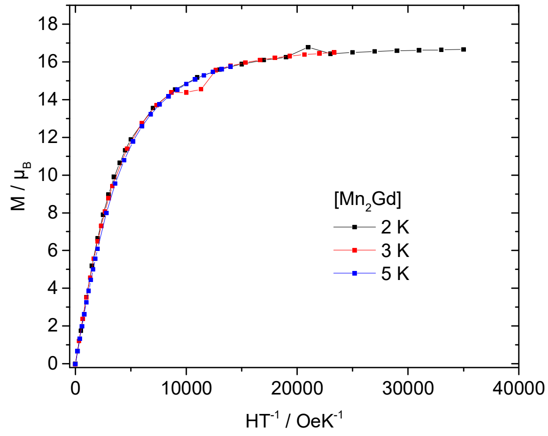
M / μ_B
0
2
4
6
8
10
12
14
16
18
0
10000
20000
30000
40000
HT^{-1} / OeK^{-1}
[Mn$_2$Gd]
2 K
3 K
5 K

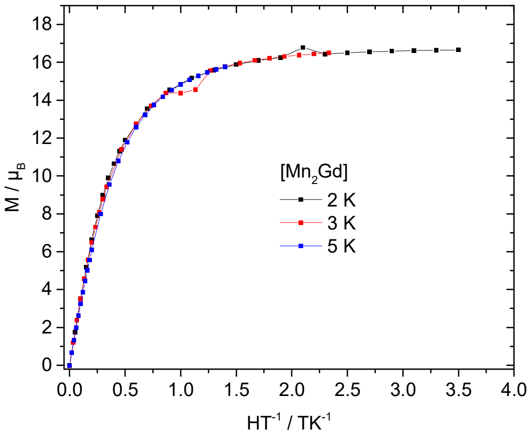
M / μ_B
0
2
4
6
8
10
12
14
16
18
0.0
0.5
1.0
1.5
2.0
2.5
3.0
3.5
4.0
HT^{-1} / TK^{-1}
[Mn$_2$Gd]
2 K
3 K
5 K

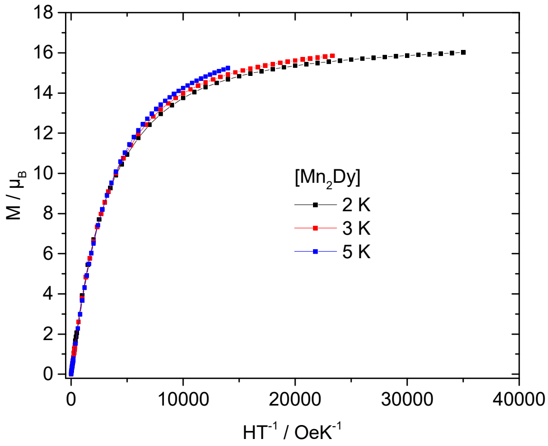
M / μ_B
0
2
4
6
8
10
12
14
16
18
0
10000
20000
30000
40000
HT^{-1} / OeK^{-1}
[Mn$_2$Dy]
2 K
3 K
5 K

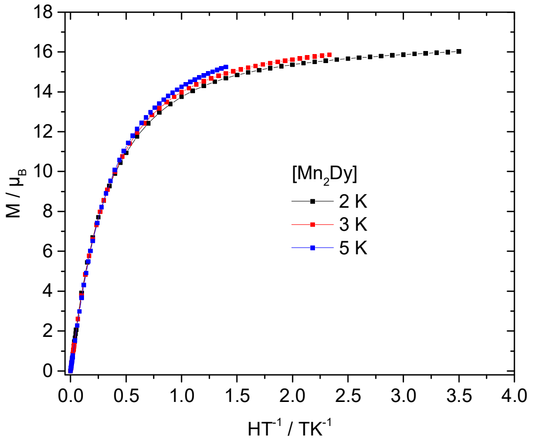
M / μ_B
0
2
4
6
8
10
12
14
16
18
0.0
0.5
1.0
1.5
2.0
2.5
3.0
3.5
4.0
HT^{-1} / TK^{-1}
[Mn$_2$Dy]
2 K
3 K
5 K

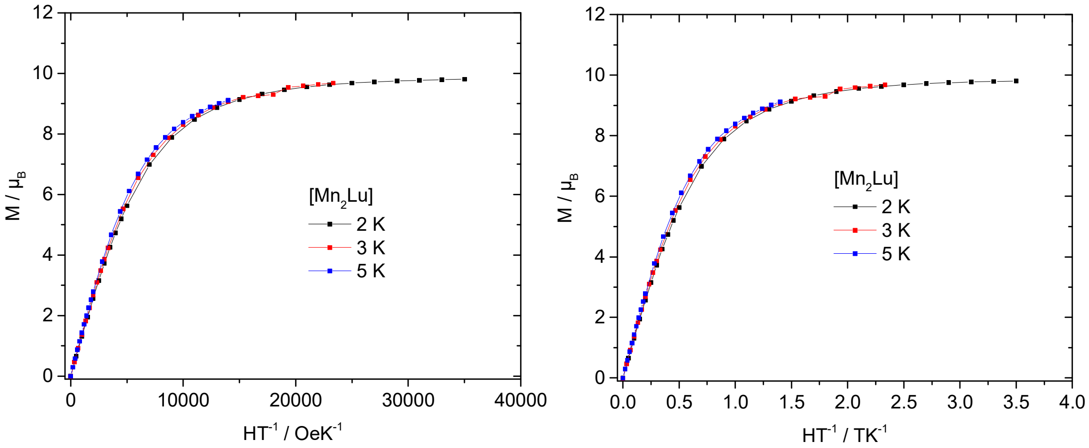

Figure S5: DC magnetic data. Field dependence of magnetization of the [Mn_2Ln]-type complexes (Ln = Nd, Eu, Gd, Dy, Lu) as M vs. H/T plots.

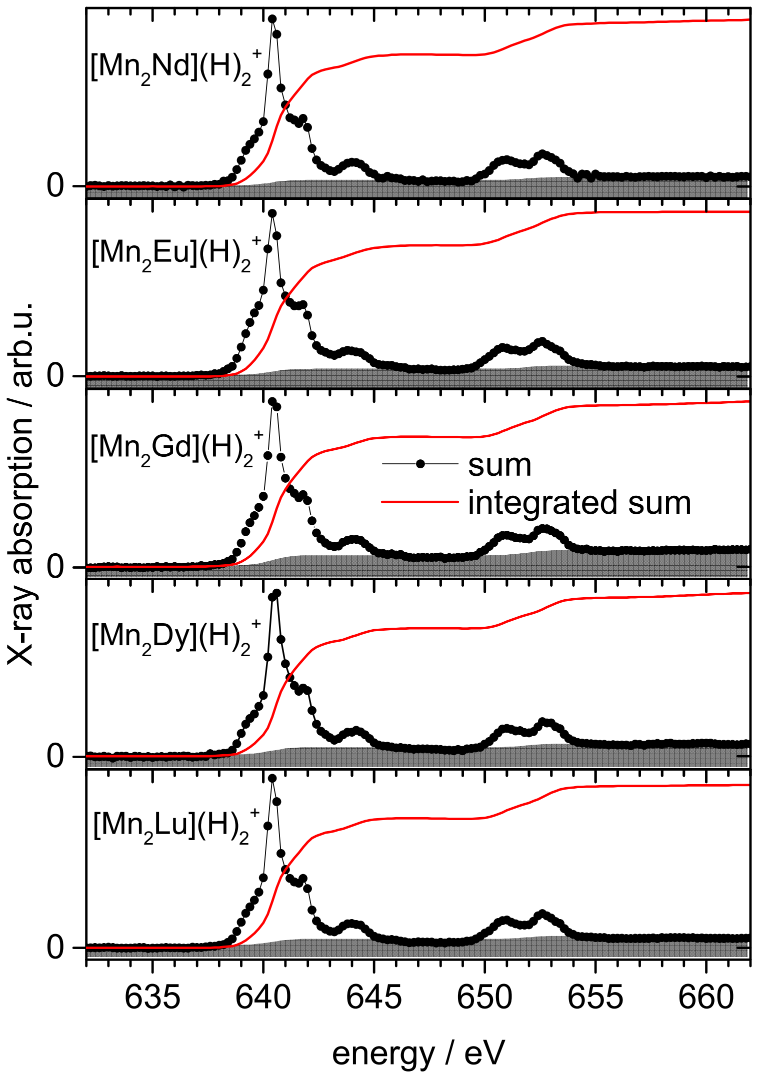

Figure S6: Sum of positive and negative XA spectra (black) and their integrated sum (red) for five isostructural bimetallic 3*d*-4*f* trinuclear complexes [Mn$_2$Ln](H)$_2^+$ (Ln = Nd, Eu, Gd, Dy, Lu). The grey shaded areas represent the two-step functions subtracted after normalization, approximating the direct 2*p* photoionization and 2*p* → *ns*, *nd* (*n* > 3) contributions.[39] Note, that the ordinates for the sum spectra and their integrals are different.

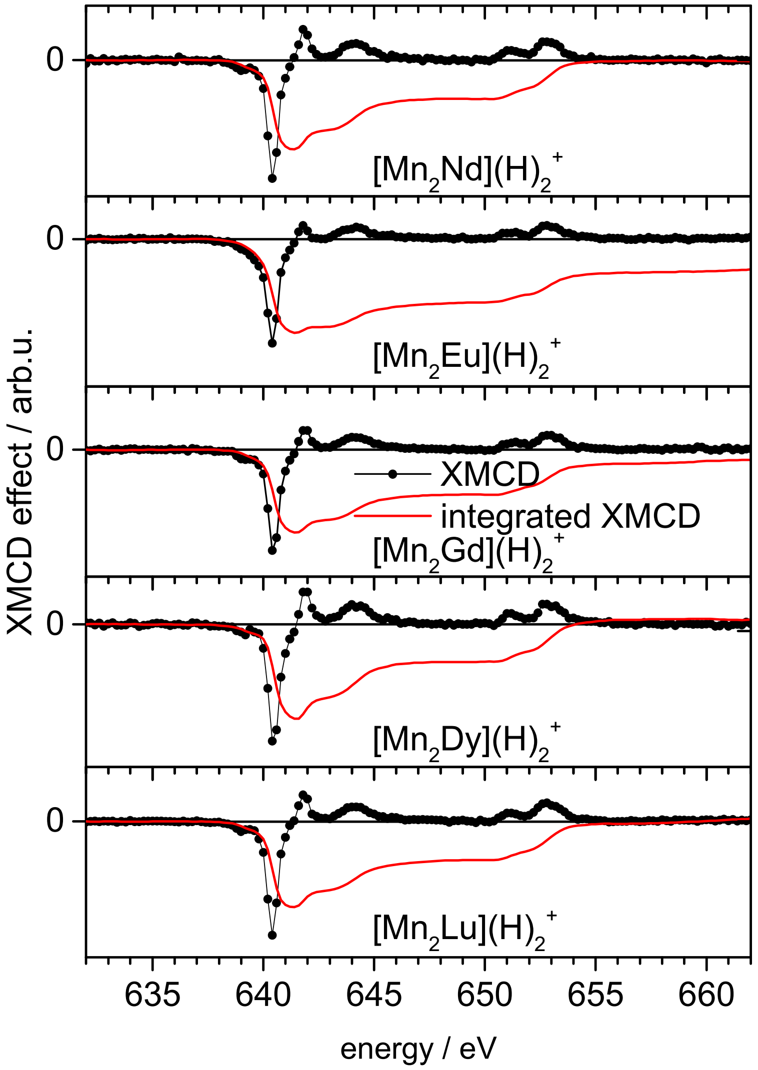

Figure S7: XMCD spectra (black) and their integrated sum (red) for five isostructural bimetallic 3*d*-4*f* trinuclear complexes $[Mn_2Ln](H)_2^+$ (Ln = Nd, Eu, Gd, Dy, Lu).

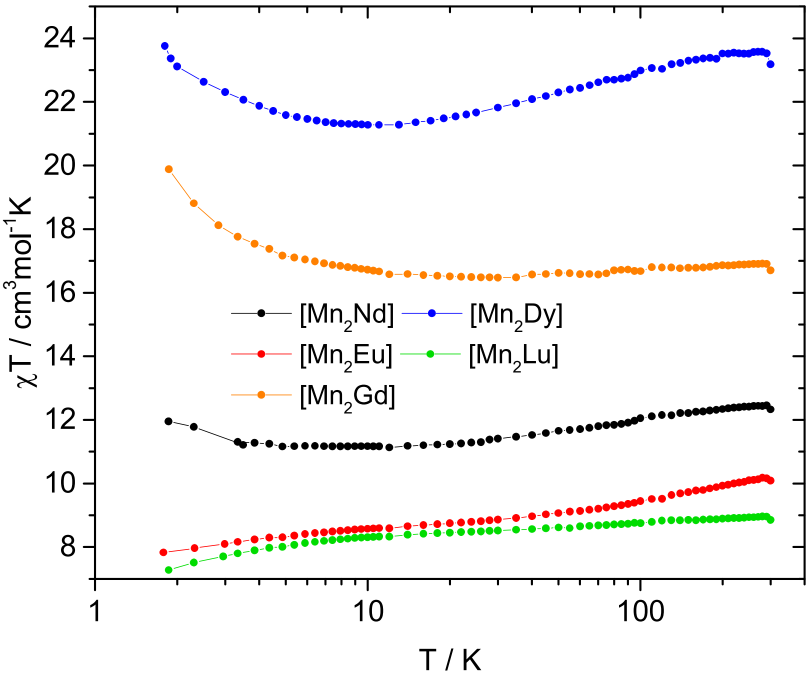

Figure S8: Semi-logarithmic plot of the measured temperature dependence of χT of five isostructural complexes of the [Mn_2Ln]-type (sum formula: [$C_{44}H_{44}N_8O_{12}LnMn_2(C_6H_{16}N)_2(ClO_4)(H_2O)_2$], with Ln = Nd, Eu, Gd, Dy, Lu).

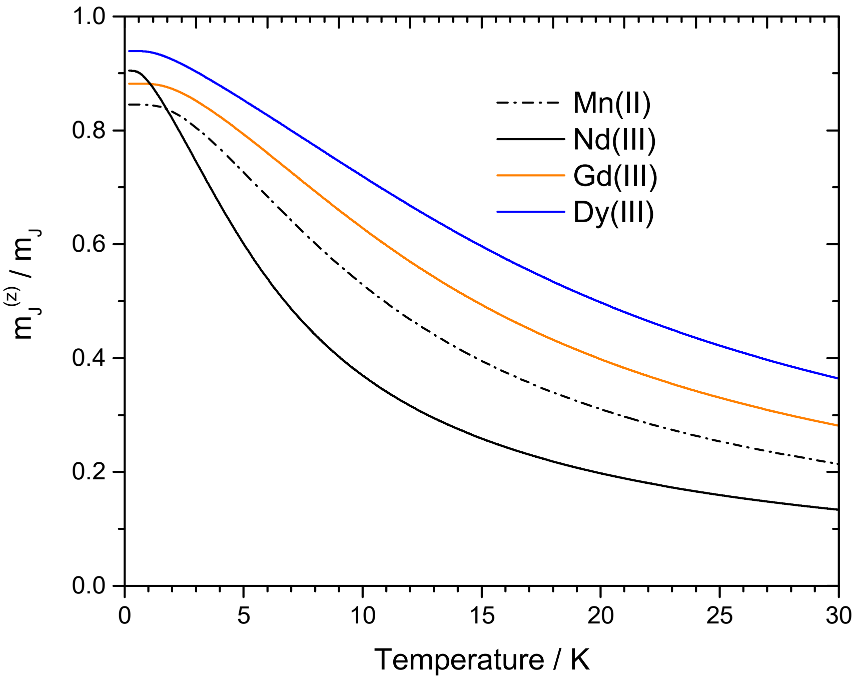

Figure S9: Relative orientation of the total magnetic moments $m_J^{(z)}/m_J$ as Brillouin function of the temperature for Mn^{2+}, Nd^{3+}, Gd^{3+} and Dy^{3+}.

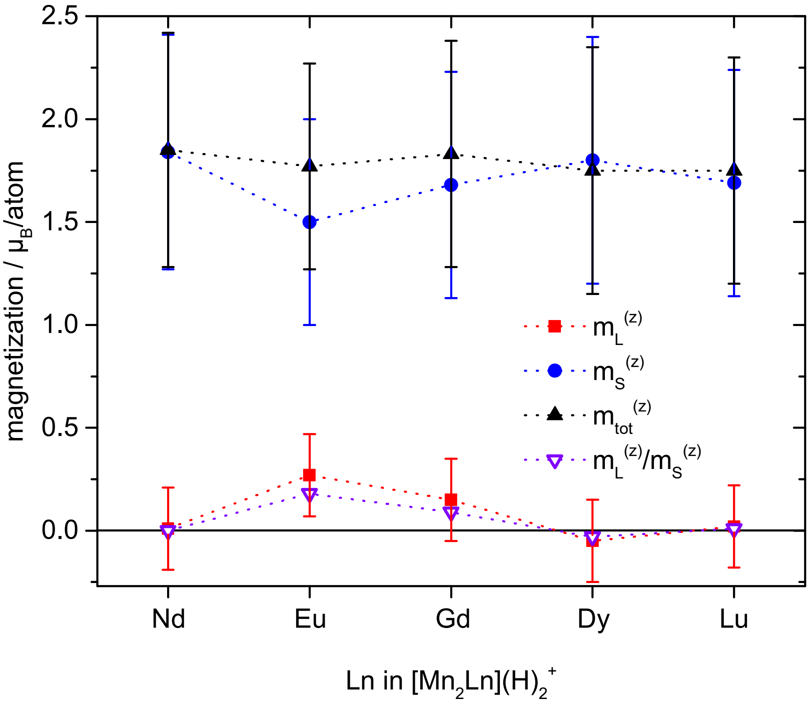

Figure S10: Calculated Magnetizations of the Mn^{2+} cations by the original sum rules: contributions by spin ($m_S^{(z)}$, filled blue circles), contributions by orbit ($m_L^{(z)}$, filled red squares), total values ($m_J^{(z)}$, filled black triangles); together with the $m_L^{(z)}$ to $m_S^{(z)}$ ratio (open purple triangles) on the manganese ions within the investigated mixed 3*d*-4*f* trinuclear complexes of the type $[Mn_2Ln](H)_2^+$.[51, 52]

Table S5: Experimental orbital ($m_L^{(z)}$), spin ($m_S^{(z)}$), total ($m_{tot}^{(z)}$) magnetization and the orbital to spin ratios ($m_L^{(z)}/m_S^{(z)}$) at the manganese ions of the $[Mn_2Ln](H)_2^+$ complexes obtained by the original sum rules. [51, 52]

	$m_L^{(z)}$ / μ$_B$/atom	$m_S^{(z)}$ / μ$_B$/atom	$m_{tot}^{(z)}$ / μ$_B$/atom	$m_L^{(z)}/m_S^{(z)}$
$[Mn_2Nd](H)_2^+$	0.01	1.84	1.85	0.00
$[Mn_2Eu](H)_2^+$	0.27	1.50	1.77	0.18
$[Mn_2Gd](H)_2^+$	0.15	1.68	1.83	0.09
$[Mn_2Dy](H)_2^+$	-0.05	1.80	1.75	-0.03
$[Mn_2Lu](H)_2^+$	0.02	1.69	1.75	0.01

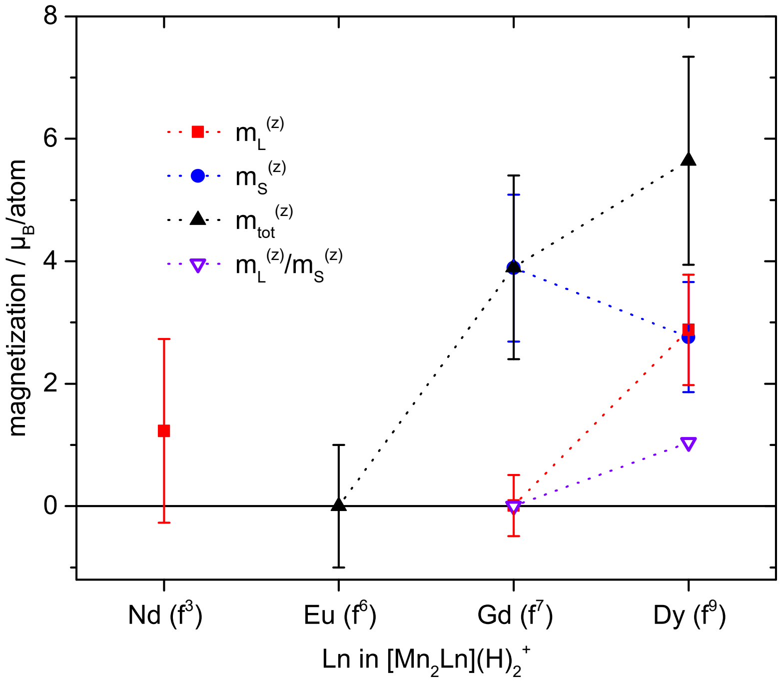

Figure S11: Calculated Spin ($m_S^{(z)}$, filled blue circles), orbital ($m_L^{(z)}$, filled red squares), total ($m_{tot}^{(z)}$, filled black triangles) magnetizations by the original sum rules and the $m_L^{(z)}$ to $m_S^{(z)}$ ratio (open purple triangles) on the Ln atoms within the investigated bimetallic 3*d*-4*f* trinuclear complexes of the type $[Mn_2Ln](H)_2^+$.[51, 52]

Table S6: Experimental orbital ($m_L^{(z)}$), spin ($m_S^{(z)}$), total ($m_{tot}^{(z)}$) magnetizations and the orbital to spin ratios ($m_L^{(z)}/m_S^{(z)}$) at the Ln^{3+} ions of the $[Mn_2Ln](H)_2^+$ complexes obtained by the original sum rules.[51, 52]

	$m_L^{(z)}$ / μ_B/atom	$m_S^{(z)}$ / μ_B/atom	$m_{tot}^{(z)}$ / μ_B/atom	$m_L^{(z)}/m_S^{(z)}$
$[Mn_2Nd](H)_2^+$	1.23	-2.41	-1.18	-0.51
$[Mn_2Eu](H)_2^+$			≈0	
$[Mn_2Gd](H)_2^+$	0.01	3.89	3.90	0.00
$[Mn_2Dy](H)_2^+$	2.88	2.76	5.64	1.04

4 Gas Phase XMCD Spectroscopy of an Octahedral Iron(II) Spin-Crossover Complex

Joachim M. Hewer[a], Matthias Tombers[a], Johannes Lang[a], Markus Schmitz[a], Vicente Zamudio-Bayer[b,c], J. Tobias Lau[b], Bernd von Issendorff[c], Akira Terasaki[d], Thomas Schlathölter[e], Ronnie Hoekstra[e], Hans-Jörg Krüger[a], and Gereon Niedner-Schatteburg[a]

(a) *Fachbereich Chemie and Forschungszentrum OPTIMAS, Kaiserslautern, Germany*

(b) *Institut für Methoden und Instrumentierung der Forschung mit Synchrotronstrahlung, Helmholtz-Zentrum Berlin für Materialien und Energie, Berlin, Germany*

(c) *Physikalisches Institut, Universität Freiburg, Germany*

(d) *Department of Chemistry, Kyushu University, Fukuoka, Japan*

(e) *Zernike Institute for Advanced Materials, University of Groningen, Groningen, The Netherlands*

4.1 Preamble

The following chapter is prepared as a manuscript for publication. I conducted the XMCD experiments, data evaluation and the quantum chemical calculations. I received experimental support by Matthias Tombers and Johannes Lang and Vicente Zamudio-Bayer. Markus Schmitz synthesized the samples in the group of Hans-Jörg Krüger. Tobias Lau, Bernd von Issendorf and Akira Terasaki operate the NanoCluster Trap experimental setup at the BESSY II synchrotron. Thomas Schlathölter and Ronnie Hoekstra provided the Electrospray Ionization (ESI). I wrote the manuscript and revised it with the help of Matthias Tombers and Gereon Niedner-Schatteburg.

4.2 Abstract

Spin-Crossover complexes have become an attractive field of research due to their potential application in e.g. electronic devices. Extensive research has contributed to a nearly outright understanding of the phenomenon. However, most investigations focus on the design, synthesis and application of Spin-Crossover complexes. In order to gain more fundamental insight to the phenomenon, investigations on isolated systems are necessary. We report the first X-ray magnetic circular dichroism (XMCD) spectroscopic study of an isolated octahedral iron(II) Spin-Crossover complex in the gas phase. The combination of temperature dependent XMCD spectroscopy and sum rule analysis allows for the temperature dependent determination of magnetic moments of transition metal complexes. Our investigations show, that the determination of a Spin-Crossover process in the gas phase is demanding. Though, first results suggest an actual transition from low spin to high spin upon increasing the ion temperature.

4.3 Introduction

Spin-Crossover complexes represent a highly active and growing field of research due to their potential application in molecular electronic devices.[1-3] The transition occurs as an entropy-driven redistribution of electrons in the valence *d*-orbitals of transition metal compounds due to an external perturbation e.g. changes in temperature, pressure or photon irradiation.[4-10] Many reported octahedral iron(II) complexes display representatives of Spin-Crossover properties.[3-5, 11-14] The $^1A_{1g}$ low spin ground state due to a $(t_{2g})^6$ electron configuration can be thermally excited into a $^5T_{2g}$ high spin state with a $(t_{2g})^4(e_g)^2$ electron configuration.[3] The transition can be observed in elongated bond lengths originating from the occupation of the σ-antibonding e_g-orbitals in the high spin state.[3] The observed transition temperatures can vary widely, depending on different parameters like e.g. ligand field strength, packing effects, counterions, residual solvent molecules in the crystal etc.[3, 4] Dissolving a Spin-Crossover complex in suitable solvents can lead to a drastic reduction of the transition temperature.[15] However, investigations of the Spin-Crossover behavior in the gas phase are missing so far. Due to the missing crystal pressure, the transition temperature is expected to be reduced once again compared to dissolved Spin-Crossover complexes. We present an approach for investigations on the Spin-Crossover behavior in the gas phase, using X-ray magnetic circular dichroism (XMCD) spectroscopy on isolated ions in the gas phase. The magnetic moments of Spin-Crossover ions, cooled by Helium buffer gas to cryogenic temperatures, orient in an external magnetic field. The combination of XMCD spectroscopy and sum rule analysis allows for a temperature dependent determination of magnetic moments of transition metal ions or complex ions.[16-21].

In this work, we investigated an octahedral iron(II) complex showing a gradual Spin-Crossover in SQUID measurements of crystalline samples from a singlet state to a quintet state in the range of 250 – 380 K.[15] The detailed sum formula of the complex is $[(C_{28}H_{28}N_4)Fe(C_6H_4NO_2)(ClO_4)]$ (abbreviated as $[Fe(L\text{-}N_4Bz_2)(pyc)]ClO_4$ or as **1**). The central iron(II) ion is in an octahedral coordination sphere, coordinated by a tetraazamacrocyclic ligand: N,N'-Dibenzyl-2,11-diaza[3.3](2,6)pyridinophane (abbreviated as $L\text{-}N_4Bz_2$) and a picolinate anion (abbreviated as pyc). The perchlorate anion acts as a counterion. The macrocyclic ligand contributes two amine and two pyridine nitrogen donor atoms. The picolinate anion coordinates the metal ion by the nitrogen donor atom and the carboxyl oxygen donor atom. The nitrogen atoms of the pyridine rings and the nitrogen and oxygen atoms of the picolinate anion form the equatorial coordination plane, the amine nitrogen atoms are bound to the metal at the axial coordination sites.[3] The pyridine units and the small ring size of the macrocyclic ligand are responsible for the rather steric rigidity of the complex.[3] The crystal structure of **1** can be found in the thesis of M. SCHMITZ.[15]

4.4 Computational and Experimental methods

4.4.1 Theoretical methods

We performed density functional theory (DFT) calculations on the Spin-crossover complex for geometry optimization starting from the crystal structure and IR frequencies at 298.15 K. Electron spin density ($\rho^s(r)$) isosurfaces were calculated using the *multiwfn* software ($\rho^s(r) = \rho^\alpha(r) - \rho^\beta(r)$) and plotted using the *GaussView 3.0* software.[22-24] The calculations were conducted at the B3LYP[25-27]/cc-pVDZ/cc-pVTZ[28-33] (N, C, H) level of theory with the Stuttgart RSC 1997 effective core potential[34, 35] representing the iron atoms as implemented in the Gaussian 09 program package[36]. Due to the over stabilization of high spin states in B3LYP caused by the exact Hartree-Fock exchange H_x^{HF} (20 %), we performed additional calculations using B3LYP with a reduced H_x^{HF}: B3LYP* (15 %) and B3LYP** (10 %).[26, 37, 38]

4.4.2 Experimental methods and setup

Recording XMCD spectra of isolated complexes

The presented polarization dependent X-ray Absorption (XA) spectra were recorded at the NanoCluster Trap which is connected to the UE52-PGM soft X-ray beamline at the BESSY II synchrotron facility of the Helmholtz-Zentrum Berlin. The NanoCluster Trap is a custom built mass spectrometer to record Total Ion Yield (TIY) gas phase XA spectra.[21, 39, 40] For our experiments we used a custom-built Electrospray Ionization (ESI) source to transfer the iron(II) complex into the gas phase.[41]

The sample for our gas phase measurements were prepared as a solution in acetonitrile (CH_3CN) at a concentration of approx. 10^{-4} mol/L. The investigated cationic species $[C_{34}H_{32}N_5O_2Fe]^+$ (abbreviated as **1⁺** or$[Fe^{II}(L\text{-}N_4Bz_2)(pyc)]^+$) is formed already in the solution by dissolvation of the cation and counter-anion.

The cation of interest (**1⁺**) is mass selected in a linear quadrupole mass filter (Extrel, 40 – 4000 amu). The ions are guided into and stored in a linear quadrupole ion trap which is located within the high field region (5 T) of a superconducting solenoid. The trap is operated at frequencies between 2 and 4 MHz depending on the mass of the investigated ions. The linear quadrupole ion trap can be cooled down to temperatures ≤ 4 K by evaporative liquid He cooling. The ions are cooled down by collisional cooling in the vacuum chamber at a constant He backing pressure in the range of 10^{-6} to 10^{-7} mbar. The ions are thermalized at a somewhat higher temperature caused by radio frequency (RF) heating of the ion trap operation.[21] The trap is filled by a constant ion current from the source. The ions are ejected from the trap into the reflectron time of flight (ReTOF) mass spectrometer at a frequency of approx. 100 Hz. The X-ray absorption (XA) is recorded by total ion yield (TIY) spectroscopy whereas the ions are irradiated by the X-rays for 10 – 15 s at a fixed photon energy. A GaAsP diode records the X-ray intensity coming from the undulator beamline which is used for normalization of the XA spectra to the photon flux. The spectra at the Fe $L_{2,3}$ absorption edge were recorded with an exit slit size of 200 µm and a corresponding spectral resolution of ~400 meV at 707 eV photon energy. The fragment intensity amounts only a small fraction of the parent ion intensity. The XA spectra were alternately taken for left and right handed circularly polarized light (cf. Fig. 1).

Sum rule analysis of XMCD effects

The spin and orbital sum rules introduced by CARRA and THOLE link the spectral intensities of the XA spectra at different photon helicities to the projection of the spin and orbital magnetizations of a magnetic sample.[42-45] The resulting XMCD spectra were analyzed in terms of sum rule analysis:

$$m_S^{(z)} = g_S\mu_B \frac{A - bB}{c\frac{3}{2}C} n_h - g_S\mu_B \frac{d}{c}\langle T_Z\rangle$$

$$m_L^{(z)} = -g_L\mu_B \frac{A + B}{a\frac{3}{2}C} n_h$$

whereas n_h is the number of electron holes in the final state, g_S and g_L the g-factors for the electron spin and orbital angular momentum ($g_S = 2.0$, $g_L = 1.0$), μ_B the BOHR magneton and *a*,*b*,*c* and *d* are sum rule related prefactors. In this work, we assume Fe^{2+} to be in a $3d^6$ state. We chose the number of unoccupied valence orbitals to be $n_h = 4$ for Fe^{2+}. The prefactors *a*,*b*,*c* and *d* are 1/2, 2, 2/3, and 7/3 for the Fe $L_{3,2}$ absorption.[46]

The integrals **A**, **B** and **C** are extracted from the XMCD spectrum (difference spectrum of XA with different helicities) and the sum spectrum (sum of the XAS with different helicities, cf. Fig. 1). A two-step function is subtracted from the XA sum spectra to eliminate the non-resonant absorption. We follow the procedure described by CHEN *et al*. (cf. Figs. S2-S4).[42] Sum rule analysis allows us to extract the projection ($m_S^{(z)}$ and $m_L^{(z)}$) of the intrinsic spin and orbital magnetic moments (m_S and m_L) onto the quantization axis . The quantization axis coincides with the magnetic field and the X-ray propagation direction.

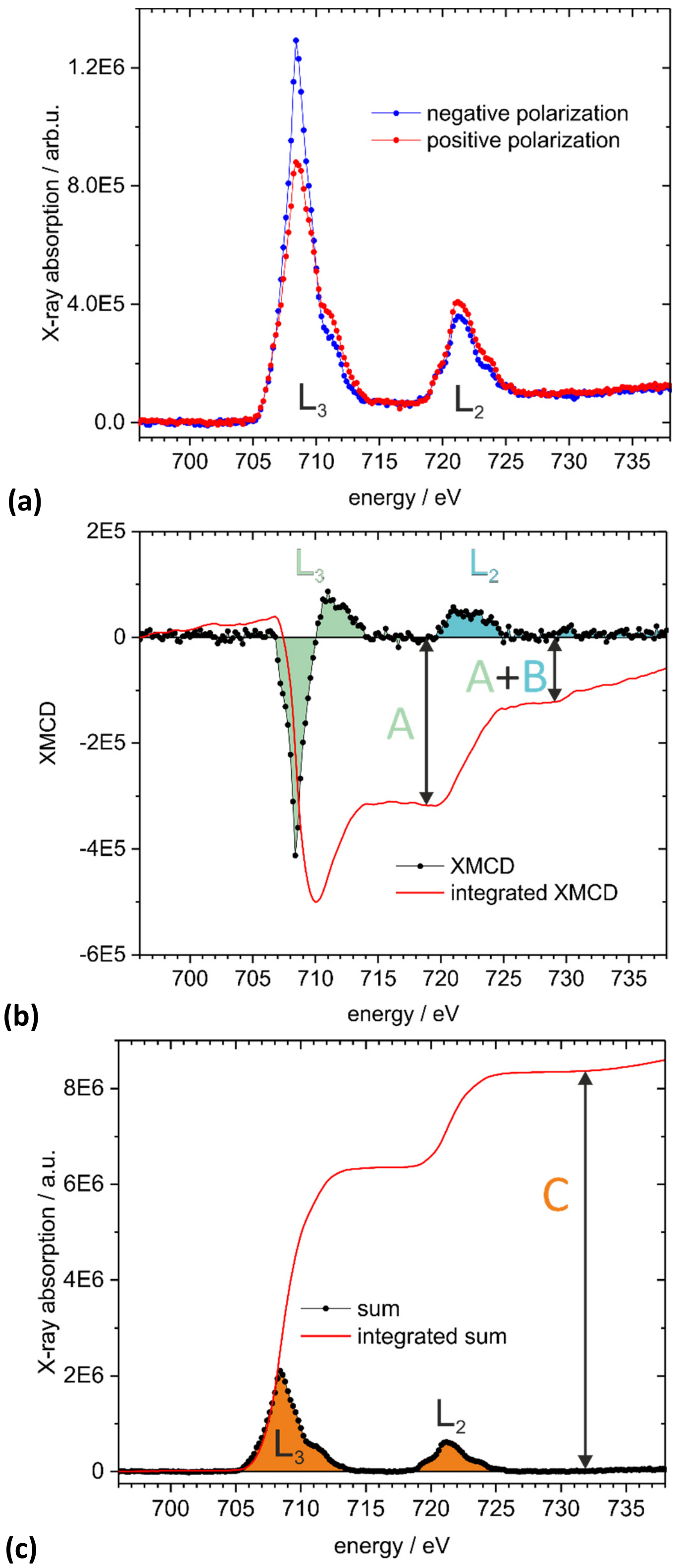

Figure 1: (a) XA spectra of the [Fe^{II}(L-N$_4$Bz$_2$)(pyc)]$^+$ ion at the L$_{3,2}$ absorption edges at both photon helicities (T_{trap} = 4 K). **(b)** XMCD spectrum / integrated XMCD intensity for the Fe L$_{3,2}$ absorption edges of the [Fe^{II}(L-N$_4$Bz$_2$)(pyc)]$^+$ ion. The Integral over the L$_3$ edge is named **A**, the integral over the L$_2$ edge is named **B**. **(c)** Sum of the XA spectra and its integral of the [Fe^{II}(L-N$_4$Bz$_2$)(pyc)]$^+$ ion. The integral over the L$_3$ and L$_2$ absorption edges is named **C**.

Correction factors:

The original sum rules only apply to transitions between well-defined shells. For the iron ions we consider the transition from the 2*p* core state to a 3*d* valence state. However, the valence states are not always completely separated. This leads to inaccuracies in the magnetic moments calculated by the sum rules, particularly for the spin sum rule.[47] The inaccuracies of the sum rules have been reviewed in many publications.[47-55] TERAMURA *et al*. have introduced correction factors for the spin sum rule based on calculations on an atomic model, taking into account the Coulomb interaction in the $L_{2,3}$ absorptions and the expectation value for the magnetic dipole operator $<T_z>$, which is not accessible in our XMCD experiment.[51-56] The presented magnetizations in this work are corrected by the suggested procedure of TERAMURA, (cf. Tab. S1) for the uncorrected data see supplement (Figs. S5, S8; Tabs. S5).

4.5 Results and Discussion

4.5.1 DFT calculations

The prediction of the spin ground state of transition metal complexes by theoretical methods is still challenging.[37, 38] Especially for spin state splittings, it is known that hybrid functionals like B3LYP overstabilize the high spin states due to the inclusion of substantial Hartree-Fock exchange E_x^{HF} (20 %). [26, 37, 57] In order to determine the relative energies of different spin states, we performed geometry optimizations with the B3LYP functional and varied the contribution of the exact Hartree-Fock exchange: standard B3LYP (20 %), B3LYP* (15 %) and B3LYP** (10 %). A low spin (LS) state (singlet, occupation of the t_{2g} orbitals only) and a high spin (HS) state (quintet) present possible electron configurations for the octahedrally coordinated Fe^{II} ion. Apparently, the triplet state could also be taken into account, but we do not discuss it here as it is not found to be important in the experimental studies (cf. Tab S4, Fig. S1).[15] The calculations were performed using cc-pVDZ and cc-pVTZ basis sets. The relative energies are listed in Tab. 1.

Table 1: Relative zero-point vibrational energies (ZVPE) and thermal free energies at 298.15 K of geometry optimized structures of **1**$^+$ at different multiplicities by variation of E_x^{HF} and basis size (in kJ/mol).

functional	basis set	ZPVE		thermal free energies (298.15 K)	
		S = 0	S = 2	S = 0	S = 2
B3LYP	cc-pVTZ	+24.8	0.0	+39.5	0.0
B3LYP	cc-pVDZ	+26.8	0.0	+41.1	0.0
B3LYP*	cc-pVDZ	+0.7	0.0	+15.1	0.0
B3LYP*	cc-pVTZ	0.0	+1.7	+13.3	0.0
B3LYP**	cc-pVDZ	0.0	+26.8	0.0	+34.7

The choice of a double or triple zeta basis has a minor impact on the relative energies of different spin states. Hence, we back on cc-pVDZ to qualify general considerations. The calculations using the original B3LYP attribute the HS state (S = 2, quintet) to the ground state by approx. 25 kJ/mol (ZPVE) or 40 kJ/mol ($\Delta G^{298.15}$). This behavior opposing to the experimental results, where the spin state transition proceeds from the singlet state to the quintet state upon increasing the temperature, is known from DFT calculations with hybrid

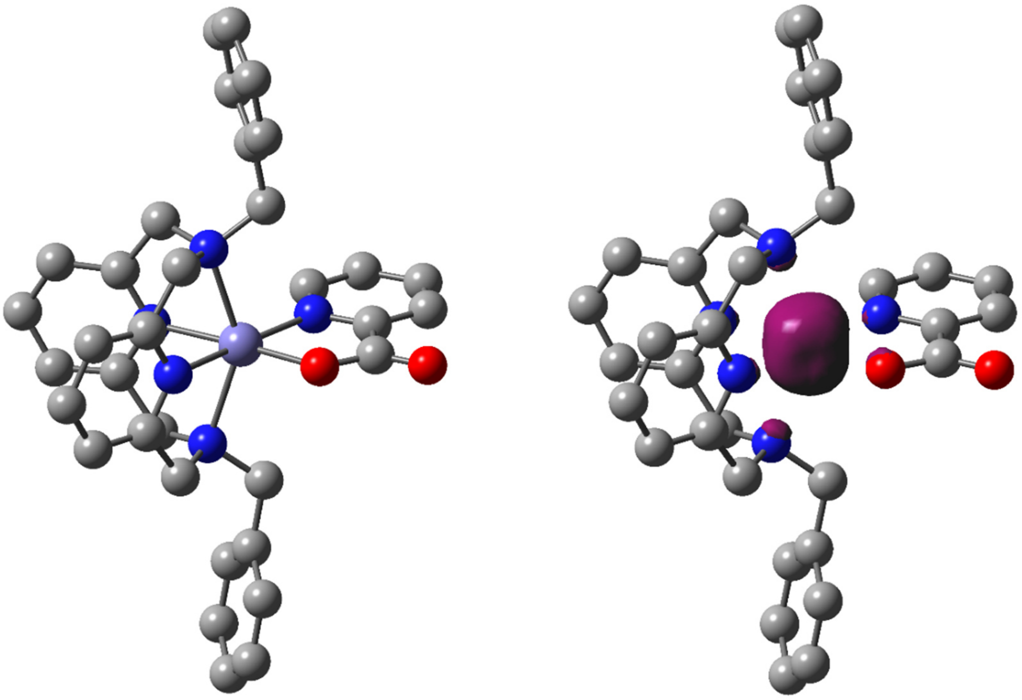

Figure 2: Left: Geometry optimized structure of **1**$^+$ in the high spin (HS) state (C: gray, O: red, N: blue, Fe: steel blue). Right: Geometry optimized structure of **1**$^+$ in the high spin (HS) state, displaying the spin density isosurface (purple) located at the iron atom. All Hydrogen atoms are omitted for clarity.

functionals with considerable Hartree-Fock exchange. Reducing the E_x^{HF} contribution to 15 % (B3LYP*) dramatically reduces the relative energies of the singlet state to 0.7 kJ/mol (ZPVE) and 15.1 kJ/mol ($\Delta G^{298.15}$). A further decrease of E_x^{HF} to 10 % (B3LYP**) results in a formally correct description of the singlet state as ground state. However, the best description of the relative energies of **1⁺** is given by B3LYP*, because the difference in the ZPVE is very small and the thermal free energies at room temperature (298.15 K) favor the quintet state as observed in the experiment. The search for an adequate theoretical description of spin state related experiments like Spin-Crossover processes is a highly active field of research.[57-63] A common approach is the adaption of various functionals to the experimental data of thoroughly studied systems in order to enable predictions for similar systems. The subsequently presented electron spin density isosurfaces and structural data from DFT calculations were obtained by calculations using the B3LYP* functional (15 % H_x^{HF}). The optimized structure of **1⁺** in the high spin (HS) state (quintet) is shown in Fig. 2 (left), the spin density is localized predominantly at the metallic iron center (Fig. 2, right, purple isosurface).

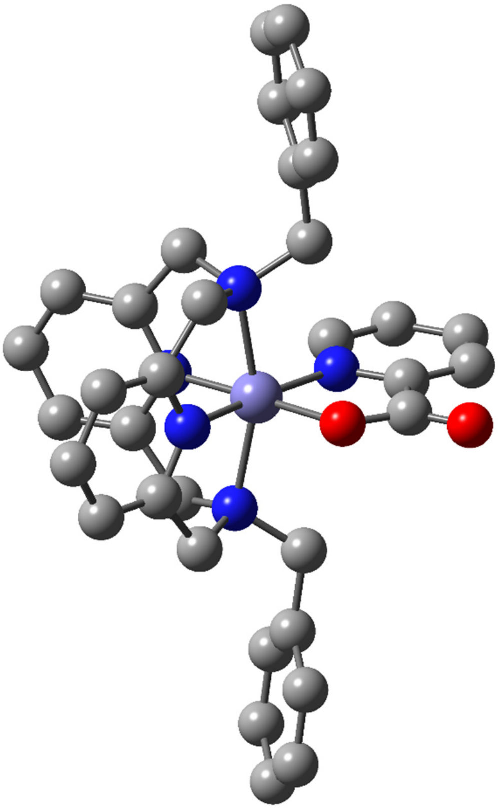

Figure 3: Geometry optimized structure of **1⁺** in the low spin (LS) state (C: gray, O: red, N: blue, Fe: steel blue). All Hydrogen atoms are omitted for clarity.

The geometry optimized structure of **1**$^+$ for the low spin (LS) state (singlet) is presented in Fig. 3. Note, that there is no electron spin density for the low spin configuration. The structural differences among the spin states are small but unambiguous. Some of the characteristic structure parameters in comparison to the crystal structure data are summarized in Tab. 2 (LS, 110 K) and Tab. 3 (HS, 333 K) (for the atomic coordinates of both structure minima, cf. Tabs. S2, S3). The high spin configuration provides elongated bond lengths between the iron atom and the six ligand atoms in the octahedral coordination sphere, that is the nitrogen atoms of the pyridine rings, the amino nitrogen atoms of the macrocyclic ligand and the nitrogen and oxygen atoms of the picolinate ligand. Also, the backbone of the macrocyclic ligand is contracted in the high spin state, resulting in a smaller angle between the two iron – pyridine nitrogen bonds and the iron – amine nitrogen bonds.

The structural parameters of the crystal structure analysis at 110 K are in very good agreement with the DFT geometry optimized singlet structure (cf. Tab. 2). The deviations of the bond lengths/angles are < 4 %.

Table 2: Selected structure parameters of LS **1**$^+$ obtained by DFT/geometry optimization (singlet, B3LYP*/cc-pVDZ) in comparison to the crystal structure data at 110 K. Bond lengths in angstrom, bond angle in degree.

Structure parameter	Crystal structure 110 K	DFT opt. **1**$^+$ (singlet)	Deviation / %
$d(\mathrm{Fe}-\mathrm{N_{py}})$	1.896 / 1.883	1.931 / 1.928	2.58 / 3.02
$d(\mathrm{Fe}-\mathrm{N_{amin}})$	2.094 / 2.088	2.157 / 2.155	3.63 / 3.83
$d(\mathrm{Fe}-\mathrm{N_{pyc}})$	1.965	2.017	3.05
$d(\mathrm{Fe}-\mathrm{O_{pyc}})$	1.978	1.957	0.05
$\beta(\mathrm{N_{py}}-\mathrm{Fe}-\mathrm{N_{py}})$	86.6	85.855	0.92
$\beta(\mathrm{N_{amin}}-\mathrm{Fe}-\mathrm{N_{amin}})$	161.5	159.984	0.46

The structural parameters of the crystal structure analysis at 333 K are still in good agreement with the DFT geometry optimized quintet structure (cf. Tab. 3). Nevertheless, the deviations of the bond lengths and angles is augmented to < 8 %. This can be explained by the gradual Spin-Crossover process, which is not yet completed at 333 K. If the crystals are heated further, the samples become amorphous and a crystal structure analysis is no longer possible.[15]

Table 3: Selected structure parameters of HS **1⁺** obtained by DFT/geometry optimization (quintet, B3LYP*/cc-pVDZ) in comparison to the crystal structure data at 333 K. Bond lengths in angstrom, bond angle in degree.

Structure parameter	Crystal structure 333 K	DFT opt. **1⁺** (quintet)	Deviation / %
d(Fe – N_{py})	2.027 / 2.030	2.181 / 2.185	7.60 / 7.64
d(Fe – N_{amin})	2.197 / 2.215	2.364 / 2.357	7.60 / 6.41
d(Fe – N_{pyc})	2.066	2.221	7.50
d(Fe – O_{pyc})	1.995	2.026	1.55
β(N_{py} – Fe – N_{py})	82.9	79.070	4.62
β(N_{amin} – Fe – N_{amin})	152.0	145.729	4.13

The differences in the iron – nitrogen and iron – oxygen bond lengths and angles in the different spin states can be explained by the different *d*-orbital occupation of the iron center. In the high spin state, the σ-antibonding e_g orbital set is occupied, resulting in elongated bond lengths.[15]

4.5.2 XMCD spectroscopy at the Fe $L_{3,2}$ absorption edges

The magnetic properties of the metal centers of the complex ion **1⁺** are studied by gas phase XMCD spectroscopy on the iron $L_{3,2}$ absorption edges. This corresponds to the transition from the spin-orbit-split $2p_{3/2}$ and $2p_{1/2}$ orbitals (L_3 and L_2) into the 3*d* valence orbitals.

The iron ion in **1⁺** is in a formal oxidation state of +II, thus the expected electron configuration is $3d^6$. There are two spin states observed in temperature dependent crystal structure analysis and in temperature dependent magnetic SQUID measurements.[15] ^{1}H-NMR spectroscopic investigations using the NMR-Evans-method show a similar magnetic behavior, shifted by ca. 100 K towards lower temperatures.[15] The data are interpreted as an electron redistribution from an initial low spin configuration with three pairs of electrons in the t_{2g} orbitals and two unoccupied e_g orbitals. The final high spin configuration at higher temperatures provides one pair of electrons in one t_{2g} orbital, two unpaired electrons in the remaining t_{2g} orbitals and one unpaired electron each in the e_g orbitals. The magnetic moments for the HS and LS are hence significantly different. The expected spin magnetic moment for the HS configuration amounts 4 μ_B per atom and 0 μ_B per atom for the low spin configuration. The non-degeneracy of the *d*-orbitals in the octahedral ligand field quenches the orbital angular momenta in first order.[64] The spin-orbit coupling steadily regenerates a certain amount of orbital momentum by mixing of degenerate excited states into the ground state.[65] Yet, the total magnetic moment m_J for a free Fe^{2+} ion (in the high spin state) is 6 μ_B as sum of the spin (m_S) and orbital angular moment (m_L), due to the spin–orbit coupling ($\zeta_{3d}(Fe^{2+}) = 410\ cm^{-1}$ [66]), which is superior to the individual coupling of the spin and orbital magnetic moments to the external magnetic field.

The polarization dependent X-ray absorption spectra for **1⁺** are recorded at three different ion trap temperatures: T_{trap} = 4 K, 15 K and 25 K (cf. Fig 5). The spectrum at T_{trap} = 4 K shows a substantial dichroic effect at the first subpeak of the L_3 absorption edge at 708.4 eV, a change of sign prior to the second subpeak at 711 eV and a less pronounced dichroism at the L_2 absorption edge at 721 eV. This indicates a distinct magnetic moment at the iron center of the complex already at very low temperatures. The overall shape of the XA spectra does not change upon increasing the ion trap temperature, though the extent of the dichroic effect decreases at higher temperatures due to randomization of the orientation of the magnetic moments.

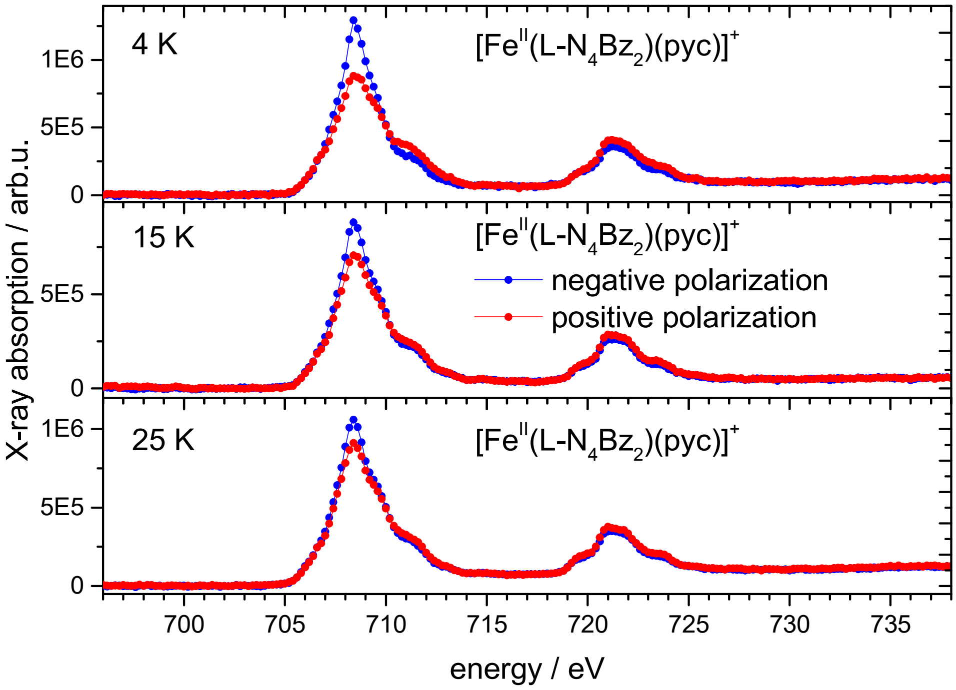

Figure 5: Polarization dependent XA spectra for negative (blue) and positive (red) circular photon polarization of **1⁺** ($[Fe^{II}(L\text{-}N_4Bz_2)(pyc)]^+$) at different ion trap temperatures. Top: T_{trap} = 4 K, middle: T_{trap} = 15 K, bottom: T_{trap} = 25 K.

The magnetizations at the iron center are extracted by sum rule analysis at the Fe $L_{3,2}$ absorption edges (Fig. 6). The background subtraction from the iron XA sum spectra originating from excitations into higher unoccupied and nonmagnetic *d* states is performed by a two-step function. The step height at the L_3 edge is 2/3 and the step height for the L_2 edge is 1/3 of the full edge jump, in agreement with the degeneracy of the spin-orbit split 2*p* initial states (cf. Figs. S2-S4 ESI).[21, 42, 46] The sum rule analysis can be performed by integration of the entire measured spectral range or by integration of the defined $L_{3,2}$ absorption range. Ideally there should be no difference. Due to small XMCD effects at higher temperatures, the signal to noise ratio increases resulting in slightly altered intensity integrals (cf. Figs. 6, S2-S4). The magnetizations obtained by integration of the entire spectral range are represented as lucent data in Fig. 6. We chose the limited integration range for the subsequent evaluation.

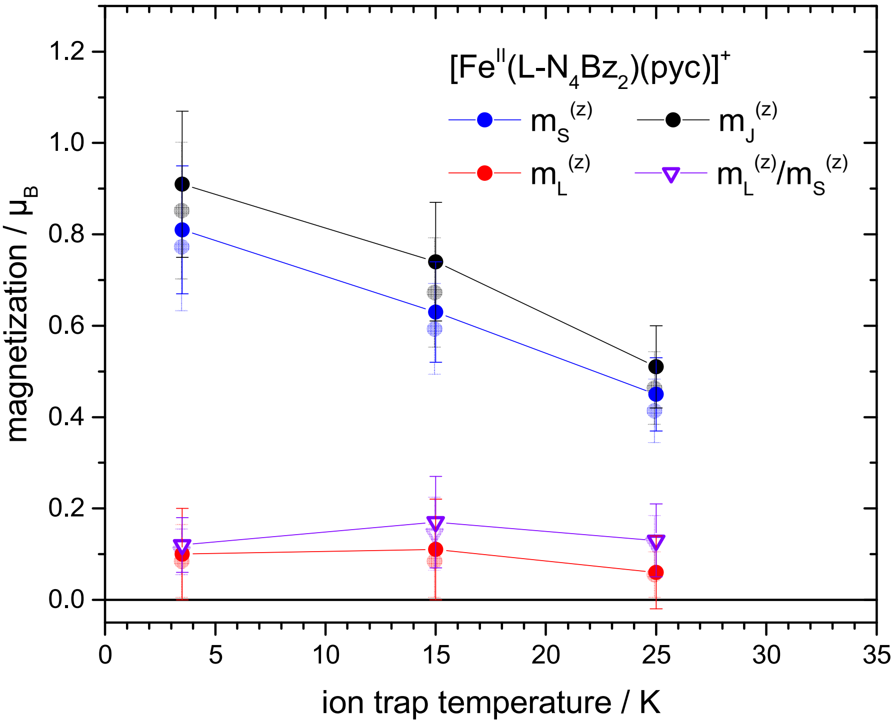

Figure 6: Spin ($m_S^{(z)}$, filled blue circles), orbital ($m_L^{(z)}$, filled red squares), total ($m_J^{(z)}$, filled black triangles) magnetizations and the $m_L^{(z)}$ to $m_S^{(z)}$ ratio (open purple triangles) on the Fe^{2+} ions in **1⁺** ($[Fe^{II}(L\text{-}N_4Bz_2)(pyc)]^+$) obtained with tight integration limits. The shaded data represent the magnetizations obtained by integration of the entire measured range.

The values for the spin ($m_S^{(z)}$), orbital ($m_L^{(z)}$), total ($m_J^{(z)}$) magnetizations and the $m_L^{(z)}$ to $m_S^{(z)}$ ratio are summarized in Tab. 4. The total magnetizations $m_J^{(z)}$ vary from 0.51 to 0.91 μ_B per atom and are dominated by the spin magnetization, which varies from 0.45 to 0.81 μ_B per atom. The orbital angular magnetization is relatively constant (0.06 to 0.11 μ_B per atom). This results in an almost invariable $m_L^{(z)}$ / $m_S^{(z)}$ ratio as well. We assume the low values of orbital angular magnetization, which is zero in between the error bars, to originate from the quenching of the orbital angular momenta in non-degenerated *d*-orbitals as described previously. The residual values may be induced by spin-orbit coupling.

Table 4: Corrected experimental spin, orbital angular, total magnetizations and the orbital to spin magnetization ratio of **1**$^+$ obtained by sum rule analysis.

T_{trap} / K	$m_S^{(z)}$ / μ_B	$m_L^{(z)}$ / μ_B	$m_J^{(z)}$ / μ_B	$m_L^{(z)}$ / $m_S^{(z)}$
4 K	0.81	0.10	0.91	0.12
15 K	0.63	0.11	0.74	0.17
25 K	0.45	0.06	0.51	0.13

The significant XMCD effect and the substantial spin magnetizations show, that the ions are not exclusively in the low spin configuration. Though, the values are too low to represent exclusively high spin configuration of the iron(II) ions. We have probably a mixture of low spin and high spin ions in the experiment, resulting in an intermediate averaged magnetization, since the method is not able to address different spin states of the same element separately.

In order to check our assumption, we simulate the temperature dependent Brillouin behavior of a Fe^{2+} ion in the ground state. If all ions are entirely in the high spin state, they should behave Brillouin-like. In the first step, we estimate the ion temperatures by projection of the experimentally determined total magnetizations $m_J^{(z)}$ onto the temperature axis via the temperature dependent Brillouin function of a free high spin Fe^{2+} ion at a constant magnetic field of 5 T (cf. Fig. 7). The resulting ion temperatures are 63, 77 and 114 K, respectively. These values are much too high compared to the values from similar experiments under similar conditions.[67, 68] Though, we have neglected the partially quenched orbital angular momentum being overestimated in the simulation. Therefore, we focus on the Brillouin behavior of the spin magnetization $m_S^{(z)}$ (cf. Fig. 8). The resulting ion temperatures of 33, 42 and 59 K are lower compared to those derived by $m_J^{(z)}$, but still too high to match the experimental conditions.[67, 68]

The precise estimation of the difference between the trap temperature and the ion temperature is challenging. The ion temperature is certainly higher than the trap temperature due to radio frequency (RF) heating from the trap operation. Computer simulations are unreliable, due to the high amount of operation parameters that can have a tremendous impact on the ion temperature. In our approach we want to derive the temperature on the basis of similar experiments, where the ion temperature is determined fairly accurate.

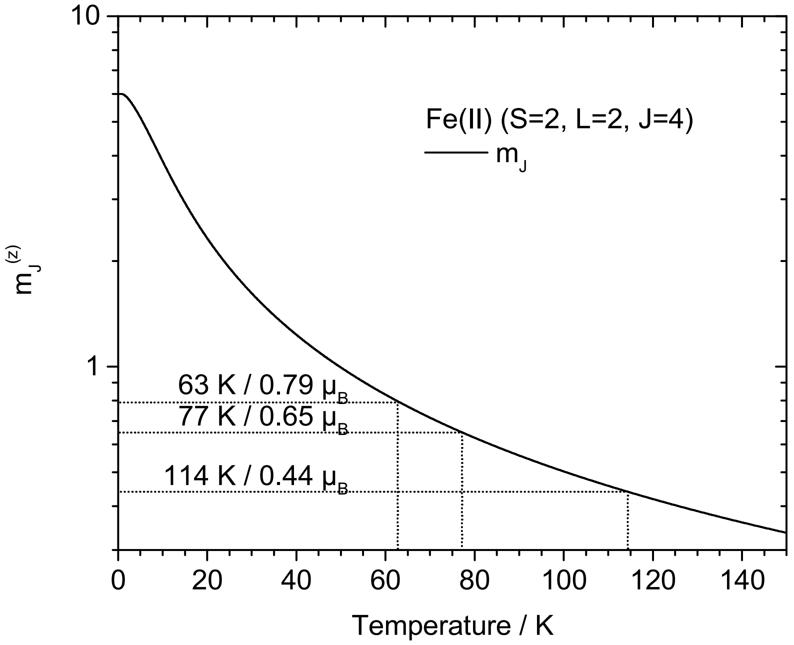

Figure 7: Simulated total magnetization $m_J^{(z)}$ of the Fe^{2+} ion in the ground state, represented as Brillouin function of the ion temperature at a magnetic field of B = 5 T. The experimentally determined total magnetizations ($m_J^{(z)}$) are projected onto the Brillouin function to identify the ion temperature.

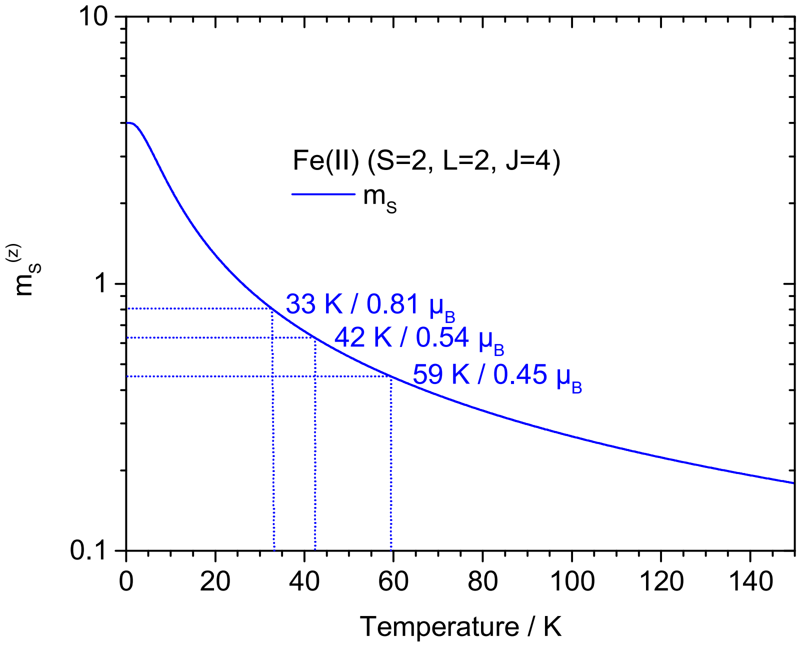

Figure 8: Simulated spin magnetizations $m_S^{(z)}$ of the Fe^{2+} ion in the ground state, represented as Brillouin function of the ion temperature at a magnetic field of B = 5 T. The experimentally determined magnetizations ($m_S^{(z)}$) are projected onto the Brillouin function to identify the ion temperature.

Assuming a constant temperature offset, we can build the derivative of the magnetizations with respect to the temperature for the experimental data, fitted linearly in approximation (cf. Fig. 9), and the simulated Brillouin functions for $m_J^{(z)}$ (cf. Fig. 10) and $m_S^{(z)}$ (cf. Fig. 11). The linear fit of the experimental data results in slopes of -0.019 and -0.017 μ_B/K, respectively.

$$\frac{dm_J^{(z)}}{dT} = -0.019 \pm 0.003 \ \frac{\mu_B}{K}$$

$$\frac{dm_S^{(z)}}{dT} = -0.017 \pm 0.003 \ \frac{\mu_B}{K}$$

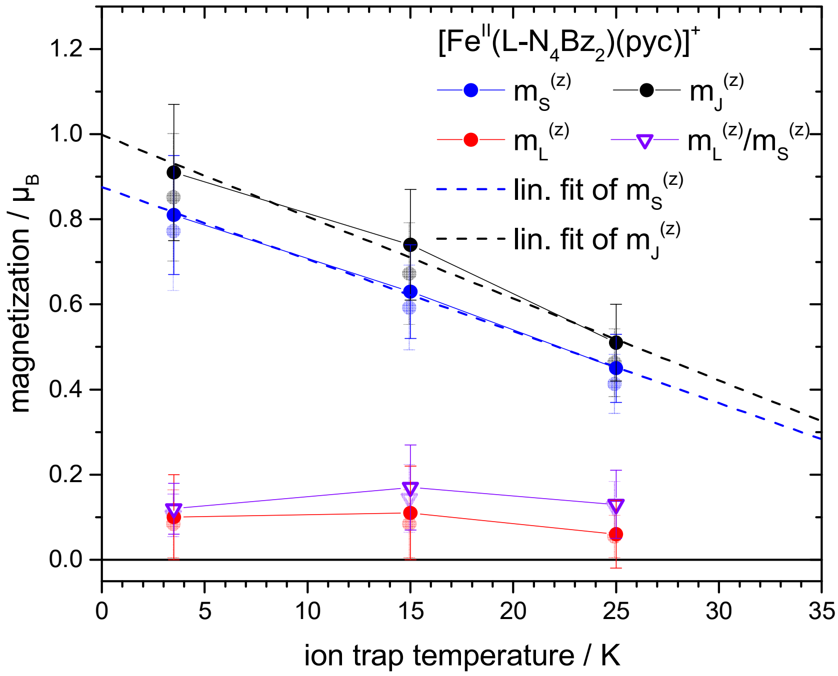

Figure 9: Spin ($m_S^{(z)}$, filled blue circles), orbital ($m_L^{(z)}$, filled red squares), total ($m_{tot}^{(z)}$, filled black triangles) magnetizations and the $m_L^{(z)}$ to $m_S^{(z)}$ ratio (open purple triangles) on the Fe^{2+} ions in complex **1**$^+$ obtained by tight integration limits. The dashed line represents a linear fit of $m_J^{(z)}$ and $m_S^{(z)}$ respectively. The shaded data represent the magnetizations obtained by integration of the entire measured range.

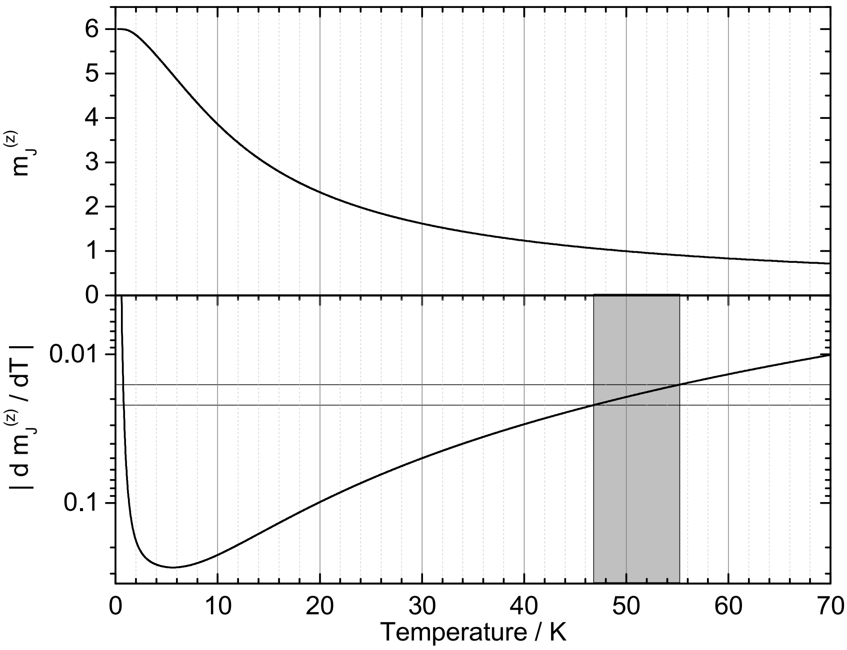

Figure 10: Top: Simulated magnetization of the Fe^{2+} ion in the ground state as a Brillouin function of the temperature. Bottom: Derivative of $m_J^{(z)}$ with respect to the temperature. The grey shaded area represents the slope of the linear fit of the experimentally determined magnetization.

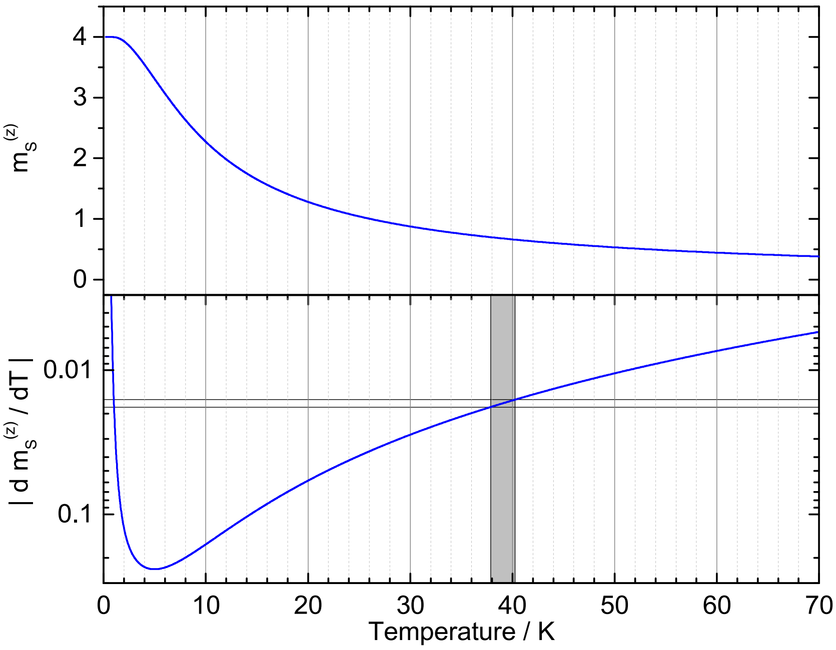

Figure 11: Top: Simulated magnetization of the Fe^{2+} ion in the ground state as a Brillouin function of the temperature. Bottom: Derivative of $m_s^{(z)}$ with respect to the temperature. The grey shaded area represents the slope of the linear fit of the experimentally determined magnetization.

A comparison of the slope of the linearly fitted experimental data to the derivative of the simulated Brillouin curves results in an ion temperature range of 47 to 55 K for $m_J^{(z)}$ and 38 to 40 K (cf. Figs. 10,11). Again, the obtained temperatures are too high to match the results of similar experiments.[67, 68] We assume having a mixture of both, high spin and low spin configuration in the gas phase molecular ion ensemble. Since the contribution of the RF heating to the ion temperature is demanding, we calculate the high spin and low spin fractions for different assumed ion temperature in four different scenarios. The respective fractions are calculated by:

$$x_{HS} \cdot m_{J,HS}^{(z)} + x_{LS} \cdot m_{J,LS}^{(z)} = m_{J,exp.}^{(z)} \quad \text{and}$$

$$x_{HS} \cdot m_{S,HS}^{(z)} + x_{LS} \cdot m_{S,LS}^{(z)} = m_{S,exp.}^{(z)},$$

assuming $m_{J,LS}^{(z)} = m_{S,LS}^{(z)} = 0$. In the low spin state all six *d*-electrons are paired in the t_{2g} orbitals and, thus there is no spin magnetization expected. The contribution of the orbital angular momentum is assumed to be negligible due to the non-degeneracy of the *d*-orbitals and we estimate $m_{L,LS}^{(z)} \approx 0$. Although, the total magnetization $m_J^{(z)}$ is not representative due to the quenching of the orbital angular momentum, we run through the scenarios of various RF heating impacts taking both into account, the total magnetization $m_J^{(z)}$ and the spin magnetization $m_S^{(z)}$.

Scenario 1: No temperature offset

In the first scenario, we assume $T_{trap} = T_{ion}$. Regarding the total magnetization $m_J^{(z)}$, there is an increasing fraction of high spin ions increasing the temperature (cf. Tab. 5).

Table 5: Calculation of the HS fractions using the experimental and theoretical total magnetizations $m_J^{(z)}$ assuming $T_{trap} = T_{ion}$.

T_{trap} / K	T_{ion} / K	$m_{J,exp}^{(z)}$	$m_J^{(z)}{}_{HS}$	$m_J^{(z)}{}_{LS}$	x_{HS}
4	4	0.91	5.41	0	0.168
15	15	0.74	2.93	0	0.252
25	25	0.51	1.91	0	0.267

Regarding the spin magnetization $m_S^{(z)}$, there is also an increasing fraction of high spin ions upon increasing the temperature (cf. Tab. 6).

Table 6: Calculation of the HS fractions using the experimental and theoretical spin magnetizations $m_S^{(z)}$ assuming $T_{trap} = T_{ion}$.

T_{trap} / K	T_{ion} / K	$m_{S,exp}^{(z)}$	$m_S^{(z)}{}_{HS}$	$m_S^{(z)}{}_{LS}$	x_{HS}
4	4	0.81	3.54	0	0.229
15	15	0.63	1.65	0	0.382
25	25	0.45	1.04	0	0.433

This scenario supports the assumption of a Spin-Crossover process in the gas phase, though it appears unlikely at once. The ions are obviously warmer than the ion trap, caused by RF heating of the linear quadrupole ion trap operation.

Scenario 2: Constant temperature offset

In the second scenario, we assume a constant temperature shift of $\Delta T \approx 9$ K. At maximum cooling power ($T_{trap} = 4$ K) the ion temperature is about 15 K (cf. chapter 3). The difference of 9 K is applied also for $T_{trap} = 15$ and 25 K, resulting in $T_{ion} = 15$, 24 and 34 K respectively. Regarding the total magnetization $m_J^{(z)}$, the high spin fraction increases by 6 % from $T_{trap} = 4$ K to 15 K and decreases by 2 % from $T_{trap} = 15$ K to 25 K (cf. Tab. 7).

Table 7: Calculation of the HS fractions using the experimental and theoretical total magnetizations $m_J^{(z)}$ assuming a constant temperature offset $\Delta T = 9$ K.

T_{trap} / K	T_{ion} / K	$m_{J,exp}^{(z)}$	$m_J^{(z)}{}_{HS}$	$m_J^{(z)}{}_{LS}$	x_{HS}
4	15	0.91	2.93	0	0.311
15	24	0.74	1.98	0	0.374
25	34	0.51	1.44	0	0.354

Regarding the spin magnetization $m_s^{(z)}$ there is also a maximum in the high spin fraction at $T_{trap} = 15$ K. The high spin fraction increases from $T_{trap} = 4$ K to 15 K by approx. 10 % and decreases by less than 1 % from $T_{trap} = 15$ K to 25 K (cf. Tab. 8).

Table 8: Calculation of the HS fractions using the experimental and theoretical spin magnetizations $m_S^{(z)}$ assuming a constant temperature offset $\Delta T = 9$ K.

T_{trap} / K	T_{ion} / K	$m_{S,exp}^{(z)}$	$m_S^{(z)}{}_{HS}$	$m_S^{(z)}{}_{LS}$	x_{HS}
4	15	0.81	1.65	0	0.491
15	24	0.63	1.08	0	0.583
25	34	0.45	0.78	0	0.577

This scenario supports the assumption of a gas phase Spin-Crossover in parts. The rise in the high spin fraction from $T_{trap} = 4$ to 15 K is much more significant compared to the decrease from $T_{trap} = 15$ to 25 K. This scenario 2 appears more likely than assuming a total absence of RF heating in scenario 1.

Scenario 3: Increasing Temperature offset

In the third scenario, we assume the energy input via RF heating to increase linearly with the temperature. We chose an increasing temperature offset of ΔT = 9, 15 and 20 K for the trap temperatures T_{trap} = 4, 15 and 25 K to an ion temperature of T_{ion} = 15, 30 and 45 K respectively.

Table 9: Calculation of the HS fractions using the experimental and theoretical total magnetizations $m_J^{(z)}$ assuming an increasing temperature offset ΔT = 9, 15 and 20 K.

T_{trap} / K	T_{ion} / K	$m_{J,exp}^{(z)}$	$m_J^{(z)}{}_{HS}$	$m_J^{(z)}{}_{LS}$	x_{HS}
4	15	0.91	2.93	0	0.311
15	30	0.74	1.62	0	0.457
25	45	0.51	1.10	0	0.464

Regarding the total magnetization $m_J^{(z)}$, we see an increasing high spin fraction with the temperature (cf. Tab. 9). The amount rises from 31.1 % to 45.7 % increasing the trap temperature from 4 to 15 K. A further increase of the trap temperature to 25 K yields in a further increase of the high spin fraction by 0.7 %.

Table 10: Calculation of the HS fractions using the experimental and theoretical spin magnetizations $m_S^{(z)}$ assuming an increasing temperature offset ΔT = 9, 15 and 20 K.

T_{trap} / K	T_{ion} / K	$m_{S,exp}^{(z)}$	$m_S^{(z)}{}_{HS}$	$m_S^{(z)}{}_{LS}$	x_{HS}
4	15	0.81	1.65	0	0.491
15	30	0.63	0.88	0	0.716
25	45	0.45	0.59	0	0.763

A similar behavior is observed regarding the spin magnetization $m_s^{(z)}$ (cf. Tab. 10). The first temperature raise yields a high spin fraction increase by 22.5 %. A further increase in temperature yields only 4.7 % higher high spin fraction.

This scenario also indicates an actual Spin-Crossover process in the gas phase. The increase in the high spin fraction from T_{trap} = 4 to 15 K is very clear, the increase from T_{trap} = 15 to 25 K much smaller, but significant. This finding is as well independent of the consideration of $m_J^{(z)}$ or $m_S^{(z)}$.

Scenario 4: Decreasing Temperature offset

In the fourth and last scenario, we assume a decreasing energy input into the ions via RF heating upon increasing the trap temperature. The temperature offset thus decreases from $\Delta T = 9$ K at $T_{trap} = 4$ K, to $\Delta T = 5$ K at $T_{trap} = 15$ K to $\Delta T = 0$ K at $T_{trap} = T_{ion} = 25$ K.

Table 11: Calculation of the HS fractions using the experimental and theoretical total magnetizations $m_J^{(z)}$ assuming a decreasing temperature offset $\Delta T = 9$, 5 and 0 K.

T_{trap} / K	T_{ion} / K	$m_{J,exp}^{(z)}$	$m_J^{(z)}{}_{HS}$	$m_J^{(z)}{}_{LS}$	x_{HS}
4	15	0.91	2.93	0	0.311
15	20	0.74	2.33	0	0.318
25	25	0.51	1.91	0	0.267

Relating to the total magnetization $m_J^{(z)}$, the high spin fraction scarcely increases from $T_{trap} = 4$ to 15 K by 0.7 % and drops by 5.1 % at further increase of the trap temperature (cf. Tab. 11). Referring to the spin magnetization $m_S^{(z)}$, the calculated high spin fraction decreases upon increasing the trap temperature as well (cf. Tab. 12).

Table 12: Calculation of the HS fractions using the experimental and theoretical spin magnetizations $m_S^{(z)}$ assuming ad decreasing temperature offset $\Delta T = 9$, 5 and 0 K.

T_{trap} / K	T_{ion} / K	$m_{S,exp}^{(z)}$	$m_S^{(z)}{}_{HS}$	$m_S^{(z)}{}_{LS}$	x_{HS}
4	15	0.81	1.65	0	0.491
15	20	0.63	1.28	0	0.492
25	25	0.45	1.04	0	0.433

Assuming a decreasing energy input into the molecular ions via RF heating upon increasing the temperature, the Spin-Crossover doesn’t take place in the gas phase. On the contrary, the calculated high spin fraction of the ions decreases, independent of the consideration of $m_J^{(z)}$ or $m_S^{(z)}$. However, this scenario is the most implausible.

Evaluation of the scenarios

The first scenario is very unlikely. Various experiments at this experimental setup have shown a distinct RF heating of the ions from the operation of the linear quadrupole ion trap.[18, 19, 21, 39-41, 67-70] The effective energy input caused by the RF heating depends on many parameters e.g. trap type and geometry, the type of the buffer gas, buffer gas pressure, trap voltage and amplitude and much more.[71-74] A systematic study of the temperature dependence of the RF heating of transition metal complexes in the NanoCluster Trap is missing so far. Most applications of cryogenic ion traps aim for maximum cooling in order to orient magnetic moments best possible (XMCD studies) or enable tagging of e.g. noble gases for high resolution vibrational and rotational spectroscopy.[16-18, 69, 71, 75-82] Though simulations and experiments indicate an increasing energy input by RF heating when increasing the ion trap temperature.[71, 77, 83] The fourth scenario, assuming a decreasing temperature offset appears less likely as previously observed.[77] We assume a constant (scenario 2) or an increasing temperature offset (scenario 3) to be most likely. Both scenarios 2 and 3 indicate a Spin-Crossover to be present in the gas phase, showing an increasing high spin fraction of the molecular ions upon increasing the trap temperature.

This experiment, investigating the Spin-Crossover process of a transition metal complex in the gas phase using a cryogenic linear quadrupole ion trap in combination with total ion yield (TIY) spectroscopy using the X-ray magnetic circular dichroism (XMCD), is the first of its kind. The lack of data points prevents an unambiguous assertion. Nevertheless, these first results show a drop in the magnetizations upon increasing temperatures deviating from the expected Brillouin behavior, indicating a transition in the spin state. Further temperature dependent experiments on isolated transition metal complexes without Spin-Crossover behavior will help to establish an ion temperature calibration in the experimental setup with fixed parameters. Subsequent temperature dependent measurements on Spin-Crossover complexes will allow for a more reliable confirmation for the observation of a temperature induced change in the spin state in the gas phase.

4.6 Conclusions

We have presented the first gas phase XMCD spectroscopic study of a mononuclear iron(II) Spin-Crossover complex $[Fe(L\text{-}N_4Bz_2)(pyc)]^+$ at different temperatures in combination with DFT modelling.

We have confirmed, that an accurate description of spin transitions in metal complexes along with structural reorganization via DFT calculations largely depends on the extent of exact Hartree-Fock exchange in hybrid functionals such as B3LYP. We have found B3LYP* (15 % H_x^{HF}) to sufficiently describe the proximity of the relative energies of $\mathbf{1}^+$ in different spin states, required for Spin-Crossover processes. The geometry optimized structures with different multiplicities, namely singlet and quintet, represent the crystal structure data very well. The singlet calculation can be assigned to the crystal structure at 110 K, providing reduced iron – ligand bond lengths. The vanishing magnetic moment at temperatures < 250 K is nicely matched by the non-existent spin density in the calculation. The bond lengths of the quintet calculation nicely match to the crystal structure data measured at 333 K. Also the calculated spin density located at the central iron(II) ion fits to the magnetic moment measured at T > 280 K.

We recorded polarization dependent gas phase XMCD spectra of the isolated complex cation $\mathbf{1}^+$ at the Fe $L_{3,2}$ absorption edges at three different ion temperatures. The spectra recorded with negative and positive circularly polarized photons show a significant dichroic effect at all temperatures, indicating a certain magnetic moment at the central iron(II) atom. Since the spin and total magnetic moments are much smaller than expected for an all-high spin configuration of the complex, we assume a mixture of high spin and low spin configurations as our method only provides the average magnetizations of the ion ensemble. A pure randomization of orientation of the magnetic moments at higher temperatures assuming an all high spin configuration can be excluded as the lowest ion temperature can be estimated from similar experiments.

Running through different scenarios, calculating the high spin fractions at three different temperatures, using the spin and total magnetization and simulated Brillouin functions, yields evidences for an actual Spin-Crossover process in the gas phase, as the high spin fraction increases with the temperature. Additional measurements are necessary in order to calibrate the ion temperature at a given trap temperature for a more reliable evidence. For this purpose, a manganese(II) complex with a temperature independent d^5 high spin electron configuration appears suitable.

4.7 Acknowledgements

This work was supported through the DFG funded transregional collaborative research center SFB TRR 88 “3MET.de”. We gratefully acknowledge the financial support and generous allocation of X-ray beamtime from HZB and the BESSY II synchrotron radiation facility. The endstation is jointly operated by HZB and Uni Freiburg, and is partially funded by the German Federal Ministry of Education (BMBF) through grand BMBF-05K16Vf1. We thank the Toyota Technological Institute for providing the superconducting magnet used in the XMCD experiments.

4.8 Appendix

DFT modelling and XMCD spectroscopy at the Fe $L_{3,2}$ absorption edges on a dinuclear Fe(II) Spin-Crossover complex

In this chapter we present preliminary results of investigations on a dinuclear iron(II) Spin-Crossover complex **2**. We performed DFT modelling in terms of geometry optimizations, energy and electron spin density calculations for different spin states and recorded XA spectra at negative and positive circular photon helicity at the iron $L_{3,2}$ absorption edges.

Complex **2** is a dinuclear iron(II) complex with the sum formula $[(C_{16}H_{20}N_4)Fe(C_{14}N_4H_8)Fe(C_{16}H_{20}N_4)\,(ClO_4)_2] \cdot 2$ EtCN synthesized and characterized by Michèle GRAF.[84] The iron(II) ions are each coordinated by a tetraazamacrocyclic ligand: N,N′-Dimethyl-2,11-diaza[3.3](2,6)pyridinophane (abbreviated as L-N_4Me_2) and connected by a dianionic 2,2′-bibenzimidazolate molecule (abbreviated as $BiBzIm^{2-}$). The perchlorate anions act as counterions. The nitrogen atoms of the of the pyridine rings and the nitrogen atoms of the bibenzimidazolate anion form the equatorial coordination plane of the dinuclear complex, the amine nitrogen atoms of the macrocyclic ligands occupy the axial coordination sites of the iron(II) ions (cf. Fig. A1). The investigated cationic complex in the gas phase has the sum formula $[C_{46}H_{48}N_{12}Fe_2]^{2+}$ (abbreviated as $\mathbf{2}^{2+}$ or $[\{Fe^{II}(L\text{-}N_4Me_2)\}_2(BiBzIm)]^{2+}$).

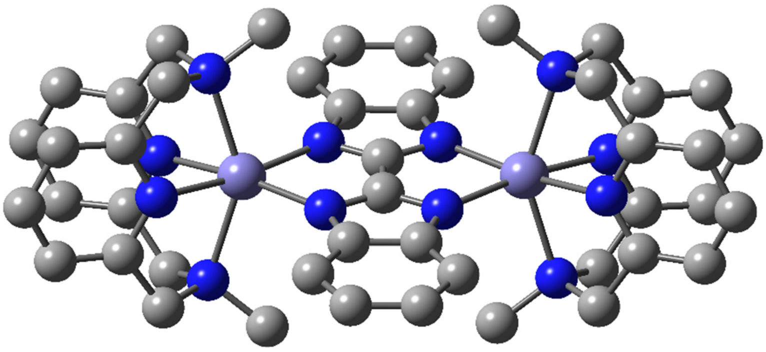

Figure A1: Crystal structure of the complex cation $\mathbf{2}^{2+}$ at 293 K in sideview (C: gray, N: blue, Fe: steel blue).[84]

SQUID measurements of a crystalline sample of **2** show a sharp spin transition at the transition temperature T = 175 K. Decreasing the temperature causes one of two iron(II) ions to change from high spin to low spin. The other iron(II) ion remains in the high spin state. Although there are two iron(II) ions in the complex, a low spin / low spin (LS / LS) configuration can neither be detected by crystal structure nor SQUID measurements even at low temperatures. This behavior can be explained by the ring strain in the bibenzimidazolate ligand. The coordination of a low spin iron(II) ion reduces the bond lengths between the iron ion and the nitrogen donor atoms and induces a bending of the ligand backbone. This results in a degradation of the overlap between the metal orbitals and the ligand orbitals and the low spin state of the second iron(II) ion can no longer be stabilized.[84] The synthesis and a detailed characterization of **2** can be found in the PhD thesis of M. GRAF.[84]

We performed DFT calculations on the B3LYP(*)/cc-pVDZ(C, H, N)/Stuttgart RSC 1997 ECP (Fe) level of theory, to calculate the relative energies and optimize the geometry of the cationic species of the spin-crossover complex ion $\mathbf{2}^{2+}$ in different spin states, hence multiplicities.[25-36] We conducted the calculations with the standard B3LYP (20 % H_x^{HF}) and with the modified B3LYP* (15 % H_x^{HF}) functional (cf. chapter 3.1). The intermediate spin state triplet and septet are not discussed here, as they are not found in the experiment. Both Fe^{II} centers have a $3d^6$ electron configuration, resulting in a nonet state for the high spin / high spin (HS / HS) configuration (eight unpaired electrons, 2 S + 1 = 9) and a quintet state for the low spin / high spin (LS / HS) configuration (four unpaired electrons, 2 S + 1 = 5). The relative energies of the nonet, quintet and the conceivable singlet state are summarized in Tab A1.

Table A1: Relative zero-point vibrational energies (ZVPE) and thermal free energies at 298.15 K of geometry optimized structures of $\mathbf{2}^{2+}$ at different multiplicities by variation of H_x^{HF} (in kJ/mol).

functional	ZPVE			thermal free energies (298.15 K)		
	S = 0 LS/LS	S = 2 LS/HS	S = 4 HS/HS	S = 0 LS/LS	S = 2 LS/HS	S = 4 HS/HS
B3LYP	+91.6	+43.1	0.0	+113.9	+52.0	0.0
B3LYP*	+42.1	+18.0	0.0	+63.2	+25.4	0.0

Just as in the DFT calculations for the mononuclear $\mathbf{1}^{+}$ complex (cf. chapter 3.1), the high spin states are significantly energetically favored using the original B3LYP functional. Reducing H_x^{HF}

to 15 % causes an equalization of the relative zero-point vibrational and thermal free energies. The singlet state is invariably highest in energy. However, further modelling of DFT functionals is necessary for an adequate computational description of the ground state of **2**$^{2+}$. The subsequently presented minimum structures and electron spin density isosurfaces were calculated using B3LYP*/cc-pVDZ (C, H, N)/Stuttgart RSC 1997 ECP (Fe).

The optimized structure of **2**$^{2+}$ in the HS / HS state (nonet) is shown in Fig. A2, the optimized structure of **2**$^{2+}$ in the LS / HS state (quintet) is shown in Fig. A3. The electron spin density is each plotted as purple isosurface.

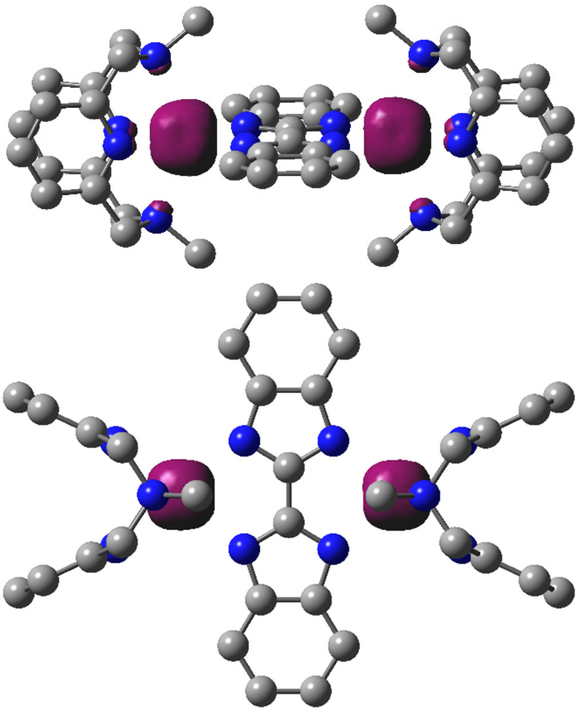

Figure A2: Geometry optimized sturcture of **2**$^{2+}$ in the HS / HS state (nonet) by DFT in sideview (top) and topview (bottom) (C: gray, N: blue, Fe: steel blue). The purple isosurfaces represent the spin density. All hydrogen atoms are omitted for clarity.

The spin density of **2**$^{2+}$ in the nonet calculation (HS/HS) is equally distributed among both iron(II) center atoms (cf. Fig. A2). This indicates both iron atoms to be in an equivalent d^6 high spin state, providing four unpaired electrons each, two in the elevated e_g orbital set and two in the t_{2g} orbital set. The spin density of **2**$^{2+}$ in the quintet (LS/HS) calculation is localized on one iron(II) center (cf. Fig. A3). The extension of the spin density is equal to those of both iron(II) ions in the nonet calculation, indicating an equivalent d^6 high spin state. The other iron(II) ion provides no spin density, suggesting a low spin d^6 configuration with three electron pairs occupying the t_{2g} orbital set.

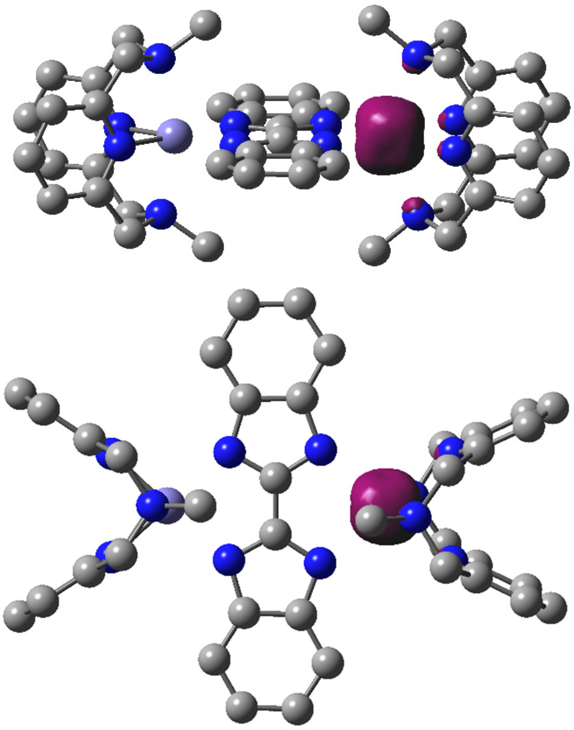

Figure A3: Geometry optimized sturcture of **2**$^{2+}$ in the LS / HS state (quintet) by DFT in sideview (top) and topview (bottom) (C: gray, N: blue, Fe: steel blue). The purple isosurface represents the spin density. All hydrogen atoms are omitted for clarity.

A comparison of selected structure parameters, namely bond lengths and bond angles, of the quintet and nonet calculations shows, that the coordination geometry of the iron(II) ions in the nonet calculation is very similar, resulting in a highly symmetric structure for **2**$^{2+}$ (cf. Fig. A3 and Tab. A2).

In the quintet calculation, the coordination geometry of Fe(2) is similar to those of both iron ions in the nonet calculation. Though, the bond lengths and angles of Fe(1) are significantly different (cf. Tab A2). For example, the iron – nitrogen bond lengths are significantly reduced. The structure parameters of our DFT/B3LYP* calculations of **2**$^{2+}$ in the quintet and nonet state nicely represent the crystal structure data of complex **2** at 150 and 293 K, respectively.[84]

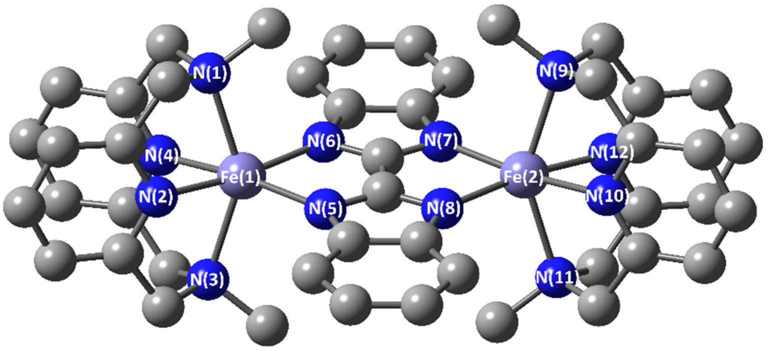

Figure A4: Geometry optimized sturcture of $\mathbf{2}^{2+}$ in the high spin state (nonet) by DFT in sideview (C: gray, N: blue, Fe: steel blue). The numbering relates to Tab. A2, indicating the structure parameters.

Table A2: Selected structure parameters of $\mathbf{2}^{2+}$ obtained by DFT/B3LYP* geometry optimization calculations in the LS (quintet) and HS (nonet) state in comparison to the crystal structures of **2** at 150 and 293 K respectively. Bond lengths in angstrom, bond angles in degree.[84]

Structure parameter	DFT: HS/LS (quintet)	Crystal struct. at 150 K[84]	DFT: HS/HS (nonet)	Crystal struct. at 293 K[84]
d(Fe(1) – N(1))	2.158	2.095	2.358	2.262
d(Fe(1) – N(2))	1.947	1.908	2.205	2.133
d(Fe(1) – N(3))	2.159	2.079	2.356	2.238
d(Fe(1) – N(4))	1.947	1.904	2.206	2.116
d(Fe(1) – N(5))	2.107	2.045	2.201	2.135
d(Fe(1) – N(6))	2.106	2.044	2.198	2.139
d(Fe(2) – N(9))	2.360	2.260	2.356	
d(Fe(2) – N(10))	2.207	2.127	2.206	
d(Fe(2) – N(11))	2.359	2.286	2.358	
d(Fe(2) – N(12))	2.206	2.151	2.205	
d(Fe(2) – N(8))	2.213	2.182	2.198	
d(Fe(2) – N(7))	2.214	2.174	2.201	
β(N(1)-Fe(1)-N(3))	160.339	161.54	144.344	146.89
β(N(2)-Fe(1)-N(4))	86.107	85.13	78.737	79.71
β(N(5)-Fe(1)-N(6))	82.214	82.96	81.179	81.97
β(N(9)-Fe(2)-N(11))	144.288	146.72	144.343	
β(N(10)-Fe(2)-N(12))	78.697	79.61	78.737	
β(N(7)-Fe(2)-N(8))	82.102	83.31	81.180	

In order to determine the spin and orbital magnetizations of $\mathbf{2}^{2+}$ in the gas phase, we measured XA spectra with negative and positive circularly polarized photons at the iron $L_{3,2}$ absorption edges (cf. Fig. A5). The trap was cooled to approx. T_{trap} = 4 K. The first peak at the L_3 absorption edge is split, resulting in two subpeaks at 708 and 709 eV and an additional shoulder at 711 eV.

There is a substantial dichroic effect at the L_3 edge, changing sign at 710 eV, indicating some magnetizations on the iron centers.

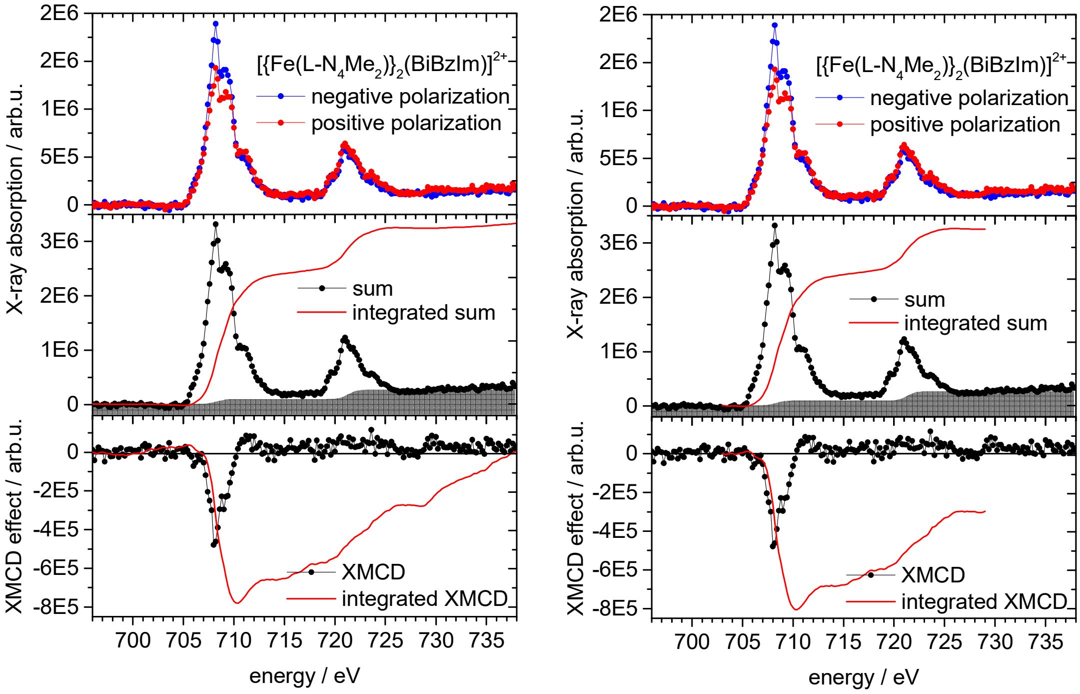

Figure A5: Top: The iron $L_{3,2}$ edges: Polarization dependent X-ray absorption spectra for negative (blue) and positive (red) circular photon polarization of $\mathbf{2^{2+}}$ at 4 K trap temperature. Middle: Sum spectrum (black) of XAS of negative and positive circular photon polarization and the integrated intensity (red). The gray shaded areas represent the two-step functions subtracted after normalization, approximating the direct $2p$ photoionization and $2p \rightarrow ns, nd$ $(n > 3)$ contributions.[21] Bottom: The resulting XMCD spectrum (black) as difference between the XAS of positive and negative circular polarization and the integrated intensity (red). In the left figure, the integration was performed over the entire measured spectral range. In the right figure, the integration was limited to the area of the absorption edges.

The splitting at the L_3 edge may hint to different spin states of the iron ions, compared to the XAS spectra of the mononuclear iron complex $\mathbf{1^+}$, discussed in the main text. The dichroic effect on the L_2 edge at 720 – 725 eV is in contrast rather small. Due to the increased the signal to noise ratio, we integrated the sum spectra and XMCD spectra only in the range of 703 – 729 eV (cf. Fig. A5).

The resulting spin, orbital angular and total magnetizations, as well as the orbital to spin magnetization ratio are summarized in Tab. A3. We corrected the spin sum rule for the magnetic anisotropy term $<T_z>$ and the 2*p*-3*d* interaction by the method of TERAMURA *et al*. (cf. Tab. S1).[51] The spin magnetization yields 0.92 μ_B / atom. For the HS / HS configuration a maximum value of 4 μ_B / atom would be expected due to four unpaired electrons at both iron(II) centers, assuming a ferromagnetic coupling scheme. The LS / HS configuration would yield 2 μ_B /atom in average as a low spin iron ion does not contribute to a spin magnetic moment. The orbital angular magnetization yields 0.12 μ_B / atom. The non-degeneracy of the *d*-orbitals in the octahedral ligand field quenches the orbital angular magnetic moment in first order.[64] Some orbital moment may be retained due to the spin-orbit coupling (cf. chapter 3.1). The calculated magnetizations of **2**$^{2+}$ are very similar to those, obtained for **1**$^{+}$. Since the coupling constants of the iron ions are unknown and there are no data for augmented trap temperatures yet, we do not estimate the ion temperature simulating a Brillouin function. An assignment of HS / HS or LS / HS configuration is hence not possible at this point. Additional measurements on this complex are intended.

Table A3: Experimental spin, orbital angular magnetizations and the orbital to spin magnetization ratio per metal ion of **2**$^{2+}$ obtained by sum rule analysis. Trap temperature T_{trap} = 4 K.

	$m_S^{(z)}$ / μ_B/atom	$m_L^{(z)}$ / μ_B/atom	$m_L^{(z)}$ / $m_S^{(z)}$	$m_J^{(z)}$ / μ_B/atom
Corr. Sum rule	0.92	0.12	0.13	1.04
Original Sum rule	0.78	0.12	0.15	0.90

4.9 References

[1] J. F. Letard, P. Guionneau, L. Goux-Capes, "*Towards spin crossover applications*", *Spin Crossover in Transition Metal Compounds III*, **2004**, *235*, 221-249.

[2] O. Kahn, J. Launay, "*Molecular bistability: An overview*", *Chemtronics*, **1988**, *3*, 140-151.

[3] H.-J. Krüger, "*Spin transition in octahedral metal complexes containing tetraazamacrocyclic ligands*", *Coord. Chem. Rev.*, **2009**, *253*, 2450-2459.

[4] M. Schmitz, M. Seibel, H. Kelm, S. Demeshko, F. Meyer, H. J. Krüger, "*How does a coordinated radical ligand affect the spin crossover properties in an octahedral iron(II) complex?*", *Angew. Chem. Int. Ed.*, **2014**, *53*, 5988-5992.

[5] P. Gütlich, A. Hauser, H. Spiering, "*Thermal and optical switching of iron(II) complexes*", *Angew. Chem. Int. Ed. in Engl.*, **1994**, *33*, 2024-2054.

[6] P. Gütlich, H. A. Goodwin, "*Spin crossover in transition metal compounds I*", Springer Science & Business Media, **2004**.

[7] M. A. Halcrow, "*Spin-crossover materials: properties and applications*", John Wiley & Sons, **2013**.

[8] Y. Ogawa, S.-Y. Koshihara, K. Koshino, T. Ogawa, C. Urano, H. Takagi, "*Dynamical aspects of the photoinduced phase transition in spin-crossover complexes*", *Phys. Rev. Lett.*, **2000**, *84*, 3181.

[9] A. Hauser, in *Spin Crossover in Transition Metal Compounds II*, Springer, **2004**, pp. 155-198.

[10] S. Bonhommeau, G. Molnár, A. Galet, A. Zwick, J. A. Real, J. J. McGarvey, A. Bousseksou, "*One Shot Laser Pulse Induced Reversible Spin Transition in the Spin-Crossover Complex $[Fe(C_4H_4N_2)\{Pt(CN)_4\}]$ at Room Temperature*", *Angew. Chem. Int. Ed.*, **2005**, *44*, 4069-4073.

[11] P. Gütlich, Y. Garcia, H. A. Goodwin, "*Spin crossover phenomena in Fe(ii) complexesDedicated to Professor FA Cotton on occasion of his 70th birthday*", *Chem. Soc. Rev.*, **2000**, *29*, 419-427.

[12] V. Niel, J. M. Martinez-Agudo, M. C. Munoz, A. B. Gaspar, J. A. Real, "*Cooperative spin crossover behavior in cyanide-bridged Fe(II)–M(II) bimetallic 3D Hofmann-like networks (M= Ni, Pd, and Pt)*", *Inorg. Chem.*, **2001**, *40*, 3838-3839.

[13] Y. Garcia, P. J. van Koningsbruggen, E. Codjovi, R. Lapouyade, O. Kahn, L. Rabardel, "*Non-classical Fe^{II} spin-crossover behaviour leading to an unprecedented extremely large apparent thermal hysteresis of 270 K: application for displays*", *J. Mater. Chem.*, **1997**, *7*, 857-858.

[14] J.-F. Létard, "*Photomagnetism of iron(II) spin crossover complexes—the T (LIESST) approach*", *J. Mater. Chem.*, **2006**, *16*, 2550-2559.

[15] M. Schmitz, "*Spincrossover-Prozesse und Π-Radikalliganden*", **2016**.

[16] S. Peredkov, A. Savci, S. Peters, M. Neeb, W. Eberhardt, H. Kampschulte, J. Meyer, M. Tombers, B. Hofferberth, F. Menges, G. Niedner-Schatteburg, "*X-ray absorption spectroscopy of mass-selected transition metal clusters using a cyclotron ion trap: An experimental setup for measuring XMCD spectra of free clusters*", *J. Electron Spectrosc. Relat. Phenom.*, **2011**, *184*, 113-118.

[17] J. Meyer, M. Tombers, C. van Wüllen, G. Niedner-Schatteburg, S. Peredkov, W. Eberhardt, M. Neeb, S. Palutke, M. Martins, W. Wurth, "*The spin and orbital contributions to the total magnetic moments of free Fe, Co, and Ni clusters*", *J. Chem. Phys.*, **2015**, *143*, 104302.

[18] K. Hirsch, J. Lau, P. Klar, A. Langenberg, J. Probst, J. Rittmann, M. Vogel, V. Zamudio-Bayer, T. Möller, B. Von Issendorff, "*X-RAY SPECTROSCOPY ON SIZE-SELECTED CLUSTERS IN AN ION TRAP: FROM THE MOLECULAR LIMIT TO BULK PROPERTIES*", *J. Phys. B: At., Mol. Opt. Phys.*, **2009**, *42*, 154029.

[19] M. Niemeyer, K. Hirsch, V. Zamudio-Bayer, A. Langenberg, M. Vogel, M. Kossick, C. Ebrecht, K. Egashira, A. Terasaki, T. Möller, B. v. Issendorff, J. T. Lau, "*SPIN COUPLING AND ORBITAL ANGULAR MOMENTUM QUENCHING IN FREE IRON CLUSTERS*", *Phys. Rev. Lett.*, **2012**, *108*, 057201.

[20] V. Zamudio-Bayer, L. Leppert, K. Hirsch, A. Langenberg, J. Rittmann, M. Kossick, M. Vogel, R. Richter, A. Terasaki, T. Möller, "*COORDINATION-DRIVEN MAGNETIC-TO-NONMAGNETIC TRANSITION IN MANGANESE-DOPED SILICON CLUSTERS*", *Phys. Rev. B*, **2013**, *88*, 115425.

[21] A. Langenberg, K. Hirsch, A. Ławicki, V. Zamudio-Bayer, M. Niemeyer, P. Chmiela, B. Langbehn, A. Terasaki, B. v. Issendorff, J. T. Lau, "*SPIN AND ORBITAL MAGNETIC MOMENTS OF SIZE-SELECTED IRON, COBALT, AND NICKEL CLUSTERS*", *Phys. Rev. B*, **2014**, *90*, 184420.

[22] T. Lu, F. Chen, "*MULTIWFN: A MULTIFUNCTIONAL WAVEFUNCTION ANALYZER*", *J. Comput. Chem.*, **2012**, *33*, 580-592.

[23] L. Tian, **2016**.

[24] T. K. GaussView Version 3.09 Roy Dennington, Joahn Milliam, *Semichem Inc.*, **2009**, *Shawnee Mission KS*.

[25] A. D. Becke, "*DENSITY-FUNCTIONAL EXCHANGE-ENERGY APPROXIMATION WITH CORRECT ASYMPTOTIC BEHAVIOR*", *Phys. Rev. A*, **1988**, *38*, 3098.

[26] A. D. Becke, "*DENSITY-FUNCTIONAL THERMOCHEMISTRY. III. THE ROLE OF EXACT EXCHANGE*", *J. Chem. Phys.*, **1993**, *98*, 5648-5652.

[27] B. Miehlich, A. Savin, H. Stoll, H. Preuss, "*RESULTS OBTAINED WITH THE CORRELATION ENERGY DENSITY FUNCTIONALS OF BECKE AND LEE, YANG AND PARR*", *Chem. Phys. Lett.*, **1989**, *157*, 200-206.

[28] E. R. Davidson, "*COMMENT ON "COMMENT ON DUNNING'S CORRELATION-CONSISTENT BASIS SETS"*", *Chem. Phys. Lett.*, **1996**, *260*, 514-518.

[29] T. H. Dunning Jr, "*GAUSSIAN BASIS SETS FOR USE IN CORRELATED MOLECULAR CALCULATIONS. I. THE ATOMS BORON THROUGH NEON AND HYDROGEN*", *J. Chem. Phys.*, **1989**, *90*, 1007-1023.

[30] R. A. Kendall, T. H. Dunning Jr, R. J. Harrison, "*ELECTRON AFFINITIES OF THE FIRST-ROW ATOMS REVISITED. SYSTEMATIC BASIS SETS AND WAVE FUNCTIONS*", *J. Chem. Phys.*, **1992**, *96*, 6796-6806.

[31] A. K. Wilson, T. van Mourik, T. H. Dunning, "*GAUSSIAN BASIS SETS FOR USE IN CORRELATED MOLECULAR CALCULATIONS. VI. SEXTUPLE ZETA CORRELATION CONSISTENT BASIS SETS FOR BORON THROUGH NEON*", *THEOCHEM*, **1996**, *388*, 339-349.

[32] D. E. Woon, T. H. Dunning Jr, "*GAUSSIAN BASIS SETS FOR USE IN CORRELATED MOLECULAR CALCULATIONS. III. THE ATOMS ALUMINUM THROUGH ARGON*", *J. Chem. Phys.*, **1993**, *98*, 1358-1371.

[33] D. E. W. Kirk A. Peterson, Thom H. Dunning Jr., "*BENCHMARK CALCULATIONS WITH CORRELATED MOLECULAR WAVE FUNCTIONS. IV. THE CLASSICAL BARRIER HEIGHT OF THE* $H + H_2 \rightarrow H_2 + H$ *REACTION*", *J. Chem. Phys.*, **1994**, *100*, 7410-7415.

[34] D. Andrae, U. Haeussermann, M. Dolg, H. Stoll, H. Preuss, "*ENERGY-ADJUSTED ABINITIO PSEUDOPOTENTIALS FOR THE SECOND AND THIRD ROW TRANSITION ELEMENTS: MOLECULAR TEST FOR* M_2 *(M = AG, AU) AND MH (M = RU, OS)*", *Theor. Chem. Acc.*, **1991**, *78*, 247-266.

[35] M. Dolg, U. Wedig, H. Stoll, H. Preuss, "*ENERGY-ADJUSTED ABINITIO PSEUDOPOTENTIALS FOR THE FIRST ROW TRANSITION ELEMENTS*", *J. Chem. Phys.*, **1987**, *86*, 866-872.

[36] M. J. Frisch, G. W. Trucks, H. B. Schlegel, G. E. Scuseria, M. A. Robb, J. R. Cheeseman, G. Scalmani, V. Barone, G. A. Petersson, H. Nakatsuji, X. Li, M. Caricato, A. Marenich, J. Bloino, B. G. Janesko, R. Gomperts, B. Menucci, H. P. Hratchian, J. V. Ortiz, A. F. Izmaylov, J. L. Sonnenberg, D. Williams-Young, F. Ding, F. Lipparini, F. Egidi, J. Goings, B. Peng, A. Petrone, T. Henderson, D. Ranasinghe, V. G. Zakrzewski, J. Gao, N. Rega, G. Zheng, W. Liang, M. Hada, M. Ehara, K. Toyota, R. Fukuda, J. Hasegawa, M. Ishida, T. Nakajima, Y. Honda, O. Kitao, H. Nakai, T. Vreven, K. Throssel, J. A. Montgomery, J. E. Peralta, F. Ogliaro, M. Bearpark, J. J. Heyd, E. Brothers, K. N. Kudin, V. N. Staroverov, T. Keith, R. Kobayashi, J. Normand, K. Raghavachari, A. Rendell, J. C. Burant, S. S. Iyengar, J. Tomasi, M. Cossi, J. M. Millam, M. Klene, C. Adamo, R. Cammi, J. W. Ochterski, R. L. Martin, K. Morokuma, O. Farkas, Fores, "*GAUSSIAN09, REVISION D.01, GAUSSIAN, INC., WALLINGFORD, CT*", *University of Minnesota, Minneapolis*, **2009**.

[37] M. Swart, "*ACCURATE SPIN-STATE ENERGIES FOR IRON COMPLEXES*", *J. Chem. Theory Comput.*, **2008**, *4*, 2057.

[38] M. Swart, A. R. Groenhof, A. W. Ehlers, K. Lammertsma, "*VALIDATION OF EXCHANGE−CORRELATION FUNCTIONALS FOR SPIN STATES OF IRON COMPLEXES*", *J. Phys. Chem. A*, **2004**, *108*, 5479-5483.

[39] K. Hirsch, V. Zamudio-Bayer, A. Langenberg, M. Niemeyer, B. Langbehn, T. Möller, A. Terasaki, B. v. Issendorff, J. T. Lau, "*MAGNETIC MOMENTS OF CHROMIUM-DOPED GOLD CLUSTERS: THE ANDERSON IMPURITY MODEL IN FINITE SYSTEMS*", *Phys. Rev. Lett.*, **2015**, *114*, 087202.

[40] V. Zamudio-Bayer, K. Hirsch, A. Langenberg, M. Niemeyer, M. Vogel, A. Ławicki, A. Terasaki, J. T. Lau, B. von Issendorff, "*MAXIMUM SPIN POLARIZATION IN CHROMIUM DIMER CATIONS AS DEMONSTRATED BY X-RAY MAGNETIC CIRCULAR DICHROISM SPECTROSCOPY*", *Angew. Chem. Int. Ed.*, **2015**, *54*, 4498-4501.

[41] E. Dmitrii, S. Bari, H. Ronnie, L. Arkadiusz, H. Konstantin, Z.-B. Vicente, L. Tobias, I. Bernd von, S. Thomas, "*AN INTENSE ELECTROSPRAY IONIZATION SOURCE FOR SOFT X-RAY PHOTOIONIZATION OF GAS PHASE PROTEIN IONS*", *J. Phys. Conf. Ser.*, **2015**, *635*, 112083.

[42] C. T. Chen, Y. U. Idzerda, H. J. Lin, N. V. Smith, G. Meigs, E. Chaban, G. H. Ho, E. Pellegrin, F. Sette, "*EXPERIMENTAL CONFIRMATION OF THE X-RAY MAGNETIC CIRCULAR DICHROISM SUM RULES FOR IRON AND COBALT*", *Phys. Rev. Lett.*, **1995**, *75*, 152-155.

[43] B. T. Thole, P. Carra, F. Sette, G. van der Laan, "*X-RAY CIRCULAR DICHROISM AS A PROBE OF ORBITAL MAGNETIZATION*", *Phys. Rev. Lett.*, **1992**, *68*, 1943-1946.

[44] P. Carra, "*X-RAY CIRCULAR DICHROISM AS A PROBE OF ORBITAL AND SPIN MAGNETIZATIONS*", *Synchrotron Radiat. News*, **1992**, *5*, 21-24.

[45] P. Carra, B. T. Thole, M. Altarelli, X. Wang, "*X-RAY CIRCULAR DICHROISM AND LOCAL MAGNETIC FIELDS*", *Phys. Rev. Lett.*, **1993**, *70*, 694-697.

[46] G. Schütz, E. Goering, H. Stoll, in *Handbook of Magnetism and Advanced Magnetic Materials*, John Wiley & Sons, Ltd, **2007**.

[47] C. Piamonteze, P. Miedema, F. M. F. de Groot, "*ACCURACY OF THE SPIN SUM RULE IN XMCD FOR THE TRANSITION-METAL L-EDGES FROM MANGANESE TO COPPER*", *Phys. Rev. B*, **2009**, *80*, 184410.

[48] W. Heiko, "*RECENT ADVANCES IN X-RAY ABSORPTION SPECTROSCOPY*", *Rep. Prog. Phys.*, **2004**, *67*, 2105.

[49] T. Funk, A. Deb, S. J. George, H. Wang, S. P. Cramer, "*X-RAY MAGNETIC CIRCULAR DICHROISM—A HIGH ENERGY PROBE OF MAGNETIC PROPERTIES*", *Coord. Chem. Rev.*, **2005**, *249*, 3-30.

[50] F. M. F. de Groot, "*X-ray absorption and dichroism of transition metals and their compounds*", *J. Electron Spectrosc. Relat. Phenom.*, **1994**, *67*, 529-622.

[51] Y. Teramura, A. Tanaka, T. Jo, "*Effect of coulomb interaction on the X-Ray magnetic circular dichroism spin sum rule in 3D transition elements*", *J. Phys. Soc. Jpn.*, **1996**, *65*, 1053-1055.

[52] Y. Teramura, A. Tanaka, B. T. Thole, T. Jo, "*Effect of Coulomb Interaction on the X-Ray Magnetic Circular Dichroism Spin Sum Rule in Rare Earths*", *J. Phys. Soc. Jpn.*, **1996**, *65*, 3056-3059.

[53] S. Qiao, A. Kimura, H. Adachi, K. Iori, K. Miyamoto, T. Xie, H. Namatame, M. Taniguchi, A. Tanaka, T. Muro, S. Imada, S. Suga, "*Direct evidence of ferromagnetism without net magnetization observed by X-ray magnetic circular dichroism*", *Phys. Rev. B*, **2004**, *70*, 134418.

[54] S. Qiao, A. Kimura, H. Adachi, K. Iori, K. Miyamoto, T. Xie, H. Namatame, M. Taniguchi, A. Tanaka, T. Muro, S. Imada, S. Suga, "*Temperature dependence of spin and orbital magnetic moments of Sm 4F electrons in (Sm,Gd)Al$_2$*", *J. Electron Spectrosc. Relat. Phenom.*, **2005**, *144–147*, 749-752.

[55] F. Bondino, C. Cepek, N. Tagmatarchis, M. Prato, H. Shinohara, A. Goldoni, "*Element-Specific Probe of the Magnetic and Electronic Properties of Dy incar-Fullerenes*", *J. Phys. Chem. B*, **2006**, *110*, 7289-7295.

[56] T. Jo, "*The 3D–4F exchange interaction, X-ray second-order optical processes and the magnetic circular dichroism (MCD) spin sum rule in rare earths*", *J. Electron Spectrosc. Relat. Phenom.*, **1997**, *86*, 73-82.

[57] K. P. Kepp, "*Consistent descriptions of metal–ligand bonds and spin-crossover in inorganic chemistry*", *Coord. Chem. Rev.*, **2013**, *257*, 196-209.

[58] M. C. Holthausen, "*Benchmarking approximate density functional theory. I. s/d excitation energies in 3d transition metal cations*", *J. Comput. Chem.*, **2005**, *26*, 1505-1518.

[59] K. P. Jensen, B. O. Roos, U. Ryde, "*Performance of density functionals for first row transition metal systems*", *J. Chem. Phys.*, **2007**, *126*, 014103.

[60] K. P. Jensen, U. Ryde, "*Theoretical Prediction of the Co−C Bond Strength in Cobalamins*", *J. Phys. Chem. A*, **2003**, *107*, 7539-7545.

[61] K. P. Chemical Physics LettersJensen, J. Cirera, "*Accurate Computed Enthalpies of Spin Crossover in Iron and Cobalt Complexes*", *J. Phys. Chem. A*, **2009**, *113*, 10033-10039.

[62] M. Reiher, O. Salomon, B. Artur Hess, "*Reparameterization of hybrid functionals based on energy differences of states of different multiplicity*", *Theor. Chem. Acc.*, **2001**, *107*, 48-55.

[63] M. Reiher, "*Theoretical Study of the Fe(phen)$_2$(NCS)$_2$ Spin-Crossover Complex with Reparametrized Density Functionals*", *Inorg. Chem.*, **2002**, *41*, 6928-6935.

[64] F. S. Ham, "*Dynamical Jahn-Teller effect in paramagnetic resonance spectra: orbital reduction factors and partial quenching of spin-orbit interaction*", *Phys. Rev.*, **1965**, *138*, A1727.

[65] A. F. Orchard, "*Magnetochemistry*", *Oxford Chemistry Primers*, **1999**, *75*, ALL-ALL.

[66] H. Lueken, "*Magnetochemie*", *Teubner Studienbücher Chemie*, **1999**.

[67] S. T. Akin, V. Zamudio-Bayer, K. Duanmu, G. Leistner, K. Hirsch, C. Bülow, A. Ławicki, A. Terasaki, B. v. Issendorff, D. G. Truhlar, J. T. Lau, M. A. Duncan, "*Size-Dependent Ligand Quenching of Ferromagnetism in Co$_3$(benzene)$_n^+$ Clusters Studied with X-ray Magnetic Circular Dichroism Spectroscopy*", *J. Phys. Chem. Lett.*, **2016**, *7*, 4568-4575.

[68] V. Zamudio-Bayer, R. Lindblad, C. Bülow, G. Leistner, A. Terasaki, B. v. Issendorff, J. T. Lau, "*Electronic ground state of Ni_2^+*", *J. Chem. Phys.*, **2016**, *145*, 194302.

[69] L. F. Chibotaru, L. Ungur, C. Aronica, H. Elmoll, G. Pilet, D. Luneau, "*Structure, magnetism, and theoretical study of a mixed-valence $Co^{II}_3Co^{III}_4$ heptanuclear wheel: lack of SMM behavior despite negative magnetic anisotropy*", *J. Am. Chem. Soc.*, **2008**, *130*, 12445-12455.

[70] V. Zamudio-Bayer, K. Hirsch, A. Langenberg, A. Ławicki, A. Terasaki, B. v. Issendorff, J. Lau, "*Electronic ground states of Fe_2^+ and Co_2^+ as determined by x-ray absorption and x-ray magnetic circular dichroism spectroscopy*", *J. Chem. Phys.*, **2015**, *143*, 244318.

[71] O. Asvany, S. Schlemmer, "*Numerical simulations of kinetic ion temperature in a cryogenic linear multipole trap*", *Int. J. Mass Spectrom.*, **2009**, *279*, 147-155.

[72] J. P. Schiffer, M. Drewsen, J. S. Hangst, L. Hornekær, "*Temperature, ordering, and equilibrium with time-dependent confining forces*", *Proc. Natl. Acad. Sci.*, **2000**, *97*, 10697-10700.

[73] D. Gerlich, "*Inhomogeneous RF fields: a versatile tool for the study of processes with slow ions*", *State-selected and state-to-state ion-molecule reaction dynamics, part*, **1992**, *1*, 1-176.

[74] W. Roland, "*Radiofrequency multipole traps: tools for spectroscopy and dynamics of cold molecular ions*", *J. Phys. B: At., Mol. Opt. Phys.*, **2009**, *42*, 154001.

[75] O. Asvany, P. Kumar, B. Redlich, I. Hegemann, S. Schlemmer, D. Marx, "*Understanding the infrared spectrum of bare CH_5^+*", *Science*, **2005**, *309*, 1219-1222.

[76] O. Asvany, O. Ricken, H. S. Müller, M. C. Wiedner, T. F. Giesen, S. Schlemmer, "*High-resolution rotational spectroscopy in a cold ion trap: H_2D^+ and D_2H^+*", *Phys. Rev. Lett.*, **2008**, *100*, 233004.

[77] S. Brünken, L. Kluge, A. Stoffels, J. Pérez-Ríos, S. Schlemmer, "*Rotational state-dependent attachment of He atoms to cold molecular ions: An action spectroscopic scheme for rotational spectroscopy*", *J. Mol. Spectrosc.*, **2017**, *332*, 67-78.

[78] C. M. Leavitt, A. B. Wolk, J. A. Fournier, M. Z. Kamrath, E. Garand, M. J. Van Stipdonk, M. A. Johnson, "*Isomer-specific IR–IR double resonance spectroscopy of D_2-tagged protonated dipeptides prepared in a cryogenic ion trap*", *J. Phys. Chem. Lett.*, **2012**, *3*, 1099-1105.

[79] E. Garand, M. Z. Kamrath, P. A. Jordan, A. B. Wolk, C. M. Leavitt, A. B. McCoy, S. J. Miller, M. A. Johnson, "*Determination of noncovalent docking by infrared spectroscopy of cold gas-phase complexes*", *Science*, **2012**, *335*, 694-698.

[80] J. Roithová, "*Characterization of reaction intermediates by ion spectroscopy*", *Chem. Soc. Rev.*, **2012**, *41*, 547-559.

[81] S. Peredkov, M. Neeb, W. Eberhardt, J. Meyer, M. Tombers, H. Kampschulte, G. Niedner-Schatteburg, "*Spin and Orbital Magnetic Moments of Free Nanoparticles*", *Phys. Rev. Lett.*, **2011**, *107*, 233401.

[82] D. Dieleman, M. Tombers, L. Peters, J. Meyer, S. Peredkov, J. Jalink, M. Neeb, W. Eberhardt, T. Rasing, G. Niedner-Schatteburg, "*Orbit and spin resolved magnetic properties of size selected $[Co_NRh]^+$ and $[Co_NAu]^+$ nanoalloy clusters*", *Phys. Chem. Chem. Phys.*, **2015**, *17*, 28372-28378.

[83] R. Otto, A. von Zastrow, T. Best, R. Wester, "*Internal state thermometry of cold trapped molecular anions*", *Phys. Chem. Chem. Phys.*, **2013**, *15*, 612-618.

[84] M. Graf, "*Untersuchungen zu Spincrossover und Valenztautomerie an an Eisen(II)- bzw. Kobalt(II)-Komplexen*", **2008**.

4.10 Supplementary Material

Gas Phase XMCD Spectroscopy of an Octahedral Iron(II) Spin-Crossover Complex

Joachim M. Hewer[a], Matthias Tombers[a], Johannes Lang[a], Markus Schmitz[a], Vicente Zamudio-Bayer[b,c], J. Tobias Lau[b], Bernd von Issendorff[c], Akira Terasaki[d], Thomas Schlathölter[e], Ronnie Hoekstra[e], Hans-Jörg Krüger[a], and Gereon Niedner-Schatteburg[a]

(a) Fachbereich Chemie and Forschungszentrum OPTIMAS, Kaiserslautern, Germany
(b) Institut für Methoden und Instrumentierung der Forschung mit Synchrotronstrahlung, Helmholtz-Zentrum Berlin für Materialien und Energie, Berlin, Germany
(c) Physikalisches Institut, Universität Freiburg, Germany
(d) Department of Chemistry, Kyushu University, Fukuoka, Japan
(e) Zernike Institute for Advanced Materials, University of Groningen, Groningen, The Netherlands

Content

Table S1: The expectation values of magnetic quantities and the ratio of X_I to X_E of the S_z sum rule for Fe^{2+} calculated with 10 Dq = 1.5 eV.

Table S2 Atom coordinates of the DFT geometry optimized (**B3LYP*/cc-pVDZ**) complex ion $\mathbf{1}^+$ in the **low spin** configuration (**singlet**).

Table S3: Atom coordinates of the DFT geometry optimized (**B3LYP*/cc-pVDZ**) complex ion $\mathbf{1}^+$ in the **high spin** configuration (**quintet**).

Table S4: Relative zero-point vibrational energies (ZVPE) and thermal free energies at 298.15 K of geometry optimized structures of $\mathbf{1}^+$ at S = 0,1,2 by variation of exact exchange and basis size (in kJ/mol).

Figure S1: Left: Geometry optimized structure of $\mathbf{1}^+$ in the intermediate triplet state (C: gray, O: red, N: blue, Fe: steel blue).

Figure S2: Sum of positive and negative XA spectra (black) and their integrated sum (red) of $\mathbf{1}^+$ at **4 K** trap temperature. XMCD spectra (black) and their integrated sum (red) at **4 K** trap temperature.

Figure S3: Sum of positive and negative XA spectra (black) and their integrated sum (red) of **1**$^+$ at **15 K** trap temperature. XMCD spectra (black) and their integrated sum (red) at **15 K** trap temperature.

Figure S4: Sum of positive and negative XA spectra (black) and their integrated sum (red) of **1**$^+$ at **25 K** trap temperature. XMCD spectra (black) and their integrated sum (red) at **25 K** trap temperature.

Figure S5: Uncorrected spin ($m_S^{(z)}$, filled blue circles), orbital ($m_L^{(z)}$, filled red squares), total ($m_{tot}^{(z)}$, filled black triangles) magnetizations and the $m_L^{(z)}$ to $m_S^{(z)}$ ratio (open purple triangles) on the Fe^{2+} ions in **1**$^+$ ([Fe^{II}(L-N_4Bz_2)(pyc)]$^+$) obtained with tight integration limits.

Table S5: Uncorrected spin, orbital angular magnetizations and the orbital to spin magnetization ratio of **1**$^+$ obtained by sum rule analysis.

Figure S6: Simulated magnetizations $m_J^{(z)}$ of the Fe^{2+} ion in the ground state, as Brillouin function of the ion temperature at a magnetic field of B = 5 T.

Figure S7: Simulated magnetizations $m_S^{(z)}$ of the Fe^{2+} ion in the ground state, as Brillouin function of the ion temperature at a magnetic field of B = 5 T.

Figure S8: Uncorrected Spin ($m_S^{(z)}$, filled blue circles), orbital ($m_L^{(z)}$, filled red squares), total ($m_{tot}^{(z)}$, filled black triangles) magnetizations and the $m_L^{(z)}$ to $m_S^{(z)}$ ratio (open purple triangles) on the Fe^{2+} ions in complex **1** ([Fe^{II}(L-N_4Bz_2)(pyc)]$^+$) obtained with tight integration limits.

Figure S9: Top: Simulated total magnetization of the Fe^{2+} ion in the ground state as a Brillouin function of the temperature.

Figure S10: Top: Simulated spin magnetization of the Fe^{2+} ion in the ground state as a Brillouin function of the temperature.

Table S6: Atom coordinates of the DFT geometry optimized (B3LYP*/cc-pVDZ) complex ion **2**$^{2+}$ in the HS/HS configuration (nonet).

Table S7: Atom coordinates of the DFT geometry optimized (B3LYP*/cc-pVDZ) complex ion **2**$^{2+}$ in the LS/HS configuration (quintet).

Table S8: Relative zero-point vibrational energies (ZVPE) and thermal free energies at 298.15 K of DFT geometry optimized structures of **2**$^{2+}$ at S = 0,1,2,3,4 by variation of exact exchange: B3LYP / B3LYP* (in kJ/mol).

Figure S11: DFT/B3LYP* geometry optimized structures of **2**$^{2+}$ (a) singlet sideview (b) singlet topview (c) triplet sideview (d) triplet topview (e) septet sideview (f) septet topview (C: gray, N: blue, Fe: steel blue).

Correction of the spin sum rules by Takeo Jo *et al*..[51, 52]

The S_z sum rule for the $L_{2,3}$ edge in **3*d* transition metal** systems is expressed as:

$$X_I = X_E.$$

The relative integrated magnetic circular dichroism (MCD) intensity is defined as

$$X_I = \frac{\int_{L_3}\big(\mu_+(\omega)-\mu_-(\omega)\big)d\omega - 2\int_{L_2}\big(\mu_+(\omega)-\mu_-(\omega)\big)d\omega}{\int_{L_3+L_2}\big(\mu_+(\omega)+\mu_0(\omega)+\mu_-(\omega)\big)d\omega}$$

and the expectation value is given by

$$X_E = \frac{2}{3(10-n)}\langle S_z\rangle + \frac{7}{3(10-n)}\langle T_z\rangle.$$

The absorption spectra with positive and negative light helicity are given by $\mu_\pm(\omega)$, with linearly polarized light by $\mu_0(\omega)$ along the *z* direction. L_3 and L_2 denote the integrated region with respect to ω, the number of 3d electrons is given by n.

Table S1: The expectation values of magnetic quantities and the ratio of X_I to X_E of the S_z sum rule for Fe^{2+} calculated with 10 Dq = 1.5 eV.[51]

	n	$\langle S_z\rangle$	$\langle T_z\rangle$	X_I/X_E
Fe^{2+}	6	-1.69	0.0126	0.875

Table S2: Atom coordinates of the DFT geometry optimized (**B3LYP*/cc-pVDZ**) complex ion **1^+** in the **low spin** configuration (**singlet**).

atom	x	y	z
N	-0.377053	-0.188631	-0.116116
C	0.907024	0.207958	-0.336485
C	1.19248	1.336586	-1.134425
H	2.239206	1.648787	-1.30658
C	0.114386	2.056653	-1.700184
H	0.309294	2.942941	-2.33268
C	-1.214057	1.638689	-1.452655
H	-2.073519	2.189842	-1.877221
C	-1.425457	0.500512	-0.645311
C	1.937406	-0.608571	0.435315
H	2.057794	-0.117816	1.429693
H	2.936488	-0.597729	-0.063735
N	1.459346	-2.025191	0.705285
C	-2.786012	-0.017308	-0.192223
H	-3.587606	0.213096	-0.935058
H	-3.041593	0.524728	0.748465
N	-2.749362	-1.496628	0.153459
C	-2.973635	-2.35745	-1.078006
H	-3.743729	-1.918298	-1.757774
H	-3.377052	-3.335091	-0.720191
C	1.773648	-2.94797	-0.459677
H	1.826671	-3.983989	-0.046763
H	2.773044	-2.727584	-0.907709
C	-1.669528	-2.643499	-1.823001
N	-0.571048	-2.66953	-1.010901
C	0.670033	-2.933608	-1.518056
C	-1.559614	-2.918991	-3.202341
H	-2.455996	-2.893297	-3.849635
C	-0.283709	-3.21701	-3.73747
H	-0.169725	-3.432159	-4.816389
C	0.848617	-3.218272	-2.888337
H	1.858177	-3.429532	-3.287426
C	2.103455	-2.545461	1.999638
H	1.689363	-1.904951	2.809656
H	1.704391	-3.574637	2.144753
C	-3.80645	-1.798452	1.227192
H	-3.715419	-2.886604	1.443959
H	-3.471501	-1.243622	2.131648
Fe	-0.705978	-1.892647	0.761623
N	-1.048458	-3.56297	1.854232
O	-0.822763	-1.008689	2.528847
C	-1.181973	-3.27811	3.190656
C	-1.048461	-1.79107	3.570428

C	-1.423771	-4.27649	4.157066
H	-1.516793	-3.956122	5.210725
C	-1.53443	-5.620606	3.743001
H	-1.724129	-6.426977	4.476641
C	-1.397041	-5.918509	2.365753
H	-1.474981	-6.955885	1.990957
C	-1.155679	-4.866703	1.458382
H	-1.042666	-5.059683	0.37414
O	-1.152835	-1.450069	4.754264
C	3.637392	-2.55307	2.053685
C	4.341365	-1.470487	2.649108
H	3.777407	-0.625732	3.092463
C	4.388657	-3.65146	1.55148
H	3.865862	-4.532459	1.128872
C	5.800856	-3.653872	1.612685
H	6.367198	-4.521397	1.223086
C	5.753645	-1.470347	2.713449
H	6.282124	-0.622001	3.188761
C	6.487277	-2.559249	2.188272
H	7.592527	-2.563729	2.243881
C	-5.259744	-1.44074	0.886557
C	-5.813133	-0.199936	1.306487
H	-5.196443	0.504809	1.899205
C	-7.153189	0.136318	1.006482
H	-7.567004	1.103707	1.349763
C	-7.966876	-0.768217	0.285788
H	-9.018005	-0.509197	0.056142
C	-7.437901	-2.015743	-0.119816
H	-8.0763	-2.739688	-0.661529
C	-6.098096	-2.34929	0.183148
H	-5.710935	-3.345008	-0.111625

Table S3: Atom coordinates of the DFT geometry optimized (**B3LYP*/cc-pVDZ**) complex ion **1**$^+$ in the **high spin** configuration (**quintet**).

atom	x	y	z
N	-0.385243	-0.096563	-0.062745
C	0.897172	0.231834	-0.369266
C	1.189567	1.262495	-1.290921
H	2.23841	1.524067	-1.525433
C	0.114469	1.94201	-1.908877
H	0.31217	2.75427	-2.633639
C	-1.214323	1.557732	-1.615549
H	-2.072215	2.053498	-2.107119
C	-1.426513	0.516721	-0.683632
C	1.967954	-0.558272	0.392563
H	2.08438	-0.077289	1.392962
H	2.956204	-0.486611	-0.12574
N	1.578791	-1.996491	0.648556
C	-2.815475	0.026409	-0.256772
H	-3.585575	0.314644	-1.014603
H	-3.07591	0.551098	0.693224
N	-2.858952	-1.45587	0.040026
C	-2.97866	-2.293466	-1.21036
H	-3.723142	-1.865585	-1.927066
H	-3.368185	-3.291735	-0.895406
C	1.817098	-2.886989	-0.546704
H	1.848726	-3.936435	-0.165519
H	2.807936	-2.685255	-1.024857
C	-1.630368	-2.514344	-1.909213
N	-0.564353	-2.678552	-1.075985
C	0.693026	-2.801176	-1.58784
C	-1.481818	-2.565202	-3.313216
H	-2.360851	-2.43705	-3.97232
C	-0.190506	-2.76284	-3.853645
H	-0.044378	-2.806683	-4.949409
C	0.91779	-2.860689	-2.98124
H	1.945293	-2.967702	-3.376583
C	2.288578	-2.531477	1.895557
H	1.922658	-1.905611	2.741817
H	1.896779	-3.563563	2.050922
C	-3.975079	-1.774737	1.03894
H	-3.904229	-2.870074	1.235603
H	-3.694073	-1.249353	1.980545
Fe	-0.761289	-1.973134	0.983113
N	-1.117922	-3.822944	2.160134
O	-0.940133	-1.192254	2.843752
C	-1.256364	-3.505306	3.484391
C	-1.156373	-2.005287	3.865428

C	-1.482199	-4.489389	4.473224
H	-1.583116	-4.155428	5.521343
C	-1.568477	-5.842066	4.083835
H	-1.744425	-6.635394	4.83544
C	-1.426811	-6.172045	2.713564
H	-1.488192	-7.219393	2.364407
C	-1.202952	-5.133164	1.788131
H	-1.085282	-5.341138	0.705717
O	-1.281977	-1.691721	5.053045
C	3.823622	-2.543429	1.862554
C	4.566212	-1.456144	2.39893
H	4.034517	-0.604516	2.868039
C	5.979727	-1.459323	2.370852
H	6.539939	-0.607262	2.801092
C	6.675342	-2.555813	1.810774
H	7.78187	-2.562569	1.794481
C	4.537582	-3.648312	1.322417
H	3.985074	-4.530269	0.941444
C	5.950806	-3.654217	1.291881
H	6.488806	-4.526788	0.874363
C	-5.403009	-1.397993	0.620038
C	-5.965192	-0.154201	1.017662
H	-5.377409	0.536849	1.654158
C	-7.279395	0.202593	0.637731
H	-7.701777	1.172137	0.964153
C	-8.057442	-0.684326	-0.141894
H	-9.088861	-0.409372	-0.433941
C	-7.519281	-1.934136	-0.528019
H	-8.131102	-2.643754	-1.117312
C	-6.205078	-2.288113	-0.145869
H	-5.810126	-3.284331	-0.428636

Table S4: Relative zero-point vibrational energies (ZVPE) and thermal free energies at 298.15 K of geometry optimized structures of **1^+** at S = 0,1,2 by variation of exact exchange and basis size (in kJ/mol).

functional	basis set	ZPVE			thermal free energies (298.15 K)		
		S = 0	S = 1	S = 2	S = 0	S = 1	S = 2
B3LYP	cc-pVTZ	+24.8	+29.3	0.0	+39.5	+34.1	0.0
B3LYP	cc-pVDZ	+26.8	+32.3	0.0	+41.1	+37.1	0.0
B3LYP*	cc-pVDZ	+0.7	+13.9	0.0	+15.1	+18.9	0.0
B3LYP**	cc-pVDZ	0.0	+21.4	+26.8	0.0	+26.2	+34.7

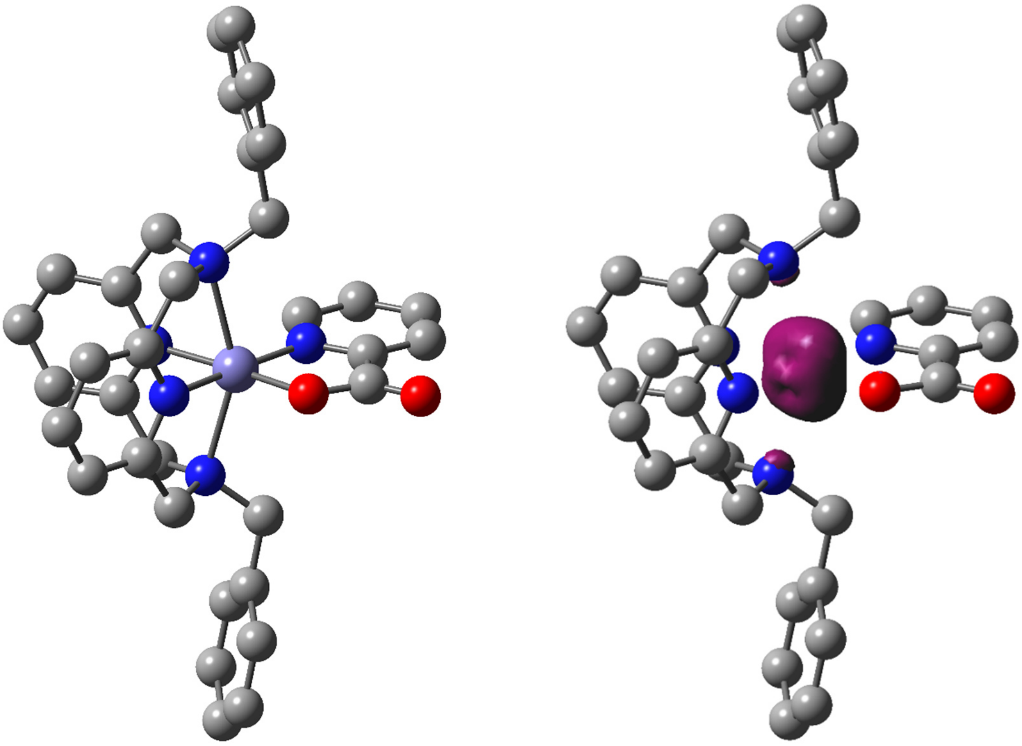

Figure S1: Left: Geometry optimized structure of **1**$^{+}$ in the intermediate triplet state (C: gray, O: red, N: blue, Fe: steel blue). Right: Geometry optimized structure of **1**$^{+}$ in the intermediate triplet state, displaying the spin density surface (purple) located at the iron atom. All Hydrogen atoms are omitted for clarity.

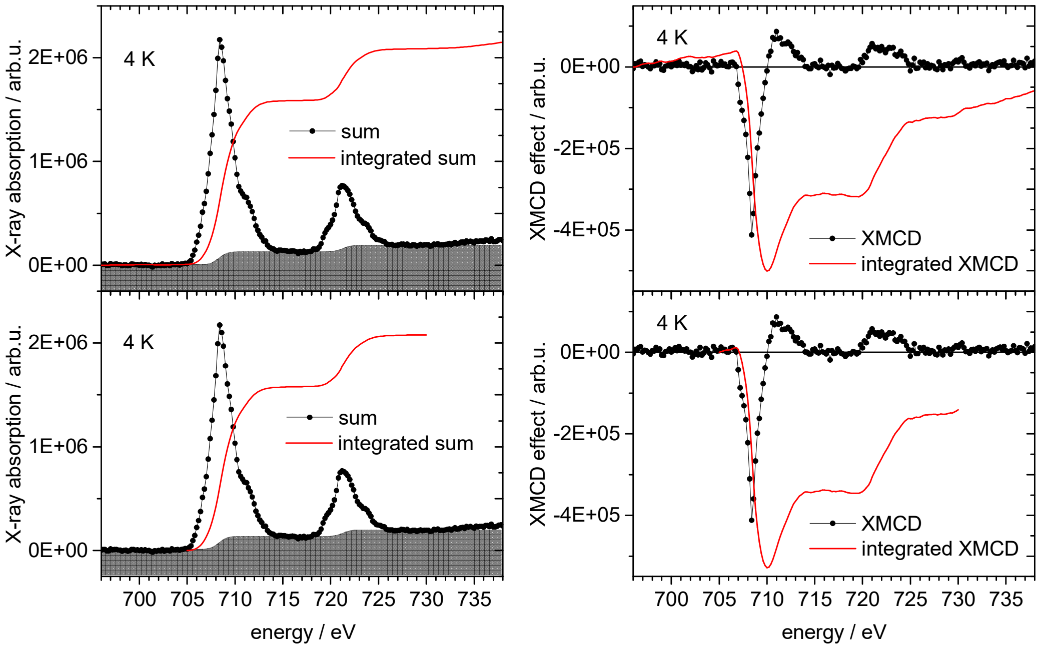

Figure S2: Left: Sum of positive and negative XA spectra (black) and their integrated sum (red) of **1**$^{+}$ at **4 K** trap temperature. The grey shaded areas represent the two-step functions subtracted after normalization, approximating the direct 2*p* photoionization and 2*p* → *ns*, *nd* (*n* > 3) contributions.[21] Note, that the ordinates for the sum spectra and their integrals are different. Right: XMCD spectra (black) and their integrated sum (red) at **4 K** trap temperature. The integrals in top left and top right represent the whole measured spectral region. The integrals in bottom left and bottom right are restricted to close proximity of the absorption bands.

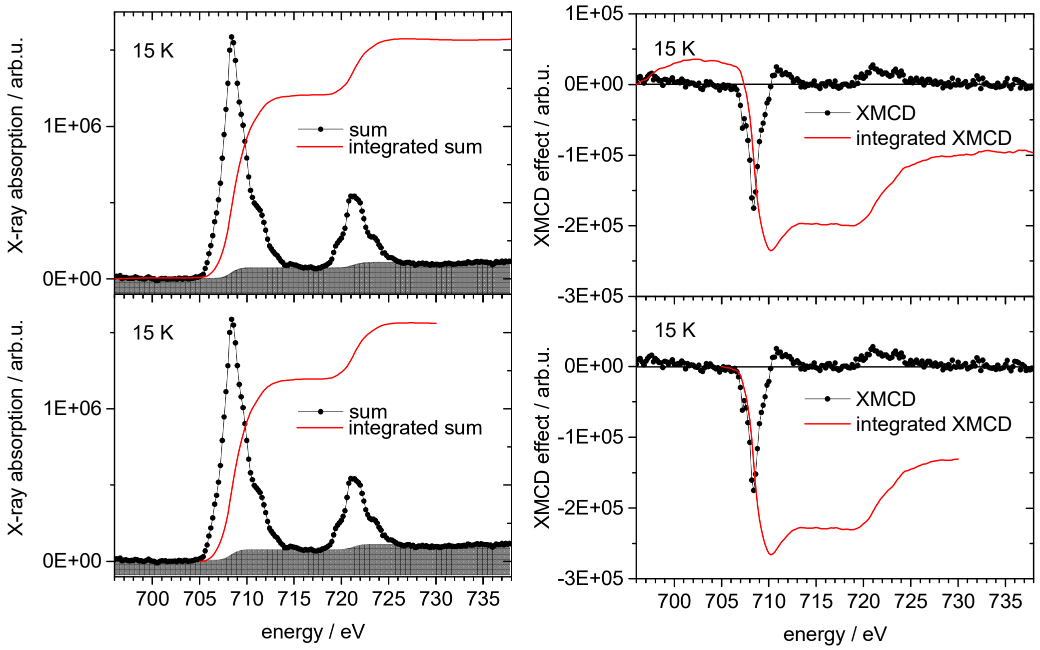

Figure S3: Left: Sum of positive and negative XA spectra (black) and their integrated sum (red) of **1**$^+$ at **15 K** trap temperature. The grey shaded areas represent the two-step functions subtracted after normalization, approximating the direct 2*p* photoionization and 2*p* → *ns*, *nd* (*n* > 3) contributions.[21] Note, that the ordinates for the sum spectra and their integrals are different. Right: XMCD spectra (black) and their integrated sum (red) at **15 K** trap temperature. The integrals in top left and top right represent the whole measured spectral region. The integrals in bottom left and bottom right are restricted to close proximity of the absorption bands.

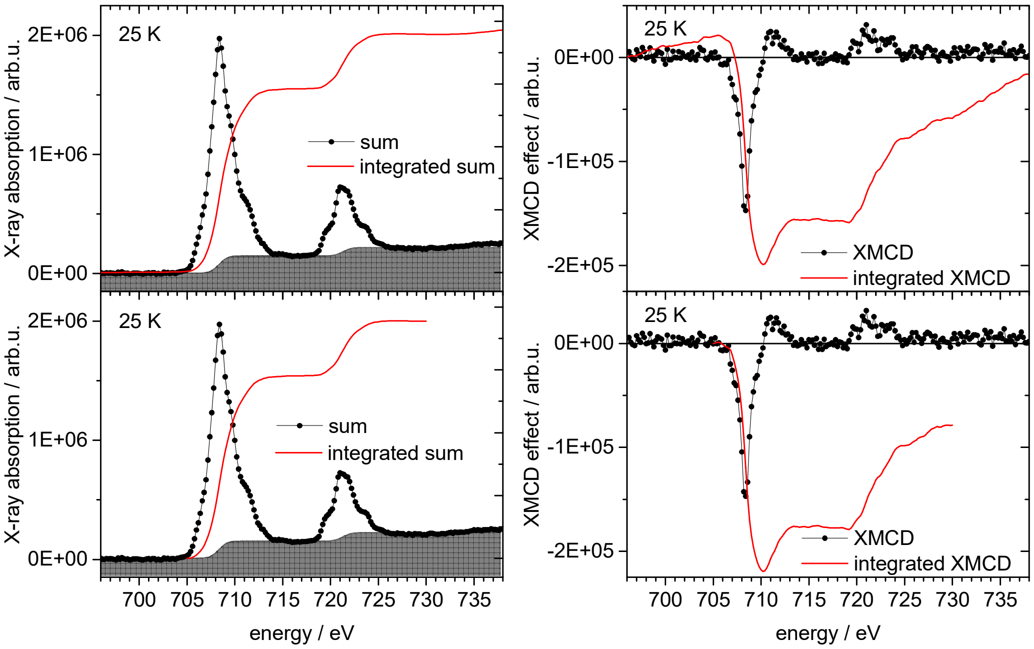

Figure S4: Left: Sum of positive and negative XA spectra (black) and their integrated sum (red) of **1**$^+$ at **25 K** trap temperature. The grey shaded areas represent the two-step functions subtracted after normalization, approximating the direct 2*p* photoionization and 2*p* → *ns*, *nd* (*n* > 3) contributions.[21] Note, that the ordinates for the sum spectra and their integrals are different. Right: XMCD spectra (black) and their integrated sum (red) at **25 K** trap temperature. The integrals in top left and top right represent the whole measured spectral region. The integrals in bottom left and bottom right are restricted to close proximity of the absorption bands.

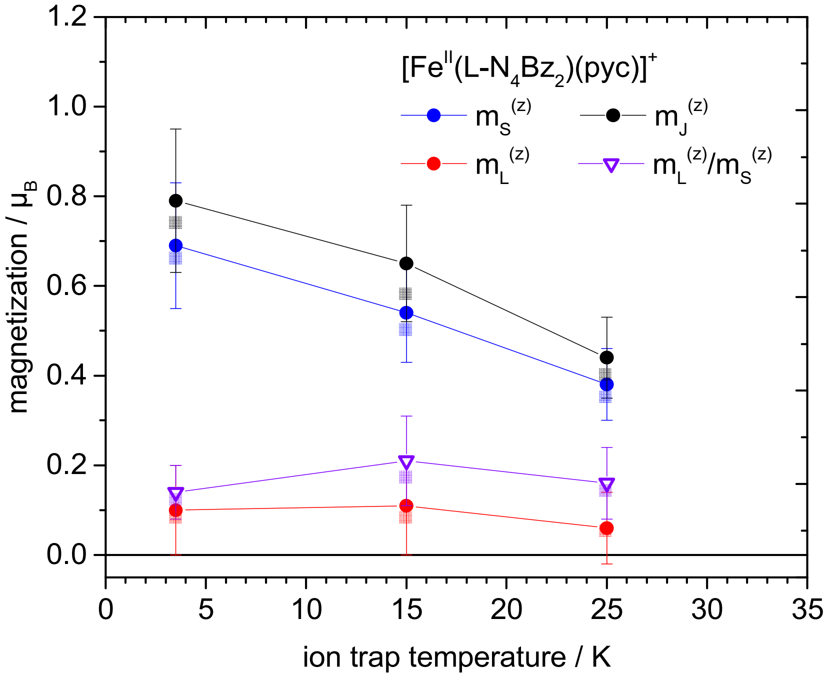

Figure S5: Uncorrected spin ($m_S^{(z)}$, filled blue circles), orbital ($m_L^{(z)}$, filled red squares), total ($m_{tot}^{(z)}$, filled black triangles) magnetizations and the $m_L^{(z)}$ to $m_S^{(z)}$ ratio (open purple triangles) on the Fe^{2+} ions in **1**$^+$ ([Fe^{II}(L-N$_4$Bz$_2$)(pyc)]$^+$) obtained with tight integration limits. The shaded data represent the magnetizations obtained by integration of the entire measured range.

Table S5: Uncorrected spin, orbital angular magnetizations and the orbital to spin magnetization ratio of **1**$^+$ obtained by sum rule analysis.

T_{trap} / K	$m_S^{(z)}$ / μ_B	$m_L^{(z)}$ / μ_B	$m_L^{(z)}$ / $m_S^{(z)}$	
3.5	0.69	0.10	0.14	0.27
15 K	0.54	0.11	0.21	0.40
25 K	0.38	0.06	0.16	0.36

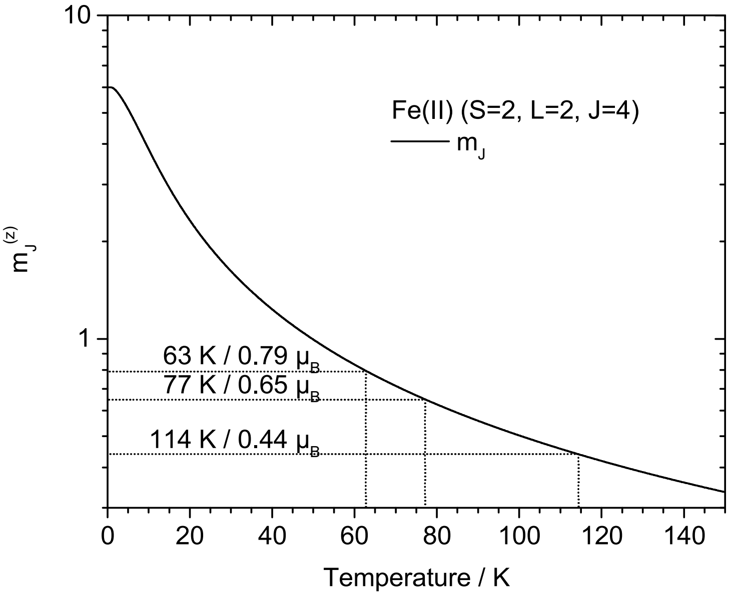

Figure S6: Simulated magnetizations $m_J^{(z)}$ of the Fe^{2+} ion in the ground state, as Brillouin function of the ion temperature at a magnetic field of B = 5 T. The experimentally determined but uncorrected total magnetizations ($m_J^{(z)}$) are projected onto the Brillouin function to identify the ion temperature.

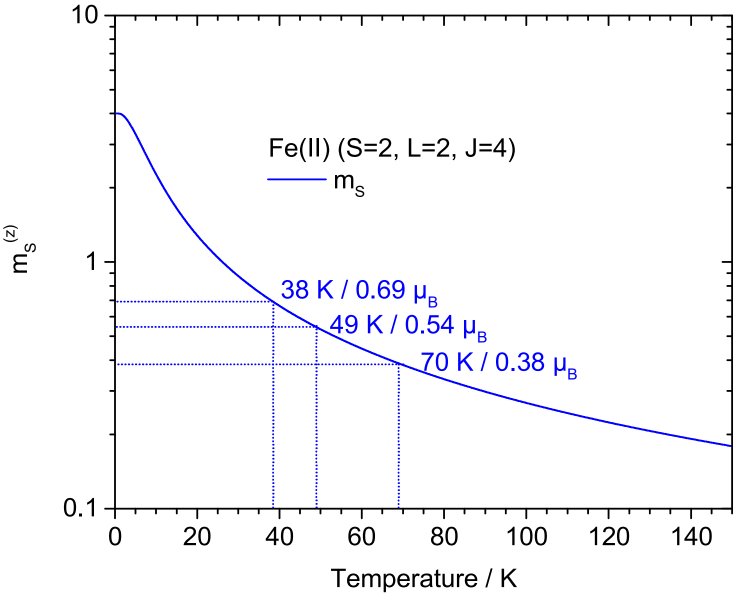

Figure S7: Simulated magnetizations $m_S^{(z)}$ of the Fe^{2+} ion in the ground state, as Brillouin function of the ion temperature at a magnetic field of B = 5 T. The experimentally determined but uncorrected spin magnetizations ($m_S^{(z)}$) are projected onto the Brillouin function to identify the ion temperature.

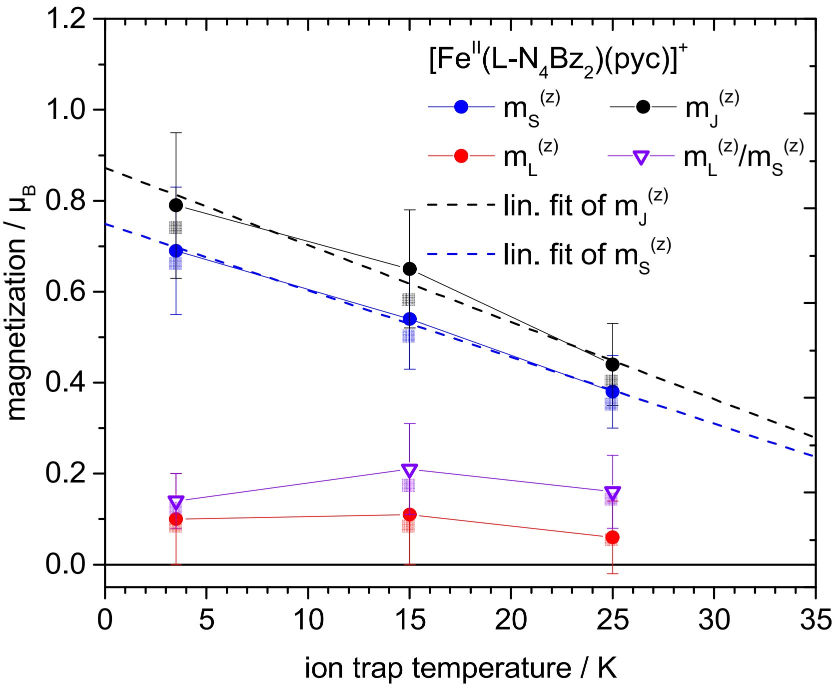

Figure S8: Uncorrected Spin ($m_S^{(z)}$, filled blue circles), orbital ($m_L^{(z)}$, filled red squares), total ($m_{tot}^{(z)}$, filled black triangles) magnetizations and the $m_L^{(z)}$ to $m_S^{(z)}$ ratio (open purple triangles) on the Fe^{2+} ions in complex **1** ($[Fe^{II}(L\text{-}N_4Bz_2)(pyc)]^+$) obtained with tight integration limits. The dashed line is a linear fit of $m_J^{(z)}$ and $m_S^{(z)}$ respectively. The shaded data represent the magnetizations obtained by integration of the entire measured range.

Slope of the linear fits:

$$\frac{d\, m_J^{(z)}}{d\, T} = -0.017 \pm 0.003$$

Temperature range: 49 – 59 K (cf. Fig. S9).

$$\frac{d\, m_S^{(z)}}{d\, T} = -0.015 \pm 0.001$$

Temperature range: 40 – 43 K (cf. Fig. S10).

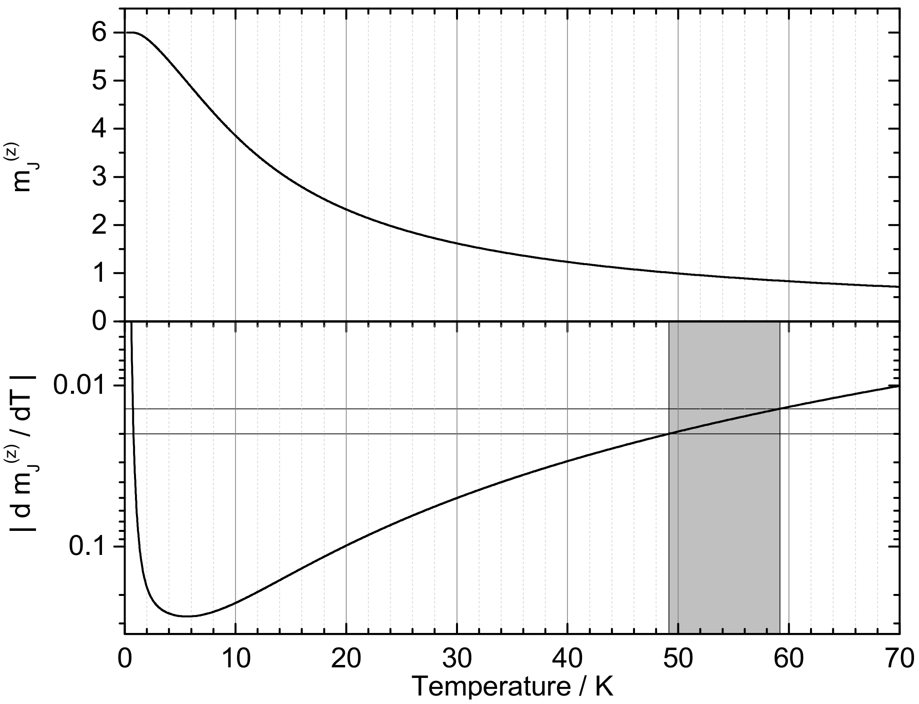

Figure S9: Top: Simulated total magnetization of the Fe^{2+} ion in the ground state as a Brillouin function of the temperature. Bottom: Derivative of $m_J^{(z)}$ with respect to the Temperature.

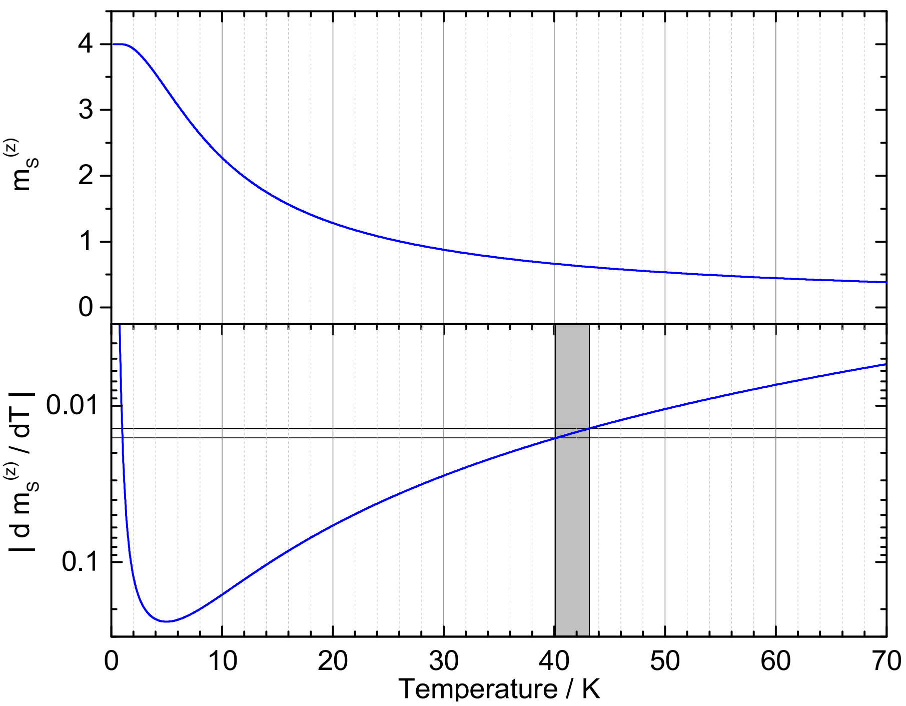

Figure S10: Top: Simulated spin magnetization of the Fe^{2+} ion in the ground state as a Brillouin function of the temperature. Bottom: Derivative of $m_s^{(z)}$ with respect to the Temperature.

Table S6: Atom coordinates of the DFT geometry optimized (**B3LYP*/cc-pVDZ**) complex ion **2**$^{2+}$ in the **HS/HS** configuration (**nonet**).

atom	x	y	z
Fe	10.2731	2.85071	7.77041
N	8.27606	2.01868	8.70322
N	8.88868	4.56394	7.64468
N	11.7038	4.72224	7.66325
N	10.3157	3.59225	9.84705
N	10.2638	2.18797	5.67485
N	11.1761	0.50452	4.34483
C	7.16707	2.93489	8.23423
H	6.84807	2.56648	7.2293
H	6.27528	2.86278	8.90813
C	7.61218	4.3945	8.08438
C	6.77157	5.49824	8.35182
H	5.7338	5.34164	8.70101
C	7.28979	6.80214	8.17707
H	6.65532	7.68582	8.37819
C	8.63662	6.9672	7.77975
H	9.07854	7.97576	7.67514
C	9.41435	5.81405	7.53116
C	10.8828	5.85785	7.09229
H	10.9151	5.75037	5.98109
H	11.3399	6.84951	7.34119
C	12.1609	4.99617	9.07905
H	13.043	4.33699	9.26599
H	12.5129	6.05374	9.18993
C	11.0948	4.67051	10.1321
C	10.9333	5.40113	11.3306
H	11.5805	6.27107	11.549
C	9.92183	5.00303	12.235
H	9.77299	5.5539	13.1828
C	9.07808	3.91878	11.9008
H	8.2536	3.61299	12.5717
C	9.30017	3.24012	10.6816
C	8.45711	2.05157	10.2052
H	8.99366	1.11268	10.4844
H	7.46761	2.03374	10.7296
C	7.96826	0.61092	8.27475
H	8.80919	-0.05157	8.57925
H	7.87094	0.58233	7.16604
H	7.01821	0.23435	8.73483
C	12.9051	4.49233	6.78962
H	12.5614	4.24636	5.76001
H	13.4845	3.63028	7.19038
H	13.5699	5.39368	6.75042
C	11.0503	1.08049	5.57275
C	9.80491	2.37282	4.35148
C	8.94785	3.35553	3.79207
H	8.50914	4.1541	4.4207
C	8.6704	3.2778	2.41119
H	8.00458	4.02934	1.94629
C	9.22872	2.24631	1.59648
H	8.98335	2.22069	0.51788

C	10.0816	1.26189	2.13828
H	10.5083	0.46126	1.50409
C	10.3712	1.32768	3.52575
N	12.5107	-0.57939	6.63295
N	11.5984	1.10408	7.96294
C	11.7243	0.52809	6.73503
C	12.9696	-0.76424	7.95633
C	13.8267	-1.74695	8.51577
H	14.2654	-2.54554	7.88715
C	14.1041	-1.66922	9.89664
H	14.7699	-2.42076	10.3616
C	13.5458	-0.63771	10.7113
H	13.7911	-0.61208	11.7899
C	12.693	0.34672	10.1695
H	12.2662	1.14736	10.8037
C	12.4033	0.28092	8.78205
Fe	12.5014	-1.24212	4.53739
N	14.4985	-0.41005	3.60463
N	13.8859	-2.95533	4.66312
N	11.0708	-3.11367	4.64447
N	12.4589	-1.98363	2.46073
C	15.6075	-1.32624	4.07365
H	15.9264	-0.95785	5.0786
H	16.4993	-1.2541	3.39979
C	15.1624	-2.78586	4.22346
C	16.003	-3.88958	3.95603
H	17.0408	-3.73297	3.60687
C	15.4848	-5.1935	4.13074
H	16.1193	-6.07716	3.92962
C	14.138	-5.35858	4.52802
H	13.6961	-6.36715	4.63259
C	13.3602	-4.20545	4.7766
C	11.8918	-4.24929	5.21543
H	11.8594	-4.14183	6.32663
H	11.4346	-5.24095	4.96649
C	10.6137	-3.38758	3.22866
H	9.73162	-2.72841	3.04171
H	10.2617	-4.44515	3.11775
C	11.6798	-3.06189	2.17564
C	11.8414	-3.79249	0.97712
H	11.1942	-4.66243	0.75871
C	12.8528	-3.39436	0.07272
H	13.0017	-3.94521	-0.87505
C	13.6966	-2.31011	0.40701
H	14.5211	-2.0043	-0.26389
C	13.4744	-1.63147	1.62624
C	14.3175	-0.44292	2.10263
H	13.781	0.49596	1.82346
H	15.307	-0.42509	1.57826
C	14.8063	0.99771	4.03312
H	13.9653	1.66019	3.7286
H	14.9035	1.02629	5.14183
H	15.7563	1.37431	3.57308
C	9.86941	-2.8838	5.51808
H	10.2131	-2.63783	6.5477
H	9.29005	-2.02175	5.11732
H	9.20461	-3.78516	5.55725

Table S7: Atom coordinates of the DFT geometry optimized (**B3LYP*/cc-pVDZ**) complex ion **2**$^{2+}$ in the **LS/HS** configuration (**quintet**).

atom	x	y	z
Fe	3.2465	2.25939	19.6966
Fe	5.38955	5.95613	16.0929
N	1.49987	1.62445	18.5987
N	1.99671	2.29002	21.1887
N	4.71324	2.40852	21.2729
N	3.41666	0.35283	20.0507
N	3.11398	4.31686	19.2668
N	4.58578	2.29812	18.0703
N	5.51552	3.79106	16.5353
N	3.9751	5.91066	17.7951
N	3.85341	6.22234	14.3225
N	5.41805	8.12618	15.6965
N	7.48212	6.65054	16.9351
N	6.67214	6.05149	14.2996
C	0.31125	1.9547	19.4888
H	-0.54993	1.27008	19.2862
H	-0.01659	2.98747	19.2188
C	0.69064	1.96311	20.9668
C	-0.19766	1.74023	22.0402
H	-1.25398	1.47621	21.8469
C	0.29262	1.8569	23.3624
H	-0.38071	1.6819	24.2223
C	1.65116	2.18798	23.5788
H	2.05785	2.27901	24.6032
C	2.4833	2.3979	22.4588
C	3.94345	2.83798	22.5128
H	3.95761	3.95443	22.5301
H	4.44791	2.4853	23.4467
C	5.28613	1.00884	21.4365
H	5.65454	0.84031	22.4792
H	6.17033	0.94163	20.7579
C	4.29339	-0.06809	21.0077
C	4.28815	-1.40293	21.4651
H	5.00503	-1.73193	22.2401
C	3.34723	-2.30519	20.9149
H	3.31778	-3.35597	21.2588
C	2.43692	-1.85342	19.9303
H	1.68869	-2.53889	19.4908
C	2.49889	-0.50522	19.5187
C	1.65064	0.12174	18.4157
H	2.18724	-0.03287	17.4488
H	0.65423	-0.37841	18.3254
C	1.27427	2.25085	17.2489
H	2.14685	2.02513	16.598
H	1.19196	3.35225	17.3755
H	0.34113	1.85939	16.7693
C	5.8517	3.36932	21.0598
H	6.55578	3.36689	21.9306
H	5.43674	4.39149	20.9224
H	6.4006	3.07442	20.139
C	3.9181	4.61575	18.2142

C	2.55663	5.56982	19.6028
C	1.6343	5.94788	20.615
H	1.21719	5.20219	21.3183
C	1.26555	7.30679	20.6988
H	0.54917	7.62873	21.4782
C	1.79742	8.28065	19.7998
H	1.48305	9.33648	19.9024
C	2.71364	7.92343	18.789
H	3.12806	8.68205	18.0974
C	3.09534	6.56052	18.6882
C	4.68616	3.56507	17.5925
C	5.45767	1.57446	17.2283
C	5.8078	0.19808	17.1988
H	5.37602	-0.51849	17.9231
C	6.72408	-0.22973	16.2155
H	7.014	-1.29656	16.1695
C	7.2873	0.68418	15.2737
H	8.00029	0.306	14.5169
C	6.95164	2.05385	15.2886
H	7.38596	2.7577	14.5526
C	6.03284	2.50341	16.2721
C	3.44117	7.67806	14.3377
H	2.6293	7.77154	15.0988
H	3.00707	7.98413	13.3516
C	4.58168	8.61886	14.7424
C	4.75918	9.91204	14.2017
H	4.06414	10.2997	13.4336
C	5.85018	10.6901	14.653
H	6.01532	11.7066	14.2488
C	6.74969	10.1437	15.5971
H	7.63351	10.7157	15.9366
C	6.50358	8.84345	16.0926
C	7.39825	8.14866	17.1261
H	8.41882	8.61028	17.1365
H	6.9527	8.32025	18.1358
C	8.50746	6.25532	15.8949
H	8.75301	5.18177	16.0808
H	9.45534	6.83842	16.0214
C	7.98294	6.38111	14.46
C	8.78244	6.78114	13.366
H	9.84825	7.03731	13.5137
C	8.18711	6.85888	12.0857
H	8.7876	7.16764	11.2094
C	6.80943	6.57569	11.9417
H	6.31037	6.66847	10.959
C	6.07657	6.18197	13.084
C	4.58241	5.83905	13.0536
H	4.0921	6.29476	12.1555
H	4.48788	4.73095	12.951
C	2.6287	5.36322	14.4661
H	2.11639	5.6194	15.4205
H	2.9385	4.2942	14.4992
H	1.91473	5.51007	13.6147
C	7.83492	6.00467	18.2452
H	7.85988	4.90043	18.1086
H	7.05116	6.25685	18.9949
H	8.83042	6.35116	18.6261

Table S8: Relative zero-point vibrational energies (ZVPE) and thermal free energies at 298.15 K of DFT geometry optimized structures of $\mathbf{2}^{2+}$ at S = 0, 1, 2, 3, 4 by variation of exact exchange: B3LYP / B3LYP* (in kJ/mol).

	B3LYP		B3LYP*	
Spin state	ZPVE	Th. Free Energy (298.15 K)	ZPVE	Th. Free Energy (298.15 K)
S = 0 (singlet)	+91.6	+113.9	+42.1	+63.2
S = 1 (triplet)	+101.9	+112.9	+61.5	+72.7
S = 2 (quintet)	+43.1	+52.0	+18.0	+25.4
S = 3 (septet)	+55.2	+57.3	+39.4	+39.9
S = 4 (nonet)	0	0	0	0

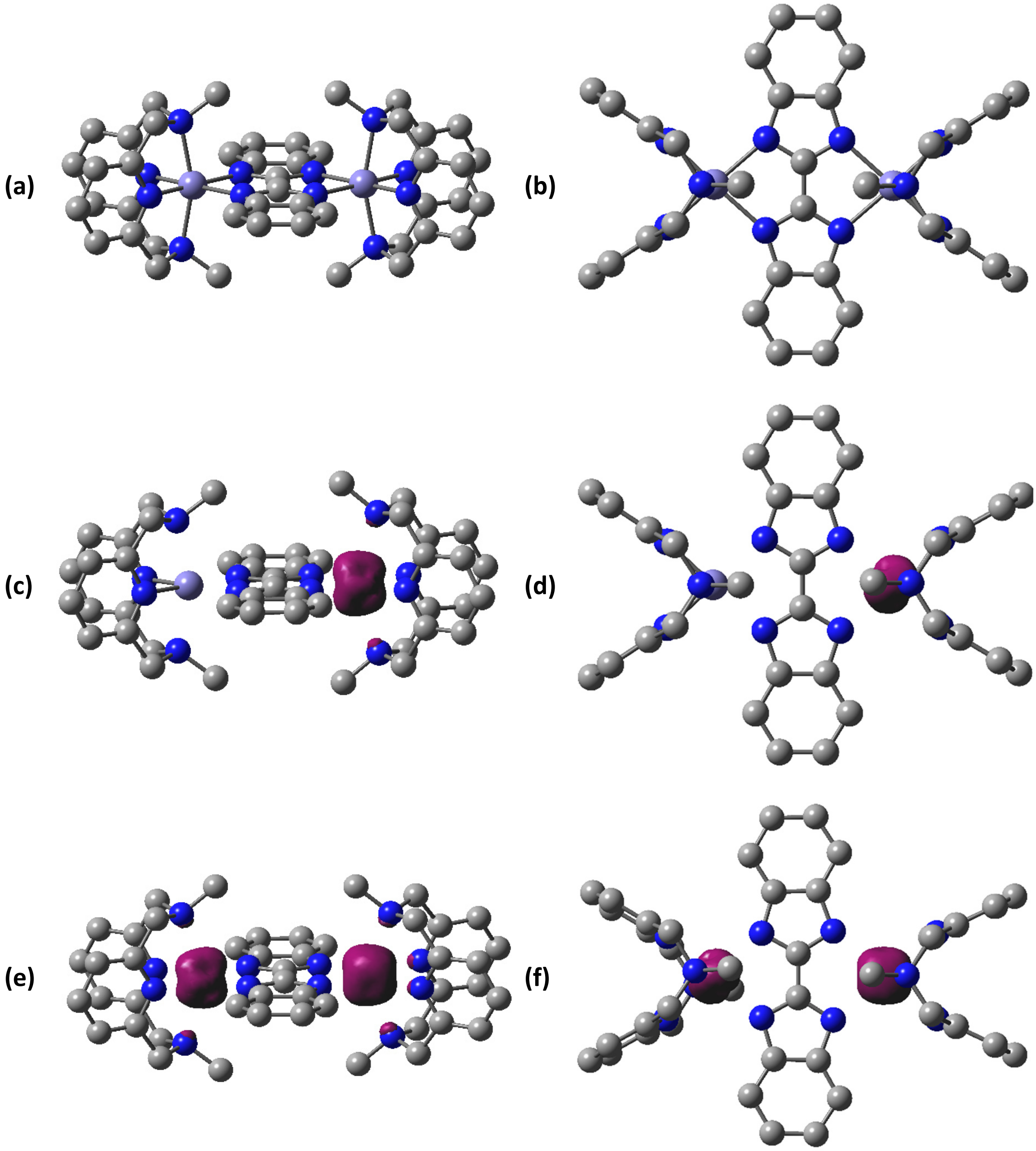

Figure S11: DFT/B3LYP* geometry optimized structures of **2^{2+}** (a) singlet sideview (b) singlet topview (c) triplet sideview (d) triplet topview (e) septet sideview (f) septet topview (C: gray, N: blue, Fe: steel blue). The purple isosurfaces represent the electron spin density. All hydrogen atoms are omitted for clarity.

5 Structural Characterization of (Methylated) Thymine/Uracil-Tetracyanoplatinate(II)-Aggregates by Two Color Enhanced Infrared Multiple Photon Dissociation (IRMPD) Spectroscopy

Joachim M. Hewer, Yevgeniy Nosenko, Michael Lembach, Christoph Riehn and Gereon Niedner-Schatteburg

Fachbereich Chemie and Forschungszentrum OPTIMAS, Kaiserslautern, Germany

5.1 Preamble

The following chapter is prepared as a manuscript for publication. I conducted the InfraRed Multiple Photon Dissociation (IRMPD) experiments, data evaluation and the quantum chemical calculations. I received experimental support by Michael Lembach. Yevgeniy Nosenko and Gereon Niedner-Schatteburg helped to interpret the data. I wrote and revised this manuscript with the help of Christoph Riehn.

5.2 Abstract

We present IR spectroscopic investigations of isolated gas phase aggregates of tetracyanoplatinate(II) dianions and thymine or uracil nucleobases and their methyl-substituted derivatives. These aggregates are regarded as model systems for the exploration of photophysical processes associated with photodynamic therapy (PDT). The two-color infrared multiple photon dissociation (IRMPD) technique reveals dark bands by overcoming intramolecular vibrational redistribution (IVR) bottlenecks. Associated density functional theory (DFT) calculations provide several stable isomeric structures, which we identify by comparing their linear absorption spectra with the recorded two-color IRMPD spectra. Aggregates with unsubstituted nucleobases exhibit strong (N1H) hydrogen bonds between the cyanide ligands of $Pt(CN)_4^{2-}$ and the secondary amino groups of the nucleobases. Further CH – NC interactions stabilize the geometrically planar aggregates. The methyl substituted species bind to the tetracyanoplatinate(II) solely mediated by CH – NC interactions, forming planar clusters as well.

5.3 Introduction

Transition metal complexes of e.g. platinum and rhenium still play an important role in recent pharmaceutical research, as they are employed in the treatment of various types of tumors.[1, 2] *Cis*-diamminedichloridoplatinum(II), known as cisplatin, is an example for an extensively used drug in the treatment of testicular, ovarian, bladder and cervical cancer.[3-7] Cisplatin targets the cellular DNA at the guanine nucleobases and forms cross-links between two adjacent strands of DNA.[3] The photodynamic therapy (PDT) and photoactivated chemotherapy (PACT) represent promising developments to avoid damage to healthy cells and tissue.[1, 8, 9] PDT involves administration of a photosensitizing chemical substance followed by its activation by light irradiation.[9, 10] There is a particular focus on platinum II and IV complexes in the current research for new PDT pharmaceuticals to control the metal reactivity by photoexcitation in clinical situations.[3, 11, 12]

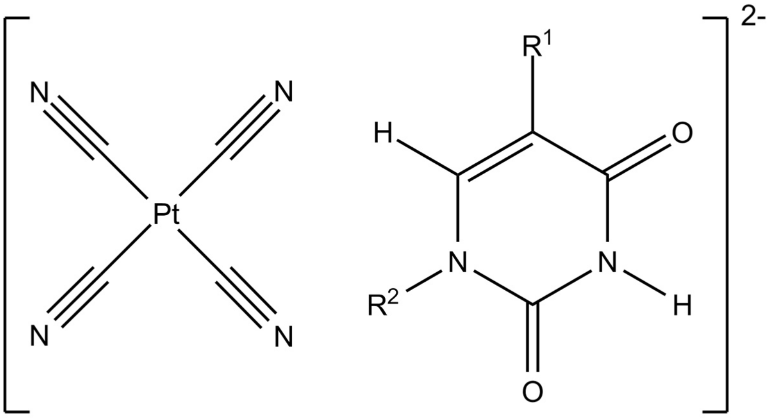

Figure 1: General depiction of the nucleobase – tetracyanoplatinate(II) Aggregates.

Tetracyanoplatinate(II) – nucleobase adducts are established model systems for the exploration of fundamental photophysical and photochemical processes in PDT with platinum(II) pharmaceuticals.[13-16] Investigations on isolated complexes help to improve the understanding of the platinate(II) – nucleobase binding.[16] A. SEN *et al.* have studied the UV photophysics of isolated $[Pt(CN)_4]^{2-}$ – nucleobase (nucleobase = uracil, thymine, cytosine, adenine) complexes in detail.[15] Structural information is paramount to acquire fundamental insight into their reactivity. In this work, we report the first IR spectroscopic investigations on the gas-phase structures of nucleobase – $[Pt(CN)_4]^{2-}$ complexes. We chose the DNA nucleobase thymine and the RNA nucleobase uracil as well as their respective methylated forms (cf. Fig 1, Tab.1). The substitution of the proton in position 1 by a methyl group is the first step to mimic nucleotides/nucleosides being the components of the single-stranded RNA and the double-stranded DNA double helices in the cell.

Table 1: Key to the (substituted) nucleobases depending on substituents R^1 and R^2 (refer to Fig. 1).

R^1	R^2	Nucleobase	Abbreviation
$-CH_3$	-H	Thymine	T
$-CH_3$	$-CH_3$	1-Methylthymine	1-mT
$-CH_3$	$-C_5H_9O_3$	Deoxythymidine	dT
-H	-H	Uracil	U
-H	$-CH_3$	1-Methyluracil	1-mU
-H	$-C_5H_9O_4$	Uridine	rU

5.4 Experimental and computational methods

A detailed description of the experimental setup has been published previously.[17] The dianionic aggregates were generated via electrospray ionization (ESI) from an aqueous solution of the respective (substituted) nucleobases or nucleosides and $K_2Pt(CN)_4$ with a stoichiometric ratio of 1:1 at a concentration of approximately 1 mM. The solutions were infused continuously into the ESI chamber with a syringe pump at a flow rate of 2 µL/min. We used nitrogen as nebulizer gas at a pressure of 7 to 8 psi and as a drying gas with a temperature of 150 °C and a flow rate of 1 to 2 L/min. The electrospray needle was held at 4.5 kV. The IRMPD experiments were performed using a modified Paul-type ion trap mass spectrometer (AmaZon SL, *Bruker Daltonics*). The ion source was operated in the negative electrospray ionization mode. The scan speed was 13000 m/z per second with a resolution of 0.3 FWHM, the scan range was at least from 50 to 600 m/z. The Instrument was controlled by *BrukerTrapControl 7.0* software, data analysis was done with *BrukerDataAnalysis 4.0* software.

A KTP/KTA (KTP = potassium titanyl phosphate; KTA = potassium titanyl arsenate) optical parametric oscillator/amplifier (OPO/OPA, *LaserVision*) system pumped by a pulsed 10 Hz injection seeded Nd:YAG laser (PL8000, *Continuum*) was used as a source of tunable IR radiation ($\delta\tilde{\nu}$ = 0.9 cm^{-1}, δt = 7 – 10 ns) for recording the vibrational spectra. The idler wave (≤ 10 mJ/per pulse) was used to record the spectra in the range of 2500 – 3700 cm^{-1}. The difference frequency (DF) generated radiation in a $AgGaSe_2$ crystal (≤ 2 mJ/per pulse) was applied in the range of 1150 – 2200 cm^{-1}. The idler radiation was focused by a CaF lens with a focal length of 50 cm. The DF beam was focused by a parabolic mirror with a focal length of 15 cm. The two-color (2c-) IRMPD experiments were facilitated using a second IR OPO/A system set to a selected vibrational resonance frequency. The respective idler radiation was focused by a CaF lens with a focal length of 75 cm. The frequency fixed laser pulses were delayed by 100 ns with respect to the first scanning IR laser. The IR spectra were measured as ion chromatograms while continuously scanning the IR laser frequency. An IRMPD spectrum is achieved by plotting the total IRMPD yield as a function of the IR laser frequency. The total IRMPD yield ($Y(v)$) is defined by:

$$Y(v) = \frac{\sum_i I_i^{fr}}{\sum_i I_i^{fr} + \sum_i I_i^{pr}}$$

where I_i^{fr} and I_i^{fr} are the respective ion intensities of fragment and parent ions. The IR frequency was calibrated using a 821B-NIR *Bristol Instruments* wave meter. The IR beam was detected by a power meter after passing through the ion trap. Due to the intrinsically nonlinear power dependencies of IRMPD yields, the spectra were not normalized.

The minimum energy structures, binding energies and linear IR absorption spectra were calculated at the DFT/B3LYP[18-20] level of theory, using the aug-cc-pVTZ [21, 22](C, H, N, O) basis set and the Stuttgart RSC 1997[23, 24] (Pt) effective core potential as implemented in the *Gaussian 09* program package.[25] All geometry optimized isomers represent true energy minima as they were checked for the absence of imaginary vibrational frequencies. The harmonic vibrational frequencies of the stretching modes (> 2500 cm^{-1}) were scaled by a factor of 0.958. All other frequencies (< 2500 cm^{-1}) were scaled by a factor of 0.986. The line spectra were deconvoluted by *GaussSum* using a Lorentzian function with FWHM = 10 cm^{-1}.[26] The counterpoise method was used to calculate the basis set superposition error (BSSE).[27]

The visualization of weak interactions such as hydrogen bonds or van der Waals-interactions was realized using the *multiwfn* and *VMD* software based on the non-covalent interaction (*NCI*) technique.[28-31] Details of this method and its application have already been published elsewhere.[32, 33] The method is based on the analysis of the electron densities ρ and their reduced gradients $s(\rho)$. When weak interactions are present, the electron density ρ is low and its reduced gradient $s(\rho)$ is close to zero. The typical weak interaction regions can be identified as troughs in plots of the reduced gradient $s(\rho)$ in dependence of the sign of the second eigenvalue λ_2 of the Hessian matrix. The nature of the weak interaction can be evaluated by sign and value of λ_2. Positive values correspond to nonbonding or repulsive interactions and negative values correspond to bonding, favorable or attractive interactions, respectively. Visualization of the interactions is realized by plotting isosurfaces of the reduced gradient, with sign and value of λ_2 related to a RGB coloring scheme. Red isosurfaces correspond to a positive sign of λ_2 and represent unfavorable interactions e.g. steric repulsion. Blue isosurfaces correspond to a negative sign of λ_2 and represent strong favorable interactions, e.g. hydrogen bonds. Green isosurfaces correspond to van der Waals interactions and λ_2 very close to zero.

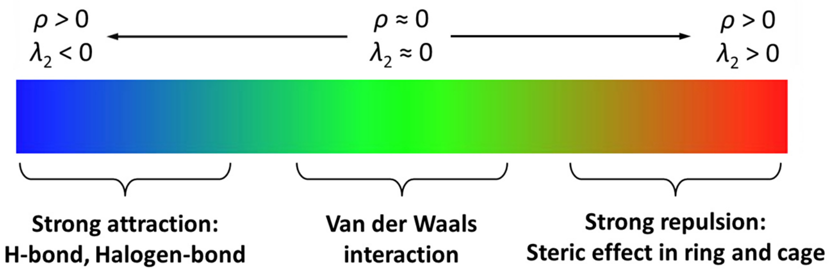

Figure 2: RGB coloring scheme for the visualization of type and strength of non-covalent interactions in molecules and clusters.[34]

5.5 Results and Discussion

The formation of the self-assembled (methylated) nucleobase – tetracyanoplatinate(II) aggregates was deduced from the recording of anion signals at the respective masses in the mass spectra (Figs. S1 – S8, ESI). The dianionic character of the investigated species is demonstrated by the 0.5 m/z spacings between the isotope peaks in the mass spectra. The fragment ions of $[T \cdot Pt(CN)_4]^{2-}$ and $[U \cdot Pt(CN)_4]^{2-}$ upon resonant infrared irradiation are in accordance with the fragment ions observed in CID-experiments by A. Sen *et al.*.[16] At higher laser energies we observed an additional fragment ion: $[Pt(CN)_3]^-$ (Tab. S1, ESI). Substitution of the proton in position 1 with a methyl group [1-mT, 1-mU] prevents a proton transfer from the nucleobase to the tetracyanoplatinate(II) (Tab. S1, ESI).

The structure of the self-assembled aggregates is elucidated by comparison of experimental IRMPD spectra with calculated harmonic vibration spectra of geometry optimized minimum structures. The presented minimum structures are based on the nucleobases in the lactam form. Enolic structures were also considered in the calculations but resulted in significantly increased relative energies (+ > 50 kJ/mol), hence they are not discussed here. IRMPD spectra often depend non-linearly on laser power flux.[17] Due to incoherent multiple photon absorption, bands in IRMPD spectra can be broadened, shifted or deformed.[35, 36] The low density of states in small systems can hinder the internal vibrational redistribution, and, together with vibrational anharmonicities, result in a bottleneck for the multiple photon absorption and hence for dissociation.[17, 37] Large molecules and clusters reveal large heat capacities and may require more laser power for weaker bands to appear in IRMPD spectra.[38] Several multi-excitation schemes have been suggested to overcome these limitations.[39-42] We have already presented several examples for a two-color (2c)-excitation scheme revealing additional bands, not visible in the one-color (1c) IRMPD spectrum.[17, 43] In this study we use this 2c-IRMPD technique in the frequency range of 1150 – 2200 cm^{-1} to reveal or augment weak bands. For fragmentation channels, calculated binding energies and bond lengths of the following discussed structures see Tabs. S1-S3.

5.5.1 Thymine – Tetracyanoplatinate(II): $[T \cdot Pt(CN)_4]^{2-}$

Computed binding isomers

By geometry optimization calculations we obtained three minimum structures for the thymine – $Pt(CN)_4^{2-}$ complex (cf. Fig. 3). In the most stable isomer **T_A,** the tetracyanoplatinate(II) is bound to the thymine via a hydrogen bond between the N1H group and a nitrogen atom of a cyanide ligand. The structure is additionally stabilized by several CH – cyanide ligand interactions resulting in a planar structure. In contrast, in the second minimum structure **T_B** (+12 kJ/mol), the thymine and $Pt(CN)_4^{2-}$ planes are orthogonal. The connection is also mediated by a hydrogen bond of the N1H group to a cyanide nitrogen atom and stabilized further by an additional interaction of the C6H proton with the same cyanide nitrogen atom. Interactions to further CN groups are missing due to the perpendicular planes of thymine and tetracyanoplatinate(II). The energetically highest lying isomer **T_C** (+79 kJ/mol) has only one almost linear (β(N3-H-N) = 178.7 °) hydrogen bond between the N3H group and a cyanide nitrogen ligand. The C=O groups have a shielding effect (electrostatic and steric), preventing further CH – NC interactions. The pyrimidinic and $Pt(CN)_4^{2-}$ planes are orthogonal. The relative energies of the minimum structures and NCI plots in Fig. 3 show, that the main part of the binding between thymine and $Pt(CN)_4^{2-}$ is mediated by the N1H – NC hydrogen bonds (blue isosurface) and further stabilization by the CH – NC interactions (green isosurface). The ring strain of the hetero-aromatic cycle is represented as red isosurface in the NCI plot.

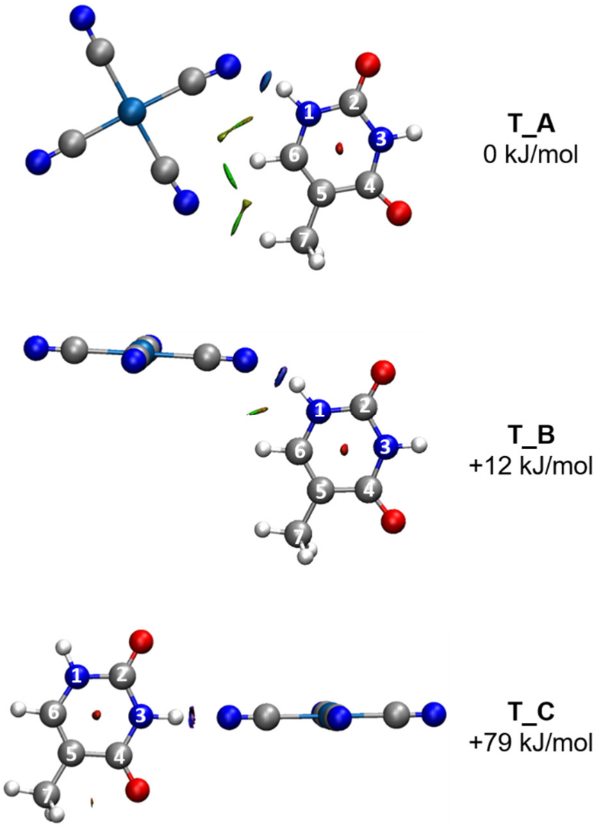

Figure 3: DFT/B3LYP calculated minimum structures and NCI plots of thymine – $Pt(CN)_4^{2-}$ aggregates.

Comparison of experimental IRMPD spectra and calculated harmonic vibration frequencies

The experimental one-color IRMPD spectrum of $[T \cdot Pt(CN)_4]^{2-}$ exhibits one sharp band at 3457 cm^{-1} and at least three bands in the region of 2600 to 3200 cm^{-1} (cf. Fig. 4). In the fingerprint region between 1150 and 2200 cm^{-1}, we observe three bands at 1673 cm^{-1}, 1725 cm^{-1} and 2111 cm^{-1}. Using the 2c-IRMPD technique (IR_{fix} = 3457 cm^{-1}, cf. section 2) additional dark bands at 1201, 1488 and 1644 cm^{-1} occur, as well as enhanced one-color IRMPD bands. The sharp band at 3457 cm^{-1} can be assigned to a free NH stretching vibration, the broad bands between 2700 – 3200 cm^{-1} originate from the CH stretching vibrations and a hydrogen bonded NH vibration. The sharp band at 2111 cm^{-1} can be assigned to the cyanide C≡N stretching modes, the intense bands at 1673 and 1725 cm^{-1} to the two C=O stretching modes of thymine.

The calculated harmonic spectrum of **T_A** is in very good agreement with the experimental 1c/2c-IRMPD spectrum (cf. Fig. 4). The recorded band at 3457 cm^{-1} is unambiguously assigned to the free N3H stretching mode. The C6H stretching vibration mode of **T_A** is represented by the absorption at 3056 cm^{-1} in the experimental spectrum. It is broadened due to a significant interaction of the C6H proton with the cyanide ligands. The broadened bands around 2873 and 2937 cm^{-1} fit quite well to the calculated C7H stretching and hydrogen bonded N1H stretching modes. The C≡N stretching modes at 2111 cm^{-1} are not sensitive to the binding motif, as the perturbation by CH or NH protons in close proximity is very small (approx. 5 cm^{-1}) and not resolved in the experiment. The C=O stretching vibrations are as well not very sensitive to the structure since there is no considerable interaction of these functional groups to $Pt(CN)_4^{2-}$. The bands at 1673 and 1725 cm^{-1} are referred to the C4=O and C2=O stretching

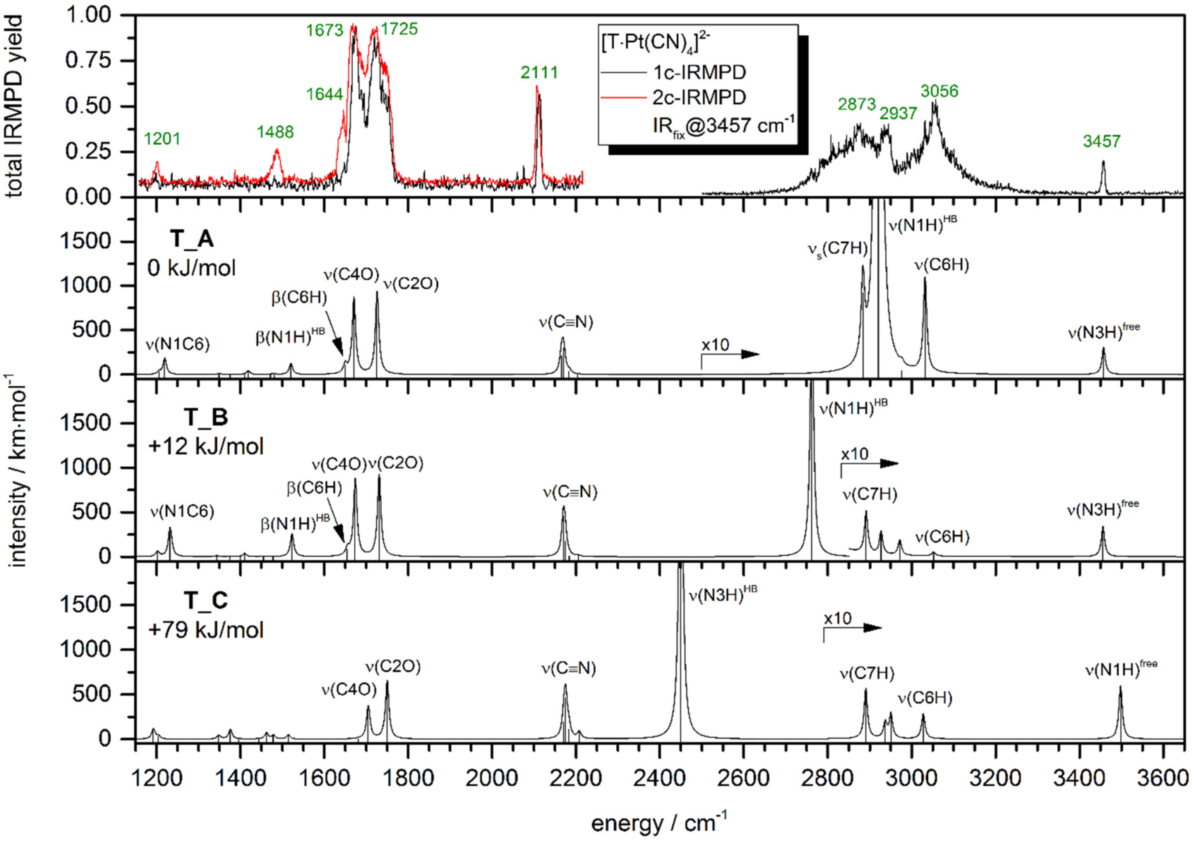

Figure 4: Experimental one and two color IRMPD spectrum of the thymine – $Pt(CN)_4^{2-}$ aggregate (probe frequency: 3457 cm^{-1}) in comparison to the calculated harmonic absorption spectra of the minimum structures (cf. Fig. 3). Note, that above 2500 cm^{-1} (**T_A**), 2850 cm^{-1} (**T_B**) or 2800 cm^{-1} (**T_C**) the intensities of the calculated spectra are multiplied by a factor of 10.

modes, the band at 1644 cm^{-1} can be assigned to the C6H bending mode. The band 1488 cm^{-1} represents the hydrogen bound N1H bending vibration. The band at 1201 cm^{-1} can be assigned to a mode, best described as N1 – C6 stretching vibration which is moderately intense in the calculated harmonic spectra. Overall, the spectral signature of the **T_A** minimum structure fits best to the IRMPD spectrum, especially in the CH-stretching region which is also most sensitive to the binding motif. The spectroscopic data presented here, cannot exclude presence of **T_B**, the calculated relative energies render the population of **T_B** and **T_C** unlikely (cf. Tab.1).

Table 1: Population of the minimum structures **T_A**, **T_B**, and **T_C** calculated by the Maxwell-Boltzmann-distribution at 300, 400, and 500 K.

Temperature / K	T_A 0 kJ/mol	T_B +12 kJ/mol	T_C +79 kJ/mol
300	0.9919	0.0081	~10^{-14}
400	0.9736	0.0264	~10^{-11}
500	0.9472	0.0528	~10^{-9}

5.5.2 Methylthymine – Tetracyanoplatinate(II): $[1\text{-mT} \cdot Pt(CN)_4]^{2-}$

Computed binding isomers

For 1-methylthymine, we found four minimum structures (cf. Fig. 5). The most stable isomer **1-mT_A** exhibits several CH – NC interactions mediating the binding between the nucleobase and the tetracyanoplatinate(II) anion. A methyl proton of C8H interacts with two adjacent cyanides. There are interactions between the C6H proton and a proton of the C7H methyl group and a cyanide ligand, respectively. In total, the structure **1-mT_A** provides four CH – NC interactions, leading to a planar geometry. The second most stable is planar as well. There are CH – NC interactions between a C8H methyl proton and a cyanide ligand, between the C6H proton and the same cyanide ligand and between a C7H methyl proton and an adjacent cyanide ligand. **1-mT_B** has in total only three CH – NC interactions, leading to a destabilization of +5 kJ/mol compared to **1-mT_A**. In the third most stable isomer **1-mT_C** (+9 kJ/mol), the bond between 1-mT and $Pt(CN)_4^{2-}$ is also mediated by CH – NC interactions. The plane of the heteroaromatic cycle and $Pt(CN)_4^{2-}$ are perpendicular. Two protons of the C8 methyl group each interact with an adjacent cyanide ligand. The C6H proton is in the center and interacts with both vicinal cyanide ligands equally. The least stable isomer **1-mT_D** (+55 kJ/mol) is in analogy to **T_C** stabilized by one single linear hydrogen bond between the N3H proton and a cyanide ligand. Both C=O groups have a shielding effect, preventing further CH – NC interactions. The planes of 1-mT and $Pt(CN)_4^{2-}$ are perpendicular as well.

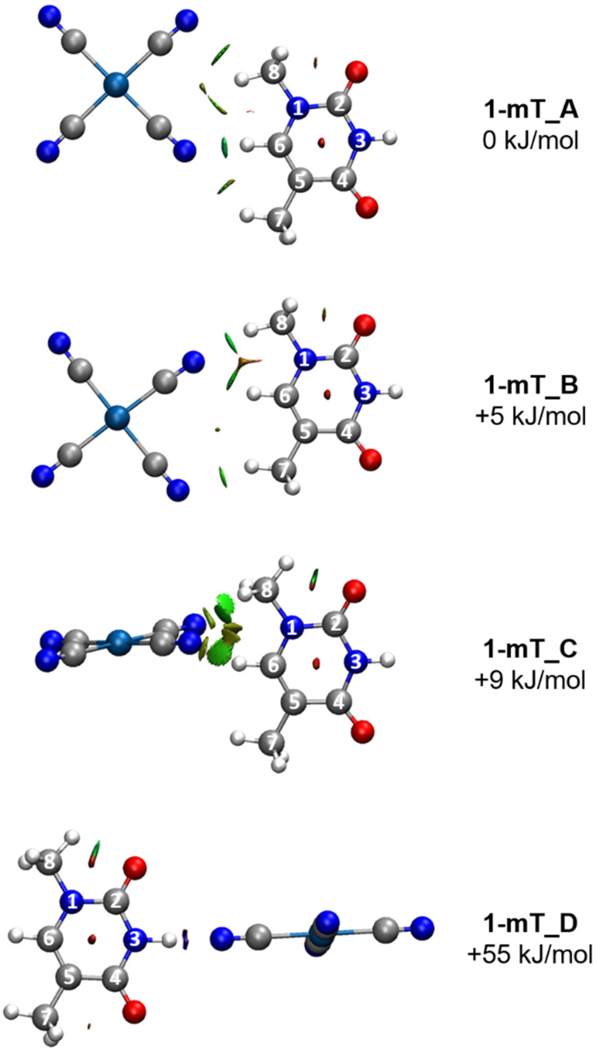

Figure 5: DFT/B3LYP calculated minimum structures and NCI plots of 1-methylthymine – $Pt(CN)_4^{2-}$ aggregates.

Comparison of experimental IRMPD spectra and calculated harmonic vibration frequencies

The experimental one and two color IRMPD spectra and the calculated harmonic absorption spectra of the minimum structures are shown in Fig. 6. The IRMPD spectrum reveals a sharp band at 3457 cm^{-1} and at least three absorptions in the CH stretching region between 2800 and 3200 cm^{-1}. There are three absorptions in the fingerprint region of the one color spectrum at 2107, 1686 and 1703 cm^{-1}, with the two color technique four additional bands at 1642, 1470, 1446 and 1320 cm^{-1} emerge. The sharp band at 3457 cm^{-1} can be assigned to a free NH stretching vibration, the broadened region bands are expected to be CH stretching vibrations. The band at 2107 cm^{-1} is assigned to the C≡N stretching vibrations of the cyanide ligands. The intense absorptions at 1686 and 1703 cm^{-1} are referred to the carbonyl C=O stretching vibrations. The calculated harmonic spectra of **1-mT_A**, **1-mT_B** and **1-mT_C** are very similar, apart from the CH stretching region and the range below 1600 cm^{-1}. In total, **1-mT_A** fits best to the experimental spectrum. The band at 3457 cm^{-1} represents the free N3H stretching

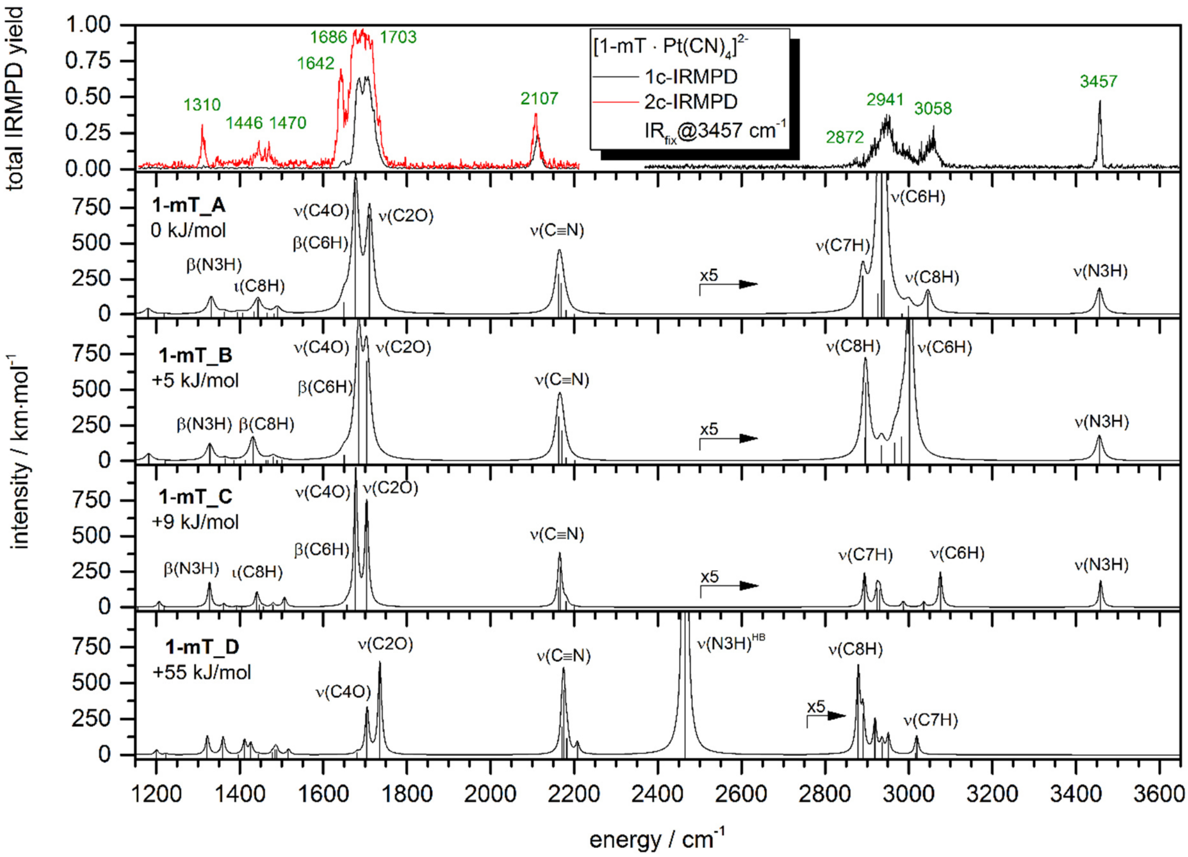

Figure 6: Experimental one and two color IRMPD spectrum of the 1-Methylthymine – $Pt(CN)_4^{2-}$ aggregate (probe frequency: 3457 cm^{-1}) in comparison to the DFT calculated harmonic absorption spectra of the minimum structures (cf. Fig. 5). Note, that above 2500 cm^{-1} (**1-mT_A**, **1-mT_B**, **1-mT_C**), and 2750 cm^{-1} (**1-mT_D**) the intensities of the calculated spectra are multiplied by a factor of 5.

vibration. We assign the band at 3058 cm^{-1} to a C8H methyl stretching vibration, which is broadened due to the interaction of one proton with the cyanide ligand. The absorption at 2941 cm^{-1} matches the C6H stretching vibration and is also broadened due to the oriented binding of the proton to a cyanide. The weak absorption band at 2872 cm^{-1} is less shifted and broadened and can be referred to the C7H methyl stretching vibration forming weaker interactions with the cyanide ligand. The C≡N stretching vibrations are rather insensitive to the structural geometry and do not shift or split significantly in the calculated harmonic absorption spectra but can be assigned to the measured band at 2107 cm^{-1}. We assign the two strong absorption bands at 1686 and 1703 cm^{-1} to the two C=O carbonyl stretching vibrations present in all harmonic absorption spectra, the smaller absorption at 1642 cm^{-1} represents the C6H bending mode which is considerably strong in the calculated spectra of **1-mT_A** and **1-mT_B**. The fingerprint region is dominated by CH bending modes and NH bending modes. The spectral signature of **1-mT_A** fits best to the experimental spectrum regarding the absorption bands at 1310 cm^{-1}, which is assigned to the bending motion of free N3H. The experimental bands at 1446 and 1470 cm^{-1} match the spectrum of **1-mT_A**, regarding frequency difference and relative intensity. However, the differences in the harmonic spectra of **1-mT_A**, **1-mT_B** and **1-mT_C** are small and cannot be excluded by comparison with the experimental IRMPD spectrum only. The difference in the thermal free energies makes a population of **1-mT_C** and **1-mT_D** very unlikely, **1-mT_B** is structurally similar to **1-mT_A** and may contribute by 12 % (cf. Tab. 2).

Table 2: Population of the minimum structures **1-mT_A**, **1-mT_B**, **1-mT_D** and **1-mT_D** calculated by the Maxwell-Boltzmann-distribution at 300, 400, and 500 K.

Temperature / K	**1-mT_A** 0 kJ/mol	**1-mT_B** +5 kJ/mol	**1-mT_C** +9 kJ/mol	**1-mT_D** +55 kJ/mol
300	0.8607	0.1159	0.0233	~10^{-10}
400	0.7757	0.1725	0.0518	~10^{-08}
500	0.7067	0.2122	0.0811	~10^{-06}

5.5.3 Uracil – Tetracyanoplatinate(II): $[U \cdot Pt(CN)_4]^{2-}$

Computed binding isomers

Geometry optimization calculations of uracil – tetracyanoplatinate(II) aggregates resulted in only two minimum structures (cf. Fig. 7). The most stable minimum **U_A** provides a N1H hydrogen bond to a cyanide ligand and two additional CH – NC interactions of the C6H proton with two adjacent cyanides, resulting in a planar overall structure. The binding motif of **U_A** is very similar to **T_A**. Isomer **U_B** is +80 kJ/mol less stable compared to **U_A**. Uracil and $Pt(CN)_4^{2-}$ are connected by a quasi linear N3H hydrogen bond to a cyanide ligand. The electrostatic and steric shielding effects of adjacent carbonyl groups prevent further NH or CH interactions with the tetracyanoplatinate(II). The planes of uracil and $Pt(CN)_4^{2-}$ are perpendicular. The binding motif is in analogy to **T_C** and **1-mT_D**.

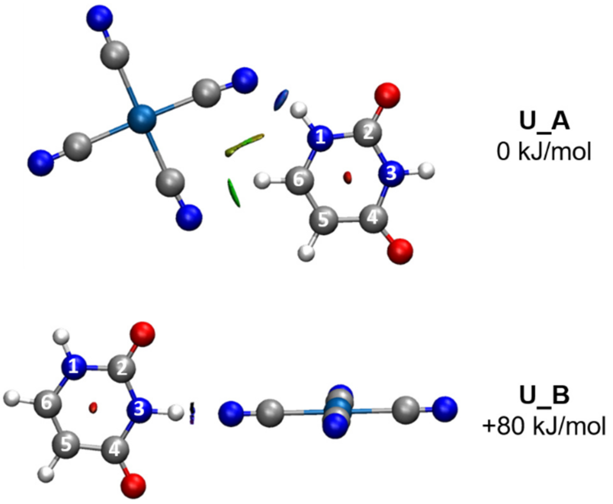

Figure 7: DFT/B3LYP calculated minimum structures and NCI plots of Uracil – $Pt(CN)_4^{2-}$ aggregates.

Comparison of experimental IRMPD spectra and calculated harmonic vibration frequencies

The experimental one and two color IRMPD spectra and the calculated harmonic absorption spectra of the minimum structures of $[U \cdot Pt(CN)_4]^{2+}$ are shown in Fig. 8. The IRMPD spectrum reveals a sharp band at 3457 cm^{-1}. The CH stretching region between 2600 and 3200 cm^{-1} is very broadened, including at least three absorptions at approx. 2812, 2929 and 3061 cm^{-1}. In the fingerprint region we observe three absorptions in the one color spectrum at 2108, 1686 and 1732 cm^{-1}: The second IR laser reveals additional bands at 1616, 1488 and 1214 cm^{-1}.

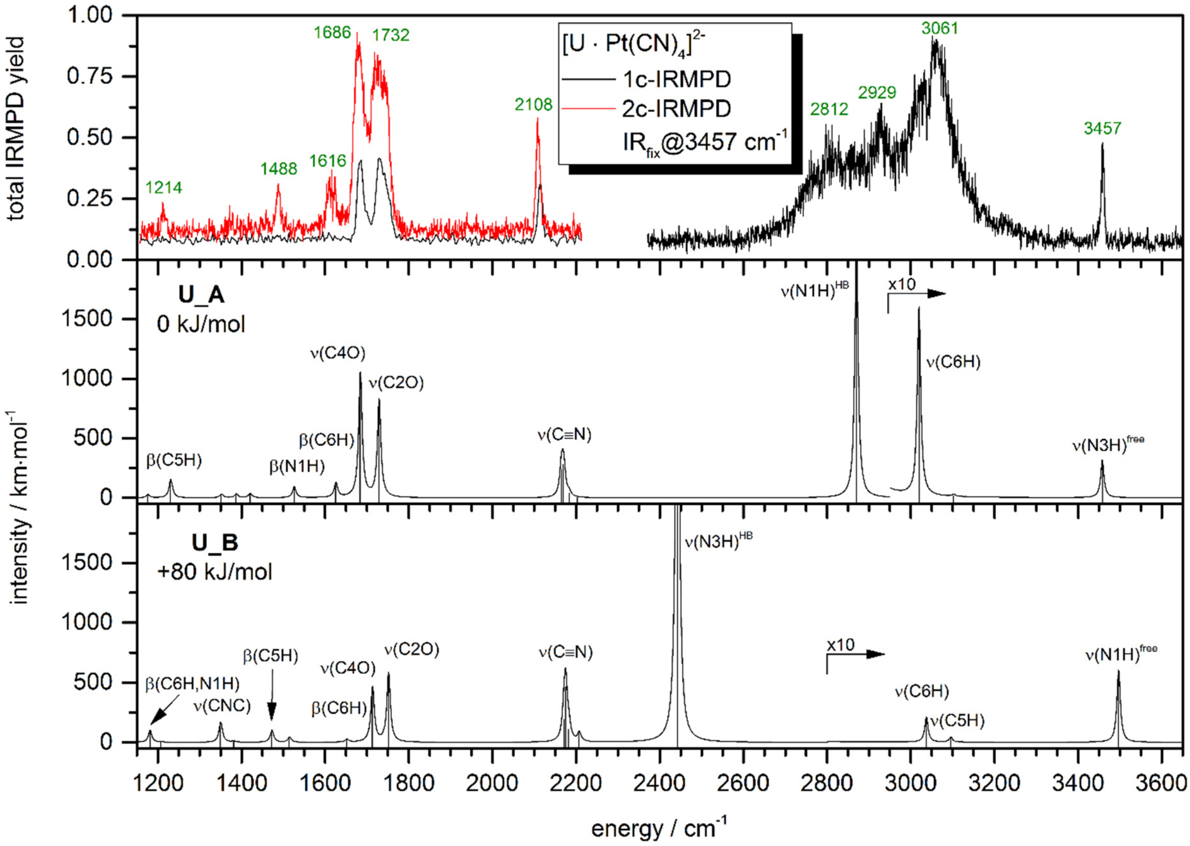

Figure 8: Experimental one and two color IRMPD spectrum of the Uracil – $Pt(CN)_4^{2-}$ aggregate (probe frequency: 3457 cm^{-1}) in comparison to the DFT calculated harmonic absorption spectra of the minimum structures (cf. Fig. 7). Note, that above 2950 cm^{-1} (**U_A**) and 2800 cm^{-1} (**U_B**) the intensities of the calculated spectra are multiplied by a factor of 10.

Comparison of the IRMPD spectrum with the calculated harmonic spectra shows, that the linear absorption spectrum of **U_A** is in very good agreement with the experiment. The sharp band at 3457 cm^{-1} is assigned to a free NH stretching vibration. The broad CH stretching region represents the C5H and C6H stretching vibrations and a hydrogen bound N1H stretching vibration. The band at 2108 cm^{-1} is referred to the C≡N stretching vibrations of the cyanide ligands. The two carbonyl C2=O and C4=O stretching modes can be assigned to the bands at 1686 and 1732 cm^{-1} regarding their splitting and relative intensities. The C6H bending mode is visible at 1616 cm^{-1} in the IRMPD spectrum, the N1H bending mode at 1488 cm^{-1} and the

C5H bending mode at 1214 cm^{-1}. The harmonic spectrum of **U_B** has some similarities with the IRMPD spectrum but the intense hydrogen bound N3H mode is not observed in the IRMPD spectrum, the spectral fingerprint in the region below 1700 cm^{1} does not fit well and the relative energy of +80 kJ/mol makes a population of **U_B** very unlikely (~10^{-16} at 300 K)

5.5.4 1-Methyluracil – Tetracyanoplatinate(II): [1-mU · Pt(CN)$_4$]$^{2-}$

Computed binding isomers

The geometry optimization calculations of 1-methyluracil – tetracyanoplatinate(II) aggregates resulted in four minimum structures (cf. Fig. 9). The most stable isomer **1-mU_A** provides CH – NC interactions between a C7H methyl proton and two vicinal cyanide ligands and the C6H proton is straight bound to a cyanide nitrogen atom. The binding motif is similar to the **1-mT_A** isomer. The second most stable isomer **1-mU_B** (+5 kJ/mol) has a binding motif similar to **1-mT_B**. There is a C7H methyl proton cyanide interaction, the central C6H proton binds to two vicinal cyanides, and the C5H proton interacts with a cyanide nitrogen. **1-mU_A** and **1-mU_B** provide a planar geometry. The binding motif of **1-mU_C** (+57 kJ/mol) is in analogy to **T_C**, **1-mT_D** and **U_B** respectively. There is one linear hydrogen bond between the N3H proton and a cyanide nitrogen, while the pyrimidinic plane and the tetracyanoplatinate(II) are oriented perpendicular. There is an additional minimum structure **1-mU_D** (+57 kJ/mol), where the Pt(CN)$_4^{2-}$ is tied by one NH3 – NC hydrogen bond and a CH – NC interaction between a C7H methyl proton and an adjacent cyanide ligand. The pyrimidinic plane and tetracyanoplatinate(II) are perpendicular.

Comparison of experimental IRMPD spectra and calculated harmonic vibration frequencies

The experimental one and two color IRMPD spectra and the calculated harmonic absorption spectra of the minimum structures of [1-mU · Pt(CN)$_4$]$^{2+}$ are shown in Fig. 10. The IRMPD spectrum reveals a sharp band at 3457 cm^{-1}. The CH stretching bands between 2900 and 3100 cm^{-1} are broadened and scarcely resolved. We can identify at least two absorptions at approx. 2963 and 3051 cm^{-1}. The one color IRMPD in the fingerprint region shows three bands

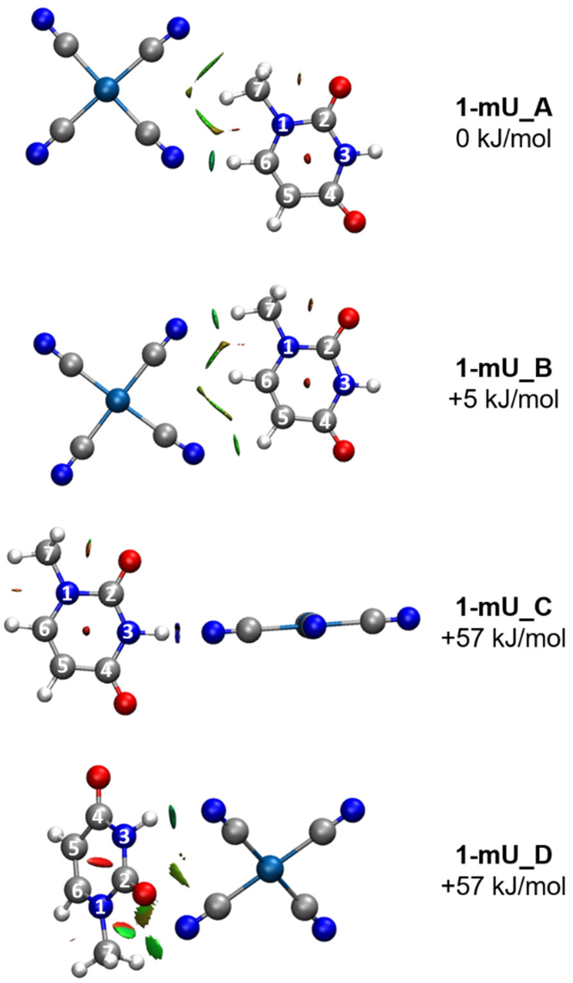

Figure 9: DFT/B3LYP calculated minimum structures and NCI plots of 1-methyluracil – $Pt(CN)_4^{2-}$ aggregates.

at 2111, 1710 and 1686 cm^{-1}, the second laser reveals two additional bands at 1626 and 1316 cm^{-1}. The calculated spectra of **1-mU_A** and **1-mU_B** are very similar, apart from the CH stretching region and the different splitting of the two carbonyl stretching vibrations C4=O and C2=O. The band at 3457 cm^{-1} is assigned to the free N3H stretching mode, present in both, **1-mU_A** and **1-mU_B**. The broadened CH stretching region makes an assignment challenging. However, the broad IRMPD spectrum hints to **1-mU_A**, due to the relatively strong bond of the C6H proton to the cyanide nitrogen, increasing also the absorption intensity, in the calculated spectrum. The band at 2111 cm^{-1} is referred to the C≡N stretching vibrations. Both absorptions at 1710 and 1686 cm^{-1} are assigned to the C2=O and C4=O carbonyl stretching vibrations. The weak absorption at 1626 cm^{-1} represents the C6H bending mode, the weak

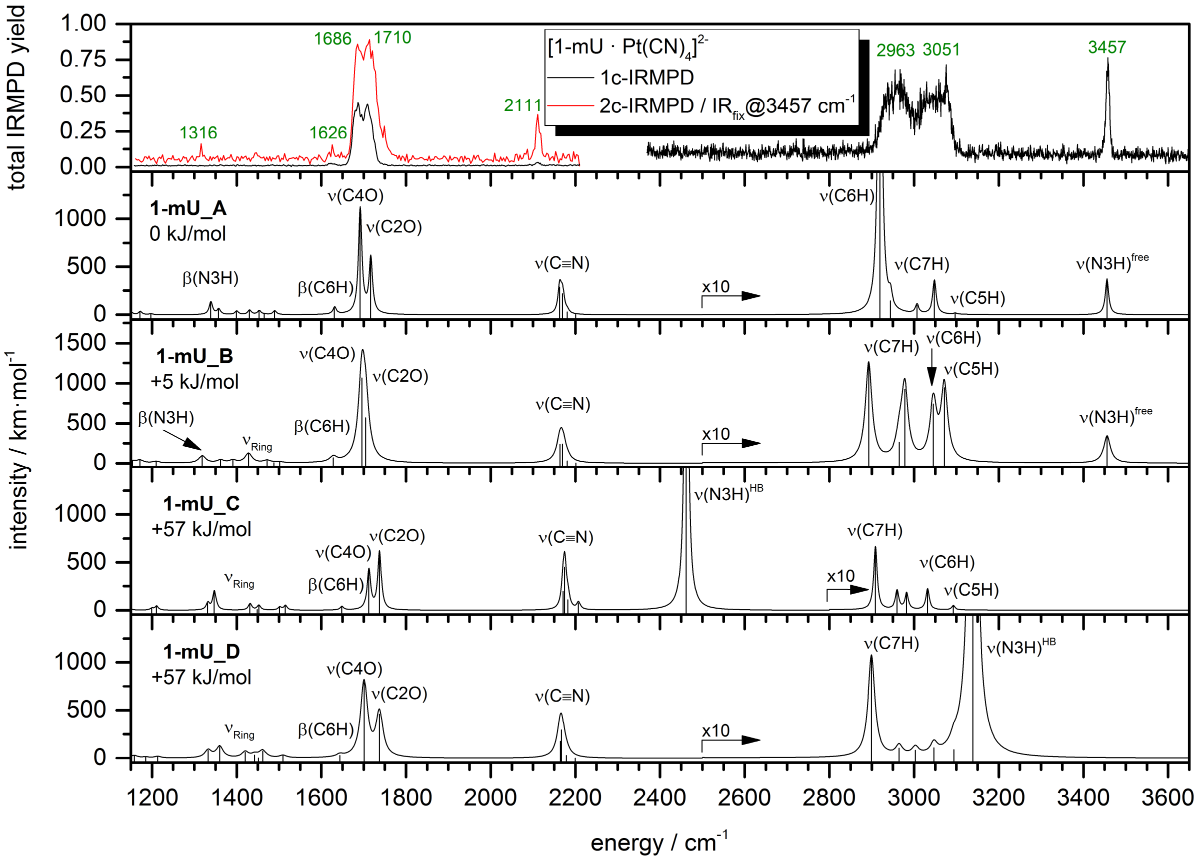

Figure 10: Experimental one and two color IRMPD spectrum of the 1-methyluracil – $Pt(CN)_4^{2-}$ aggregate (probe frequency: 3457 cm^{-1}) in comparison to the DFT calculated harmonic absorption spectra of the minimum structures (cf. Fig. 9). Note, that above 2500 cm^{-1} (**1-mU_A**, **1-mU_B**, **1-mU_D**) and above 2800 cm^{-1} (**1-mU_C**) the intensities of the calculated spectra are multiplied by a factor of 10.

absorption at 1316 cm^{-1} represents the N3H bending mode. Since the IRMPD spectra of **1-mU_A** and **1-mU_B** differ only slightly in the CH stretching range, the experimental spectrum cannot be assigned unambiguously. The consideration of the thermal free energies shows, that besides **1-mU_A**, **1-mU_B** may be populated by ca. 12 % (cf. Tab. 2). Due to their high relative energy, **1-mU_C** and **1-mU_D** are not taken into account.

Table 3: Population of the minimum structures **1-mU_A**, **1-mU_B**, **1-mU_C** and **1-mU_D** calculated by the Maxwell-Boltzmann-distribution at 300, 400, and 500 K.

Temperature / K	**1-mU_A** 0 kJ/mol	**1-mU_B** +5 kJ/mol	**1-mU_C** +57 kJ/mol	**1-mU_D** +57 kJ/mol
300	0.8813	0.1187	~10^{-10}	~10^{-10}
400	0.8181	0.1819	~10^{-08}	~10^{-08}
500	0.7690	0.2122	~10^{-07}	~10^{-07}

5.6 Conclusions

We presented one and two color infrared multiple photon dissociation action spectra of $[T \cdot Pt(CN)_4]^{2-}$, $[1\text{-}mT \cdot Pt(CN)_4]^{2-}$, $[U \cdot Pt(CN)_4]^{2-}$ and $[1\text{-}mU \cdot Pt(CN)_4]^{2-}$ in combination with computational geometry optimizations and calculated harmonic vibrational spectra. The recorded vibrational spectra are reproduced well by DFT harmonic spectra of optimized structures. The observed binding motifs of the non-methylated and methylated nucleobases to the tetracyanoplatinate(II) are analogous.

Thymine and uracil are bound primarily via a N1H hydrogen bond to a nitrogen atom of a cyanide ligand, supported by various CH – CN interactions. For both nucleobases, we find experimentally similar aggregate geometries to those reported by A. Sen *et al.* which are solely based on computations.[13-16] The methylated nucleobases bind the tetracyanoplatinate(II) complex only by CH – NC interactions. A concomitant stabilization via a strong NH – NC and weaker CH – NC interactions is not possible due to the carbonyl groups adjacent to the remaining N3H proton. Instead, solely CH – NC interactions mediate the loosely bound nucleobase – tetracyanoplatinate(II) aggregate. The two energetically most favorable isomers **1-mT_A/B** and **1-mU_A/B** are very close in structure and energy, enabling both isomers to contribute in the gas phase.

First IRMPD experiments on the aggregates of the nucleosides thymidine and uridine representing the next step in mimicking DNA/RNA strands were conducted (cf. Figs. S9-S18) The binding motif of the nucleosides thymidine and uridine and is unlike. The N1H proton of the nucleobase is replaced by a cyclic sugar side chain. In the case of the DNA nucleoside thymidine it is deoxyribose, in the case of the RNA nucleoside uridine it is ribose. The CH – NC interactions become less pronounced and the pentose's hydroxyl groups form stable hydrogen bonds with the cyanide ligands of tetracyanoplatinate(II). The flexibility of the sugar backbone and the large number of polarized functional groups allow for a vast number of possible isomers. This and the highly broadened absorption bands in the CH / OH / NH stretching region make an assignment difficult. Yet, calculations show that the binding motif compared to the nucleobases changes in favor of CN – HO hydrogen bonds.

Additional IR(M)PD experiments on tetracyanoplatinate(II) – nucleobase adducts using messenger spectroscopy (e.g. He tagging) in cryogenically cooled ion traps may help in resolving the significant CH-stretching region superimposed to the broadened hydrogen bound NH region.

5.7 References

[1] E. Shaili, "*Platinum anticancer drugs and photochemotherapeutic agents: recent advances and future developments*", *Science progress*, **2014**, *97*, 20-40.

[2] A. Leonidova, V. Pierroz, R. Rubbiani, J. Heier, S. Ferrari, G. Gasser, "*Towards cancer cell-specific phototoxic organometallic rhenium(I) complexes*", *Dalton Trans.*, **2014**, *43*, 4287-4294.

[3] E. R. Jamieson, S. J. Lippard, "*Structure, Recognition, and Processing of Cisplatin−DNA Adducts*", *Chem. Rev.*, **1999**, *99*, 2467-2498.

[4] P. J. Loehrer, L. H. Einhorn, "*Cisplatin*", *Ann. Intern. Med.*, **1984**, *100*, 704-713.

[5] P. G. Rose, B. N. Bundy, E. B. Watkins, J. T. Thigpen, G. Deppe, M. A. Maiman, D. L. Clarke-Pearson, S. Insalaco, "*Concurrent cisplatin-based radiotherapy and chemotherapy for locally advanced cervical cancer*", *N. Engl. J. Med.*, **1999**, *340*, 1144-1153.

[6] H. M. Keys, B. N. Bundy, F. B. Stehman, L. I. Muderspach, W. E. Chafe, C. L. Suggs, J. L. Walker, D. Gersell, "*Cisplatin, radiation, and adjuvant hysterectomy compared with radiation and adjuvant hysterectomy for bulky stage IB cervical carcinoma*", *N. Engl. J. Med.*, **1999**, *340*, 1154-1161.

[7] L. H. Einhorn, "*Treatment of testicular cancer: a new and improved model*", *J. Clin. Oncol.*, **1990**, *8*, 1777-1781.

[8] N. J. Farrer, L. Salassa, P. J. Sadler, "*Photoactivated chemotherapy (PACT): the potential of excited-state d-block metals in medicine*", *Dalton Trans.*, **2009**, 10690-10701.

[9] T. J. Dougherty, C. J. Gomer, B. W. Henderson, G. Jori, D. Kessel, M. Korbelik, J. Moan, Q. Peng, "*Photodynamic therapy*", *J. Natl. Cancer Inst.*, **1998**, *90*, 889-905.

[10] J. D. Knoll, C. Turro, "*Control and utilization of ruthenium and rhodium metal complex excited states for photoactivated cancer therapy*", *Coord. Chem. Rev.*, **2015**, *282*, 110-126.

[11] Y. Zhao, G. M. Roberts, S. E. Greenough, N. J. Farrer, M. J. Paterson, W. H. Powell, V. G. Stavros, P. J. Sadler, "*Two-Photon-Activated Ligand Exchange in Platinum (II) Complexes*", *Angew. Chem. Int. Ed.*, **2012**, *51*, 11263-11266.

[12] N. J. Farrer, J. A. Woods, L. Salassa, Y. Zhao, K. S. Robinson, G. Clarkson, F. S. Mackay, P. J. Sadler, "*A Potent Trans-Diimine Platinum Anticancer Complex Photoactivated by Visible Light*", *Angew. Chem. Int. Ed.*, **2010**, *49*, 8905-8908.

[13] A. Sen, C. E. H. Dessent, "*Communication: Photoactivation of nucleobase bound platinumII metal complexes: Probing the influence of the nucleobase*", *J. Chem. Phys.*, **2014**, *141*, 241101.

[14] A. Sen, C. E. H. Dessent, "*Mapping the UV Photophysics of Platinum Metal Complexes Bound to Nucleobases: Laser Spectroscopy of Isolated Uracil·Pt(CN)$_4^{2-}$ and Uracil·Pt(CN)$_6^{2-}$ Complexes*", *J. Phys. Chem. Lett.*, **2014**, *5*, 3281-3285.

[15] A. Sen, G.-L. Hou, X.-B. Wang, C. E. H. Dessent, "*Electron Detachment as a Probe of Intrinsic Nucleobase Dynamics in Dianion-Nucleobase Clusters: Photoelectron Spectroscopy of the Platinum II Cyanide Dianion Bound to Uracil, Thymine, Cytosine, and Adenine*", *J. Phys. Chem. B*, **2015**, *119*, 11626-11631.

[16] A. Sen, T. F. M. Luxford, N. Yoshikawa, C. E. H. Dessent, "*Solvent evaporation versus proton transfer in nucleobase-Pt(CN)$_{4,6}^{2-}$ dianion clusters: a collisional excitation and electronic laser photodissociation spectroscopy study*", *Phys. Chem. Chem. Phys.*, **2014**, *16*, 15490-15500.

[17] Y. Nosenko, F. Menges, C. Riehn, G. Niedner-Schatteburg, "*INVESTIGATION BY TWO-COLOR IR DISSOCIATION SPECTROSCOPY OF HOOGSTEEN-TYPE BINDING IN A METALATED NUCLEOBASE PAIR MIMIC*", *Phys. Chem. Chem. Phys.*, **2013**, *15*, 8171-8178.

[18] A. D. Becke, "*DENSITY-FUNCTIONAL THERMOCHEMISTRY. III. THE ROLE OF EXACT EXCHANGE*", *J. Chem. Phys.*, **1993**, *98*, 5648-5652.

[19] A. D. Becke, "*DENSITY-FUNCTIONAL EXCHANGE-ENERGY APPROXIMATION WITH CORRECT ASYMPTOTIC BEHAVIOR*", *Phys. Rev. A*, **1988**, *38*, 3098.

[20] B. Miehlich, A. Savin, H. Stoll, H. Preuss, "*RESULTS OBTAINED WITH THE CORRELATION ENERGY DENSITY FUNCTIONALS OF BECKE AND LEE, YANG AND PARR*", *Chem. Phys. Lett.*, **1989**, *157*, 200-206.

[21] R. A. Kendall, T. H. Dunning Jr, R. J. Harrison, "*ELECTRON AFFINITIES OF THE FIRST-ROW ATOMS REVISITED. SYSTEMATIC BASIS SETS AND WAVE FUNCTIONS*", *J. Chem. Phys.*, **1992**, *96*, 6796-6806.

[22] D. E. Woon, T. H. Dunning Jr, "*GAUSSIAN BASIS SETS FOR USE IN CORRELATED MOLECULAR CALCULATIONS. III. THE ATOMS ALUMINUM THROUGH ARGON*", *J. Chem. Phys.*, **1993**, *98*, 1358-1371.

[23] M. Dolg, U. Wedig, H. Stoll, H. Preuss, "*ENERGY-ADJUSTED ABINITIO PSEUDOPOTENTIALS FOR THE FIRST ROW TRANSITION ELEMENTS*", *J. Chem. Phys.*, **1987**, *86*, 866-872.

[24] D. Andrae, U. Haeussermann, M. Dolg, H. Stoll, H. Preuss, "*ENERGY-ADJUSTEDAB INITIO PSEUDOPOTENTIALS FOR THE SECOND AND THIRD ROW TRANSITION ELEMENTS: MOLECULAR TEST FOR M_2 (M = AG, AU) AND MH (M = RU, OS)*", *Theor. Chem. Acc.*, **1991**, *78*, 247-266.

[25] M. J. Frisch, G. W. Trucks, H. B. Schlegel, G. E. Scuseria, M. A. Robb, J. R. Cheeseman, G. Scalmani, V. Barone, G. A. Petersson, H. Nakatsuji, X. Li, M. Caricato, A. Marenich, J. Bloino, B. G. Janesko, R. Gomperts, B. Menucci, H. P. Hratchian, J. V. Ortiz, A. F. Izmaylov, J. L. Sonnenberg, D. Williams-Young, F. Ding, F. Lipparini, F. Egidi, J. Goings, B. Peng, A. Petrone, T. Henderson, D. Ranasinghe, V. G. Zakrzewski, J. Gao, N. Rega, G. Zheng, W. Liang, M. Hada, M. Ehara, K. Toyota, R. Fukuda, J. Hasegawa, M. Ishida, T. Nakajima, Y. Honda, O. Kitao, H. Nakai, T. Vreven, K. Throssel, J. A. Montgomery, J. E. Peralta, F. Ogliaro, M. Bearpark, J. J. Heyd, E. Brothers, K. N. Kudin, V. N. Staroverov, T. Keith, R. Kobayashi, J. Normand, K. Raghavachari, A. Rendell, J. C. Burant, S. S. Iyengar, J. Tomasi, M. Cossi, J. M. Millam, M. Klene, C. Adamo, R. Cammi, J. W. Ochterski, R. L. Martin, K. Morokuma, O. Farkas, Fores, "*GAUSSIAN09, REVISION D.01, GAUSSIAN, INC., WALLINGFORD, CT*", *University of Minnesota, Minneapolis*, **2009**.

[26] N. M. O'Boyle, A. L. Tenderholt, K. M. Langner, "*CCLIB: A LIBRARY FOR PACKAGE-INDEPENDENT COMPUTATIONAL CHEMISTRY ALGORITHMS*", *J. Comput. Chem.*, **2008**, *29*, 839-845.

[27] S. F. Boys, F. d. Bernardi, "*THE CALCULATION OF SMALL MOLECULAR INTERACTIONS BY THE DIFFERENCES OF SEPARATE TOTAL ENERGIES. SOME PROCEDURES WITH REDUCED ERRORS*", *Mol. Phys.*, **1970**, *19*, 553-566.

[28] J. Contreras-García, E. R. Johnson, S. Keinan, R. Chaudret, J.-P. Piquemal, D. N. Beratan, W. Yang, "*NCIPLOT: A PROGRAM FOR PLOTTING NONCOVALENT INTERACTION REGIONS*", *J. Chem. Theory Comput.*, **2011**, *7*, 625-632.

[29] T. Lu, F. Chen, "*MULTIWFN: A MULTIFUNCTIONAL WAVEFUNCTION ANALYZER*", *J. Comput. Chem.*, **2012**, *33*, 580-592.

[30] W. Humphrey, A. Dalke, K. Schulten, "*VMD: VISUAL MOLECULAR DYNAMICS*", *J. Mol. Graphics*, **1996**, *14*, 33-38.

[31] E. R. Johnson, S. Keinan, P. Mori-Sánchez, J. Contreras-García, A. J. Cohen, W. Yang, "*REVEALING NONCOVALENT INTERACTIONS*", *J. Am. Chem. Soc.*, **2010**, *132*, 6498-6506.

[32] J. Lang, J. Mohrbach, S. Dillinger, J. M. Hewer, G. Niedner-Schatteburg, "*Vibrational blue shift of coordinated N2 in [$Fe_3O(OAc)_6(N_2)_n]^+$:"non-classical" dinitrogen complexes*", *Chem. Commun.*, **2017**, *53*, 420-423.

[33] A. Bouchet, J. Klyne, G. Piani, O. Dopfer, A. Zehnacker, "*Diastereo-specific conformational properties of neutral, protonated and radical cation forms of (1R,2S)-cis- and (1R,2R)-trans-amino-indanol by gas phase spectroscopy*", *Phys. Chem. Chem. Phys.*, **2015**, *17*, 25809-25821.

[34] L. Tian, "*Multiwfn -A Multifunctional Wavefunction Analyzer- Software Manual Version 3.4 (dev)*", **2016**.

[35] J. Oomens, B. G. Sartakov, G. Meijer, G. Von Helden, "*Gas-phase infrared multiple photon dissociation spectroscopy of mass-selected molecular ions*", *Int. J. Mass Spectrom.*, **2006**, *254*, 1-19.

[36] J. Oomens, A. Tielens, B. G. Sartakov, G. von Helden, G. Meijer, "*Laboratory infrared spectroscopy of cationic polycyclic aromatic hydrocarbon molecules*", *Astrophys. J.*, **2003**, *591*, 968.

[37] T. Pankewitz, A. Lagutschenkov, G. Niedner-Schatteburg, S. S. Xantheas, Y.-T. Lee, "*Infrared spectrum of $NH_4^+(H_2O)$: Evidence for mode specific fragmentation*", *J. Chem. Phys.*, **2007**, *126*, 074307.

[38] A. Simon, C. Joblin, N. Polfer, J. Oomens, "*Infrared Spectroscopy of $[XFeC_{24}H_{12}]^+$ ($X = C_5H_5$, $C_5(CH_3)_5$) Complexes in the Gas Phase: Experimental and Computational Studies of Astrophysical Interest*", *J. Phys. Chem. A*, **2008**, *112*, 8551-8560.

[39] E. Garand, J. A. Fournier, M. Z. Kamrath, N. D. Schley, R. H. Crabtree, M. A. Johnson, "*Characterization of an activated iridium water splitting catalyst using infrared photodissociation of H_2 tagged ions*", *Phys. Chem. Chem. Phys.*, **2012**, *14*, 10109-10113.

[40] L. Yeh, M. Okumura, J. Myers, J. Price, Y. Lee, "*Vibrational spectroscopy of the hydrated hydronium cluster ions $H_3O^+(H_2O)_n$ (n= 1, 2, 3)*", *J. Chem. Phys.*, **1989**, *91*, 7319-7330.

[41] C. H. Watson, J. A. Zimmerman, J. E. Bruce, J. R. Eyler, "*Resonance-enhanced two-laser infrared multiple photon dissociation of gaseous ions*", *J. Phys. Chem.*, **1991**, *95*, 6081-6086.

[42] G. Altinay, R. B. Metz, "*Comparison of IRMPD, Ar-tagging and IRLAPS for vibrational spectroscopy of $Ag^+(CH_3OH)$*", *Int. J. Mass Spectrom.*, **2010**, *297*, 41-45.

[43] Y. Nosenko, C. Riehn, G. Niedner-Schatteburg, "*Self-pairing of 1-methylthymine mediated by two and three Ag(I) ions: a gas phase study using infrared dissociation spectroscopy and density functional theory*", *Phys. Chem. Chem. Phys.*, **2016**, *18*, 8491-8501.

5.8 Supplementary Material

Structural Characterization of (Methylated) Thymine/Uracil-Tetracyano-platinate(II)-Aggregates by Two Color Enhanced Infrared Multiple Photon Dissociation (IRMPD) Spectroscopy

Joachim M. Hewer, Yevgeniy Nosenko, Michael Lembach, Christoph Riehn and Gereon Niedner-Schatteburg

Fachbereich Chemie und Forschungszentrum OPTIMAS, Kaiserslautern, Germany

Content

Figure S1: Mass spectrum of the isolated $[T \cdot Pt(CN)_4]^{2-}$ aggregate without (black) and with resonant infrared photon irradiation (red).

Figure S2: Experimental and simulated mass peaks of the fragments of $[T \cdot Pt(CN)_4]^{2-}$.

Figure S3: Mass spectrum of the isolated $[1\text{-mT} \cdot Pt(CN)_4]^{2-}$ aggregate without (black) and with resonant infrared photon irradiation (red).

Figure S4: Experimental and simulated mass peaks of the fragments of $[1\text{-mT} \cdot Pt(CN)_4]^{2-}$.

Figure S5: Mass spectrum of the isolated $[U \cdot Pt(CN)_4]^{2-}$ aggregate without (black) and with resonant infrared photon irradiation (red).

Figure S6: Experimental and simulated mass peaks of the fragments of $[U \cdot Pt(CN)_4]^{2-}$.

Figure S7: Mass spectrum of the isolated $[1\text{-mU} \cdot Pt(CN)_4]^{2-}$ aggregate without (black) and with resonant infrared photon irradiation (red).

Figure S8: Experimental and simulated mass peaks of the fragments of $[1\text{-mU} \cdot Pt(CN)_4]^{2-}$.

Table S1: Fragmentation channels of the $[Nu \cdot Pt(CN)_4]^{2-}$ aggregates upon infrared photon irradiation, sorted by their m/z ratio.

Table S2: DFT computed binding energies of $[Nu \cdot Pt(CN)_4]^{2-}$ geometry optimized minimum structures at 0 and 298 K (B3LYP/aug-cc-pVTZ).

Table S3: Hydrogen bond distances for the NH – CN and CH – CN interactions in $[Nu \cdot Pt(CN)_4]^{2-}$ sorted by length.

Figure S9: DFT/B3LYP (aug-cc-pVDZ (C, H, N, O); Stuttgart 1997 ECP (Pt)) calculated four most stable minimum structures and NCI plots of Thymidine – $Pt(CN)_4^{2-}$ aggregates.

Figure S10: Experimental one and two color IRMPD spectrum of the Thymidine – $Pt(CN)_4^{2-}$ aggregate (probe frequency: 3454 cm^{-1}) in comparison to the DFT calculated harmonic absorption spectra of the four most stable minimum structures.

Figure S11: DFT/B3LYP (aug-cc-pVDZ (C, H, N, O); Stuttgart 1997 ECP (Pt)) calculated less stable minimum structures and NCI plots of Thymidine – $Pt(CN)_4^{2-}$ aggregates **dT_E** to **dT_K**.

Figure S12: Experimental one and two color IRMPD spectrum of the Thymidine – $Pt(CN)_4^{2-}$ aggregate (probe frequency: 3454 cm^{-1}) in comparison to the DFT calculated harmonic absorption spectra of the less stable minimum structures.

Figure S13: DFT/B3LYP (aug-cc-pVDZ (C, H, N, O); Stuttgart 1997 ECP (Pt)) calculated four most stable minimum structures and NCI plots of Uridine – $Pt(CN)_4^{2-}$ aggregates.

Figure S14: Experimental one and two color IRMPD spectrum of the Uridine – $Pt(CN)_4^{2-}$ aggregate (probe frequency: 3454 cm^{-1}) in comparison to the DFT calculated harmonic absorption spectra of the four most stable minimum structures.

Figure S15: DFT/B3LYP (aug-cc-pVDZ (C, H, N, O); Stuttgart 1997 ECP (Pt)) calculated less stable minimum structures and NCI plots of Uridine – $Pt(CN)_4^{2-}$ aggregates **rU_E** to **rU_M**.

Figure S16: Experimental one and two color IRMPD spectrum of the Uridine – $Pt(CN)_4^{2-}$ aggregate (probe frequency: 3454 cm^{-1}) in comparison to the DFT calculated harmonic absorption spectra of the less stable minimum structures.

Figure S17: DFT/B3LYP (aug-cc-pVDZ (C, H, N, O); Stuttgart 1997 ECP (Pt)) calculated less stable minimum structures and NCI plots of Uridine – $Pt(CN)_4^{2-}$ aggregates **rU_N** to **rU_V**.

Figure S18: Experimental one and two color IRMPD spectrum of the Uridine – $Pt(CN)_4^{2-}$ aggregate (probe frequency: 3454 cm^{-1}) in comparison to the DFT calculated harmonic absorption spectra of the less stable minimum structures.

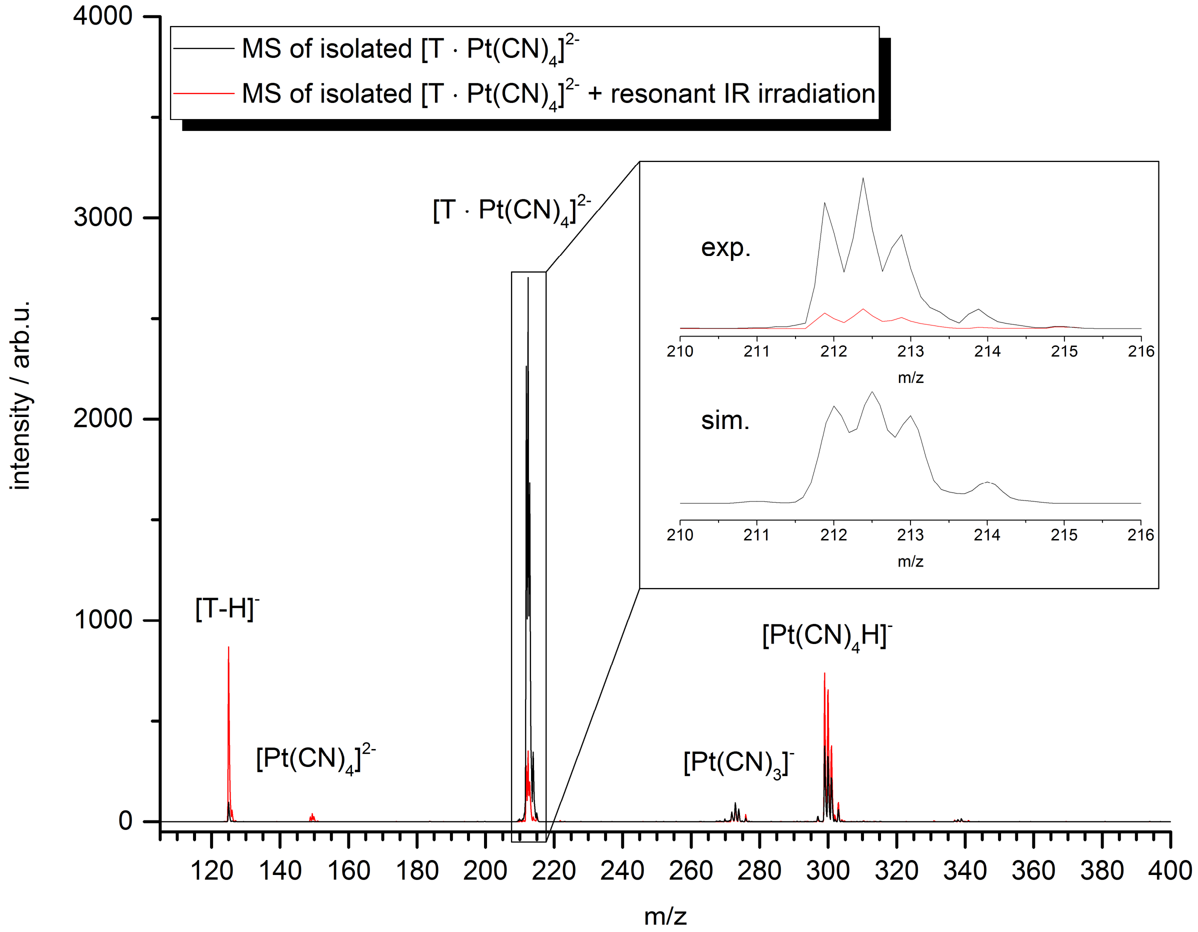

Figure S1: Mass spectrum of the isolated [T · Pt(CN)$_4$]$^{2-}$ aggregate without (black) and with resonant infrared photon irradiation (red). Note, that there is basic fragmentation due to stiff isolation conditions. The inset shows the experimental and simulated isotopic pattern of [T · Pt(CN)$_4$]$^{2-}$.

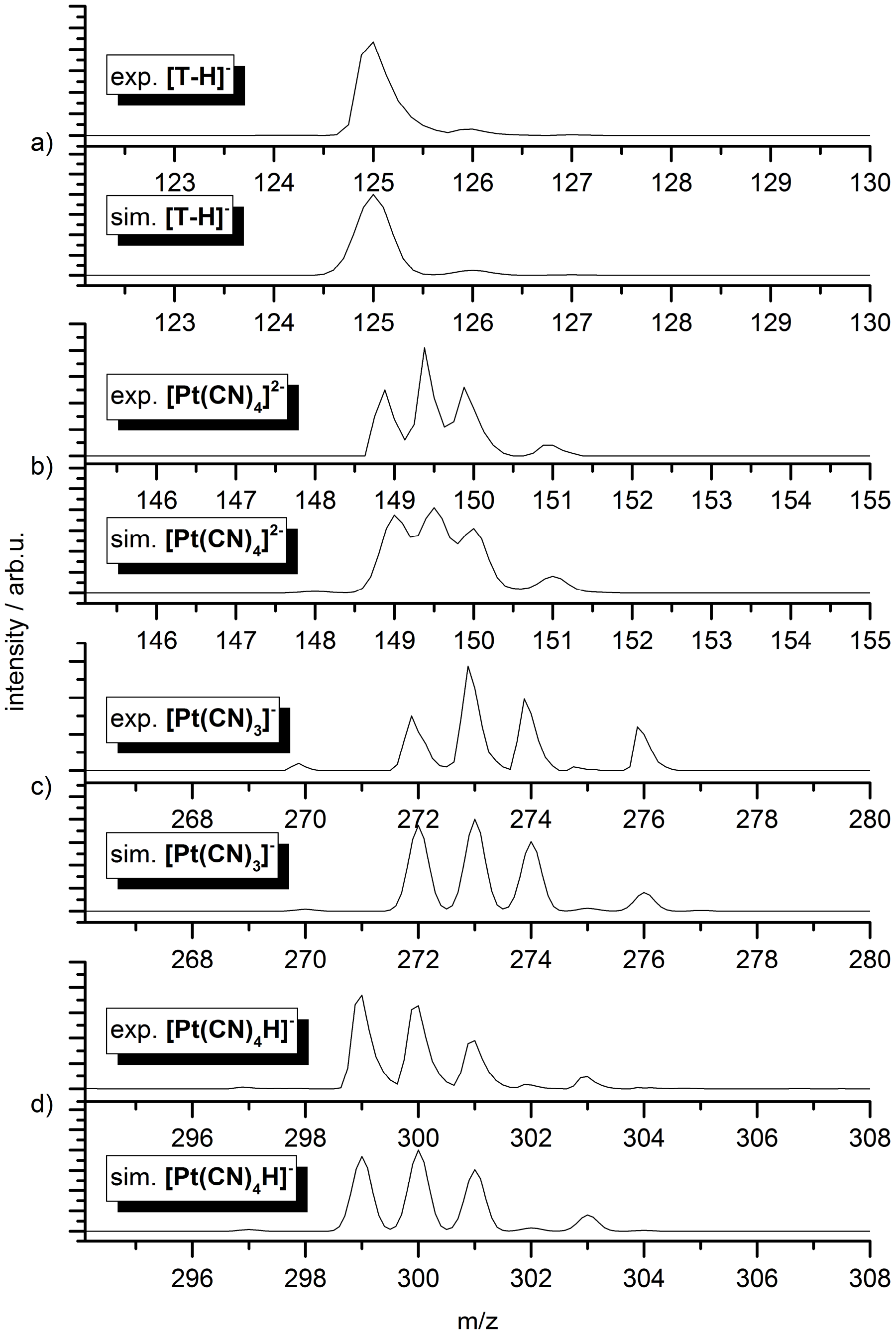

Figure S2: Experimental and simulated mass peaks of the fragments of $[T \cdot Pt(CN)_4]^{2-}$: a) deprotonated thymine $[T\text{-}H]^-$; b) tetracyanoplatinate(II) dianion $[Pt(CN)_4]^{2-}$; c) triscyanoplatinate(II) anion $[Pt(CN)_3]^-$; d) protonated tetracyanoplatinate(II) anion $[Pt(CN)_4H]^-$.

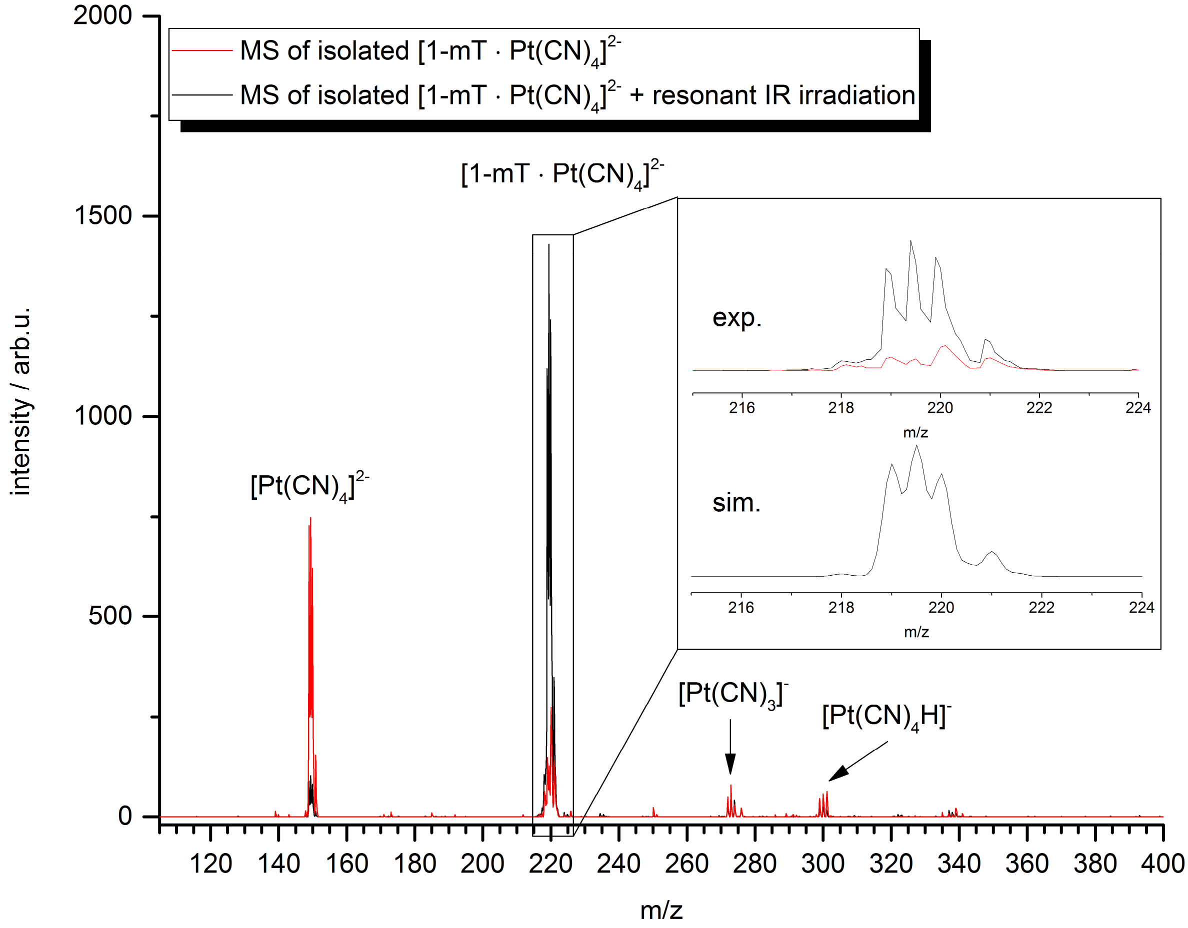

Figure S3: Mass spectrum of the isolated [1-mT · Pt(CN)$_4$]$^{2-}$ aggregate without (black) and with resonant infrared photon irradiation (red). Note, that there is basic fragmentation due to stiff isolation conditions. The inset shows the experimental and simulated isotopic pattern of [1-mT · Pt(CN)$_4$]$^{2-}$.

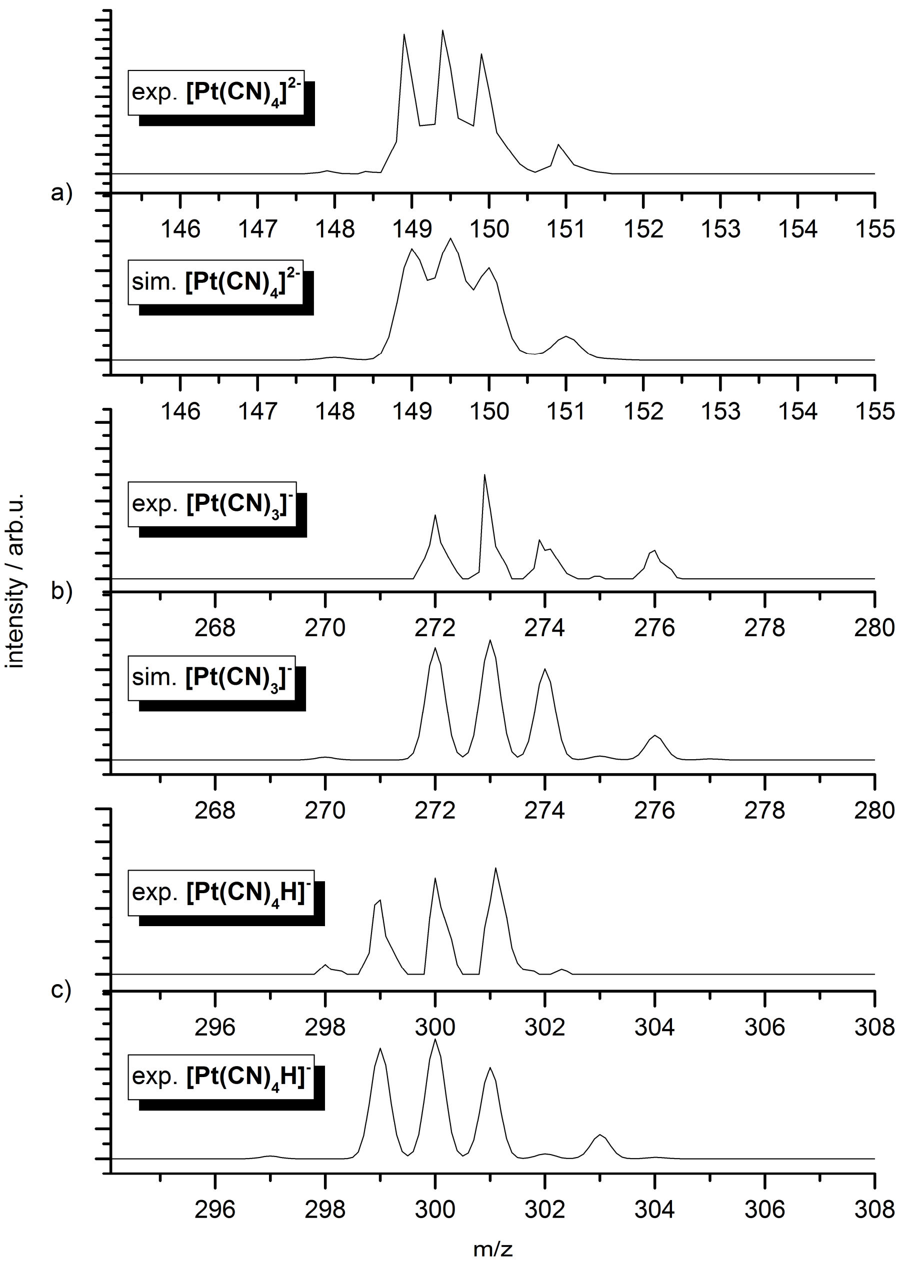

Figure S4: Experimental and simulated mass peaks of the fragments of $[1\text{-mT} \cdot Pt(CN)_4]^{2-}$: a) tetracyanoplatinate(II) dianion $[Pt(CN)_4]^{2-}$; b) triscyano-platinate(II) anion $[Pt(CN)_3]^-$; c) protonated tetracyanoplatinate(II) anion $[Pt(CN)_4H]^-$.

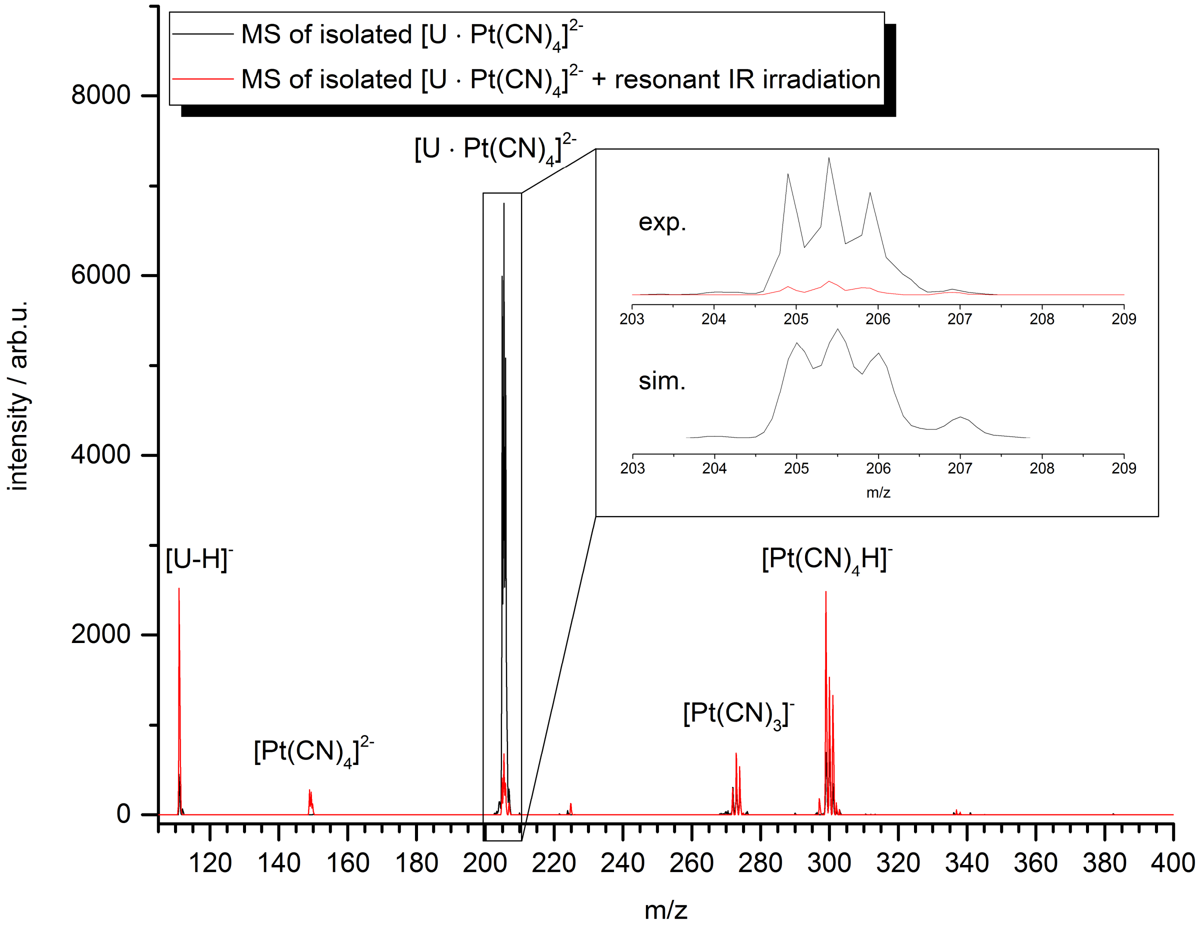

Figure S5: Mass spectrum of the isolated [U · Pt(CN)$_4$]$^{2-}$ aggregate without (black) and with resonant infrared photon irradiation (red). Note, that there is basic fragmentation due to stiff isolation conditions. The inset shows the experimental and simulated isotopic pattern of [U · Pt(CN)$_4$]$^{2-}$.

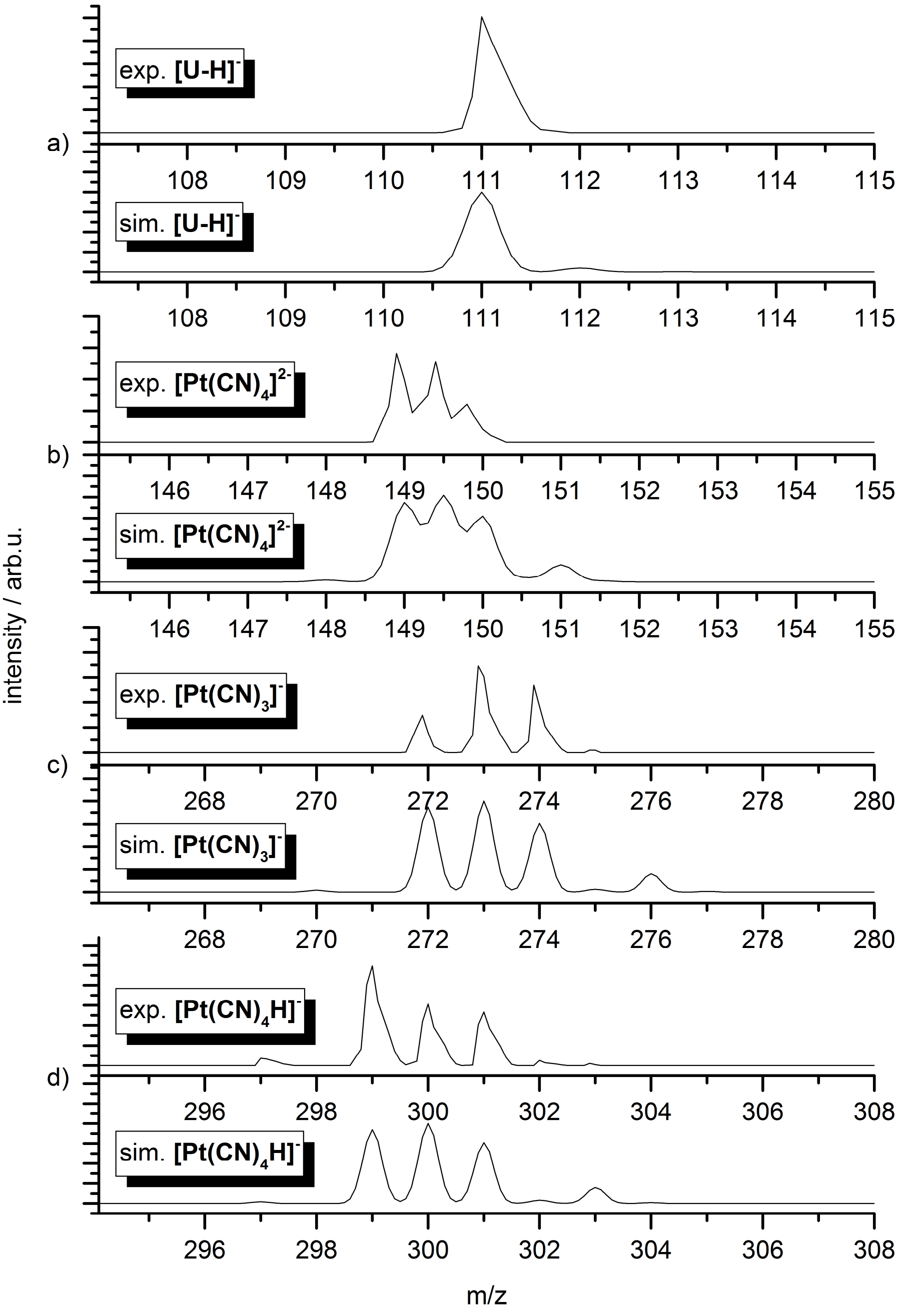

Figure S6: Experimental and simulated mass peaks of the fragments of $[U \cdot Pt(CN)_4]^{2-}$: a) deprotonated uracil $[U\text{-}H]^-$; b) tetracyanoplatinate(II) dianion $[Pt(CN)_4]^{2-}$; c) triscyano-platinate(II) anion $[Pt(CN)_3]^-$; d) protonated tetracyanoplatinate(II) anion $[Pt(CN)_4H]^-$.

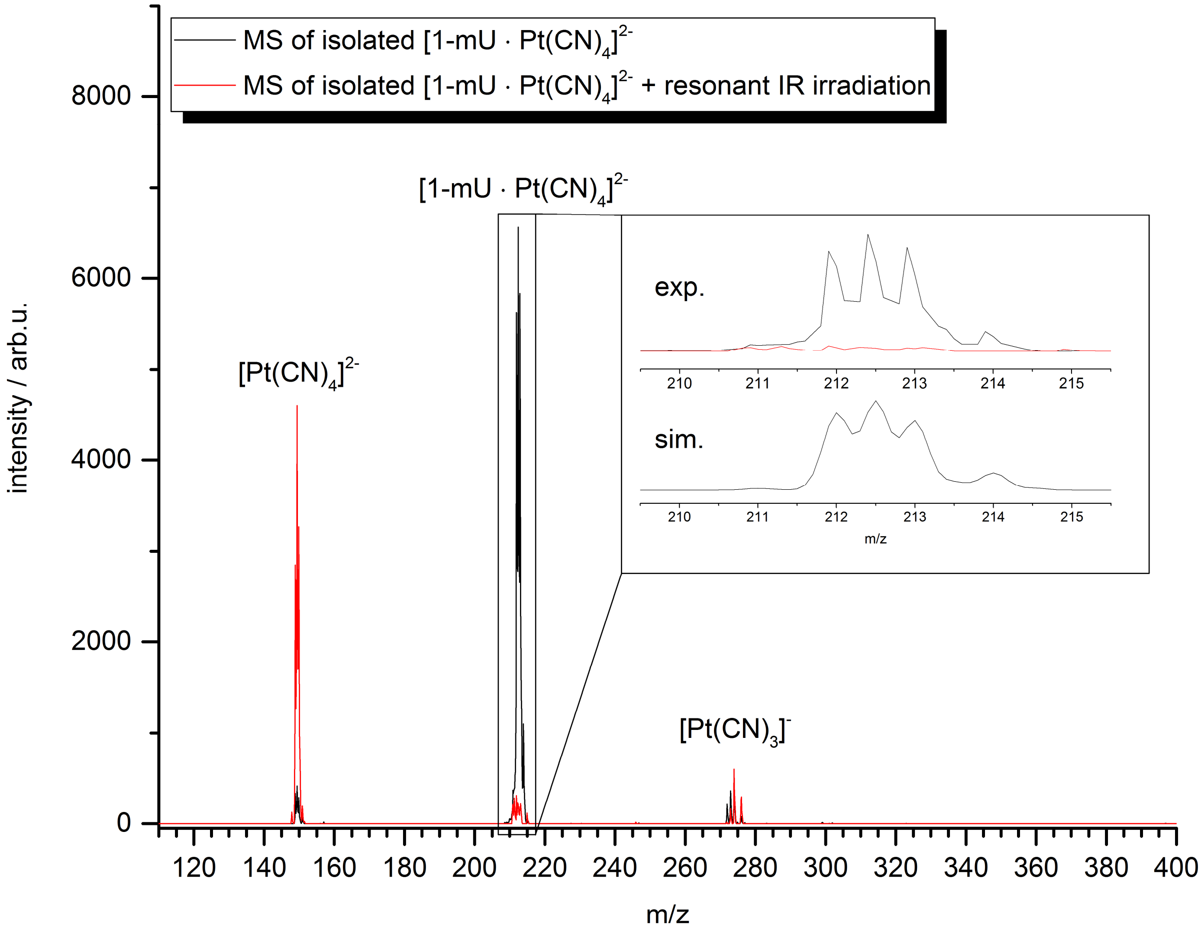

Figure S7: Mass spectrum of the isolated [1-mU · Pt(CN)$_4$]$^{2-}$ aggregate without (black) and with resonant infrared photon irradiation (red). Note, that there is basic fragmentation due to stiff isolation conditions. The inset shows the experimental and simulated isotopic pattern of [1-mU · Pt(CN)$_4$]$^{2-}$.

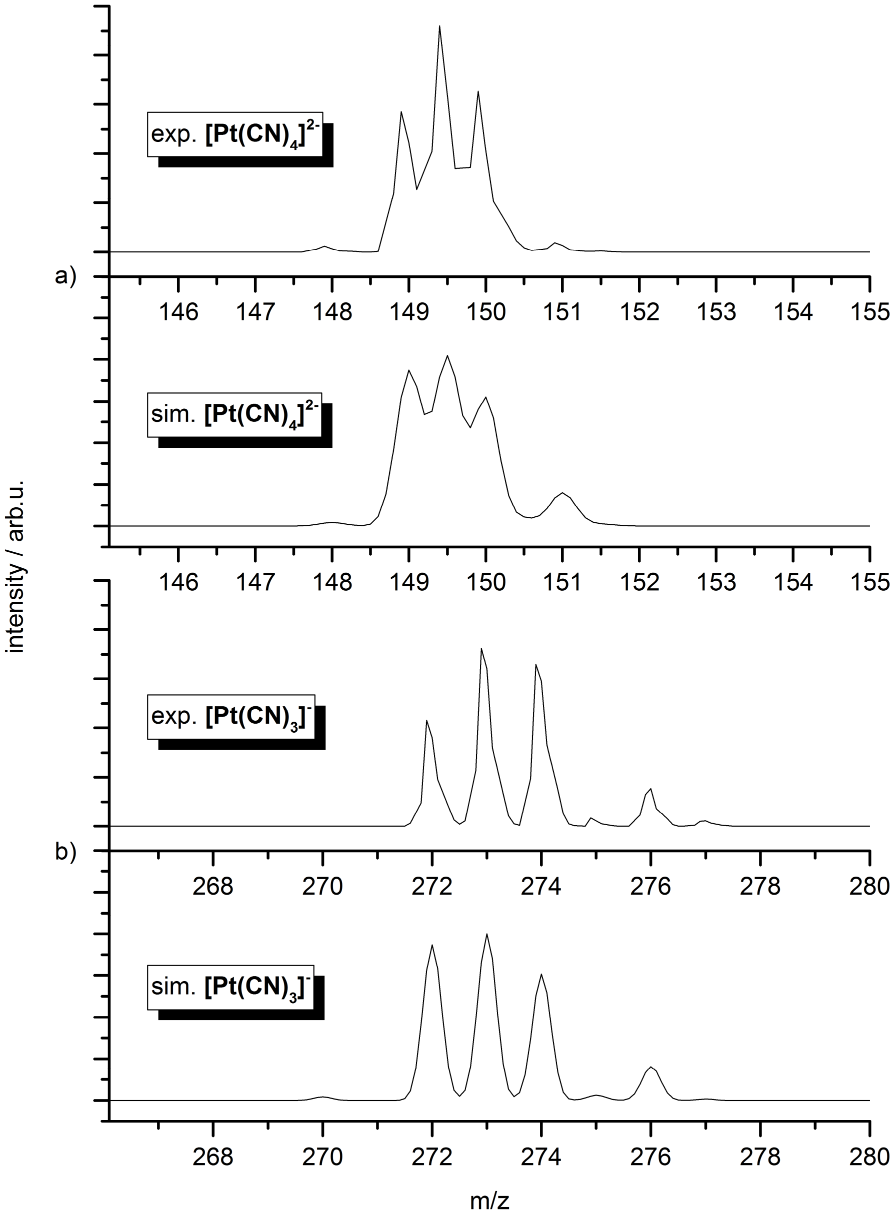

Figure S8: Experimental and simulated mass peaks of the fragments of [1-mU · Pt(CN)$_4$]$^{2-}$: a) tetracyanoplatinate(II) dianion [Pt(CN)$_4$]$^{2-}$; b) triscyanoplatinate(II) anion [Pt(CN)$_3$]$^-$.

Table S1: Fragmentation channels of the $[Nu \cdot Pt(CN)_4]^{2-}$ aggregates upon infrared photon irradiation, sorted by their m/z ratio. Note, that the deprotonated nucleobase as product ion is only present at thymine and uracil, which have a NH – NC hydrogen bond in their lowest lying minimum structure.

Parent ion	Product ion	Neutral / ionic loss
$[T \cdot Pt(CN)_4]^{2-}$	**$[T\text{-}H]^-$**	$[Pt(CN)_4H]^-$
	$[Pt(CN)_4]^{2-}$	$[T]$
	$[Pt(CN)_3]^-$	$[T]+[CN]^-$
	$[Pt(CN)_4H]^-$	$[T\text{-}H]^-$
$[1\text{-}mT \cdot Pt(CN)_4]^{2-}$	$[Pt(CN)_4]^{2-}$	$[1\text{-}mT]$
	$[Pt(CN)_3]^-$	$[1\text{-}mT]+[CN]^-$
	$[Pt(CN)_4H]^-$	$[1\text{-}mT\text{-}H]^-$
$[U \cdot Pt(CN)_4]^{2-}$	**$[U\text{-}H]^-$**	$[Pt(CN)_4H]^-$
	$[Pt(CN)_4]^{2-}$	$[U]$
	$[Pt(CN)_3]^-$	$[U]+[CN]^-$
	$[Pt(CN)_4H]^-$	$[U\text{-}H]^-$
$[1\text{-}mU \cdot Pt(CN)_4]^{2-}$	$[Pt(CN)_4]^{2-}$	$[1\text{-}mU]$
	$[Pt(CN)_3]^-$	$[1\text{-}mU]+[CN]^-$

Table S2: DFT computed binding energies of $[Nu \cdot Pt(CN)_4]^{2-}$ geometry optimized minimum structures at 0 and 298 K (B3LYP/aug-cc-pVTZ). The values are corrected by the basis set superposition error (BSSE).

Nucleobase	Binding energy / kJmol^{-1}	
	0 K	298 K
Thymine		
T_A	131	85
T_B	119	73
T_C	45	6
1-Methylthymine		
1-mT_A	99	57
1-mT_B	95	51
1-mT_C	96	48
1-mT_D	42	2
Uracil		
U_A	134	89
U_B	47	8
1-Methyluracil		
1-mU_A	102	60
1-mU_B	98	55
1-mU_C	49	3
1-mU_D	43	3

Table S3: Hydrogen bond distances for the NH – CN and CH – CN interactions in $[\mathrm{Nu} \cdot \mathrm{Pt(CN)_4}]^{2-}$ sorted by length. All H-bonds lengths below 3.3 Å are listed.

Nucleobase		H-bond length / Å
Thymine		
T_A	N1H – NC1	1.81
	C6H – NC1	2.97
	C6H – NC2	2.48
T_B	N1H – NC1	1.74
	C6H – NC1	2.77
T_C	N1H – NC1	1.67
1-Methylthymine		
1-mT_A	C7H – NC1	2.69
	C7H – NC2	3.05
	C6H – NC2	2.09
	C8H – NC2	2.99
1-mT_B	C7H – NC1	2.21
	C6H – NC1	2.30
	C8H – NC2	2.60
1-mT_C	C7H – NC1	2.57
	C7H – NC2	2.55
	C6H – NC1	2.76
	C6H – NC2	2.81
1-mT_D	N3H – NC	1.67
Uracil		
U_A	N1H – NC1	1.79
	C6H – NC1	3.05
	C5H – NC2	2.40
U_B	N3H – NC	1.67
1-Methyluracil		
1-mU_A	C7H – NC1	2.85
	C7H – NC2	2.70
	C6H – NC2	2.07
1-mU_B	C7H – NC1	2.19
	C6H – NC1	2.62
	C6H – NC2	3.00
	C5H – NC2	2.47
1-mU_C	N3H – NC	1.67
1-mU_D	N3H – NC1	2.02
	C5H – NC2	2.38

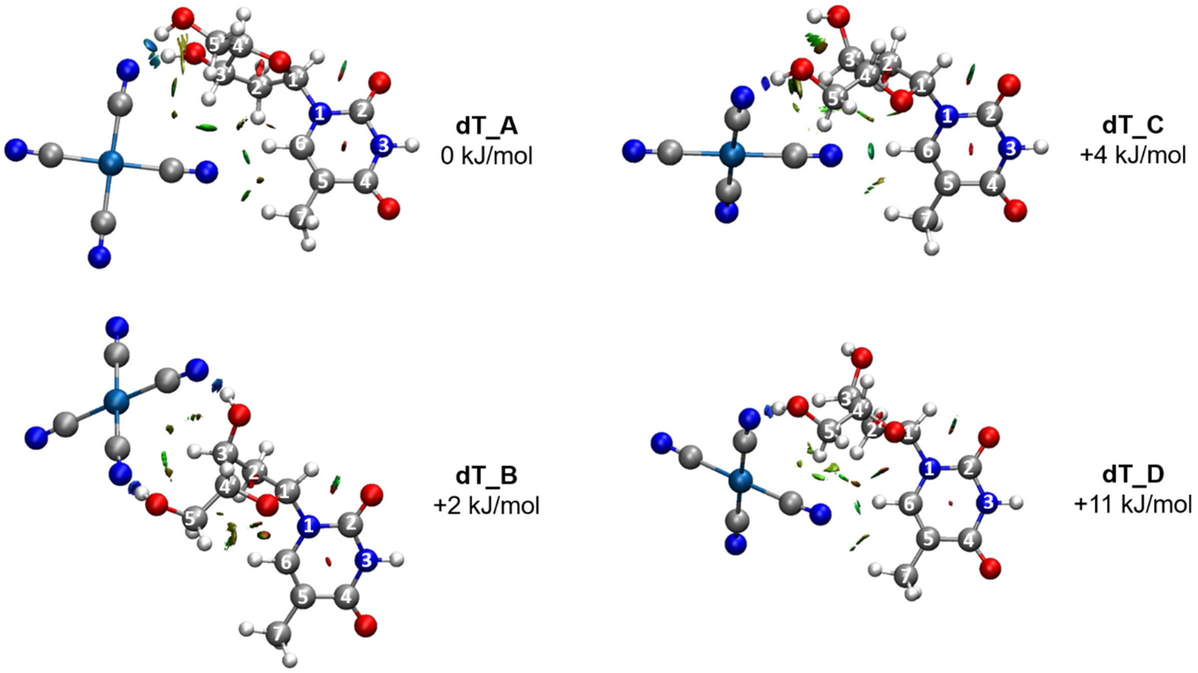

Figure S9: DFT/B3LYP (aug-cc-pVDZ (C, H, N, O); Stuttgart 1997 ECP (Pt)) calculated four most stable minimum structures and NCI plots of Thymidine – $Pt(CN)_4^{2-}$ aggregates.

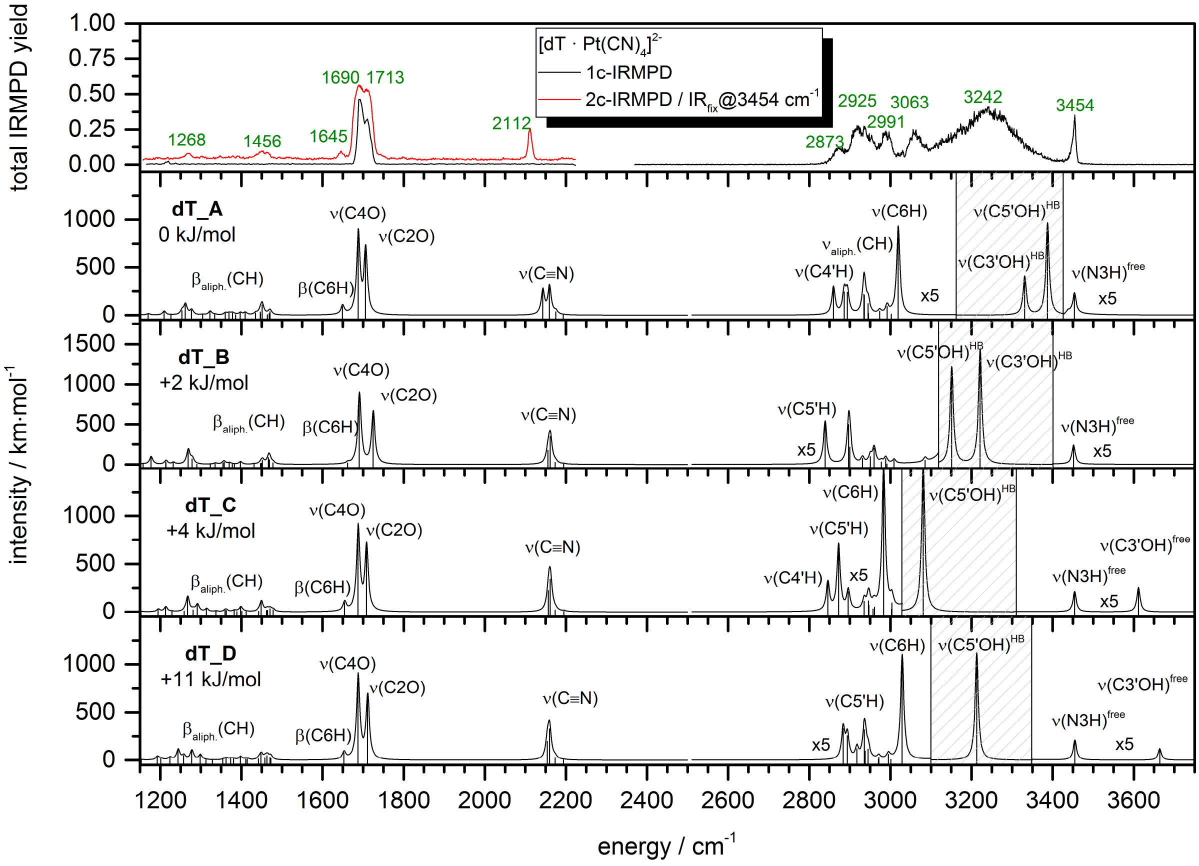

Figure S10: Experimental one and two color IRMPD spectrum of the Thymidine – $Pt(CN)_4^{2-}$ aggregate (probe frequency: 3454 cm^{-1}) in comparison to the DFT calculated harmonic absorption spectra of the four most stable minimum structures (cf. Fig. S9). Note, that above 2500 cm^{-1} the intensities of the calculated spectra are multiplied by a factor of 5, except for the grey shaded area.

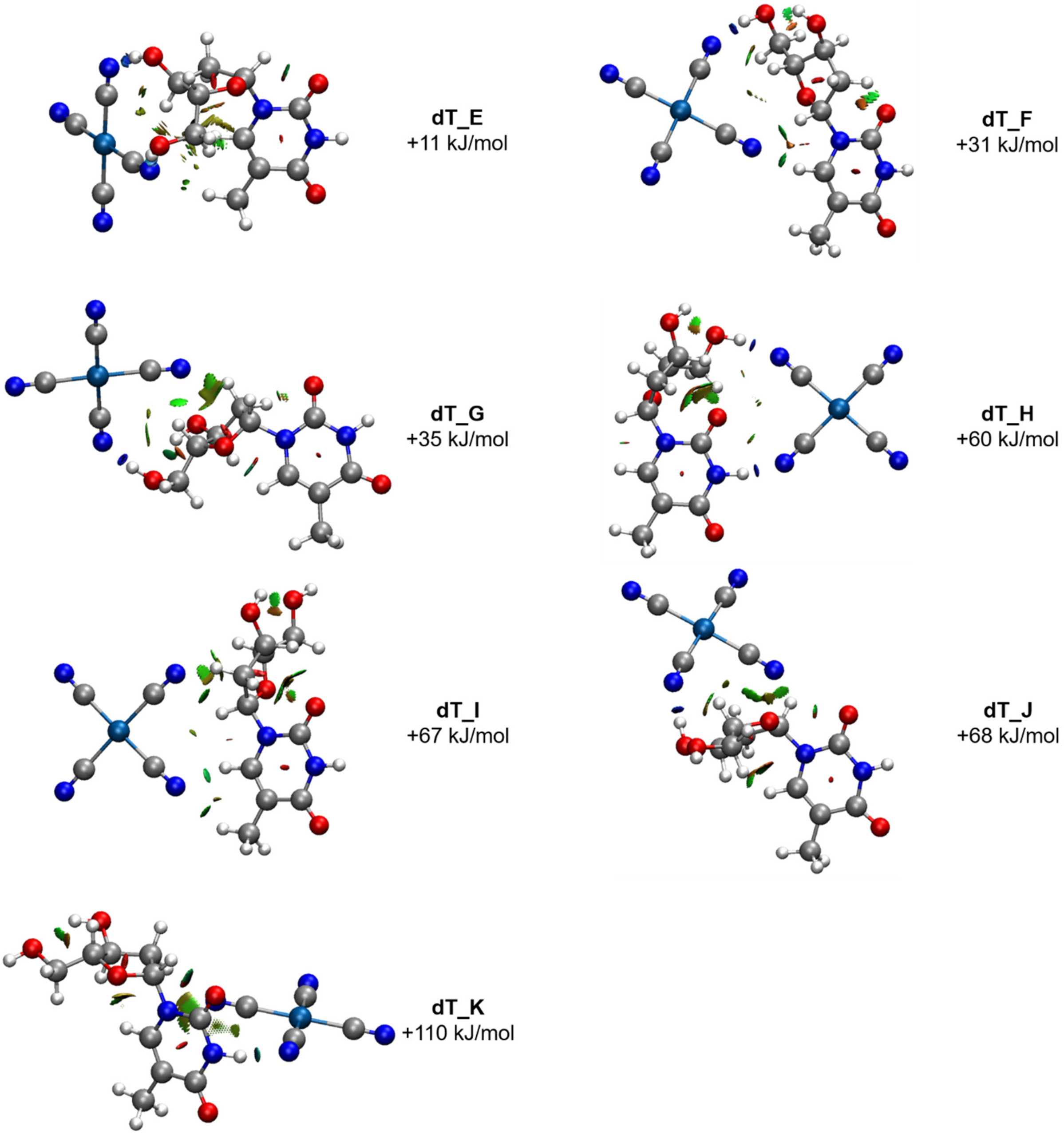

Figure S11: DFT/B3LYP (aug-cc-pVDZ (C, H, N, O); Stuttgart 1997 ECP (Pt)) calculated less stable minimum structures and NCI plots of Thymidine – $Pt(CN)_4^{2-}$ aggregates **dT_E** to **dT_K**.

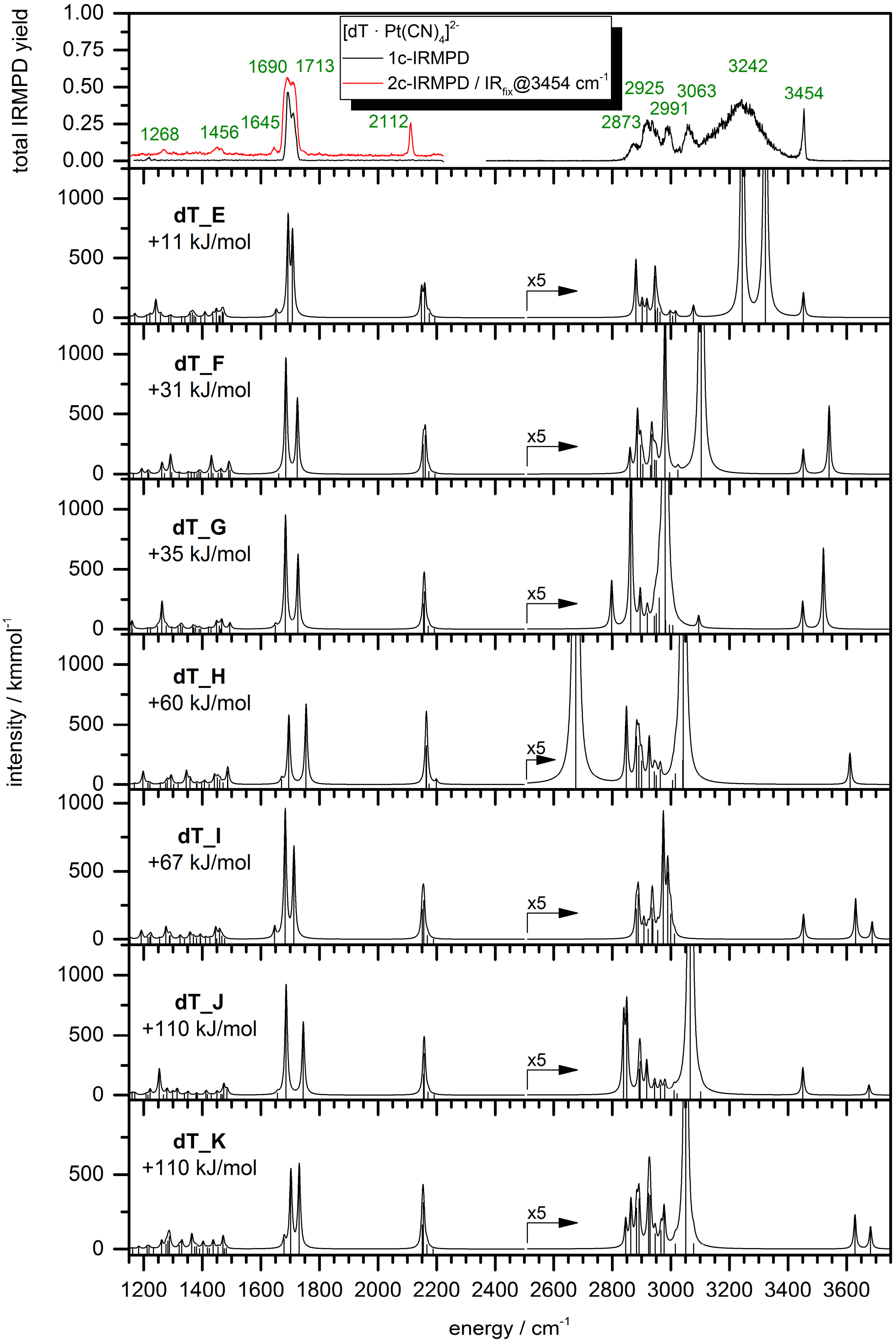

Figure S12: Experimental one and two color IRMPD spectrum of the Thymidine – $Pt(CN)_4^{2-}$ aggregate (probe frequency: 3454 cm^{-1}) in comparison to the DFT calculated harmonic absorption spectra of the less stable minimum structures (cf. Fig. S11). Note, that above 2500 cm^{-1} the intensities of the calculated spectra are multiplied by a factor of 5.

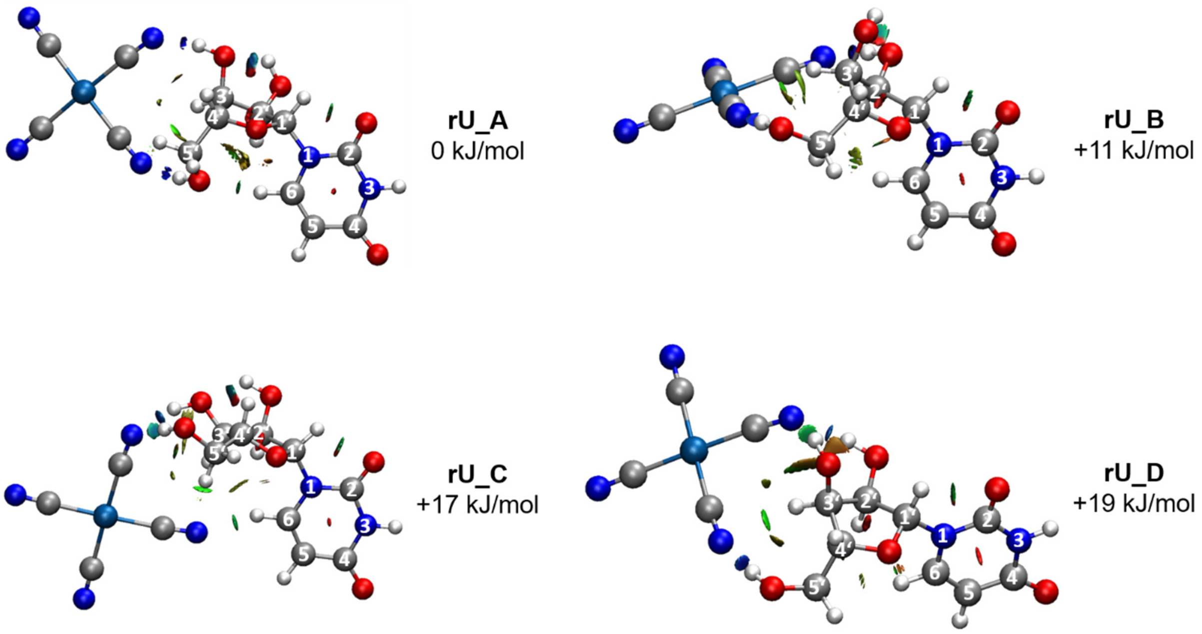

Figure S13: DFT/B3LYP (aug-cc-pVDZ (C, H, N, O); Stuttgart 1997 ECP (Pt)) calculated four most stable minimum structures and NCI plots of Uridine – $Pt(CN)_4^{2-}$ aggregates.

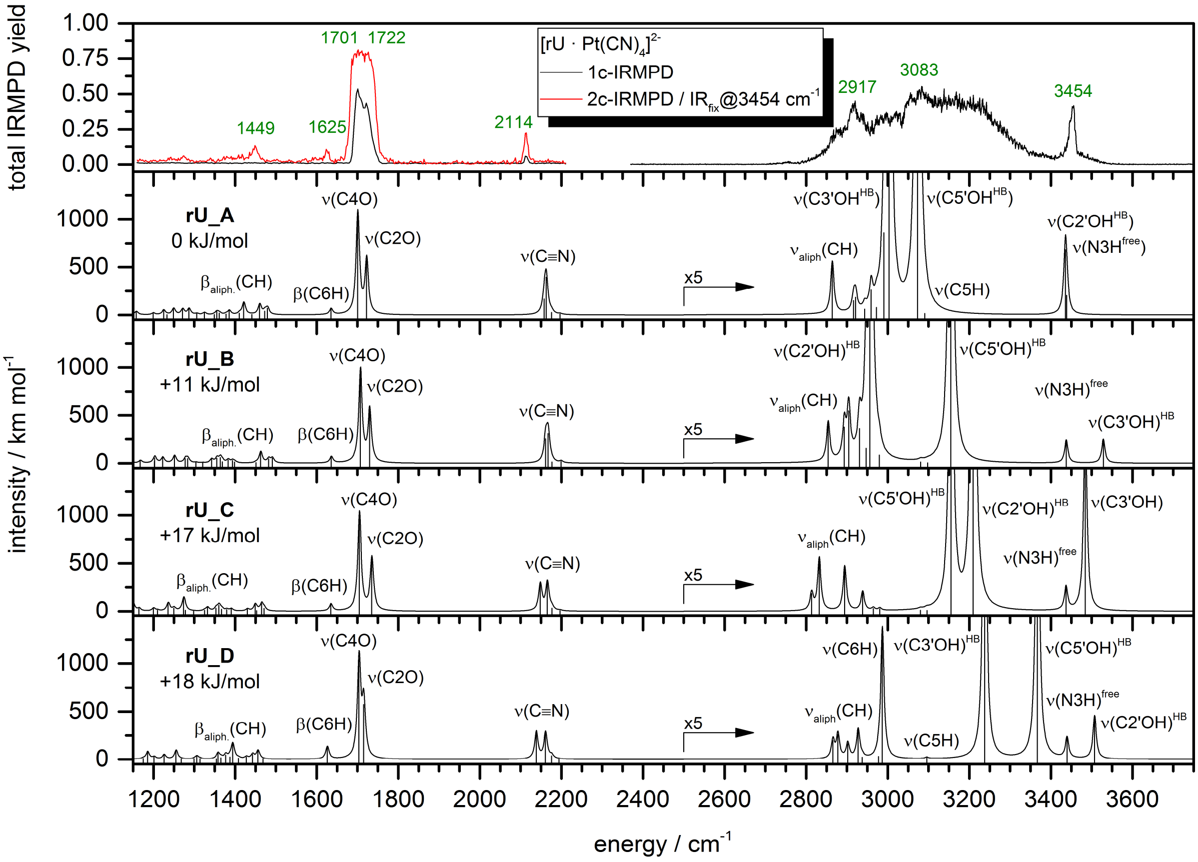

Figure S14: Experimental one and two color IRMPD spectrum of the Uridine – $Pt(CN)_4^{2-}$ aggregate (probe frequency: 3454 cm^{-1}) in comparison to the DFT calculated harmonic absorption spectra of the four most stable minimum structures (cf. Fig. S13). Note, that above 2500 cm^{-1} the intensities of the calculated spectra are multiplied by a factor of 5.

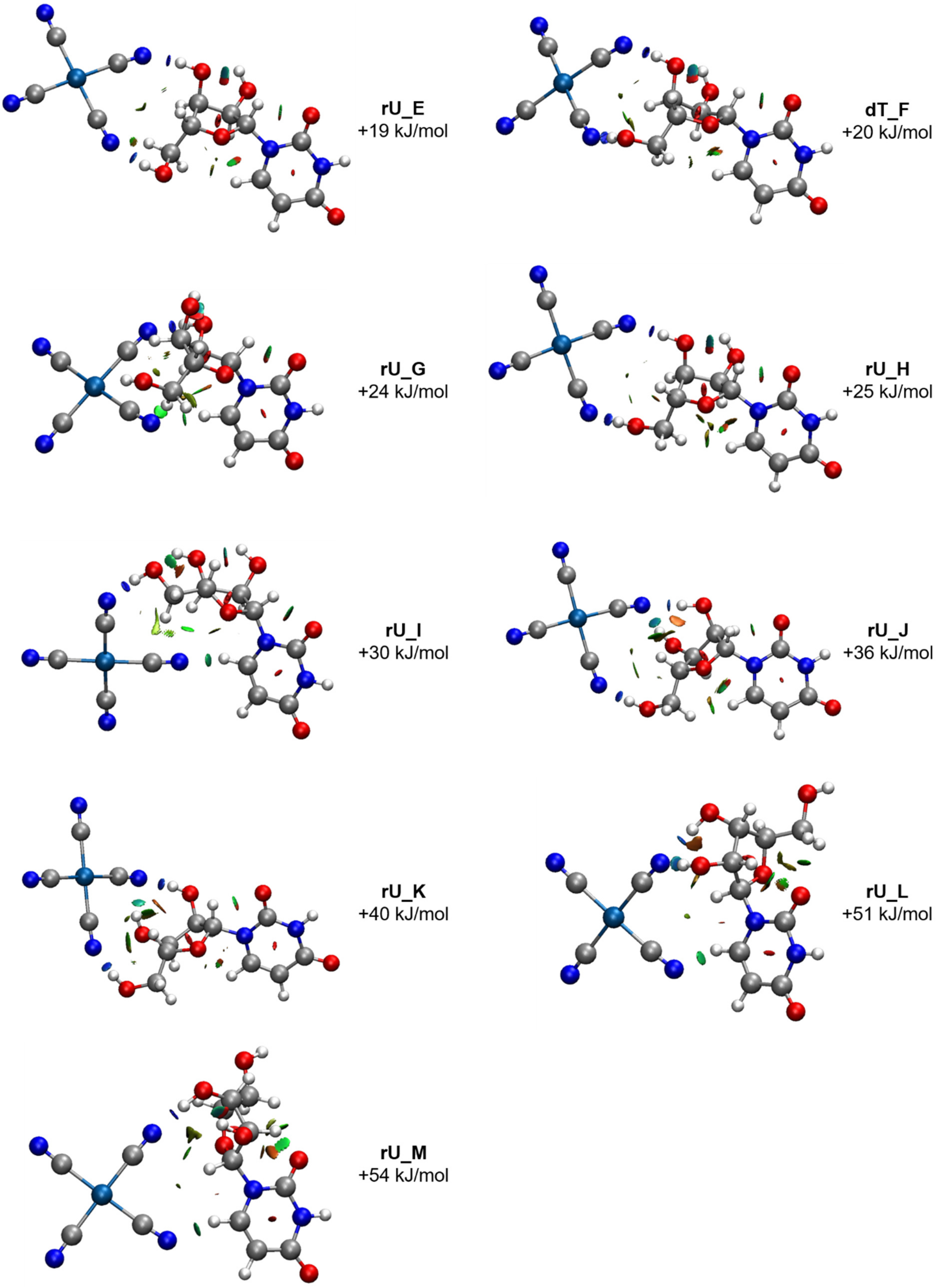

rU_E
+19 kJ/mol

dT_F
+20 kJ/mol

rU_G
+24 kJ/mol

rU_H
+25 kJ/mol

rU_I
+30 kJ/mol

rU_J
+36 kJ/mol

rU_K
+40 kJ/mol

rU_L
+51 kJ/mol

rU_M
+54 kJ/mol

Figure S15: DFT/B3LYP (aug-cc-pVDZ (C, H, N, O); Stuttgart 1997 ECP (Pt)) calculated less stable minimum structures and NCI plots of Uridine – $Pt(CN)_4^{2-}$ aggregates **rU_E** to **rU_M**.

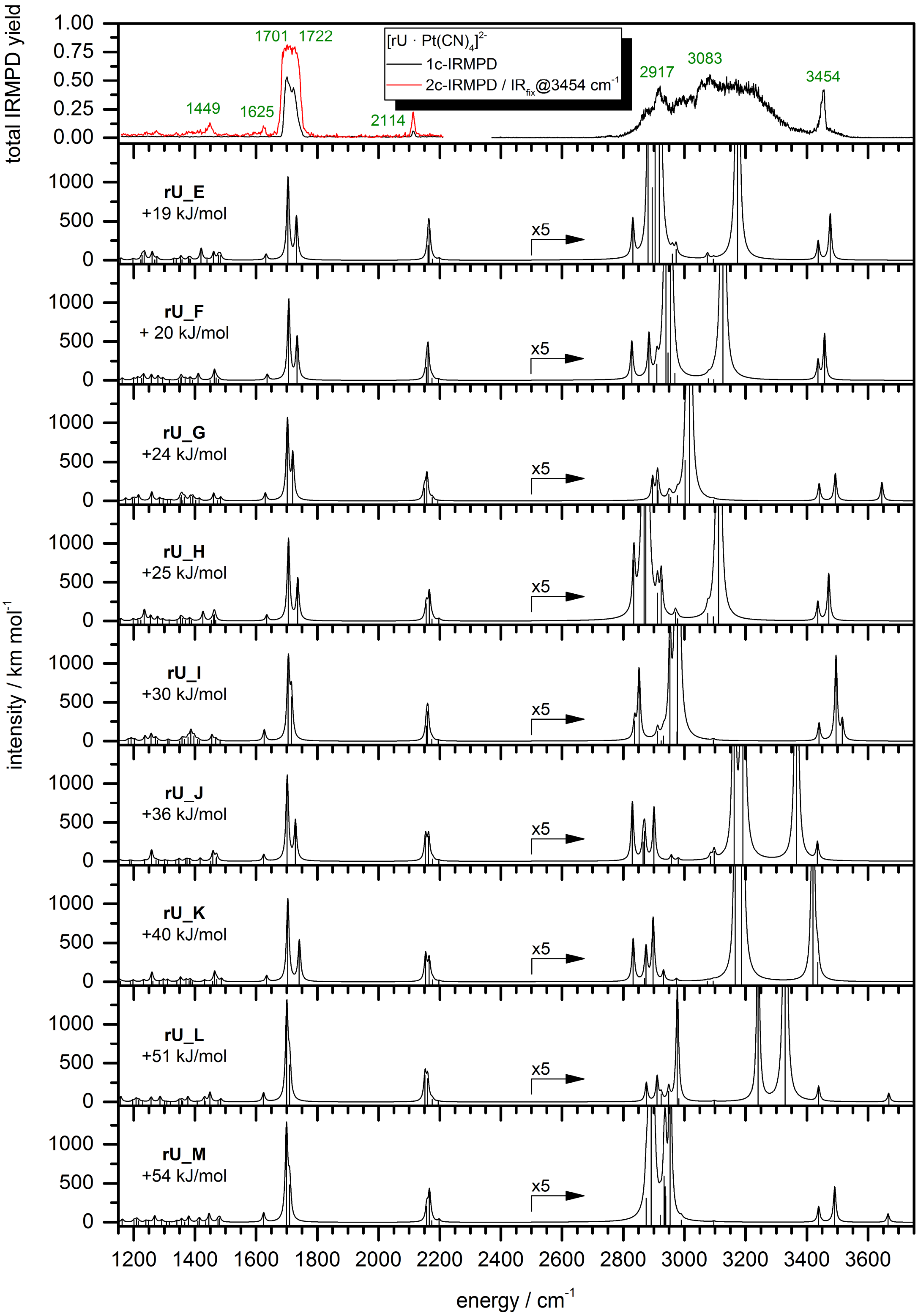

Figure S16: Experimental one and two color IRMPD spectrum of the Uridine – $Pt(CN)_4^{2-}$ aggregate (probe frequency: 3454 cm^{-1}) in comparison to the DFT calculated harmonic absorption spectra of the less stable minimum structures (cf. Fig. S15). Note, that above 2500 cm^{-1} the intensities of the calculated spectra are multiplied by a factor of 5.

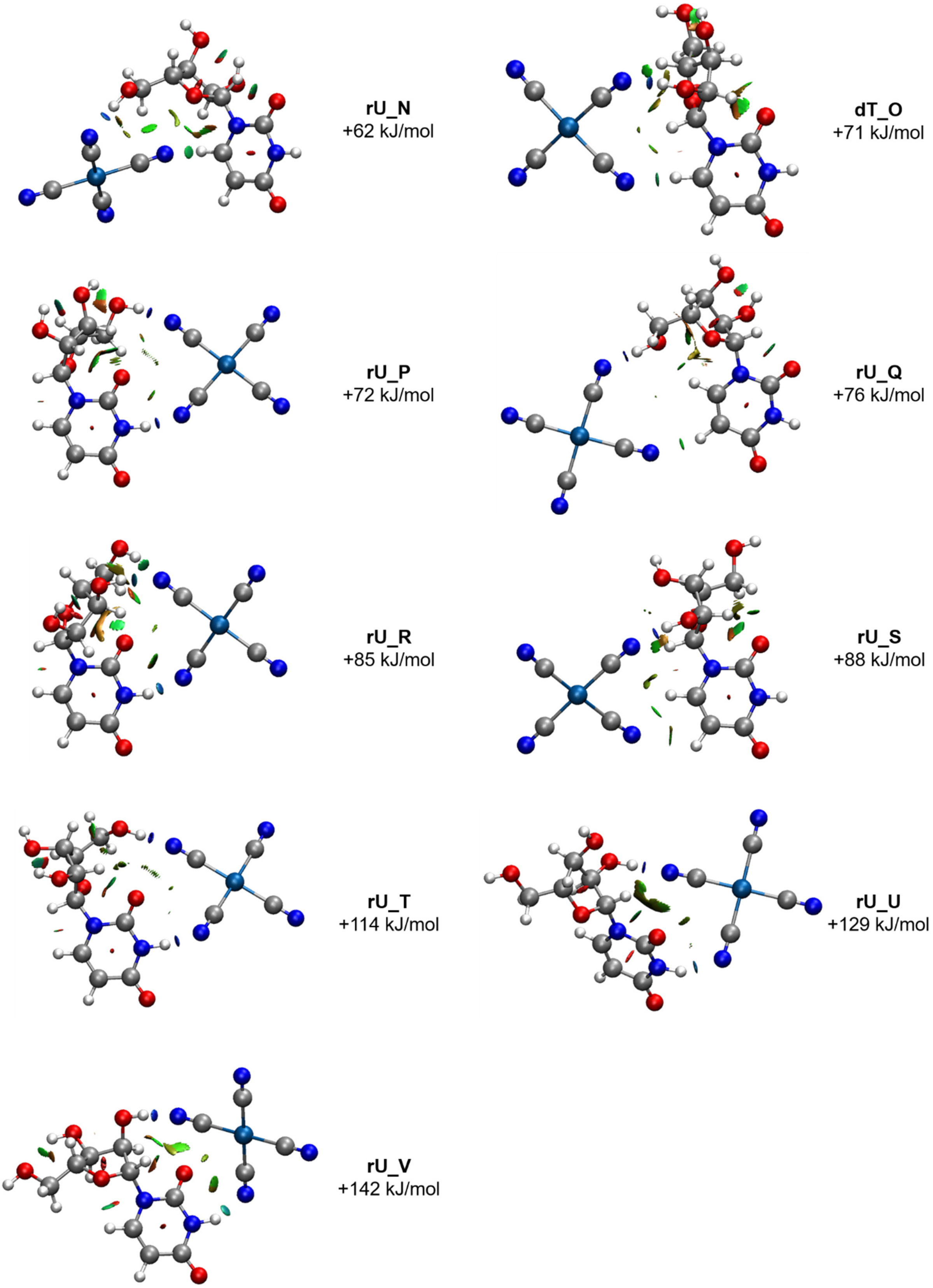

Figure S17: DFT/B3LYP (aug-cc-pVDZ (C, H, N, O); Stuttgart 1997 ECP (Pt)) calculated less stable minimum structures and NCI plots of Uridine – $Pt(CN)_4^{2-}$ aggregates **rU_N** to **rU_V**.

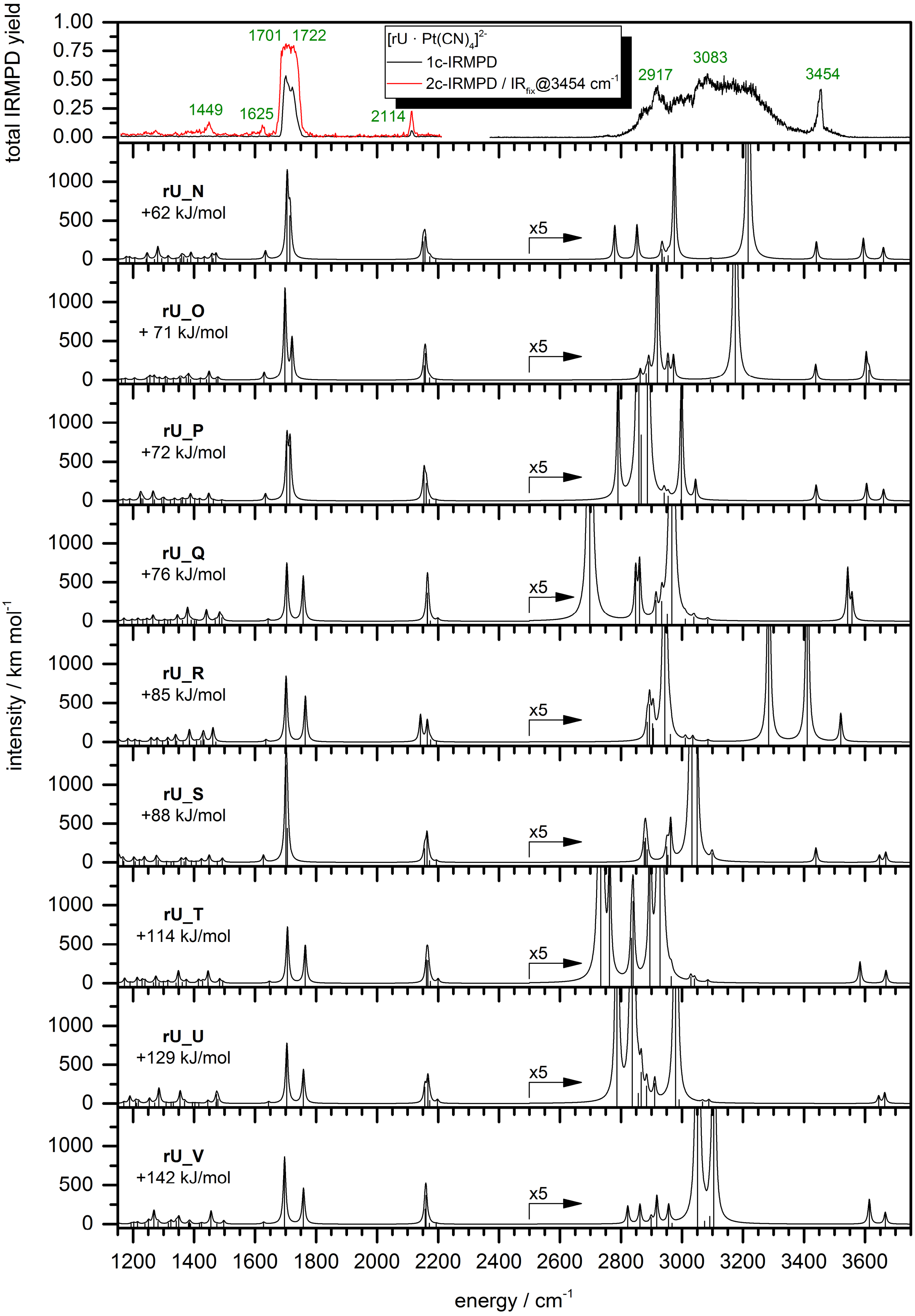

Figure S18: Experimental one and two color IRMPD spectrum of the Uridine – $Pt(CN)_4^{2-}$ aggregate (probe frequency: 3454 cm^{-1}) in comparison to the DFT calculated harmonic absorption spectra of the less stable minimum structures (cf. Fig. S17). Note, that above 2500 cm^{-1} the intensities of the calculated spectra are multiplied by a factor of 5.

6 Gas Phase Structure of Fluorescein, 2,7-Dichlorofluorescein and 5-Nitrofluorescein Ions by Infrared Multiple Photon Dissociation Spectroscopy and Density Functional Theory

Joachim M. Hewer, Sebastian Becker, Dimitri Imanbaew and Gereon Niedner-Schatteburg

Fachbereich Chemie and Forschungszentrum OPTIMAS, Kaiserslautern, Germany

6.1 Preamble

The following chapter is prepared as a manuscript for publication. I conducted the infrared multiple photon dissociation (IRMPD) experiments, data evaluation and the density functional theory (DFT) calculations. I received experimental support by Sebastian Becker. Dimitri Imanbaew helped with discussions and interpreting the data. I wrote the manuscript and revised it with the help of Gereon Niedner-Schatteburg.

6.2 Abstract

Fluorescein and its derivatives are prominent fluorescent dyes known for almost 150 years. The photophysical properties strongly depend on respective functionalization groups and the examined prototropic form. We report an IRMPD spectroscopic study of isolated gas phase fluorescein [F], 2’,7’-dichlorofluorescein [DCF] and 5-nitrofluorescein [5NF] in the dianionic, monoanionic and cationic form for structural elucidation. The infrared multiple photon dissociation (IRMPD) experiments are conducted using a two-color excitation scheme, to reveal dark bands and overcome intramolecular vibrational redistribution (IVR) bottlenecks The experimental data are supported by density functional theory (DFT) calculations in terms of geometry optimization, harmonic vibrational spectra, relative energies and rotational barriers. The experimental spectra are in an excellent agreement with the calculated harmonic spectra. The assigned gas phase structures are strongly correlated to the relative energies of different isomers in the gas phase and in the solution.

6.3 Introduction

Fluorescein (F) was first synthesized by Adolf von Baeyer in 1871, using phthalic anhydride and resorcinol.[1] Owing to its bright fluorescence and the feasibility of functionalization fluoresceins have been extensively studied, characterized and are used in a large variety of applications.[2-14] One of the most valuable application of fluorescein derivatives like fluorescein isothiocyanate is the labelling of proteins in medical diagnostics.[6, 14] The major drawbacks of fluorescein are the deactivation by photobleaching and the strong dependence of the fluorescence on solvent properties and pH level even in the physiological area.[9, 15] Much effort has been spent in the development of more robust dyes based on fluorescein. For example, 2’,7’-dichlorofluoescein (DCF) is more photostable has a much lower pK_a value and is hence less dependent on the pH level at equal fluorescence properties.[16] It has been used in various fields, for example as an acid/alkaline indicator[17, 18], reactant in free radical reactions[19], fluorescent probe in micellar examination[20, 21] and in the analysis of oxidative stress[22-26]. 5-Nitrofluorescein (5NF) instead has a much less pronounced fluorescence.[27] The electron withdrawing nitro group causes a redshift of the absorption and emission maxima by rendering the positive charge of the phenyl and an electric attraction to the xanthene, stabilizing the xanthene unit and decreasing the HOMO-LUMO energy gap.[28]

The fluorescence properties e.g. lifetime and quantum yield of fluorescein derivatives are not only correlated to the respective functionalization groups but are also highly sensitive to the prototropic form. There are four prototropic forms for fluoresceins conceivable in solution: the dianion, the monoanion, the neutral and the cation.[9, 26] The dianions represent the most fluorescent prototropic forms, exhibiting quantum yield of 0.92 ([F])[9, 26, 29, 30], 0.88 ([DCF])[26, 31] and 0.29 ([5NF])[32] ([F] and [DCF] in water, [5NF] in methanol). The monoanions have a noticeably lowered quantum yield in aqueous solution: 0.37 ([F]) and 0.17 ([DCF]) due to the alterated molecular geometry and electron structure compared to the dianion.[9, 26, 29-31] The monoanions provide two different tautomeric forms depending on the respective protonation site at the xanthene carbonyl groups or at the benzoate unit. Raman and FTIR spectroscopies of fluorescein in solution suggest the protonation site at the xanthene unit to prevail.[33] Investigations on fluorescein by the Jockusch lab using potodissociation (PD) spectroscopy, infrared multiple photon dissociation (IRMPD) spectroscopy and fluorescence spectroscopy present strong evidence for the benzoate protonation site to be dominant in the gas phase.[26, 34, 35]

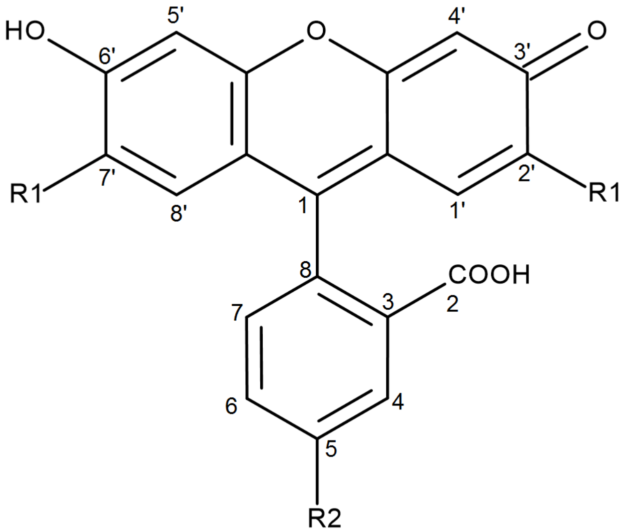

Figure 1: General depiction of the investigated fluorescein derivatives displaying the atom numbering.

In the present study, we report as well on IRMPD spectroscopy in combination with density functional theory (DFT) on the charged prototropic forms of [F], [DCF] and [5NF] (cf. Fig.1, Tab. 1). IRMPD spectroscopy has proven valuable in studying isolated molecules and ions like complexes, amino acids etc.[36-39]

We expand the spectral range, using a LaserVision optical parametric oscillator/amplifier system covering the spectral range from approx. 1000 – 4000 cm^{-1} including the OH-stretching region. DFT calculations support the experimental data regarding harmonic absorption spectra of geometry optimized minimum structures, relative energies in the gas phase and in solution and rotational barriers.

Table 1: Key to the fluorescein derivatives depending on substituents R1 and R2 (refer to Fig. 1).

R1	R2	Species	Abbreviation
-H	-H	Fluorescein	[F]
-Cl	-H	2',7'-Dichlorofluorescein	[DCF]
-H	-NO_2	5-Nitrofluorescein	[5NF]

6.4 Experimental and Computational methods

A detailed description of the experimental setup has been published elsewhere.[36] The ionic species were generated via Electrospray Ionization (ESI) from a solution of fluorescein, 2',7'-dichlorofluorescein and 5-nitrofluorescein in methanol (MeOH) at a concentration of approximately 1 mmol/L. The respective solutions were infused continuously into the ESI chamber using a syringe pump at a flow rate of approx. 3 µL/min. Nitrogen was used as nebulizer gas at a pressure of 7 to 8 psi and as a drying gas with a temperature of 200 °C and a flow rate of 2 L/min. The electrospray needle was held at 4.5 kV. All IRMPD experiments were performed using a modified PAUL-type ion trap mass spectrometer (AmaZon SL, Bruker Daltonics). The ion source was operated in the positive (for the cationic species) and negative (for the monoanionic and dianionic) electrospray ionization mode. The scan speed was 13000 m/z per second with a resolution of 0.3 FWHM, the scan range was at least from 50 to 700 m/z. The Instrument was controlled by the *BrukerTrapControl 7.0* software, data analysis was performed with *BrukerDataAnalysis 4.0* software.

A KTP/KTA (KTP = potassium titanyl phosphate; KTA = potassium titanyl arsenate) optical parametric oscillator/amplifier (OPO/OPA, *LaserVision*) system, pumped by a pulsed 10 Hz injection seeded Nd:YAG laser (*PL8000, Continuum*) was used as a source of tunable IR radiation ($\delta\tilde{\nu}$ = 0.9 cm^{-1}, δt = 7 – 10 ns) for recording the vibrational spectra. The idler wave (≤ 10 mJ per pulse) was used to record the spectra in the range of 2500 – 3700 cm^{-1}. The difference frequency generated (DFG) radiation in an $AgGaSe_2$ crystal (≤ 2 mJ per pulse) was applied in the range of approx. 1100 – 2000 cm^{-1}. The idler radiation was focused by a calcium fluoride (CaF) lens with a focal length of 50 cm. The DFG beam was focused by a parabolic mirror with a focal length of 15 cm. The two-color (2c) IRMPD experiments were facilitated using a second IR OPO/A system set to a selected vibrational resonance frequency. The respective idler radiation was focused by a calcium fluoride (CaF) lens with a focal length of 75 cm. The frequency fixed laser pulses were irradiated with a delay of 100 ns with respect to the first scanning IR laser. The IR spectra were measured as ion chromatograms while continuously scanning the IR laser frequency. The IRMPD spectra are achieved by plotting the total IRMPD yield (*Y(v)*) as a function of the IR laser frequency:

$$Y(v) = \frac{\sum_i I_i^{fr}}{\sum_i I_i^{fr} + \sum_i I_i^{pr}}$$

where I_i^{fr} and I_i^{fr} represent the respective ion intensities of fragment and parent ions. The IR frequency was calibrated using a wave meter (*821B-NIR*, *Bristol Instruments*). The IR beam intensity was detected by a power meter after passing through the ion trap. The spectra were not normalized due to the intrinsically nonlinear power dependencies of IRMPD yields.

The minimum energy structures, transition states and linear IR absorption spectra were calculated at the DFT/B3LYP[40-42] level of theory, using the 6-311++G**[43] (C, H, N, O) and 6-31++G**[44] (Cl) basis sets as implemented in the *Gaussian 09* program package.[45] All geometry optimized isomers represent true energy minima since they were checked for the absence of imaginary vibrational frequencies. The harmonic vibrational frequencies of the stretching modes (> 2500 cm^{-1}) were scaled by a factor of 0.954. All other frequencies (< 2500 cm^{-1}) were scaled by a factor of 0.978. The line spectra were deconvoluted by *Gabedit* software using a Lorentzian function with FWHM = 5 cm^{-1}.[46] The free energy of the geometry optimized minimum structures in methanolic solution were determined taking into account solvent effects by means of the self-consistent reaction field method (SCRF) with the polarized continuum (PCM) model.[47-50]

6.5 Results and Discussion

All ionic species were generated via Electrospray Ionization. The gas phase structure of the dianions, anions and cations is elucidated by comparison of experimental one (1c) and two color (2c) IRMPD spectra with calculated harmonic vibrational spectra of geometry optimized minimum structures. In most cases IRMPD spectra depend non-linearly on the laser photon flux.[36] Incoherent multiple photon absorptions cause IRMPD bands to become broad, shifted or deformed.[51, 52] The low density of states in small molecular systems can hinder the internal vibrational redistribution (IVR) and can together with anharmonicities result in a bottleneck for numerous photon absorption, thus for dissociation.[36, 53] The large heat capacities in large molecules may require higher laser power for weaker bands to become visible.[54] Diverse experimental multi-excitation schemes have been suggested for compensation.[55-58] An example for a two-color (2c) excitation scheme revealing several additional bands has already been presented.[36] In this study we use a similar 2c-IRMPD technique for the cationic species. The dianionic and monoanionic species fragment easily upon infrared photon irradiation due to the accessible fragmentation channels like electron detachment and loss of carbon dioxide. The fragmentation pattern of the cationic species is much more complicated compared to those of the anions. We assume this to originate from significantly increased fragmentation enthalpies or/and fragmentation transition states. Due to the complicated fragmentation pattern of the cations, we are not able to calculate these enthalpies/transition states. The fragmentation patterns of all ionic species is in agreement with the findings of JOCKUSCH *et al.* using IRMPD and photodissociation spectroscopy (cf. Tab. S1).[26, 34, 35]

6.5.1 Dianions

6.5.1.1 Fluorescein Dianion

Geometry optimization of the dianionic species of fluorescein ($[F\text{-}2H]^{2-}$) via DFT (B3LYP/6-311++G**) yielded a single minimum structure **$[F\text{-}2H]^{2-}$_A** (cf. Fig. 2). Both hydroxyl groups at the xanthene ring and the benzoic acid moiety are deprotonated. The structure is symmetric and provides a planar xanthene unit perpendicular connected to the planar benzoate plane.

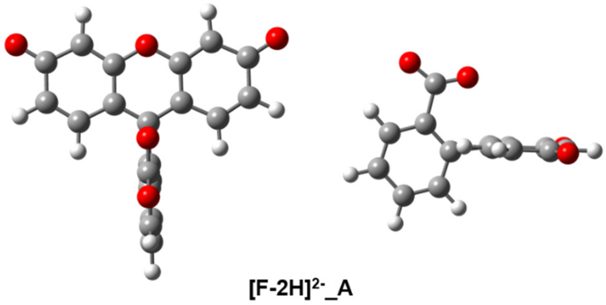

$[F\text{-}2H]^{2-}$_A

Figure 2: Calculated minimum structure of dianionic fluorescein $[F\text{-}2H]^{2-}$ (C: gray, O: red, H: white). Left: Topview. Right: Sideview.

The experimental one color IRMPD spectrum in the range of 1200 – 1850 cm^{-1} is shown in Fig. 3. It shows at least six significant absorption bands at 1352, 1377, 1477, 1578, 1628 and 1639 cm^{-1}. The absorption at 1639 cm^{-1} is assigned to the asymmetric CO stretching vibration of the benzoate moiety $\nu_{as}(CO_b)$, the more intense peak at 1628 cm^{-1} is assigned to a combination of $\nu_{as}(CO_b)$ and a CC stretching mode of the xanthene ring $\nu(CC_x)$. The intense and broad absorption band at 1578 cm^{-1} with a shoulder to lower photon energies represents a vibrational mode involving $\nu(CC_x)$ and an asymmetric stretching vibration of the CO groups of the xanthene ring $\nu_{as}(CO_x)$. The shoulder is assigned to the symmetric CO stretching mode in

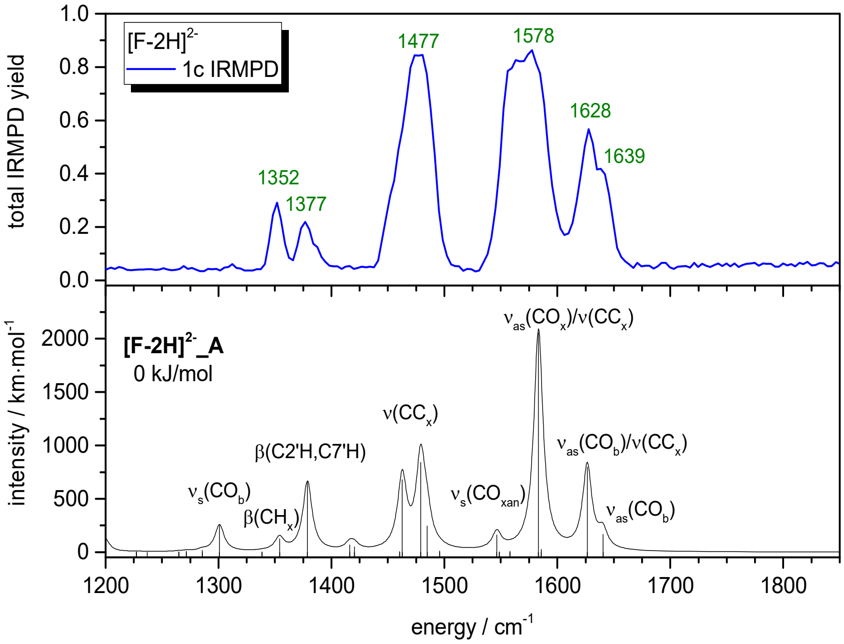

Figure 3: Experimental one color IRMPD spectrum of dianionic fluorescein $[F\text{-}2H]^{2-}$ in comparison to the calculated harmonic absorption spectrum of the minimum structure **$[F\text{-}2H]^{2-}$_A**.

the xanthene moiety $\nu_s(CO_{xan})$. The resolution of the experimental spectrum does not resolve the distinct peaks due to saturation effects based on too high photon flux in the experiment. The broad absorption at 1477 cm^{-1} can be assigned to the calculated double peak at approx. 1463 and 1473 cm^{-1} representing CC stretching modes of the xanthene ring. Two peaks at 1377 and 1352 cm^{-1} are well represented by CH bending modes in the calculated harmonic absorption spectrum (β(C2'H,C7'H) and $\beta(CH_x)$). The symmetric CO stretching mode of the benzoate $\nu_s(CO_b)$ provides a low intensity in the calculated spectrum and is not pronounced in the experimental spectrum. However, the spectral signature of the experiment fits the calculated harmonic absorption spectrum very well.

6.5.1.2 2',7'-Dichlorofluorescein Dianion

The DFT geometry optimization (B3LYP/6-311++G**(C, H, O)/6-31++G**(Cl)) of the dianionic twofold chlorine substituted fluorescein derivative in positions 2' and 7' ($[DCF\text{-}2H]^{2-}$) yields a single minimum structure (**$[DCF\text{-}2H]^{2-}$_A**) as well (cf. Fig. 4). The structure is likewise symmetric.

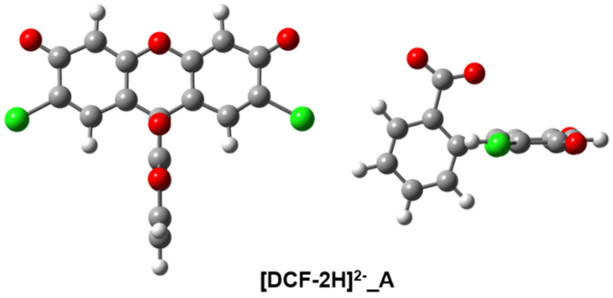

Figure 4: Calculated minimum structure of dianionic 2’,7’-dichlorofluorescein $[DCF\text{-}2H]^{2-}$ (C: gray, O: red, H: white, Cl: green). Left: Topview. Right: Sideview.

The experimental one color IRMPD spectrum in comparison to the calculated harmonic vibrational absorption spectrum of **$[DCF\text{-}2H]^{2-}$_A** is shown in Fig. 5. The IRMPD spectrum shows six absorption bands at 1315, 1364, 1486, 1578, 1626 and 1648 cm^{-1}. The overall signature of the experimental and calculated spectra is very similar to those of $[F\text{-}2H]^{2-}$, apart from the relative band intensities. The bands at 1648 and 1626 cm^{-1} are assigned to the asymmetric CO stretching vibration of the benzoate $\nu_{as}(CO_b)$ in combination with a xanthene CC stretching mode $\nu(CC_x)$. The broadened absorption band at 1578 cm^{-1} with a shoulder to lower photon energies is assigned to the most intense asymmetric CO stretching vibration in combination with CC stretching vibrations in the xanthene moiety. The calculated symmetric CO stretching vibration in the xanthene moiety has low intensity and is represented as shoulder by the asymmetric shape of the peak at 1578 cm^{-1}. The calculated xanthene CC stretching vibrations between 1450 and 1500 cm^{-1} are reported by the asymmetric shaped peak at 1486 cm^{-1} in the IRMPD spectrum. The CH bending modes at approx. 1310 and 1365 cm^{-1} are represented well by the peaks at 1364 and 1315 cm^{-1} in the experimental IRMPD spectrum. The low intensity of the peak at 1315 cm^{-1} can be explained by the decreasing laser power at lower photon energies. In general, the peak positions and intensities fit the calculated harmonic vibrational absorption spectrum remarkably well.

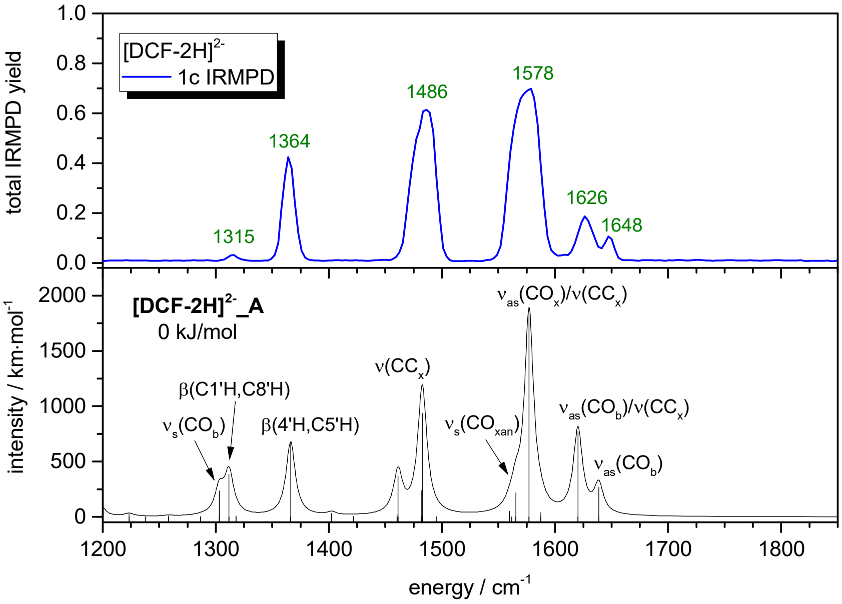

Figure 5: Experimental one color IRMPD spectrum of dianionic 2',7'-dichlorofluorescein $[DCF\text{-}2H]^{2-}$in comparison to the calculated harmonic absorption spectrum of the minimum structure **$[DCF\text{-}2H]^{2-}$_A**.

6.5.1.3 5-Nitrofluorescein Dianion

The geometry optimized structure of dianionic 5-nitrofluorescein is shown in Fig. 6. Also here, geometry optimization via DFT (B3LYP/6-311++G**) resulted in a single minimum structure **$[5NF\text{-}2H]^{2-}$_A**.

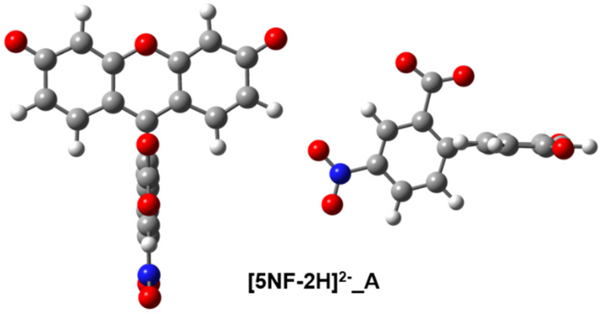

Figure 6: Calculated minimum structure of dianionic 5-nitrofluorescein $[5NF\text{-}2H]^{2-}$ (C: gray, O: red, H: white, N: blue). Left: Topview. Right: Sideview.

The one and two color IRMPD spectra in comparison to the calculated harmonic vibrational absorption spectrum of **$[5NF\text{-}2H]^{2-}$_A** is shown in Fig. 7. In the two color experiment, the frequency fixed IR laser was irradiated at the CH stretching absorption at 3044 cm^{-1} with a delay of 100 ns subsequent to the scanning laser (cf. Chapter 2). The two color IRMPD spectrum shows a slightly increased fragmentation yield for all absorptions. Additional or dark bands could not be revealed. The spectra show seven absorption bands in the region of 1200 – 1800 cm^{-1}. The absorption bands at 1657 and 1628 cm^{-1} are assigned to the asymmetric CO stretching vibrations of the benzoate in combination with CC stretching vibrations of the xanthene moiety ($\nu_{as}(CO_b)$ and $\nu(CC_x)$). The intense absorptions at 1580 and 1560 cm^{-1} are assigned to the asymmetric and symmetric CO stretching mode of the carbonyl groups of the xanthene plane ($\nu_{as/s}(CO_x)$ and $\nu(CC_x)$). The broad peak at 1485 cm^{-1} represents two calculated intense CC stretching modes in the xanthene moiety $\nu(CC_x)$. The measured peak at 1376 cm^{-1} represents an intense CH bending mode β(C2'H,C7'H) and the peak at 1354 cm^{-1} presumably represents the symmetric NO and CN stretching mode of the nitro group $\nu_s(NO)$ / $\nu(CN)$. The calculated harmonic absorption spectrum is well represented by the one and two color IRMPD spectra.

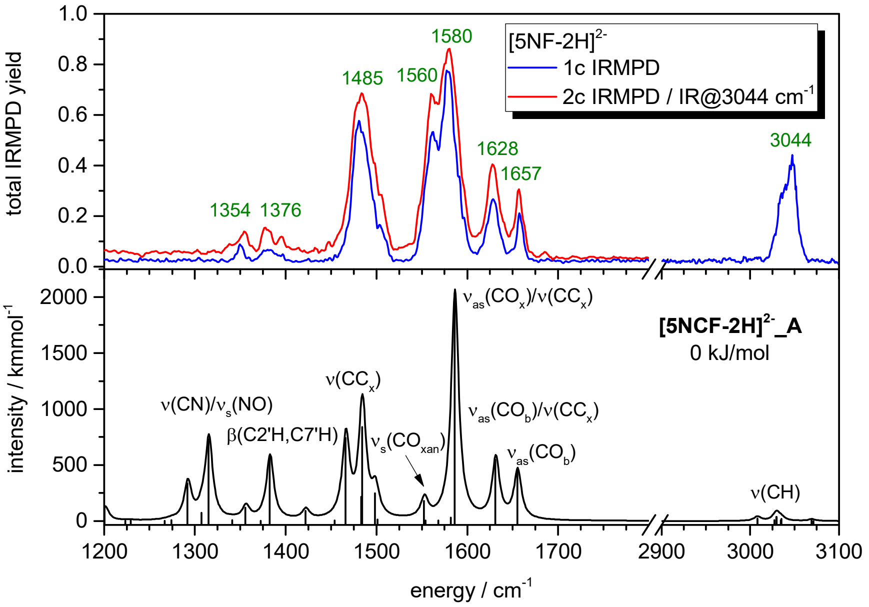

Figure 7: Experimental one and two color IRMPD spectrum of dianionic 5-nitrofluorescein $[5NF\text{-}2H]^{2-}$ in comparison to the calculated harmonic absorption spectrum of the minimum structure **$[5NF\text{-}2H]^{2-}$_A**.

The calculated minimum structures of the dianionic species of all fluorescein derivatives are very similar, due to their lack in conformational degrees of freedom. They all provide a planar xanthene unit perpendicularly connected to plane of the benzoate unit. The positions and relative intensities of the peaks of the scaled harmonic absorption spectra are very well represented by the one and two color IRMPD spectra. These findings are in good agreement with the free electron laser (FEL) IRMPD measurements reported by YAO *et al.*.[26]

6.5.2 Cations

The cationic species of fluorescein, 2',7'-dichlorofluorescein and 5-nitrofluorescein ($[F+2H]^+$, $[DCF+2H]^+$, $[5NF+2H]^+$) are protonated at both xanthene carbonyl groups and the benzoic acid unit. The resulting hydroxy groups provide many possible conformational isomers, by rotation of the hydroxy groups and the COOH group. Only the most stable isomers are discussed in the main text. For less stable minimum structures and harmonic vibrational absorption spectra see Figs. S1 – S6.

6.5.2.1 Fluorescein cation

The DFT based geometry optimization calculations of the cationic fluorescein species $[F+H]^+$ resulted in twelve minimum structures **$[F+H]^+$_A** – **$[F+H]^+$_L**. Due to energetic considerations, only **$[F+H]^+$_A** to **$[F+H]^+$_F** are discussed in the following.

The minimum structures **$[F+H]^+$_A** to **$[F+H]^+$_F** only differ in the relative orientation of the hydroxy protons (cf. Fig. 8). They can be divided into two sets of isomers (**$[F+H]^+$_A** to **$[F+H]^+$_C** and **$[F+H]^+$_D** to **$[F+H]^+$_F**, respectively), which are close in energy. The relative orientation of the COOH group is equal in each set of isomers. The protonation of the COOH oxygen atom opposite to the xanthene unit is energetically favorable. The isomers in the individual sets differ in the relative orientation of the hydroxy protons of the xanthene moiety. In all isomers, the OH group is in one plane with the xanthene moiety. The difference of < 1 kJ / mol shows, that there is no energetically prevailing isomer in the cationic species of unsubstituted fluorescein.

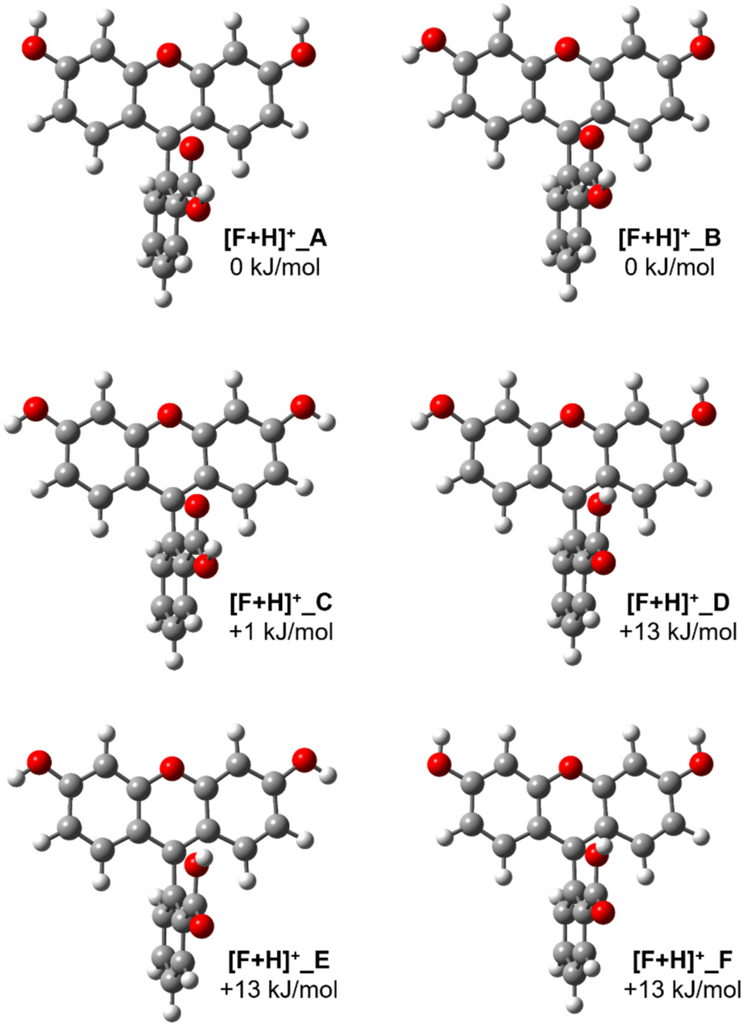

Figure 8: The six most stable minimum structures **$[F+H]^+$_A** to **$[F+H]^+$_F** of the cationic species of fluorescein $[F+H]^+$ calculated by DFT/B3LYP.

The experimental one and two color IRMPD spectra of $[F+H]^+$ in comparison to calculated harmonic absorption spectra of the six energetically most stable isomers is shown in Fig. 9. All calculated spectra are very similar, since the only conformational degrees of freedom are given by rotation of the hydroxy groups of the xanthene unit and the rotation around the CC axis in the benzoic acid unit. Major differences are restricted to the spectral region below 1300 cm^{-1}. The experimental spectra show two peaks at 3617 and 3576 cm^{-1} in the OH stretching region. The intense peak at 3617 cm^{-1} is assigned to the symmetric and asymmetric stretching modes of the hydroxy groups in the xanthene unit. The peak at 3576 cm^{-1} is assigned to the OH stretching mode of the benzoic acid unit. The one color IRMPD spectrum in the region from 1000 – 1850 cm^{-1} shows no significant absorption. Though, with the two color technique at least nine bands in the region from 1191 to 1746 cm^{-1} are revealed. Due to

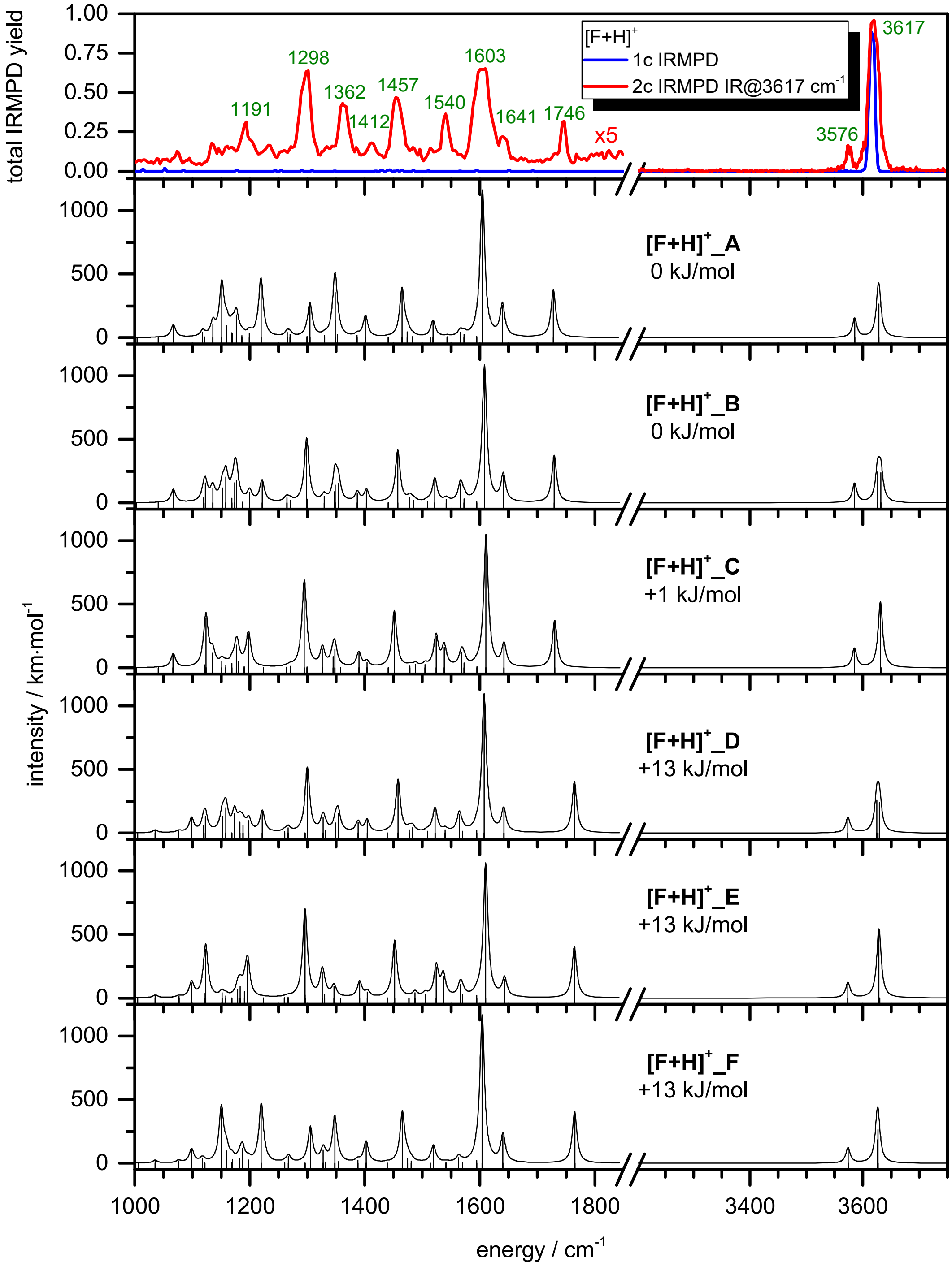

Figure 9: Experimental one and two color IRMPD spectrum of cationic fluorescein [F+H]$^+$ in comparison to the calculated harmonic absorption spectra of the six most stable minimum structures **[F+H]$^+$_A** to **[F+H]$^+$_F**. Note, that the intensity of the two color IRMPD spectrum < 1850 cm^{-1} is multiplied by a factor of 5.

the lack of significant differences in the calculated harmonic spectra, we will not discuss the region from 1000 – 1850 cm^{-1} in detail. But we state, that the spectral signature of the two color IRMPD spectrum fits the calculated harmonic spectra very well. Due to the difference of approx. 13 kJ / mol, the population of isomers **[F+H]$^+$_D** to **[F+H]$^+$_F** can be neglected under our experimental conditions. The distinction between the population of **[F+H]$^+$_A, [F+H]$^+$_B** and **[F+H]$^+$_C** based on the IRMPD spectra is not possible, due to the similar harmonic absorption spectra. An even population of all three isomers appears likely.

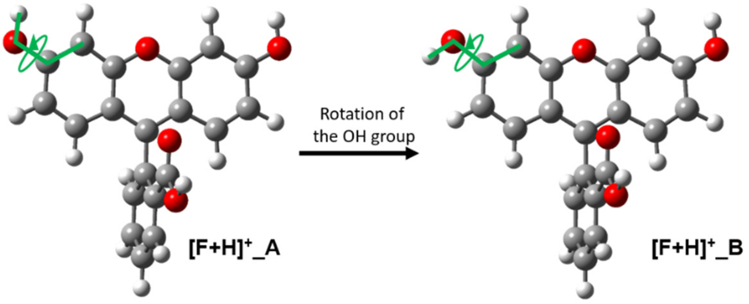

Figure 10: Definition of the dihedral angle for the rotation of the hydroxy group of the xanthene ring in cationic [F+H]$^+$ isomers. Rotation by 180° converts **[F+H]$^+$_A** into **[F+H]$^+$_B**.

In order to check for a conversion from one isomer to the other in the gas phase we calculate the rotational barrier of the hydroxy groups of the xanthene ring. We define the respective dihedral angle (cf. Fig. 10) and calculate a potential energy surface (PES, in terms of single point calculations without geometrical relaxation) for the rotation around the CO bond. A rotation by 180° converts **[F+H]$^+$_A** into **[F+H]$^+$_B**. Additionally, we calculate the transition states at 90° and 270° to determine a more reliable barrier height.

The calculated potential energy surface for the rotation of the hydroxy group is shown in Fig. 11. The barrier height obtained by single point calculations amounts 33 kJ / mol. The transition state calculated with geometrical relaxation yields a barrier height of only 28 kJ / mol. The PES at 180° identifies Isomer **[F+H]$^+$_B** as minimum structure but it is described less stable by 8 kJ / mol. From energetic considerations we can conclude, that at our experimental conditions (300 – 450 K, 10^{-4} mbar He) a conversion of one isomer into the other is doubtful. It is more likely, that **[F+H]$^+$_A**, **[F+H]$^+$_B** and **[F+H]$^+$_C** are populated already in solution and are transferred into the gas phase by the ESI. Furthermore, a conversion during the ESI process is also conceivable.

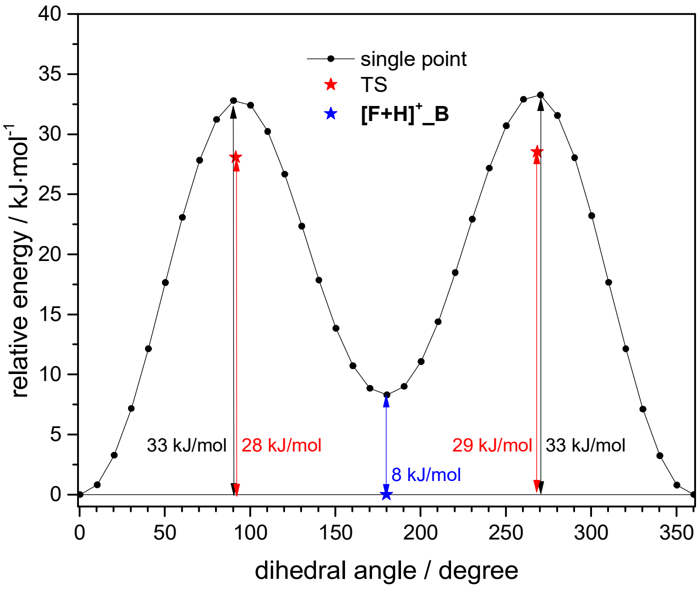

Figure 11: Potential energy surface for the rotation of the hydroxy group of the xanthene ring of **[F+H]$^+$_A**. The single point calculations result in a rotational barrier of 33 kJ/mol. The transition state (TS) calculations result in an effective rotational barrier of 28 and 29 kJ/mol, respectively. The relative energy of isomer **[F+H]$^+$_B** is not represented satisfactorily in the single point calculations.

6.5.2.2 2',7'-Dichlorofluorescein cation

The DFT based geometry optimization calculations on the substituted cationic 2',7'-dichlorofluorescein species [DCF+H]$^+$ resulted in eleven minimum structures **[DCF+H]$^+$_A** – **[F+H]$^+$_K**. Due to energetic considerations, only **[DCF+H]$^+$_A** to **[DCF+H]$^+$_E** are discussed in the following.

The two already stated only possible conformational degrees of freedom are again represented by the rotation of the hydroxy groups of the xanthene unit and the rotation of the COOH group of the benzoic acid around the CC bond. The five most stable minimum structures of cationic 2',7'-dichlorofluorescein obtained by DFT geometry optimization are shown in Fig. 12. Here again, the minima can be divided in two groups, with similar orientation of the COOH group. In **[DCF+H]$^+$_A, [DCF+H]$^+$_B** and **[DCF+H]$^+$_D** the acidic proton is bound to the oxygen atom opposite to the xanthene unit. In **[DCF+H]$^+$_C** and **[DCF+H]$^+$_E** the acidic proton is bound to the oxygen atom neighboring the xanthene unit. In between the minima sets, the relative orientation of the xanthene hydroxy groups varies. In DCF, the chlorine atoms in positions 2′ and 7′ interact with the xanthene hydroxy groups. If the hydroxy proton of the xanthene moiety is oriented towards the chlorine atom, weak hydrogen bonds are formed. The resulting energy gain (+11 kJ / mol) is exhibited in the relative energy of the isomers **[DCF+H]$^+$_A** and **[DCF+H]$^+$_B** with two and one stabilizing OH-Cl hydrogen bond, respectively.

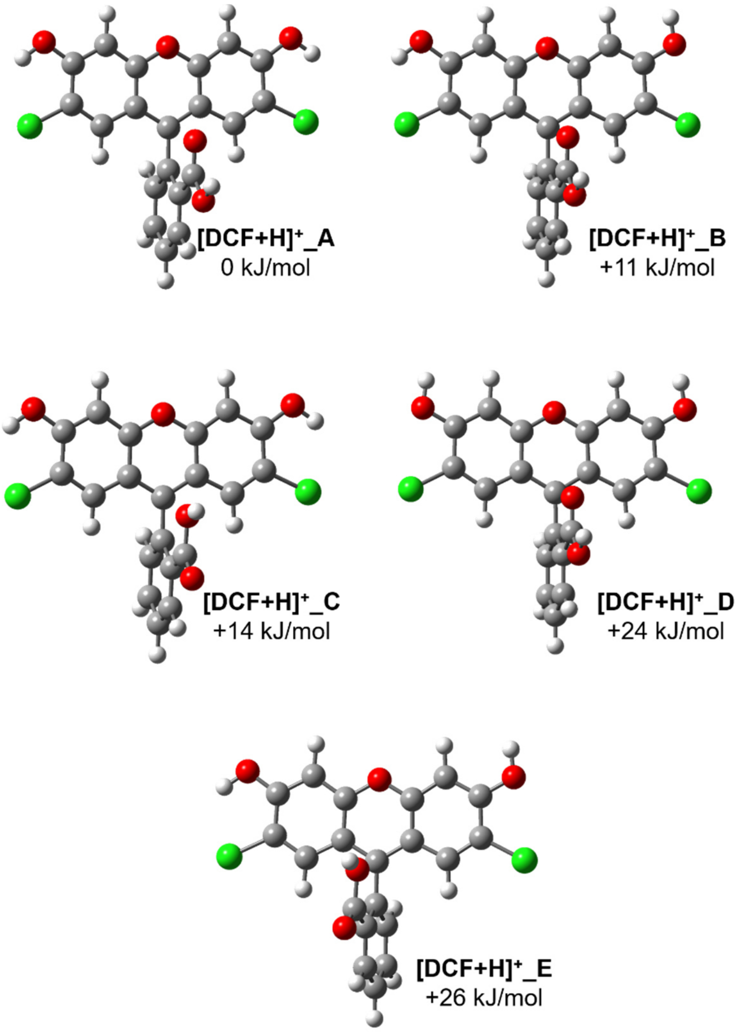

Figure 12: The five most stable minimum structures **[DCF+H]$^+$_A** to **[DCF+H]$^+$_E** of the cationic species of 2′,7′-dichlorofluorescein [DCF+H]$^+$ calculated by DFT/B3LYP.

The experimental one color IRMPD spectrum of [DCF+H]$^+$ in comparison to the calculated harmonic spectra of the five most stable minimum structures is shown in Fig. 13. Significant

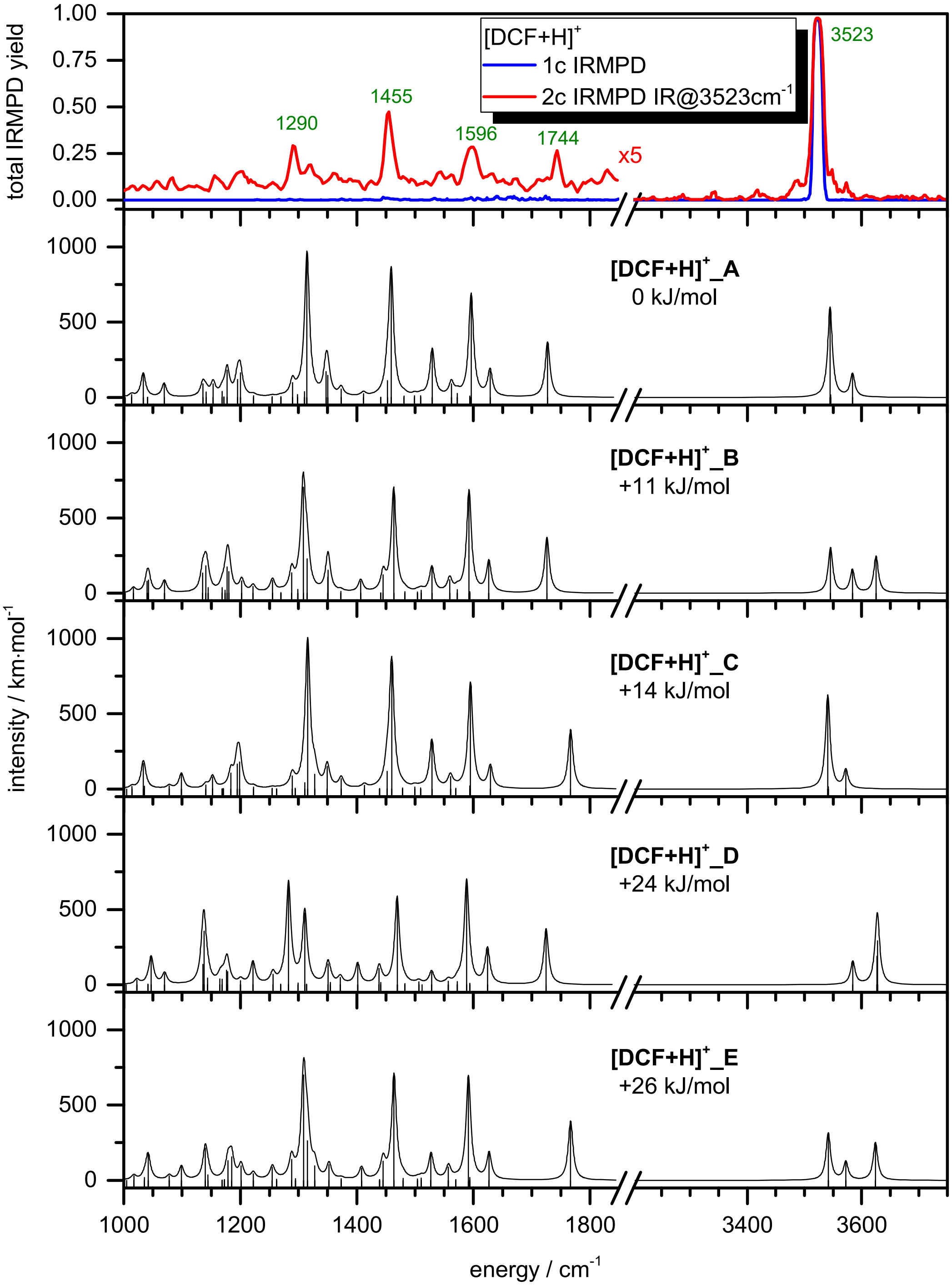

Figure 13: Experimental one and two color IRMPD spectrum of cationic 2’,7’-dichlorofluorescein [DCF+H]$^+$ in comparison to the calculated harmonic absorption spectra of the five most stable minimum structures **[DCF+H]$^+$_A** to **[DCF+H]$^+$_E**. Note, that the intensity of the two color IRMPD spectrum < 1850 cm^{-1} is multiplied by a factor of 5.

differences are visible in the OH stretching region due to the redshift of the OH stretching vibration of hydrogen bound protons. Apart from the relative intensities, the region from 1000 to 1850 cm^{-1} is quite similar for all isomers. The one color IRMPD spectrum shows a single intense absorption at 3523 cm^{-1} (cf. Fig. 13). Due to the stability of the complex, the IR laser power in the region from 1000 to 1850 cm^{-1} induces no fragmentation. Using the two color technique (IR_{fix}@3523 cm^{-1}) several absorption bands at 1290, 1455, 1596 and 1744 cm^{-1} become visible. Unfortunately, the two color IRMPD spectrum in the OH stretching region does not reveal clear additional absorption bands. The intense band at 3523 cm^{-1} is assigned to the OH stretching vibration of the hydrogen bound hydroxy groups of the xanthene unit which appears at approx. 3545 cm^{-1} in the calculated spectra of **[DCF+H]$^+$_A/B/C/E**. Due to the repeated lack of significant differences in the calculated harmonic spectra, we will not discuss the region from 1000 – 1850 cm^{-1} in detail. But we state once more, that the spectral signature of the two color IRMPD spectrum matches the calculated harmonic spectra very well. From energetic considerations, we can assume only isomer **[DCF+H]$^+$_A** to be populated under our experimental conditions.

In order to check for the energetic impact of the OH-Cl hydrogen bonds on a conceivable conversion from isomer **[DCF+H]$^+$_A** into isomer **[DCF+H]$^+$_B**, we calculate the rotational barrier of the OH groups of the xanthene ring. We define the respective dihedral angle (cf. Fig. 14) and calculate an analogous potential energy surface (PES, in terms of single point calculations without geometrical relaxation) for the rotation around the CO bond. A rotation by 180° converts **[DCF+H]$^+$_A** into **[DCF+H]$^+$_B**. Furthermore, we calculate the transition states to determine a more precise barrier height.

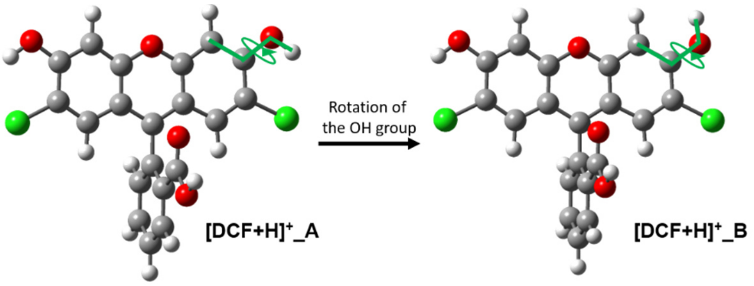

Figure 14: Definition of the dihedral angle for the rotation of the hydroxy group of the xanthene ring in cationic [DCF+H]$^+$ isomers. Rotation by 180° converts **[DCF+H]$^+$_A** into **[DCF+H]$^+$_B**.

The calculated potential energy surface for the rotation of the OH group in $[DCF+H]^+$ is shown in Fig. 15. The barrier height obtained by single point calculations amounts 42 kJ / mol. The transition state calculated with geometrical relaxation yields a barrier height of approx. 37 kJ / mol. The PES at 180° identifies Isomer **$[DCF+H]^+$_B** as minimum structure, but is described less stable by 6 kJ / mol. The interaction of the OH-Cl hydrogen bonds causes the dihedral angles of the transition states structures to change from 90°/270° to approx. 100°/260°. From energetic considerations we can assume, that at the experimental conditions (300 – 450 K, 10^{-4} mbar He) a conversion of isomers is unlikely, resulting in the population of only **$[DCF+H]^+$_A**.

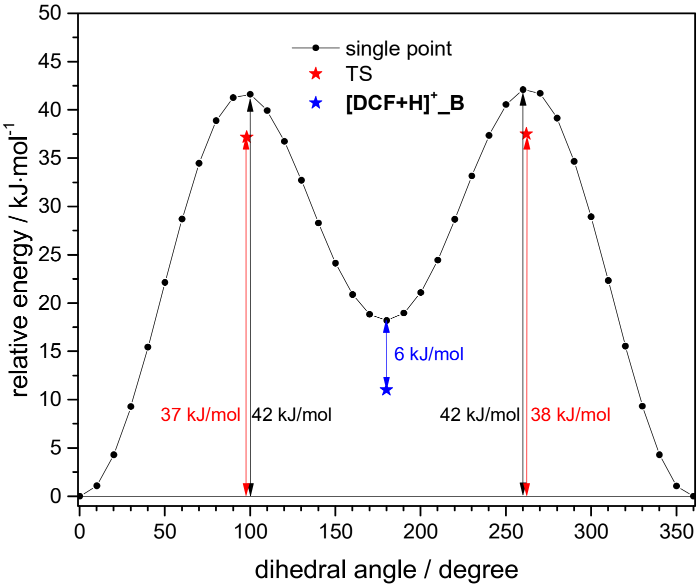

Figure 15: Potential energy surface for the rotation of the hydroxy group of the xanthene ring of **$[DCF+H]^+$_A**. The single point calculations result in a rotational barrier of 42 kJ/mol. The transition state (TS) calculations result in an effective rotational barrier of 37 and 38 kJ/mol, respectively. The relative energy of isomer **$[F+H]^+$_B** is well represented in the single point calculations.

6.5.2.3 5-Nitrofluorescein cation

The DFT based geometry optimization calculations of the substituted cationic 5-nitrofluorescein species $[5NF+H]^+$ resulted in ten minimum structures **$[5NF+H]^+$_A** to **$[5NF+H]^+$_J**. Due to energetic considerations, only **$[5NF+H]^+$_A** to **$[5NF+H]^+$_F** are discussed hereinafter.

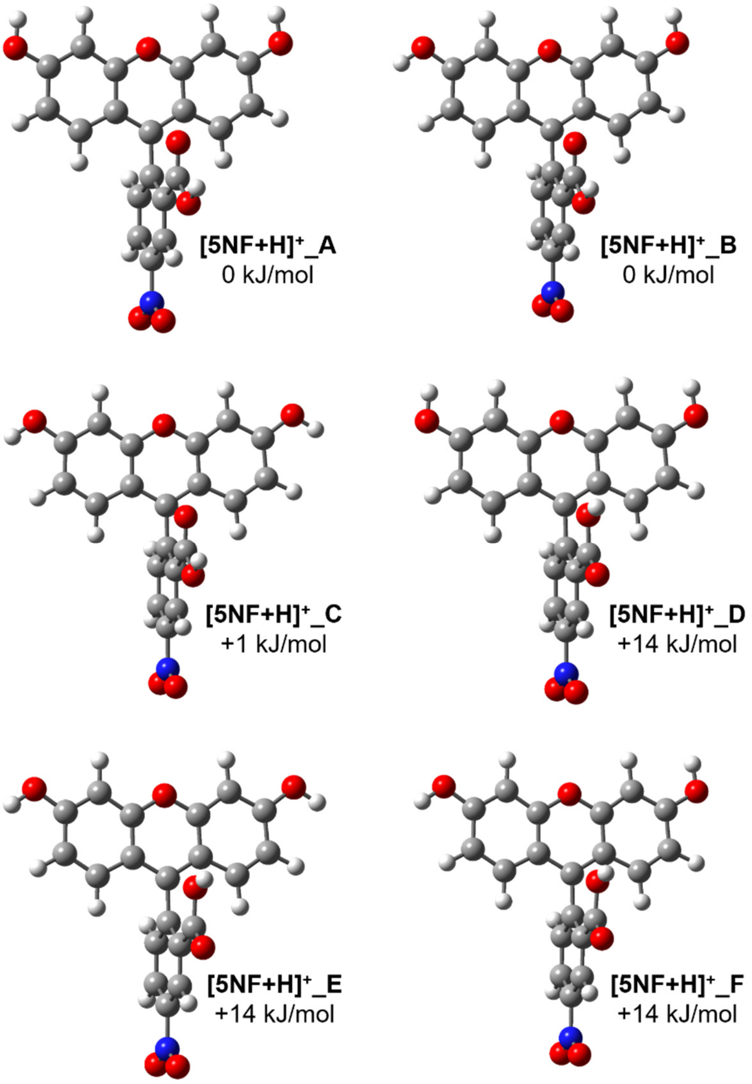

Figure 16: The six most stable minimum structures **[5NF+H]$^+$_A** to **[5NF+H]$^+$_F** of the cationic species of 5-nitrofluorescein [5NF+H]$^+$ calculated by DFT/B3LYP.

The conformational degrees of freedom for variation of the isomers are represented by the rotation of the OH groups of the xanthene unit and the rotation of the COOH group of the benzoic acid around the CC bond. The six most stable minimum structures of cationic 5-nitrofluorescein obtained by geometry optimization via DFT are shown in Fig. 16. As in the case of unsubstituted fluorescein, the minima can be divided in two groups, with similar orientation of the COOH group. In **[5NF+H]$^+$_A**, **[5NF+H]$^+$_B** and **[5NF+H]$^+$_C** the acidic proton is bound to the oxygen atom opposite to the xanthene unit. In **[5NF+H]$^+$_D**, **[DCF+H]$^+$_E** and **[DCF+H]$^+$_F** the acidic proton is bound to the oxygen atom oriented towards the xanthene moiety. In between the minima sets, the relative orientation of the xanthene OH groups

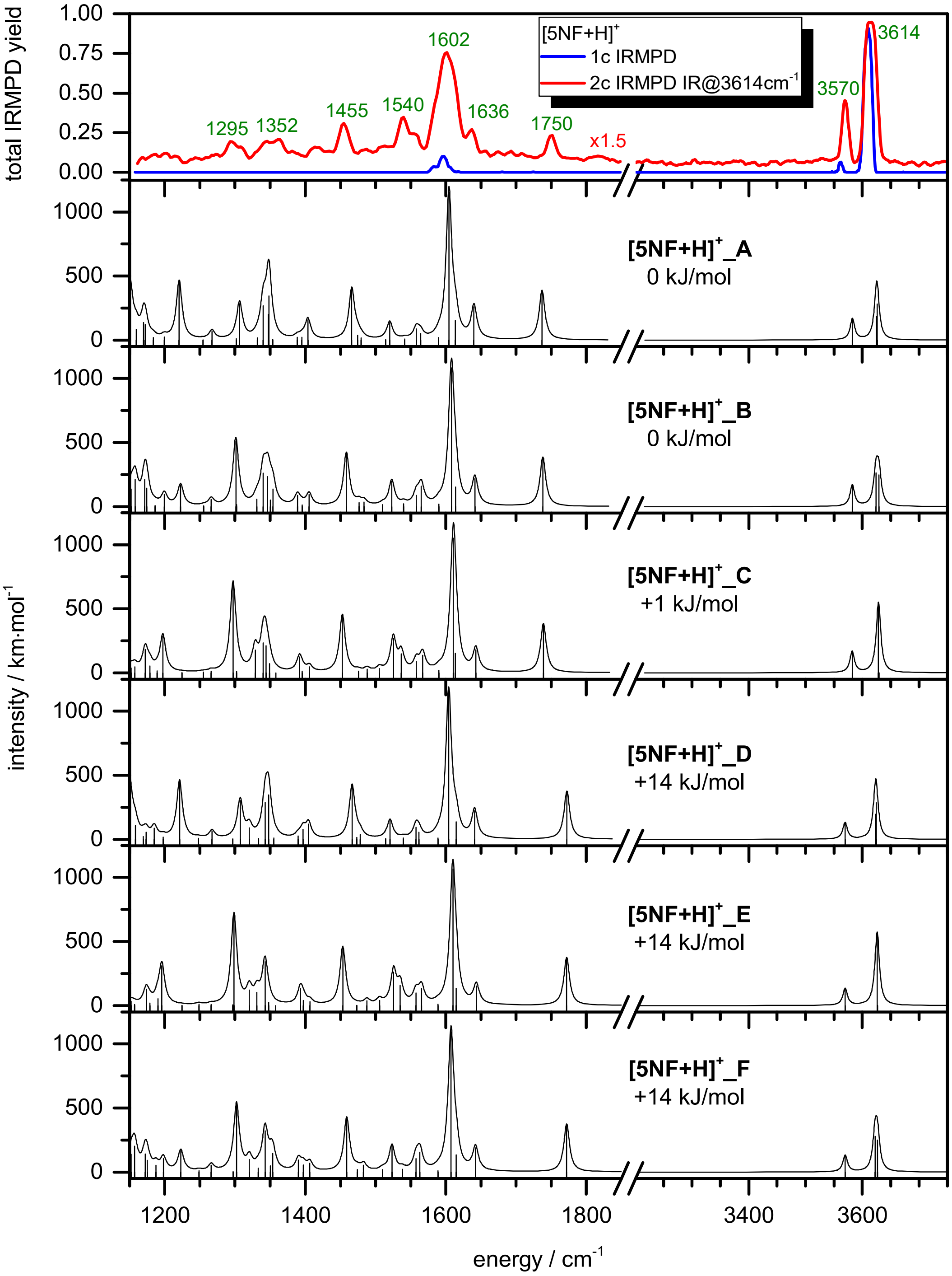

Figure 17: Experimental one and two color IRMPD spectrum of cationic 5-nitrofluorescein [5NF+H]$^+$ in comparison to the calculated harmonic absorption spectra of the six most stable minimum structures **[5NF+H]$^+$_A** to **[5NF+H]$^+$_F**.

changes. There is no hydrogen bond interaction or similar possible in 5NF. As for unsubstituted fluorescein, the individual isomers of each group of isomers are very close in energy

(< 1 kJ / mol). A rotation of 180° around the CC bond between phenyl ring and COOH destabilizes the isomers by 14 kJ / mol.

The experimental one and two color IRMPD spectra of $[5NF+H]^+$ in comparison to the calculated harmonic spectra of the six most stable minimum structures is shown in Fig. 17. Due to the missing interactions of the OH protons to nearby atoms, no significant differences are visible in the calculated harmonic spectra. Apart from the relative intensities, only the regions < 1250 cm^{-1} are different. The one color IRMPD spectrum shows two bands at 3614 and 3570 cm^{-1} in the OH stretching region and one band at 1603 cm^{-1}. Using the two color technique with an additional laser irradiating at 3614 cm^{-1}, at least six further absorptions at 1295, 1352, 1455, 1540, 1636 and 1750 cm^{-1} are revealed. The most intense band at 3613 cm^{-1} is assigned to the OH stretching vibration of the OH groups of the xanthene unit, the band at 3570 cm^{-1} is assigned to the OH stretching vibration of the COOH group. Because of the lack of substantial differences in the calculated harmonic spectra we will not discuss the region from 1000 – 1850 cm^{-1} in detail. Nevertheless, the spectral signature of the two color IRMPD spectrum is in good agreement with the calculated harmonic spectra. Comparing the relative energies the isomers, we assume a uniform distribution of the population of the isomers **$[5NF+H]^+$_A/B/C** under our experimental conditions.

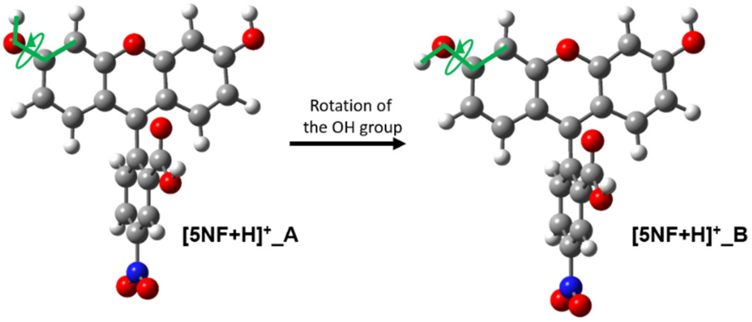

Figure 18: Definition of the dihedral angle for the rotation of the hydroxyl group of the xanthene ring in cationic $[5NF+H]^+$ isomers. Rotation by 180° converts **$[5NF+H]^+$_A** into **$[5NF+H]^+$_B**.

To further investigate a possible energetic impact of the nitro group at the benzoic acid unit on a conversion from isomer **$[5NF+H]^+$_A** into isomer **$[5NF+H]^+$_B/C**, we compute the rotational barrier of the hydroxy groups of the xanthene ring. We define the respective dihedral angle (cf. Fig. 18) and compute the corresponding potential energy surface (PES, in terms of single point calculations without geometrical relaxation) for the rotation around the CO bond. A rotation by 180° converts **[5NF+H]$^+$_A** into **[5NF+H]$^+$_B**. Additionally, we calculate the transition states in order to determine a more accurate rotational barrier height.

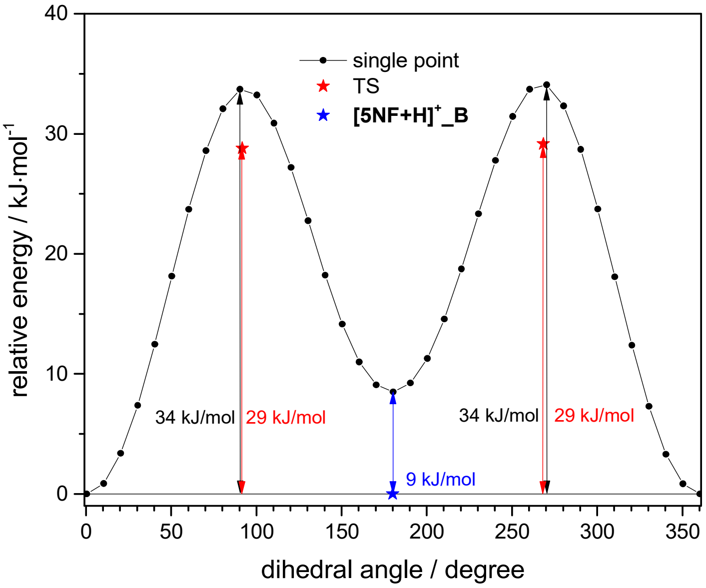

Figure 19: Potential energy surface for the rotation of the hydroxy group of the xanthene ring of **[5NF+H]$^+$_A**. The single point calculations result in a rotational barrier of 34 kJ/mol. The transition state calculations result in an effective rotational barrier of 28 and 29 kJ/mol, respectively. The relative energy of isomer **[5NF+H]$^+$_B** is not represented satisfactorily in the single point calculations.

The calculated PES for the rotation of the hydroxy group in [5NF+H]$^+$ is depicted in Fig. 19. The calculated barrier heights (single point calculations) amount 34 kJ / mol. The transition states calculated with geometrical relaxation yield barrier heights of approx. 29 kJ / mol. The potential energy surfaces at a dihedral angle of 180° identifies Isomer **[5NF+H]$^+$_B** as local minimum structure, but is described less stable by 9 kJ / mol. These values are similar to those, obtained for unsubstituted fluorescein, thus the nitro group has very little influence on the rotational barrier of the OH groups of the xanthene unit or the gas phase structure of [5NF+H]$^+$ at all. We assume, a uniform population of **[5NF+H]$^+$_A/B/C** at the experimental conditions (300 – 450 K, 10^{-4} mbar He). Due to the rotational barrier height, a conversion in the gas phase is unlikely.

For the cationic species of the fluorescein derivatives, we have identified multiple low-energy rotamers. Several rotamers are not unambiguously distinguishable by IR spectroscopy due to the lack of significant differences in the calculated harmonic spectra. The conversion of isomers by rotation of the hydroxy groups seems unlikely regarding the respective calculated potential energy surface. The presented IRMPD spectra are in excellent agreement with the computed harmonic absorption spectra and the investigations by YAO *et al.*.[26]

6.5.3 Monoanions

We also studied the gas phase structure of monoanionic fluorescein derivatives by IRMPD spectroscopy and accompanying DFT calculations. The monoanions provide several isomeric structures due to the possibilities of the deprotonation. The remaining acidic hydrogen atom is located either at the xanthene moiety or the benzoic acid unit. Additional conformational degrees of freedom are given by the rotation of the xanthene OH group and the rotation of the COOH group of the benzoic acid unit. The main text discusses only the most stable isomers, for the less stable isomers see Figs. S7-S12.

6.5.3.1 Fluorescein anion

Geometry optimization of different start geometries for the anionic fluorescein species $[F\text{-}H]^-$ by DFT/B3LYP resulted in seven different minimum structures. The five most stable minimum structures are shown in Fig. 20. The minimum structures **[F-H]$^-$_A/B/C** are deprotonated at the hydroxy groups of the xanthene unit compared to the neutral fluorescein molecule. They differ in the relative orientation of the COOH group of the benzoic acid moiety. Deprotonation at the formally more acidic COOH group results in the (up to 31 kJ / mol) less stable isomers **[F-H]$^-$_D**, and **[F-H]$^-$_E**, differing in the relative orientation of the hydroxy group of the xanthene unit.

The experimental one color IRMPD spectrum is in comparison to the calculated harmonic absorption spectra on the DFT/B3LYP level of theory is shown in Fig. 21. The experiment shows an intense absorption at 3420 cm^{-1} and a weak absorption at 3657 cm^{-1} in the OH stretching region. The range between 1200 and 1900 cm^{-1} exhibits six absorption bands at 1750, 1628 1588, 1485, 1388 and 1350 cm^{-1}. The calculated spectra of the isomers **[F-H]$^-$_A**, **[F-H]$^-$_B**, and

[F-H]$^{-}$_C differ significantly in the position of the OH and CO stretching vibrations of the benzoic acid ($\nu(\mathrm{OH}_{\mathrm{benz}}) \approx 3400 - 3600$ cm^{-1}, $\nu(\mathrm{CO}_{\mathrm{benz}}) \approx 1700 - 1800$ cm^{-1}). The band at 3420 cm^{-1} is assigned to the redshifted OH stretching vibration of the benzoic acid proton hydrogen bound to the xanthene carbon atom in **[F-H]$^{-}$_A**. The redshift of the OH stretching mode from **[F-H]$^{-}$_B** to **[F-H]$^{-}$_A** amounts 141 cm^{-1}. The conceivable conversion from **[F-H]$^{-}$_A** to **[F-H]$^{-}$_B** was calculated in terms of a potential energy surface for the rotation of the C-O bond, though the barrier amounts 40 kJ/mol and is hence unlikely (cf. Fig. S13). The band at

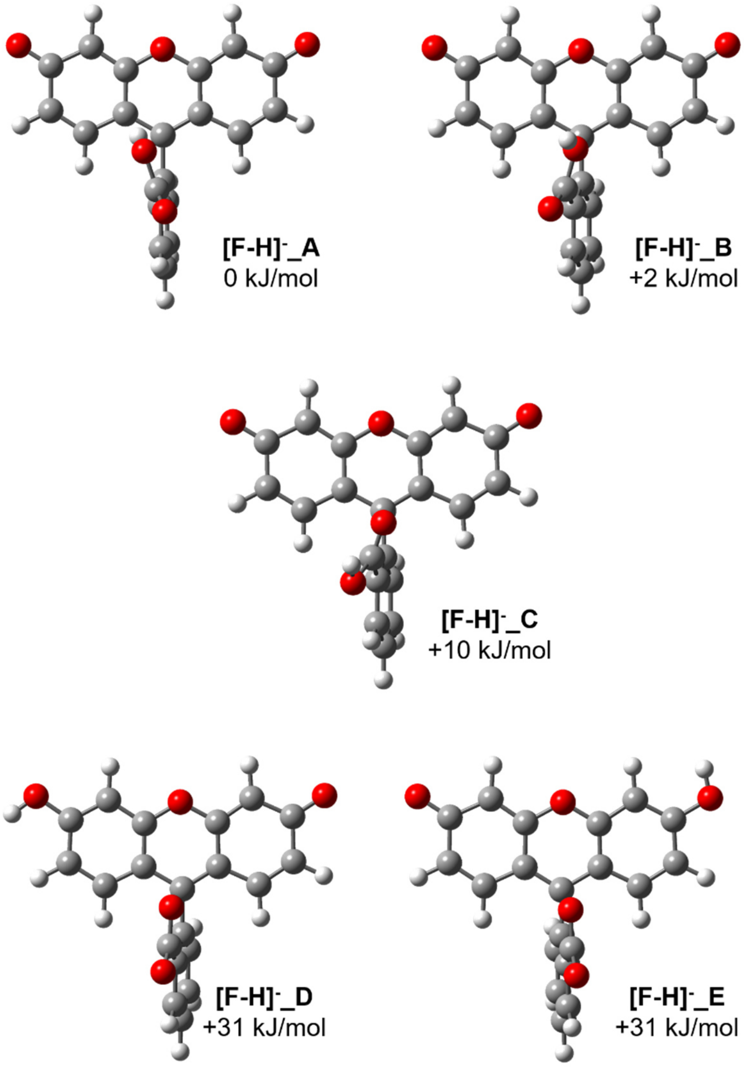

Figure 20: The five most stable minimum structures **[F-H]$^{-}$_A** to **[F-H]$^{-}$_E** of the anionic species of fluorescein [F-H]$^{-}$ calculated by DFT/B3LYP. Note, that the structures **[F-H]$^{-}$_A** to **[F-H]$^{-}$_C** are deprotonated at the xanthene ring and the structures **[F-H]$^{-}$_D** and **[F-H]$^{-}$_E** are deprotonated at the benzoate moiety.

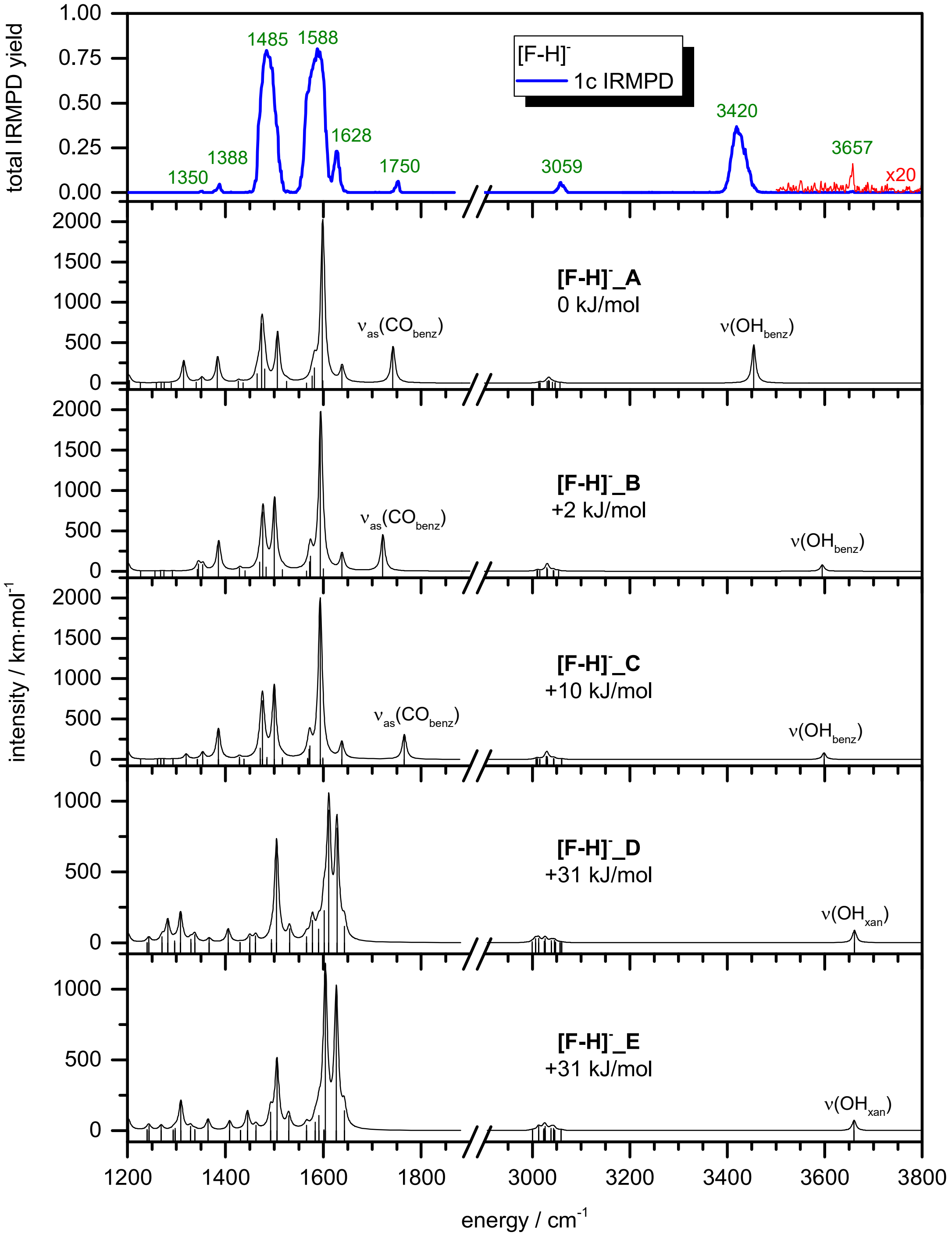

Figure 21: Experimental one color IRMPD spectrum of anionic fluorescein species $[F\text{-}H]^-$ in comparison to the calculated harmonic absorption spectra of the five most stable minimum structures **$[F\text{-}H]^-$_A** to **$[F\text{-}H]^-$_E**. Note, that the red graph in the experimental spectrum is magnified by a factor of 20, exposing a weak absorption at 3657 cm^{-1}.

1750 cm^{-1} is assigned to the asymmetric stretching CO stretching vibration of the benzoic acid carbonyl group. Apart from the weak band at 3657 cm^{-1}, the experimental spectrum is in good agreement with the harmonic spectrum of **[F-H]$^{-}$_A**. Neither the benzoic acid OH stretching vibration of **[F-H]$^{-}$_B** nor the benzoic acid OH stretching vibration of **[F-H]$^{-}$_C** are able to represent this band, due to the relative shift of > 50 cm^{-1}. Instead the OH stretching vibrations of the xanthene OH group of the isomers **[F-H]$^{-}$_D** and **[F-H]$^{-}$_E** fit the frequency very well. Regarding solely the IRMPD spectrum, a majoritarian population of **[F-H]$^{-}$_A** with a spare population of **[F-H]$^{-}$_D/E** appears reasonable. A natural population of **[F-H]$^{-}$_D/E** in the gas phase seems unlikely due to their elevated relative energy of 31 kJ / mol. We calculated the relative energy of all minimum structures in the gas phase and in methanolic solution (cf. Tab. 2). Due to solvation effects, the energetic order is very different. A deprotonation of the benzoic acid is favored in solution, whereas the most stable isomer in the gas phase **[F-H]$^{-}$_A** is destabilized by 13 kJ / mol. Assuming a decent energy input to the ions during the transfer from solution to the gas phase via electrospray ionization, we suggest the majority of the ions to be converted from **[F-H]$^{-}$_D/E** to **[F-H]$^{-}$_A**. Apparently, some of the **[F-H]$^{-}$_D/E** ions retain their molecular structure.

Table 2: Relative thermal free energies (ΔG_{rel}) of the calculated minimum structures of anionic fluorescein [F-H]$^{-}$ (DFT/B3LYP) at 298.15 K in the gas phase and in solution (methanol).

Minimum structure	ΔG_{rel} (gas phase) / kJ·mol^{-1}	$\Delta G_{rel,solv}$ (methanol) / kJ·mol^{-1}
[F-H]$^{-}$_A	0.0	+13.0
[F-H]$^{-}$_B	+1.7	+3.5
[F-H]$^{-}$_C	+9.5	+0.8
[F-H]$^{-}$_D	+30.7	+2.3
[F-H]$^{-}$_E	+31.0	0.0

6.5.3.2 2’,7’-Dichlorofluorescein anion

The four most stable geometry optimized minimum structures of anionic 2’,7’-dichlorofluorescein [DCF-H]$^{-}$ obtained by DFT/B3LYP are shown in Fig. 22. The most stable structures **[DCF-H]$^{-}$_A/B/C** are as well deprotonated at the xanthene hydroxyl group compared to the neutral species, and differ in the relative orientation of the COOH group. A deprotonation at the benzoic acid in isomer **[DCF-H]$^-$_D** results in a destabilization of 37 kJ/mol.

The experimental one and two color IRMPD spectra in comparison to the calculated harmonic absorption spectra of the four most stable isomers are shown in Fig. 23. The experimental spectra provide an intense absorption at 3450 cm^{-1} and a moderately intense absorption at3580 cm^{-1} in the OH stretching region. The area between 1200 and 1850 cm^{-1} exhibits eight absorptions at 1325, 1354, 1492, 1575, 1602, 1626, 1742 and 1757 cm^{-1}. Significant differences between **[DCF-H]$^-$_A/B/C** are exhibited in the position/intensity of the OH stretching vibration of the COOH group. The intense absorption at 3450 cm^{-1} is assigned to the OH stretching vibration (ν(OH_{benz})) in **[DCF-H]$^-$_B**. The redshift of the OH stretching mode from

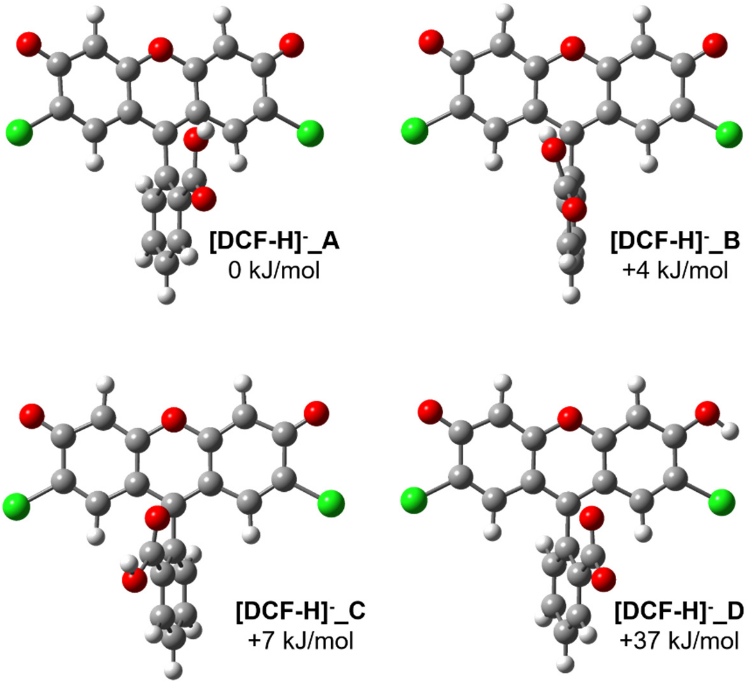

Figure 22: The four most stable minimum structures **[DCF-H]$^-$_A** to **[DCF-H]$^-$_D** of the anionic species of 2',7'-dichlorofluorescein [DCF-H]$^-$ calculated by DFT/B3LYP. Note, that the structures **[DCF-H]$^-$_A** to **[DCF-H]$^-$_C** are deprotonated at the xanthene ring and the structure **[DCF-H]$^-$_D** is deprotonated at the benzoate moiety.

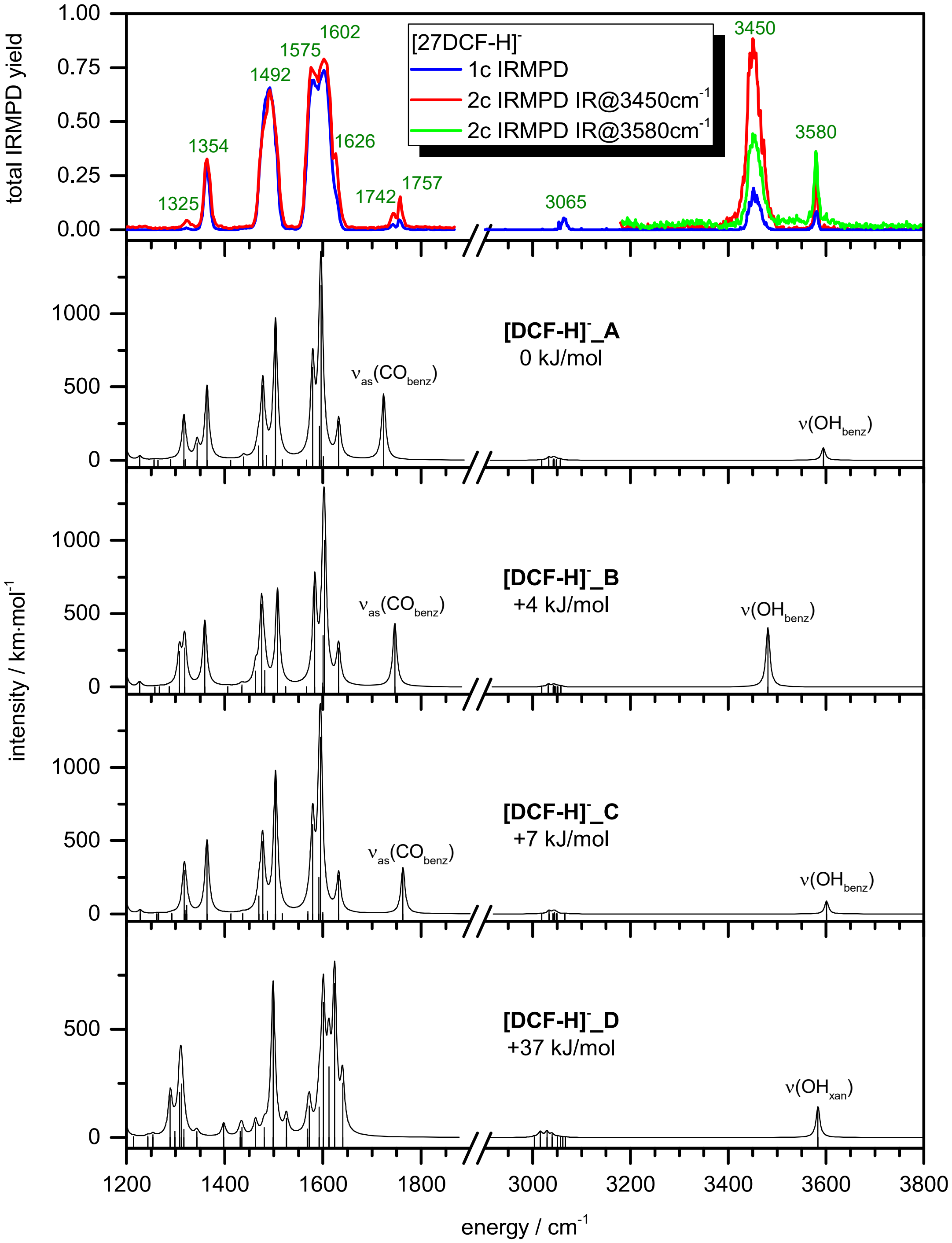

Figure 23: Experimental one and two color IRMPD spectrum of anionic 2',7'-dichlorofluorescein species [DCF-H]$^-$ in comparison to the calculated harmonic absorption spectra of the four most stable minimum structures **[DCF-H]$^-$_A** to **[DCF-H]$^-$_D**.

[DCF-H]$^-$_A to **[DCF-H]$^-$_B** amounts 113 cm^{-1}. The conceivable conversion from **[F-H]$^-$_A** to **[F-H]$^-$_B** was calculated in terms of a potential energy surface for the rotation of the C-O bond, though the barrier amounts 40 kJ/mol and is hence unlikely (cf. Fig. S14). The band at 3580 cm^{-1} is assigned to the OH stretching vibration of the COOH group (ν(OH$_{benz}$)) averted from the molecule in **[DCF-H]$^-$_A**. The assumption of the presence of both isomers **[DCF-H]$^-$_A/B** is supported by the double peak at 1742/1757 cm^{-1} reflecting the relative shift of the asymmetric CO stretching vibration of the COOH unit (ν(CO$_{benz}$)). Due to the lack of significant differences, contributions from isomer **[DCF-H]$^-$_C** to the IRMPD spectrum cannot be excluded, though the relative energy of +7 kJ / mol make it unlikely. In contrast to the unsubstituted fluorescein, the chlorine substituted anion seems to have no contribution from isomer **[DCF-H]$^-$_D** which is deprotonated at the benzoate site. This hypothesis is supported by comparison of the relative energies of the isomers in methanolic solution (cf. Tab. 3). Unlike [F-H]$^-$, [DCF-H]$^-$ prefers the xanthene deprotonation site in the gas phase and in methanolic solution.

Table 3: Relative thermal free energies (ΔG$_{rel}$) of the calculated minimum structures of anionic 2’,7’-dichlorofluorescein [DCF-H]$^-$ (DFT/B3LYP) at 298.15 K in the gas phase and in solution (methanol).

Minimum structure	ΔG$_{rel}$ (gas phase) / kJ·mol^{-1}	ΔG$_{rel,solv}$ (methanol) / kJ·mol^{-1}
[DCF-H]$^-$_A	0.0	+2.9
[DCF-H]$^-$_B	+3.5	+15.0
[DCF-H]$^-$_C	+6.8	0.0
[DCF-H]$^-$_D	+37.3	+15.4

6.5.3.3 5-Nitrofluorescein anion

The five most stable minimum structures of anionic 5-nitrofluorescein [5NF-H]$^-$ obtained by geometry optimization via DFT/B3LYP are shown in Fig. 24. The most stable structures **[5NF-H]$^-$_A/B/C** are deprotonated at the hydroxy group of the xanthene unit. Deprotonation at the benzoic acid results in a destabilization of 16 kJ/mol in **[5NF-H]$^-$_D/E**. The isomers of different deprotonation sites differ in the relative orientation of the remaining COOH and OH group, respectively. The energetic order of the different isomers is equal to that, observed for unsubstituted fluorescein [F-H]$^-$, but the relative energy is significantly different. The isomers of [5NF-H]$^-$ are closer in energy.

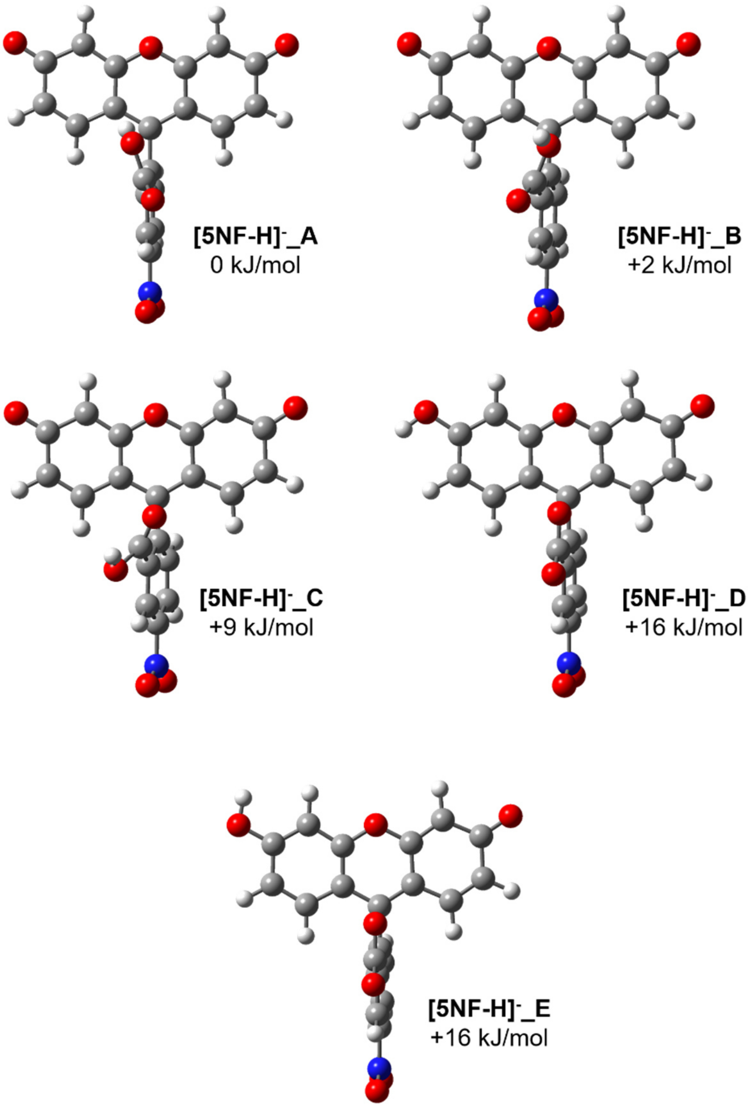

Figure 24: The five most stable minimum structures **[5NF-H]$^-$_A** to **[5NF-H]$^-$_E** of the anionic species of 5-nitrofluorescein [5NF-H]$^-$ calculated by DFT/B3LYP. Note, that the structures **[5NF-H]$^-$_A** to **[5NF-H]$^-$_C** are deprotonated at the xanthene ring and the structures **[5NF-H]$^-$_D** and **[5NF-H]$^-$_E** are deprotonated at the benzoate moiety.

The experimental one and two color IRMPD spectra of [5NF-H]$^-$ in comparison to the calculated harmonic absorption spectra of the most stable minimum structures are shown in Fig. 25. The IRMPD spectrum shows three absorptions in the OH stretching region at 3404, 3575 and 3649 cm^{-1}. The range between 1200 and 1900 cm^{-1} shows at least nine absorption bands with two very broad absorptions, each involving at least three distinct bands (1487 – 1534 cm^{-1} and 1550 – 1661 cm^{-1}). Significant differences in the calculated absorption

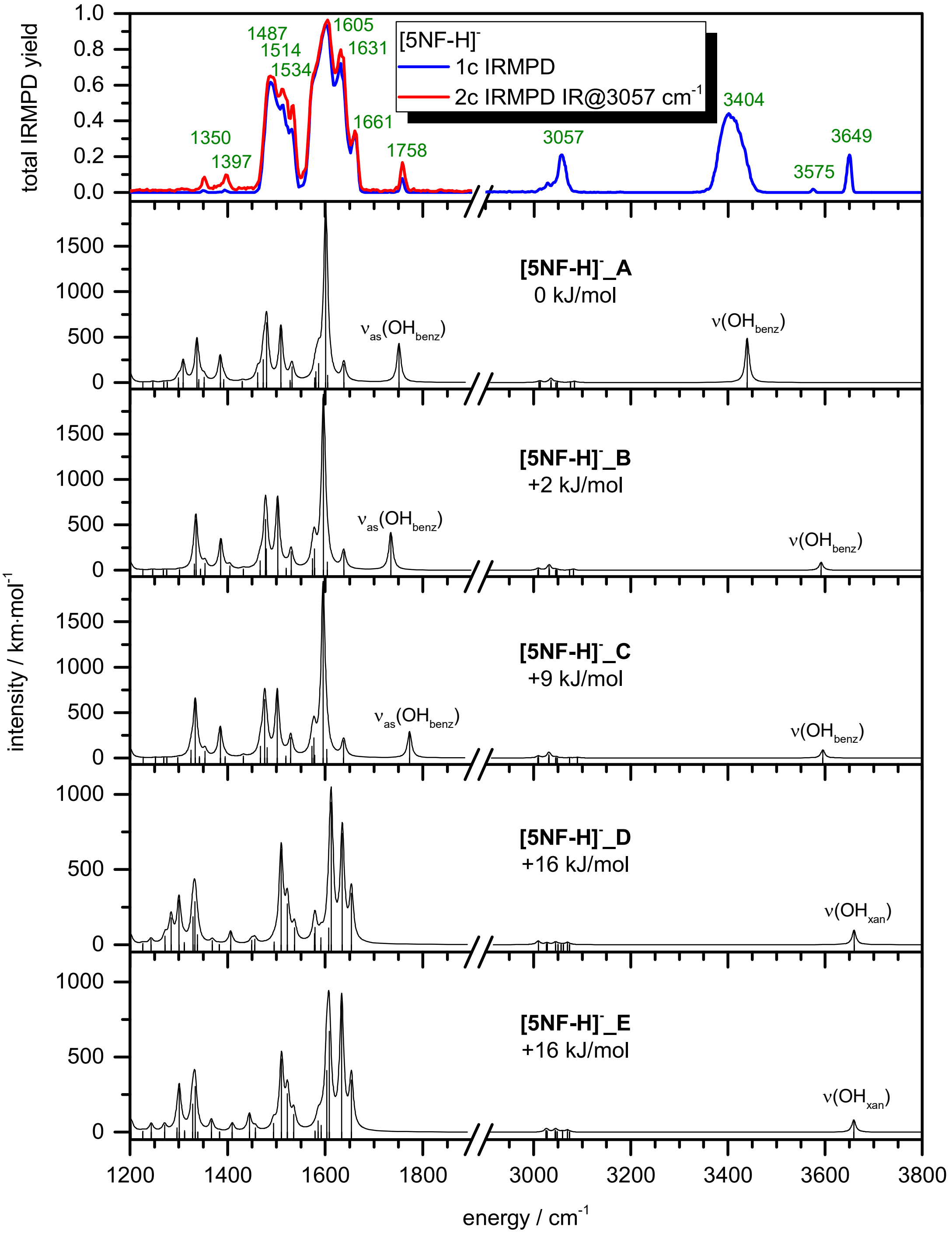

Figure 25: Experimental one and two color IRMPD spectrum of anionic 5-nitrofluorescein species $[5NF-H]^-$ in comparison to the calculated harmonic absorption spectra of the five most stable minimum structures **$[5NF-H]^-$_A** to **$[5NF-H]^-$_E**.

spectra occur in the OH stretching region, whereat **$[5NF-H]^-$_B** and **$[5NF-H]^-$_C** as well as **$[5NF-H]^-$_D** and **$[5NF-H]^-$_E** cannot be distinguished unambiguously. The intense absorption at 3404 cm^{-1} is assigned to the COO-H stretching vibration ν(OH_{benz}) in **$[5NF-H]^-$_A**. The redshift of the OH stretching mode from **$[5NF\text{-}H]^-$_B** to **$[5NF\text{-}H]^-$_A** amounts 153 cm^{-1}. The conceivable conversion from **$[5NF\text{-}H]^-$_A** to **$[5NF\text{-}H]^-$_B** was calculated in terms of a potential energy surface for the rotation of the C-O bond, though the barrier amounts 39 kJ/mol and is hence unlikely (cf. Fig. S15). The weak absorption at 3575 cm^{-1} is assigned to the OH stretching vibration of the unaltered COOH group of **$[5NF\text{-}H]^-$_B**. The medium intense band at 3649 cm^{-1} is allocated to the free OH stretching modes of the energetically unfavorable isomers **$[5NF\text{-}H]^-$_D/E**. Thus, the OH stretching area indicates a population of at least three different isomers. The bulky absorptions in the CO stretching region indicate the presence of multiple isomers as well. Considering the relative energy in the gas phase, only **$[5NF\text{-}H]^-$_A/B** should be populated at the experimental conditions. Isomer **$[5NF\text{-}H]^-$_C** is the most stable in methanolic solution (cf. Tab. 4). As described for $[F\text{-}H]^-$ before, we assume **$[5NF\text{-}H]^-$_C** to retain its structure during the transfer from the solution into the gas phase via ESI.

Table 4: Relative thermal free energies (ΔG_{rel}) of the calculated minimum structures of anionic 5-nitrofluorescein $[5NF\text{-}H]^-$ (DFT/B3LYP) at 298.15 K in the gas phase and in solution (methanol).

Minimum structure	ΔG_{rel} (gas phase) / kJ·mol^{-1}	$\Delta G_{rel,solv}$ (methanol) / kJ·mol^{-1}
$[5NF\text{-}H]^-$_A	0.0	+23.5
$[5N F\text{-}H]^-$_B	+2.0	+11.5
$[5N F\text{-}H]^-$_C	+8.8	+10.3
$[5N F\text{-}H]^-$_D	+15.7	0.0
$[5N F\text{-}H]^-$_E	+16.3	+0.2

The monoanionic species show a rather unexpected deprotonation site in the gas phase. For all fluorescein derivatives, a deprotonation at the xanthene unit is favored, whereas the actual acidic COOH groups retain the proton. Nevertheless, unsubstituted fluorescein shows a weak absorption in the OH stretching region at 3657 cm^{-1} indicating a partial population of fluorescein deprotonated at the benzoate which is assumed to originate from the solvated phase. In 2’,7’-dichlorofluorescein the assignment is more challenging due to the redshift of the OH stretching vibration based on the hydrogen bond to the neighboring chlorine atom. According to the relative free energies, the favored deprotonation site of the solvated ions is likewise the xanthene unit. The spectra of anionic 5-nitrofluorescein show presence of several deprotonation sites and rotamers. The assumption is supported by the comparison of the relative free energies of the different isomers in the gas phase and in methanolic solution. The electron withdrawing nitro group favors a deprotonation at the benzoic acid.

6.6 Conclusions

We performed gas phase one and two color IRMPD experiments on the three charged prototropic forms of fluorescein, 2',7'-dichlorofluorescein and 5-nitrofluorescein in combination with DFT calculations elucidating minimum structures, relative free energies, transition states, and rotational barriers.

The dianionic species are entirely deprotonated, resulting in a single minimum structure. Our experimental IRMPD spectra match the calculated harmonic spectra very well, regarding peak position and intensity. The cationic species show excellent agreements between the two color IRMPD spectra and the calculated harmonic spectra. Due to the lack of significant differences in the calculated harmonic absorption spectra an unequivocal assignment is challenging. The calculated potential energy surfaces representing a conversion by rotation of the hydroxyl group shows, that a transformation of the ions in the gas phase is very unlikely. The initially unexpected deprotonation site of monoanionic fluorescein was first reported by YAO *et al.* and endorsed by this study, additionally taking the vibrational OH stretching region into account.[26] The utilized two color IRMPD technique has repeatedly proven valuable to overcome bottlenecks and enhance weak IRMPD absorption bands of stable molecules and allows for a more exhaustive spectral range and advanced spectral resolution in comparison to Yao's Free Electron Laser (FEL) data.

We have shown that the favored deprotonation site of monoanionic fluorescein derivatives in the gas phase and in methanolic solution is thoroughly represented by DFT energy calculations and largely depends on inherent substituents. The presented data provide strong evidence for a partial conservation of the favored minimum structures in methanolic solution during the transfer into the gas phase via ESI. Investigations using different ionization techniques, e.g. the Laser Induced Liquid Bead Ion Desorption (LILBID) in combination with mass spectrometry could help to elucidate the properties of defined dye-solvent cluster ions. The presented work contributes to a better understanding of the interactions between solvent molecules and dyes and may help for tuning properties in the future development of dyes.

6.7 References

[1] A. Baeyer, "*Ueber eine neue Klasse von Farbstoffen*", *Ber. Dtsch. Chem. Ges.*, **1871**, *4*, 555-558.

[2] P. Ehrlich, "*Ueber provocirte Fluorescenzerscheinungen am Auge*", *Dtsch. Med. Wochenschr.*, **1882**, *8*, 21-22.

[3] P. Ehrlich, "*Ueber provocirte Fluorescenzerscheinungen am Auge Fortsetzung aus No. 2*", *Dtsch. Med. Wochenschr.*, **1882**, *8*, 35-37.

[4] P. Ehrlich, "*Ueber provocirte Fluorescenzerscheinungen am Auge (Schluss aus No. 3.)*", *Dtsch. Med. Wochenschr.*, **1882**, *8*, 54-55.

[5] A. H. Coons, H. J. Creech, R. N. Jones, E. Berliner, "*The Demonstration of Pneumococcal Antigen in Tissues by the Use of Fluorescent Antibody*", *J. Immunol.*, **1942**, *45*, 159-170.

[6] J. L. Riggs, R. J. Seiwald, J. H. Burckhalter, C. M. Downs, T. G. Metcalf, "*Isothiocyanate Compounds as Fluorescent Labeling Agents for Immune Serum*", *Am. J. Pathol.*, **1958**, *34*, 1081-1097.

[7] D. L. Taylor, Y. L. Wang, "*Molecular cytochemistry: incorporation of fluorescently labeled actin into living cells*", *Proc. Natl. Acad. Sci.*, **1978**, *75*, 857-861.

[8] H. Giloh, J. W. Sedat, "*Fluorescence microscopy: reduced photobleaching of rhodamine and fluorescein protein conjugates by n-propyl gallate*", *Science*, **1982**, *217*, 1252.

[9] R. Sjöback, J. Nygren, M. Kubista, "*Absorption and fluorescence properties of fluorescein*", *Spectrochim. Acta, Part A*, **1995**, *51*, L7-L21.

[10] I. Vermes, C. Haanen, H. Steffens-Nakken, C. Reutellingsperger, "*A novel assay for apoptosis Flow cytometric detection of phosphatidylserine expression on early apoptotic cells using fluorescein labelled Annexin V*", *J. Immunol. Methods*, **1995**, *184*, 39-51.

[11] B. A. Griffin, S. R. Adams, R. Y. Tsien, "*Specific Covalent Labeling of Recombinant Protein Molecules Inside Live Cells*", *Science*, **1998**, *281*, 269.

[12] B. S. Gaylord, A. J. Heeger, G. C. Bazan, "*DNA Hybridization Detection with Water-Soluble Conjugated Polymers and Chromophore-Labeled Single-Stranded DNA*", *J. Am. Chem. Soc.*, **2003**, *125*, 896-900.

[13] M. J. Levene, D. A. Dombeck, K. A. Kasischke, R. P. Molloy, W. W. Webb, "*In Vivo Multiphoton Microscopy of Deep Brain Tissue*", *J. Neurophysiol.*, **2004**, *91*, 1908.

[14] R. P. Haugland, "*The handbook - A Guide to Fluorescent Probes and Lbeling Tchnologies*", Invitrogen, San Diego, **2005**.

[15] M. M. Martin, "*Hydrogen bond effects on radiationless electronic transitions in xanthene dyes*", *Chem. Phys. Lett.*, **1975**, *35*, 105-111.

[16] I. M. Kolthoff, W. M. Lauer, C. J. Sunde, "*The Use of Dichlorofluorescein as an Adsorption Indicator for Argentometric Titration if Chlorides*", *J. Am. Chem. Soc.*, **1929**, *51*, 3273-3277.

[17] K. Hiraki, Y. Nishikawa, "*Acid-Base Titration by Use of Fluorescent Indicators (Differential Titration Method)*", *Bunseki Kagaku*, **1981**, *30*, 45-50.

[18] A. Minta, J. P. Kao, R. Y. Tsien, "*FLUORESCENT INDICATORS FOR CYTOSOLIC CALCIUM CASED ON RHODAMINE AND FLUORESCEIN CHROMOPHORES*", *J. Biol. Chem.*, **1989**, *264*, 8171-8178.

[19] M. Wrona, K. Patel, P. Wardman, "*REACTIVITY OF 2′,7′-DICHLORODIHYDROFLUORESCEIN AND DIHYDRORHODAMINE 123 AND THEIR OXIDIZED FORMS TOWARD CARBONATE, NITROGEN DIOXIDE, AND HYDROXYL RADICALS*", *Free Radic. Biol. Med.*, **2005**, *38*, 262-270.

[20] T. Nash, "*ORIGIN OF TIME-DEPENDENT ORGANIZATION IN A MICELLE SERIES*", *Nature*, **1958**, *182*, 1536-1536.

[21] J. E. Lovelock, T. Nash, "*A COLOUR REACTION FOR NON-IONIC AND AMPHOTERIC SOAPS*", *Nature*, **1958**, *181*, 1263-1264.

[22] C. P. LeBel, H. Ischiropoulos, S. C. Bondy, "*EVALUATION OF THE PROBE 2',7'-DICHLOROFLUORESCIN AS AN INDICATOR OF REACTIVE OXYGEN SPECIES FORMATION AND OXIDATIVE STRESS*", *Chem. Res. Toxicol.*, **1992**, *5*, 227-231.

[23] H. Zhu, G. L. Bannenberg, P. Moldéus, H. G. Shertzer, "*OXIDATION PATHWAYS FOR THE INTRACELLULAR PROBE 2′,7′-DICHLOROFLUORESCIN*", *Arch. Toxicol.*, **1994**, *68*, 582-587.

[24] A. K. Patel, M. B. Hallett, A. K. Campbell, "*THRESHOLD RESPONSES IN PRODUCTION OF REACTIVE OXYGEN METABOLITES IN INDIVIDUAL NEUTROPHILS DETECTED BY FLOW CYTOMETRY AND MICROFLUORIMETRY*", *Biochem. J.*, **1987**, *248*, 173.

[25] J. A. Royall, H. Ischiropoulos, "*EVALUATION OF 2′,7′-DICHLOROFLUORESCIN AND DIHYDRORHODAMINE 123 AS FLUORESCENT PROBES FOR INTRACELLULAR H_2O_2 IN CULTURED ENDOTHELIAL CELLS*", *Arch. Biochem. Biophys.*, **1993**, *302*, 348-355.

[26] H. Yao, J. D. Steill, J. Oomens, R. A. Jockusch, "*INFRARED MULTIPLE PHOTON DISSOCIATION ACTION SPECTROSCOPY AND COMPUTATIONAL STUDIES OF MASS-SELECTED GAS-PHASE FLUORESCEIN AND 2′,7′-DICHLOROFLUORESCEIN IONS*", *J. Chem. Phys. A*, **2011**, *115*, 9739-9747.

[27] M. T. Bogert, R. G. Wright, "*SOME EXPERIMENTS ON THE NITRO DERIVATIVES OF FLUORESCEIN*", *J. Am. Chem. Soc.*, **1905**, *27*, 1310-1316.

[28] X.-F. Zhang, J. Zhang, L. Liu, "*FLUORESCENCE PROPERTIES OF TWENTY FLUORESCEIN DERIVATIVES: LIFETIME, QUANTUM YIELD, ABSORPTION AND EMISSION SPECTRA*", *Journal of Fluorescence*, **2014**, *24*, 819-826.

[29] N. Klonis, W. H. Sawyer, "*SPECTRAL PROPERTIES OF THE PROTOTROPIC FORMS OF FLUORESCEIN IN AQUEOUS SOLUTION*", *Journal of Fluorescence*, **1996**, *6*, 147-157.

[30] D. Magde, R. Wong, P. G. Seybold, "*FLUORESCENCE QUANTUM YIELDS AND THEIR RELATION TO LIFETIMES OF RHODAMINE 6G AND FLUORESCEIN IN NINE SOLVENTS: IMPROVED ABSOLUTE STANDARDS FOR QUANTUM YIELDS¶*", *Photochemistry and Photobiology*, **2002**, *75*, 327-334.

[31] H. Leonhardt, L. Gordon, R. Livingston, "*ACID-BASE EQUILIBRIUMS OF FLUORESCEIN AND 2',7'-DICHLOROFLUORESCEIN IN THEIR GROUND AND FLUORESCENT STATES*", *The Journal of Physical Chemistry*, **1971**, *75*, 245-249.

[32] X.-F. Zhang, "*THE EFFECT OF PHENYL SUBSTITUTION ON THE FLUORESCENCE CHARACTERISTICS OF FLUORESCEIN DERIVATIVES VIA INTRAMOLECULAR PHOTOINDUCED ELECTRON TRANSFER*", *Photochemical & Photobiological Sciences*, **2010**, *9*, 1261-1268.

[33] L. Wang, A. Roitberg, C. Meuse, A. K. Gaigalas, "*RAMAN AND FTIR SPECTROSCOPIES OF FLUORESCEIN IN SOLUTIONS*", *Spectrochim. Acta, Part A*, **2001**, *57*, 1781-1791.

[34] P. D. McQueen, S. Sagoo, H. Yao, R. A. Jockusch, "*ON THE INTRINSIC PHOTOPHYSICS OF FLUORESCEIN*", *Angewandte Chemie International Edition*, **2010**, *49*, 9193-9196.

[35] H. Yao, R. A. Jockusch, "*FLUORESCENCE AND ELECTRONIC ACTION SPECTROSCOPY OF MASS-SELECTED GAS-PHASE FLUORESCEIN, 2′,7′-DICHLOROFLUORESCEIN, AND 2′,7′-DIFLUOROFLUORESCEIN IONS*", *J. Chem. Phys. A*, **2013**, *117*, 1351-1359.

[36] Y. Nosenko, F. Menges, C. Riehn, G. Niedner-Schatteburg, "*Investigation by two-color IR dissociation spectroscopy of Hoogsteen-type binding in a metalated nucleobase pair mimic*", *Phys. Chem. Chem. Phys.*, **2013**, *15*, 8171-8178.

[37] Y. Nosenko, C. Riehn, G. Niedner-Schatteburg, "*Self-pairing of 1-methylthymine mediated by two and three Ag(I) ions: a gas phase study using infrared dissociation spectroscopy and density functional theory*", *Phys. Chem. Chem. Phys.*, **2016**, *18*, 8491-8501.

[38] M. Gaffga, I. Munstein, P. Müller, J. Lang, W. R. Thiel, G. Niedner-Schatteburg, "*Multistate-Mediated Rearrangements and $FeCl_2$ Elimination in Dinuclear FePd Complexes*", *J. Phys. Chem. A*, **2015**, *119*, 12587-12598.

[39] J. Lang, J. Mohrbach, S. Dillinger, J. M. Hewer, G. Niedner-Schatteburg, "*Vibrational blue shift of coordinated N_2 in $[Fe_3O(OAc)_6(N_2)_n]^+$:"non-classical" dinitrogen complexes*", *Chem. Commun.*, **2017**, *53*, 420-423.

[40] A. D. Becke, "*Density-functional thermochemistry. III. The role of exact exchange*", *J. Chem. Phys.*, **1993**, *98*, 5648-5652.

[41] A. D. Becke, "*Density-functional exchange-energy approximation with correct asymptotic behavior*", *Phys. Rev. A*, **1988**, *38*, 3098.

[42] B. Miehlich, A. Savin, H. Stoll, H. Preuss, "*Results obtained with the correlation energy density functionals of Becke and Lee, Yang and Parr*", *Chem. Phys. Lett.*, **1989**, *157*, 200-206.

[43] R. Krishnan, J. S. Binkley, R. Seeger, J. A. Pople, "*Self-consistent molecular orbital methods. XX. A basis set for correlated wave functions*", *J. Chem. Phys.*, **1980**, *72*, 650-654.

[44] M. M. Francl, W. J. Pietro, W. J. Hehre, J. S. Binkley, M. S. Gordon, D. J. DeFrees, J. A. Pople, "*Self-consistent molecular orbital methods. XXIII. A polarization-type basis set for second-row elements*", *J. Chem. Phys.*, **1982**, *77*, 3654-3665.

[45] M. J. Frisch, G. W. Trucks, H. B. Schlegel, G. E. Scuseria, M. A. Robb, J. R. Cheeseman, G. Scalmani, V. Barone, G. A. Petersson, H. Nakatsuji, X. Li, M. Caricato, A. Marenich, J. Bloino, B. G. Janesko, R. Gomperts, B. Menucci, H. P. Hratchian, J. V. Ortiz, A. F. Izmaylov, J. L. Sonnenberg, D. Williams-Young, F. Ding, F. Lipparini, F. Egidi, J. Goings, B. Peng, A. Petrone, T. Henderson, D. Ranasinghe, V. G. Zakrzewski, J. Gao, N. Rega, G. Zheng, W. Liang, M. Hada, M. Ehara, K. Toyota, R. Fukuda, J. Hasegawa, M. Ishida, T. Nakajima, Y. Honda, O. Kitao, H. Nakai, T. Vreven, K. Throssel, J. A. Montgomery, J. E. Peralta, F. Ogliaro, M. Bearpark, J. J. Heyd, E. Brothers, K. N. Kudin, V. N. Staroverov, T. Keith, R. Kobayashi, J. Normand, K. Raghavachari, A. Rendell, J. C. Burant, S. S. Iyengar, J. Tomasi, M. Cossi, J. M. Millam, M. Klene, C. Adamo, R. Cammi, J. W. Ochterski, R. L. Martin, K. Morokuma, O. Farkas, Fores, "*GAUSSIAN09, Revision D.01, Gaussian, Inc., Wallingford, CT*", *University of Minnesota, Minneapolis*, **2009**.

[46] A.-R. Allouche, "*Gabedit—A graphical user interface for computational chemistry softwares*", *J. Comput. Chem.*, **2011**, *32*, 174-182.

[47] J. Tomasi, M. Persico, "*Molecular Interactions in Solution: An Overview of Methods Based on Continuous Distributions of the Solvent*", *Chem. Rev.*, **1994**, *94*, 2027-2094.

[48] C. J. Cramer, D. G. Truhlar, "*Structure and Reactivity in Aqueous Solution*", *Vol. 568*, American Chemical Society, **1994**.

[49] T. Mineva, N. Russo, E. Sicilia, "*Solvation effects on reaction profiles by the polarizable continuum model coupled with the Gaussian density functional method*", *J. Comput. Chem.*, **1998**, *19*, 290-299.

[50] V. Barone, M. Cossi, J. Tomasi, "*GEOMETRY OPTIMIZATION OF MOLECULAR STRUCTURES IN SOLUTION BY THE POLARIZABLE CONTINUUM MODEL*", *J. Comput. Chem.*, **1998**, *19*, 404-417.

[51] J. Oomens, B. G. Sartakov, G. Meijer, G. Von Helden, "*GAS-PHASE INFRARED MULTIPLE PHOTON DISSOCIATION SPECTROSCOPY OF MASS-SELECTED MOLECULAR IONS*", *Int. J. Mass Spectrom.*, **2006**, *254*, 1-19.

[52] J. Oomens, A. Tielens, B. G. Sartakov, G. von Helden, G. Meijer, "*LABORATORY INFRARED SPECTROSCOPY OF CATIONIC POLYCYCLIC AROMATIC HYDROCARBON MOLECULES*", *Astrophys. J.*, **2003**, *591*, 968.

[53] T. Pankewitz, A. Lagutschenkov, G. Niedner-Schatteburg, S. S. Xantheas, Y.-T. Lee, "*INFRARED SPECTRUM OF* $NH_4^+(H_2O)$*: EVIDENCE FOR MODE SPECIFIC FRAGMENTATION*", *J. Chem. Phys.*, **2007**, *126*, 074307.

[54] A. Simon, C. Joblin, N. Polfer, J. Oomens, "*INFRARED SPECTROSCOPY OF* $[XFeC_{24}H_{12}]^+$ $(X=C_5H_5, C_5(CH_3)_5)$ *COMPLEXES IN THE GAS PHASE: EXPERIMENTAL AND COMPUTATIONAL STUDIES OF ASTROPHYSICAL INTEREST*", *J. Phys. Chem. A*, **2008**, *112*, 8551-8560.

[55] E. Garand, J. A. Fournier, M. Z. Kamrath, N. D. Schley, R. H. Crabtree, M. A. Johnson, "*CHARACTERIZATION OF AN ACTIVATED IRIDIUM WATER SPLITTING CATALYST USING INFRARED PHOTODISSOCIATION OF* H_2 *TAGGED IONS*", *Phys. Chem. Chem. Phys.*, **2012**, *14*, 10109-10113.

[56] L. Yeh, M. Okumura, J. Myers, J. Price, Y. Lee, "*VIBRATIONAL SPECTROSCOPY OF THE HYDRATED HYDRONIUM CLUSTER IONS* $H_3O^+(H_2O)_N$ $(N= 1, 2, 3)$", *J. Chem. Phys.*, **1989**, *91*, 7319-7330.

[57] C. H. Watson, J. A. Zimmerman, J. E. Bruce, J. R. Eyler, "*RESONANCE-ENHANCED TWO-LASER INFRARED MULTIPLE PHOTON DISSOCIATION OF GASEOUS IONS*", *J. Phys. Chem.*, **1991**, *95*, 6081-6086.

[58] G. Altinay, R. B. Metz, "*COMPARISON OF IRMPD, AR-TAGGING AND IRLAPS FOR VIBRATIONAL SPECTROSCOPY OF* $Ag^+(CH_3OH)$", *Int. J. Mass Spectrom.*, **2010**, *297*, 41-45.

6.8 Supplementary Material

Gas Phase Structure of Fluorescein, 2,7-Dichlorofluorescein and 5-Nitrofluorescein ions by Infrared Multiple Photon Dissociation Spectroscopy and Density Functional Theory

Joachim M. Hewer, Sebastian Becker, Dimitri Imanbaew and Gereon Niedner-Schatteburg

Fachbereich Chemie and Forschungszentrum OPTIMAS, Kaiserslautern, Germany

Content

Table S1: Fragmentation channels of the dianionic and monoanionic fluorescein, 2’,7’-dichlorofluorescein and 5-nitrofluorescein species

Figure S1: Less stable minimum structures **$[F+H]^+$_G** to **$[F+H]^+$_L** of the cationic species of fluorescein $[F+H]^+$ calculated by DFT/B3LYP.

Figure S2: Experimental one and two color IRMPD spectrum of cationic fluorescein $[F+H]^+$ in comparison to the calculated harmonic absorption spectra of the less stable minimum structures **$[F+H]^+$_G** to **$[F+H]^+$_L**.

Figure S3: Less stable minimum structures **$[DCF+H]^+$_F** to **$[F+H]^+$_K** of the cationic species of 2’,7’-dichlorofluorescein $[DCF+H]^+$ calculated by DFT/B3LYP.

Figure S4: Experimental one and two color IRMPD spectrum of cationic 2’,7’-dichlorofluorescein $[DCF+H]^+$ in comparison to the calculated harmonic absorption spectra of the less stable minimum structures **$[DCF+H]^+$_F** to **$[DCF+H]^+$_K**.

Figure S5: Less stable minimum structures **$[5NF+H]^+$_G** to **$[5NF+H]^+$_J** of the cationic species of 5-nitrofluorescein $[5NF+H]^+$ calculated by DFT/B3LYP.

Figure S6: Experimental one and two color IRMPD spectrum of cationic 5-nitrofluorescein $[5NF+H]^+$ in comparison to the calculated harmonic absorption spectra of the less stable minimum structures **$[5NF+H]^+$_G** to **$[5NF+H]^+$_J**.

Figure S7: Less stable minimum structures **$[F-H]^-$_F** and **$[F-H]^-$_G** of the anionic species of fluorescein $[F-H]^-$ calculated by DFT/B3LYP.

Figure S8: Experimental one color IRMPD spectrum of anionic fluorescein species $[F-H]^-$ in comparison to the calculated harmonic absorption spectra of the less stable minimum structures **$[F-H]^-$_F** and **$[F-H]^-$_G**.

Figure S9: Less stable minimum structures **$[DCF-H]^-$_E** to **$[DCF-H]^-$_G** of the anionic species of 2’,7’-dichlorofluorescein $[DCF-H]^-$ calculated by DFT/B3LYP.

Figure S10: Experimental one and two color IRMPD spectrum of anionic 2’,7’-dichlorofluorescein species $[DCF-H]^-$ in comparison to the calculated harmonic absorption spectra of the less stable minimum structures **$[DCF-H]^-$_E** to **$[DCF-H]^-$_G**.

Figure S11: Less stable minimum structures **$[5NF-H]^-$_F** and **$[5NF-H]^-$_G** of the anionic species of 5-nitrofluorescein $[5NF-H]^-$ calculated by DFT/B3LYP.

Figure S12: Experimental one and two color IRMPD spectrum of anionic 5-nitrofluorescein species $[5NF-H]^-$ in comparison to the calculated harmonic absorption spectra of the less stable minimum structures **$[5NF-H]^-$_F** and **$[5NF-H]^-$_G**.

Figure S13: Potential energy surface (PES) for the conversion of **$[F-H]^-$_A** to **$[F-H]^-$_B** by rotation of the OH group around the C-O bond.

Figure S14: Potential energy surface (PES) for the conversion of **$[DCF-H]^-$_A** to **$[DCF-H]^-$_B** by rotation of the OH group around the C-O bond.

Figure S15: Potential energy surface (PES) for the conversion of **$[5NF-H]^-$_A** to **$[5NF-H]^-$_B** by rotation of the OH group around the C-O bond.

Table S1: Fragmentation channels of the dianionic and monoanionic fluorescein, 2',7'-dichlorofluorescein and 5-nitrofluorescein species. The respective main fragmentation channel is highlighted in bold.

Parent ion	Parent ion mass	Fragment ion mass	Neutral/ionic loss
$[F\text{-}2H]^{2-}$	165	286	$-CO_2$, $-e^-$
		285	**$-CO_2H$, $-e^-$**
$[DCF\text{-}2H]^{2-}$	199	354	$-CO_2$, $-e^-$
		353	$-CO_2H$, $-e^-$
		319	**$-CO_2$, $-HCl$, $-e^-$**
$[5NF\text{-}2H]^{2-}$	188	**331**	**$-CO_2$, $-e^-$**
		301	$-CO_2$, $-NO$, $-e^-$
		285	$-CO_2$, $-NO_2$, $-e^-$
$[F\text{-}H]^-$	331	287	$-CO_2$
		286	$-CO_2H$
$[DCF\text{-}H]^-$	399	355	$-CO_2$
		354	$-CO_2H$
		319	**$-CO_2H$, $-HCl$**
$[5NF\text{-}H]^-$	376	**332**	**$-CO_2$**
		331	$-CO_2H$
		315	$-CO_2$, $-H_2O$
		302	$-CO_2$, $-NO$
		285	$-CO_2H$, $-NO_2$

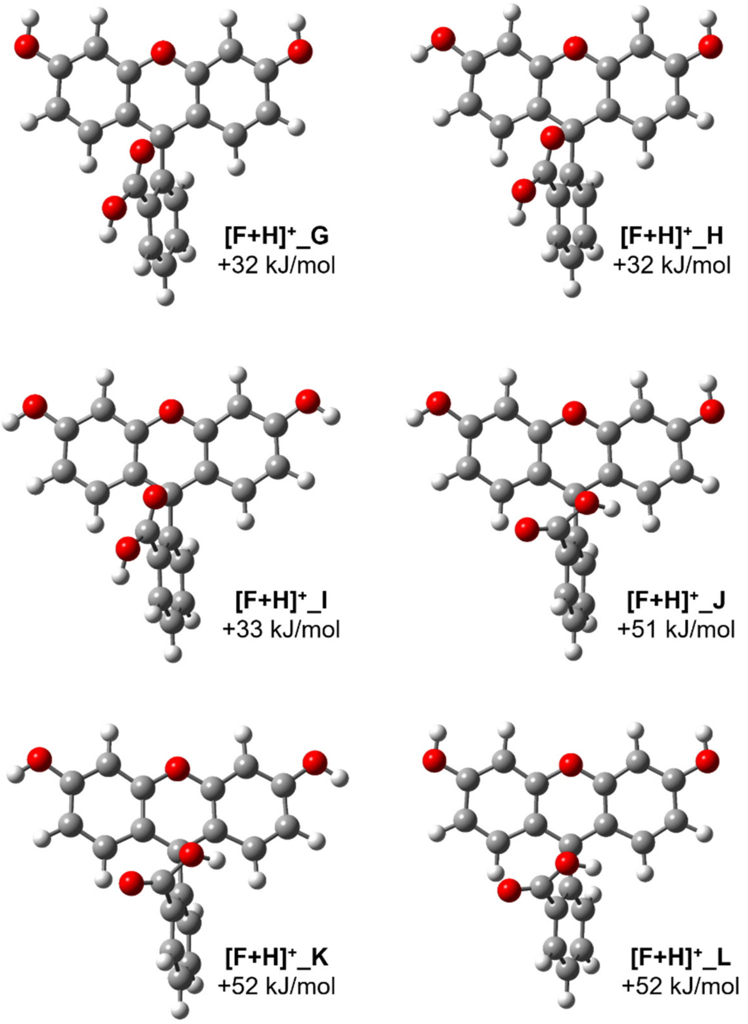

Figure S1: Less stable minimum structures **$[F+H]^+$_G** to **$[F+H]^+$_L** of the cationic species of fluorescein $[F+H]^+$ calculated by DFT/B3LYP.

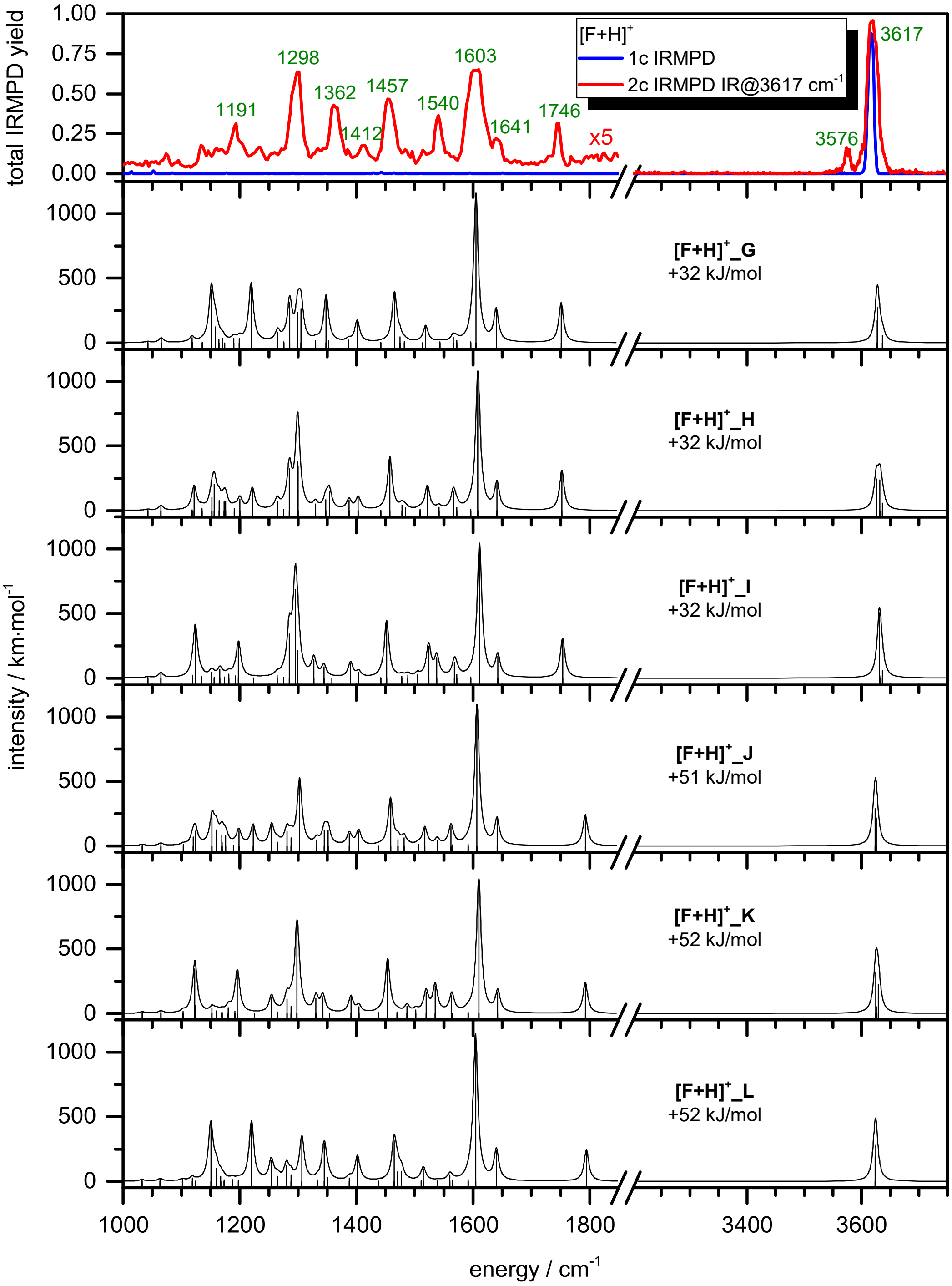

Figure S2: Experimental one and two color IRMPD spectrum of cationic fluorescein [F+H]$^+$ in comparison to the calculated harmonic absorption spectra of the less stable minimum structures **[F+H]$^+$_G** to **[F+H]$^+$_L**.

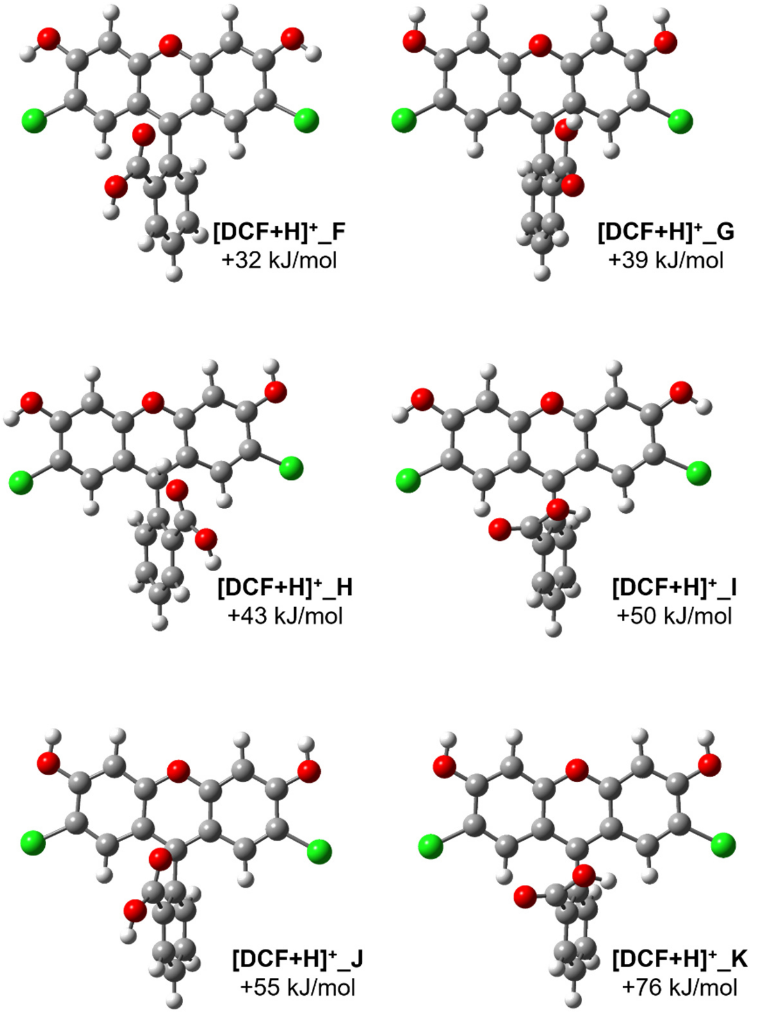

Figure S3: Less stable minimum structures **$[DCF+H]^+$_F** to **$[F+H]^+$_K** of the cationic species of 2’,7’-dichlorofluorescein $[DCF+H]^+$ calculated by DFT/B3LYP.

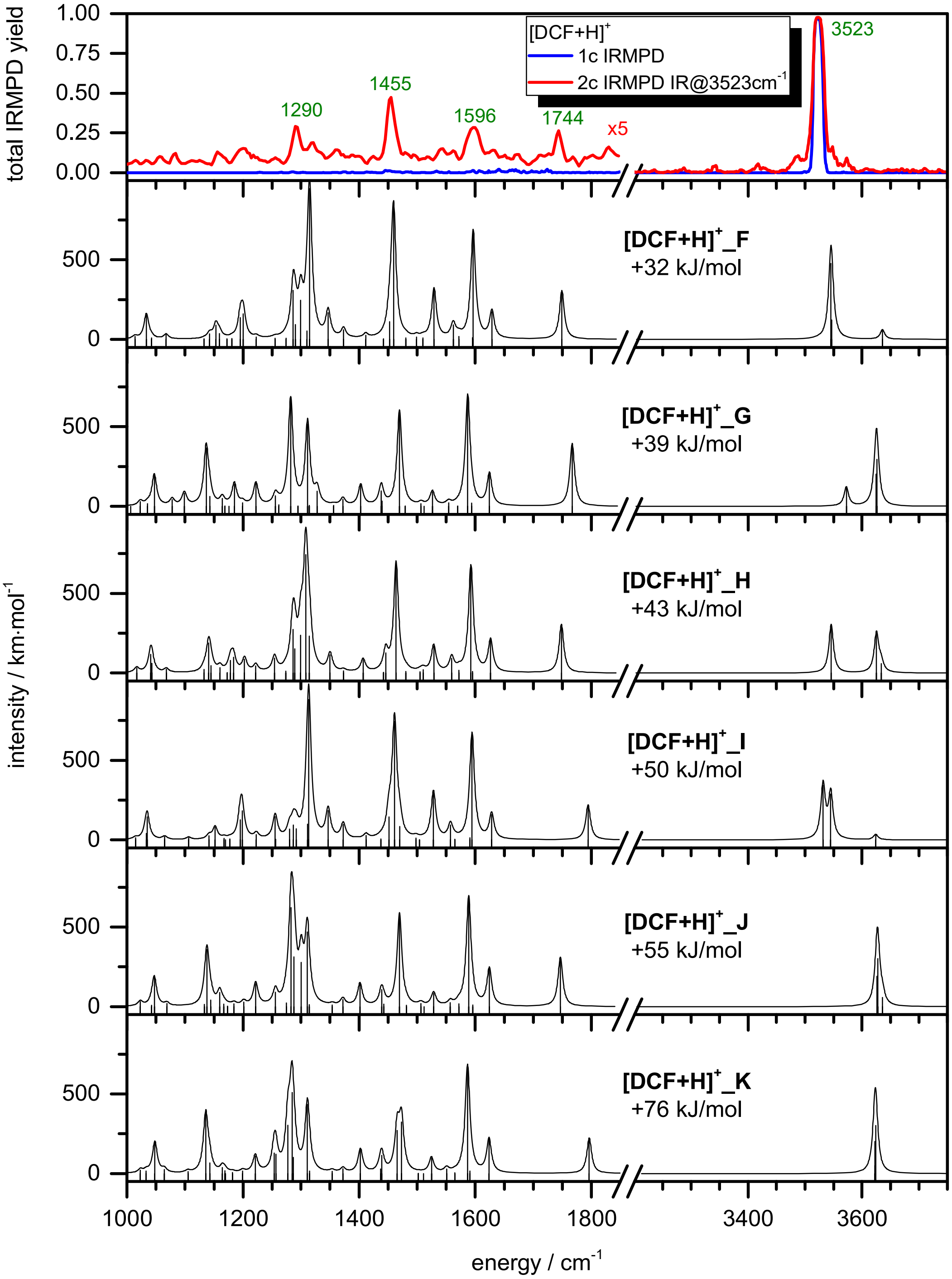

Figure S4: Experimental one and two color IRMPD spectrum of cationic 2',7'-dichlorofluorescein [DCF+H]$^+$ in comparison to the calculated harmonic absorption spectra of the less stable minimum structures **[DCF+H]$^+$_F** to **[DCF+H]$^+$_K**.

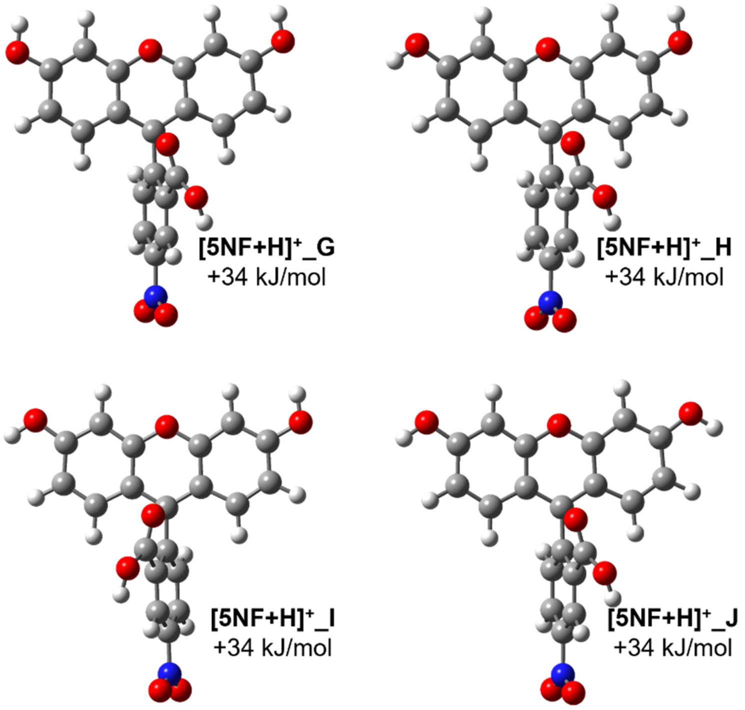

Figure S5: Less stable minimum structures **[5NF+H]$^+$_G** to **[5NF+H]$^+$_J** of the cationic species of 5-nitrofluorescein [5NF+H]$^+$ calculated by DFT/B3LYP.

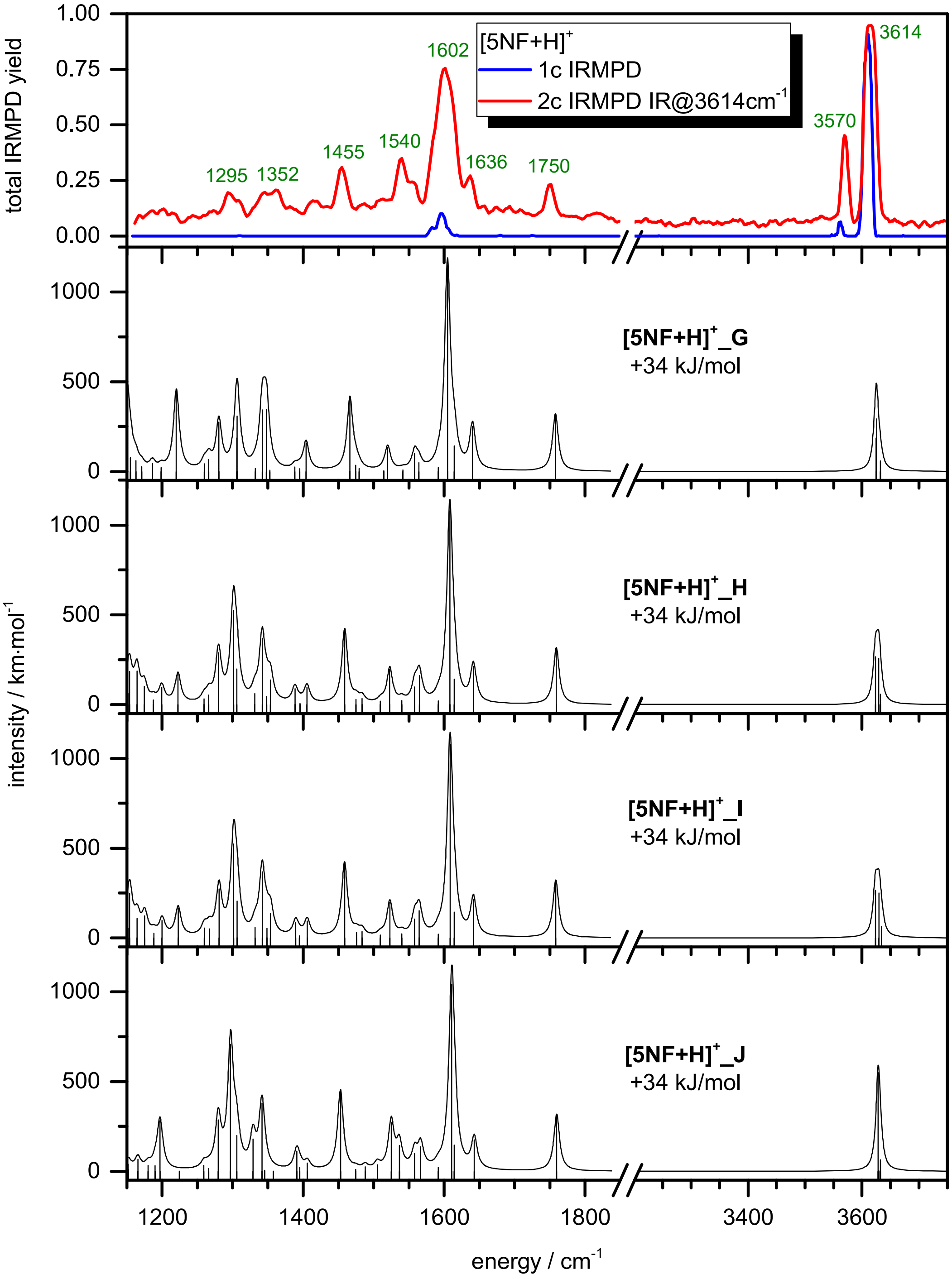

Figure S6: Experimental one and two color IRMPD spectrum of cationic 5-nitrofluorescein $[5NF+H]^+$ in comparison to the calculated harmonic absorption spectra of the less stable minimum structures **$[5NF+H]^+$_G** to **$[5NF+H]^+$_J**.

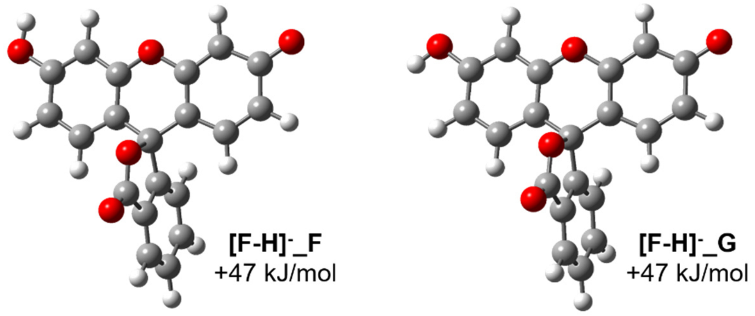

Figure S7: Less stable minimum structures **[F-H]$^-$_F** and **[F-H]$^-$_G** of the anionic species of fluorescein [F-H]$^-$ calculated by DFT/B3LYP.

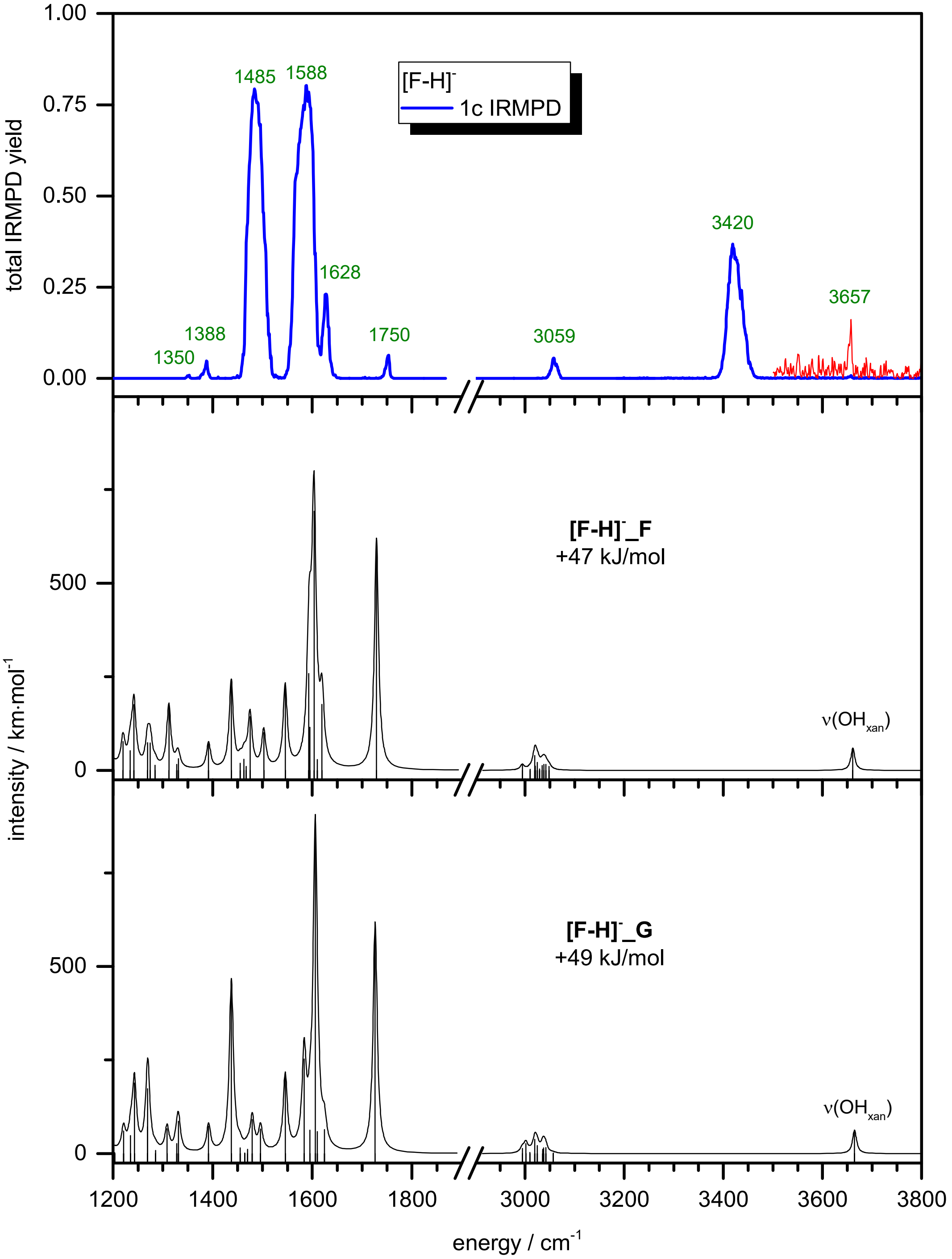

Figure S8: Experimental one color IRMPD spectrum of anionic fluorescein species [F-H]$^-$ in comparison to the calculated harmonic absorption spectra of the less stable minimum structures **[F-H]$^-$_F** and **[F-H]$^-$_G**. Note, that the red graph in the experimental spectrum is magnified by a factor of 20, exposing a weak absorption at 3657 cm^{-1}.

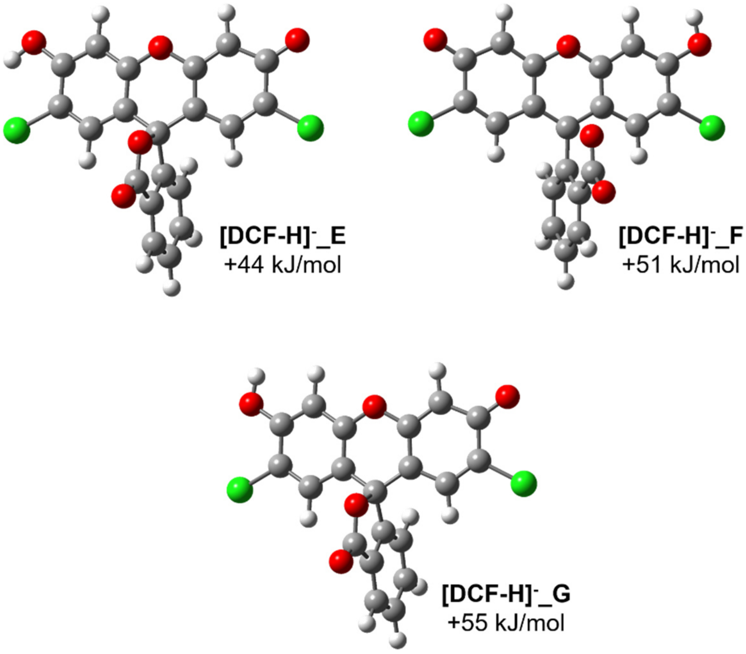

Figure S9: Less stable minimum structures **[DCF-H]$^-$_E** to **[DCF-H]$^-$_G** of the anionic species of 2',7'-dichlorofluorescein [DCF-H]$^-$ calculated by DFT/B3LYP.

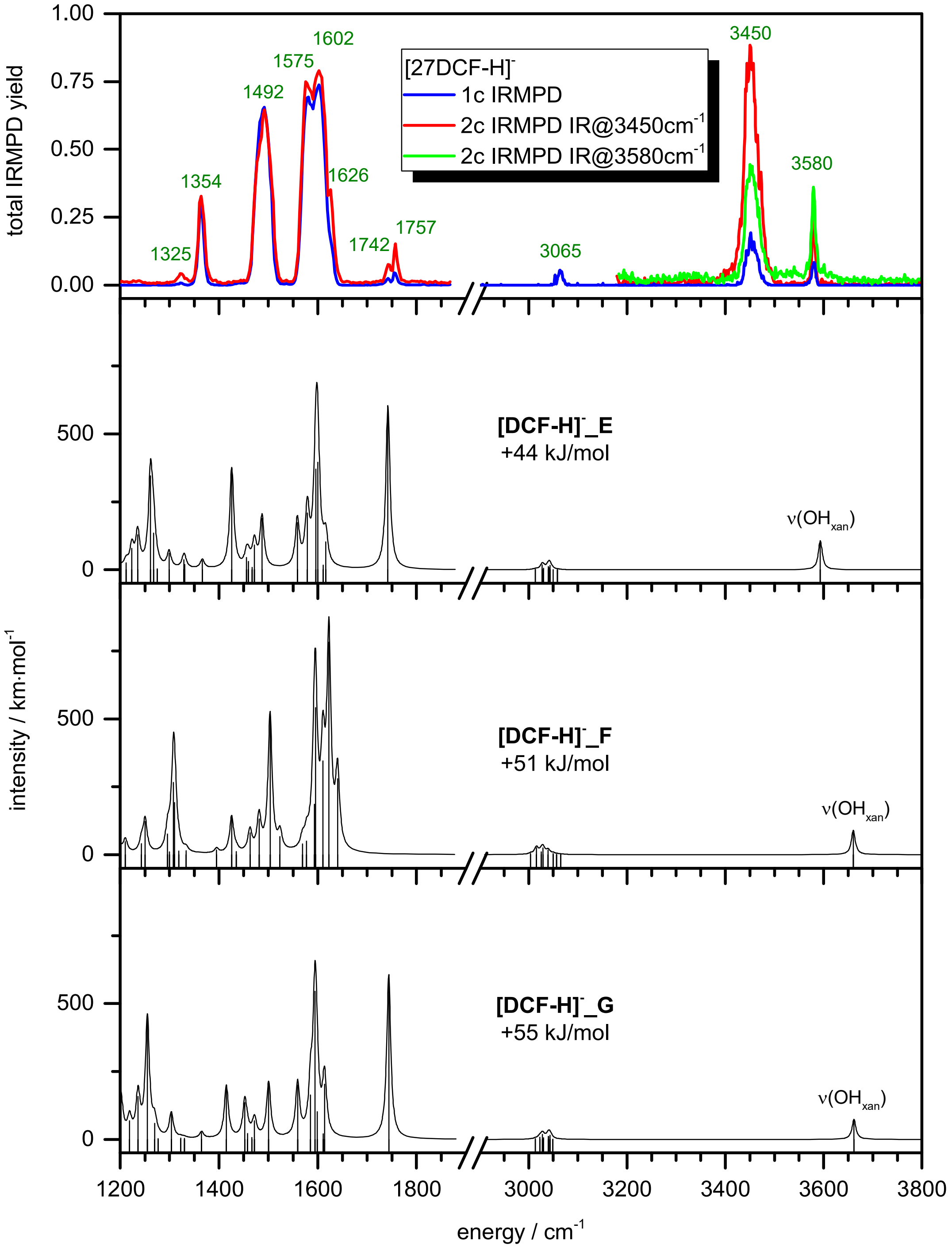

Figure S10: Experimental one and two color IRMPD spectrum of anionic 2',7'-dichlorofluorescein species [DCF-H]$^-$ in comparison to the calculated harmonic absorption spectra of the less stable minimum structures **[DCF-H]$^-$_E** to **[DCF-H]$^-$_G**.

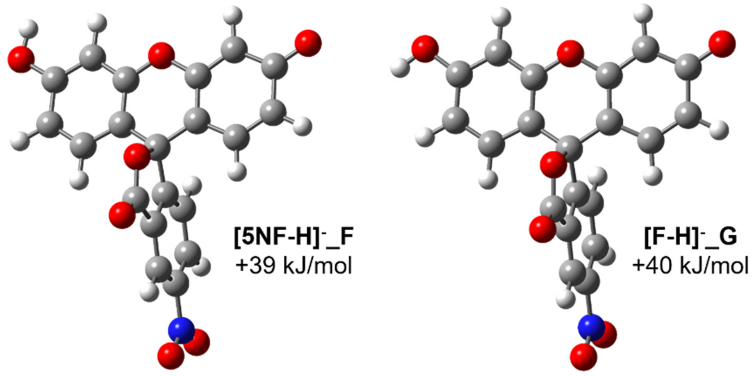

Figure S11: Less stable minimum structures **[5NF-H]$^-$_F** and **[5NF-H]$^-$_G** of the anionic species of 5-nitrofluorescein [5NF-H]$^-$ calculated by DFT/B3LYP.

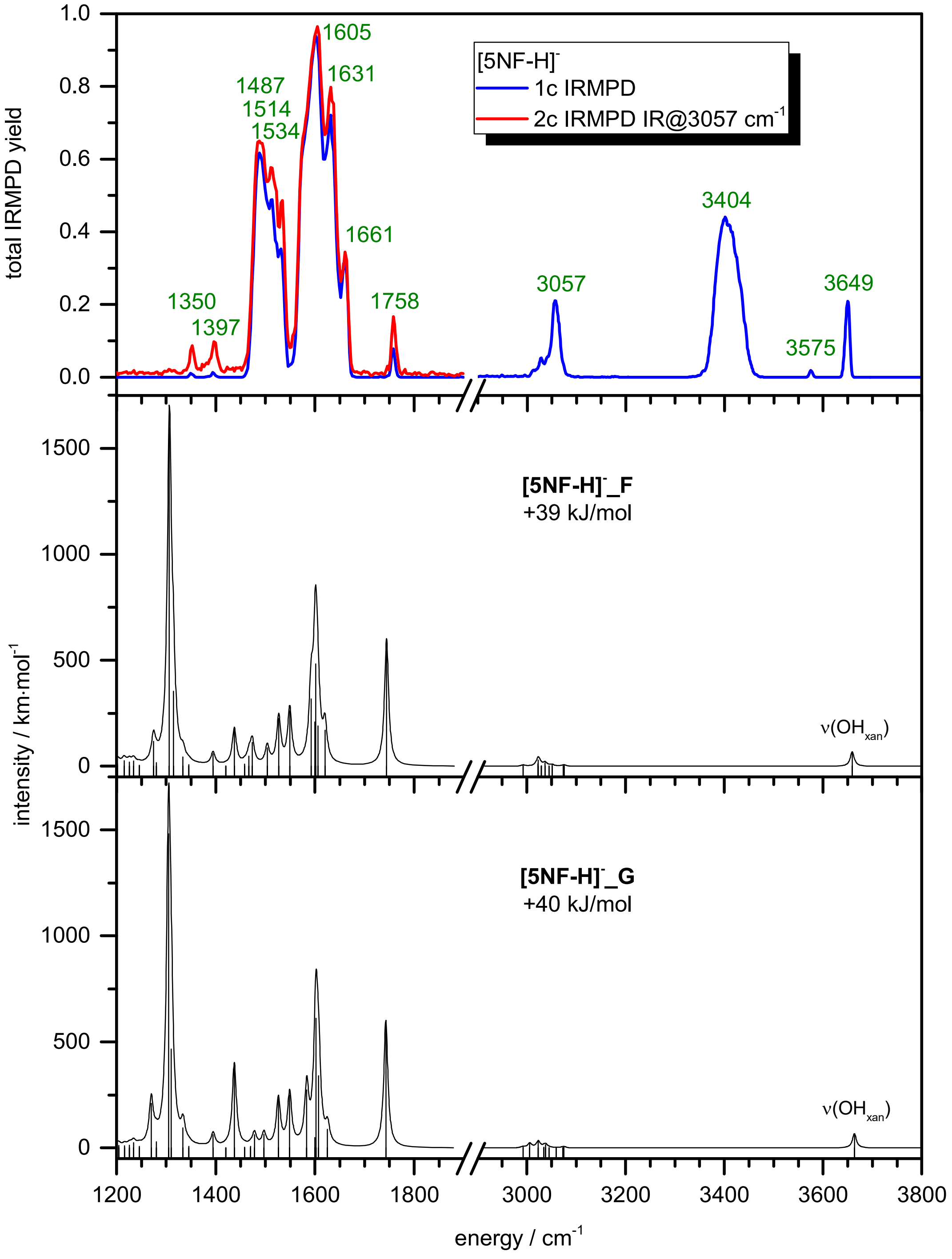

Figure S12: Experimental one and two color IRMPD spectrum of anionic 5-nitrofluorescein species [5NF-H]$^-$ in comparison to the calculated harmonic absorption spectra of the less stable minimum structures **[5NF-H]$^-$_F** and **[5NF-H]$^-$_G**.

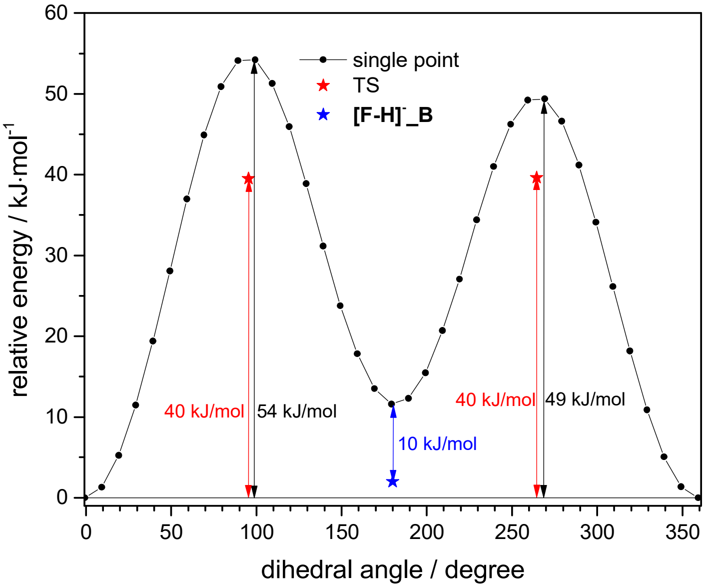

Figure S13: Potential energy surface (PES) for the conversion of **[F-H]$^-$_A** to **[F-H]$^-$_B** by rotation of the OH group around the C-O bond. The dihedral angle is defined by the C-C-O-H atoms of the benzoic acid moiety.

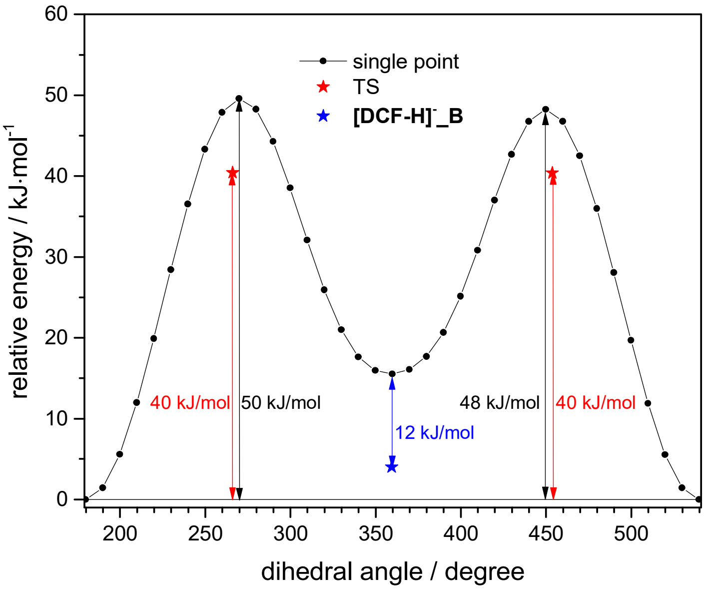

Figure S14: Potential energy surface (PES) for the conversion of **[DCF-H]$^-$_A** to **[DCF-H]$^-$_B** by rotation of the OH group around the C-O bond. The dihedral angle is defined by the C-C-O-H atoms of the benzoic acid moiety.

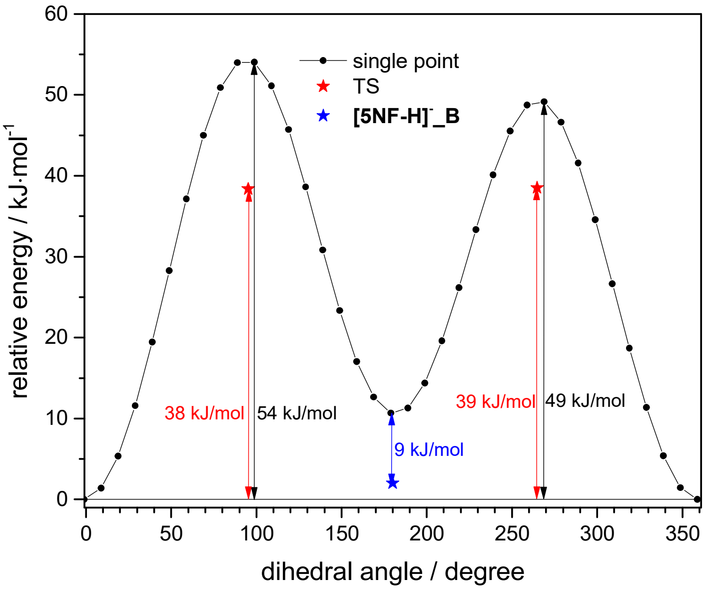

Figure S15: Potential energy surface (PES) for the conversion of **[5NF-H]$^-$_A** to **[5NF-H]$^-$_B** by rotation of the OH group around the C-O bond. The dihedral angle is defined by the C-C-O-H atoms of the benzoic acid moiety.

7 Summary and Outlook

The presented work encompasses magnetic investigations on metal complexes and structural investigations on metal complexes and fluorescein derivatives as isolated ions, transferred into the gas phase by Electrospray Ionization (ESI). The experimental conditions in ion traps facilitate exploration of intrinsic molecular magnetic and structural properties exempt from any influences of e.g. solvent, bulk or auxiliary surfaces.

X-ray Magnetic Circular Dichroism (XMCD) spectroscopy in combination with sum rule analysis allows to separately address the spin and orbital contributions to the magnetic moments of open valence metal ions. The XMCD experiments were conducted at the NanoCluster Trap connected to the UE52-PGM soft X-ray beamline at the BESSY II synchrotron facility of the Helmholtz-Zentrum für Materialien und Energie GmbH in Berlin.

The structural studies using InfraRed Multiple Photon Dissociation (IRMPD) spectroscopy were conducted with a modified *Bruker amaZon SL* PAUL-trap mass spectrometer in combination with two *LaserVision* OPO/OPA laser systems providing tunable infrared light covering a spectral region from 1000 – 4000 cm^{-1}. Quantum chemical calculations based on density functional theory (DFT) serve to determine of geometry minimum structures and to calculate the corresponding linear harmonic IR absorption spectra in order to identify isomer populations by comparison of calculated to experimental spectra.

Gas phase XMCD studies on a set of structurally analogous trinuclear hetero-bimetallic 3*d*-4*f* complexes [Mn_2Ln] containing two manganese(II) ions and a lanthanide(III) ion (neodymium, europium, gadolinium, dysprosium or lutetium) provided insight into the spin and orbital contributions of the individual metal centers to the total molecular magnetic moment. Due to the vanishing orbital angular momenta on the manganese ions and the substantial spin magnetizations, a d^5 high spin configuration was determined for all complexes. The XMCD effects and the respective spin and orbital angular momenta of the lanthanide ions vary, in conjunction with the *f*-orbital occupancy. We have confirmed the diamagnetic ground state of Eu^{3+}. The m_L/m_S ratios reported for Nd^{3+}, Gd^{3+} and Dy^{3+} are in excellent agreement with the expected values derived from HUND's rules. By comparing the experimental total magnetization $m_J^{(z)}$ at the given experimental conditions with a Brillouin plot for the Mn^{2+} and the respective Ln^{3+} ground states as a function of the temperature at a constant magnetic field of 5 T, we were able to approximate the ion temperature of the hetero-bimetallic complexes. The values of approx. 14 K are in the expected ion temperature range, due to RF heating of the ions caused by the trap operation. Correction terms for the application of the spin sum rule were found to be indispensable for qualitative and quantitative analysis of magnetic moments in isolated metal complexes studied by XMCD spectroscopy. The results from gas phase studies were corroborated bulk magnetometry in terms of SQUID measurements on crystalline samples. SQUID measurements reveal weak ferromagnetic interactions between the paramagnetic trivalent lanthanide ions (Nd^{3+}, Gd^{3+} and Dy^{3+}) and the adjacent Mn^{2+} ions at temperatures < 10 K. A magnetic coupling of the manganese ions via the diamagnetic lanthanide ions (Eu^{3+} and Lu^{3+}) was not observed. The magnetization measurements show a good agreement between the expected magnetization for weakly exchange coupled ions and the measured saturation value at high fields. In summary, we have shown that a combination of XMCD spectroscopy on complexes in the gas phase and sum rule analysis is a powerful tool to determine the intrinsic magnetic properties of isolated molecules.

The have presented for the first time an extensive experimental and theoretical study of a mononuclear octahedral iron(II) Spin-Crossover complex $[Fe(L\text{-}N_4Bz_2)(pyc)]^+$ (**1**$^+$) by XMCD measurements at different temperatures in the gas phase in combination with DFT modeling. We have confirmed that an accurate description of spin transitions in metal complexes along with structural reorganization via DFT calculations is challenging, due to the large dependence of the relative energies at different multiplicities on the extent of exact Hartree-Fock (HF) exchange in hybrid functionals such as B3LYP. A customized B3LYP* (15 % H_x^{HF}) functional, employing 15 % of exact HF exchange was found to satisfactorily describe the energetic spacing of the spin states of **1**$^+$, required for Spin-Crossover processes. The geometry optimized structures in singlet and quintet states are in excellent agreement with crystallographic data. The singlet calculation can be assigned to the crystal structure measured at 110 K, revealing reduced iron – ligand bond lengths. The vanishing magnetic moment at temperatures < 250 K is nicely matched by the non-existent spin density in the calculation. The bond lengths of the quintet calculation match the crystal structure data at 333 K very well. The calculated spin density at the iron(II) center is in accordance with the magnetic moment measured at temperatures > 280 K.

Photon polarization dependent gas phase XMCD spectra of the isolated complex cation $\mathbf{1}^+$ recorded at the Fe $L_{3,2}$ absorption edges at different ion trap temperatures show significant dichroic effects. This indicates a certain magnetic moment at the iron(II) metal center. As the spin and total magnetic moments are much smaller than expected for an all-high spin configuration of the complex, we assume a coexistence of high spin and low spin configurations, since the method only provides an average magnetization of the ion ensemble. A pure orientational randomization of the magnetic moments at higher temperatures, assuming an all-high spin configuration seems unlikely as the lowest ion temperature can be estimated to approx. 15 K from similar experiments. Calculating the high spin fractions at three different temperatures using the spin and total magnetization and simulated Brillouin functions, provides strong evidence for a Spin-Crossover process in the gas phase, as the high spin fraction was found to increase with temperature. Future studies including an ion temperature calibration are necessary to prove our assumption. Manganese(II) complexes exhibiting a temperature independent d^5 high spin configuration appear to be suitable systems for this purpose.

We performed structural characterization of (methylated) pyrimidine-based thymine (T) and uracil (U) nucleobases bound to dianionic tetracyanoplatinate(II), which are a popular model system to explore fundamental photophysical and photochemical processes in photodynamic therapy (PDT). Using a one and two color IRMPD technique in combination with DFT for geometry optimization and harmonic frequency calculation, we were able to conclusively determine the structures of $[T \cdot Pt(CN)_4]^{2-}$, $[1\text{-mT} \cdot Pt(CN)_4]^{2-}$, $[U \cdot Pt(CN)_4]^{2-}$ and $[1\text{-mU} \cdot Pt(CN)_4]^{2-}$ aggregates. The observed binding motifs of the non-methylated and methylated nucleobase complexes are identical, although the intermolecular interactions differ significantly. The non-methylated nucleobases thymine and uracil are bound primarily via a N1H hydrogen bond to a nitrogen atom of a cyanide ligand. The found geometries are similar to those, reported in a purely theoretical study by JOCKUSCH *et al.* solely based on computations. Calculations on the methylated nucleobases reveal a similar binding motif to tetracyanoplatinate(II). However, the concomitant stabilization via a strong NH – NC and weaker CH – NC interactions is not reconcilable, due to shielding carbonyl groups adjacent to the remaining N3H proton. Solely CH – NC interactions mediate the loosely bound nucleobase – tetracyanoplatinate(II) aggregate.

First experiments on the respective binding motif of the nucleosides thymidine and uridine suggest a remarkably different behavior. The N1H proton of the nucleobases is replaced by a cyclic sugar side chains. The CH – NC interactions become less pronounced and the pentose's hydroxy groups form stable hydrogen bonds with the cyanide ligands of tetracyanoplatinate(II). The flexibility of the sugar backbone and the large number of polarized functional groups result in numerous possible isomers. Definite structural assignments were not possible, owing to the highly broadened experimental absorption bands in the CH/OH/NH stretching region. Additional experiments using messenger spectroscopy (e.g. He tagging) in a cryogenically cooled ion trap may help to resolve the band structure in the crucial CH stretching region, which is superimposed by the hydrogen bound OH/NH stretching region. However, our calculations at least show that the binding motif compared to the (methylated) nucleobases changes in favor of CN – HO hydrogen bonds.

The second structural characterization study was performed on the three charged forms of fluorescein (F), 2',7'-dichlorofluorescein (DCF) and 5-nitrofluorescein (5NF). Fluorescein derivatives are frequently used for protein labeling in medical diagnostics, owing to their bright fluorescence and the easy conjugation to biomolecules. The fluorescence properties, however, are strongly influenced by functional groups and the charge state. We performed gas phase one and two color IRMPD experiments in combination with DFT calculations to elucidate minimum structures, their relative free energies, transition states, and rotational barriers for interconversion of rotamers. The dianionic species are entirely deprotonated resulting in a single minimum structure. The experimental IRMPD spectra match the calculated harmonic IR spectra extraordinarily well, with regard to peak position and intensity. The experimental two color IRMPD spectra are in excellent agreement with calculated harmonic IR spectra of geometry optimized minimum structures. However, a lack of distinct spectral features in the calculated harmonic absorption spectra make an unequivocal assignment challenging. The unsuspected deprotonation site of monoanionic fluorescein at the xanthene moiety was first reported in an IRMPD study by JOCKUSCH *et al.* and endorsed by this study, additionally taking the vibrational OH stretching region into account. We have shown that the deprotonation site of monoanionic fluorescein derivatives in the gas phase and in methanolic solution is described accurately by DFT energy calculations on minimum structures and depends on the substituents. The presented data provide strong evidence for a partial conservation of the favored minimum structures in methanolic solution during the transfer into the gas phase via ESI. The utilized two color IRMPD technique has once more proven valuable to overcome bottlenecks and enhance weak IRMPD absorption bands of stable molecules and allows for a wider spectral range and improved spectral resolution in comparison to experimental data obtained with Free Electron Laser (FEL) sources. Future investigations using different ionization techniques, e.g. the Laser Induced Liquid Bead Ion Desorption (LILBID) in combination with mass spectrometry and spectroscopy could help to elucidate the properties of defined dye-solvent cluster ions.

8 Zusammenfassung und Ausblick

Die vorliegende Arbeit beschäftigt sich mit magnetischen Untersuchungen an isolierten ionischen Metallkomplexen und strukturellen Untersuchungen an isolierten ionischen Metallkomplexen und Fluoresceinderivaten. Dafür wurden die Proben durch Elektrospray-Ionisation (ESI) aus einer Lösung in die Gasphase überführt. Die experimentellen Bedingungen in Ionenfallen erlauben die Erforschung von intrinsischen molekularen magnetischen und strukturellen Eigenschaften ohne störende äußere Einflüsse durch beispielsweise Lösungsmitteleffekte, Packungseffekte in Kristallen oder Wechselwirkungen mit Oberflächen.

Der Zirkulare Magnetische Dichroismus mit Röntgenstahlung (XMCD-Spektroskopie) in Kombination mit der Anwendung der sogenannten Summenregeln erlaubt es, die Spin- und Bahnbeiträge zum gesamten magnetischen Moment von offenschaligen Metallkernen getrennt voneinander getrennt zu bestimmen. Die XMCD-Experimente wurden an der NanoCluster Trap durchgeführt, welche an der UE52-PGM-Beamline für weiche Röntgenstrahlung an der BESSY II-Synchrotronanlage des Helmholtz-Zentrum für Materialien und Energie GmbH in Berlin angeschlossen ist.

Die Studien zur Strukturaufklärung mithilfe der mit infraroten Multiphotonen-Dissoziation (IRMPD-Spektroskopie) wurden mit einem modifizierten *Bruker amaZon SL* PAULfallen-Massenspektrometer in Kombination mit zwei optisch parametrischen Oszillator-/Verstärkersystemen (OPO/OPA) der Firma *LaserVision* durchgeführt. Dabei wird der infrarote Spektralbereich von etwa 1000 bis 4000 cm^{-1} abgedeckt. Quantenchemische Berechnungen auf Basis der Dichtefunktionaltheorie (DFT) dienen zur Bestimmung von geometrischen Minimumstrukturen und deren linearen harmonischen IR Absorptionsspektren um die Population von Isomeren durch den Vergleich von berechneten und experimentellen Spektren zu bestimmen.

Untersuchungen an einem Satz von isostrukturellen trinuklearen hetero-bimetallischen 3*d*-4*f*-Komplexen [Mn_2Ln] unter Verwendung der XMCD-Spektroskopie in der Gasphase, lieferten die jeweiligen Spin- und Bahnbeiträge der einzelnen Metallzentren zum gesamten magnetischen Moment. Die Komplexe verfügen dabei jeweils über zwei Mangan(II)-Ionen und ein Ion(III) der Gruppe der Seltenen Erden (Neodym, Europium, Gadolinium, Dysprosium oder Lutetium). Aufgrund des verschwindenden magnetischen Bahnmoments an den

Manganionen und den signifikanten Spinmomenten konnte eine d^5 high spin Konfiguration bestätigt werden. Die XMCD-Effekte und die jeweiligen Spin- und Bahnmomente der Lanthanid-Ionen variieren stark, je nach der Besetzung der jeweiligen *f*-Orbitale. Dabei konnte der diamagnetische Grundzustand von Eu^{3+} bestätigt werden. Die experimentell bestimmten m_L/m_S-Verhältnisse für Nd^{3+}, Gd^{3+} und Dy^{3+} stimmen mit den erwarteten Werten nach den HUND'schen Regeln sehr gut überein. Durch Vergleichen der experimentell bestimmten Gesamtmagnetisierung $m_J^{(z)}$ bei den gegebenen experimentellen Bedingungen mit einem Brillouin-Diagramm für die Mn^{2+} und Ln^{3+} Ionen im jeweiligen Grundzustand als Funktion der Temperatur bei einem konstanten Magnetfeld von 5 T, konnte die Ionentemperatur der $[Mn_2Ln]$-Komplexe abgeschätzt werden. Die Werte von ca. 14 K liegen im erwarteten Temperaturbereich der Ionen die sich aufgrund der Hochfrequenzspannung die an der Falle anliegt im Vergleich zur Fallentemperatur erwärmen. Korrekturen für die Anwendung der Spin-Summenregel haben es erstmals ermöglicht nicht nur qualitative, sondern auch quantitative Aussagen über die magnetischen Momente von isolierten Metallkomplexen zu treffen. Die Ergebnisse der Gasphasenuntersuchungen wurden durch die Festkörpermessungen in Form von SQUID-Messungen an kristallinen Proben untermauert. Die SQUID-Messungen zeigen schwache ferromagnetische Wechselwirkungen zwischen den paramagnetischen dreiwertigen Lanthanidionen (Nd^{3+}, Gd^{3+} und Dy^{3+}) und den benachbarten Mn^{2+}-Ionen bei Temperaturen <10 K. Eine magnetische Kopplung der Manganionen über die diamagnetischen Lanthanidionen (Eu^{3+} und Lu^{3+}) wird nicht beobachtet. Die gemessenen Magnetisierungen zeigen eine gute Übereinstimmung zwischen der erwarteten Magnetisierung für schwach austauschgekoppelte Ionen und dem gemessenen Sättigungswert bei hohen Feldern. In dieser Studie haben wir gezeigt, dass eine Kombination von XMCD-Spektroskopie an isolierten Komplexen in der Gasphase und Summenregelanalyse ein leistungsfähiges Werkzeug für die Untersuchung interessanter magnetischer Verbindungen frei von Lösungsmitteleffekten, Kristallpackungseffekten oder Wechselwirkungen mit Oberflächen darstellt.

Wir haben erstmals eine umfassende experimentelle und theoretische Untersuchung an einem mononuklearen oktaedrischen Eisen(II) Spin-Crossover Komplexes $[Fe(L\text{-}N_4Bz_2)(pyc)]^+$ (**1**$^+$) mittels XMCD Spektroskopie bei verschiedenen Temperaturen in der Gasphase in Kombination mit DFT-Berechnungen durchgeführt. Wir konnten bestätigen, dass eine angemessene Beschreibung von Spinübergängen in Metallkomplexen zusammen mit struktureller Reorganisation durch DFT-Berechnungen schwierig ist. Das liegt hauptsächlich an der starken Abhängigkeit der relativen Energien bei unterschiedlichen Multiplizitäten vom Ausmaß des exakten Hartree-Fock-Austausches H_x^{HF} in Hybridfunktionalen wie z.B. B3LYP. Ein modifiziertes Funktional B3LYP* mit 15 % exaktem Hartree-Fock-Austausch zeigt eine verhältnismäßig genaue Beschreibung der Nähe der energetischen Abstände von **1**$^+$ in verschiedenen Spin-Zuständen. Diese energetische Nähe unterschiedlicher Spinzustände ist Voraussetzung für Spin-Crossover-Prozesse. Die geometrieoptimierten Strukturen im Singulett- und Quintettzustand geben die Kristallstrukturdaten sehr gut wieder. Die Singulettrechnung kann der Kristallstruktur bei 110 K zugeordnet werden, die sich durch reduzierte Eisen-Ligand-Bindungslängen auszeichnet. Das verschwindende magnetische Moment bei Temperaturen < 250 K wird durch die nicht vorhandene Spindichte in der Rechnung korrekt dargestellt. Die Bindungslängen der Quintettrechnung spiegeln die Kristallstruktur bei 333 K sehr gut wieder. Die berechnete Spindichte am zentralen Eisen(II) -Ion, wird experimentell durch das gemessene magnetische Moment bei Temperaturen > 280 K wiedergegeben.

Polarisationsabhängige XMCD-Spektren des isolierten Komplexkations **1**$^+$ an den Fe $L_{3,2}$-Absorptionskanten bei verschiedenen Ionenfallentemperaturen in der Gasphase, zeigen bei allen Temperaturen signifikante dichroitische Effekte. Das beweist ein bestimmtes magnetisches Moment am zentralen Eisen(II)-Atom. Die Spinmomente und die totalen magnetischen Momente sind viel kleiner sind als man es für eine reine high-Spin-Konfiguration des Komplexes erwarten würde. Da die Methode nur durchschnittliche Magnetisierungen des Ionenensembles liefert, nehmen wir eine Koexistenz von high spin und low spin-Konfiguration in der Ionenwolke an. Eine reine Randomisierung der Orientierung der magnetischen Momente bei höheren Temperaturen unter der Annahme einer reinen high spin Konfiguration ist unwahrscheinlich, da die niedrigste Ionentemperatur aus ähnlichen Experimenten auf etwa 15 K geschätzt werden kann. In verschiedenen Szenarien zur Auswirkung der Hochfrequenz-Aufheizung der Ionen berechnen wir den high spin Anteil bei verschiedenen Temperaturen unter Verwendung der Spin-/Totalmagnetisierung und simulierten Brillouin-Funktionen. Die Ergebnisse deuten auf einen Spin-Crossover Prozess in der Gasphase hin, da der high spin-Anteil mit der Temperatur zunimmt. Ergänzende Studien einschließlich einer Kalibrierung der

Ionentemperatur sind für zuverlässigere Aussagen notwendig. Hierfür würden sich beispielsweise Mangan(II)-Komplexe mit einer temperaturunabhängigen d^5 high spin Konfiguration eignen.

Es wird weiterhin über eine strukturelle Charakterisierung von (methylierten) Pyrimidin-basierten Nukleobasen Thymin (T) und Uracil (U) die an dianionisches Tetracyanoplatinat(II) gebunden sind berichtet. Diese stellen ein prominentes Modellsystem zur Erforschung grundlegender photophysikalischer und photochemischer Prozesse in der photodynamischen Therapie (PDT) dar. Durch die verwendeten ein- und zwei-Farben IRMPD-Techniken in Kombination mit DFT-basierten Rechnungen in Form von Geometrieoptimierung und harmonischen Schwingungsspektren erhielten wir schlüssige Strukturzuordnungen für die Aggregate $[T \cdot Pt(CN)_4]^{2-}$, $[1\text{-}mT \cdot Pt(CN)_4]^{2-}$, $[U \cdot Pt(CN)_4]^{2-}$ und $[1\text{-}mU \cdot Pt(CN)_4]^{2-}$. Die beobachteten Bindungsmotive der nicht-methylierten und methylierten Nukleobasen, die an Tetracyanoplatinat (II) gebunden sind, sind identisch. Es gibt jedoch deutliche Unterschiede in der Natur der intermolekularen Wechselwirkungen. Die nicht-methylierten Nukleobasen Thymin und Uracil werden primär über eine N1H-Wasserstoffbrückenbindung an ein Stickstoffatom eines Cyanidliganden gebunden und durch verschiedene CH – CN Wechselwirkungen stabilisiert. Die geometrischen Zuordnungen sind in Übereinstimmung mit den Ergebnissen von A. SEN *et al.* die ausschließlich auf Rechnungen basieren. Die methylsubstituierten Nukleobasen zeigen ein abweichendes Bindungsmotiv zum Tetracyanoplatinat(II)-dianion. Eine gleichzeitige Stabilisierung über eine starke NH – NC und schwächere CH – NC Wechselwirkungen ist durch die Abschirmung der Carbonylgruppen neben dem verbleibenden N3H Proton nicht möglich. Lediglich CH – NC Wechselwirkungen vermitteln das locker gebundene Nukleobase - Tetracyanoplatinat (II) - Aggregat. Erste Experimente zum jeweiligen Bindungsmotiv der Nukleoside Thymidin und Uridin deuten auf ein ganz anderes Verhalten hin. In Nukleosiden ist das N1H Proton durch eine cyclische Zuckerseitenkette substituiert. Die CH – NC Wechselwirkungen verlieren an Bedeutung und die Hydroxygruppen der Pentose bilden mit den Cyanidliganden des Tetracyanoplatinats(II) stabile Wasserstoffbrückenbindungen. Die Flexibilität des Zuckerrückgrats und die große Anzahl polarer funktioneller Gruppen führen zu einer großen Zahl an möglichen Bindungsisomeren. Zuverlässige Zuordnungen werden durch die stark verbreiterten Absorptionsbanden im CH/OH/NH-Streckschwingungsbereich erschwert. Zusätzliche

Experimente unter Anwendung sog. Messenger-Spektroskopie (z.B. He *tagging*) in tiefgekühlten Ionenfallen könnten dazu beitragen, die Bandenstruktur des CH-Streckschwingungsbereichs aufzulösen, die mit dem verbreiterten wasserstoffbrücken-gebundenen OH/NH-Streckschwingungsbereich überlagert ist. Berechnungen zeigen jedoch, dass sich das Bindungsmotiv gegenüber den (methylierten) Nukleobasen zugunsten von CN – HO Wasserstoffbrücken ändert.

Die zweite Studie zur Strukturaufklärung mittels IRMPD-Spektroskopie wurde an den drei geladenen Formen von Fluorescein (F), 2',7'-Dichlorfluorescein (DCF) und 5-Nitrofluorescein (5NF) durchgeführt. Fluoresceinderivate werden aufgrund ihrer hellen Fluoreszenz und der leicht zugänglichen Funktionalisierung häufig zur Proteinetikettierung in der medizinischen Diagnostik eingesetzt. Die Fluoreszenzeigenschaften sind stark von funktionellen Gruppen und dem Ladungszustand abhängig. Es wurden ein- und zwei-Farben IRMPD Experimente in der Gasphase in Kombination mit DFT-Rechnungen durchgeführt. Die Rechnungen liefern hierbei Minimum-Strukturen, relative freie Energien, Übergangszustände und Rotationsbarrieren. Die dianionischen Spezies sind vollständig deprotoniert, was zu einer einzigen möglichen Minimum-Struktur führt. Die experimentellen IRMPD-Spektren entsprechen den berechneten harmonischen Spektren hinsichtlich der Bandenpositionen und -intensitäten außerordentlich gut. Die kationischen Spezies zeigen eine ausgezeichnete Übereinstimmung zwischen den zwei-Farben IRMPD-Spektren und den berechneten harmonischen Spektren der geometrieoptimierten Minimum-Strukturen. Das Fehlen von signifikanten Unterschieden in den berechneten harmonischen Absorptionsspektren macht eine eindeutige Zuordnung von Isomeren schwierig. Über die unerwartete Deprotonierungsstelle von monoanionischem Fluorescein an der Xantheneinheit wurde erstmals von JOCKUSCH *et al*. in einer IRMPD Studie berichtet. Die vorliegende Studie bestätigt diese Ergebnisse, wobei der Spektralbereich um den OH-Streckschwingungsbereich erweitert wurde. Wir konnten zeigen, dass die favorisierte Deprotonierungsstelle von monoanionischen Fluoresceinderivaten in der Gasphase und in methanolischer Lösung von inhärenten Substituenten abhängig ist und durch DFT-Rechnungen treffend wiedergegeben wird. Die gezeigten Ergebnisse liefern einen starken Hinweis für eine partielle Erhaltung der bevorzugten Struktur in methanolischer Lösung während des Transfers in die Gasphase über ESI. Die verwendete zwei-Farben IRMPD-Technik hat sich wiederholt als wertvoll erwiesen um einerseits energetische Flaschenhälse (bzgl. der intramolekularen Schwingungsumverteilung) zu überwinden und schwache IRMPD-Absorptionsbanden von stabilen Molekülen zu verstärken und andererseits einen größeren Spektralbereich und eine verbesserte spektrale Auflösung im Vergleich zu Freie Elektronen Laser (FEL) Daten zu ermöglichen. Zukünftige Untersuchungen unter Verwendung unterschiedlicher Ionisationstechniken, z.B. laserinduzierte Flüssigtropfen-Ionen-Desorption (Laserinduced Liquid Bead Ion Desorption, LILBID) in Kombination mit Massenspektrometrie und Spektroskopie könnten es ermöglichen, die Eigenschaften definierter Farbstoff-Lösungsmittel-Cluster-Ionen zu erforschen.

9 Appendix: Joint Publications

Content:

9.1 Infrared spectroscopy of N_2 adsorption on size selected cobalt cluster cations in isolation

9.2 Vibrational Blue Shift of Coordinated N_2 in $[Fe_3O(OAc)_6(N_2)_n]^+$: “Non Classical” Dinitrogen Complexes

9.3 Doubly Regioselective C-H Hydroarylation of Unsymmetrical Alkynes Using Carboxylates as Deciduous Directing Groups

9.1 Infrared spectroscopy of N_2 adsorption on size selected cobalt cluster cations in isolation

Sebastian Dillinger, Jennifer Mohrbach, Joachim Hewer, Maximilian Gaffga
and Gereon Niedner-Schatteburg

Fachbereich Chemie and Forschungszentrum OPTIMAS,
Technische Universität Kaiserslautern,
67663 Kaiserslautern, Germany

9.1.1 Preamble

The following chapter is a reprint of a publication in the journal “Physical Chemistry Chemical Physics”.

A team consisting of Sebastian Dillinger, Jennifer Mohrbach, Maximilian Gaffga and myself performed the measurements. Sebastian Dillinger evaluated the experimental data and conducted the presented quantum chemical calculations. The manuscript was written by Sebastian Dillinger and revised with the help of Gereon Niedner-Schatteburg and Jennifer Mohrbach.

Full Reference:

Infrared spectroscopy of N2 adsorption on size selected cobalt cluster cations in isolation

S. Dillinger, J. Mohrbach, J. Hewer, M. Gaffga and G. Niedner-Schatteburg, Physica*l Chemistry Chemical Physics,* **2015**, 17, 10358-10362.

http://dx.doi.org/10.1039/C5CP00047E

9.1.2 Reprint

Reprint Licence

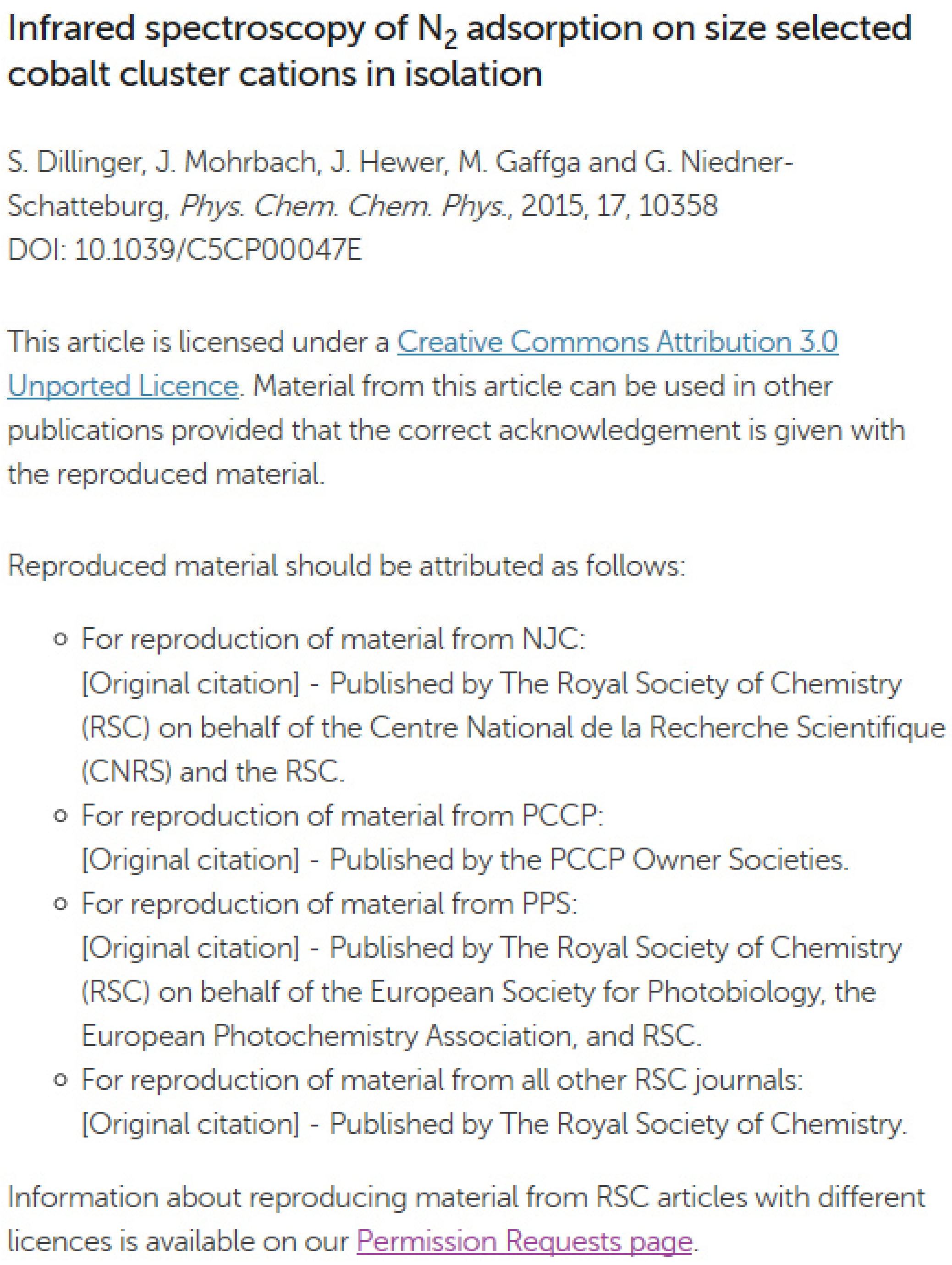

Infrared spectroscopy of N_2 adsorption on size selected cobalt cluster cations in isolation

S. Dillinger, J. Mohrbach, J. Hewer, M. Gaffga and G. Niedner-Schatteburg, *Phys. Chem. Chem. Phys.*, 2015, 17, 10358
DOI: 10.1039/C5CP00047E

PCCP

COMMUNICATION

View Article Online
View Journal | View Issue

Cite this: *Phys. Chem. Chem. Phys.*, 2015, **17**, 10358

Received 5th January 2015, Accepted 18th March 2015

DOI: 10.1039/c5cp00047e

www.rsc.org/pccp

Infrared spectroscopy of N_2 adsorption on size selected cobalt cluster cations in isolation

Sebastian Dillinger, Jennifer Mohrbach, Joachim Hewer, Maximilian Gaffga and Gereon Niedner-Schatteburg

We report IR active N_2 stretching frequencies in isolated and size selected cobalt cluster nitrogen adsorbate complexes, $[Co_n(N_2)_1]^+$ as recorded by virtue of InfraRed Photon Dissociation (IRPD) spectroscopy. The observed frequencies of the $[Co_n(N_2)_1]^+$ complexes (n = 8–17) are significantly redshifted (2180 to 2290 cm^{-1}) with respect to the IR inactive vibrations of free N_2 (2359 cm^{-1}). These bands are assigned to a μ_1 head-on type of coordination of the N_2 to the cobalt cluster surface, revealing remarkable cluster size dependent features to interpret.

It is often difficult to investigate heterogeneously catalyzed reactions due to their complexity. Reactions of isolated transition metal clusters may serve to elucidate elementary processes in such reactions. The initial adsorption event is often the rate limiting step in multistep bond activation that precedes any further activation and the phenomenon of gas adsorption in layers became an early subject of research.[1,2] Historically adsorption is classified into chemisorption and physisorption by phenomenological persistence of the adsorbate. Physisorbed species often serve as precursors for activation. The initial adsorption and activation of N_2 is the rate limiting step in the Haber–Bosch process. Therefore the characterization of the precursor state is of great importance for the mechanistic understanding of this catalytic conversion.[3]

CO adsorption on metal surfaces has been characterized by numerous kinetic[4–7] and spectroscopic studies.[8–10] The observed redshift of the CO stretching vibration is understood to indicate the CO coordination site – on top (μ_1), on bridge (μ_2) or on hollow (μ_3). It moreover reflects interaction strength and of course charge effects. Complementary insights arise from the IR based characterization of CO adsorbates on the surfaces of isolated metal clusters.[11–13]

There is equally great interest in the kinetics of the N_2 adsorption on metal surfaces.[14–16] Spectroscopic and kinetic studies of N_2 adsorbed on Fe(111) revealed that there are three characteristic α-, δ- and γ-states, which refer to side-on, and head-on adsorption to highly and to less coordinated metal surface atoms.[17–19] Many reaction studies have been performed for a better understanding of the N_2 adsorption kinetics with metal clusters.[20–25] Two of these studies[24,25] have drawn far reaching structural conclusions from so called uptake plots of average association numbers of multiple N_2 molecules under flow reactor conditions. They discuss icosahedral, hexagonal (hcp) and face centered cubic (fcc) packing speculating about pressure dependent inter conversion. Despite obvious need merely a single spectroscopic study elucidated the N_2 adsorption on isolated metal clusters, namely those of Ruthenium,[26] with no unambiguous assignment of the recorded spectral features.

Common interpretation of the head-on adsorption of CO and N_2 to surfaces of extended bulk metal samples and of size selected clusters arises in terms of a σ-donor π-acceptor synergistic bonding scheme according to the so called Blyholder model.[27] *Ab initio* DFT modelling reaches its limits when it comes to the appropriate choice of exchange correlation functionals.[7]

The present study probes the N–N stretching frequency of N_2 when adsorbed on size selected cobalt cluster cations at cryogenic temperatures. We aim to gain insight into the binding motifs of the adsorbates and towards the structure of the cobalt clusters themselves. Preliminary *ab initio* DFT calculations augment the current experiments, failing to provide unambiguous structural conclusions as of now.

A customized Fourier Transform-Ion Cyclotron Resonance (FT-ICR)-mass spectrometer (Apex Ultra Bruker Daltonics) served to perform the cluster production, isolation, N_2 condensation, InfraRed Photon Dissociation (IRPD) and mass analysis. The metal clusters were generated using a home-built laser vaporization cluster ion source as described before.[28,29] In brief, cobalt atoms are evaporated from a rotating 1 mm thick cobalt foil by the second harmonic of a pulsed Nd:YAG laser. The hot plasma is captured by a He gas pulse (40 μs, 10–15 bar) created by a home-built piezoelectric valve.[30] The atoms and ions are cooled and aggregate to clusters in the subsequent jet expansion through a 60 mm long channel (2 mm diameter) into vacuum (10^{-6} mbar).

Fachbereich Chemie and Forschungszentrum OPTIMAS, Technische Universität Kaiserslautern, 67663 Kaiserslautern, Germany

The clusters are skimmed and injected into a cryogenic hexapole ion trap passing different ion lenses, a 90 degrees ion beam bender and a quadrupole mass filter. The ion trap is cooled to 26 K by a closed cycle He cryostat. Buffer or reaction gas can be introduced both pulsed and continuously. In this work we used the continuous gas inlet. He or Ar (He: $[\text{Co}_{8\text{–}10}(\text{N}_2)_1]^+$, Ar: $[\text{Co}_{11\text{–}17}(\text{N}_2)_1]^+$) is used to increase the pressure in the ion trap from 1.7×10^{-7} mbar up to 1.0×10^{-6} mbar to accomplish the efficient trapping and cooling of the ions. The attachment of nitrogen is achieved due to impurities in the buffer gas and can only be observed at temperatures below 28 K. After storage of the ions for a variable time (0–10 s), the manipulated ions are guided by electrostatic lenses into the FT-ICR cell of the so-called "infinity" type.[31] This cell is held at a temperature of 10 K with a closed cycle He cryostat to prevent heating of the clusters by black body radiation. The cell is also used for isolation and detection of the ions.

For the acquisition of the (IRPD) spectra the FT-ICR cell is coupled to a tunable IR laser ($\delta n = 0.9$ cm^{-1}, $\delta t = 7$ ns). This laser is a KTP/KTA optical parametric oscillator/amplifier (OPO/A, LaserVision) system pumped by a pulsed 10 Hz injection seeded Nd:YAG laser (PL8000, Continuum). The difference frequency (DF) between the OPA signal and idler waves is generated in a AgGaSe_2 crystal. This generates IR radiation in the range of 1400–2400 cm^{-1}. Each trapped and isolated package of ions is irradiated by 10–15 laser pulses (0.1–1.2 mJ per pulse) to yield a sufficient amount of fragment ions. The IR spectra were recorded as ion chromatograms while continuously scanning the IR wavelength. The IRPD signal was evaluated as $\Sigma_i F_i/(\Sigma_i F_i + \Sigma_i P_i)$, where F_i and P_i indicate fragment and the parent ion signals, respectively. An experimental IRPD spectrum arises from a plot of the fragmentation efficiency as a function of laser frequency. We employed the IRPD spectroscopy in the 2100–2350 cm^{-1} range on the $[\text{Co}_n(\text{N}_2)_1]^+$ species (n = 8–17). In this range we expected the N_2 stretching frequencies of the species. For all complexes the loss of the N_2 was the only observed fragmentation channel.

The cold IRPD spectra of the cryo cooled $[\text{Co}_n(\text{N}_2)_1]^+$ cluster adsorbate complexes reveal well resolved bands (*cf.* Fig. 1). All complexes show a single or multiple IR active bands within the range of 2180 to 2290 cm^{-1} (2110–2350 cm^{-1} probed). These bands are significantly redshifted with respect to the IR inactive stretching mode of free N_2 (at 2359 cm^{-1}[32]). Some clusters show multiple bands (n = 14–17), other clusters reveal single bands (n = 8–13). Dissociative $[\text{N–Co}_n\text{–N}]^+$ adsorption would inevitably lead to much lower Co–N stretching frequencies which may become as low as 600 cm^{-1} when interstitial nitrides form. Therefore we confirm molecular (intact) adsorption (physisorption) of N_2 on naked cobalt cluster surfaces. While we cannot exclude some (at present invisible) dissociation of N_2 we do not find forcing evidence. Such an activation would, if any, occur in competition to intact adsorption.

The observed cluster size dependence reveals continuous variations and "jumps"/discontinuities alike. The dotted red line serves to guide the eye. It is slightly tilted towards the red with cluster size. A plain charge dilution effect would lead to an opposite effect namely to a blue shifting by increasing cluster size. Instead one might recall the (likely) metallic nature of the cobalt cluster allowing for electron density shifts in response to external perturbation. Such polarization may couple back to the perturbing adsorbate and enhance electron donation into empty antibinding orbitals – the more the larger the cluster. Hence this would lead to a weakening of the N–N binding strength and an increasing redshift of the stretching frequency with cluster size.

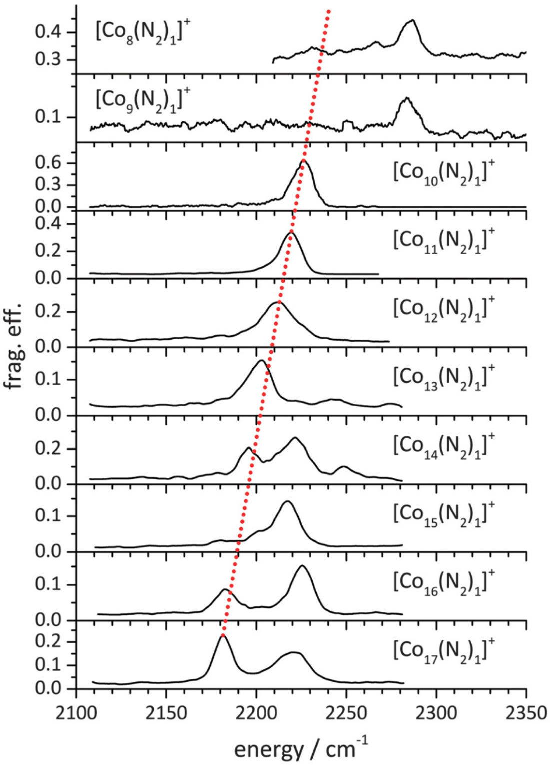

Fig. 1 IRPD spectra of $[\text{Co}_n(\text{N}_2)_1]^+$ for n = 8–17. The dotted red line serves to guide the eye. Its slight tilt with cluster size indicates a conceivable cooperative polarization effect. Note the variation in the observed peak positions and splittings. Multiple major peaks likely indicate cluster core isomers, spin isomers or N_2 bonding isomers while weak sidebands to the blue may arise from combination bands (N_2 stretching and wagging modes, *cf.* Table 1). Note the "jump" of the major peak from n = 9 to n = 10.

Looking at the bands in detail it is obvious that $[\text{Co}_8(\text{N}_2)_1]^+$ and $[\text{Co}_9(\text{N}_2)_1]^+$ do not follow the trend illustrated by the red line. The absorption of $[\text{Co}_8(\text{N}_2)_1]^+$ and $[\text{Co}_9(\text{N}_2)_1]^+$ (both at 2285 cm^{-1}) are significantly less redshifted than those of all other cluster complexes studied. The clusters with n = 10–13 show merely one strong band that aligns well to the mentioned polarization effect (2226, 2219, 2212, 2203 cm^{-1}). In the case of $[\text{Co}_{13}(\text{N}_2)_1]^+$ this main absorption band is accompanied by weak sidebands to the blue. These may arise from combination bands (N_2 stretching and wagging modes, *cf.* Table 1, as supported by calculations). Besides these sidebands of $[\text{Co}_{13}(\text{N}_2)_1]^+$, the main band is in line with a possible icosahedral structure (I_h). A major difference arises

Table 1 Computed vibrations in $[Co_{13}(N_2)_1]^+$ (I_h, $2S + 1 = 15$). Explicitly listed values document all those modes that involve significant motion of either of the two N-atoms

Mode	Type	Freq./ cm^{-1}	Scaled freq./ cm^{-1}	IR intensity/ km mol^{-1}
ν_1	N_2 wagging	33.8	32.1	0.04
ν_2	N_2 wagging	46.7	44.4	0.08
ν_3	N↑–N–Co↓ bending	78	74	0.17
$\nu_3\cdots\nu_{37}$	Co_{13}^+ skeleton modes	78...306		<2.7
ν_{38}	N↑–N↓–Co↑ bending	354	336	37
ν_{39}	N–N stretching	2338	2221	605

for even larger clusters, which reveal multiple bands. These are possibly due to cobalt cluster isomers, to spin state isomers or to N_2 bonding isomers or to combinations of all three effects. $[Co_{14}(N_2)_1]^+$ is most prominent in revealing three major bands (at 2195, 2222, 2248 cm^{-1}). A possible explanation is the presence of spin isomers. The Co_{14}^+ cluster core structure is conceivable, yet speculative. Our preliminary calculations reveal a possible adatom to a icosahedral core (little overall relaxation), alternatively: significant reorganization (from Co_{13}^+ to Co_{14}^+) through incorporation of the extra Co atom into prior Co_{13}^+ cluster surface, *e.g.* by opening the prior five membered rings to a six membered ring. This would provide for a higher (sixfold) coordinated Co surface atom in the center of the six membered ring. This working hypothesis might serve to explain the new band at 2222 cm^{-1} in $[Co_{14}(N_2)_1]^+$.

A similar picture can be found in $[Co_{15}(N_2)_1]^+$, except for the vanishing "red" peak (which was strong for $[Co_{10-14}(N_2)_1]^+$), indicative of a major change in structural binding motif. Possibly explained by a change from icosahedral to hexagonal close-packed (hcp) as found in larger cobalt clusters by Trapped Ion Electron Diffraction (TIED) experiments (Co bulk: hcp; Co cluster: icosahedral).[33]

DFT calculations of $[Co_{13}(N_2)_1]^+$ (at PBE0/ECP(Co); cc-pVTZ(N) level of theory) reveal full icosahedral I_h geometry of the Co_{13}^+ core with little relaxation by the N_2 attachment. SCF convergence is tedious and can be achieved only by tolerating relaxed SCF convergence criteria of 10^{-5} (as compared to 10^{-8} in "standard" DFT calculations). Choice of an appropriate spin multiplicity is crucial. Our previous XMCD investigations yielded a spin magnetic moment of 2.30(15) μ_B per atom for the Co_{14}^+ cluster.[34] That implies 32(2) unpaired electrons and a multiplicity of $2S + 1 = 33(2)$. Our present DFT calculations have revealed stable high spin state structures of a $[Co_{14}(N_2)_1]^+$ complex with multiplicities 30(+47), 32(0) and 34(+29), relative stabilities in kJ mol^{-1} indicated in parentheses. Both findings are in good agreement – assuming that N_2 adsorption does not alter spin states in Co_{14}^+.

On the basis of this agreement we utilized our DFT approach to undertake an extended search of minimum structures of $[Co_8(N_2)_1]^+$, $[Co_9(N_2)_1]^+$, $[Co_{10}(N_2)_1]^+$ (*cf.* Fig. 3), $[Co_{13}(N_2)_1]^+$, $[Co_{14}(N_2)_1]^+$ and $[Co_{17}(N_2)_1]^+$. The calculations reveal head-on N_2 binding in μ_1 N–Co coordination, irrespective of chosen cobalt cluster geometry – allowing for full relaxation without constraints – and irrespective of chosen N_2 coordination site, and irrespective of particular spin multiplicity. Other assumed coordinations (μ_2 or μ_3) relax towards μ_1 coordination. This finding is the more important as μ_2 or μ_3 coordinated N_2 would be weak or inactive in the IR. Any activation towards dinitride species was found vastly endothermic. The computed zero Kelvin adsorption enthalpies of N_2 to Co_{13}^+ were found to range around 80 kJ mol^{-1} in case of all likely spin states ($2S + 1 = 25$, 27, 29 and 31), the Co–N distances round 1.890(2) Å. It thus takes two to three IR photons to induce the observed IRPD processes.

Standard *ab initio* calculations reveal force constants and subsequent normal mode analysis reveal harmonic vibrational frequencies. After appropriate lump sum scaling for anharmonicities (empirical factor 0.95) the thus obtained values compare to experimental data. We chose to document the case of $[Co_{13}(N_2)_1]^+$ in more detail (*cf.* Table 1) assuming an icosahedral I_h geometry of Co_{13}^+ (*cf.* Fig. 2). The IR inactive N–N stretching mode of free N_2 at 2359 cm^{-1} redshifts through coordination with Co_{13}^+ to 2203 cm^{-1} (expt.) and 2221 cm^{-1} (calc. ν_{39}) in $[Co_{13}(N_2)_1]^+$. The concomitant N–N–Co bending mode within $[Co_{13}(N_2)_1]^+$ is predicted to occur at 336 cm^{-1} which is outside of our experimental probing range. However, the experimental spectrum reveals weak sidebands to the N_2 stretching mode which locate at $\nu_s(N_2)$ + 15 cm^{-1}, 35 cm^{-1} and (maybe) 68 cm^{-1}. We assign these sidebands to combination modes ($\nu_{39} + \nu_1$), ($\nu_{39} + \nu_2$) and ($\nu_{39} + \nu_3$), which is in qualitative agreement with the DFT computed ν_1, ν_2 and ν_3 values of +32 cm^{-1}, +44 cm^{-1} and +78 cm^{-1}.

Despite all current effort the accordingly computed vibrational spectra of other clusters (as listed above) do not recover the subtle changes in the recorded experimental spectra. Obtained N_2 stretching frequencies do indeed fall into the range of experimental values. There is, however, no further insight from calculations into the origin of the three experimental observations: general and steady increase of N_2 redshift, sudden increase of N_2 redshift when going from $[Co_{8,9}(N_2)_1]^+$ to $[Co_{10}(N_2)_1]^+$, and multiple strong vibrational peaks in the spectra of cluster $[Co_{14}(N_2)_1]^+$ and beyond.

It remains to be seen whether further calculations achieve more insight. Four improvements come to our minds. Broken symmetry

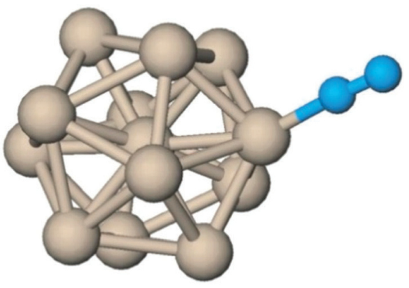

Fig. 2 Computed geometry of $[Co_{13}(N_2)_1]^+$. The assumed icosahedral Co_{13}^+ core is a low lying stable geometry, and it only physisorbs N_2 in μ_1 head-on coordination. Note, that all cobalt surface atoms are equivalent, thus giving rise to a single IR active N–N stretching vibration at about 2230 cm^{-1} (scaled by 0.95) with variations by spin multiplicity of the cobalt cluster core (likely $2S + 1 = 25$, 27, 29, 31) (see text for discussion).

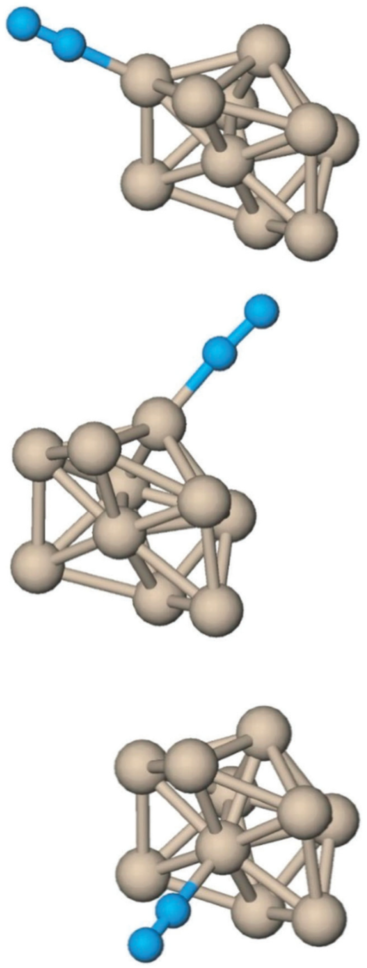

Fig. 3 Three computed geometries of $[Co_{10}(N_2)_1]^+$. The calculated species show the different binding sites of N_2 to the $Co_{10}{}^+$ core. N_2 only coordinates μ_1 head-on. The structures differ in the binding motif of the coordination site (Co atom). The structures illustrate an adsorption of N_2 on a Co atom which in turn coordinates to four- (top), five- (middle) or six- (bottom) membered cobalt atom rings. It comes somewhat as a surprise that the present DFT calculations find little variation of N_2 stretching frequencies in response to this change of coordination (*e.g.* shifts by less than 10 cm^{-1}).

DFT would allow to check for conceivable antiferromagnetic coupling.[35–38] Variation of the DFT functional is mandatory and tedious. Dispersion interaction needs to be considered. Dynamic basin hopping/annealing calculations might retrieve otherwise overlooked geometries.

Conclusions

The N_2 adsorption on cationic $Co_n{}^+$ clusters in the size range of n = 8–17 has been investigated *via* IRPD spectroscopy. The recorded spectra revealed remarkable cluster size dependent features. All species show bands within the range of 2180 to 2290 cm^{-1}, suggesting a head-on μ_1 coordination of the N_2 on the cluster surface. Current DFT calculations reveal a possible icosahedral $Co_{13}{}^+$ core. Nevertheless the calculations do not allow for a final assignment of the observed spectral features (*e.g.* the "jump" from n = 9 to n = 10 or the presence of multiple bands). It is mandatory to spend further effort in *ab initio* calculations to gain invaluable insight into the binding motifs of the nitrogen and of conceivable activation routes.

Acknowledgements

This work was supported by the DFG founded transregional collaborative research center SFB/TRR 88 "3MET.de" and by the state research center OPTIMAS.

Notes and references

1 I. Langmuir, *J. Am. Chem. Soc.*, 1918, **40**, 1361–1403.

2 S. Brunauer, P. H. Emmett and E. Teller, *J. Am. Chem. Soc.*, 1938, **60**, 309–319.

3 G. Ertl, *Catal. Rev.*, 1980, **21**, 201–223.

4 D. M. Cox, K. C. Reichmann, D. J. Trevor and A. Kaldor, *J. Chem. Phys.*, 1988, **88**, 111–119.

5 G. A. Somorjai, *Introduction to Surface Chemistry and Catalysis*, John Wiley & Sons, 1994.

6 G. Ertl, M. Neumann and K. M. Streit, *Surf. Sci.*, 1977, **64**, 393–410.

7 A. Nilsson and L. G. M. Pettersson, in *Chemical Bonding at Surfaces and Interfaces*, ed. A. N. G. M. P. K. Nørskov, Elsevier, Amsterdam, 2008, pp. 57–142.

8 A. Crossley and D. A. King, *Surf. Sci.*, 1977, **68**, 528–538.

9 R. M. Hammaker, S. A. Francis and R. P. Eischens, *Spectrochim. Acta*, 1965, **21**, 1295–1309.

10 F. M. Hoffmann, *Surf. Sci. Rep.*, 1983, **3**, 107–192.

11 A. Fielicke, P. Gruene, G. Meijer and D. M. Rayner, *Surf. Sci.*, 2009, **603**, 1427–1433.

12 A. Fielicke, G. von Helden, G. Meijer, D. B. Pedersen, B. Simard and D. M. Rayner, *J. Chem. Phys.*, 2006, **124**, 194305.

13 J. T. Lyon, P. Gruene, A. Fielicke, G. Meijer and D. M. Rayner, *J. Chem. Phys.*, 2009, **131**, 184706.

14 D. A. King and M. G. Wells, *Proc. R. Soc. London, Ser. A*, 1974, **339**, 245–269.

15 D. A. King and M. G. Wells, *Surf. Sci.*, 1972, **29**, 454–482.

16 G. Ertl, S. B. Lee and M. Weiss, *Surf. Sci.*, 1982, **114**, 515–526.

17 C. N. R. Rao and G. R. Rao, *Surf. Sci. Rep.*, 1991, **13**, 221–263.

18 M. C. Tsai, U. Ship, I. C. Bassignana, J. Küppers and G. Ertl, *Surf. Sci.*, 1985, **155**, 387–399.

19 J. J. Mortensen, L. B. Hansen, B. Hammer and J. K. Nørskov, *J. Catal.*, 1999, **182**, 479–488.

20 M. B. Knickelbein, *Annu. Rev. Phys. Chem.*, 1999, **50**, 79–115.

21 M. D. Morse, M. E. Geusic, J. R. Heath and R. E. Smalley, *J. Chem. Phys.*, 1985, **83**, 2293–2304.

22 A. Berces, P. A. Hackett, L. Lian, S. A. Mitchell and D. M. Rayner, *J. Chem. Phys.*, 1998, **108**, 5476–5490.

23 L. Fuyi, L. Ming, T. Lin and P. B. Armentrout, *J. Chem. Phys.*, 2008, **128**, 194313.
24 J. Ho, E. K. Parks, L. Zhu and S. J. Riley, *Chem. Phys.*, 1995, **201**, 245–261.
25 S. J. Riley, *J. Non-Cryst. Solids*, 1996, **205–207**(Part 2), 781–787.
26 C. Kerpal, D. J. Harding, J. T. Lyon, G. Meijer and A. Fielicke, *J. Phys. Chem. C*, 2013, **117**, 12153–12158.
27 G. Blyholder, *J. Phys. Chem.*, 1964, **68**, 2772–2777.
28 S. Maruyama, L. R. Anderson and R. E. Smalley, *Rev. Sci. Instrum.*, 1990, **61**, 3686–3693.
29 C. Berg, T. Schindler, G. Niednerschatteburg and V. E. Bondybey, *J. Chem. Phys.*, 1995, **102**, 4870–4884.
30 D. Proch and T. Trickl, *Rev. Sci. Instrum.*, 1989, **60**, 713–716.
31 P. Caravatti and M. Allemann, *Org. Mass Spectrom.*, 1991, **26**, 514–518.
32 W. M. Haynes, *CRC Handbook of Chemistry and Physics*, Taylor & Francis, 93rd edn, 2012.
33 T. Rapps, R. Ahlrichs, E. Waldt, M. M. Kappes and D. Schooss, *Angew. Chem., Int. Ed.*, 2013, **52**, 6102–6105.
34 S. Peredkov, M. Neeb, W. Eberhardt, J. Meyer, M. Tombers, H. Kampschulte and G. Niedner-Schatteburg, *Phys. Rev. Lett.*, 2011, **107**, 233401.
35 E. M. V. Kessler, S. Schmitt and C. van Wullen, *J. Chem. Phys.*, 2013, **139**, 184110.
36 C. van Wullen, *J. Phys. Chem. A*, 2009, **113**, 11535–11540.
37 F. Neese, *J. Phys. Chem. Solids*, 2004, **65**, 781–785.
38 F. Neese, *Coord. Chem. Rev.*, 2009, **253**, 526–563.

9.2 Vibrational Blue Shift of Coordinated N_2 in $[Fe_3O(OAc)_6(N_2)_n]^+$: “Non Classical” Dinitrogen Complexes

Johannes Lang, Jennifer Mohrbach, Sebastian Dillinger, Joachim M. Hewer
and Gereon Niedner-Schatteburg

Fachbereich Chemie and Forschungszentrum OPTIMAS,
Technische Universität Kaiserslautern,
67663 Kaiserslautern, Germany

9.2.1 Preamble

The following chapter is a reprint of a publication in the journal “Chemical Communications”.

A team consisting of Jennifer Mohrbach, Sebastian Dillinger, Johannes Lang and myself performed the measurements. Johannes Lang evaluated the experimental data and conducted the presented quantum chemical calculations. The manuscript was written by Johannes Lang and revised with the help of Gereon Niedner-Schatteburg and Jennifer Mohrbach.

Full Reference:

Vibrational Blue Shift of coordinated N_2 in $[Fe_3O(OAc)_6(N_2)_n]^+$:“Non Classical” Dinitrogen Complexes

J. Lang, J. Mohrbach, S. Dillinger, **J. M. Hewer** and G. Niedner-Schatteburg, *Chemical Communications,* **2017**, 53, 420-423.

http://dx.doi.org/10.1039/C6CC07481B

9.2.2 Reprint

Reprint Licence

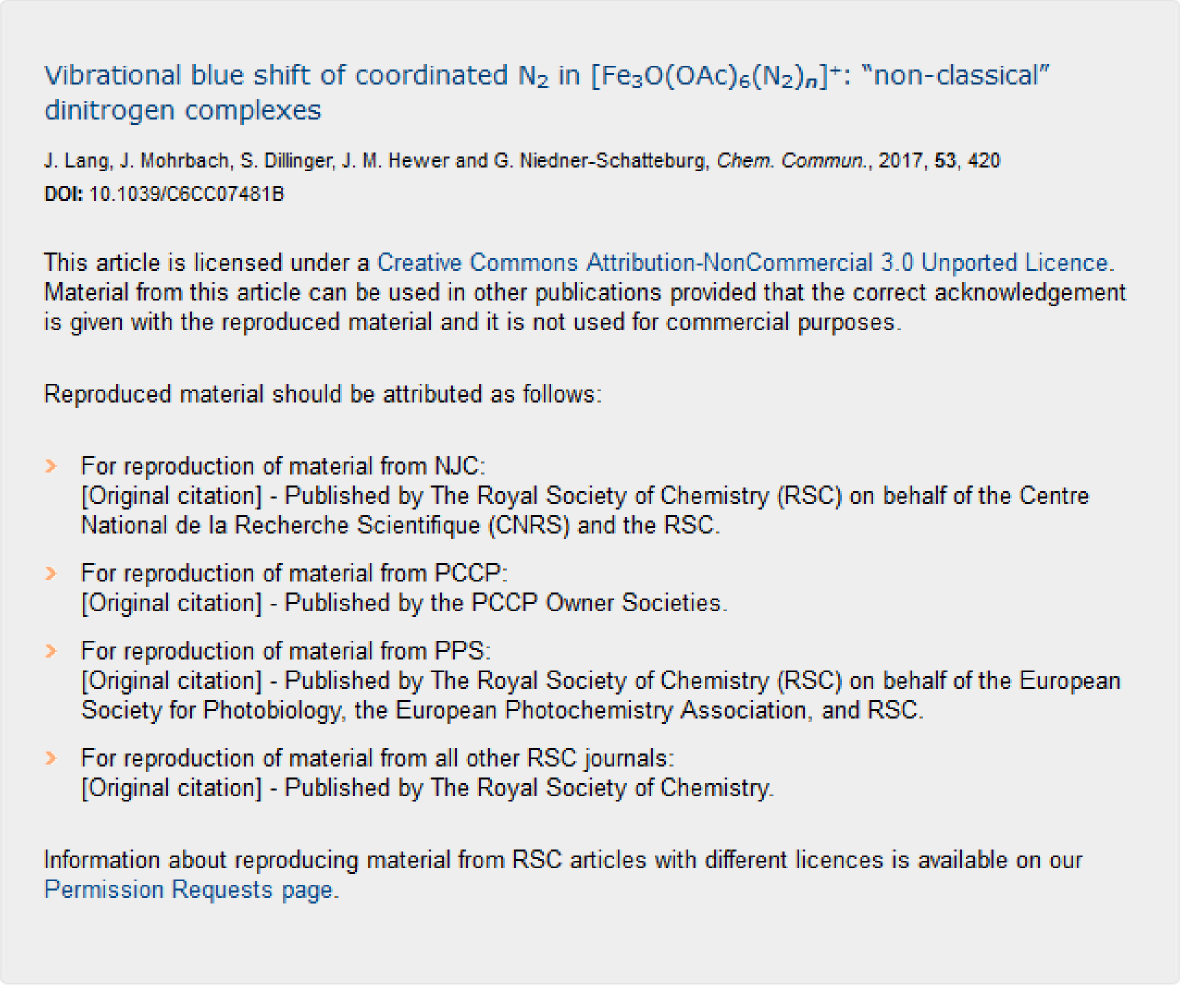

Vibrational blue shift of coordinated N_2 in $[Fe_3O(OAc)_6(N_2)_n]^+$: "non-classical" dinitrogen complexes

J. Lang, J. Mohrbach, S. Dillinger, J. M. Hewer and G. Niedner-Schatteburg, *Chem. Commun.*, 2017, **53**, 420
DOI: 10.1039/C6CC07481B

This article is licensed under a Creative Commons Attribution-NonCommercial 3.0 Unported Licence. Material from this article can be used in other publications provided that the correct acknowledgement is given with the reproduced material and it is not used for commercial purposes.

Reproduced material should be attributed as follows:

- For reproduction of material from NJC:
  [Original citation] - Published by The Royal Society of Chemistry (RSC) on behalf of the Centre National de la Recherche Scientifique (CNRS) and the RSC.
- For reproduction of material from PCCP:
  [Original citation] - Published by the PCCP Owner Societies.
- For reproduction of material from PPS:
  [Original citation] - Published by The Royal Society of Chemistry (RSC) on behalf of the European Society for Photobiology, the European Photochemistry Association, and RSC.
- For reproduction of material from all other RSC journals:
  [Original citation] - Published by The Royal Society of Chemistry.

Information about reproducing material from RSC articles with different licences is available on our Permission Requests page.

ChemComm

ROYAL SOCIETY OF CHEMISTRY

COMMUNICATION

View Article Online
View Journal

Cite this: DOI: 10.1039/c6cc07481b

Received 14th September 2016,
Accepted 2nd December 2016

DOI: 10.1039/c6cc07481b

www.rsc.org/chemcomm

Vibrational blue shift of coordinated N_2 in $[Fe_3O(OAc)_6(N_2)_n]^+$: "non-classical" dinitrogen complexes†

Johannes Lang,* Jennifer Mohrbach, Sebastian Dillinger, Joachim M. Hewer and Gereon Niedner-Schatteburg

We present "non-classical" dinitrogen Fe(III) oxo acetate complexes *in vacuo* utilizing Infrared Photodissociation (IR-PD) at cryo temperatures. The IR-PD spectra reveal a blue shift of the N_2 stretching vibration frequencies in the complexes. Density Functional Theory (DFT) calculations confirm the experiments and indicate strengthened N–N bonds due to pronounced σ bonding and a lack of π back donation.

The discovery of transition metal dinitrogen complexes in 1965[1] launched the ever growing research field of N_2 coordination chemistry.[2,3] One of the main goals is the conversion of N_2 to ammonia under mild conditions[4] by homogenous catalysis.[5,6] The basic idea is to weaken N–N bonds upon coordination to enable subsequent functionalization. Precursors to N_2 activation manifest by elongated N–N distances and by red shifting of stretching frequencies[7,8] with respect to the vibration of the free N_2 molecule. Such bond activation and vibrational red shifts have been interpreted before, *e.g.* in terms of the Dewar–Chatt–Duncanson (DCD) model,[9] and the Blyholder surface coordination (BSC)[10] model. Theoretical as well as spectroscopic investigations confirmed these interpretations.[11] However, FT-IR studies on N_2 coordinated to Lewis acid centers in zeolites[12] and alumina[13] revealed blue shifted vibrational N_2 stretching frequencies (up to 24 cm^{-1}). This indicates N–N bond strengthening rather than weakening – much beyond these established models. A similar effect has been observed in the case of isoelectronic carbon monoxide: so called "non-classical" metal carbonyl complexes[14,15] exhibit blue shifted vibrational CO stretching frequencies (up to 138 cm^{-1}).[16] Gas phase studies of isolated non-classical metal carbonyl clusters[17,18] proved the intrinsic molecular origin of this effect. The cause for the CO blue shift was a topic of debate[19] and is now understood in terms of an interplay between π back donation and electrostatic effects.[20] It is paramount to characterize the geometrical and electronic structures of such complexes in order to acquire a fundamental insight into the prevailing interactions leading to such non-classical behaviour.

The combination of Electrospray Ionization Mass Spectrometry[21] (ESI-MS) and infrared (IR) laser spectroscopy is suitable for the characterization of isolated coordination complexes with defined stoichiometry. Infrared (Multiple) Photon Dissociation (IR-(M)PD) provides direct access to structural and vibrational information, both under cryogenic conditions[22,23] and at room temperature.[24] The experimental results and dedicated *ab initio* calculations are combined in order to obtain detailed insight into the geometrical structure and intrinsic properties of the isolated molecular ions.

In this work we investigate isolated dinitrogen complexes $[Fe_3O(OAc)_6(N_2)_n]^+$ (n = 1–3, OAc = $CH_3CO_2^-$, *cf.* Scheme 1), which exhibit a significant blue shift (17 cm^{-1}) of N_2 vibrations in the complex with respect to the free N_2 molecule. We examine the N_2 coordination in detail to rationalize the blue shift and N–N bond strengthening. This is, to the best of our knowledge, the first report on the "non-classical" behaviour of isolated N_2 complexes.

We utilize a customized Fourier Transform-Ion Cyclotron Resonance (FT-ICR)-mass spectrometer (Apex Ultra, Bruker Daltonics) equipped with an ESI ion source (Apollo 2, Bruker).

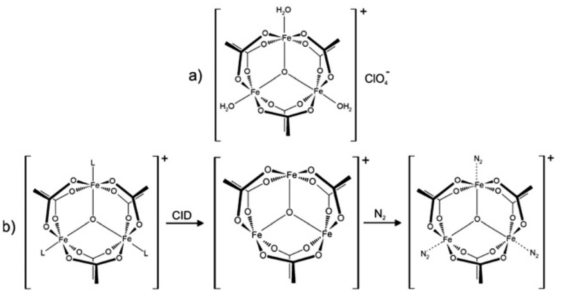

Scheme 1 (a) Molecular structure of the precursor $[Fe_3O(OAc)_6(H_2O)_3](ClO_4)$ salt. In solution the water molecules exchange with solvent molecules (L = *e.g.* acetonitrile). (b) ESI-MS reveals the formation of $[Fe_3O(OAc)_6(L)_n]^+$ (n = 0, 1, 2, 3). Collision induced dissociation (CID) of L yields the under-coordinated $[Fe_3O(OAc)_6]^+$ complex, which binds 1–3 N_2 molecules at 26 K.

Fachbereich Chemie und Forschungszentrum OPTIMAS, Technische Universität Kaiserslautern, 67663 Kaiserslautern, Germany. E-mail: jlang@chemie.uni-kl.de

† Electronic supplementary information (ESI) available. See DOI: 10.1039/c6cc07481b

We coupled the ICR cell with a KTP/KTA optical parametric oscillator/amplifier (OPO/A) IR laser system (LaserVision). Optimized minimum energy structures and linear IR absorption spectra were calculated at the B3LYP[25] level of theory using cc-pVTZ basis sets[26] and Stuttgart RSC 1997[27] effective core potential basis sets (Gaussian 09[28]). We present calculations with 15 unpaired alpha electrons yielding a spin multiplicity of 16 with other multiplicities (2–18) found to be significantly less stable (*cf.* Fig. S12, ESI†). We scale the calculated frequencies with two different scaling factors: one scaling factor (0.951) is specifically designed to elucidate N_2 stretching bands in $[Fe_3O(OAc)_6(N_2)_n]^+$. It scales the calculated N_2 stretching frequencies such that a calculated free N_2 stretching vibration frequency matches the experimental value[29] of 2330 cm^{-1}. This approach conveniently reveals any effects of Fe–N_2 coordination on N_2 stretching frequencies. A second unspecific scaling factor (0.986) is applied for all other bands below 1800 cm^{-1}. It scales the calculated asymmetric carboxylate stretching vibration frequencies of $[Fe_3O(OAc)_6(N_2)_1]^+$ to match our own experimental value of 1587 cm^{-1}. Unscaled spectra are provided in the ESI† (*cf.* Fig. S4).

Upon spraying the sample solution and recording mass spectra in the ICR-cell, we observe a series of isotopic peaks matching convincingly with simulated isotopic patterns (*cf.* Fig. S1, ESI†). We assign those peaks to $[Fe_3O(OAc)_6(L)_n]^+$ (L = H_2O, acetonitrile, acetic acid; n = 0, 1, 2, 3). Elimination of L by Collision Induced Dissociation (CID) and subsequent coordination of N_2 in the hexapole at cryo temperatures (26 K) leads to the formation of $[Fe_3O(OAc)_6(N_2)_n]^+$ (*cf.* Scheme 1b and Fig. S2, ESI†). Note that we observe $n_{max} = 3$, thus "titrating" the three available Fe coordination sites. The calculated Gibbs energies at various temperatures reveal N_2 binding energies of 11, 9, and 8 kJ mol^{-1} for the first, second, and third N_2 (26 K; BSSE corrected, *cf.* Fig. S3, ESI†). The N_2 binding Gibbs energies diminish with increasing temperature, vanishing above 80 K.

We recorded IR-PD spectra of cryocooled $[Fe_3O(OAc)_6(N_2)_n]^+$ (n = 1, 2, 3, Fig. 1, black traces) and conducted DFT simulations to obtain their linear IR absorption spectra (Fig. 1, green traces). The DFT calculations reveal optimized minimum structures as depicted in the insets of Fig. 1. We observe several bands between 1300 cm^{-1} and 1500 cm^{-1}, coinciding with the predicted CH_3 bending modes of the acetate ligands. While the calculated band frequencies around 1423 cm^{-1} and 1467 cm^{-1} agree well with the IR-PD spectrum, the calculated intensities differ significantly. Switching the DFT functional from B3LYP to PBE0 yields a much better match of IR intensities but significant deviations of calculated and observed vibrational frequencies (*cf.* Fig. S5, ESI†). Neither of these empirical functionals predicts both entities correctly. In the following we utilize the B3LYP results for further discussion.

The amount of N_2 coordination (n = 1, 2, 3) has no significant influence on the frequency and intensity of the CH_3 bending bands (neither in the IR-PD experiments nor in the DFT calculations). This finding likely originates from the spatial separation of the affected methyl groups from the Fe–N_2 coordination sites.

We find a strong IR-PD band at 1587, 1590, and 1591 cm^{-1} in the cases of n = 1, 2, 3. We assign this band to carboxylic CO stretching bands of the six coordinated acetate ligands. The n = 1 CO stretching band is red shifted by ≈3–4 cm^{-1} with

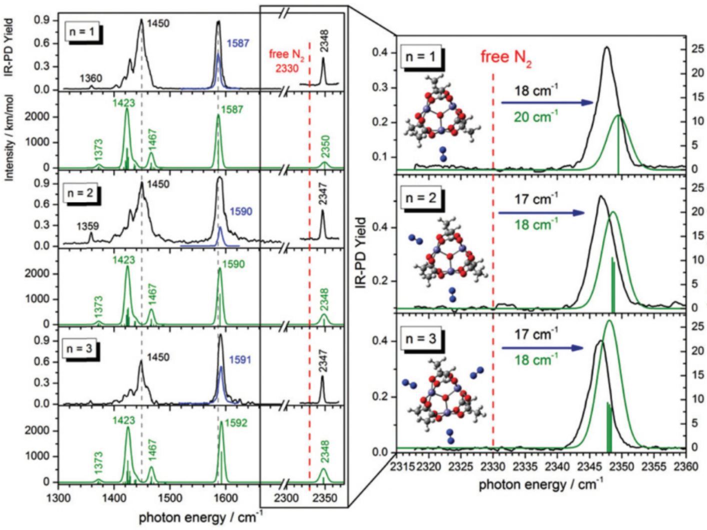

Fig. 1 Left: IR-PD spectra of $[Fe_3O(OAc)_6(N_2)_n]^+$ (n = 1, 2, 3) at 26 K (black and blue curves) and calculated IR absorption spectra of optimized $[Fe_3O(OAc)_6(N_2)_n]^+$ (n = 1–3) (green curves) in the range of 1300–2400 cm^{-1}. The blue IR-PD spectrum shows the CO stretching band (recorded with highly attenuated laser power to avoid saturation effects). The calculations were performed at the B3LYP/cc-pVTZ (H,C,N,O) and Stuttgart 1997 ECP (Fe) level of theory. The multiplicity is 16 and frequencies are scaled with 0.951 (0.986) above 2300 cm^{-1} (below 2300 cm^{-1}). Calculated stick spectra were convoluted with a Gaussian envelope of FWHM = 7 cm^{-1}. Right: A zoom into the N_2 stretching vibration region. Calculated lines were convoluted with a Gaussian envelope of FWHM = 3.5 cm^{-1}. Insets show associated geometry optimized structures.

respect to the n = 2, 3 bands, and with respect to the corresponding band of the free acetate anion[30] at 1591 cm^{-1}. The DFT calculated asymmetric carboxylate stretching frequencies – scaled to match the experiment at n = 1 – reproduce well the reduced redshift of the experiments on n = 2, 3. The coordinated carboxylate groups thus sense N_2 coordination through their common Fe centers. We provide an illustrative visualization of the calculated displacement vectors of these modes in Fig. S6 of the ESI.† Note that the n = 1 and 2 coordinations lift the sixfold degeneracy of these asymmetric stretching bands of the six coordinated acetate ligands. The recorded bands (slightly broadened to FWHM $\approx$ 7 cm^{-1}) may well contain the predicted splittings of $\approx$0.5 cm^{-1} – yet unresolved (*cf.* Fig. S7, ESI†).

We observe sharp bands (FWHM $\approx$ 3.5 cm^{-1}) above 2300 cm^{-1} revealing the IR active N_2 stretching vibrations of $[Fe_3O(OAc)_6(N_2)_n]^+$ (*cf.* the displacement vector visualization of these modes in Fig. S8, ESI†). Isotope labeling of the N_2 molecule confirms our assignment of these IR-PD bands to the N_2 stretching frequencies. We observe a red shift of the $^{15}N–^{15}N$ vibration band relative to the $^{14}N–^{14}N$ vibration band (79 cm^{-1}; *cf.* Fig. S17, ESI†) and the same blue shift with respect to the free N_2 in both isotopomers.

In all cases (n = 1, 2, 3) the solitary $^{14}N_2$ stretching bands of the experimental IR-PD spectra shift to the blue (17–18 cm^{-1}) with respect to the (IR inactive) stretching frequency of the free $^{14}N_2$ molecule (2330 cm^{-1}).[29] These blue shifts indicate N–N bond strengthening upon coordination. Our DFT calculations predict this blue shift remarkably well (18–20 cm^{-1}). Multiple coordinated N_2 molecules have almost identical stretching frequencies. There seems to be no coupling between the N_2 molecules adsorbing at distinct, equivalent Fe sites. In contrast to the carboxylate asymmetric stretching bands the N_2 stretching bands shift slightly to lower frequencies with increasing n (IR-PD spectrum: 1 cm^{-1}; DFT: 1.5 cm^{-1}). However, in all three cases (n = 1–3) the N_2 stretching band is blue shifted with respect to the free N_2.

The DFT calculations reveal subtle distortions of the triangular Fe_3O-core upon coordination of N_2 (*cf.* Scheme 2 and Table S2, ESI†). Each N_2 molecule binds end on to the respective Fe atom. In general, the coordination of N_2 enlarges Fe–Fe distances and Fe–$O_{central}$ bond lengths (by 0.03 Å resp. 0.01 Å) of those bonds which involve the N_2 coordinating Fe-center. All the other Fe–Fe distances and Fe–$O_{central}$ bond lengths shorten by approx. 0.03 Å or 0.01 Å. Natural Population Analysis (NPA) of $[Fe_3O(OAc)_6(N_2)_n]^+$ (n = 0, 1, 2, 3) reveals the dependence upon n of local charge densities within the triangular Fe_3O-core (*cf.* Scheme 2). The Fe centers gain 0.058–0.064 e electron density per coordinating N_2. The non-coordinated N atoms donate 0.121–0.134 e electron density in about equal parts to the coordinating N and Fe atoms. Free, non-polar N_2 molecules thus polarize and oxidize significantly upon Fe coordination, both magnitudes decreasing with n – as does the blue shift of the N_2 stretching bands. Note that the N–N bond length contracts slightly upon coordination (−0.002 Å). The high positive charge on the Fe centers (1.862–1.922 e) diminishes their electron donating capability and thus inhibits the π back donation. Such charge effects seem to increase the "non-classical" effect in metal carbonyl complexes.[31]

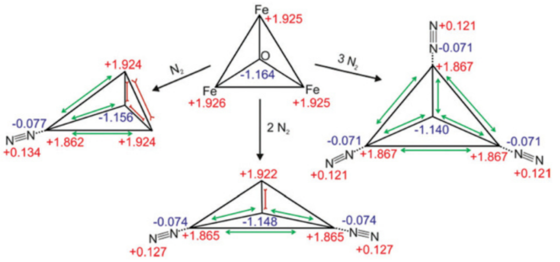

Scheme 2 Calculated geometries and natural charge distributions of the Fe_3O-core and the coordinated N_2 in $[Fe_3O(OAc)_6(N_2)_n]^+$ (n = 0, 1, 2, 3).

Non covalent interaction (*cf.* Fig. 2 for n = 1 and Fig. S11 for n = 2, 3, ESI†) analysis reveals a rather strong attractive, but non covalent interaction between the Fe atoms and the coordinated N atoms at rather long Fe–N coordination distances of 2.451–2.501 Å (n = 1–3). At such distances the π back donation is doomed to weakness due to scant π orbital overlap. Instead, it stands to reason that σ-donation of the N_2 molecule constitutes the driving force of attraction in the Fe–N_2 coordination in $[Fe_3O(OAc)_6(N_2)_n]^+$. Besides the obvious attractive Fe–N interaction, we identify repulsive interactions between the carboxylate O atoms and the coordinated N atoms.

Simple considerations as *e.g.* by the DCD and BSC models do not explain the observed blue shift of the N_2 stretching vibrations upon coordination. To rationalize this effect in a fairly perspicuous way we refer to the molecular orbital (MO) diagram of N_2 (*cf.* Scheme S1, ESI†): all bonding MOs are populated. When ruling out short range π back donation into empty anti-bonding MOs (inhibited by the net positive charge of the coordinating complex), there is a way to increase the formal N–N bond order (and thus strengthen the N–N bond and increase the stretching frequency): this is a depopulation of the antibonding 4σ* orbital into appropriate Fe centered acceptor orbitals. We have elucidated the prevailing coordination and bonding by inspection of computed molecular orbitals in $[Fe_3O(OAc)_6(N_2)_n]^+$. Indeed, we found that the 4σ* MO of the N_2 unit overlaps efficiently with MOs located at the Fe centers and at the carboxylate oxygen atoms of the $[Fe_3O(OAc)_6]^+$ subunit (*cf.* Fig. 3 for n = 1 and

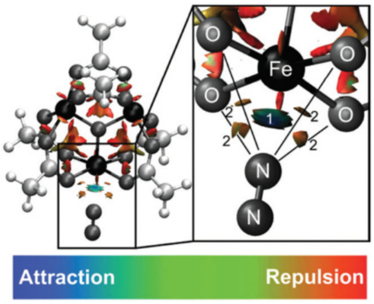

Fig. 2 NCI plot of geometry optimized $[Fe_3O(OAc)_6(N_2)_1]^+$ (*cf.* Fig. S10 for n = 2, 3, ESI†). The NCI plot reveals attractive interaction between the Fe center and the coordinated N atom (1) and repulsive interaction between of the O atoms and the N atom (2).

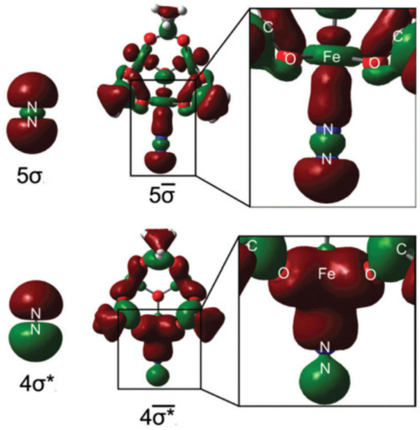

Fig. 3 Left: $4\sigma^*/5\sigma$ molecular orbitals of free N_2. Right: Selected molecular orbitals of $[Fe_3O(OAc)_6(N_2)_1]^+$ involving the former $4\sigma^*(N_2)$ and $5\sigma(N_2)$ orbitals. $4\sigma^*(N_2)$ electron density delocalizes into the whole complex, thus strengthening the N–N bond.

Fig. S13 for $n = 2, 3$, ESI†). The electrons of the anti-bonding $4\sigma^*(N_2)$ orbital delocalize into a $4\bar{\sigma}^*$ MO of the whole complex, whereby the $4\sigma^*(N_2)$ orbital polarizes towards the Fe center. Note that the node plane of $4\sigma^*(N_2)$ (between the N atoms) shifts somewhat towards the Fe center. The depletion of the anti-bonding electron density along the N–N bond increases the net bond order of N_2 and blue shifts the N_2 stretching vibration. The bonding $5\sigma(N_2)$ contributes to a $5\bar{\sigma}$ MO of the complex. This is expected to result in N–N bond weakening counteracting the effect of $4\sigma^*(N_2)$ delocalization. However, $5\sigma(N_2)$ receives a partial $4\sigma^*(N_2)$ character to form the $5\bar{\sigma}$ MO *via* hybridization. The strengthening effect of $4\sigma^*(N_2)$ electron density delocalization thus seems to be the critical factor for the "non-classical" behavior of $[Fe_3O(OAc)_6(N_2)_n]^+$. The involvement of the $4\sigma^*(N_2)$ orbital in the M–N_2 bonding scheme as well as $4\sigma^*/5\sigma$ hybridization has been suggested in the context of X-ray absorption studies of N_2 adsorbed on metal surfaces.[32] Inspection of all other delocalized MOs in the $[Fe_3O(OAc)_6(N_2)_1]^+$ complex reveals a total lack of π back donation from the $[Fe_3O(OAc)_6]^+$ unit to empty $\pi^*(N_2)$ orbitals. Considering the high charge on the Fe center and the long Fe–N_2 distance (see above) this seems reasonable. The N_2 coordination and thus the "non-classical" behavior of $[Fe_3O(OAc)_6(N_2)_n]^+$ originate from σ bonding effects.

Our fundamental insight into the class of "non-classical" N_2–Fe complexes is remarkable in view of the industrial use of bulk iron for N_2 activation and hydrogenation. It might help to advance a general understanding of dinitrogen chemistry beyond established coordination models.

This work was supported by the German Research Foundation DFG within the Transregional Collaborative Research Center SFB/TRR 88 "Cooperative effects in homo and heterometallic complexes" (3MET).

Notes and references

1 M. D. Fryzuk, *Chem. Commun.*, 2013, **49**, 4866–4868.
2 J. L. Crossland and D. R. Tyler, *Coord. Chem. Rev.*, 2010, **254**, 1883–1894.
3 N. Khoenkhoen, B. de Bruin, J. N. H. Reek and W. I. Dzik, *Eur. J. Inorg. Chem.*, 2015, 567–598.
4 S. F. McWilliams and P. L. Holland, *Acc. Chem. Res.*, 2015, **48**, 2059–2065.
5 D. V. Yandulov and R. R. Schrock, *Science*, 2003, **301**, 76–78.
6 H. Tanaka, K. Arashiba, S. Kuriyama, A. Sasada, K. Nakajima, K. Yoshizawa and Y. Nishibayashi, *Nat. Commun.*, 2014, **5**, 1–11.
7 N. Lehnert and F. Tuczek, *Inorg. Chem.*, 1999, **38**, 1659–1670.
8 N. Lehnert and F. Tuczek, *Inorg. Chem.*, 1999, **38**, 1671–1682.
9 J. Chatt and L. A. Duncanson, *J. Chem. Soc.*, 1953, 2939–2947.
10 G. Blyholder, *J. Phys. Chem.*, 1964, **68**, 2772–2777.
11 F. Studt and F. Tuczek, *J. Comput. Chem.*, 2006, **27**, 1278–1291.
12 K. Hadjiivanov and H. Knözinger, *Catal. Lett.*, 1999, **58**, 21–26.
13 R. Wischert, C. Coperet, F. Delbecq and P. Sautet, *Chem. Commun.*, 2011, **47**, 4890–4892.
14 H. Willner and F. Aubke, *Angew. Chem., Int. Ed.*, 1997, **36**, 2402–2425.
15 A. J. Lupinetti, G. Frenking and S. H. Strauss, *Angew. Chem., Int. Ed.*, 1998, **37**, 2113–2116.
16 P. K. Hurlburt, J. J. Rack, J. S. Luck, S. F. Dec, J. D. Webb, O. P. Anderson and S. H. Strauss, *J. Am. Chem. Soc.*, 1994, **116**, 10003–10014.
17 J. Velasquez, B. Njegic, M. S. Gordon and M. A. Duncan, *J. Phys. Chem. A*, 2008, **112**, 1907–1913.
18 A. Fielicke, G. von Helden, G. Meijer, B. Simard and D. M. Rayner, *J. Phys. Chem. B*, 2005, **109**, 23935–23940.
19 A. S. Goldman and K. Krogh-Jespersen, *J. Am. Chem. Soc.*, 1996, **118**, 12159–12166.
20 G. Bistoni, S. Rampino, N. Scafuri, G. Ciancaleoni, D. Zuccaccia, L. Belpassi and F. Tarantelli, *Chem. Sci.*, 2016, **7**, 1174–1184.
21 J. B. Fenn, *Angew. Chem., Int. Ed.*, 2003, **42**, 3871–3894.
22 N. Heine and K. R. Asmis, *Int. Rev. Phys. Chem.*, 2014, **34**, 1–34.
23 J. Jašík, J. Žabka, J. Roithová and D. Gerlich, *Int. J. Mass Spectrom.*, 2013, **354–355**, 204–210.
24 J. Lang, M. Gaffga, F. Menges and G. Niedner-Schatteburg, *Phys. Chem. Chem. Phys.*, 2014, **16**, 17417–17421.
25 A. D. Becke, *J. Chem. Phys.*, 1993, **98**, 5648–5652.
26 T. H. Dunning, *J. Chem. Phys.*, 1989, **90**, 1007–1023.
27 M. Dolg, H. Stoll, H. Preuss and R. M. Pitzer, *J. Phys. Chem.*, 1993, **97**, 5852–5859.
28 M. J. Frisch, G. W. Trucks, H. B. Schlegel, G. E. Scuseria, M. A. Robb, J. R. Cheeseman, G. Scalmani, V. Barone, B. Mennucci, G. A. Petersson, H. Nakatsuji, M. Caricato, X. Li, H. P. Hratchian, A. F. Izmaylov, J. Bloino, G. Zheng, J. L. Sonnenberg, M. Hada, M. Ehara, K. Toyota, R. Fukuda, J. Hasegawa, M. Ishida, T. Nakajima, Y. Honda, O. Kitao, H. Nakai, T. Vreven, J. A. Montgomery, Jr., J. E. Peralta, F. Ogliaro, M. Bearpark, J. J. Heyd, E. Brothers, K. N. Kudin, V. N. Staroverov, R. Kobayashi, J. Normand, K. Raghavachari, A. Rendell, J. C. Burant, S. S. Iyengar, J. Tomasi, M. Cossi, N. Rega, J. M. Millam, M. Klene, J. E. Knox, J. B. Cross, V. Bakken, C. Adamo, J. Jaramillo, R. Gomperts, R. E. Stratmann, O. Yazyev, A. J. Austin, R. Cammi, C. Pomelli, J. W. Ochterski, R. L. Martin, K. Morokuma, V. G. Zakrzewski, G. A. Voth, P. Salvador, J. J. Dannenberg, S. Dapprich, A. D. Daniels, Ö. Farkas, J. B. Foresman, J. V. Ortiz, J. Cioslowski and D. J. Fox, *Gaussian 09, Revision E.01*, Gaussian, Inc., Wallingford CT, 2009.
29 K. P. Huber and G. Herzberg, *Constants of Diatomic Molecules*, Van Norstrand, New York, 1979.
30 J. D. Steill and J. Oomens, *J. Phys. Chem. A*, 2009, **113**, 4941–4946.
31 A. M. Ricks, J. M. Bakker, G. E. Douberly and M. A. Duncan, *J. Phys. Chem. A*, 2009, **113**, 4701–4708.
32 A. Nilsson and L. G. M. Pettersson, *Surf. Sci. Rep.*, 2004, **55**, 49–167.

9.3 Doubly Regioselective C-H Hydroarylation of Unsymmetrical Alkynes Using Carboxylates as Deciduous Directing Groups

Agostino Biafora(a), Bilal A. Khan(b,c), Janet Bahri(b), Joachim M. Hewer(a)
and Lukas J. Goossen(c)

(a) Fachbereich Chemie and Forschungszentrum OPTIMAS, Technische Universität Kaiserslautern, 67663 Kaiserslautern, Germany

(b) Department of Chemistry, University of Azad Jammu and Kashmir, 13100 Muzaffarabad, AJK, Pakistan

(c) Fakultät für Chemie und Biochemie, Ruhr-Universität Bochum, Universitätsstraße 150, 44801 Bochum, Germany

9.3.1 Preamble

The following chapter is a reprint of a publication in the journal "Organic Letters".

The concept was developed by Agostino Biafora, who also performed the screening and isolation of reaction products, together with Bilal Khan. The first version of the manuscript was written by Bilal Khan and revised by Agostino Biafora and Lukas Goossen. Janet Bahri performed the microwave experiments. The ESI-MS control experiments were conducted by Agostino Biafora and myself.

Full Reference:

Doubly Regioselective C-H Hydroarylation of Unsymmetrical Alkynes Using Carboxylates as Deciduous Directing Groups

A. Biafora, B. A. Kahn, J. Bahri, **J. M. Hewer** and L. J. Goossen, *Organic Letters,* **2017**, 19, 1232-1235.

http://dx.doi.org/10.1021/acs.orglett.7b00300

9.3.2 Reprint

Reprint Licence

Title:	Doubly Regioselective C–H Hydroarylation of Unsymmetrical Alkynes Using Carboxylates as Deciduous Directing Groups
Author:	Agostino Biafora, Bilal A. Khan, Janet Bahri, et al
Publication:	Organic Letters
Publisher:	American Chemical Society
Date:	Mar 1, 2017

Copyright © 2017, American Chemical Society

If you're a copyright.com user, you can login to RightsLink using your copyright.com credentials. Already **a RightsLink user** or want to learn more?

PERMISSION/LICENSE IS GRANTED FOR YOUR ORDER AT NO CHARGE

This type of permission/license, instead of the standard Terms & Conditions, is sent to you because no fee is being charged for your order. Please note the following:

- Permission is granted for your request in both print and electronic formats, and translations.
- If figures and/or tables were requested, they may be adapted or used in part.
- Please print this page for your records and send a copy of it to your publisher/graduate school.
- Appropriate credit for the requested material should be given as follows: "Reprinted (adapted) with permission from (COMPLETE REFERENCE CITATION). Copyright (YEAR) American Chemical Society." Insert appropriate information in place of the capitalized words.
- One-time permission is granted only for the use specified in your request. No additional uses are granted (such as derivative works or other editions). For any other uses, please submit a new request.

Organic LETTERS
Letter
pubs.acs.org/OrgLett

Doubly Regioselective C−H Hydroarylation of Unsymmetrical Alkynes Using Carboxylates as Deciduous Directing Groups

Agostino Biafora,[§] Bilal A. Khan,[*,‡] Janet Bahri,[†] Joachim M. Hewer,[§] and Lukas J. Goossen[*,†]

[†] Fakultät für Chemie und Biochemie, Ruhr-Universität Bochum, Universitätsstrasse 150, 44801 Bochum, Germany
[‡] Department of Chemistry, University of Azad Jammu and Kashmir, 13100 Muzaffarabad, AJK, Pakistan
[§] FB Chemie und Forschungszentrum OPTIMAS, Technische Universität Kaiserslautern, Erwin-Schroedinger-Strasse Geb 52-54, 67663 Kaiserslautern, Germany

Supporting Information

ABSTRACT: A catalyst system composed of $[(C_6Me_6)RuCl_2]_2$, potassium carbonate/guanidine carbonate, and mesitoic acid efficiently promotes the doubly regioselective C−H hydroarylation of unsymmetrical alkynes. The process involves carboxylate-directed *ortho*-C−H bond activation followed by regioselective addition to the alkyne C−C triple bond with concerted decarboxylation. This action of the carboxylate as a deciduous directing group ensures exclusive monovinylation with high selectivity for the (*E*)-1,2-diarylalkene.

Styrenes are prevalent structures often encountered in functional materials, pharmaceuticals, and natural and synthetic products.[1] Stoichiometric methods to access this structural motif, including Wittig[2] or Peterson olefinations[3] and insertions of alkynes into organometallic reagents,[4] are waste-intensive and require prefunctionalized substrates. Catalytic alternatives such as the Mizoroki−Heck reaction[5] and olefin metathesis[6] are more atom-economic but also require prefunctionalized arenes. C−H vinylations of the Fujiwara−Moritani type[7] have emerged as a powerful alternative but rely on stoichiometric oxidants.

C−H hydroarylations of alkynes compare favorably to the above concepts, especially when the regioselectivity is controlled effectively, e.g., by chelation assistance. Following early reports on ruthenium-catalyzed carbonyl-directed hydroarylations of alkynes,[8] several transition-metal catalysts, including precious[9−12] and first-row metals,[13,14] have been found to efficiently promote the insertion of alkynes into the C−H bond *ortho* to various directing groups. However, most of these directing groups, including phenol, ketone, pyridine, amide, and sulfoxide, require additional chemical steps for their synthesis, removal, or modification.

In this context, the use of carboxylates as directing groups is particularly desirable because they are easily accessible at low cost and in great structural diversity, can be transformed into a wealth of other compound classes, may serve as leaving groups in decarboxylative couplings, and are tracelessly removable by a subsequent protodecarboxylation step.[15,16] Over the years, extensive research has led to the discovery of carboxylate-directed substitutions of *ortho*-C−H atoms with (hetero)aryl, alkyl, acyl, allyl, alkoxy, olefin, amine, amide, and halogen groups.[17] The discovery that carboxylates can act as deciduous directing groups[18] that stay in place just long enough to direct one group into their *ortho*-position further improves the versatility of this group. A deciduous-type reaction pathway, in which the CO_2 is released concomitantly to C−C bond formation, intrinsically prevents unwanted double functionalization, a typical side reaction in *ortho*-C−H functionalizations (Scheme 1).[19]

Scheme 1. CO_2H as Deciduous vs Removable Directing Group (DG) in Catalytic Hydroarylations

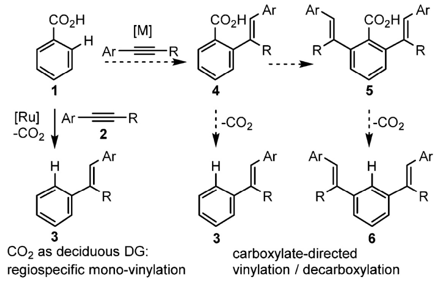

The development of carboxylate-directed regiospecific C−H hydroarylations is challenging because of the weak coordinating ability of the carboxylate group and the known reactivity of alkynes to undergo carboxylate addition to the enol esters in the presence of Ru^{II}[20] and because carboxylate groups reduce the electron density at the arene ring, thereby lowering its reactivity.

Received: January 30, 2017
Published: February 14, 2017

DOI: 10.1021/acs.orglett.7b00300
Org. Lett. 2017, 19, 1232−1235

The Ackermann group, the group of Hartwig and Zhao, and our own group have independently developed Ru-catalyzed carboxylate-directed C−H hydroarylations of internal alkynes.[19a−c] All of these processes allow the decarboxylative hydroarylation of diarylalkynes in high yields. However, examples with alkylarylalkynes as coupling partners were provided only by Hartwig and Zhao, and these reactions did not proceed via a deciduous-type pathway. Selectivity for the monovinylated, decarboxylated product was achieved by using a 2-fold excess of the arenecarboxylate and a powerful copper protodecarboxylation catalyst. Satisfactory yields and selectivities were obtained merely for a few substrates.[19c]

We herein report a catalyst system that requires only low Ru loadings and no copper mediator to promote the regioselective decarboxylative monovinylation using unsymmetrical alkynes. In the search for an efficient protocol for the desired transformation, we used the reaction of *p*-methoxybenzoic acid **1a** and 1-phenyl-1-propyne **2a** as a model (Table 1).

Table 1. Optimization of the Reaction Conditions[a]

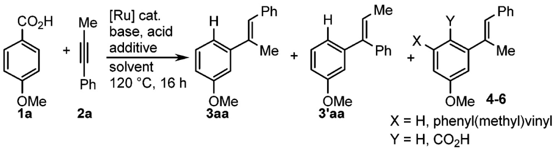

#	[Ru]	base (mol %)	acid	additive (mol %)	yield (%)		
					3aa	**3'aa**	**4-6**
1[b]	**[Ru1]**	-	-	Cu(OAc)$_2$ (20)	59	5	n.d.[19c]
2[b]	"	-	-	-	13	2	8
3[c]	**[Ru2]**	GuanCO$_3$ (20)	AcOH	2-picoline (20)	25	n.d.	21
4[c]	**[Ru3]**	"	"	"	38	"	20
5	"	"	"	"	53	3	23
6	"	"	"	-	53	3	29
8	"	K$_2$CO$_3$ (20)	"	-	31	16	8
9	"	Cs$_2$CO$_3$ (20)	"	-	23	9	8
10	"	K$_2$CO$_3$ (10)	"	-	39	3	5
11	"	GuanCO$_3$ (5) + K$_2$CO$_3$ (10)	"	-	60	9	13
12	"	"	TMBA	-	71	2	n.d.
13[d]	"	GuanCO$_3$ (10)	"	-	76	9	n.d.

[a] Method A: **1a** (0.5 mmol), **2a** (0.75 mmol), [Ru] (4 mol %), base, acid (1 equiv), additive, NMP (1 mL), 120 °C, 16 h. [b] Method A: **1a** (1 mmol), **2a** (0.5 mmol), [**Ru1**] (10 mol %) in dioxane/mesitylene/*n*-heptane (2:2:1), 80 °C, 48 h. [c] Method A: **2a** (0.5 mmol) in PhMe. [d] Method B: **1a** (1 mmol), **2a** (0.5 mmol), [Ru] (4 mol %), guanidine carbonate (10 mol %), TMBA (0.5 equiv), NMP (2 mL), 180 °C μW, 5 min. Yields were determined by GC analysis after esterification with MeI/K$_2$CO$_3$ using *n*-tetradecane as internal standard. [**Ru1**] = (*p*-cym)Ru(OAc)$_2$, [**Ru2**] = [(*p*-cym)RuCl$_2$]$_2$, [**Ru3**] = [(C$_6$Me$_6$)RuCl$_2$]$_2$. GuanCO$_3$ = guanidinium carbonate. TMBA = 2,4,6-trimethylbenzoic (mesitoic) acid.

When Hartwig and Zhao's conditions were used, i.e., treatment a 2-fold excess of **1a** with **2a** in the presence of [**Ru1**] and 20 mol % Cu(OAc)$_2$ in dioxane/mesitylene/*n*-heptane at 80 °C for 48 h,[19c] the desired styrene **3aa** was formed in 59% yield and a **3aa**/**3′aa** regioselectivity of 12:1 (Table 1, entry 1). Unsatisfactory results and formation of products **4**−**6** in notable amounts were observed without the copper mediator (entry 2). Our conditions previously optimized for diarylalkynes, namely **1a** (0.5 mmol), **2a** (1 equiv), [(*p*-cymene)RuCl$_2$]$_2$ (4 mol %, [**Ru2**]), guanidine carbonate (20 mol %), AcOH (1 equiv), and 2-picoline (20 mol %) in toluene, provided **3aa** in 25% yield along with 21% of **4aa**−**6aa**, which are products arising from a competing nondeciduous directing mode of the carboxylate group (entry 3). Screening of various catalysts, additives, and solvents showed that the combination of a [(C$_6$Me$_6$)RuCl$_2$]$_2$ ([**Ru3**]) catalyst and the polar aprotic solvent NMP gave greater conversion and good regioselectivity (entry 4 and Table S1). Increasing the amount of **2a** to 1.5 equiv further improved the yield (entry 5). Interestingly, 2-picoline, which was an important component of our original conditions, did not affect the outcome here (entry 6). Higher yields were obtained when the acetic medium was buffered with 5 mol % of guanidine carbonate and 10 mol % of potassium carbonate (entries 8−11). Substituting acetic by mesitoic acid shifted the reaction completely toward the desired pathway, so that products **4**−**6** arising from competing pathways were no longer detected. Within 16 h under optimal conditions, i.e., **1a** (0.5 mmol), **2a** (0.75 mmol), [(C$_6$Me$_6$)RuCl$_2$]$_2$ (4 mol %), guanidine carbonate (5 mol %), K$_2$CO$_3$ (10 mol %), and mesitoic acid (1 equiv) in NMP (1 mL) at 120 °C, the monovinylated product **3aa** was obtained exclusively and with an impressive **3aa**/**3′aa** regioselectivity of 36:1 in favor of the less sterically hindered alkyl-branched product (entry 12, method A). The regiochemical preference is in agreement with findings by Fagnou, Miura, Rovis, Li, Ackermann, Larock, and others on mechanistically related oxidative annulation reactions.[21]

When a preformed *o*-vinylbenzoic acid (**4ba**) was subjected to the reaction conditions, no decarboxylation was observed (see the Supporting Information), which confirms that C−C bond formation and decarboxylation indeed occur concertedly. Further control experiments established that both base and acid additive are required (Table S1).

The only drawback of this protocol was the long reaction time. However, this can be shortened to only 5 min by employing microwave irradiation (method B) after small adjustments to the catalyst system (10 mol % of guanidine carbonate as the only base and with the amount of mesitoic acid reduced to 0.5 equiv).[22]

With two effective sets of conditions in hand, the scope and selectivity of the ruthenium-catalyzed decarboxylative C−H hydroarylation of **2a** with substituted benzoic acids **1** were evaluated (Scheme 2). The scope extends from electron-rich to electron-poor benzoic acids with various functional groups in the *ortho*, *meta*, or *para* positions, as well as heterocyclic carboxylates. Benzoic acids bearing *ortho* substituents generally gave excellent yields (**3ba**−**ka**). *Para*-substituted benzoic acids afforded monofunctionalized products (**3aa**,**la**−**oa**) exclusively and in good yields. *p*-Toluic acid (**1m**) afforded 30% of non-decarboxylated product **4ma** along with **3ma**, which presumably result from a competing nondeciduous pathway. Extending the reaction time to 48 h did not shift the product distribution further toward **3ma** (see the SI). This clearly indicates that the decarboxylated product results from a concerted C−C bond formation/decarboxylation process, and that once the non-decarboxylated product is released, it does not re-enter the catalytic cycle. The reactivity of *meta*-substituted acids was lower (**3pa**,**qa**). Deactivating substituents such as nitro groups reduced the yields (**3wa**). With 2-allyl benzoate, the side-chain double bond isomerized into conjugation under the reaction conditions (**3da**). The efficiency of the microwave method was generally

DOI: 10.1021/acs.orglett.7b00300
Org. Lett. 2017, 19, 1232−1235

Scheme 2. Scope with Respect to the Benzoic Acids[a]

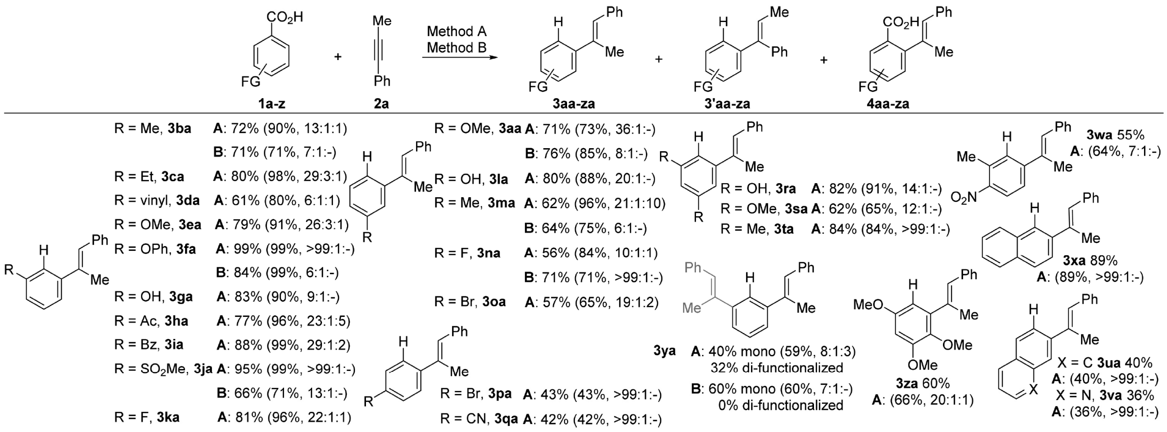

[a]Isolated yields. GC yields and product ratios of **3**:**3′**:**4**, in parentheses, after esterification using *n*-tetradecane as internal standard.

comparable, although the higher reaction temperature somewhat affected the regioselectivity. Only for unsubstituted benzoic acid (**1y**) was nondecarboxylative hydroarylation a major side reaction under thermal conditions, leading to the formation of substantial amounts of disubstituted products. However, under microwave conditions, the carboxylate acted as a deciduous directing group again, and only monovinylated product **3ya** was observed.

We next investigated the alkyne substrate scope in combination with *p*-anisic (**1a**), *p*-fluorobenzoic (**1n**), and *o*-toluic acid (**1b**) (Scheme 3). For alkylarylalkynes **2b**−**f**, high yields and excellent regioselectivities of the desired products were achieved. Electron-poor propiolates (**2b**) were successfully converted to *β*,*β*-diaryl acrylates, which are valuable synthons for further decarboxylative couplings.[18,23] Terminal alkynes did not react under the reaction conditions.

Scheme 3. Scope with Respect to the Alkynes[a]

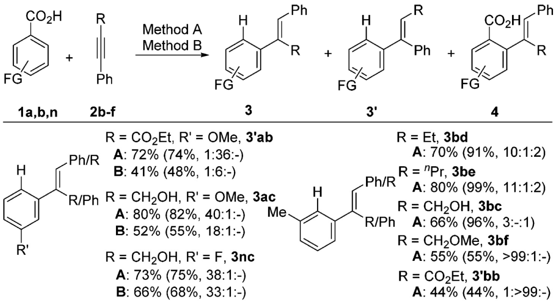

[a]Isolated yields. GC yields and product ratios of **3**:**3′**:**4**, in parentheses, after esterification using *n*-tetradecane as internal standard.

A plausible reaction pathway derived from mechanistic experiments (see the SI) is outlined in Scheme 4. Following C−H activation, the *ortho*-ruthenated complex **A** coordinates the alkyne substrate. Migratory insertion leads to the seven-membered ruthenacycle **B**. Possible next steps involve either decarboxylation to intermediate **C**, which is then protodemetalated to product **3aa**, or early protodemetalation of **B**, resulting in the nondecarboxylated compound **4aa**. Ruthenium is not capable by itself of decarboxylating **4aa** under these conditions. CO_2 extrusion can occur only in the presence of copper or silver decarboxylation catalysts, as previously reported.[16]

Scheme 4. Proposed Mechanism for the Ruthenium-Catalyzed Decarboxylative Hydroarylation

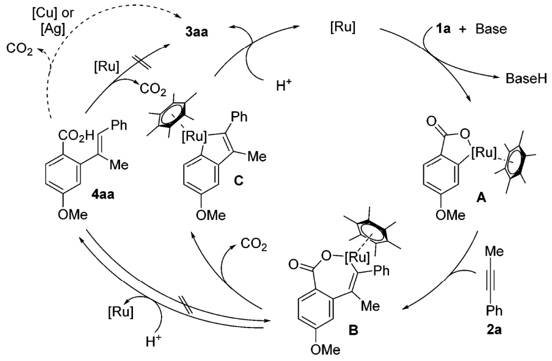

In conclusion, an effective and broadly applicable C−H hydroarylation of unsymmetrical alkynes has developed on the basis of the inexpensive and easy-to-handle catalyst $[(C_6Me_6)RuCl_2]_2$. The concerted C−C bond formation/CO_2 extrusion process ensures nearly exclusive formation of monovinylated products and obviates a subsequent protodecarboxylation step.

■ ASSOCIATED CONTENT

Ⓢ Supporting Information

The Supporting Information is available free of charge on the ACS Publications website at DOI: 10.1021/acs.orglett.7b00300.

Detailed screening tables, experimental procedures, analytical data for all the products, and NMR spectra (PDF)

■ AUTHOR INFORMATION

Corresponding Authors

*E-mail: bkhan@ajku.edu.pk.
*E-mail: lukas.goossen@rub.de.

ORCID

Lukas J. Goossen: 0000-0002-2547-3037

Notes

The authors declare no competing financial interest.

■ ACKNOWLEDGMENTS

We thank Umicore for donating chemicals, the DFG (SFB/TRR-88, "3MET") and XC/1069 "RESOLV" for financial support, and the AG Clusterchemie for providing technical equipment.

■ REFERENCES

(1) (a) Rosazza, J. P. N.; Huang, Z.; Dostal, L.; Volm, T.; Rousseau, B. *J. Ind. Microbiol.* **1995**, *15*, 457−471. (b) Ali, M. S.; Mahmud, S.; Perveen, S.; Ahmad, V. U.; Rizwani, G. H. *Phytochemistry* **1999**, *50*, 1385−1389. (c) Rukachaisirikul, V.; Rodglin, A.; Sukpondma, Y.; Phongpaichit, S.; Buatong, J.; Sakayaroj, J. *J. Nat. Prod.* **2012**, *75*, 853−858. (d) Hassam, M.; Taher, A.; Arnott, G. E.; Green, I. R.; van Otterlo, W. A. L. *Chem. Rev.* **2015**, *115*, 5462−5569. (e) Roseblade, S. J.; Pfaltz, A. *Acc. Chem. Res.* **2007**, *40*, 1402−1411.

(2) March, J. *Advanced Organic Chemistry: Reactions, Mechanisms, And Structure*, 4th ed.; Wiley: New York, 1992.

(3) Kürti, L.; Czakó, B. *Strategic Applications of Named Reactions in Organic Synthesis: Background and Detailed Mechanisms*; Elsevier Academic Press: Amsterdam, 2005.

(4) (a) Xu, X.; Chen, J.; Gao, W.; Wu, H.; Ding, J.; Su, W. *Tetrahedron* **2010**, *66*, 2433−2438. (b) Fagnou, K.; Lautens, M. *Chem. Rev.* **2003**, *103*, 169−196. (c) Shirakawa, E.; Yamagami, T.; Kimura, T.; Yamaguchi, S.; Hayashi, T. *J. Am. Chem. Soc.* **2005**, *127*, 17164−17165.

(5) Beletskaya, I. P.; Cheprakov, A. V. *Chem. Rev.* **2000**, *100*, 3009−3066.

(6) (a) Grubbs, R. H.; Chang, S. *Tetrahedron* **1998**, *54*, 4413−4450. (b) Fürstner, A. *Angew. Chem., Int. Ed.* **2000**, *39*, 3012−3043.

(7) (a) Moritani, I.; Fujiwara, Y. *Tetrahedron Lett.* **1967**, *8*, 1119−1122. (b) Yokota, T.; Tani, M.; Sakaguchi, S.; Ishii, Y. *J. Am. Chem. Soc.* **2003**, *125*, 1476−1477. (c) Nishikata, T.; Lipshutz, B. H. *Org. Lett.* **2010**, *12*, 1972−1975.

(8) (a) Kakiuchi, F.; Yamamoto, Y.; Chatani, N.; Murai, S. *Chem. Lett.* **1995**, *24*, 681−682. (b) Kakiuchi, F.; Sato, T.; Tsujimoto, T.; Yamauchi, M.; Chatani, N.; Murai, S. *Chem. Lett.* **1998**, *27*, 1053−1054. (c) Kakiuchi, F.; Uetsuhara, T.; Tanaka, Y.; Chatani, N.; Murai, S. *J. Mol. Catal. A: Chem.* **2002**, *182−183*, 511−514.

(9) (a) Arockiam, P. B.; Bruneau, C.; Dixneuf, P. H. *Chem. Rev.* **2012**, *112*, 5879−5918. (b) Hashimoto, Y.; Hirano, K.; Satoh, T.; Kakiuchi, F.; Miura, M. *Org. Lett.* **2012**, *14*, 2058−2061. (c) Manikandan, R.; Jeganmohan, M. *Org. Biomol. Chem.* **2015**, *13*, 10420−10436. (d) Hashimoto, Y.; Hirano, K.; Satoh, T.; Kakiuchi, F.; Miura, M. *J. Org. Chem.* **2013**, *78*, 638−646. (e) Cheng, K.; Yao, B.; Zhao, J.; Zhang, Y. *Org. Lett.* **2008**, *10*, 5309−5312. (f) Itoh, M.; Hashimoto, Y.; Hirano, K.; Satoh, T.; Miura, M. *J. Org. Chem.* **2013**, *78*, 8098−8104. (g) Manikandan, R.; Jeganmohan, M. *Org. Lett.* **2014**, *16*, 912−915.

(10) (a) Hong, P.; Cho, B.-R.; Yamazaki, H. *Chem. Lett.* **1979**, *8*, 339−342. (b) Hong, P.; Cho, B.-R.; Yamazaki, H. *Chem. Lett.* **1980**, *9*, 507−510. (c) Schipper, D. J.; Hutchinson, M.; Fagnou, K. *J. Am. Chem. Soc.* **2010**, *132*, 6910−6911. (d) Shibata, Y.; Otake, Y.; Hirano, M.; Tanaka, K. *Org. Lett.* **2009**, *11*, 689−692. (e) Katagiri, T.; Mukai, T.; Satoh, T.; Hirano, K.; Miura, M. *Chem. Lett.* **2009**, *38*, 118−119. (f) Parthasarathy, K.; Jeganmohan, M.; Cheng, C.-H. *Org. Lett.* **2008**, *10*, 325−328. (g) Colby, D. A.; Bergman, R. G.; Ellman, J. A. *J. Am. Chem. Soc.* **2008**, *130*, 3645−3651. (h) Patureau, F. W.; Besset, T.; Kuhl, N.; Glorius, F. *J. Am. Chem. Soc.* **2011**, *133*, 2154−2156.

(11) (a) Kuninobu, Y.; Kawata, A.; Takai, K. *J. Am. Chem. Soc.* **2005**, *127*, 13498−13499. (b) Kuninobu, Y.; Tokunaga, Y.; Kawata, A.; Takai, K. *J. Am. Chem. Soc.* **2006**, *128*, 202−209. (c) Tsuchikama, K.; Kasagawa, M.; Hashimoto, Y.-K.; Endo, K.; Shibata, T. *J. Organomet. Chem.* **2008**, *693*, 3939−3942.

(12) (a) Tsukada, N.; Mitsuboshi, T.; Setoguchi, H.; Inoue, Y. *J. Am. Chem. Soc.* **2003**, *125*, 12102−12103. (b) Liu, Z.; Derosa, J.; Engle, K. M. *J. Am. Chem. Soc.* **2016**, *138*, 13076−13081. (c) Shibuya, T.; Shibata, Y.; Noguchi, K.; Tanaka, K. *Angew. Chem., Int. Ed.* **2011**, *50*, 3963−3967.

(13) (a) Ilies, L.; Chen, Q.; Zeng, X.; Nakamura, E. *J. Am. Chem. Soc.* **2011**, *133*, 5221−5223. (b) Gao, K.; Lee, P.-S.; Fujita, T.; Yoshikai, N. *J. Am. Chem. Soc.* **2010**, *132*, 12249−12251. (c) Cera, G.; Ackermann, L. *Top. Curr. Chem. (Z)* **2016**, *374*, 57. (d) Wong, M. Y.; Yamakawa, T.; Yoshikai, N. *Org. Lett.* **2015**, *17*, 442−445.

(14) (a) Nakao, Y.; Idei, H.; Kanyiva, K. S.; Hiyama, T. *J. Am. Chem. Soc.* **2009**, *131*, 15996−15997. (b) Mukai, T.; Hirano, K.; Satoh, T.; Miura, M. *J. Org. Chem.* **2009**, *74*, 6410−6413. (c) Nakao, Y.; Kashihara, N.; Kanyiva, K. S.; Hiyama, T. *J. Am. Chem. Soc.* **2008**, *130*, 16170−16171. (d) Tsukada, N.; Murata, K.; Inoue, Y. *Tetrahedron Lett.* **2005**, *46*, 7515−7517. (e) Gooßen, L. J. *Angew. Chem., Int. Ed.* **2002**, *41*, 3775−3778.

(15) (a) Goossen, L. J. *Science* **2006**, *313*, 662−664. (b) Goossen, L. J.; Rodríguez, N.; Melzer, B.; Linder, C.; Deng, G.; Levy, L. M. *J. Am. Chem. Soc.* **2007**, *129*, 4824−4833. (c) Gooßen, L. J.; Rodríguez, N.; Gooßen, K. *Angew. Chem., Int. Ed.* **2008**, *47*, 3100−3120. (d) Rodríguez, N.; Goossen, L. J. *Chem. Soc. Rev.* **2011**, *40*, 5030. (e) *Inventing Reactions*; Goossen, L. J., Ed.; Topics in Organometallic Chemistry; Springer: New York, 2013.

(16) (a) Zhang, Y.; Zhao, H.; Zhang, M.; Su, W. *Angew. Chem., Int. Ed.* **2015**, *54*, 3817−3821. (b) Luo, J.; Preciado, S.; Larrosa, I. *J. Am. Chem. Soc.* **2014**, *136*, 4109−4112. (c) Cornella, J.; Righi, M.; Larrosa, I. *Angew. Chem., Int. Ed.* **2011**, *50*, 9429−9432. (d) Bhadra, S.; Dzik, W. I.; Gooßen, L. J. *Angew. Chem., Int. Ed.* **2013**, *52*, 2959−2962. (e) Qin, X.; Sun, D.; You, Q.; Cheng, Y.; Lan, J.; You, J. *Org. Lett.* **2015**, *17*, 1762−1765.

(17) (a) Pichette-Drapeau, M.; Gooßen, L. J. *Chem. - Eur. J.* **2016**, *22*, 18654−18677. (b) Shi, G.; Zhang, Y. *Adv. Synth. Catal.* **2014**, *356*, 1419−1442. (c) Biafora, A.; Krause, T.; Hackenberger, D.; Belitz, F.; Gooßen, L. J. *Angew. Chem., Int. Ed.* **2016**, *55*, 14752−14755. (d) Mei, R.; Zhu, C.; Ackermann, L. *Chem. Commun.* **2016**, *52*, 13171−13174. (e) Simonetti, M.; Cannas, D. M.; Panigrahi, A.; Kujawa, S.; Kryjewski, M.; Xie, P.; Larrosa, I. *Chem. - Eur. J.* **2017**, *23*, 549−553. (f) Huang, L.; Weix, D. J. *Org. Lett.* **2016**, *18*, 5432−5435.

(18) Tang, J.; Hackenberger, D.; Goossen, L. J. *Angew. Chem., Int. Ed.* **2016**, *55*, 11296−11299.

(19) (a) Huang, L.; Biafora, A.; Zhang, G.; Bragoni, V.; Gooßen, L. J. *Angew. Chem., Int. Ed.* **2016**, *55*, 6933−6937. (b) Kumar, N. Y. P.; Bechtoldt, A.; Raghuvanshi, K.; Ackermann, L. *Angew. Chem., Int. Ed.* **2016**, *55*, 6929−6932. (c) Zhang, J.; Shrestha, R.; Hartwig, J. F.; Zhao, P. *Nat. Chem.* **2016**, *8*, 1144−1151. (d) Simonetti, M.; Larrosa, I. *Nat. Chem.* **2016**, *8*, 1086−1088.

(20) (a) Goossen, L. J.; Paetzold, J.; Koley, D. *Chem. Commun.* **2003**, 706−707. (b) Bruneau, C.; Dixneuf, P. H. *Angew. Chem., Int. Ed.* **2006**, *45*, 2176−2203. (c) Miura, H.; Tsutsui, K.; Wada, K.; Shishido, T. *Chem. Commun.* **2015**, *51*, 1654−1657.

(21) (a) Guimond, N.; Gouliaras, C.; Fagnou, K. *J. Am. Chem. Soc.* **2010**, *132*, 6908−6909. (b) Hyster, T. K.; Rovis, T. *J. Am. Chem. Soc.* **2010**, *132*, 10565−10569. (c) Mochida, S.; Umeda, N.; Hirano, K.; Satoh, T.; Miura, M. *Chem. Lett.* **2010**, *39*, 744−746. (d) Ackermann, L.; Lygin, A. V.; Hofmann, N. *Angew. Chem.* **2011**, *123*, 6503−6506. (e) Li, B.; Feng, H.; Xu, S.; Wang, B. *Chem. - Eur. J.* **2011**, *17*, 12573−12577. (f) Larock, R. C.; Yum, E. K.; Refvik, M. D. *J. Org. Chem.* **1998**, *63*, 7652−7662.

(22) Goossen, L. J.; Manjolinho, F.; Khan, B. A.; Rodríguez, N. *J. Org. Chem.* **2009**, *74*, 2620−2623.

(23) Zhang, L.; Hang, Z.; Liu, Z.-Q. *Angew. Chem., Int. Ed.* **2016**, *55*, 236−239.

DOI: 10.1021/acs.orglett.7b00300
Org. Lett. 2017, 19, 1232−1235

List of Publications

1. *"Benzene activation and H/D isotope effects in reactions if mixed cobalt platinum clusters: The influence of charge and of composition"*
   L. Barzen, M. Tombers, C. Merkert**, J. Hewer** and G. Niedner-Schatteburg
   International Journal of Mass Spectrometry, **2012**, *330-332*, 271-276.
   http://dx.doi.org/10.1016/j.ijms.2012.09.008

2. *"Infrared spectroscopy of N_2 adsorption on size selected cobalt cluster cations in isolation"*
   S. Dillinger, J. Mohrbach, M. Gaffga, **J. Hewer**, and G. Niedner-Schatteburg
   Physical Chemistry Chamical Physics, 2015 17, 10358
   http://dx.doi.org/10.1039/C5CP00047E

3. *"Vibrational Blue Shift of coordinated N_2 in $[Fe_3O(OAc)_6(N_2)_n]^+$: "Non Classical" Dinitrogen Complexes"*
   J. Lang, J. Mohrbach, S. Dillinger, **J. M. Hewer** and G. Niedner-Schatteburg
   Chemical Communications, **2017**, 53, 420-423.
   http://dx.doi.org/10.1039/C6CC07481B

4. *"Doubly Regioselective C-H Hydroarylation of Unsymmetrical Alkynes Using Carboxylates as Deciduous Directing Groups"*
   A. Biafora, B.A. Khan, J. Bari, **J.M. Hewer** and L.J. Goossen
   Organic Letters, **2017**, 19, 1232-1235
   http://dx.doi.org/10.1021/acs.orglett.7b00300

Contribution to Conferences: Oral Presentations

2014

Joachim Hewer, Maximilian Gaffga, Yevgeniy Nosenko, Gereon Niedner-Schatteburg "Two color enhanced IRMPD spectroscopy of a mononuclear Ag(I)-Bispyridine-complex", Frühjahrstagung der Deutschen Physikalischen Gesellschaft, Berlin, 17.-21.03.2014.

2016

Joachim Hewer, Matthias Tombers, Johannes Lang, Gereon Niedner-Schatteburg, Tobias Lau, "X-ray Magnetic Circular Dichroism Spectroscopy on Heterometallic Complexes in Isolation", Frühjahrstagung der Deutschen Physikalischen Gesellschaft, Hannover, 29.02.-04.03.2016.

Joachim Hewer, "X-ray magnetic circular dichroism (XMCD) spectroscopy of single molecule magnets and 3d-4f mixed bimetallic complexes in isolation", Zernike Seminar, Rijksuniversiteit Groningen, Groningen, NL, 17.10.2016 (eingeladener Vortrag).

Contribution to Conferences: Poster Presentations

2015

Joachim Hewer, Gereon Niedner-Schatteburg "Two color enhanced IRMPD spectroscopy of mono- an dinuclear silver complexes" Frühjahrstagung der Deutschen Physikalischen Gesellschaft, Heidelberg, 23-27.03.2015.

Joachim Hewer, Gereon Niedner-Schatteburg "Two color enhanced IRMPD spectroscopy of mono- an dinuclear silver complexes" 114. Bunsentagung für Physikalische Chemie, Bochum, 14.-16.05.2015.

Joachim Hewer, Matthias Tombers, Johannes Lang, Gereon Niedner-Schatteburg, Christine Bülow, Tobias Lau "Investigations on isolated Singe Molecule Magnets by X-ray Magnetic Circular Dichroism spectroscopy" Seventh Joint BER II and BESSY II User Meeting, Berlin, 9.-11.12.2015.

2016

Joachim Hewer, Matthias Tombers, Johannes Lang, Marc Prosenc, Gereon Niedner-Schatteburg, Peter Roesky, Christine Bülow, Tobias Lau "X-ray Magnetic Circular Dichroism of Heteronuclear Complexes in Isolation" GRS: Molecular and Ionic Clusters, Ventura, CA, USA, 16.-17.01.2016.

Joachim Hewer, Matthias Tombers, Johannes Lang, Marc Prosenc, Gereon Niedner-Schatteburg, Peter Roesky, Christine Bülow, Tobias Lau "X-ray Magnetic Circular Dichroism of Heteronuclear Complexes in Isolation" GRC: Molecular and Ionic Clusters, Ventura, CA, USA, 16.-17.01.2016.

Joachim Hewer, Matthias Tombers, Johannes Lang, Marc H. Prosenc, Gereon. Niedner-Schatteburg, Peter Roesky, Christine Bülow, T. Lau, "X-ray Magnetic Circular Dichroism of Heteronuclear Complexes in Isolation", International Symposium on Small Particles and Inorganic Clusters XVIII, Jyväskylä, Finnland, 14.08.2016 - 19.08.2016.

Joachim Hewer, Matthias Tombers, Johannes Lang, Sebastian Dillinger, Gereon Niedner-Schatteburg, Peter W. Roesky, Christine Bülow, Tobias Lau, „X-ray Magnetic Circular Dichroism, of Heteronuclear Complexes in Isolation", 3rd International Conference on Bimetallic Complexes, Kaiserslautern, 05.-07.10.2016.

Danksagung

Ich danke Prof. Gereon Niedner-Schatteburg für die Betreuung der Doktorarbeit, die gute Zusammenarbeit und für die stetige Diskussionsbereitschaft. Ebenso möchte ich mich für die Ratschläge jenseits des Fachlichen bedanken.

Ich möchte mich bei Herrn Prof. Gerhards für die Übernahme des Zweitgutachtens und bei Herrn Prof. Ernst für die Übernahme des Prüfungsvorsitzes der Promotionskomission bedanken.

Danke an die vorherige Generation an Doktoranden des AK GNS: Fabian Menges, Lars Barzen, Christine Merkert und Jennifer Meyer für die freundliche Aufnahme in den Arbeitskreis und die Geduld beim Anlernen.

Ich bedanke mich bei Maximilian Gaffga für die äußerst angenehme Zusammenarbeit, die Einarbeitung in die IR-Laser, die Hilfsbereitschaft bei allerlei Problemen und die Gute Laune!

Ich danke Matthias Tombers für die Einführung in die Arbeit mit Synchrotronstrahlung, die Hilfsbereitschaft, Aufmunterungen und Ratschläge hinsichtlich der XMCD-Projekte.

Ich danke meinen Leidensgenossen Sebastian Dillinger, Dimitri Imanbaew, Johannes Lang und Jennifer Mohrbach für die tolle Zeit an der Uni und privat, die gegenseitige Unterstützung, für den Zusammenhalt und natürlich für die Freundschaft.

Ich bedanke mich bei Matthias Klein, Michael Lembach, Björn Kwasigroch und Annika Steiner für ihr Engagement und der Sicherung der Zukunft des AK GNS.

Ich danke Yevgeniy Nosenko und Thomas Kolling für jegliche Unterstützung und die Hilfsbereitschaft bei jeglichen Problemen.

Christoph Riehn danke ich für die gute Zusammenarbeit, die stete Diskussionsbereitschaft und Ratschläge jeglicher Art.

Ich bedanke mich bei Tobias Lau für die Möglichkeit, Messungen an der NanoCluster Trap durchzuführen und für die Diskussionen und hilfreichen Ratschläge. Vicente Zamudio-Bayer, Rebecka Lindblad, Christine Bülow, Georg Leistner und Martin Timm danke ich für die Unterstützung während den Strahlzeiten bei BESSY.

Bei Thomas Schlathölter möchte ich mich für die großzügige Bereitstellung der ESI-Quelle für die Messungen an der NanoCluster Trap bedanken.

Ich möchte mich bei allen aktuellen und ehemaligen Mitarbeitern der physikalischen und theoretischen Chemie (inkl. Agostino Biafora und Alexander Jones) für die gute Zusammenarbeit und/oder die gute Arbeitsatmosphäre bedanken.

Vielen Dank an unsere Sekretärinnen Hilde Seelos, Sybille Heieck, Petra Wetzel und Birgit Harrison-Weber für die Hilfe in den letzten Jahren.

Ich danke all meinen Freunden für ihre Unterstützung, ihr offenes Ohr und die Ablenkung vom Promotionsstress.

Ein besonderer Dank gilt Anne für ihre Unterstützung in den letzten Jahren, ihr Verständnis für die zeitintensive Arbeit und die Ablenkung vom Uni-Stress.

Ich danke meiner Familie, insbesondere meinen Eltern Cäcilia und Helmut, für die Ermöglichung des Chemiestudiums, die stetige Unterstützung, den immerwährenden Rückhalt und die Geduld.

Eidesstattliche Erklärung

Hiermit bestätige ich, Joachim Hewer, dass die vorliegende Arbeit mit dem Titel „*Magnetic and Structural Characterization of Isolated Gasous Ions by XMCD and IRMPD Spectroscopy*“ gemäß der Promotionsordnung des Fachbereichs Chemie der Technischen Universität Kaiserslautern selbstständig und mit keinen anderen als den hier angegebenen Quellen und Hilfsmitteln erstellt wurde.

Kaiserslautern, im Juni 2017 Joachim Hewer